Merete Tangstad, Harry Rong, Aasgeir Valderhaug, Birger Andresen, Halvor Dalaker and Ingrid Gamst Page (Ed.)

Silicon for the chemical and solar industry XVIII

Kristiansand, Norway, 7-10 September 2026

Photo: Casper van der Eijk / SINTEF

FAGBOKFORLAGET

First published 2026 by Vigmostad & Bjørke AS.

© 2026 copyright of the selection and editorial matter, Merete Tangstad, Harry Morten Rong, Aasgeir Valderhaug, Birger Andresen, Halvor Dalaker, Ingrid Gamst Page
© 2026 copyright of the individual chapters is held by the respective authors.

This work, available from https://oa.fagbokforlaget.no, is licensed under the Creative Commons Attribution 4.0 International (CC BY 4.0) license.

This license grants permission to copy and redistribute the material in any medium or format, and to remix, transform, and build upon the material for any purpose, even commercially. The exercise of these freedoms is granted on the following terms: You must give appropriate credit, provide a link to the license, and indicate if changes were made. You may do so in any reasonable manner, but not in any way that suggests the licensor endorses you or your use. You may not apply legal terms or technological measures that legally restrict others from doing anything the license permits.

The license text in full is available at https://creativecommons.org/licenses/by/4.0/

The license may not give you all the permissions necessary for your intended use. For example, other rights such as publicity, privacy, or moral rights may limit how you use the material.

ISBN digital edition: 978-82-450-6423-0
DOI: https://doi.org/10.55669/oa9008

Enquiries about this book can be directed to:
fagbokforlaget@fagbokforlaget.no
www.fagbokforlaget.no

Cover design by Vigmostad & Bjørke AS
Coverphoto: Temperature measurements through the tap hole during a pilot scale experiment
Photographer: Casper Van der Eijk

Monsen, I., V. K. Risinggård, and S. A. Halvorsen. 2026. Characterization of Electrode Currents: A Basis for Current Control without Electrode Interaction. In *Silicon for the Chemical and Solar Industry XVIII*, edited by M. Tangstad, H. Rong, A. Valderhaug, B. Andresen, H. Dalaker, and I. G. Page. Kristiansand, Norway, September 7–10, 2026. https://doi.org/10.55669/oa900801

Characterization of electrode currents A basis for current control without electrode interaction

I. Monsen[1], V.K. Risinggård[1], and S.A. Halvorsen[1]
[1]NORCE Research AS, Norway, idam@norceresearch.no

Keywords: symmetrical components, electrode currents, furnace control

Abstract – The power distribution in submerged arc furnaces is controlled either with current or with resistance control. Current control only requires current measurements and is widely used for small furnaces. For larger furnaces, the current interaction effect is large. Alternatively, furnaces can run on resistance control, which requires unreliable voltage measurements.

We propose a novel way of characterizing transformer and electrode currents that gives information about circulating current and imbalance, and outline how this characterization can be used to design current control that can neutralize the interaction effect. Our method is based on high-frequency measurements, enabling us to compute both phase and magnitude of each transformer current. The currents can then be decomposed into a circulating current that will not enter the furnace, a balanced three-phase current, which is the desired current, and an unbalanced single-phase current, which we want to minimize. This decomposition into effective balanced current and unbalanced current can be used to propose synchronized electrode movements. To correct for the imbalance, one electrode must be moved down and the other two moved up, or vice versa. Provided correctly calibrated movements, the interaction effect will be reduced or neutralized. To correct for a too high or too low total current, all electrodes are moved up or down simultaneously. This paper details the theoretical foundations. Further investigation and testing are required to develop a robust control strategy.

1. INTRODUCTION

Electrical control of submerged arc furnaces has two objectives, to maintain a stable and high power and to maintain a suitable power distribution around each electrode. The total power is normally controlled by adjusting the transformer tap positions and the power distribution is normally controlled by individually adjusting the vertical position of each electrode (Stewart, 1980), where raising an electrode increases the resistance and lowering it decreases the resistance. This is implemented either as current control, where an electrode is moved to maintain a given current, or resistance control, where the electrode is moved to maintain a given electrode resistance (Valderhaug, 1992).

Both current and resistance control have their own set of advantages and challenges. For resistance control, both voltage and current measurements are needed to find the electrode resistances. This is a weakness, since measuring electrode voltage is complicated and uncertain (Reuter *et al.*, 1995). However, if the resistances are known they can each easily be adjusted independently by moving a single electrode. Current control only requires electrode current measurements, which are more accurate, and having direct control over the current is useful for making sure we stay inside the operational constraints (Valderhaug, 1992). But this method poses its own challenges. Moving one electrode changes the current distribution inside the furnace, thus affecting the current of all three electrodes (Barker *et al.*, 1991). This is called the interaction effect and is most prevalent in larger furnaces with low power factors (Barker *et al.*, 1991). This means that current control on large furnaces can create the need for new

This work is licensed under the Creative Commons Attribution 4.0 International License. To view a copy of this license, visit https://creativecommons.org/licenses/by/4.0/

adjustments, which in turn creates the need for even new adjustments, and so on. Therefore, a current control algorithm should ideally take the interaction effect into account and make coordinated electrode movements. For example, a decoupling strategy where all three electrodes are moved synchronously so that they only change one current for current control has been suggested (Valderhaug, 1992).

In this paper, we propose a basis for an alternative method for current control that counteracts the interaction effect. Instead of measuring only current magnitudes, we propose using high-frequency current measurements to obtain information about both the magnitude and phase of the currents. This is used to decompose the transformer currents into a net balanced positive rotation current, with equal magnitude and 120° phase shifts, a circulating current, and a single-phase current imbalance. We can then adjust for current imbalance and total delivered current separately by using synchronous electrode movements instead of individual adjustments. The method does require non-standard measurements, but the added phase information can be useful for more than a control algorithm, since it, for example, gives information about circulating current and a direct way of quantifying imbalance in the furnace (Monsen, 2025). We first explain the theory of symmetrical components and the needed measurements, before presenting the current decomposition that the control scheme is based on. Then we outline the suggested control strategy and discuss its possible advantages and challenges.

2. THEORY

2.1 Simplified furnace model

We will be working on a simplified, linear circuit model of the furnace, where the secondary side transformers are modelled as voltage sources connected in a delta-star to impedance elements representing the electrodes (Barker and Stewart, 1980). We assume that there is no mutual inductance between the elements and no current paths inside the furnace other than those going down through the electrodes and connecting to the charge material. In particular, this means that we disregard arcing, mutual inductance between the electrodes, and complicated current paths. The simplified circuit model is shown in Figure 1, where the transformers are labelled A, B, and C and the electrodes are labelled 1, 2, and 3. The simplified model is suitable for analysing current distribution between the electrodes, but more advanced models are needed for other studies.

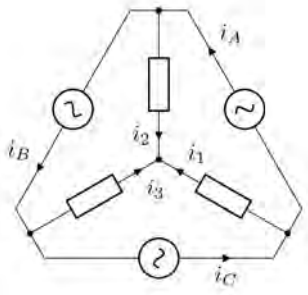

Figure 1: Simplified equivalent circuit for a submerged arc furnace.

Normally in furnaces, only current and voltage magnitudes are measured and presented. However, both magnitudes and phase angles are needed to fully specify systems with alternating currents like this one. This can be done with phasors, complex numbers that contain information about both phase and magnitude. The phasor $A\exp(\theta j)$, where j is the

imaginary unit, has magnitude A and phase θ. Going forward, we will assume currents and voltages are given as phasors unless otherwise specified.

Assuming the simplified equivalent circuit in Figure 1, it is possible to calculate electrode currents from transformer currents, but we cannot calculate transformer currents from electrode currents. Similarly, it is possible to calculate transformer voltages from electrode voltages, but not the other way around. In general, we say that the model has three degrees of freedom for both current and voltage. This means that if we know the value of three independent currents, we can determine all currents, and similarly for voltages.

2.2 Symmetrical components

Instead of specifying the three transformer currents directly as three current phasors, we will use a combination of three different basis vectors. This method is known as symmetrical components (Anderson, 1995). The first basis vector is $[1, \alpha^2, \alpha]^T$, where $\alpha = \exp(2\pi j/3)$ and j is the imaginary unit. This vector contains three phasors with magnitude 1 and phase angles $0°$, $240°$, and $120°$, in that order. It has a positive rotation, which for the circuit in Figure 1 means that the current reaches its peak value in the transformers A, B, and C, in that order. The vector $[1, \alpha^2, \alpha]^T$ is therefore called the positive sequence. The second basis vector is $[1, \alpha, \alpha^2]^T$, which has opposite rotation of $0°$, $120°$, and $240°$ and is called the negative sequence. This current will reach its peak value in the transformers in the order A, C, and B. The third basis vector is called the zero sequence and has three equal phasors with magnitude 1 and phase angle $0°$, namely $[1,1,1]^T$. In linear systems like this one, decomposing the currents into symmetrical components has the benefit that calculations can be done on the different sequences separately and added together in the end, which can simplify calculations.

Let $[i_A, i_B, i_C]^T$ be the three transformer current phasors. Symmetrical decomposition consists of determining how much of each of the three basis vector currents are present, that is, we need to find the three complex numbers $[i_0, i_+, i_-]^T$ such that the transformer currents can be written as a linear combination of the basis vectors. Then, we can write the currents as

$$\begin{bmatrix} i_A \\ i_B \\ i_C \end{bmatrix} = \begin{bmatrix} 1 & 1 & 1 \\ 1 & \alpha^2 & \alpha \\ 1 & \alpha & \alpha^2 \end{bmatrix} \begin{bmatrix} i_0 \\ i_+ \\ i_- \end{bmatrix}. \quad [1]$$

Any three-phase current system can be similarly decomposed using symmetrical components (Anderson, 1995).

The phasor i_+ specifies the magnitude and phase angle for a balanced three-phase current. Ideally, this should be the only component. The phasor i_- specifies the magnitude and phase angle of a balanced three-phase current with negative rotation, which will introduce current imbalance. The phasor i_0 specifies the amount and phase angle for a common component. The decomposition is illustrated in Figure 2, where we can see the positive sequence, the negative sequence, the zero sequence, and how they add up.

For the furnace circuit in Figure 1, the different sequences have different physical interpretations. Both for the transformers and electrodes, the positive sequence is the current we want, a perfectly balanced three-phase current with positive rotation. The negative sequence introduces imbalance. It is a three-phase current with negative rotation, which added to the positive sequence gives an unbalanced current. The larger the negative sequence is relative to the positive sequence, the greater the imbalance. The zero sequence is mathematically defined as one third of the sum of the phasors. For the transformers, this means that the zero sequence coincides with the definition of circulating current (Monsen, 2025). In other words, the zero sequence is a measure of circulating current in the transformer

delta. The current must sum to zero in the star connection between the electrodes due to charge conservation, which means that the zero sequence component will always be zero for the electrode currents.

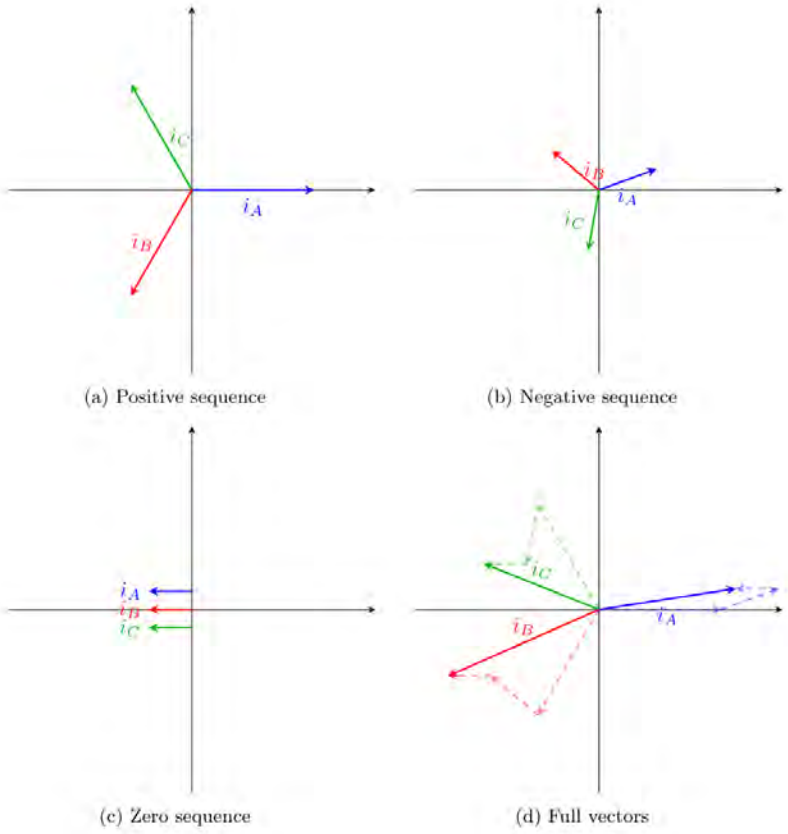

Figure 2: Decomposition of the three current phasors i_A, i_B, and i_C by symmetrical components. The different graphs show the positive sequence, the negative sequence, the zero sequence, and lastly how they add up to the full vectors.

2.3 Electrode currents

When the transformer currents are known, the electrode currents are given by

$$\begin{aligned} i_1 &= i_C - i_A, \\ i_2 &= i_A - i_B, \\ i_3 &= i_B - i_C. \end{aligned} \qquad [2]$$

The electrode currents can also be written as a linear combination of the symmetrical components of the transformer currents, as

$$\begin{bmatrix} i_1 \\ i_2 \\ i_3 \end{bmatrix} = \begin{bmatrix} -1 & 0 & 1 \\ 1 & -1 & 0 \\ 0 & 1 & -1 \end{bmatrix} \begin{bmatrix} i_A \\ i_B \\ i_C \end{bmatrix} = \begin{bmatrix} \alpha - 1 \\ 1 - \alpha^2 \\ \alpha^2 - \alpha \end{bmatrix} i_+ + \begin{bmatrix} \alpha^2 - 1 \\ 1 - \alpha \\ \alpha - \alpha^2 \end{bmatrix} i_-. \qquad [3]$$

The vector $[\alpha - 1, 1 - \alpha^2, \alpha^2 - \alpha]^T$ represents a balanced set of three current phasors, with magnitude $\sqrt{3}$ and phase angles 150°, 30°, and 270°, respectively, that is a positive rotation. Similarly, the vector $[\alpha^2 - 1, 1 - \alpha, \alpha - \alpha^2]^T$ is a set of currents with magnitude $\sqrt{3}$ and the negative rotation 210°, 330°, and 90°. This is in accordance with theory for a balanced delta-star system, where the currents entering the star connection will be $\sqrt{3}$ times larger than those in the delta connection and with a phase angle shift of 30°.

2.4 Measurement equipment

To have access to phase information, we need equipment that can measure and log currents with sufficiently high frequency to resolve the sinusoidal current waveform, not just RMS values, and from that extract the phase and amplitude of the signal. The sampling frequency must therefore be many times higher than the current frequency. As explained previously, it is possible to calculate electrode currents if we know the transformer currents. Thus, either measuring the transformer currents or the electrode currents will work.

Measurements of secondary side transformer currents are not standard in submerged arc furnaces but can for example be done with Rogowski coils (Monsen, 2025). Alternatively, one can make high-frequency measurements of the electrode currents, but this will not give access to information about the circulating current in the transformer delta. Measuring electrode current is a standard process (Sævarsdóttir, 2013), the difference being that one will need to log high-frequency measurements. More work is needed to identify typical errors for the high-frequency measurements and how to best mitigate them, regardless of which method is used. For example, care must be taken to synchronize the three measurements to obtain the correct phases.

Given high-frequency measurements, a Fourier transform can be used to estimate the phases and amplitude of the signal frequencies (Monsen, 2025). The simplified circuit in Figure 1 will have a perfect sinusoidal signal and thus only one frequency, but higher harmonics of the fundamental frequency can be present in a real furnace (Reuter *et al*., 1995; Stewart, 1980). This needs to be taken into account when designing the full control algorithm, but will not be further considered here.

3. RESULTS AND DISCUSSION

We first present the mathematical results, detailing the calculations that need to be done on the high-frequency current measurements. Then we explain its potential application, by describing how it can be used to design a practical control scheme.

3.1 Decomposition of transformer currents

Let $[i_A, i_B, i_C]^{\mathrm{T}}$ be the secondary side transformer currents in a furnace, and choose the global phase such that $i_+/M = 1$ and $i_-/M = r\exp(j\beta)$, where M and r are real numbers. In other words, i_+ has phase angle 0 and i_- has phase angle β. The currents can then be decomposed with symmetrical components as

$$\begin{bmatrix} i_A \\ i_B \\ i_C \end{bmatrix} = \begin{bmatrix} 1 \\ 1 \\ 1 \end{bmatrix} i_0 + \begin{bmatrix} 1 \\ \alpha^2 \\ \alpha \end{bmatrix} i_+ + \begin{bmatrix} 1 \\ \alpha \\ \alpha^2 \end{bmatrix} i_-. \qquad [4]$$

From this, we add and subtract a vector with the same phase as i_+ and the same magnitude as i_-, that is $[1, \alpha^2, \alpha]^T rM$. We then get

$$\begin{bmatrix} i_A \\ i_B \\ i_C \end{bmatrix} = \begin{bmatrix} 1 \\ 1 \\ 1 \end{bmatrix} i_0 + \begin{bmatrix} 1 \\ \alpha^2 \\ \alpha \end{bmatrix} i_+ + \begin{bmatrix} 1 \\ \alpha \\ \alpha^2 \end{bmatrix} i_- = \begin{bmatrix} 1 \\ 1 \\ 1 \end{bmatrix} i_0 + \begin{bmatrix} 1 \\ \alpha^2 \\ \alpha \end{bmatrix} (i_+ - rM) + \begin{bmatrix} 1 \\ \alpha^2 \\ \alpha \end{bmatrix} rM + \begin{bmatrix} 1 \\ \alpha \\ \alpha^2 \end{bmatrix} i_-. \qquad [5]$$

The first term is the zero sequence, which can be interpreted as the circulating current in the transformer delta (Monsen, 2025). The second term, with amplitude $i_+ - rM = M(1-r)$ is the net transformer currents having the desired behaviour, namely a balanced three-phase current in positive rotation. We will call this the net positive sequence. The last two terms constitute the unbalanced part. Denoting the unbalanced components of the transformer currents as $[i'_{\mathrm{A}}, i'_B, i'_{\mathrm{C}}]$, the unbalanced components can be written out as

$$
\begin{aligned}
i'_{\mathrm{A}} &= rM + i_{-} = rM\big(1 + \exp(j\beta)\big) = 2rM\cos\left(\frac{\beta}{2}\right)\exp\left(\frac{j\beta}{2}\right), \\
i'_{\mathrm{B}} &= \alpha^2 rM + \alpha i_{-} = \alpha rM\big(\alpha + \exp(j\beta)\big) = 2rM\cos\left(\frac{\pi}{3} - \frac{\beta}{2}\right)\exp\left(j\left(\pi + \frac{\beta}{2}\right)\right), \\
i'_{\mathrm{C}} &= \alpha rM + \alpha^2 i_{-} = \alpha^2 rM\left(\frac{1}{\alpha} + \exp(j\beta)\right) = 2rM\cos\left(\frac{\pi}{3} + \frac{\beta}{2}\right)\exp\left(j\left(\pi + \frac{\beta}{2}\right)\right),
\end{aligned}
\qquad [6]
$$

where $2\cos\phi = \exp(j\phi) + \exp(-j\phi)$. The arguments, or angles, of the unbalanced components are then

$$
\begin{aligned}
\arg(i'_{\mathrm{A}}) &= \frac{\beta}{2}, \\
\arg(i'_{\mathrm{B}}) &= \pi + \frac{\beta}{2}, \\
\arg(i'_{\mathrm{C}}) &= \pi + \frac{\beta}{2}.
\end{aligned}
\qquad [7]
$$

This means that the unbalanced part of the current has the same phase for all three transformers, just with different signs. The decomposition is shown visually in Figure 3, where we see how the net positive sequence, the single-phase imbalance sequence, and the zero sequence add up to the full vectors. Note the main difference to the symmetrical decomposition shown in Figure 2, that we have a single-phase unbalance instead of a negative rotation sequence.

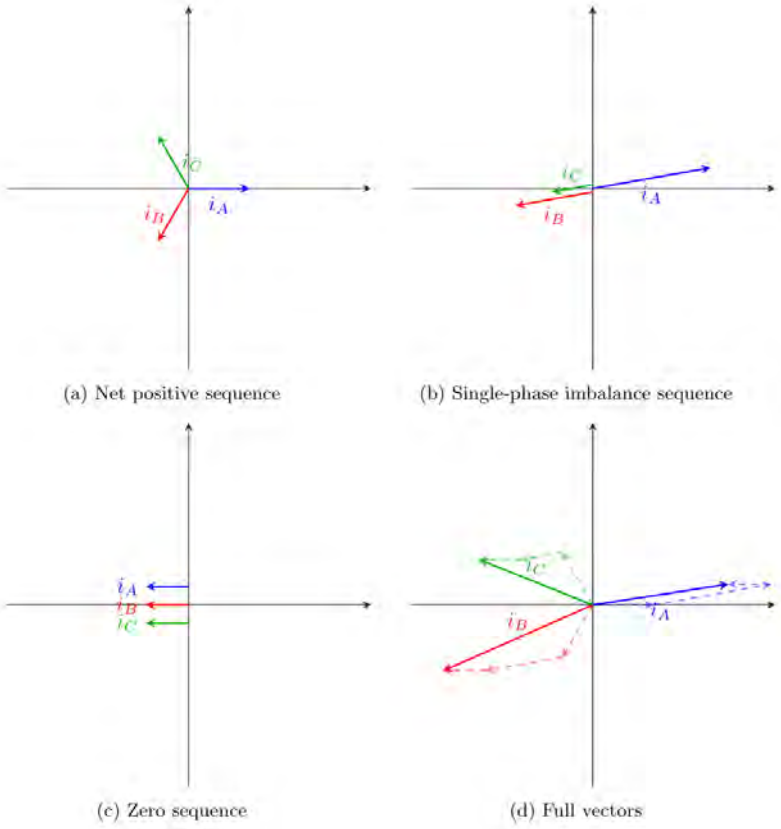

Figure 3: Decomposition of the three current phasors i_A, i_B, and i_C into a net positive rotation, a single-phase unbalance and the zero sequence. The bottom right graph shows how they sum to the full vectors.

3.2 Implications for electrode currents

We take advantage of the fact that we have a linear system and look at each part of the decomposed transformer currents separately. For a balanced delta-star system, the currents entering the star connection will be $\sqrt{3}$ times larger than those in the delta connection and with a phase angle shift of 30°, as previously explained. This applies to the net positive sequence. The circulating current, i.e. the zero sequence component of the transformer current, does not enter the electrodes, and the electrode current will have no zero sequence component.

Looking at the single-phase unbalanced transformer currents, we find that the unbalanced electrode currents are

$$\begin{aligned} i_1' &= i_C' - i_A' = 2rM\left(-\cos\left(\frac{\pi}{3}+\frac{\beta}{2}\right)-\cos\left(\frac{\beta}{2}\right)\right)\exp\left(\frac{j\beta}{2}\right), \\ i_2' &= i_A' - i_B' = 2rM\left(\cos\left(\frac{\beta}{2}\right)+\cos\left(\frac{\pi}{3}-\frac{\beta}{2}\right)\right)\exp\left(\frac{j\beta}{2}\right), \\ i_3' &= i_B' - i_C' = 2rM\left(\cos\left(\frac{\pi}{3}+\frac{\beta}{2}\right)-\cos\left(\frac{\pi}{3}-\frac{\beta}{2}\right)\right)\exp\left(\frac{j\beta}{2}\right). \end{aligned} \quad [8]$$

The unbalanced currents can all be written on the form

$$i_n' = 2rM \cdot x_n \cdot \exp\left(\frac{j\beta}{2}\right), \quad [9]$$

where $n = 1,2,3$ and

$$\begin{aligned} x_1 &= -\cos\left(\frac{\pi}{3}+\frac{\beta}{2}\right)-\cos\left(\frac{\beta}{2}\right), \\ x_2 &= \cos\left(\frac{\beta}{2}\right)+\cos\left(\frac{\pi}{3}-\frac{\beta}{2}\right), \\ x_3 &= \cos\left(\frac{\pi}{3}+\frac{\beta}{2}\right)-\cos\left(\frac{\pi}{3}-\frac{\beta}{2}\right). \end{aligned} \quad [10]$$

The absolute values of x_1, x_2, and x_3 determine the distribution of the unbalanced current between the three electrodes. The larger the absolute value of x_n, the more unbalanced current passes through electrode n. x_1, x_2, and x_3 always adds up to zero, but their individual values vary as a function of β, where $\beta/2$ is the phase angle of the unbalanced current. The behaviour of x_1, x_2, and x_3 is plotted in Figure 4.

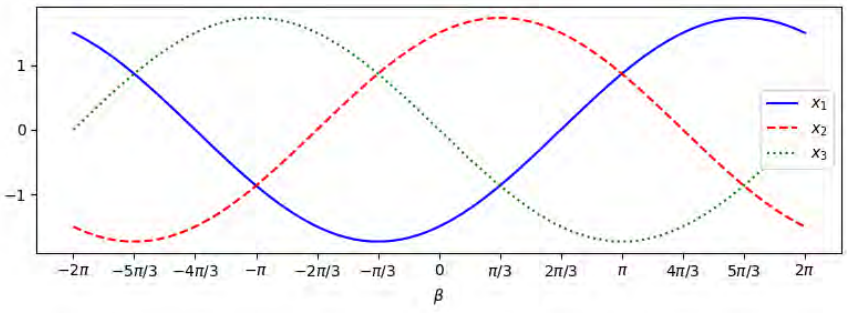

Figure 4: x_1, x_2, and x_3, representing the distribution of the single-phase unbalanced electrode currents, as functions of beta.

3.3 Control scheme outline

We can use the mathematical results from the previous section to outline a practical control scheme. Suppose we have measurement equipment that can measure the high-frequency secondary side transformer currents and extract phases and amplitudes. We can then give information on circulating current, the desired current entering the furnace, the unbalanced current, and how it is distributed between the electrodes.

Specifically, suppose we have a program that uses these measurements to calculate the unbalanced electrode currents as explained in the previous section, particularly to calculate x_1, x_2, and x_3, which represents the amount of unbalanced current in electrode 1, 2, and 3, respectively. We can now control for total current and current imbalance separately. To increase the total current, which is the balanced plus the unbalanced parts, all electrodes can be moved down. Or vice versa, all electrodes can be moved up to decrease the total current.

For the single-phase unbalanced current, since we know how this current is distributed in the electrodes, we can move the electrodes synchronously to counteract the imbalance. Suppose we are in the case of $\beta = \pi$ as shown in Figure 4, where $x_1 = x_2$ and $x_1 + x_2 = -x_3$. This can be interpreted as an unbalanced current going down into electrode 3 and divided equally to go up through electrodes 1 and 2. To counteract the imbalance, we then need to increase the resistance of electrode 3 and decrease the resistances of electrodes 1 and 2. Physically, this means raising electrode 3 and lowering electrodes 1 and 2.

As another example, suppose $\beta = -2\pi$, such that $x_1 = -x_2$ and $x_3 = 0$. Then there is no unbalanced current in electrode 3, all of it is oscillating between electrodes 1 and 2. This means that the resistances of electrodes 1 and 2 must be increased compared to the resistance of electrode 3. So, electrodes 1 and 2 should be raised. But the current going through electrode 3 will also be affected by these increased resistances, and electrode 3 should be lowered to compensate.

The conditions around each electrode are likely to differ, and if all electrodes are moved by the same amount, the currents are not necessarily changed equally. For control of the total current, we recommend establishing a running estimate on the relative change in electrode positions needed to change all three currents by the same amount. Such an estimate can be checked, and possibly updated, after each total current correction. Similarly, we recommend running estimates for the situations where all the unbalanced current is oscillation between two electrodes. The estimate would then be on the relative change in the three electrode positions required to change two currents while keeping the third one unchanged. The running estimates, one for the balanced current and three for the unbalanced cases, are probably closely linked, and constitutes a topic for further research.

The general case where the unbalanced current enters one electrode and is distributed to the two others, can be written as the sum of two currents, each with zero unbalanced current in one electrode. The total correction will then be the sum of two corrections, following the method previously outlined.

Some thought must be offered to the absolute value of the imbalance. This can for example be to only make adjustments when the magnitude of the imbalance is outside of some deadband, or to move more quickly if the absolute value is larger. Questions about the step size of electrode movements, relative step size for each electrode, and time between steps also need to be addressed. Specific algorithms should be simulated on a model of the furnace to get a good understanding of how it will behave under various conditions and to test it against other control strategies.

3.4 Higher harmonics

There might be higher harmonics of the fundamental frequency present in the furnace, which will complicate the symmetrical components analysis. High-frequency measurements previously done on a silicon submerged-arc furnace indicate that the current harmonics are small compared to the imbalance of the fundamental, even though the electrode voltage is

clearly distorted due to arcing (Monsen, 2025). Further study is needed to determine whether this is applicable in general, and how much higher harmonics will affect the performance of a control strategy like the one we have proposed. It is not difficult to do the calculations and adjustments presented here only based on the fundamental frequency, but the presence of higher harmonics might still influence the performance of the control strategy. If necessary, the method should therefore be extended to account for the effect of higher harmonics.

3.5 Further work

Our characterization of electrode currents constitutes a sound theoretical basis for a current control without electrode interaction, but more studies are needed to develop and test robust control algorithms. While our simple model is sufficient for analysing current distributions, a more realistic model is required for properly studying the control strategy. Such a model should include typical induction effects, non-linearities, and changes in the furnace conditions. The latter is needed to study robustness against changes due to variation in raw material properties and uneven material flow.

For further research, we propose at least the following. A first step would be to investigate the behaviour of the running estimates described above and to test the control strategy on a simple furnace model. Then, it should be tested on more complex and realistic models. Measurements should also be performed on real furnaces, and the behaviour of the symmetrical components should be studied regarding variations, typical time constants and so on. Lastly, a successfully developed control strategy should be tested on real furnaces. If successfully implemented, the current interaction effect will be properly counteracted. If not, we assume that the novel strategy at least will substantially reduce current interaction effects.

4. CONCLUSIONS

We have shown that the electrode currents can be decomposed into one perfectly balanced three phase system in positive rotation and one single-phase imbalanced current. This lays the theoretical foundation for a novel current control method which effectively eliminates, or substantially reduces, the interaction effect. The single-phase imbalance can be counteracted by moving one electrode down and the other two up, or vice versa, while the total current shows whether all electrodes should be moved up or down to maintain the set point for the electric current.

The method requires high-frequency current measurements, to compute magnitude and phase for each transformer current. In addition, decomposition of transformer currents shows the amount and phase of a current circulating between the transformers without entering the furnace. Further studies are needed to design a proper control algorithm and to investigate the effect of higher harmonics in the current. Simulating and testing the method are important next steps to validate the proposed method and to compare its performance with those of other control strategies.

5. ACKNOWLEDGEMENTS

This work was supported by the project “Submerged-arc furnaces: Improved electrical conditions for increased energy efficiency and decarbonization” (SAPPHIRE) funded by the Research Council of Norway (grant number 358034) and the Norwegian Ferroalloy Producers’ Research Association (FFF) with the member companies Elkem ASA, Eramet Norway AS, Finnfjord AS, and Wacker Chemicals Norway AS.

6. REFERENCES

Anderson, P.M. 1995. *Analysis of Faulted Power Systems*. IEEE. https://ieeexplore.ieee.org/book/5263441

Barker, I.J., De Waal, A., Rennie, M.S. and Klopper, J. 1991. The interaction effect in submerged arc furnaces. *Proceedings of the 49th Electric Furnace Conference*, Toronto, Canada, pp.305-310.

Barker, I.J. and Stewart, A.B. 1980. Inductive reactance, and the operation of large submerged-arc furnaces. *Journal of The South African Institute of Mining and Metallurgy*, Vol.80, pp.123-128. http://www.saimm.org.za/Journal/v080n03p123.pdf

Monsen, I. 2025. Circuit Modelling of Submerged Arc Furnaces and Their Power Supply Systems. Master's thesis. University of Oslo. https://hdl.handle.net/10852/120820

Reuter, M.A., Oosthuizen, M., Barker, I.J., Rennie, M.S. and De Waal, A. 1995. The dynamic response of submerged-arc furnaces to electrode movement. *IFAC Proceedings Volumes*, Vol.28, pp.121-127. https://doi.org/10.1016/s1474-6670(17)46753-x

Stewart, A.B. 1980. An Analysis of the Electrical Circuit of Submerged-Arc Furnaces. PhD thesis. University of Cape Town. http://hdl.handle.net/11427/14048

Sævarsdóttir, G.A. 2013. Electric and thermal operations of furnaces for ferroalloys production. In: M. Gasik, ed. *Handbook of Ferroalloys*. Butterworth-Heinemann. pp. 139-175. https://doi.org/10.1016/B978-0-08-097753-9.00005-8

Valderhaug, A.M. 1992. Modelling and Control of Submerged-Arc Furnaces. PhD thesis. The Norwegian Institute of Technology. https://hdl.handle.net/11250/260770

Ida Monsen

Researcher, NORCE Research

Ida Monsen holds a master's degree in Computational Physics. She has been working as a researcher at NORCE for about a year, mainly within the fields of metallurgy and other process industry.

Fromreide, M., I. Monsen, J. O. Sundli, Ø. S. Sortland, U. Thisted, M. Sparta, and V. K. Risinggård. 2026. Modelling of neutral-point drift in a silicon furnace. In Silicon for the chemical and solar industry XVIII, edited by M. Tangstad, H. Rong, A. Valderhaug, B. Andresen, H. Dalaker, and I. G. Page. Kristiansand, Norway, September 7-10, 2026.
https://doi.org/10.55669/oa900802

Modelling of neutral-point drift in a silicon furnace

M. Fromreide[1], I. Monsen[1], J.O. Sundli[2], Ø.S. Sortland[1], U. Thisted[1], M. Sparta[1], V.K. Risinggård[1]
[1]NORCE Research AS, Norway, mafr@norceresearch.no
[2]Wacker Chemicals Norway AS, Norway

Keywords: Bøckman system, Neutral-point drift, Submerged Arc Furnace, Finite Element Model

Abstract – Stable and efficient production of silicon in three-phase submerged arc furnaces relies on precise heat-control of the reaction zone. As the heat is generated by the electric currents flowing through each of the three electrodes, the heat-control translates to controlling the electric power in each electrode. To determine the electrode powers, the electrode voltages must be determined through measurements. Typically, the electrode voltages are measured relative to the neutral point of the electrodes' notional star connection using the so-called Bøckman method. The Bøckman method relies on three measurement leads outside the furnace, each connected to the furnace bottom, to cancel voltages induced by the large magnetic fields in the vicinity of the furnace. The two main sources of error associated with the Bøckman method are induction and neutral-point drift. For an idealized and symmetric furnace, the induced voltages in three symmetrically placed leads cancel, and the true neutral point of the voltage will be at the furnace centre. However, during operation the induced voltages will change with the dynamically changing current paths inside the furnace, and the neutral point will dynamically drift, leading to errors in the measured voltages.
To study these effects, we have developed Finite Element Method (FEM) simulation models of industry-scale three-phase silicon furnaces. The models are implemented in COMSOL Multiphysics and are used to calculate the electromagnetic fields within the furnace (including the electrodes, linings and steel casing) as well as the induced voltages in leads placed around the furnace, mimicking the Bøckman measurement system.

Through simulations we have investigated how asymmetric furnace conditions lead to neutral point drift. Furthermore, we have estimated the contribution to the measured neutral point drift from an asymmetric or poorly calibrated Bøckman system. The model results have been considered together with industrial measurements of neutral point drift.

1. INTRODUCTION

Production of Silicon requires vast amounts of energy to heat up and transform quartz into a metal alloy. The production process takes place in submerged arc furnaces (SAFs), where the necessary energy is provided by electric current through three large electrodes. In a stepwise process, the solid quartz (SiO_2) is transformed into liquid silicon (Si) of varying grade. The Si-yield and production of by-products are highly dependent on temperature. Thus, to run an optimal Si-production the heat balance within the furnace must be properly controlled, to ensure the desired temperatures (Westly, 1974; Westly, 1975; Stewart, 1980; Schei, Tuset and Tveit, 1998).

Efficient control of the heat balance in the furnace hearth requires a good estimate of the electric power provided through each of the three electrodes, which in turn requires good measurements of the electrode currents and the voltage drop over the electrodes. The electrode currents are most readily available and can be measured outside the furnace itself. As for the

This work is licensed under the Creative Commons Attribution 4.0 International License. To view a copy of this license, visit https://creativecommons.org/licenses/by/4.0/

voltage drops, there is no single accessible neutral point, for which to measure the potential difference. The three electrode currents will connect through a notional star connection at some point in the furnace hearth (Stewart, 1980; Barker and Stewart, 1980; Stewart and Barker, 1980; Gerritsen, Tracy and Saber, 2015). For a perfectly symmetric furnace, the electric potential will be zero at the vertical centre axis. A common way to estimate the voltage drop is the so-called Bøckman measurement system which applies three leads between a common centre point at the bottom of the furnace and the top of each electrode (Bøckman, 1973a; Bøckman, 1973b). The use of electric leads around the furnace is prone to measurement errors due to induced voltages from the strong magnetic fields surrounding the furnace. However, the use of three leads allows to cancel out induction errors, due to the three-part rotational symmetry of the three-phase electrode currents.

For precise measurements, two main obstacles occur. Firstly, setting up three leads perfectly symmetric around the furnace is in practice very difficult. Secondly, the neutral point inside the furnace is not fixed, as it will vary with dynamical changes to the inner geometry and material properties of the furnace. It will also vary with electrode movements and arcing. This effect is referred to as *neutral point drift* (Stewart and Barker, 1980; Barker 1980). An asymmetric set-up of the leads will affect the inductive cancellation by skewing the contribution to each lead. This effect can be counteracted by having an adjustable resistance for each lead, which can be tuned to achieve balance between the three leads. Usually, this is a procedure that takes place at a single point in time at the start of the furnace's lifespan. When tuning the resistance network, it is assumed that the neutral point is well defined in the centre of the furnace. Thus, if due to material imbalance, the true neutral point is significantly off centre, the tuning of the resistances will be affected (Sparta, Risingård, Thisted, 2024a; Sparta, Risingård, Thisted, 2024b).

In this publication, a finite element model of a three-phase submerged arc furnace is presented. The model builds on previous research of both inner conditions as well as models of the Bøckman system (Herland, Sparta and Halvorsen, 2018; Sparta, Risinggård and Thisted, 2024a; Sparta, Risinggård and Thisted, 2024b). The novelty of this work is in the investigation of simulation cases with quantitively different asymmetries, to investigate the impact on neutral point drift and thereby the effect on the Bøckman compensation. The study is partly motivated by industrial measurement campaigns that observed neutral point drift, the key findings of which are briefly presented in this publication.

2. Furnace model and simulations

A furnace model has been simulated using the *Magnetic and Electric Fields* interface in *COMSOL Multiphysics* (COMSOL, 2025). Here, Maxwell's equations were solved for the electric potential and magnetic vector potential in the frequency domain. The model is a continuation of previous modelling work of three-phase furnaces, and further details about the implementation can be found in (Herland, Sparta and Halvorsen, 2018; Sparta *et al.*, 2021; Sparta *et al.*, 2022; Sparta, Risinggård and Thisted, 2024a; Sparta, Risinggård and Thisted, 2024b). The electromagnetic fields are governed by Maxwell's equations, which in the frequency domain can be written as (assuming no accumulation of charge)

$$i\omega\mathbf{B} + \operatorname{curl}\mathbf{E} = \mathbf{0}, \quad [1]$$

$$i\omega\mathbf{D} - \operatorname{curl}\mathbf{H} = -\mathbf{J}, \quad [2]$$

$$\operatorname{div}\mathbf{B} = 0, \quad [3]$$

$$\operatorname{div}\mathbf{E} = 0. \quad [4]$$

Each of the vector fields represent the complex amplitude of the respective fields, where **B** is the magnetic induction, **H** is the magnetic field, **E** is the electric field, **D** is the electric displacement and **J** is the electric current density. In addition to Maxwell's equations, Ohms law, $\boldsymbol{J} = \sigma \boldsymbol{E}$, is also included in the model formulation. The model is solved in terms of the scalar electric potential V and magnetic vector potential **A**, defined as $\mathbf{B} = \mathbf{curl}\ \mathbf{A}$ and $\text{grad}\ V = -\mathbf{E} + i\omega\mathbf{A}$.

The furnace model includes a steel shell, steel roof, carbon lining, alumina refractories and electrodes. In addition, a large region of non-conducting air surrounds the domain to secure a well posed boundary condition for the magnetic field. The mathematical model is completed with introducing appropriate boundary conditions for **A** and V. An electric potential is fixed on top of each of the electrodes, while magnetic insulation is assumed for the remaining outer boundary of the computational domain. In addition, the model utilizes the impedance boundary conditions to remove the computationally costly steel shell domain from the computations (Herland, Sparta and Halvorsen, 2018; Fromreide *et al.* 2023). The computational domain is discretized using mainly tetrahedral mesh elements, with refined rectangular boundary elements at the boundaries of very well conducting domains, such as the electrodes and metal alloy. The Bøckman leads which are located outside the furnace are meshed using edge-elements.

The interior of the furnace is divided into zones with bulk properties to represent the distribution of material and heat zones of a real industrial furnace. The charge material is divided into three zones, a cold top layer, a middle outer reaction zone and an inner high-temperature reaction zone. Each of the vertically stacked layers are further divided in three sections, so that the conditions around each individual electrode can be adjusted. At the bottom of each electrode a crater with surrounding crater walls is defined. The model is fully parameterized and further includes the possibility of side arcs (electrode – crater wall) and a bottom arc (electrode – alloy). Side-arcs are included if the distance between the electrode and crater wall is 15 cm or less and is approximated by cylindrical resistive domains. The same is true for the bottom arc for the distance between the electrode and alloy. However, for the simulations treated in this publication, no bottom arcs are included as only higher electrode positions are considered. A sketch of the different material zones can be seen in Figure 1.

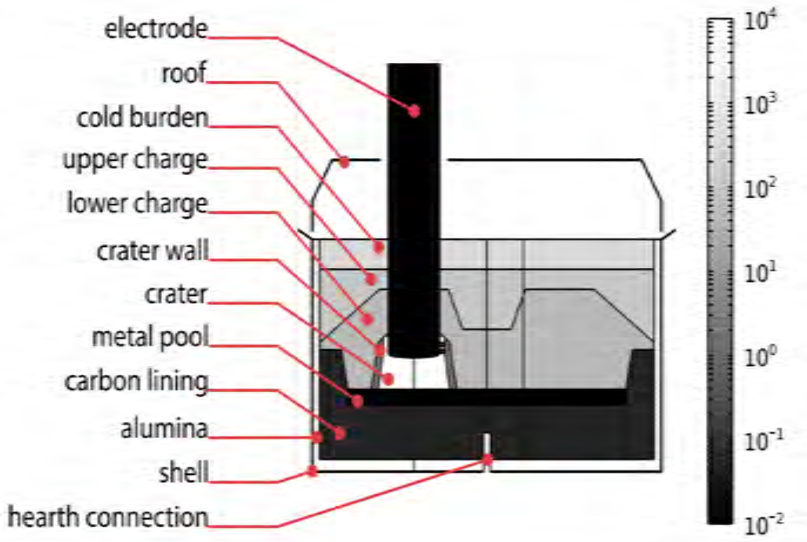

Figure 1: Schematic representation of model geometry and material zones.
The color bar shows the resistivity of the materials inside the furnace in mΩ·m.

2.1 Simulation cases

Surrounding the furnace model a network of possible Bøckman leads is placed. In general, any three symmetrically (120° separation) placed leads will give perfect cancellation. A perfect symmetric placement is difficult to obtain in practice, the simulations carried out in this work considered asymmetric leads (Sparta, Risinggård and Thisted, 2024a; Sparta, Risinggård and Thisted, 2024b). Three leads have been chosen, with angular separations of 100°, 150° and 110°. The angular position relative to the electrodes is shown in the 2D furnace sketch in Figure 2. This work only considers angular displacement of the leads, keeping the radial distance from the furnace constant for each lead. In reality, the displacement will generally vary in both the angular and radial direction as a function of the furnace height.

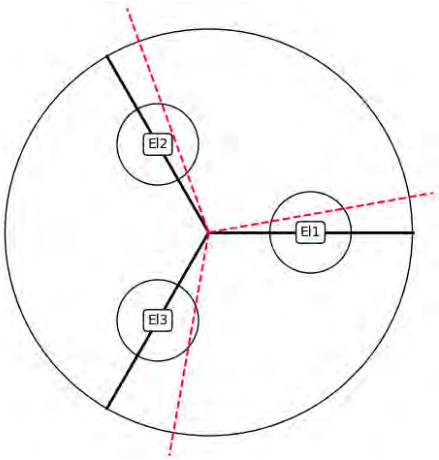

Figure 2: Placement of asymmetric Bøckman leads

A default case has been defined where the furnace is completely symmetric with each electrode in the same position. Then, more cases have been chosen by introducing an unbalance in the resistivities of the inner material zone surrounding the three electrodes. Due to the geometry of the model and the typical value range (20-80 mΩ·m) for the bulk resistivity of these regions, they have the single most impact on the current distribution (Fromreide *et al.*, 2021). For each simulation case, the electrode resistances are kept constant by allowing the electrodes to shift down or up to account for the change in material resistivity. The bulk resistivity in each inner reaction zone can be either decreased, increased or be kept constant. Thus, there are a total of $3^3 = 27$ qualitatively different combinations to explore. However, due to rotational symmetry (e.g. (0 - -) can be rotated to give (– 0 –) and so forth) and the fact that some combinations will be scaled versions of others (e.g. (- - 0) and (- - +) will give the same asymmetry), only four asymmetric settings are needed to span the set of possibilities and get an estimate for how different variations will affect the model. The full factorial design with the four selected cases is shown in Table 1.

The default setting for the bulk resistivity of the inner charge zone has been set to 47 mΩ·m. The asymmetries have then been introduced by either keeping this value approximately constant, increasing it to approximately 70 mΩ·m or lowered to approximately 30 mΩ·m for each individual region between and surrounding the electrodes. To get constant electrode resistances within reasonable electrode positions, some adjustments have been made to the different cases. The value used for each case is defined in Table 2, together with electrode tip positions which are adjusted as a response to the chosen bulk resistivities.

Table 1: Factorial design of the 27 qualitatively different combinations of variations in material resistivity. 0 denotes a medium value, - a low value and + a high value. The five selected simulation cases are indicated.

#	Value	#	Value	#	Value
1	− − −	10	0 − −	19	+ − −
2	− − 0	11	0 − 0	20	+ − 0
3 (D)	− − +	12	0 − +	21 (A)	+ − +
4	− 0 −	13	0 0 −	22 (C)	+ 0 −
5	− 0 0	14 (Sym)	0 0 0	23	+ 0 0
6 (B)	− 0 +	15	0 0 +	24	+ 0 +
7	− + −	16	0 + −	25	+ + −
8	− + 0	17	0 + 0	26	+ + 0
9	− + +	18	0 + +	27	+ + +

Table 2: Parameter settings for the varying parameters for the five simulation cases.

Parameter	Sym.	A	B	C	D
Electrode 1 tip position (m)	0.80	0.61	0.82	0.73	0.86
Electrode 2 tip position (m)	0.80	0.94	0.87	0.78	1.01
Electrode 3 tip position (m)	0.80	0.80	0.57	0.95	0.76
Resistivity inner zone 1-2 (mΩ·m)	47	70	28	72	40
Resistivity inner zone 2-3 (mΩ·m)	47	31	50	50	40
Resistivity inner zone 3-1 (mΩ·m)	47	71	72	40	70

3. Results

Each of the simulations defined in Table 2 has been solved in COMSOL Multiphysics. From the calculations, the induced voltage in the defined asymmetric Bøckman leads has been extracted as complex amplitudes together with the calculated electric potential at the point of access (PA) at the furnace bottom. Given the amplitudes for the individual leads, the resistances needed to compensate for neutral point drift is found by solving two equations, on for the real part and one for the imaginary part of the three vectors. Thus, one of the leads resistances are kept constant while two are scaled. The value of the two scalars is found numerically using the least square fit algorithm in the python library *scipy* (Virtanen *et al.*, 2020), accounting for small numerical errors arising from the FEM simulations. Figure 3 shows

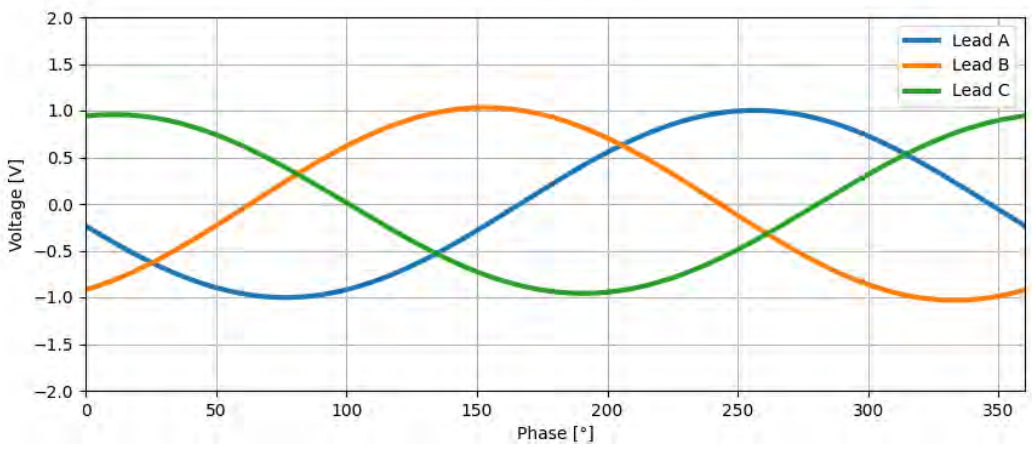

Figure 3: Induced voltage in the three Bøckman leads for the symmetric furnace. The values have been scaled by the voltage amplitude measured in Lead A.

the induced voltage in each of the three Bøckman leads for the symmetric case. For confidentiality, the scales have been adjusted, but the relative trends are kept in all the subsequent plots by scaling with the same value The results are illustrated as curves over one phase. The value for each lead is then added together with the contribution from the voltage at PA to find the measured Bøckman potential, which for a perfect symmetric Bøckman measurement should be zero. The result is shown in Figure 4 together with the measured potential at PA and the compensated Bøckman measurement. As the figure shows, the uncompensated measured neutral point is different from the true voltage at PA due to the asymmetric Bøckman set up. However, the scaling of two of the lead resistances perfectly compensates the measured value.

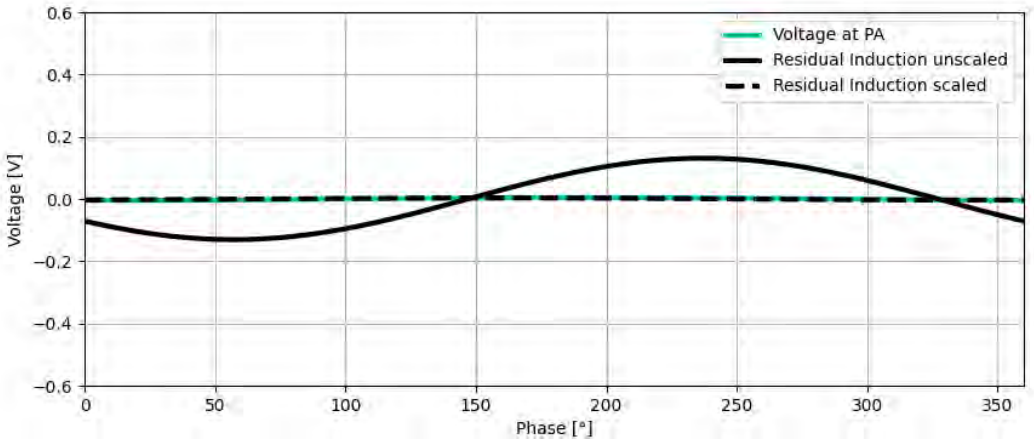

Figure 4: Measured voltage at connection point at the furnace bottom (PA), unscaled neutral point measured from the leads and scaled induction. The values have been scaled by the voltage amplitude of measured in Lead A.

Figure 5 shows the results from the four asymmetric simulation cases. There are notable differences between the cases, both in terms of magnitude and phase shift. Further, it is seen that the simple tuning of resistances does not fully compensate for the neutral point drift in any of the cases. For the uncompensated cases the magnitude of the simulated measured Bøckman voltage varies between 1.13 and 2.61 times the "true" zero potential measured at the furnace bottom (PA). Likewise, the phase error varies between 4° and 42°. Similarly, for the compensated leads, the magnitudes vary between 1.20 and 1.60 times the measured voltage at PA, with phase errors in the range 0° to 24°. The overestimation of the voltage magnitude and the variation in phase is in line with previous results in (Sparta, Risinggård and Thisted, 2024a; Sparta, Risinggård and Thisted, 2024b). The results are summarized in Table 3, which states the offset in terms of both the relative amplitude and absolute phase for each case. The results show that a single calibration of the resistance network is not sufficient for proper compensation. However, apart from case A, which showed a good agreement between the uncompensated Bøckman voltage and the voltage at PA, the compensation works in a positive way as it reduces the offset. It is a notable significant positive effect on the phase shift, which is important for furnace control.

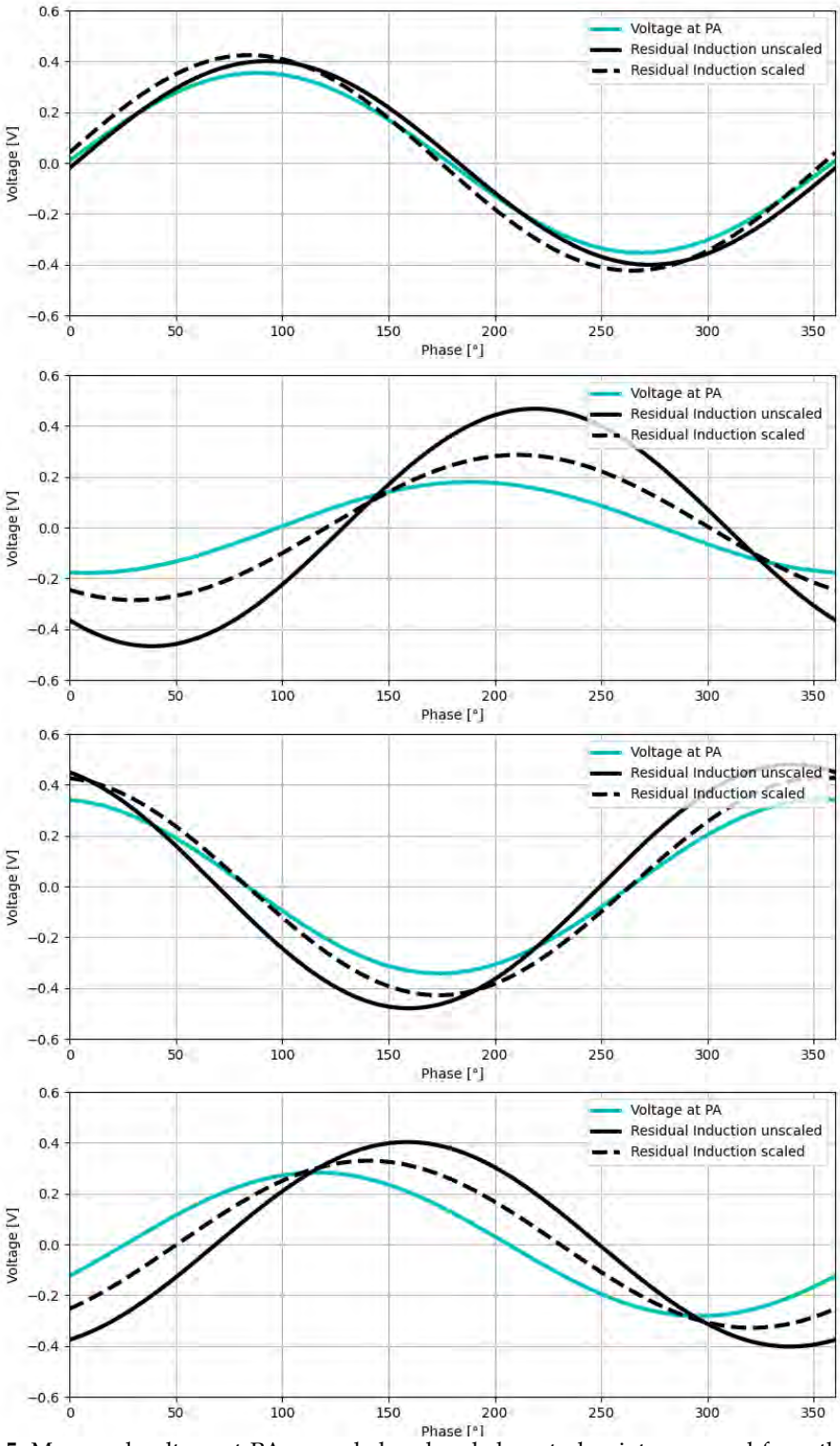

Figure 5: Measured voltage at PA, unscaled and scaled neutral point measured from the leads. Cases A, B, C and D (from top to bottom). The values have been scaled by the voltage amplitude measured in Lead A.

Table 3: Deviation of the "measured" neutral point voltage and the voltage at PA in terms of the relative amplitude (first row) and phase angle (last row) for the four asymmetric cases. U and C denote uncompensated and compensated, respectively.

	A		**B**		**C**		**D**	
	U	C	U	C	U	C	U	C
$\left\|\frac{\|V_{PA}\| - \|V_0\|}{\|V_{PA}\|}\right\|$	0.13	0.19	1.6	0.60	0.40	0.25	0.42	0.16
$\angle V_{PA} - \angle V_0$	-4.1°	4.5°	-30.4°	-22.3°	14.3°	0.28°	-42.6°	-24.3°

The numerical studies have partly been motivated by measurement campaigns performed at an industrial silicon furnace. The furnace is approximately 30 MW and has a geometry and dimensions which are reasonably close to those used in the numerical models. The furnace was equipped with sensors capable of measuring the electrode voltages at a high frequency, enabling a good resolution of one phase period (50 Hz). Figure 6 shows a 20-minute data window from one measurement campaign. The magnitude of the potential is omitted for confidentiality, while relative trends and phase errors are presented. Preliminary results from this measurement campaign have previously been published in a master's thesis (Monsen, 2025), where more information about the measurements set up can be found. As the figure shows, the potential circles around the neutral point with some notable distinct drifts in the region 250°- 360°. The figure highlights that neutral point drift can cause significant errors in measured electrode voltages.

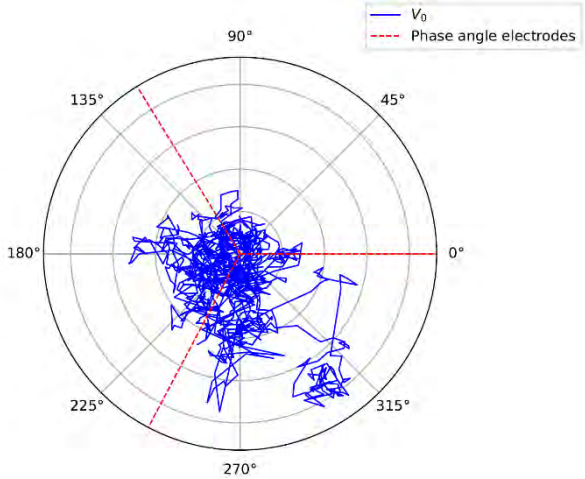

Figure 6: Measured neutral point drift over a 20-minute period from an industrial silicon furnace. The magnitude of the voltage has been omitted for confidentiality; relative trends are preserved.

5. CONCLUSIONS

Measurements of electrode voltages in an industrial silicon furnace indicate that neutral-point drift is significant as a source of error in the electrode voltage. it has been shown how significant drift in the neutral point phase occur over a short time-period during normal operation. The error arising from neutral point drift has a larger impact compared to previous

estimates of induction-related errors. Contributions to the neutral-point measurement from asymmetries in the placement of the Bøckman leads have been estimated using finite-element simulations. It has been shown that different asymmetries give variations in the measured off-set and that a single calibration is insufficient for proper compensation. The simulations highlight the critical role of practical procedures for compensating for geometric asymmetries in the voltage measurement system.

In this study, the compensation was based on a fully symmetric furnace, and the simulation cases were established assuming constant electrode resistance. Both assumptions represent idealized operating conditions. Future work will extend the analysis to investigate Bøckman lead compensation in asymmetric furnace configurations and to employ constant electrode current as the governing condition, thereby providing a more realistic representation of industrial furnace operation.

6. ACKNOWLEDGEMENTS

This work was supported by the project "Submerged-arc furnaces: Improved electrical conditions for increased energy efficiency and decarbonization" (SAPPHIRE) funded by the Research Council of Norway (grant number 358034) and the Norwegian Ferroalloy Producers' Research Association (FFF) with the member companies Elkem ASA, Eramet Norway AS, Finnfjord AS, and Wacker Chemicals Norway AS.

7. REFERENCES

Barker, I.J. 1980. *IFAC Proc. Vol.*, vol. 13, pp. 611–21, https://doi.org/10.1016/s1474-6670(17)64768-2.

Barker, I.J. and Stewart, A.B. 1980 *J. South. Afr. Inst. Min. Metall.*, 1980, vol. 80, pp. 123–28, http://www.saimm.org.za/Journal/v080n03p123.pdf.

Bøckman, O.C. 1973. NO126288B, Jan. 1973, https://patents.google.com/patent/NO126288B/en.

Bøckman, O.C. 1973. US3757021, Sep. 1973, https://patents.google.com/patent/US3757021/en.

COMSOL Inc.: *AC/DC Module User's Guide*, 2025.

Fromreide, M., Gomez, D., Halvorsen, S. A., Herland, E. V. and Salgado, P. 2021. Reduced 2D/1D mathematical models for analyzing inductive effects in submerged arc furnaces. Applied Mathematical Modelling, 98,59-70.

Fromreide, M, Gomez, D., Halvorsen, S. A. and Salgado, P. 2023 Induced currents in the lining and steel shell of submerged arc furnaces. Journal of Sustainable Metallurgy 9.1: 375-385.

Gerritsen, T., Tracy, P. and Saber, F. 2015. in *Proc. INFACON XIV*, International Committee on Ferro-Alloys, Kyiv, Ukraine, 2015, pp. 338–48, https://www.pyrometallurgy.co.za/InfaconXIV/338-Gerritsen.pdf.

Herland, E.V., Sparta, M. and Halvorsen, S.A. 2018 *J. South. Afr. Inst. Min. Metall.*, vol. 118, pp. 607–18, https://doi.org/10.17159/2411-9717/2018/v118n6a8.

Monsen, I. 2025, Circuit Modelling of Submerged Arc Furnaces and Their Power Supply Systems, M.Sc. thesis, University of Oslo

Schei, A., Tuset, J.K. and Tveit, H. 1998, Production of High Silicon Alloys, Tapir forlag, Trondheim,

Sparta, M., Fromreide, M. Risinggård, V.K. Halvorsen, S.A. 2022 in *Proc. Silicon Chem. Sol. Industry XVI*, SSRN Electronic Journal, Trondheim, 2022, https://doi.org/10.2139/ssrn.4118651.

Sparta, M., Risinggård, V.K. and Thisted U. 2024 in *Proc. Silicon Chem. Sol. Industry XVII*, Social Science Research Network, Trondheim, Norway, 2024, https://doi.org/10.2139/ssrn.4942623.

Sparta, M., Risinggård, V.K. and Thisted U. 2024. NORCE Research AS, Kristiansand, Norway, 2024.

Sparta, M., Varagnolo, D. Stråbø, K., Halvorsen, S.A., Herland, E.V. and Martens, H. 2021. *Metall. Mat. Trans. B*, vol. 52, pp. 1267–78, https://doi.org/10.1007/s11663-021-02089-7.

Stewart, A.B. 1980. PhD Thesis, University of Cape Town, 1980, http://hdl.handle.net/11427/14048.

Stewart, A.B. and Barker, I.J. 1980. in *Proc. INFACON II*, International Committee on Ferro-Alloys, Lausanne, Switzerland, 1980, pp. 71–82, https://www.pyrometallurgy.co.za/InfaconII/071-Stewart.pdf.

Pauli Virtanen, Ralf Gommers, Travis E. Oliphant, Matt Haberland, Tyler Reddy, David Cournapeau, Evgeni Burovski, Pearu Peterson, Warren Weckesser, Jonathan Bright, Stéfan J. van der Walt, Matthew Brett, Joshua Wilson, K. Jarrod Millman, Nikolay Mayorov, Andrew R. J. Nelson, Eric Jones, Robert Kern, Eric Larson, CJ Carey, İlhan Polat, Yu Feng, Eric W. Moore, Jake VanderPlas, Denis Laxalde, Josef Perktold, Robert Cimrman, Ian Henriksen, E.A. Quintero, Charles R Harris, Anne M. Archibald, Antônio H. Ribeiro, Fabian Pedregosa, Paul van Mulbregt, and SciPy 1.0 Contributors. 2020 SciPy 1.0: Fundamental

Algorithms for Scientific Computing in Python. Nature Methods, 17(3), 261-272. DOI: 10.1038/s41592 019-0686-2.
Westly, J. 1974. in *Proc. INFACON I*, International Committee on Ferro-Alloys, Johannesburg, South Africa, pp. 121–27, https://www.pyrometallurgy.co.za/InfaconI/121-Westly.pdf.
Westly, J. 1975. in *Proc. Elec. Furn. Conf.*, Iron & Steel Society, pp. 47–53.

Mads Fromreide
Senior Researcher, NORCE Research AS
Mads Fromreide holds a PhD in Applied Mathematics from the University of Santiago de Compostela. He has worked at NORCE for over a decade, mainly working on modelling towards the metallurgical industry.

Låstad, J., and J. Safarian. 2026. Vacuum refining techniques for End-of-life solar silicon. In *Silicon for the chemical and solar industry XVIII,* edited by M. Tangstad, H. Rong, A. Valderhaug, B. Andresen, H. Dalaker, and I. G. Page. Kristiansand, Norway, September 7–10, 2026. https://doi.org/10.55669/oa900804

Vacuum refining techniques for End-of-life solar silicon

J. Låstad[1], J. Safarian[2]
[1]NTNU, Norway, Jonas.Lastad@ntnu.no
[2]NTNU, Norway, Jafar.Safarian@ntnu.no

Keywords: Photovoltaics, Silicon, Vacuum refining, low vacuum gas flow

Abstract – End-of-life (EoL) photovoltaic (PV) silicon wafers are currently downcycled into lower value metallurgical silicon, losing much of its value. To address this, EoL silicon purification via vacuum refining was studied using the temperatures 1450 °C, 1600 °C, 1700 °C and a pressure of approximately 20 Pa. The sample vapor was collected by a novel approach utilizing a water-cooled plate condenser placed above the crucible holding molten silicon. The condensate and refined silicon samples were studied using glow discharge mass spectroscopy (GDMS). The results indicated that the condensation technique provided improved mass flux data. The impact of temperature indicated improved silicon yield with increased temperature. It was found that the evaporation from the melt, and hence the corresponding deposition on the condenser surface are affected by temperature and it is the highest at 1700C°, and the lowest at 1600C°. This could be explained by a surface slag layer originating from glass component and passivated layers impacted the mass transfer rate during vacuum refining by limiting the effective area of the melt due to partially surface coverage. This impact was reduced at 1700 °C temperature, where deoxidation of the melt and slag phase removal occurred. Regarding the properties of the material, a mechanism for mass transport of elements under vacuum for processing EoL PV silicon was proposed.

1. INTRODUCTION

Waste from the spent solar panels is a growing issue and current estimates reach 78 million tons of PV waste by 2050. Processes are being developed for recycling the bulk of the panel, namely glass and aluminum, as well as for the valuable silver electric busbars (Wade et al., 2016). However, the remaining wafer, which retains the value of higher purity, tends to be downcycled into metallurgical grade silicon. This results in the potential cost of upgrading the spent PV silicon by the existing Siemens process, which is both costly and has a high impact on climate.(Chen et al., 2023) Estimates for energy consumption for upgrading metallurgical Si to solar grade (SoG) polysilicon reaches 63.9 kWh per kg Si compared with only 12 kWh/kg for the initial smelting of metallurgical grade Si (Frischknecht et al., 2015). This estimate informs the headroom of alternative processes for reducing energy consumption.

Vacuum refining is a potential approach suited for recycling EoL PV silicon as the technique exploits the low volatility of silicon compared with most other metals.(Harris and Davenport, 1982) The technique is also suited for achieving high purity silicon as the purification is not dependent on an equilibrium, meaning that the concentration of volatile elements approaches zero. (Safarian and Tangstad, 2012b)However, all the mechanisms of mass transfer are not completely understood for all the relevant vacuum refining conditions. At low to medium vacuum the impact of chemical reactions in the gas phase are poorly understood, but has been found to modify the mass transfer through the gas phase.(Hoseinpur et al., 2021)

Studying the degree of purification during vacuum refining of high purity substances such as for solar grade silicon poses a challenge as the difference in purity between the treated and untreated samples are minimal as the concentrations are low already. The concentrations also approach in the order of 0.1PPM which is the detection limit for certain analytical techniques introducing uncertainty (Di Sabatino, 2014). This paper aims to explore medium vacuum conditions for upgrading the purity of EoL PV silicon using a novel sample collection technique, with the goal of obtaining solar grade feedstock quality.

This work is licensed under the Creative Commons Attribution 4.0 International License. To view a copy of this license, visit https://creativecommons.org/licenses/by/4.0/

2. THEORY

2.1 End-of-Lifeo photovoltaic material characteristics

EoL PV waste consists of a mix of panel designs; old panel types consisted of primarily P type panels where the emitter layer is doped with phosphorous and the bulk doped with boron. Tunnel Oxide Passivated Contact (TOPCon) cell structure as presented in Figure 1 is the leading PV cell in 2026. The figure represents the different layers such as of the TOPCon cell. The dopant in the emitter and bulk layer depends on the wafer type and has historically been primarily P-type wafers with B in the bulk layer and P in the emitter. Newer cell designs using N-type wafers doped with P in the bulk and B in the emitter. The list of expected elements in the different layers of a PV Cell is presented in Table I. During recycling, the panel is typically disassembled and metal contacts recovered, leaving behind primarily the doped silicon wafer, but with contamination from glass and oxide wafer layers. (Vodapally and Ali, 2022)

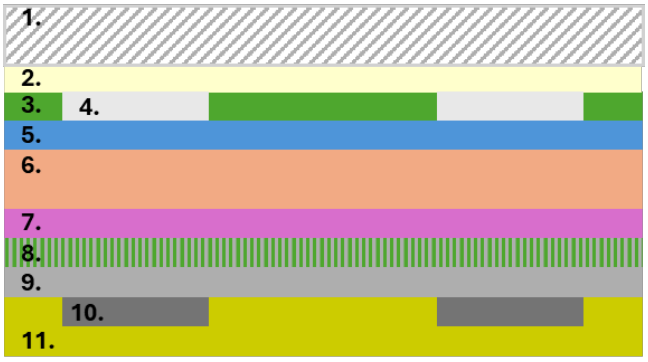

Figure 1 Schematic showing structure of a typical TOPCon panel. 1. PV glass, 2. Binding polymer, 3. Anti-reflective coating, 4. Front electrical contacts, 5. Doped emitter, 6. Bulk layer, 7. Doped Thin Film, 8. Tunnel oxide passivated rear contact, 9. Rear metallization, 10. Rear electrical contacts, and 11. Polymer backsheet.

Table I Element distribution in Si PV (Granata et al., 2014; Sharma, 2019; Lozac'h, Nunomura and Matsubara, 2020; Ghosh et al., 2022)

Layer	Element
Glass	MgO, Al_2O_3, SiO_2, CaO, TiO_2, SnO, K_2O, Sb_2O_3
Polymer	H, C, O
Anti reflective coating	MgF_2, Al_2O_3, $AlSiO_2$ SiN_x, TiO_2
Front contacts	Ni, Cu, Ag, Zn, Pb
Emitter layer	Si, B, Al, Ga
Bulk layer	Si, P, As
Back surface field	Si, P, As
Tunnel oxide layer	Si, Al, Ti, O
Rear metallization	Al, Ti, Ag
Rear electrical contact	Al, Zn, Sn, Pb
Polymer backsheet	H, C, O

Other elements may enter the waste stream due to poor sorting. Thin film PV panels such as CdTe panels pose a challenge as they introduce heavy metals such as cadmium or telluride. Furthermore, perovskite and tandem modules may introduce elements otherwise unaccounted for. However, these technologies are not dominant and, assuming adequate sorting, these potential contaminants are not considered (Sundaram, Benson and Mallick, 2016).

2.2 Vacuum refining

In vacuum refining, similarly to distillation, the differences in volatility between the components of a mixture are exploited to achieve a difference in mass transport rate and obtain a targeted composition. The technique utilizes the deviation equilibrium in pressure as the mass transport from the vapor source, or the melt, which approaches p_i^e and the vapor pressure on the cold surface which approaches $p_i^c \rightarrow 0$, here i denotes element i. This is calculated in equation [1] using standard vapor pressure p_i^0 of the elements and chemical activities a_i in the melt, activity coefficient γ_i and the molar concentration X_i. The activity coefficients can be assumed constant in dilute solution known as the Henrian activity coefficients γ_i^0, which is a valid assumption for all the minor elements, and can be assumed to be 1 for the silicon solvent. Metals with low volatility such as tungsten, iron, and silicon are well suited for this purification technique as they have low vapor pressures compared to most other elements. Silicon is particularly suited for vacuum refining as it has very low vapor pressure compared to most metals, as seen in Figure 2.

$$a_i = \frac{p_i^e}{p_i^0} = \gamma_i X_i \quad [1]$$

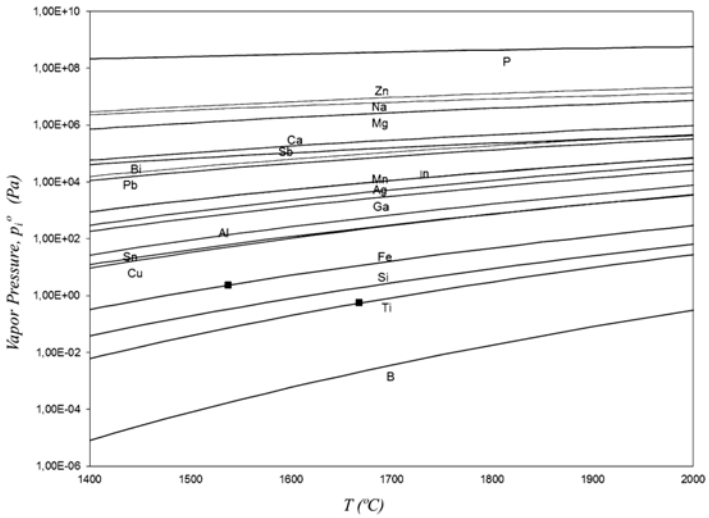

Figure 2 Vapor pressure of elements as a function of temperature, as calculated by (Safarian and Tangstad, 2012b).

The evaporation rate is controlled by the rate of transport through the different steps between the molten metal and the condensing surface. The steps are diffusion through the melt surface m, evaporation at melt-gas interface c, diffusion through the gas g and deposition d. Assuming no accumulation and that the system is in steady state, the coupled model can be presented as equation [2]. Where the mass flux for element i, $\dot{m}_i$ $\left[\frac{kg}{s}\right]$, is the momentary rate at the changing concentration c_i $[g/g\ Si]$ can be described following equation [3] using the mass transfer coefficient k_i $\left[\frac{m}{s}\right]$ in a 1st order reaction and area A assuming no interaction with the wall. For a first order reaction, the rate constant can be calculated using equation [4] (Safarian and Tangstad, 2012a) using the starting C_i and final C_c concentration of the metal, as well as the area A, volume V , and refining time t.

$$\dot{m}_i = \dot{m}_{m,i} = \dot{m}_{c,i} = \dot{m}_{g,i} = \dot{m}_{d,i} = \frac{dm}{dt} \quad [2]$$

$$\dot{m}_i = k_i * C_i * \rho_{Si} * A \quad [3]$$

$$k_i = \ln\left(\frac{C_s}{C_f}\right)\Big/\frac{A}{V}t \quad [4]$$

The total mass transport coefficient k_i can be calculated by taking the resistive sum of the different mass transport steps shown in equation [5]. These steps are mass transfer through melt boundary layer: $k_{m,i}$, mass transfer through evaporation $k_{c,i}$, mass transfer through gas phase $k_{g,i}$, and the condensation referenced as $k_{d,i}$, d representing deposition.

$$k_i = \left(\frac{1}{k_{m,i}} + \frac{1}{k_{c,i}} + \frac{1}{k_{g,i}} + \frac{1}{k_{d,i}}\right)^{-1} \quad [5]$$

Induction heating causes stirring in conductive melts, inducing a high surface velocity v_m, causing k_m to be large. Hoseinpur describes diffusion through the melt boundary layer as having a negligible impact on the flux under the relevant conditions and can be disregarded (Hoseinpur et al., 2021). The deposition rate has also been described as negligible (Malhotra, Mahajan and Sampath, 2006), leaving the evaporation rate and the gas transfer rate as the rate determining steps.

3. METHODS

The furnace used in this work, as presented in Figure 3, consists of the following parts:
The condensing plate for the collection of metal vapor is original and will be used for measuring the relative flux of the refining process. The dimensions of inner crucible were 96 mm high and 51 mm inner diameter. The distance between the bottom of the inner crucible and the cold plate was 130 mm. The thermocouple is positioned on the outside of the inner crucible and the space between the crucibles is packed with insulation. The placement of the thermocouple simplifies the geometry of the crucible, limiting the impact on gas flow. The insulation improves the accuracy of the thermocouple and holds crucible in place for sampling. The temperature T_b obtained from this thermocouple is approximate of the actual bulk temperature. From experience, the deviation is less than 50 °C from the actual value.

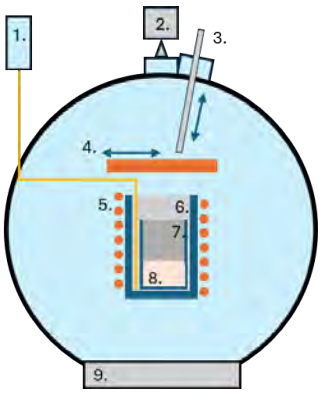

Figure 3 Schematic of vacuum induction furnace. 1. Thermocouple and 2. Pyrometer for measuring bulk temperature T_b and surface temperature T_s, 3. Quartz sampling tube for sampling the molten silicon without opening the furnace, 4. Vapor condenser for collecting the evaporated material, 5. Induction coil, 6. Outer graphite crucible, 7. Inner graphite crucible, 8. Molten Si sample, 9. Vacuum pump system.

A 100 g sample of mixed crushed EoL PV silicon with composition as presented in Figure 9 which had been separated, and treated for metal recovery was delivered by Fraunhofer CSP and used in each experiment, as seen in Figure 4, with a density 2.52 g/cm^3 (Mukai and Yuan, 2000) this corresponds to 39 682 mm^3 of molten Si, resulting a depth of 19.4 mm in the inner crucible.

Figure 4 Image of crucible setup and silicon sample.

Prior to the experiments, the crucibles are heated to remove volatile elements from the crucible and minimize contamination. Three vacuum refining experiments were performed, one each at surface temperatures T_s = 1450 °C, 1600 °C and 1700 °C. The holding time at the conditions was 60 minutes as indicated by the red lines, beginning when the vacuum reached 20 Pa. The measured temperatures are presented in Figure 5 – 7. With manual temperature controls, the temperature varied as seen in Figure 7 the sudden drop in bulk temperature T_b was caused by the shifting of the thermocouple, loosing contact with the inner crucible. The noise in the surface temperature data is caused by the condenser plate being moved in front of the pyrometer. Limited pumping rate and minimum pressure led to the pump being left running during the experiment, working at its highest rate, resulting in the presented pressure profiles rather than a set pressure, this is not believed to have a significant impact on the flux, as the change is small, and the curve is consistent between the experiments.

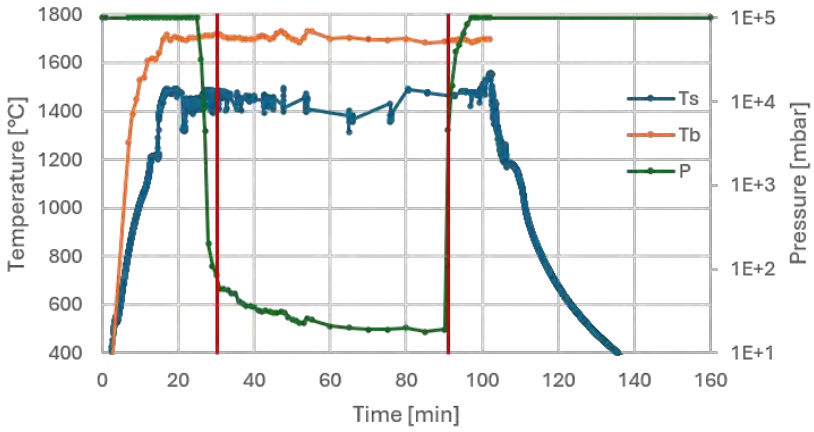

Figure 5 Furnace conditions [Ts=1450 °C].

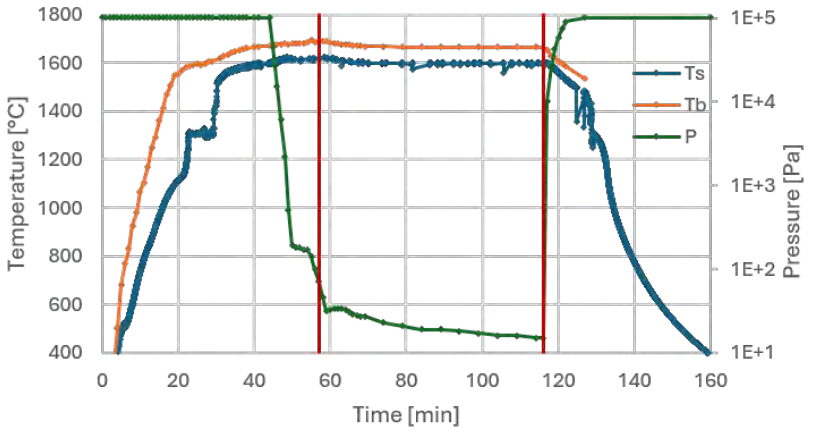

Figure 6 Furnace conditions [Ts=1600 °C].

Silicon samples were taken from the molten silicon by a pure quartz tube sampler that molten silicon was sucked into it. Once the melt reached the target temperature, once before making vacuum sampling was carried out, and again after re-pressurization after 60 minutes of refining. The samples were analyzed providing before and after compositions for the refining experiments. The vapor was deposited and collected on the water-cooled condenser plate as shown in Figure 3. The condenser plate obstructed the visibility of the pyrometer and hence was regularly moved aside for surface temperature measurements. This reduced the condensate collected for some seconds. However, the deposit loss is assumed to be insignificant in the total time of the refining. Collected metal and condensate samples were analyzed using Glow Discharge Mass Spectrometry (GDMS).

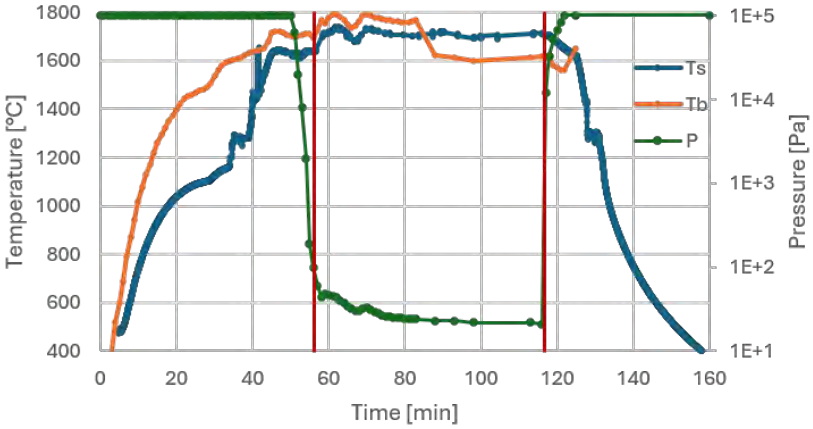

Figure 7 Furnace conditions [Ts=1700 °C].

4. RESULTS

4.1 Observations

As presented in Figure 5 and 6, the surface temperature T_s for the 1450 °C and 1600 °C experiments are consistently lower than the bulk. For the experiment at 1700 °C, shown in Figure 7, there is a sudden drop in bulk temperature T_b. This drop is suspected of being caused by displacement of the thermocouple, causing it to lose thermal contact with the melt or damage. The slightly lower surface temperature than the bulk is expected as the evaporation of silicon and other elements are endothermic and occurring at the surface of the melt. Once the target temperature had been reached and the vacuum chamber evacuated, a distinct vapor plume could be observed between the molten silicon surface and the condenser plate, as shown in Figure 8a. There is no visible plume bypassing the plate, indicating good vapor collection. The condensate could later be seen accumulating with dendrites on the plate as shown in Figure 8b. The change in mass for the crucible was minimal.

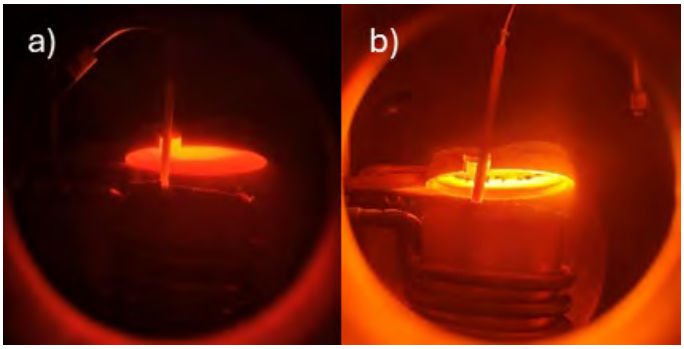

Figure 8 Images of crucible, induction coil, thermocouple, and condenser plate. A) Vapor cone visible shortly after reducing pressure. B) Dark patches of condensate visible on condenser plate.

4.2 Chemical analysis

GDMS analysis of silicon samples before and after refining is presented in Figure 9 and Figure 10 and shows minimal standard deviation in the analysis. There is significant spread in composition between the samples, despite being the same sample material. The concentration of impurities like B, Al, P, Ca, and Cu can be seen to increase after refining, loss of silicon could explain the non-volatile elements, but the volatiles indicate contamination. Carbon was detected in the metal but is assumed to have dissolved from the graphite crucible in the melt. There are differences in the concentrations of the samples, after melting. The batch refined at 1600 °C has higher concentrations of Na, K, Ca than the other temperatures. This is seen in both the before and after refining samples.

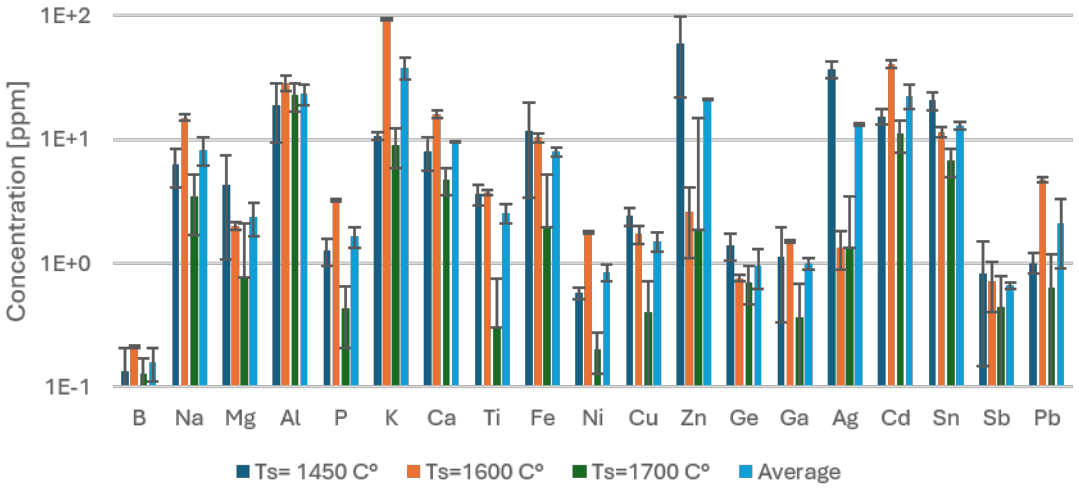

Figure 9 Starting compositions of molten silicon from GDMS analysis, individual samples and average. Error bars indicate standard deviation from analysis.

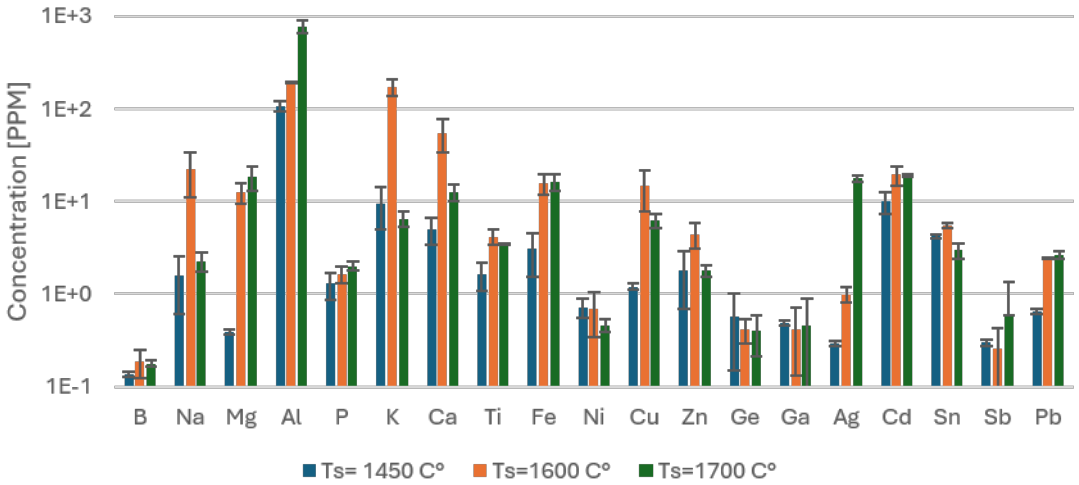

Figure 10 Final compositions of silicon melts measured by GDMS analysis, error bars indicate standard deviation.

The condensate formed during the experiments was collected and their masses are presented in Table II. These values can be used to calculate the mass flux. The 1600 °C sample deviates from the expected trend of increasing mass as temperature increases. The sample mass 1600 °C is significantly lighter than both the 1450 °C and 1700 °C samples, indicating less vapor in contact with the condenser for this experiment.

Table II Mass of collected condensate.

Sample	Mass [g]
Ts = 1450 °C	0.175
Ts = 1600 °C	0.096
Ts = 1700 °C	0.230

The condensate compositions are presented in Figure 11. The concentration of the impurities are higher orders of magnitude in the condensate than in the metal, with the exemption of Ti. This indicates they are removed from the metal faster than silicon, and Ti evaporation is insignificant as expected regarding its low vapor pressure (Fig. 1). The ratios between silicon and the different elements informs the relative flux α independent of the mass of the collected condensate. Higher temperatures correspond to lower silicon concentrations, indicating higher selectivity, mostly dominated by the increase in aluminum concentration. In a non-equilibrium reaction, a higher selectivity results in higher purity and silicon yield. K concentration is below the detectable limit for GDMS analysis despite the high concentration in the melt, and high volatility. The condensate also contained a detectable concentration of Ge, Ga and Cd which was absent from the analyses of the silicon metal. The presence of C in the condensate can be explained by the decomposition of the organic binder in the graphite or thermal insulator.

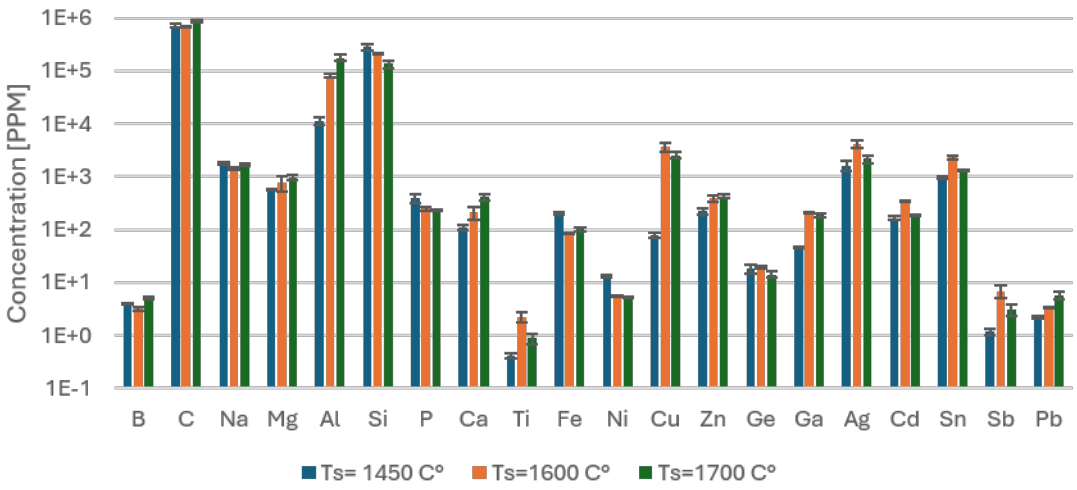

Figure 11 Composition of condensate by GDMS analysis.

5. DISCUSSION

5.1 Evaluating analysis

It is apparent that the measured initial concentrations of the samples varied. This may be explained by the presence of contaminants or from inhomogeneity in the samples. Figure 9 indicates that the inhomogeneity of the sample is a significant issue and sample melted at 1450°C contains more of some metallic impurities (Fe, Cu, Zn, Ag, Sn), while the sample melted at 1600°C contains more of the elements that are often in glass (Na, Al, K, Ti). The impact of this is exasperated by the low concentration, approaching the detectable limit of GDMS. As the concentrations are at ppm levels, the concentration of the melt is affected by even a small particle of the glass or a particle that has more metallic components. Hence, it is important to consider the initial composition of the melts for further calculations rather than the average composition presented in Figure 9. The condensate concentrations are multiple orders of magnitude greater than the corresponding metal samples and are useful for calculating mass flow.

The challenge for using the condensate is the sample collected quantity. When combining pyrometry and collection, time spent measuring temperature should therefore be subtracted from holding time. Furthermore, as can be seen in Figure 8b, there is a chance condensate could flake off and fall back into the crucible. This could potentially have caused the low mass of the condensate of the 1600 °C experiment and could explain the outlier concentration of Na, K, and Cu in this sample. However, no particles were found on the surface of the solidified sample, and this may or may not have occurred.

Considering experimental design, the flat condensing surface could have caused scattering of high volatility elements such as K, P, Zn and Pb. By texturing the surface, scattered particles would collide with the condenser multiple times before escaping to the furnace chamber. In theory of vacuum metallurgy, it is usually assumed that the atoms colliding with the cold surfaces are getting deposited due to losing the kinetic energy. However, the outer surface of the deposited layer may have high temperature and so these elements are scattered due to still high vapor pressure and kinetic energy. Texturing of the condenser surface would also double the effective surface area, improving adhesion thereby reducing the risk of scaling. Similarly, increasing the distance from the crucible opening, and size of the condenser, the area would reduce the heat flux, minimizing the vapor loss to the chamber.

There is a possibility of the vapor bypassing the condenser plate, however, the distribution of condensate on the cold plate shows a strong concentration towards the center (directly above the melt surface) and the gap between the crucible and condenser is small making this impact negligible. A larger concern is surface effects from the crucible, as the temperature of the crucible wall in upper position is lower than the molten silicon, and insignificant condensation was observed on the crucible top.

5.2 Mechanism of mass transfer in the system

The apparent mass flow of impurities into both the metal and condensate such as for aluminum, is improbable and challenges the calculation of mass transfer coefficients. A possible explanation of this is the presence of a slag phase, possibly formed from the small glass fragments, below micrometer size and the passivated layers of the wafer. This slag is a silicate phase that usually contains Na, Mg, Ca, Al, K, Ti, and some trace elements. Oxides from glass residue and passive layers such as SiO_2 and Al_2O_3 could contain the impurities detected. Given the composition and distribution as presented in Table I and incomplete separation during sorting, this is reasonable. The samples that were analyzed were taken from the bottom of the molten metal, where the suction of the melt to the quartz tube sampler was done. Therefore, the presence of a floating slag layer on top of the silicon melt would not be represented in the samples analyzed.

A thin slag layer would impact the flux in a non-linear way, as the slag layer consists of lower volatility oxides and may form a capping layer on the molten silicon as seen in Figure 12. Initially at low temperature of 1450 °C, the slag is semi-solid and clumps along the edges of the crucible. At higher temperature such as 1600 °C the slag thins and covers more of the silicon, reducing its effective surface area and therefore preventing the evaporation of the species from the melt surface. Figure 9 shows that the silicon for the test at 1600 °C has more elements that the slag contains (Na, K, Ca, and Al) than the test at 1450 °C. This indicates that we may have more slag for the test at 1600 °C and hence more Na, K, Ca and Al were transported to the silicon melt. Hence, less evaporation occurred for the test at 1600 °C, and it yielded less deposit mass on the condenser surface.

For the test at 1700 °C, there were lower concentrations of Na, Al, Ca, K than in the metal tested at 1600 °C as seen in Figure 9, and this may indicate less glass contamination and associated slag phase before the vacuum refining. However, for 1700 °C, the largest mass of the deposit on the condenser was observed. This means more evaporation in comparison with the test at 1600 °C. As for 1700 °C, the slag is more reactive with the silicon melt and causes deoxidation of the molten system (slag + metal) through the formation of SiO gas in the system. Hence, we may conclude that at higher temperatures, the silicon oxide is reduced forming SiO and CO gas, thereby slag is removed and so we have the increase of the evaporating area for the elements. This may cause a higher condensate mass for the test at 1700 °C, while the concentration of the components is not different from the other temperatures (Figure 11).

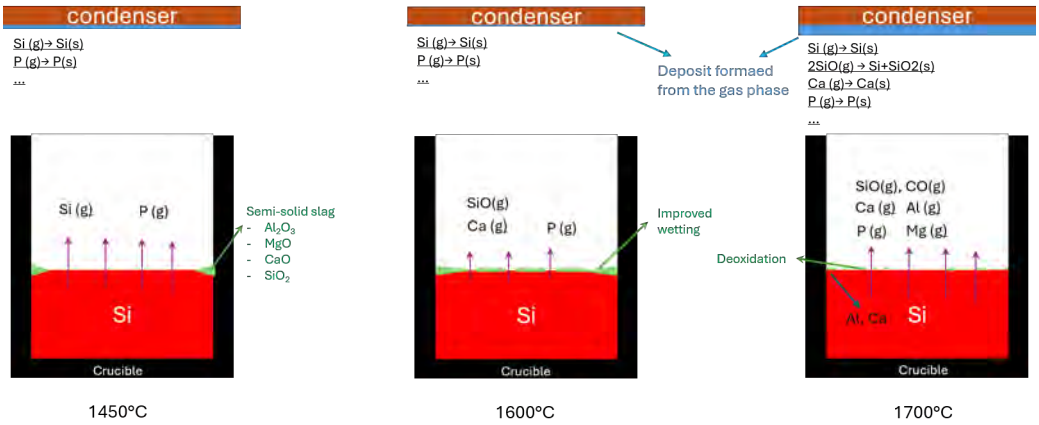

Figure 12 Schematic of the impact of a slag layer on the rate of evaporation as a function of temperature, and some typical condensation reactions from the vapor.

This mechanism is supported by thermodynamic calculations using HSC chemistry 10 (Metso, 2020) as seen in Figure 13 using a reference composition of 1mol Si, 1 mol C, and 0.1 mol of the slag components. The system changes around 1710 °C as deoxidation occurs as described by equations [6] to [9], forming SiO and CO. There is an equilibrium of metal and slag below the deoxidizing temperature, but with no oxide evaporation. The values can be considered representative of the activities and thereby evaporation rate.

$$SiO_2(l) + Si(l) = 2SiO(g) \quad [6]$$
$$SiO_2(l) + C(s) = SiO\ (g) + CO\ (g) \quad [7]$$
$$3Si(l) + Al_2O_3(s) = 3SiO\ (g) + 2Al(l) \quad [8]$$
$$Al_2O_3(s) + 3C(s) = 2Al + 3CO\ (g) \quad [9]$$

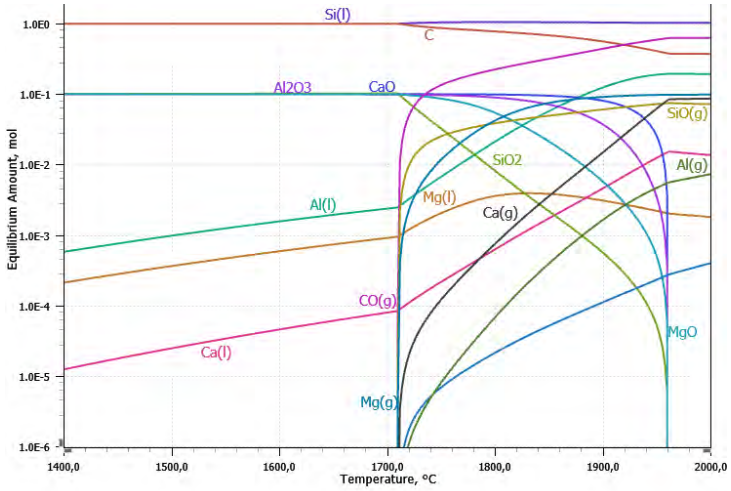

Figure 13 Equilibrium diagram of simulated Silicon-Slag system, calculated using HSC Chemistry.

5.3 Mass transport

The purity of the final product can be described by the measured concentrations of the treated sample as seen in Figure 10 or by applying the mass transfer regarding the condensate mass and composition. Considering the deoxidation reactions, slag elements simultaneous transport from slag to metal and evaporation from the metal would impact the evaporation rate calculated using the metal composition changes. This would also change the reaction order, as the concentration change is not only dependent on the evaporation rate. Figure 14 presents the composition of the melt as calculated by subtracting the mass of the elements in the condensate from the mass of the elements in the initial metal. Al and Cu reached negative, near zero values indicating more than complete removal or that those elements may originate from the slag. Cu might be explained by contamination from the copper plate while Al might be explained by the underrepresentation in the initial composition due to the slag layer or alumina in the feed silicon components seen in Table I. The change in elements such as B, Ti, Fe, and Ni is minimal as expected for the elements as they have low volatility compared with Si. Na, Mg, P, and Ga seem to drop at 1700 °C as expected from slag elements due to the slag reduction and the evaporation of the elements under vacuum. Compared with the samples from the melt, it indicates that K is still removed while not condensation on the condenser. The flux of the elements is high enough to significantly impact the purity of the sample positively, even in the given conditions.

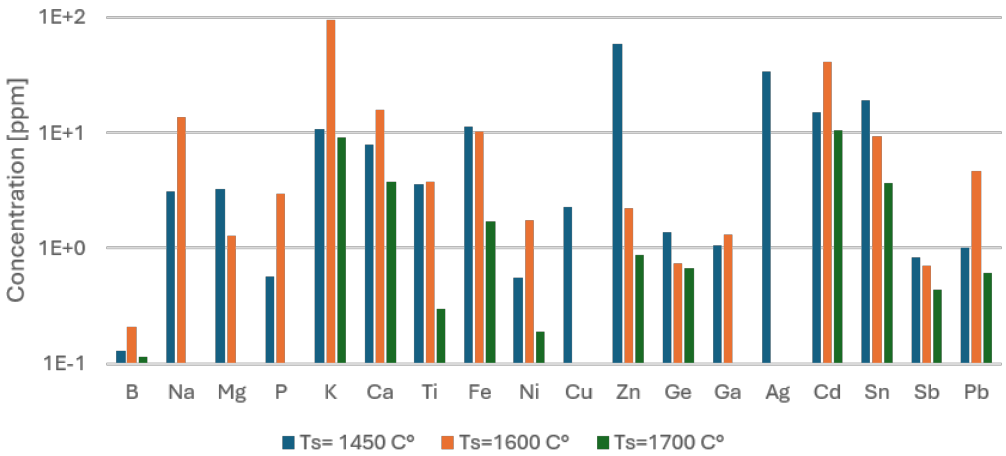

Figure 14 Calculated final composition of silicon using starting composition and mass transfer from condensate data, absent bars indicate negative values.

Assuming the collected condensate samples are representative, and a minimum of vapor was lost before collection, despite the unexpectedly low condensate mass from the 1600 °C experiment, the approximate mass transport coefficients can be calculated following equation [4]. The final composition of the metal is first calculated using the mass of the condensate, subsequently multiplying the concentration of the element with the mass of the condensate, dividing by time, thereby obtaining the mass flux of the element.

The flux can then be divided by initial concentration, area and density. The resulting mass transfer coefficients are presented in Figure 15. There is a correlation between increasing temperature and mass transfer. The values for the elements B and Ni, and Pb are higher than expected, being higher than silicon despite their vapor pressures being lower than silicon. Comparing the experimental mass transfer coefficients with theoretical ones is difficult as medium pressure regimes as this study are not well modelled. The usefulness of these conditions for vacuum refining is questionable as the impact of the process is limited. Deeper understanding of these medium vacuum environments as described by (Hoseinpur et al., 2021) is needed to improve selectivity. It is worth to note that in literature, most studies are on silicon samples without slag (glass) and the existence of small amount of glass in the feed is affecting the chemistry of the system and the surface of the melt.

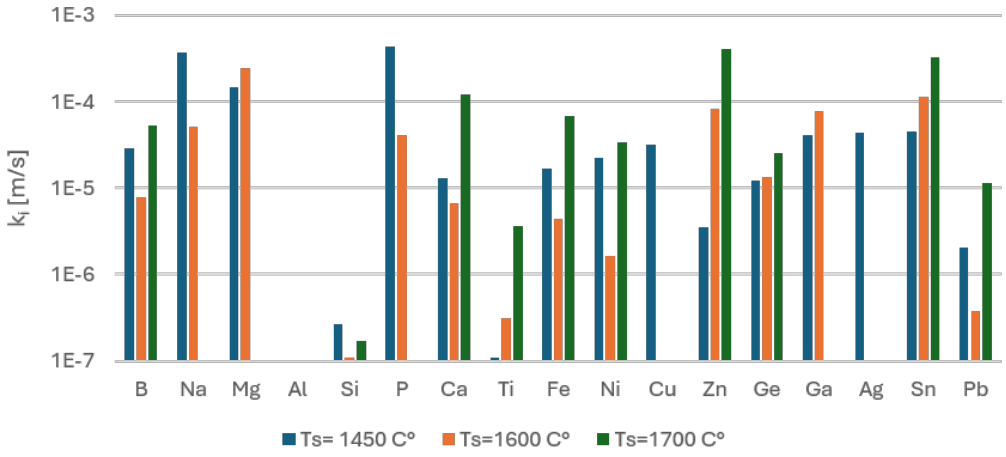

Figure 15 The overall mass transfer coefficients k_i calculated from mass and composition of condensate. Absent values indicate infinite, due to excess concentration in the condensate.

The mass transfer coefficient can also be calculated from the change in concentration in the metal for the purpose of corroboration. It is assumed that there is no change in silicon mass, which is appropriate as the relative mass change is minimal. The resulting plot in Figure 16 is sparse, indicating negative values reflecting an increase in concentration. Though being sparse indicating, disregarding the negative values, that the approximate magnitude is similar for most elements. Aluminum consistently increased in concentration as it is expected to have higher mass transport of Al (from slag or other components of EoL Si) to the silicon melt than its evaporation under vacuum. When comparing the mass transfer coefficient between the condensate and metal, the lower values for known volatiles such as K, Ca, Zn, and Pb in the condensate might indicate scattering caused by inadequate gas cooling performance. These elements have lower condensation temperatures and higher vapor pressures, and hence more chance to leave a condensate over the furnace chamber or reach the vacuum pump.

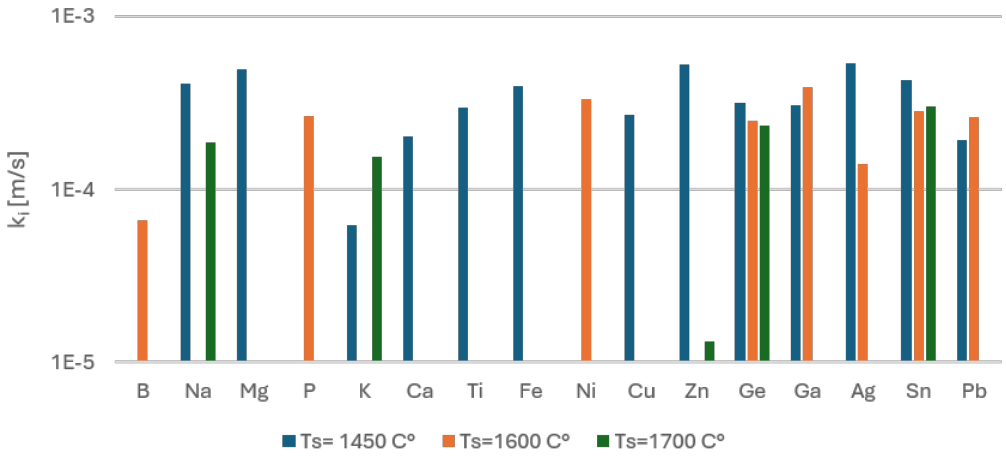

Figure 16 Mass transfer coefficients k_i calculated from the change in metal composition. Absent values indicate negative mass transfer.

6. CONCLUSION

This study demonstrates that vacuum refining is a viable technique for purification and recycling EoL PV silicon waste, evaporating volatile dopants and metallic impurities. Exploiting the differences in vapor pressures, the technique is still useful for already pure samples.

- Most of the impurities in the EoL PV Si particles are removed via the vacuum induction refining process at elevated temperatures.
- The mass transfer coefficients calculated for the experiments were higher than the theoretical values, probably due to complexity due to the existence of an adjacent thin molten slag phase.
- Mass transfer coefficients increase with increasing temperature, and lower values for many elements (B, Na, Si, P, Ca, Fe, Ni and Pb) at 1600 °C is attributed to silicon melt coverage with a molten slag.
- The applied novel method of vapor collection yields improved chemical resolution, with issues regarding complete sample collection.
- Increased temperature improved silicon yield and higher purity, and at 1700 °C it yielded the highest purification with insignificant silicon loss.
- Holding time at current conditions is insufficient for achieving high purity silicon, and longer time is needed to reach promising purity.
- Condensate samples provided more reliable data for mass transfer evaluation than the change in metal composition.
- A slag layer should be considered for the purpose of vacuum refining EoL PV Si as this can impact evaporation rate by limiting the effective area of the evaporating metal. The removal of glass particles prior to vacuum refining is crucial.

7. ACKNOWLEDGEMENTS

The authors gratefully acknowledge the financial support from the European Union to Apollo EU project in Horizon Europe program under the grant number of 101122277.

8. REFERENCES

Chen, P.-H., Chen, W.-S., Lee, C.-H., Wu, J.-Y., Chen, P.-H., Chen, W.-S., Lee, C.-H. and Wu, J.-Y., 2023. Comprehensive Review of Crystalline Silicon Solar Panel Recycling: From Historical Context to Advanced Techniques. *Sustainability*, [online] 16(1). https://doi.org/10.3390/su16010060.

Di Sabatino, M., 2014. Detection limits for glow discharge mass spectrometry (GDMS) analyses of impurities in solar cell silicon. *Measurement*, 50, pp.135–140. https://doi.org/10.1016/j.measurement.2013.12.024.

Frischknecht, R., Itten, R., Sinha, P., De Wild-Scholten, M., Zhang, J., Heath, G. and Olson, C., 2015. *Life Cycle Inventories and Life Cycle Assessments of Photovoltaic Systems*. [online] p.NREL/TP--6A20-73853, IEA-PVPS-TASK-12, IEA-PVPS-12-04:2015. https://doi.org/10.2172/1561526.

Ghosh, D.K., Bose, S., Das, G., Acharyya, S., Nandi, A., Mukhopadhyay, S. and Sengupta, A., 2022. Fundamentals, present status and future perspective of TOPCon solar cells: A comprehensive review. *Surfaces and Interfaces*, 30, p.101917. https://doi.org/10.1016/j.surfin.2022.101917.

Granata, G., Pagnanelli, F., Moscardini, E., Havlik, T. and Toro, L., 2014. Recycling of photovoltaic panels by physical operations. *Solar Energy Materials and Solar Cells*, 123, pp.239–248. https://doi.org/10.1016/j.solmat.2014.01.012.

Harris, R. and Davenport, W.G., 1982. Vacuum distillation of liquid metals: Part I. Theory and experimental study. *Metallurgical Transactions B*, 13(4), pp.581–588. https://doi.org/10.1007/BF02650015.

Hoseinpur, A., Andersson, S., Tang, K. and Safarian, J., 2021. Selective Vacuum Evaporation by the Control of the Chemistry of Gas Phase in Vacuum Refining of Si. *Langmuir*, 37(24), pp.7473–7485. https://doi.org/10.1021/acs.langmuir.1c00876.

Lozac'h, M., Nunomura, S. and Matsubara, K., 2020. Double-sided TOPCon solar cells on textured wafer with ALD SiOx layer. *Solar Energy Materials and Solar Cells*, 207, p.110357. https://doi.org/10.1016/j.solmat.2019.110357.

Malhotra, C.P., Mahajan, R.L. and Sampath, W.S., 2006. High Knudsen Number Physical Vapor Deposition: Predicting Deposition Rates and Uniformity. *Journal of Heat Transfer*, 129(11), pp.1546–1553. https://doi.org/10.1115/1.2712855.

Metso, 2020. *HSC Chemistry 10*. Available at: <https://www.metso.com/portfolio/hsc-chemistry/>.

Mukai, K. and Yuan, Z., 2000. Measurement of the Density of Molten Silicon by a Modified Sessile Drop Method. *Materials Transactions, JIM*, 41(2), pp.323–330. https://doi.org/10.2320/matertrans1989.41.323.

Safarian, J. and Tangstad, M., 2012a. Kinetics and Mechanism of Phosphorus Removal from Silicon in Vacuum Induction Refining. 31(1), pp.73–81. https://doi.org/10.1515/htmp.2011.143.

Safarian, J. and Tangstad, M., 2012b. Vacuum Refining of Molten Silicon. *Metallurgical and Materials Transactions B*, 43(6), pp.1427–1445. https://doi.org/10.1007/s11663-012-9728-1.

Sharma, R., 2019. Effect of obliquity of incident light on the performance of silicon solar cells. *Heliyon*, 5(7), p.e01965. https://doi.org/10.1016/j.heliyon.2019.e01965.

Sundaram, S., Benson, D. and Mallick, T.K., 2016. Chapter 2 - Overview of the PV Industry and Different Technologies. In: *Solar Photovoltaic Technology Production*. [online] Academic Press. pp.7–22. https://doi.org/10.1016/B978-0-12-802953-4.00002-0.

Vodapally, S.N. and Ali, M.H., 2022. A Comprehensive Review of Solar Photovoltaic (PV) Technologies, Architecture, and Its Applications to Improved Efficiency. *Energies*, [online] 16(1). https://doi.org/10.3390/en16010319.

Wade, A., Heath, G., Weckend, S., Wambach, K., Sinha, P., Jia, Z., Komoto, K. and Sander, K., 2016. *IRENA and IEA PVPS (2016) - End-of-Life Management: Solar Photovoltaic Panels*.

Jonas Låstad
PhD Candidate, NTNU

Jonas Låstad works as a part of the EU funded Apollo project researching techniques for recycling end of life PV silicon. Here he researches both hydrometallurgical and vacuum refining techniques of silicon. He completed his bachelor's degree in materials engineering at the Norwegian University of Science and technology with his work on hydrogen reduction of deep-sea manganese ore. He completed his master's degree at the same university with his work on production of electrolytic manganese dioxide from hydrogen reduced manganese ore.

Ernst, O. C., D. Uebel, and J. Acker. 2026. Isotopic Engineering of Silane: Scaling quantum grade 28SiH4 Synthesis for the Next Generation of Semiconductor Technologies. In *Silicon for the chemical and solar industry XVIII*, edited by M. Tangstad, H. Rong, A. Valderhaug, B. Andresen, H. Dalaker, and I. G. Page. Kristiansand, Norway, September 7–10, 2026. https://doi.org/10.55669/oa900805

Isotopic Engineering of Silane: Scaling quantum grade $^{28}SiH_4$ Synthesis for the Next Generation of Semiconductor Technologies

O. C. Ernst, D. Uebel, and J. Acker
Brandenburg University of Technology Cottbus-Senftenberg, Germany, owen.ernst@b-tu.de

Keywords: Isotopic Engineering, Silicon-28, Monosilane Synthesis, Quantum Technology, SiF_4 Conversion

Abstract –This work addresses a critical chemical bottleneck in quantum hardware scaling by demonstrating a high-purity, high-yield conversion from isotopically enriched silicon fluoride precursors to electronic-grade monosilane-28. An analytical framework for the synthesis and chemical vapor deposition (CVD)-validation of the isotopes are imperative to bridge the gap between specialized nuclear enrichment and global semiconductor fabrication, essential for the realization and scalability of fault-tolerant quantum computing.

While the chemical purification of natural silicon to electronic grade (9-11N) is a mature industrial process, the emerging field of 2nd generation quantum technologies impose new restrictions: the elimination of nuclear noise. Natural silicon contains ~4.7% of the stable isotope ^{29}Si, whose nuclear spin acts as a decoherence source for charge carrier spin states used as qubits. To enable fault-tolerant quantum computing, an industrial value chain for chemically and isotopically pure "quantum grade" ^{28}Si is required. Despite projections indicating that demand already surpasses 100 million USD annually, a scalable value chain for this critical material has yet to be developed.

This work revisits a pathway for the production and analytical evaluation of high quality ^{28}Si. Isotopic enrichment is achieved via gas counter current centrifugation of silicon tetrafluoride. The subsequent transformation into viable monosilane is a critical prerequisite for further processing. This is achieved using highly potent hydrogenation processes. Gas-Mass Spectrometry (G-MS) verify chemical quality of 4 N after chemical purification. The main contaminants are traced back to carbon residues from chemical conversion.

To validate the materials performance in a semiconductor environment, purified monosilane was used for the epitaxial growth of Si thin films via CVD. Secondary Ion Mass Spectrometry (SIMS) confirm the preservation of isotopic purity >99.9% throughout the deposition process and provide high-sensitivity depth profile of carbon contaminants.

1. INTRODUCTION

Isotopically engineered materials possess altered chemical and physical properties, rendering them attractive for various technical applications. One notable example of increasing relevance is the silicon-28 isotope (^{28}Si) and its precursor gas monosilane-28 ($^{28}SiH_4$).

^{28}Si is of crucial importance as a material platform for both spin-based quantum computing and spintronics (Ernst et al., 2022; Kane, 1998; Liu et al., 2022). The quality of the material platform is defined by its isotopic purity, as nuclear spins of odd-numbered isotopes such as ^{29}Si interact with the charge carrier spins via Fermi contact interaction and significantly reduce their decoherence time. Conversely, even-numbered isotopes, such as ^{28}Si, are characterized by a lack of nuclear spin ($\bar{I}$ =0 ħ). This is referred to in the literature as a "spin vacuum."

This work is licensed under the Creative Commons Attribution 4.0 International License. To view a copy of this license, visit https://creativecommons.org/licenses/by/4.0/

Reducing the ^{29}Si content from 4.7 % to 1 ppm has been shown to result in an augmentation of the decoherence time from T_2=20 µs to T_2=60 s (Witzel et al., 2010).
Two-dimensional electron gases (2DEG) and hole gases (2DHG) at the interface of ^{28}Si heterostructures are used to isolate, manipulate and measure charge carrier spins, and ultimately use them as quantum bits (qubits – basic unit of information in a quantum computer). Electron spin qubits on 300-mm Si-wafers already exhibit high fidelity values of >99% (two-qubit control fidelity and measurement fidelity), thereby demonstrating the principle scalability of the approach (Steinacker et al., 2025). However, the coherence of the systems is currently limited to T_2^{echo}≈100–800 ms (Scappucci et al., 2021; Witzel et al., 2010; Zwerver et al., 2022). The underlying reason is the present low material quality of isotopically pure ^{28}Si, which is required for the production of the qubits. In this paper, "isotopically pure ^{28}Si" refers to silicon whose isotopic ^{28}Si content has been increased from 92.2 mol-% to at least 99.9 mol-%.

Furthermore, ^{28}Si possesses the highest thermal conductivity ever measured for a dielectric. At 450 W/cm·K at 21 K, this value exceeds the conductivity of natural silicon (^{nat}Si) by a factor of 10 (Inyushkin et al., 2018, 2004). This renders the semiconductor attractive for low-temperature physics and microelectronic components with high heat generation.

Further applications are derived from the bandgap that is shifted by 58 meV (Karaiskaj et al., 2001). High-energy measurements have been shown to provide a more precise fine structure of the non-phononic photoluminescence lines of bound excitons, which result, for example, from B-doping. The optimized fine structure in the photoluminescence spectrum can be used for high-resolution studies of exciton processes in isotopically pure materials, for example in quantum sensing.

The value chain for ^{28}Si is characterized by its complexity and high cost. It necessitates the implementation of elaborate enrichment and chemical conversion processes, resulting in a distinctive chemical fingerprint. The resulting impurities reduce the coherence time of the charge carriers (Itoh and Watanabe, 2014; Witzel et al., 2010): The T_2^{echo} time decreases from 60 s to 200 ms at donor concentrations C_E=1.2×10^{14} /cm^3 with 1 ppm ^{29}Si.

Until 2022, material was globally procured from Russia through individual R&D channels. Political realities following Russia's invasion of Ukraine, characterized by geopolitical tensions and the imposition of trade restrictions, lead to a critical supply and material shortage. For industrial manufacturers, these issues present a technical and economic challenge, stemming from limited availability and inadequate material quality. The shortage lead to elevated prices, regularly exceeding 100 EUR/g for silicon-28-tetrafluoride ($^{28}SiF_4$), and 1'000 EUR/g for $^{28}SiH_4$ and ^{28}Si (Ernst et al., 2026). Its current research demand already supersedes 15 million EUR annually in Europe with the outlook to grow to 100 million EUR annually until 2030. Projections indicate that the global demand already surpasses 100 million USD annually, which corresponds to an annual volume of 100 kg.

A critical bottleneck in the value chain concerns the chemical transformation from industrially available silicon-28-tetrafluoride ($^{28}SiF_4$) to $^{28}SiH_4$ and other chemical vapor deposition (CVD) precursor materials, since this is the only step not covered by a commercial institution. Reliable instrumental methods for cost-effective purification and ensuring the chemical and isotopic purity of ultra-pure gases are still missing.

The limited availability of ^{28}Si has recently been classified as a "key vulnerability" by the Transatlantic Quantum Community (TQC) in 2025. The report *Critical Vulnerabilities in the*

Quantum Computing Supply Chain within the NATO Alliance (2025) recommends "[to] develop an understanding of the key requirements needed to support the fabrication of semiconductor spin systems, including any specialized requirements for the successful integration of isotopically pure ^{28}Si into the process flow."
In this paper, we provide a concise overview of the complex value chain for isotopically pure semiconductors and the synthesis methods for $^{28}SiH_4$ methods that have been employed to date. Laboratory-synthesized $^{28}SiH_4$ is analyzed for its chemical and isotopic purity and deposited as ^{28}Si layers using a rudimentary thermal CVD setup. Secondary ion mass spectrometry (SIMS) measurements of the layer provide a quantitative basis for demonstrating its chemical quality. The chemical quality of the layer exceeds the chemical quality of Russian samples reported in the literature and is sufficiently high to produce quantum bits from it.

2. MAJOR SECTION

2.1 Value chain

2.1.1 Isotopic separation

A multitude of physical methods have been developed for the purpose of isotopic enrichment (Ernst et al., 2024). However, from an economic standpoint, the use of counter-current gas centrifuges has proven to be the most viable option to date.

In gas centrifuges, isotopic enrichment is achieved by exploiting the mass-dependent inertia of molecules. Isotope separation is achieved using rotating cylinders. A gas introduced into the cylinders is subjected to continuous acceleration. The resulting inertial force, denoted by F, can be calculated using the simple equation

$$F = M v^2 r^{-1} \quad [1]$$

(with M – molar mass; v – rotational velocity; r – radius of the cylinder)

and ensures isotope separation.

Enrichment of ^{28}Si is typically carried out using SiF_4, as it is among the limited number of Si compounds that meets the critical chemical and physical requirements (Borisevich and Levin, 2001; Levin, 1994):

i. The vapor pressure of the substance in question must exceed 5–10 mmHg (≙ 0.7–1.3 kPa), as enrichment requires a stable gaseous source.

ii. The substance must not undergo chemical reactions with the materials of the enrichment chamber, which are typically stainless steel or specialized high-temperature alloys.

iii. For sufficient enrichment, the molecular mass of the molecules must not be less than 40 u. SiH_4, with a molecular mass of 32 u, is therefore not suitable. It has been demonstrated that higher molecular masses generally result in higher enrichment rates and lower energy consumption.

iv. The substance to be enriched must exhibit sufficiently high thermal stability.

v. No chemical reaction should occur between the molecules of the substance intended to be enriched. Anion exchange or atom exchange would result in incomplete enrichment.

Modern gas centrifuges, also known as ZIPPE or KAMENEV centrifuges, consist of vertically rotating cylinders typically made of carbon fiber-reinforced steel with a cylinder radius of 5 cm and reaching rotational speeds of 750 m/s and higher (Kushner, 2013). High rotational speeds are achieved by a rotating magnetic field that sets the cylinder itself in rotation. A force of up to 12,000 eVm (>1,000,000 g) acts on each SiF_4 molecule. This force is counteracted by a pressure gradient between the gas compressed against the cylinder wall and the vacuum generated at the axis of rotation. If the pressure at the wall is excessively high due to elevated circulation speeds, the gas may condense on the walls of the centrifuge.

In the counter-current centrifuge, in addition to the gas flow from the inside to the outside, a vertical pressure difference arises that pushes the molecules near the axis of rotation downward (or upward). By heating the cylinder head and altering the geometry of the cylinder's interior, a counter current can be generated that maintains or even amplifies the internal pressure differences. The flow generates horizontal zones within the cylinder. In each zone, horizontal enrichment occurs from the inside (light molecules) to the outside (heavy molecules). Due to the vertical pressure difference, the heavy molecules are gradually transferred to the zone above (or below), while the light molecules migrate to the zone on the opposite side. The degree of enrichment increases with each additional zone.

Two strategies were pursued in the past. On the one hand, many short centrifuges can be connected. The degree of enrichment can be increased by connecting the centrifuges in series, and throughput can be increased by connecting them in parallel. This technical solution is highly adaptable and allows for swift adjustments to system parameters or product requirements. The second strategy on the other hand is based on a small number of tall centrifuges. These enable the generation of multiple enrichment zones within a single cylinder. As a result, the process is accelerated and requires fewer maintenance-intensive individual components. Additionally, contamination from cylinder walls and gas lines is minimized. A challenge associated with this method pertains the stability of the tall cylinders. When the rotary motors start up, the bending frequencies of the cylinders must be overcome. Cylinders longer than 1 m are susceptible to critical deformation if they are not stabilized.

Urenco Ltd. is the world's largest producer of isotopically pure materials and relies exclusively on counter-current gas centrifuges. Only the enrichment plants of the Russian TVEL Fuel Company, a subsidiary of the state-owned Atomenergoprom Group, possess a comparable production capacity. Both Urenco and TVEL have demonstrated that they can achieve enrichment levels of $^{28}SiF_4$ up to 99.9999%.

Alternative isotope separation methods include gas thermodiffusion, laser separation, cyclotrons, and air nozzle processes (Ernst et al., 2026, 2024).

2.1.2 Chemical conversion

$^{28}SiF_4$ is not generally considered suitable for the majority of industrial CVD processes. One reason for this is the molecule's exceptionally high negative standard formation enthalpy (<-1500 kJ/mol (Sukkaew et al., 2016)). The Si-F bond is regarded as the strongest single bond ever measured. A variety of other silane species, including monosilane SiH_4 and trichlorosilane $HSiCl_3$, are employed in industrial settings as CVD precursors.

The transformation of inert fluorides into isotopically pure semiconductor precursors poses a particular challenge (Figure 1). The chemical reduction of $^{28}SiF_4$ has been the subject of scientific inquiry since the 1960s as a method for producing $^{28}SiH_4$.

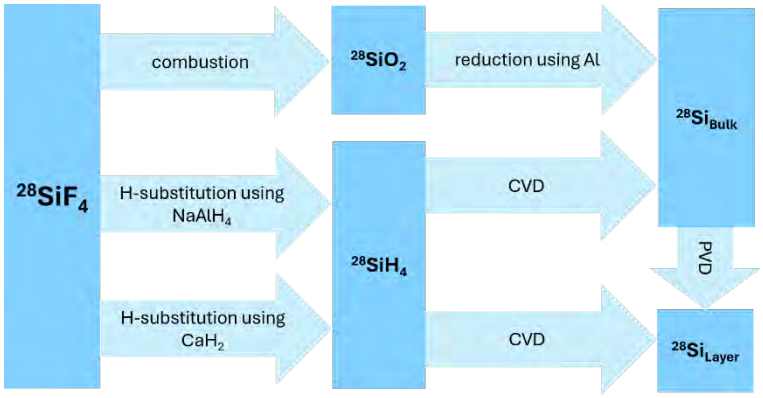

Figure 1: Strategies for the synthesis of $^{28}SiH_4$ and ^{28}Si starting from $^{28}SiF_4$.

In general, the quantitative conversion of semimetal halides (MXy) into their hydrogen compounds (MHy) is possible using hydrides (AHx).

$$MX_y + AH_x \rightarrow MH_y + AX_x \quad [2]$$

In the literature, conversions were executed using dissolved alkali hydrides containing aluminum (Al), lithium (Li), sodium (Na), or combinations thereof. However, the necessary dissolution of these hydrides in organic solvents such as dimethyl ether, diethylene glycol, or tetrahydrofuran result in indelible C-impurities (Devyatykh et al., 2003; Sennikov et al., 2015).

Alternatively, solid calcium hydride (CaH_2) can be brought into reaction with $^{28}SiF_4$ directly, thereby circumventing the introduction of critical impurities (Bulanov et al., 2008, 2004, 2002).

$$2\ CaH_2 + {}^{28}SiF_4 \rightarrow 2\ CaF_2 + {}^{28}SiH_4 \quad [3]$$

However, this conversion method is hindered by the high $^{28}SiF_4$ pressures necessary to attain sufficient reaction velocity and consequently the necessity for extensive safety measures.

2.2 Chemical and isotopic purity from literature

The enrichment of $^{28}SiF_4$ is feasible on an industrial scale, and the material is available on the global market for less than 500 EUR/g from companies such as Urenco Ltd. or Orano S.A.. The challenge lies in the chemical conversion of the fluoride to $^{28}SiH_4$ and ^{28}Si (Ernst et al., 2024).

Initial experiments were conducted in the United States in 1958 (Gordon and Bowers, 1958). The primary strategy entailed the conversion of $^{28}SiF_4$ to $^{28}SiO_2$, followed by reduction with aluminum powder at a temperature of 1100 °C.

$$^{28}SiF_4 + O_2 \rightarrow {}^{28}SiO_2 + 2\ F_2 \quad [4]$$

$$3\ {}^{28}SiO2 + 4\ Al \rightarrow 3\ {}^{28}Si + 2\ Al_2O_3 \quad [5]$$

The method was revived in 1994 in an American-Russian-German study. $^{28}SiO_2$ was sourced from the Oak Ridge National Laboratory (ORNL) and the Russian National Metrology Institute (NMI) (Becker et al., 2010, 2009). It is noteworthy that the NMI material was discarded due to high levels of impurities of unknown origin, while the ORNL material was reduced using the Al method described above in a collaboration between the Physikalisch-Technische Bundesanstalt (PTB) and Wacker-Chemitronic in Germany. The resulting ^{28}Si crystals, with a mass of 300 g, exhibited high impurity levels of C (1.3×10^{17} cm^{-3} / 2.6 ppm), O (1.1×10^{16} cm^{-3} / 0.22 ppm), and B (10^{18} cm^{-3} / 20 ppm).

In experiments conducted in the 1980s and 1990s, reduction was carried out using lithium aluminum hydride ($LiAlH_4$) and sodium aluminum hydride ($NaAlH_4$) (Ulmer et al., 1982). However, the resulting fluoride salts cause the solvent to become sludgy, making the implementation and scaling of these processes technically very difficult. Furthermore, the solvent introduces organic solvents that can act as carbon sources—electrically active donors in silicon. Furthermore, metals present in silicon exhibit electrical activity, necessitating sophisticated and expensive purification process. However, yields of over 99% have been reported (Sennikov et al., 2015, 2010).

Progress was achieved using the approach in which solid CaH_2 was used for reduction. Given the high cost of $^{28}SiF_4$, efficiency plays a pivotal role. For the CaH_2 approach, efficiencies of up to 90% have been reported (Bulanov et al., 2004; Sennikov et al., 2015, 2010).

Table I: A selection of isotopically pure silicon compounds from the literature, alongside a comparison of their purities with those in this study. Chemical impurities are measured either in SiH_4 gas (ppm) or in solid Si (cm^{-3}). However, these measurements cannot be directly compared.

	reference	compound	producer	method of synthesis	isotopic purity	chemical impurities
1	(Sennikov et al., 2010)	$^{28}SiH_4$	Russian Federal State Institution of Science Institute of Chemistry of High-Purity Substances (IChHPS)	CaH_2 / cryo-filtration/ ultra-purification	99.9 %	< 1ppm
2	this work	$^{28}SiH_4$	Brandenburg Technical University (BTU)	$LiAlH_4$	>99.9 %	0.12 % H_2O 200 ppm CO_2 80 ppm CH_4 < 10 ppm other
3	(Becker et al., 2010)	^{28}Si	ORNL / Wacker-Chemitronic	$^{28}SiO_2$-reduction	99.99 %	1.3×10^{17} cm^{-3} C 1.1×10^{16} cm^{-3} O 10^{18} cm^{-3} B
4	(Becker et al., 2009)	^{28}Si	IChHPS / Leibniz Institute of Crystal Growth (IKZ)	CaH_2 / CVD /Float zone	99.9999 %	< 10^{15} cm^{-3}
5	(Liu et al., 2022)	^{28}Si	IChHPS / Leibniz Institute of Crystal Growth (IKZ)	CaH_2 / CVD / Float zone	99.9 %	10^{18} – 10^{20} cm^{-3} C
6	this work	^{28}Si	BTU / [qgm]	$LiAlH_4$ /CVD	>99.9 %	10^{17} – 10^{19} cm^{-3} C

It has been observed that both the $NaAlH_4$ process as well as the CaH_2 process are affected by SiF_4 residues and CO_2 and CH_4 impurities (Sennikov et al., 2010). Due to their high vapor pressures, these impurities remain even during cryogenic distillation. In order to achieve the required level of chemical purity, a series of purification steps, collectively referred to as "ultrapurification", were implemented. These steps included cryofiltration and the separation of light and heavy fractions. These processes, in turn, result in a lower overall yield.

2.3 Experimental results and discussion

2.3.1 Synthesis and characterization of as-synthesized $^{28}SiH_4$

To replicate and verify literature values, $^{28}SiH_4$ was synthesized from $^{28}SiF_4$ in a laboratory-scale setup using $LiAlH_4$. The synthetic route closely follows previously published protocols (Ernst et al., 2025, 2026; Ulmer et al., 1982). To archive this, gaseous $^{28}SiF_4$ was sparged through a solution of $LiAlH_4$ in anhydrous tetrahydrofuran (THF) under an inert atmosphere. Efficient gas-liquid mixing can be ensured by utilizing a fine-pored glass frit or a Venturi system. Due to the exothermic nature of the reaction, continuous colling was applied to maintain the internal temperature strictly below the boiling point of THF (66°C). The detailed chemical procedure can be adopted from these references. The gas quality was analyzed using a GSD 320 Omnistar gas mass spectrometer (Pfeiffer Vacuum GmbH.).

The initial gas mass spectrometry analysis of the as-synthesized gas confirmed the successful formation of $^{28}SiH_4$. As illustrated in Figure 2, the mass spectrum exhibits prominent peaks at m/z=15,16,18,28,29,30,31,32,42,44,62,85. Quantitative evaluation of the impurity profile reveal that the as-synthesized gas contains significant volatile contaminants, predominantly tetrahydrofuran THF (9,4 %), methane (1,9 %), water (0,42 %), and carbon dioxide (0,39 %). THF is used as solvent for the $LiAlH_4$-agent and remains at the vapor phase after the primary reaction stage. Likewise, the methane likely originates from the solvent. The origin of the significant levels of water and carbon dioxide is not clear but may be attributed to minor atmospheric leaks within the experimental setup and residues inside the setup. While no distinct signals for molecular oxygen or nitrogen were resolved, trace amounts may be masked by the dominant $^{28}SiH_x^+$ fragmentation (m/z = 28–32) or rapidly consumed via reaction with $^{28}SiH_4$ prior to reaching the detector of the mass spectrometer.

The conversion of $^{28}SiF_4$ to $^{28}SiH_4$ is almost complete. It has been determined that only 0.35 mol% of $^{28}SiF_4$ is detectable in the as-synthesized gas. This corresponds to a chemical yield of approximately 99.6%. As a potential byproduct of the reaction, traces of disilane Si_2H_6 (21 ppm) were detected.

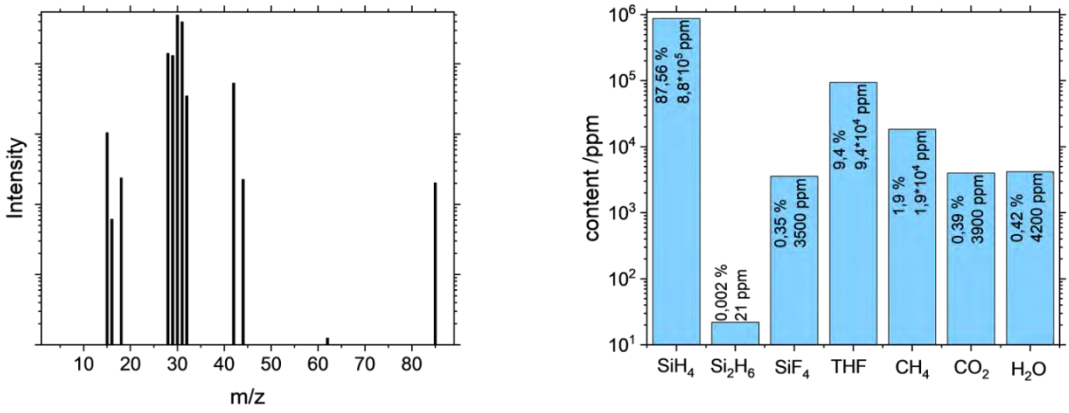

Figure 2: Results of the gas mass spectrometry analysis of the as-synthesized SiH_4. The contaminants likely originate from the $LiAlH_4$ solvent, unreacted SiF_4, and minor gas leaks.

2.3.2 Purification of $^{28}SiH_4$

To meet the stringent purity requirements for subsequent CVD deposition, the as-synthesized gas was subjected to cryogenic distillation at a temperature of 180 K. Since the boiling point of SiH_4 lies at 168 K, it is expected that all high-boiling impurities will be frozen out.

The post-purification mass spectrum (Figure 3) demonstrates a substantial reduction in all volatile impurities, shifting the baseline closer to or even below the detection limit. Specifically, THF, SiF_4 and Si_2H_6 content dropped below the detection limit of 10 ppm. Even though the boiling point of methane is lower than 180 K, the methane concentration also dropped by more than two orders of magnitude to 80 ppm. It is likely that a significant portion of the methane is redissolve in the frozen THF.

The concentrations of water (0.12%) and carbon dioxide (200 ppm) remain high. This supports the hypothesis that this contamination is caused by small leaks in the laboratory setup or residue on the setup wall.

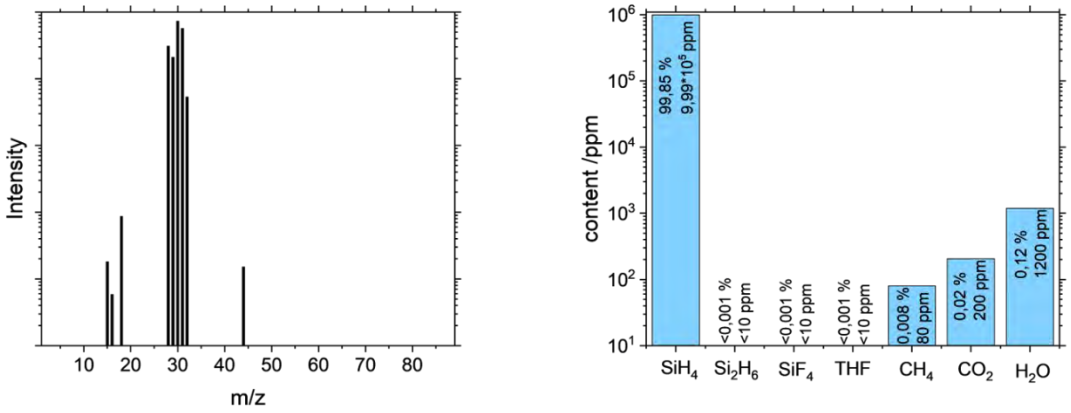

Figure 3: Results of the gas mass spectrometry analysis of the purified SiH_4. Purification was performed at 168 K.

2.3.3 Thin-film deposition and Secondary Ion Mass Spectrometry

As gas-phase mass spectrometry is primarily sensitive to chemical impurities rather than isotopic variations and the detection limits are rather high, the purified $^{28}SiH_4$ was subsequently deposited as a solid thin film.

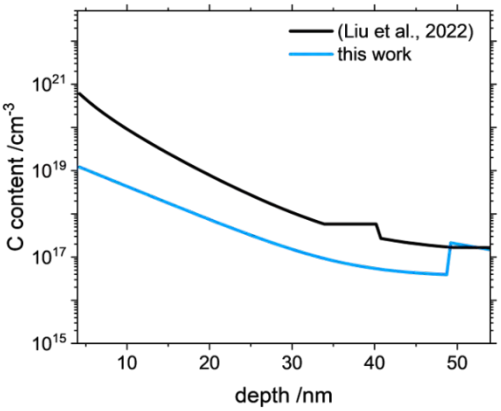

Figure 4: Results of the SIMS analysis for Carbon Content of Si layers deposited from the purified SiH_4 in comparison with previous results.

A CVD process was conducted within a quartz tube furnace at 650°C for a duration of 10 min. The substrates used in this study were HF-dipped 1×1 cm^2 Si(100) wafers. The resulting Si-layers exhibit a thickness of approx. 50 nm and were subjected to analysis by Secondary Ion Mass Spectrometry (SIMS) utilizing a Cameca ims 4f-E6 (Cs^+, 14.5 eV, SI^-) to analyze the critical C impurities.

As illustrated in Figure 4, the layers exhibit a C content ranging from 10^{17} cm^{-3} to 10^{18} cm^{-3} (5 ppm to 50 ppm). These impurities are attributed to CH_4, which deposits heavily alongside SiH_4. In a previous study (Liu et al., 2022), we obtained purified $^{28}SiH_4$ from the Russian IChHPS and deposited the material. In the initial 50 nm of the layer, a C content ranging from 10^{19} cm^{-3} to 10^{20} cm^{-3} (0,05 % to 0,5 %) was measured. Therefore, we cannot confirm the very low carbon content of the Russian material (<1 ppm) reported in the literature for the sample we received.

The isotopic content was also measured (Figure 5). It has been demonstrated that the isotopic purity of the source $^{28}SiH_4$, respectively $^{28}SiF_4$, can be transferred to the ^{28}Si layers. The isotopic distribution in natural silicon is as follows: 92.3% ^{28}Si, 4.7% ^{29}Si, and 3.0% ^{30}Si. In the $^{28}SiF_4$ employed as the source material, the ^{28}Si content was enriched to 99.9%. The isotopic composition of the deposited ^{28}Si sample was found to be approximately 0.01% ^{29}Si and 0.001% ^{30}Si, which corresponds to the purity in the $^{28}SiF_4$ source. Thus, it has been demonstrated that the chemical conversion of $^{28}SiF_4$ to $^{28}SiH_4$, followed by CVD deposition as ^{28}Si, does not result in the introduction of measurable isotopic impurities. Therefore, the process preserves isotopic purity.

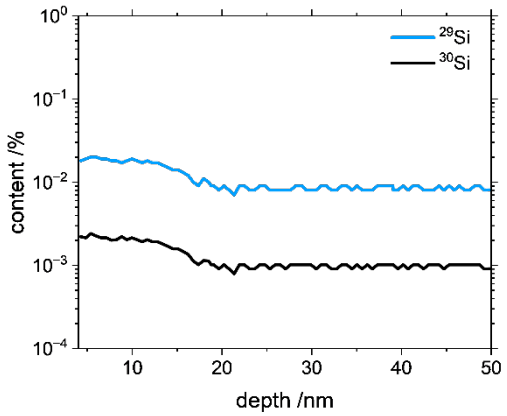

Figure 5: Results of the isotopic SIMS analysis of deposited Si layers from (Liu et al., 2022).

3. CONCLUSIONS

^{28}Si is a critical raw material that will become increasingly important as second-generation quantum technologies approach maturity. However, to date, no Western company has succeeded in establishing commercial-scale production of ^{28}Si or $^{28}SiH_4$ to supply the market with the 100 kg per year currently needed. Despite the existence of established processes for the enrichment of $^{28}SiF_4$, the subsequent conversion to $^{28}SiH_4$—and particularly its purification—remains challenging.

In this study, we have shown that $^{28}SiH_4$ can be synthesized using $LiAlH_4$ utilizing the synthesis protocols from literature. However, the C impurities introduced by the necessary

solvent, particularly CH_4, cannot be removed without multi-step cryofiltration and fractionation. This observation is consistent with reports in the literature.

A comparison of our material with Russian-produced material, manufactured using the CaH_2 process, shows that our material has a carbon content that is 1.5 to 2 orders of magnitude lower. However, the literature frequently describes lower carbon content measurements, which were generally preceded by additional solid-phase purification via Float Zone.

In this study, we also demonstrated that the isotopic purity of $^{28}SiF_4$ can be transferred to both $^{28}SiH_4$ and, in the subsequent CVD step, to ^{28}Si layers.

Based on these results, the $LiAlH_4$ route has the potential to yield high-quality $^{28}SiH_4$. However, in order to render the material suitable for utilisation within the semiconductor industry, reliable purification methods must be employed that, in contrast to established methods, do not result in a significant reduction in the overall process yield.

4. ACKNOWLEDGEMENTS

This work was funded by the EXIST research transfer project 03EFBB0063 HoCHQuant, supported by the German Federal Ministry for Economic Affairs and Energy and the ESF.

5. REFERENCES

Becker, P., Friedrich, H., Fujii, K., Giardini, W., Mana, G., Picard, A., Pohl, H.-J., Riemann, H., Valkiers, S., 2009. The Avogadro constant determination via enriched silicon-28. Meas. Sci. Technol. 20, 092002. https://doi.org/10.1088/0957-0233/20/9/092002

Becker, P., Pohl, H. -J., Riemann, H., Abrosimov, N., 2010. Enrichment of silicon for a better kilogram. physica status solidi (a) 207, 49–66. https://doi.org/10.1002/pssa.200925148

Borisevich, V.D., Levin, E. V., 2001. SEPARATION OF MULTICOMPONENT ISOTOPE MIXTURES BY GAS CENTRIFUGE. Sep. Sci. Technol. 36, 1697–1735. https://doi.org/10.1081/SS-100104759

Bulanov, A.D., Balabanov, V. V., Pryakhin, D.A., Troshin, O.Yu., 2002. Preparation and Fine Purification of SiF4 and 28SiH4. Inorganic Materials 38, 283–287. https://doi.org/10.1023/A:1014735203351

Bulanov, A.D., Mikheev, V.S., Troshin, O.Yu., Lashkov, A.Yu., 2008. Reaction of silicon tetrafluoride with calcium hydride as a propagating wave. Russian Journal of Inorganic Chemistry 53, 6–10. https://doi.org/10.1134/S0036023608010026

Bulanov, A.D., Moiseev, A.N., Troshin, O.Yu., Balabanov, V. V., Isaev, D. V., 2004. Fine Purification of Monoisotopic Silanes 28SiH4 , 29SiH4 , and 30SiH4 via Distillation. Inorganic Materials 40, 555–557. https://doi.org/10.1023/B:INMA.0000031984.83652.87

Devyatykh, G.G., Dianov, E.M., Bulanov, A.D., Troshin, O.Yu., Balabanov, V. V., Pryakhin, D.A., 2003. Preparation of High-Purity Monoisotopic Silane: 28SiH4, 29SiH4, and 30SiH4. Doklady Chemistry 391, 204–205. https://doi.org/10.1023/A:1025380518197

Ernst, O., Uebel, D., Boeck, T., 2025. EP000004486690A1: METHOD FOR PRODUCING ISOTOPE-ENRICHED GERMANIUM-HYDROGEN COMPOUNDS.

Ernst, O.C., Liu, Y., Boeck, T., 2022. Leveraging dewetting models rather than nucleation models: current crystallographic challenges in interfacial and nanomaterials research. Zeitschrift für Kristallographie-Crystalline Materials 237, 191–200.

Ernst, O.C., Uebel, D., Brendler, R., Handschick-Ernst, A., Acker, J., 2026. Halbleiter für Quantumcomptuting: Wertschöpfung und chemischer Fingerabdruck. AMA Service GmbH, Von-Münchhausen-Str. 49, 31515 Wunstorf, Germany, pp. 80–83. https://doi.org/10.5162/iCCC2026/4.6

Ernst, O.C., Uebel, D., Brendler, R., Kraushaar, K., Steudel, M., Acker, J., Kroke, E., 2024. Silicon-28-Tetrafluoride as an Educt of Isotope-Engineered Silicon Compounds and Bulk Materials for Quantum Systems. Molecules 29, 4222.

Gordon, J.P., Bowers, K.D., 1958. Microwave Spin Echoes from Donor Electrons in Silicon. Phys. Rev. Lett. 1, 368–370. https://doi.org/10.1103/PhysRevLett.1.368

Inyushkin, A. V, Taldenkov, A.N., Ager III, J.W., Haller, E.E., Riemann, H., Abrosimov, N. V, Pohl, H.-J., Becker, P., 2018. Ultrahigh thermal conductivity of isotopically enriched silicon. J. Appl. Phys. 123, 095112. https://doi.org/10.1063/1.5017778

Inyushkin, A. V, Taldenkov, A.N., Gibin, A.M., Gusev, A. V, Pohl, H.-J., 2004. On the isotope effect in thermal conductivity of silicon. physica status solidi (c) 1, 2995–2998. https://doi.org/https://doi.org/10.1002/pssc.200405341
Itoh, K.M., Watanabe, H., 2014. Isotope engineering of silicon and diamond for quantum computing and sensing applications. MRS Commun. 4, 143–157. https://doi.org/10.1557/mrc.2014.32
Kane, B.E., 1998. A silicon-based nuclear spin quantum computer. Nature 393, 133–137. https://doi.org/10.1038/30156
Karaiskaj, D., Thewalt, M.L.W., Ruf, T., Cardona, M., Pohl, H.-J., Deviatych, G.G., Sennikov, P.G., Riemann, H., 2001. Photoluminescence of Isotopically Purified Silicon: How Sharp are Bound Exciton Transitions? Phys. Rev. Lett. 86, 6010–6013. https://doi.org/10.1103/PhysRevLett.86.6010
Kushner, D., 2013. The real story of stuxnet. IEEE Spectr. 50, 48–53. https://doi.org/10.1109/MSPEC.2013.6471059
Levin, E. V., 1994. Separation of multicomponent isotopic mixtures in a gas centrifuge — approximate method for solving the system of diffusion-transport equations and analysis of some separation characteristics. Atomic Energy 77, 760–767. https://doi.org/10.1007/BF02415435
Liu, Y., Rinner, S., Remmele, T., Ernst, O., Reiserer, A., Boeck, T., 2022. 28Silicon-on-insulator for optically interfaced quantum emitters. J. Cryst. Growth 593, 126733. https://doi.org/https://doi.org/10.1016/j.jcrysgro.2022.126733
Scappucci, G., Taylor, P.J., Williams, J.R., Ginley, T., Law, S., 2021. Crystalline materials for quantum computing: Semiconductor heterostructures and topological insulators exemplars. MRS Bull. 46, 596–606. https://doi.org/10.1557/s43577-021-00147-8
Sennikov, P.G., Kornev, R.A., Abrosimov, N. V., 2015. Production of stable silicon and germanium isotopes via their enriched volatile compounds. J. Radioanal. Nucl. Chem. 306, 21–30. https://doi.org/10.1007/s10967-015-4192-4
Sennikov, P.G., Kotkov, A.P., Adamchik, S.A., Grishnova, N.D., Chuprov, L.A., Ignatov, S.A., 2010. Impurities in monosilanes synthesized by different processes. Inorganic Materials 46, 358–363. https://doi.org/10.1134/S0020168510040072
Steinacker, P., Dumoulin Stuyck, N., Lim, W.H., Tanttu, T., Feng, M., Serrano, S., Nickl, A., Candido, M., Cifuentes, J.D., Vahapoglu, E., Bartee, S.K., Hudson, F.E., Chan, K.W., Kubicek, S., Jussot, J., Canvel, Y., Beyne, S., Shimura, Y., Loo, R., Godfrin, C., Raes, B., Baudot, S., Wan, D., Laucht, A., Yang, C.H., Saraiva, A., Escott, C.C., De Greve, K., Dzurak, A.S., 2025. Industry-compatible silicon spin-qubit unit cells exceeding 99% fidelity. Nature 646, 81–87. https://doi.org/10.1038/s41586-025-09531-9
Sukkaew, P., Ojamäe, L., Kordina, O., Janzén, E., Danielsson, Ö., 2016. Thermochemical Properties of Halides and Halohydrides of Silicon and Carbon. ECS Journal of Solid State Science and Technology 5, P27–P35. https://doi.org/10.1149/2.0081602jss
Ulmer, H.E., Pickens, D., Rahl, F.J., Lefrancois, P.A., 1982. Producing silane from silicon tetrafluoride . US4407783A.
Witzel, W.M., Carroll, M.S., Morello, A., Cywiński, Ł., Sarma, S. Das, 2010. Electron spin decoherence in isotope-enriched silicon. Phys. Rev. Lett. 105, 187602.
Zwerver, A.M.J., Krähenmann, T., Watson, T.F., Lampert, L., George, H.C., Pillarisetty, R., Bojarski, S.A., Amin, P., Amitonov, S. V, Boter, J.M., Caudillo, R., Correas-Serrano, D., Dehollain, J.P., Droulers, G., Henry, E.M., Kotlyar, R., Lodari, M., Lüthi, F., Michalak, D.J., Mueller, B.K., Neyens, S., Roberts, J., Samkharadze, N., Zheng, G., Zietz, O.K., Scappucci, G., Veldhorst, M., Vandersypen, L.M.K., Clarke, J.S., 2022. Qubits made by advanced semiconductor manufacturing. Nat. Electron. 5, 184–190. https://doi.org/10.1038/s41928-022-00727-9

Dr. Owen C. Ernst
Research project lead, Brandenburg University of Technology Cottbus-Senftenberg
CEO, quantum grade materials [qgm] GmbH

Owen C. Ernst holds degrees in chemistry and physical chemistry from Humboldt University in Berlin, Germany. He led the “Local Growth and Structure Formation of Semiconductors” research group at the Leibniz Institute for Crystal Growth. Since 2024, he serves as the research project lead for "Chemistry and Physics of Isotopically Engineered Semiconductors" at Brandenburg University of Technology Cottbus-Senftenberg. In 2026, he founded the university spin-off quantum grade materials [qgm] GmbH.

Vilatela, J. J., A. Pendashteh, I. Gómez-Palos, and R. Schäufele. 2026. Towards large-scale silicon nanowire paper fabrication for batteries. In *Silicon for the Chemical and Solar Industry XVIII*, edited by M. Tangstad, H. Rong, A. Valderhaug, B. Andresen, H. Dalaker, and I. G. Page. Kristiansand, Norway, September 7–10. https://doi.org/10.55669/oa900806

Towards large-scale silicon nanowire paper fabrication for batteries

Juan J. Vilatela[1,2] , Afshin Pendashteh, [1] Isabel Gómez-Palos[1,] Richard Schäufele[1]
[1] Floatech. S.L., Spain
[2] IMDEA Materials Institute, Spain
Juanjose.vilatela@floatech.eu

Keywords: battery, CVD, nanowire, paper, silane, aerogel, free space

ABSTRACT

Si anodes are a central material for the electrification of transport in coming decades, and strategic for Europe given its lack of battery critical raw materials. They can simultaneously increase battery performance and reduce graphite consumption. Si anodes can enable electric vehicle (EV) range near 1000km and charge times below 10 minutes, while reducing pressure of natural graphite, a critical raw material, on a scale of 100s of kilo tonnes per annum (ktpa). In the processes, this could prevent accumulated CO_2 emissions on mega tonne scale during battery manufacture. This presentation introduces a new method for continuous synthesis of a paper-like, freestanding material made up entirely of Silicon nanowires directly from thermocatalytic conversion of silane in a free space reactor, and its application in battery energy storage. It shows progress in the use of the Si nanowire (SiNW) paper as 100% Si anode in Li-ion batteries with high energy density and cyclability, meeting some market entry requirements.

BACKGROUND

Credited for nearly 30% of the reduction in greenhouse gas emissions, batteries are a key technology enabler to mitigate climate change. The lifetime emissions of an electric vehicle are about 80% lower than for an internal combustion engine. Their widespread use in portable electronics, defense and recently in stationary battery energy storage systems is driving battery growth at 20-30 % CAGR. In Europe alone, the accelerated transition towards electric-powered mobility and products requires a 20-fold increase in battery energy storage capacity demand from 2020, reaching around 1000 GWh/a by 2030 in Europe alone (Figure 1).

This work is licensed under the Creative Commons Attribution 4.0 International License. To view a copy of this license, visit https://creativecommons.org/licenses/by/4.0/

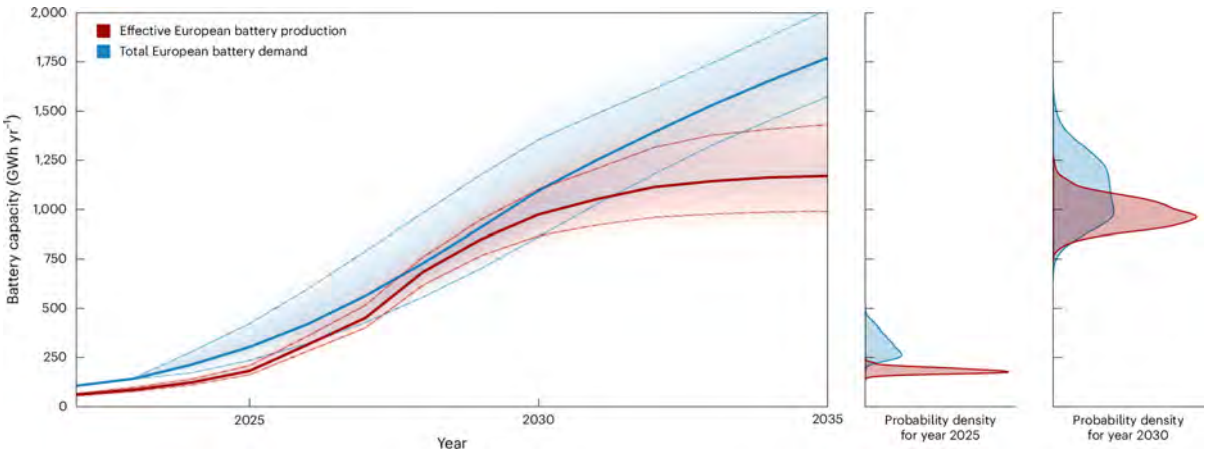

Figure 1. Projected European LIB demand. (1)

This European battery demand will require around 22 million tons per annum of different battery materials (Mtpa) by 2035. However, unlike the solar market which is dominated by a single material (Si), the battery market serves broad power/energy/cost scenarios that thus require different battery chemistries at large scale, each comprising several materials within, with a complex materials interrelation. To simplify, batteries can be visualised as layered devices allowing for multiple different combinations of constituents, but with some dominant ones. For transport and portable electronics lithium-ion batteries (LIB) are set to dominate for the next decades due to their performance. Their energy density is double that of the theoretical limit for sodium-ion batteries, for example.

In LIBs, the most significant upcoming changes are the incorporation of Si in the anode, and the elimination of solvents (in manufacture through dry-processing and in electrolytes in solid-state batteries). Si is a replacement for today's incumbent material, graphite, because of its superior performance, ease of manufacture and abundance. Whereas graphite stores lithium though intercalation of ions between its crystallographic planes ($Li + 6C \rightleftharpoons LiC_6$), silicon undergoes an alloying reaction that can store a much larger amount of Li ($15Li + 4Si \rightleftharpoons Li_{15}Si_4$). These mechanisms, result in Si having an accessible gravimetric capacity almost 10X greater than graphite (3500 mAh/g vs 372 mAh/g).

In addition to its 10-fold higher capacity, silicon is more abundant that graphite. Over 96% of both natural and synthetic battery graphite is produced and controlled by China, making it one of the most pressing critical raw materials (CRM) to replace in Europe and North America. The EU currently extracts less than 0.1% of its total needs. The recurrent introduction of export controls by graphite producers has exposed the sector's vulnerability (2), creating supply risks and potential price shocks.

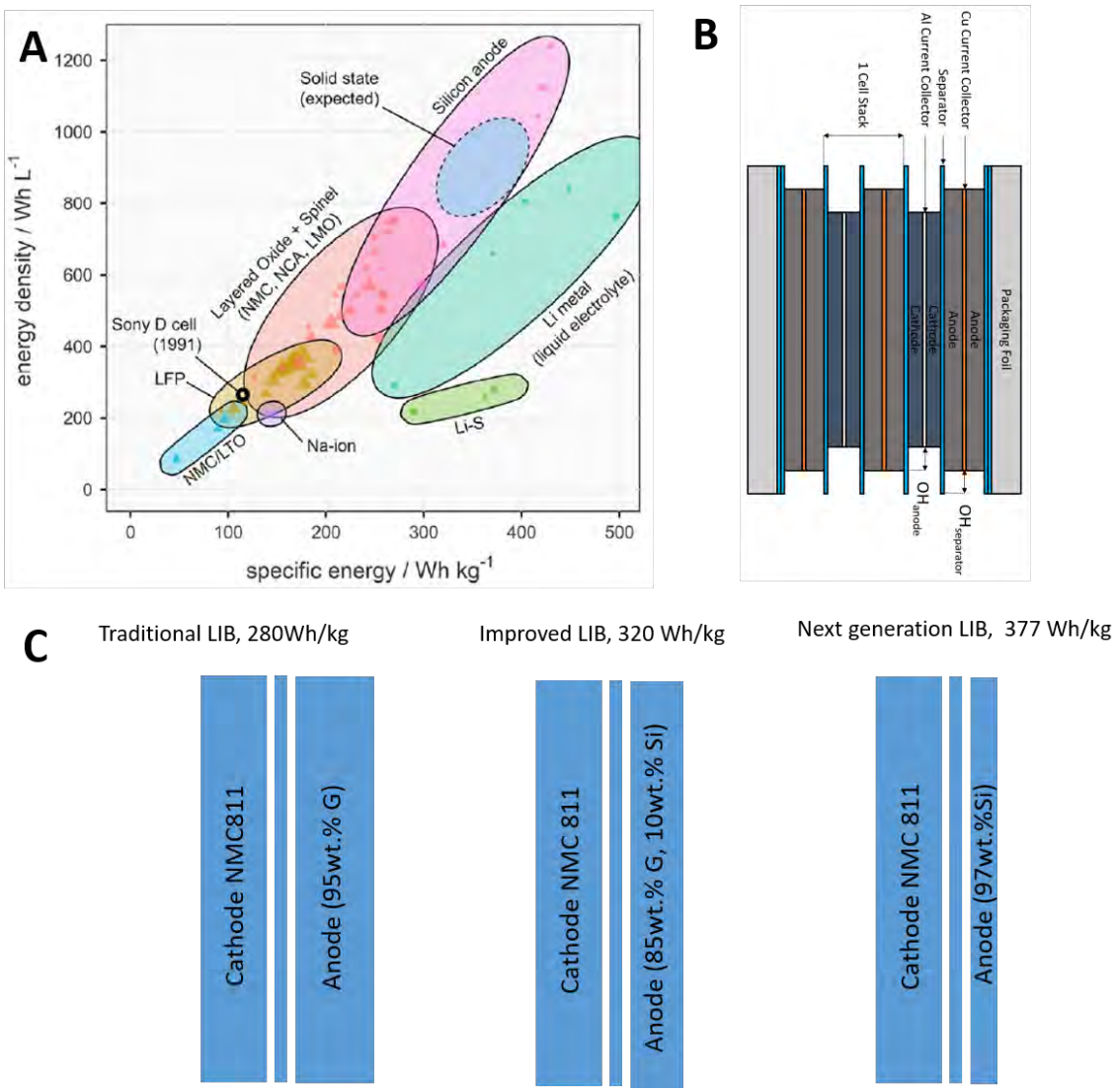

Figure 2. Si anodes for higher performance LIBs. A) Calculated cell energy densities for different battery chemistries. (3) B) Scheme of a prototypical cell (4) and C) comparison of cells with different anodes used in this analysis: conventional G, advanced Si+G, next generation Si. Cell scheme from reference.

TECHNOECONOMICS OF LIBS WITH DIFFERENT ANODES

Improvements in battery cell performance upon introduction of Si depend on multiple cell design parameter, particularly the choice of cathode material and extent of Si utilisation. Figure 2A shows the accessible performance of Si-containing batteries compared to other chemistries. Coupled with a high voltage cathode like Ni-rich layered oxides, at areal capacities above 5mAh/cm^2, full utilisation of an anode of 100% Si leads to cell energy densities above 350 Wh/kg and 1000 Wh/L, amongst the highest for any LIB. They translate into 1000 km and under 10min charge. These values have been recently realised in advanced battery cells starting commercialisation for premium applications (i.e. high performance and high margin). An alternative is to make a blend of graphite and ca. 10wt.% Si as anodes with capacity around 600 mAh/g (5). Blends are used commercially by several cell producers for portable electronics (6) and premium EVs (7).

We carry out a basic top-down technoeconomic analysis of battery silicon to meet 2030 European transport LIB demand. For this, we consider three types of hypothetical 58Ah EV cells: with 100% G, 10% Si & 90% G, and 100% Si, respectively. They are schematically shown in Figure 2B. The cell design is based on the Fraunhofer CellEst model, which enables extraction of realistic cell performance parameters and detailed composition. Their gravimetic energy density is 280 Wh/kg, 320 Wh/kg and 377 Wh/kg, respectively. They represent scenarios of business as usual, incremental improvement and accelerated Si adoption.

Table 1: Comparison of LIB anode technologies

FEATURES	GRAPHITE ANODE	ADVANCED GRAPHITE ANODE (10wt.% Silicon)	REPLACEMENT ANODE 100wt.% Silicon
Anode capacity	372 mAh/g	600 mAh/g	3,100 mAh/g
Cell Energy density	≈240 Wh/kg	>280 Wh/kg	> 350 Wh/kg
Mass anode required by 2030 to meet EU LIBs	550 ktpa	410 ktpa	67 ktpa
References for domestic EU production	1 ktpa natural graphite (2024) Projected 124 kpta synthetic graphite (2030)	1 ktpa natural graphite (2024) Projected 124 kpta synthetic graphite (2030)	400 ktpa Si production (2026)
Estimated price of finished anodes	€12 /kWh	€11/kWh	Under €10/kWh
Estimated embodied emissions levelized by energy stored	9.8 CO_2-eq/$kWh_{storage}$	7.5 CO_2-eq/$kWh_{storage}$	1.2 CO_2-eq/$kWh_{storage}$
Estimated embodied energy levelized by energy stored	66.5 $kWh_{production}$ /$kWh_{storage}$	48.6 $kWh_{production}$ /$kWh_{storage}$	6.6 $kWh_{production}$ /$kWh_{storage}$

For the three battery cell type we estimate the amount of anode required and their projected cost (at 2025 prices), embedded greenhouse gas emissions and embedded energy, levelized by electrochemical performance. The results are summarised in Table 1.

The technoeconomic analysis is carried through combination of four blocks: Si manufacture, cell performance and chemistry, cell manufacturing costs at EV scale, and projected European anode LIB demand, under these assumptions:

Si manufacture. Embedded emissions taken as 10 kg $CO_{2\text{-eq}}$/kg for graphite (average of natural 6 kg $CO_{2\text{-eq}}$/kg and synthetic 14 kg $CO_{2\text{-eq}}$/kg produced in China) (8), and 13 kg $CO_{2\text{-eq}}$/kg for metallurgical Si from China (6 kg $CO_{2\text{-eq}}$/kg for production in the EEA) (9). Emissions from further processing, either conversion of MG-Si to SiH4, or spheroidization and other treatments to make battery graphite, are assumed to be small compared to the initial chemical step and not included.

Cell performance and chemistry. The cell gravimetric energy density and full materials composition is calculated using the CellEst model for a 58Ah EV-type cell (10). The choice and areal capacity of the cathode are key parameters, as the cathode is the limiting electrode. We consider an NMC811 cathode with a high areal capacity of 6mAh/cm^2, in line with the trend of continuous increase in areal capacity communicated to Floatech by cell producers and OEMs. The choice of areal capacity explains the discrepancy with similar analysis done by others (11).
Cell manufacturing costs at EV scale. Detailed manufacturing costs (OPEX, CAPEX) are from the BatPac database of Argonne National Laboratory, which models costing for a 50GWh EV battery plant. The main information extracted is the cost distribution in manufacture of finished anodes of graphite, include the various stages of slurry preparation, coating, drying, etc.
Projected European anode demand for LIBs. European anode demand and the required mass of Si and/or G are calculated considering the projected increase in LIB demand, assuming 75% of LIB demand is for transport and Europe accounting for 33% of global Si market. Energy demand is converted into anode and materials demand data from the cell performance and chemistry module. European LIB demand is from references (12).

As seen in the table, European demand can be met with 67kpta of 100% Si, instead of 410 kpta of blends of 550kpta of G. For reference, we also include values for the domestic production of battery graphite and metallurgical Si. This shows that Europe produces 1/500 of its graphite demand, but nearly 10-fold more Si than needed for LIBs. Therefore, despite increased performance, blends of Si with graphite carry supply risks. In a blend, 1kg of Si requires 9kg of graphite. As a full anode, 1kg of Si replaces 10kg of graphite.

Because of its much higher capacity, the estimated levelized cost is approximately €10/kWh, which is below that of graphite. Similarly, the embedded emissions and energy are both nearly an order of magnitude lower for Si. The embedded emissions of anodes of 100% Si levelized by energy stored, are about 1/8 of those of anodes of graphite (Table 1).

Si ANODE PRODUCTION

Estimates of Si used in anodes are shown in Figure 3. It shows that Si went from marginal to kpta production in a few years. Most of today's capacity is for blends, produced from pyrolysis of monosilane. However, there is rapid progress in the development of new methods to manufacture Si-dominant anodes (>50wt.%) by a handful of startups and metallurgical Si producers. These companies are differently positioned along the production chain: from anode active material to anode production, to cell fabrication. The different manufacturing methods proposed include thin film deposition, crystal etching, microparticle jet-milling and thermocatalytic growth. The prevalent challenge for all these technologies is to demonstrate scalable, cost-effective manufacture of products that can be integrated in the next generation of batteries for widespread use. This landscape shows a clear trade-off: production at relatively large scale (tpa) is demonstrated for active material particles as an irregular powder, which thus need extensive postprocessing to make inks, slurries and anodes prior to cell integration. Alternative new methods apply direct fabrication of finished anodes from monosilane, enabling seamless integration of anodes in cells without any need for solvents, binders, etc. Yet, these disruptive alternative methods have currently lower production capacity.

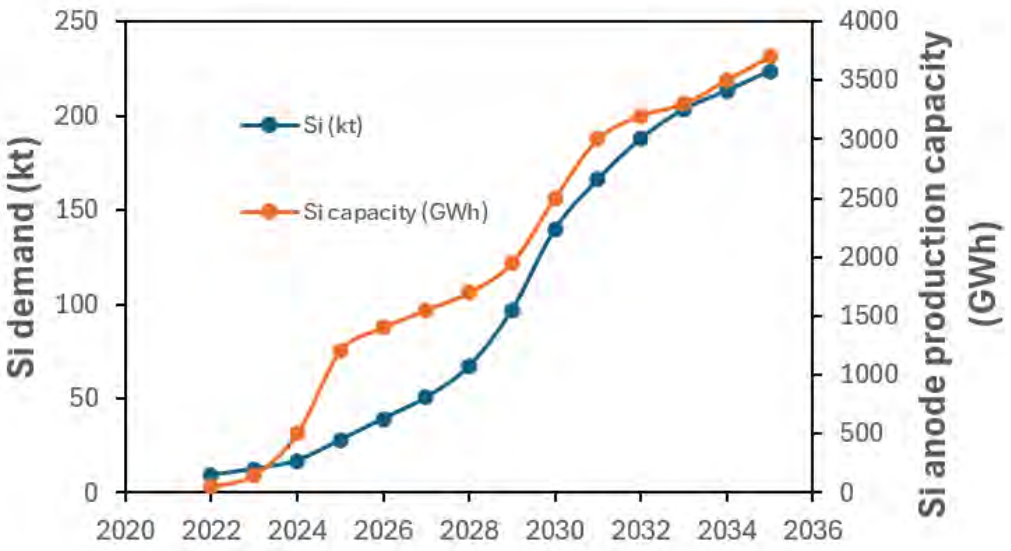

Figure 3. Estimated production of Si for LIBs, based on calculations adapted from Benchmark mineral intelligence report on Si anode production capacity and Si-based electrode market share forecast and other sources. A 10% Si content in composite electrodes is assumed, and an equivalence of 6.4 GWh/kt for Si considering highly optimised cells.

THE FLOATECH PROCESS: SILICON PAPER FROM FREE SPACE REACTORS

Floatech's manufacturing process consists in the thermocatalytic conversion of silane ($SiH_{4(gas)}$) as a precursor into a Si paper consisting of porous network of entangled nanowires. It is a single-step process, carried out continuously in a flow-through reactor. As a separate downstream processing step, the paper-like Si material collected at the reactor outlet is mechanically attached onto a copper foil (current collector used in batteries) to make a finished anode, which is then supplied to a battery producer to assemble battery cells. The manufacturing process is schematically shown in Figure 4.

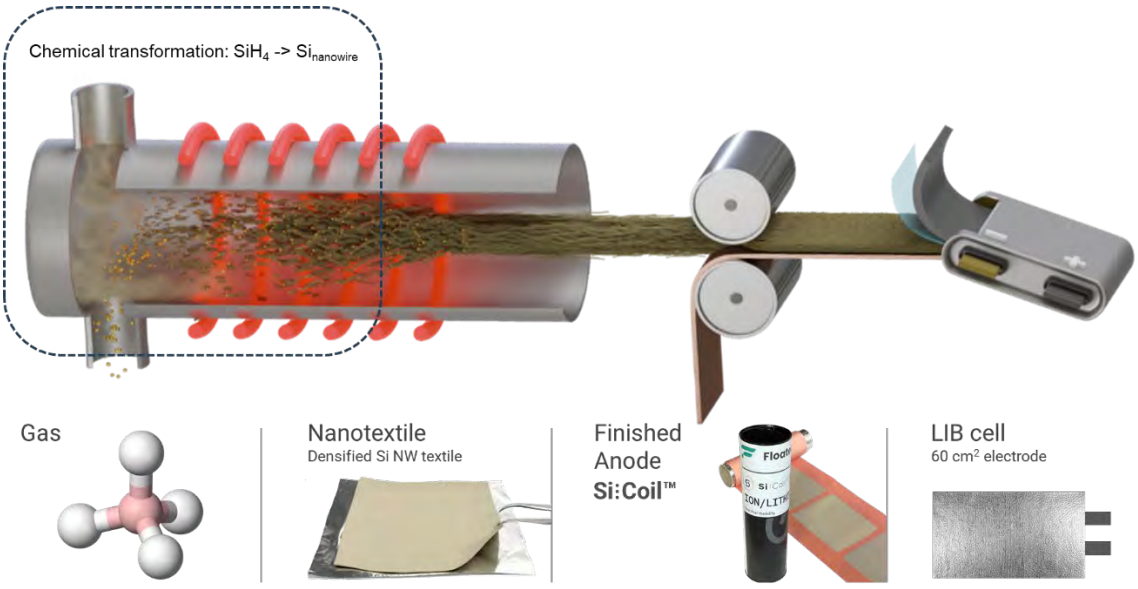

Figure 4. Overview of Floatech's manufacturing process whereby silane is thermocatalytically converted into a freestanding Si paper made of Si nanowires, which is then mechanically attached to a current collector to make a finished anode for battery cell assembly.

The key stage in the manufacturing process is the chemical transformation of silane into Si nanowires (SiNW), monocrystalline Si wires with nano-sized diameter and an aspect ratio of 55. Currently, the process is carried out by flowing reactants and gases through a hot wall tubular reactor at 650 °C. In the process a mixture of silane, a carrier gas and a catalyst aerosol have a residence time under 10s in the hot zone.

When the reactants approach the hottest part of the profile SiH_4 reacts to form an alloy with the metal nanoparticle (e.g. Si-Au). As the alloy particles supersaturate, a nanowire crystal layer nucleates, and growth of the nanowire continues provided Si incorporation into the alloy is maintained. This is known as the vapour-solid-liquid VLS mechanism. The metal nanoparticle acts as reservoir for Si, which is different from a traditional catalysts in that the nanoparticle undergoes a large chemical change during the reaction. It remains incorporated in the SiNWs.

Growth of the nanowire from the alloy particle occurs at very high rates, of the order of ~10-100 µm/s or 10^7 atoms/s, in a regime where the rate-limiting process is Si incorporation into the alloy and growth termination occurs through silane depletion. The nanowires have a diameter distribution reminiscent of that of the metal nanoparticles, and a log-normal length distribution with a mean of 1.5 µm. Because of their high aspect ratio and high concentration, the nanowires form an aerosol that evolves to form large agglomerates through diffusion-limited cluster aggregation (13) within the reaction tube and later super-agglomerates similar to flakes, visible by naked eye.

As a chemical route, Floatech's FCCVD method has a close resemblance to the free-space reactor (FSR) process for Si nanoparticle (SiNP) production. In FSR, Si nanoparticles are produced through nucleation from monosilane pyrolysis in the gas phase. The method was amply studied over the last decades. Through heat management and controlled precursor injection to prevent wall deposition, FSR monosilane conversion into SiNPs can reach over 99% and be scaled up to the industrial pilot level at hundreds of tpa (14). Work is in progress to demonstrate a similar scale-up path for SiNW growth in FSR.

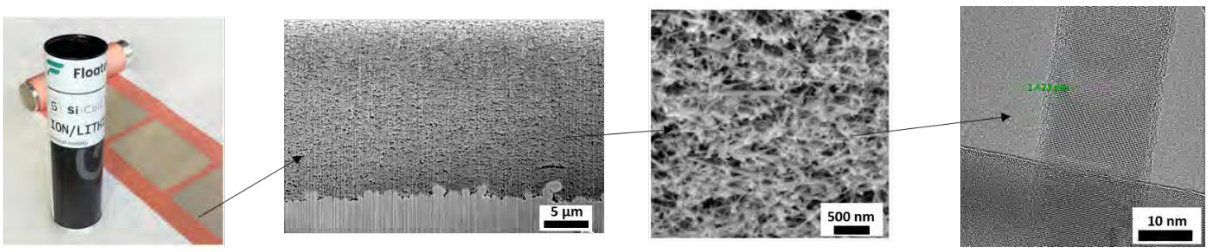

Figure 5. Paper-like silicon comprised of an interconnected network of Si nanowires. Photograph and cross-sectional electron micrographs of a finished anode before cell cycling.

Downstream of the reactor outlet SiNWs are collected as an aerogel on a conveyor belt. Upon mechanical densification the aerogel converts to a SiNW paper. The SiNW macroscopic material is freestanding, flexible and has tensile mechanical properties analogous to those of office paper (15). An example of a finished anode of SiNW on a Cu current collector is shown

in Figure 5. The electron micrographs (before cell cycling) show the interconnected network of nanowires and engineered porosity to supress cell expansion.

The SiNW anode can be directly integrated in a LIB cell. Its second cycle reversible gravimetric capacity is over 3000 mAh/g, depending on cell design and test conditions. Anode thickness can be easily adjusted during manufacture in the range 0.1 – 10 mAh/cm^2 (16). By way of example of performance in full cell, Figure 6 shows the capacity retention in a pouch cell with NMC cathode, SiNW anode and solid electrolyte. The N/P ratio is such that the cell is tested under nearly full Si utilization. This implies that the capacity retention is amongst the highest reported, meeting many market specifications and demonstrating that the full use of Si anodes to replace graphite in the next generation of LIBs is feasible and advancing at rapid pace.

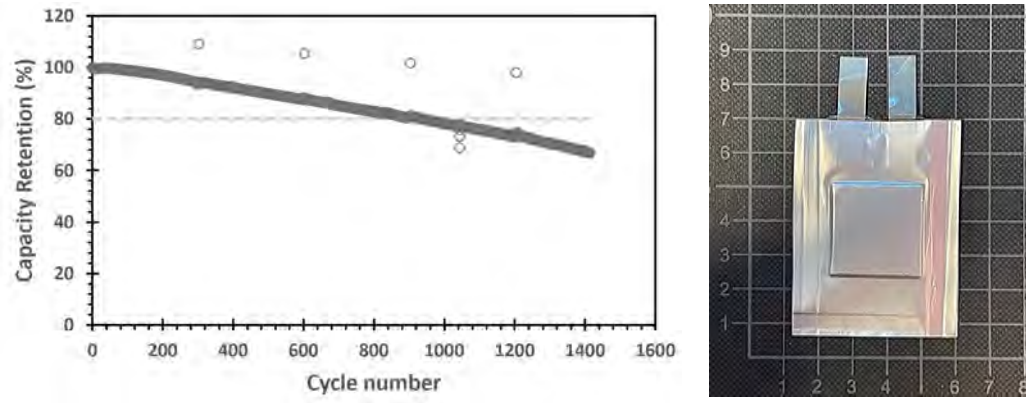

Figure 6. Electrochemical properties of battery cells with Floatech's Si anodes. Capacity retention of full cell with solid electrolyte. (17)

CONCLUSIONS

Silicon anodes are a key material to enable deployment of LIBs for electrification of transport and potentially for stationary storage in battery energy storage systems (BESS). For Europe, Si anodes offer an opportunity to meet battery demand with domestic production, while reducing embedded GHG emissions in anode manufacture.
Around 10% of Si is already blended with graphite to make improved anodes, used in commercial cells for portable electronics and premium EVs. Complete replacement of graphite with anodes of 100% Si will decrease battery time-to-charge and weight, while reducing external supply risks.
There are increasing demonstrations of prototype battery cells with 100% Si that meet market specifications. An example is shown of a solid-state battery with Floatech's SiNW anode reaching over 1000 deep cycles with more than 80% capacity retention, meeting one of the longstanding targets for EVs.
After performance demonstration, for producers of Si anodes the next challenge is scale-up to meet the exponentially growing demand, currently at ktpa and expected to reach Mtpa in ten years.

References

(1) https://www.nature.com/articles/s41560-025-01722-y
(2) https://www.iea.org/policies/17933-announcement-on-the-optimisation-and-adjustment-of-temporary-export-control-measures-for-graphite-items

(3) https://doi.org/10.1038/s41467-023-35933-2
(4) Energies, 12 (2019)
(5) https://iopscience.iop.org/article/10.1149/1945-7111/ac4545
(6) https://www.taiwannews.com.tw/news/6335800
(7) https://source.benchmarkminerals.com/article/teslas-silicon-battery-anode-tease-stands-out-but-what-is-the-commercial-reality
(8) https://source.benchmarkminerals.com/article/esg-of-graphite-how-do-synthetic-graphite-and-natural-graphite-compare; https://doi.org/10.1016/j.jclepro.2022.130474 ; https://www.sciencedirect.com/science/article/pii/S0959652622001172
(9) Journal of Sustainable Metallurgy. 2021, 7 848-857
(10) Energies 2019, 12(3), 504; https://doi.org/10.3390/en12030504
(11) https://www.linkedin.com/posts/rory-mcnulty_the-relationship-between-anode-silicon-activity-7358489521610493952-kZSa?utm_source=share&utm_medium=member_desktop&rcm=ACoAAD-Gt2oBppcL-mQsF4AlVtVX5qUSBG3dD4Y
(12) IEA 2024 Outlook for battery and energy demand, https://www.iea.org/reports/global-ev-outlook-2024/outlook-for-battery-and-energy-demand; Battery Cell Production Market Analysis, VDI/VDE Innovation + Technik GmbH, 2022
(13) Fractal Scaling in the Gas-Phase Agglomeration of Nanowires. Small 2409673, 2025. DOI: 10.1002/smll.202409673
(14) Journal of Alloys and Compounds 986 (2024) 174061
(15) Tough sheets of nanowires produced floating in the gas phase. Materials Horizons 7, 2978-2984, 2020. DOI: 10.1039/D0MH00777C
(16) Nanotextile 100% Si anodes for the next generation energy-dense Li-ion batteries. Advanced Energy Materials, 2304018, 2024. DOI: 10.1002/aenm.202304018
(17) Long Cycling of All-Silicon Solid-State Pouch Cells with Zero Expansion under Reduced Stack Pressure, submitted.

Voldsund, M., H. Wegge, S. Bublik, and Aa. Valderhaug. 2026. Pilot-Scale Silicon Production Using SiC as Reduction Material - Opportunities and Operational Challenges. In *Silicon for the chemical and solar industry XVIII*, edited by M. Tangstad, H. Rong, A. Valderhaug, B. Andresen, H. Dalaker, and I. G. Page. Kristiansand, Norway, September 7–10, 2026. https://doi.org/10.55669/oa900807

Pilot-Scale Silicon Production Using SiC as Reduction Material – Opportunities and Operational Challenges

M. Voldsund[1], H. Wegge[1], S. Bublik[1], and Aa. Valderhaug[1]
[1]Elkem ASA, Norway, mari.voldsund@elkem.com

Keywords: two-stage silicon production, Sicalo, SiC, pilot submerged-arc furnace

Abstract – Elkem is developing a two-stage silicon production process in which silicon carbide (SiC) is first produced in a dedicated reactor and subsequently used as a reducing agent in a second reactor. This approach can reduce direct emissions of dilute CO_2, enable utilisation of a concentrated CO stream, and lower energy consumption and costs. As part of this development, a pilot-scale submerged-arc furnace has been designed and constructed at Elkem's R&D facilities in Kristiansand to demonstrate silicon production with high SiC fractions in the reduction material. To date, five pilot campaigns have been conducted with progressively increasing SiC fractions, ranging from a reference case without SiC to approximately 60 percentage points SiC in the carbon coverage. The main objective of these campaigns has been to establish operating strategies for subsequent demonstration campaigns. Material balance analyses show that silicon can be produced with a high fraction of SiC. The best campaign achieved a silicon yield of 92% based on tapped metal and 88% based on filter dust, with a specific energy consumption of 11.8 MWh per tonne Si. A solid basis has been established for the planning of forthcoming demonstration campaigns.

1. INTRODUCTION

Industrial production of silicon has, in principle, remained largely unchanged for more than 100 years. Carbon-based reduction materials such as coal, coke, charcoal, and woodchips are used to reduce quartz in submerged-arc furnaces. The process involves a complex set of reactions between solids, gases, and liquids at different temperature levels within the furnace, producing liquid silicon and a process gas containing CO and some SiO. The liquid silicon is tapped at the bottom of the furnace, while the process gas ascends through the charge. The furnaces used are typically open or semi-closed, meaning that the process gas is combusted in air in the furnace hood. This configuration is required to ensure stable operation and to avoid problems with SiO condensation in the off-gas system. However, it has the drawback that valuable CO is oxidised to CO_2 and diluted significantly with air.

1.1 Two-stage silicon production process

Elkem is developing an alternative two-stage silicon production process (Figure 1) in which the overall furnace reactions are separated into two reactor stages:

- One reactor in which silicon carbide (SiC) is produced from quartz and carbon, generating a high-purity CO gas stream.
- One reactor in which silicon is produced from SiC and quartz, with combustion of process gas as in conventional silicon furnaces.

In this configuration, approximately two-thirds of the carbon entering the process is converted to CO in the SiC reactor, while the remaining one-third is emitted as CO_2 from the submerged-arc furnace. A similar process, although without focus on preserving a pure CO gas stream, was previously investigated in the Solsilc project for production of solar-grade silicon (Nygaard, 2008; Kvande, 2011).

This work is licensed under the Creative Commons Attribution 4.0 International License. To view a copy of this license, visit https://creativecommons.org/licenses/by/4.0/

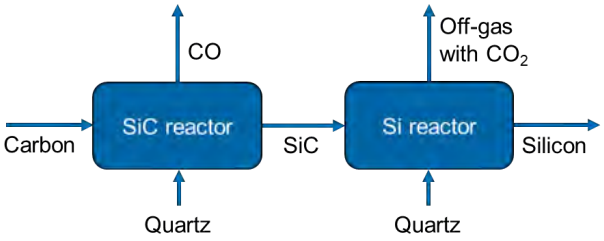

Figure 1: Schematic of the two-stage silicon production process.

The two-stage process offers several potential advantages compared with conventional silicon production:

- The chemical energy in the CO gas is preserved, enabling more efficient utilisation of off-gas carbon. This is a key advantage in the Elkem Sicalo® concept (see Section 1.2).
- The CO gas can be utilised for process heat or electricity generation. In addition, combustion of CO in gas burners or gas engines results in higher CO_2 concentration in the off-gas, which may facilitate more cost-efficient CO_2 capture. Such solutions are being investigated in the manganese industry (Enova, 2023).
- The volumetric flow rate of the off-gas is significantly reduced. For an equivalent carbon throughput, the flow rate of pure CO gas is approximately 5% of that of conventional silicon off-gas, enabling a substantial reduction in off-gas system costs.
- The process provides increased flexibility for plant expansion. Existing furnaces can increase capacity by partially substituting conventional reduction materials with SiC, while new SiC production units can potentially be located in areas with lower electricity cost.
- A fraction of the SiC produced in the first stage can potentially be further upgraded and sold for higher-value applications.
- The process may enable production of high-purity silicon, as demonstrated in the Solsilc project (Nygaard, 2008; Kvande, 2011).
- Separation of the reaction steps enables improved understanding and control of the process and may allow more systematic cost optimisation compared with conventional furnace operation.

1.2 The Elkem Sicalo® concept

The Elkem Sicalo® concept aims to significantly reduce CO_2 emissions from silicon production by closing the carbon loop through reuse of off-gas carbon in the process. In this concept, CO and CO_2 from the off-gas are converted to methane via reaction with hydrogen, followed by methane cracking to produce solid carbon and hydrogen. The solid carbon is agglomerated and reused as a reduction material, while the hydrogen is recycled. In principle, this enables substitution of fossil carbon by hydrogen and electricity. This process is illustrated for conventional furnace technology and two-stage silicon production in Figure 2.

The two-stage silicon production configuration has several advantages compared with the one-stage configuration. By preserving approximately two-thirds of the process carbon as a concentrated CO stream, it can:

- reduce hydrogen consumption by approximately one-third,
- reduce capital and operational costs for CO_2 capture, and
- reduce capital costs of the off-gas and energy recovery systems.

In addition, electrode consumption may be reduced due to the lower specific energy consumption in the silicon furnace.

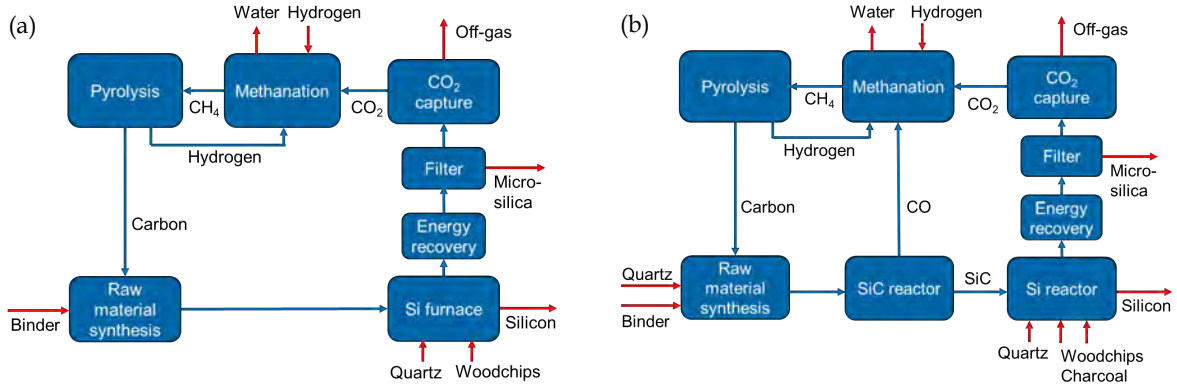

Figure 2: The Sicalo concept. (a) Sicalo one-stage. (b) Sicalo two-stage.

The Sicalo two-stage concept can also be implemented without CO_2 capture, recycling only the CO stream from the SiC reactor. In this case, CO_2 emissions could be reduced by around two-thirds compared with conventional silicon production, while the hydrogen demand would be halved compared with the full two-stage recirculation concept and reduced by around two-thirds compared with the one-stage concept. This provides an alternative with lower emissions reduction, but also lower energy use and lower capital costs per tonne of CO_2 abated.

1.3 Si reactor pilot testing

As part of the development of the two-stage silicon production process, a pilot-scale submerged-arc furnace has been designed and constructed at Elkem's R&D facilities in Kristiansand. It is intended to demonstrate the second stage of the process, namely silicon production using SiC as a reduction material. It also provides a platform for testing other novel raw materials. To date, five campaigns have been conducted with progressively increasing SiC fraction in the reduction material. The primary objective of these campaigns has been to establish an operating strategy for subsequent demonstration campaigns. This paper presents the design of the pilot furnace and selected results together with preliminary analyses from the first five campaigns.

2. THEORY

2.1 Silicon furnace process with conventional reduction materials

In conventional silicon production, the furnace is charged with quartz and carbon-based reduction materials. As these materials enter the furnace, moisture and volatile matter are released from the reduction materials and combusted at the charge top, while fixed carbon and quartz descend through the furnace.

Furnace reactions

In a simplified model, the furnace may be divided into two main zones: one hot inner zone and one slightly cooler outer zone. In the inner zone, SiO_2 reacts with Si to form SiO gas, and the SiO gas reacts with SiC to produce silicon and CO gas.

$$SiO_2(l) + Si(l) = 2\,SiO(g) \qquad \Delta H_{2000\,^\circ C} = 82\ \text{kWh/kmol SiO} \qquad \text{(I)}$$

$$SiO(g) + SiC(s) = 2\,Si(l) + CO(g) \qquad \Delta H_{2000\,^\circ C} = 48\ \text{kWh/kmol SiO} \qquad \text{(II)}$$

This gives the following highly endothermic overall reaction:

$SiO_2(l) + SiC(s) = Si(l) + SiO(g) + CO(g)$ $\Delta H_{2000\,°C} = 212$ kWh/kmol SiO (III)

The silicon produced is tapped from the bottom of the furnace, while the SiO and CO gases ascend to the outer zone, where SiO gas is recovered mainly through the following two exothermic reactions:

$SiO(g) + 2\,C(s) = SiC(s) + CO(g)$ $\Delta H_{1700\,°C} = -21$ kWh/kmol SiO (IV)

$2\,SiO(g) = SiO_2(l) + Si(l)$ $\Delta H_{1700\,°C} = -84$ kWh/kmol SiO (V)

The reaction heat from these reactions heats the descending colder materials. Reaction IV produces SiC, which descends to the inner zone, and CO, while Reaction V produces a mixture of SiO_2 and Si. The CO gas produced in both zones, together with SiO gas not recovered in the outer zone, is combusted together with the volatiles at the charge top.

Efficient SiO recovery in the outer zone is crucial for achieving a high silicon yield. Reaction IV is also essential because it generates SiC, which is required in Reaction II, whereas Reaction V is less desirable because the SiO_2/Si condensate formed may act as a binder between solid particles and reduce gas permeability and impede the descent of materials. Reaction V also generates four times as much heat as Reaction IV, which may give a temperature increase that inhibits both reactions and thereby reduces SiO recovery. Traditionally, considerable emphasis has therefore been placed on selecting reduction materials with appropriate SiO reactivity, to promote Reaction IV rather than Reaction V.

The overall reaction for both the inner and outer charge zones, when using only fixed carbon as a reducing agent and accounting for SiO losses, can be expressed as:

$SiO_2 + (1+\mu)\,C = \mu Si + (1-\mu)\,SiO + (1+\mu)\,CO$ (VI)

where μ is the fraction of silicon units converted from SiO_2 all the way to Si.

Carbon coverage

A key factor when operating the furnace is the carbon coverage, defined as the moles of fixed carbon (fix C) in the reduction materials per mole of oxygen in the quartz fed to the process:

$$FC = \frac{n_{\text{fix C}}}{2 \cdot n_{SiO_2}} \quad [1]$$

The carbon coverage is adjusted to limit SiO losses and at the same time avoid accumulation of carbon in the form of SiC in the furnace.

In practice, some fixed carbon is combusted at the charge top before meeting any SiO gas, while some of the electrode carbon participates in the furnace reactions. The effective carbon coverage is therefore defined as:

$$f_C = \frac{n_{C,rx}}{2 \cdot n_{SiO_2}} = FC - \frac{n_{\text{fixC loss}}}{2 \cdot n_{SiO_2}} + \frac{n_{\text{electrode}}}{2 \cdot n_{SiO_2}} \quad [2]$$

where $n_{C,rx}$ is the number of moles of carbon that participate in the furnace reactions. The effective carbon coverage can also be expressed in terms of μ and calculated based on the SiO loss:

$$f_C = \frac{1+\mu}{2} = \frac{(2n_{SiO_2} - n_{SiO_2,dust})}{2 \cdot n_{SiO_2}} \quad [3]$$

Process performance

The silicon yield and the specific energy consumption are important indicators of furnace performance and operating efficiency. The silicon yield is defined as the silicon tapped divided by the silicon introduced with the raw materials. When only conventional reduction material is used, all silicon enters the process as SiO_2, and the silicon yield is equal to μ and is linearly related to the effective carbon coverage:

$$\text{Si yield} = \mu = 2f_C - 1 \quad [4]$$

The specific energy consumption (SEC) is determined by the furnace thermal efficiency, the silicon yield and operating conditions. The theoretical SEC (ideal operation at 100% thermal efficiency) is given by the enthalpy difference between the input and output material streams. Assuming typical temperatures for the input and output streams, the theoretical energy consumption is around 8.4 MWh/tonne Si when all silicon units are converted (μ = 1). The theoretical SEC as a function of effective carbon coverage for conventional reduction material is shown by the upper black line in Figure 4.

2.2 Silicon furnace process with SiC as reduction material

Replacing part of the carbon in the reduction material with SiC affects the furnace conditions in several ways. Here, SiC is treated as a reduction material because the carbon bound in SiC acts as a reductant in the hot-zone reaction with SiO, while the silicon bound in SiC contributes to the silicon product. The most important changes are:

- The overall reaction is changed such that the overall extent of Reactions I and IV is reduced, resulting in lower specific energy consumption.
- Less carbon is available to capture SiO gas through Reaction IV, so a greater fraction of SiO gas must be captured by Reaction V. This leads to higher heat generation in the outer zone, potentially inhibiting the capture of SiO gas.

By assuming that all SiC is converted to silicon, the new overall reaction for the inner and outer charge zone can be expressed as:

$$SiO_2 + (1 + \mu - n)\ C + n\ SiC = (\mu + n)\ Si + (1 - \mu)\ SiO + (1 + \mu)\ CO \quad \text{(VII)}$$

where n is the number of moles SiC per mole SiO_2 added to the process. The carbon coverage is then equal to:

$$FC = \frac{(n_{fix\ C} + n_{SiC})}{2 \cdot n_{SiO2}} \quad [5]$$

Equations 2 and 3 for effective carbon coverage are still valid, while silicon yield and its relation to effective carbon coverage can be expressed as:

$$\text{Si yield} = \frac{\mu+n}{1+n} = \frac{2f_C-1+n}{1+n} \quad [6]$$

Figure 3 illustrates the expected change in furnace behaviour with increasing SiC content in the reduction material. The figure shows the theoretical SEC as a function of effective carbon coverage for different SiC fractions. The solid black line represents conventional silicon production with carbon as the only reduction material. The coloured lines correspond to 20, 40, 60, and 80 percentage points SiC in the effective carbon coverage, equivalent to n = 0.4, 0.8, 1.2, and 1.6, and illustrate how the SEC decreases with both increasing SiC fraction and increasing effective carbon coverage. Each curve terminates when the effective carbon coverage is fully provided by SiC. Constant-yield lines are shown in grey, illustrating combinations of f_C and SiC fraction that give the same silicon yield. As silicon enters the furnace both as SiO_2 and SiC, the required effective carbon coverage decreases with increasing SiC fraction for a given silicon yield. The objective is to produce silicon with low energy consumption while maintaining high yield. The preferred operating region in the diagram is therefore characterised by high f_C and low SEC.

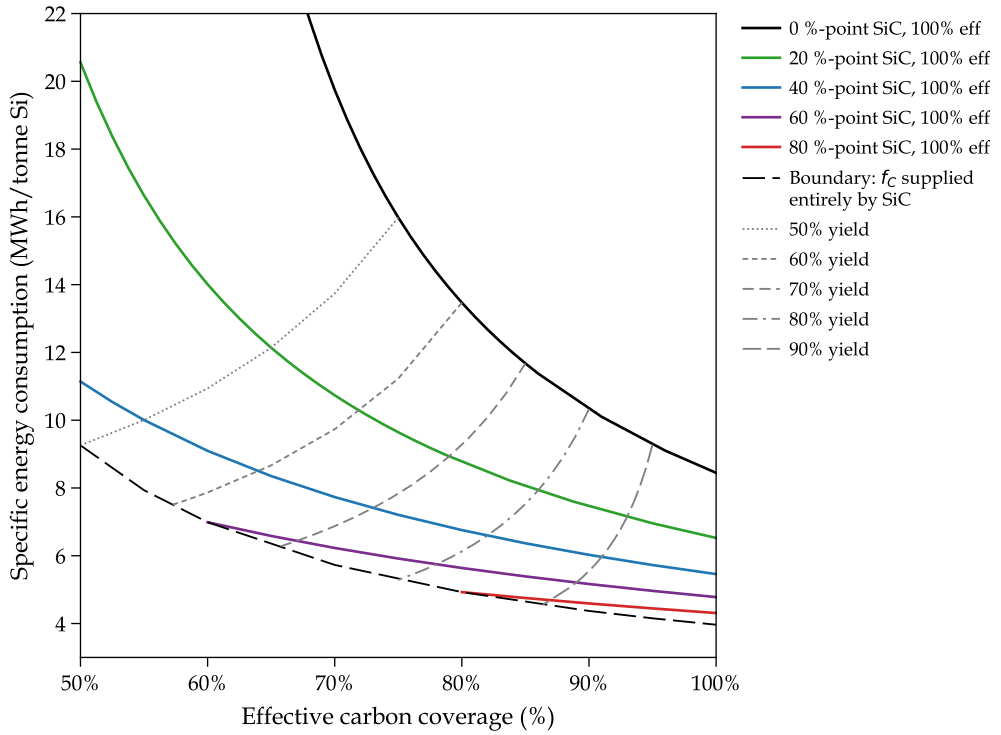

Figure 3: Theoretical specific energy consumption (SEC) as a function of effective carbon coverage (f_C) for different percentage points SiC in f_C. The dashed and dotted grey lines indicate constant yield as a function of f_C and SiC content.

This type of diagram is useful for planning and evaluation of silicon production with a fraction of SiC in the reduction material. For a given furnace load, assumed furnace thermal efficiency, and assumed carbon losses and electrode consumption, charge compositions, weights and charging frequency can be determined. Operational results can be plotted in the diagram and used to guide future furnace operation.

2.3 Previous pilot-scale testing of SiC as reduction material

Pilot-scale campaigns on silicon production with SiC as a reduction material have been conducted previously by several actors. Dow Corning has demonstrated in pilot-scale submerged arc furnace tests (200 kVA) that silicon can be successfully produced with approximately 25% SiC in the reduction material, resulting in significantly reduced energy consumption and increased production rates compared with conventional operation (Dosaj, et al., 1991). Later, the Solsilc project developed a carbothermic reduction route using SiC-

containing agglomerates for production of high-purity silicon, with pilot campaigns carried out up to 1.5 MW scale around 2007–2011, achieving several tonnes of silicon production (Nygaard, 2008; Kvande, 2011; Øvrelid & Pizzini, 2016).

3. THE PILOT SILICON FURNACE

3.1 Furnace design

The pilot silicon furnace, illustrated in Figure 4, is designed and built at Elkem's R&D facilities in Kristiansand to test new raw materials. The furnace power supply consists of a 1.5 MVA single-phase transformer with 32 secondary voltage levels in the range 40–90 V. The maximum electric current to the furnace is 4 kA, limited by the capacity of the electrode and the flexible cables connected between busbars, bus tubes and the water-cooled contact clamp.

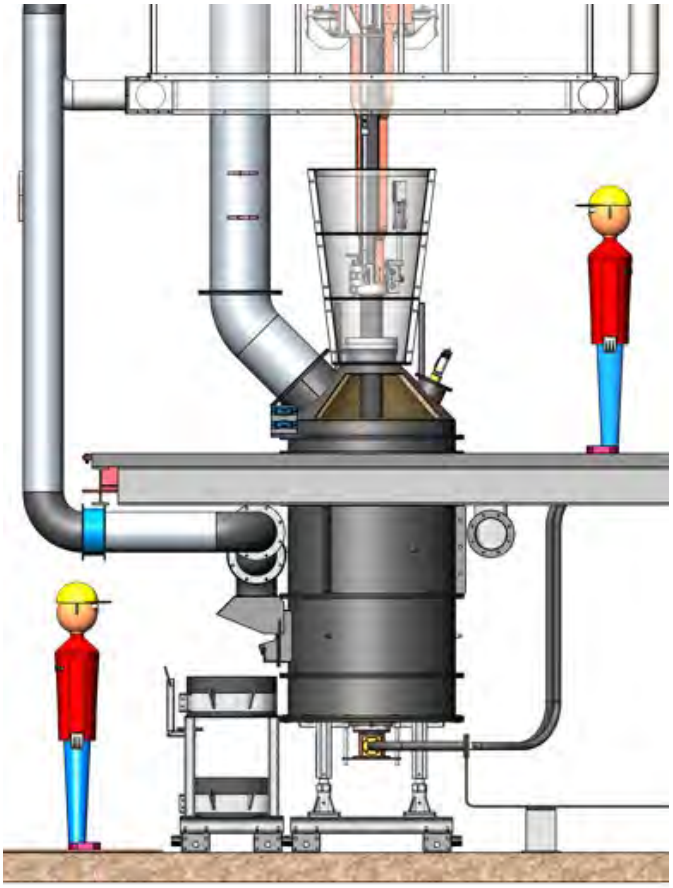

Figure 4: Pilot-scale submerged-arc furnace for silicon production.

The furnace is designed for ergonomic use and built over three levels. The taphole and tapping equipment are located at the bottom level (+6.0 m MSL), the middle level contains the furnace roof hatches for stoking and charging of raw materials (+8.7 m MSL), and the upper level, above the ventilation hood and not shown in the figure, is used for assembly of new electrode elements (+13.4 m MSL). The process chamber is 0.8 m in diameter and 0.7 m high from the bottom to the air intake. The electrode column has a diameter of 15 cm, and the water-cooled bottom contact is attached to a graphite bottom electrode with a diameter of 17.5 cm.

The electrical operating conditions are controlled by setting the voltage level and using a current controller to adjust the electrode column position to maintain the current setpoint. The

campaigns carried out to date have used an electric load of around 130 kW, a transformer secondary voltage level in the range 51–55 V and an electrode current in the range 2.7–3.0 kA.

The process gas leaves the furnace through an off-gas duct with capacity >6000 Nm^3/h. The process gas, the tapping fume and the air from the ventilation hood, which captures fume released from the furnace hatches, are sent to a bag filter with a capacity of 30 000 Nm^3/h.

3.2 Instrumentation and data collection

The measured and registered parameters used for furnace operation, process analysis, and material balance calculations are summarised in Tables I–III.

Table I: Logged parameters for furnace operation and control.

Parameter	Unit	Purpose / comment
Furnace load	kW	Monitoring electrical power input
Current	A	Furnace operation and control
Electrode holder position	mm	Electrode movement and control
Electrode voltage	V	Electrical operating condition
Transformer voltage	V	Transformer operating condition
Voltage harmonics	%	Monitoring electric arc conditions
Current harmonics	%	Monitoring electric arc conditions
Lining temperatures	°C	Thermal monitoring of furnace lining
Furnace overpressure	mmH_2O	Pressure monitoring in the furnace
Off-gas NO_x content	ppm	Indicator of combustion/blowing conditions
Off-gas dust concentration	mg/Nm^3	Indicator of blowing conditions
IR images/videos of charge top	–	Visual monitoring of charge-top conditions, including temperature measurements

Table II: Logged parameters for process analysis.

Parameter	Unit	Purpose / comment
Off-gas composition	vol%	CO_2, CO, H_2, Ar, N_2, O_2
Cooling water flow rates	L/h	Electrode holder
	L/h	Bottom contact
Cooling water inlet and outlet temperatures	°C	Electrode holder
	°C	Bottom contact
Gas flow rates	Nm^3/h	Off-gas duct
	Nm^3/h	Combustion air
Gas temperatures	°C	Off-gas duct
	°C	Combustion air

Table III: Manually measured and registered parameters for material balance.

Category	Parameter	Unit
Input materials	Baking coke bed material	kg
	Charge materials	kg
	Electrode slip	cm
	Electrode consumption/addition	cm
Output materials	Tapped metal	kg
	Filter dust	kg
	Material accumulated in furnace after the campaign	kg

4. PILOT CAMPAIGNS WITH SIC AS REDUCTION MATERIAL

4.1 Pilot campaign overview

The five pilot campaigns are summarised in Table IV, and the corresponding carbon coverage and reduction material mix are shown in Figure 5. The first campaign was carried out using only coke and woodchips, while the SiC content was subsequently increased by around 20 percentage points in each campaign. SiC was introduced in several forms, including 2 mm SiC, SiC briquettes (90 wt% SiC and 10 wt% carbon black or 100 wt% SiC), composite briquettes (1 mol SiO_2/1.5 mol SiC), or SiC agglomerates developed in the Horizon Europe project MECALO. The last two campaigns were both conducted with around 60 percentage points SiC but using different types of SiC agglomerates. The carbon coverage was around 100% in the first three campaigns and was reduced to around 95% in the fourth and fifth campaigns. The duration was four days in the first four campaigns and five days in the final campaign.

Table IV: Pilot campaign overview.

ID	FC	%-points SiC in FC	Length	Comment
0% SiC (#1)	99%	0%	4 days	Reference reduction material.
20% SiC (#2)	100%	20%	4 days	SiC: 50% SiC briquette, 50% 2 mm
40% SiC (#3)	101%	42%	4 days	SiC: 50% SiC briquette, 50% 2 mm
60% SiC comp (#4)	94%	62%	4 days	SiC: 50% SiC briquette, 50% composite briquette
60% SiC MEC (#5)	95%	60%	5 days	SiC: MECALO agglomerate.

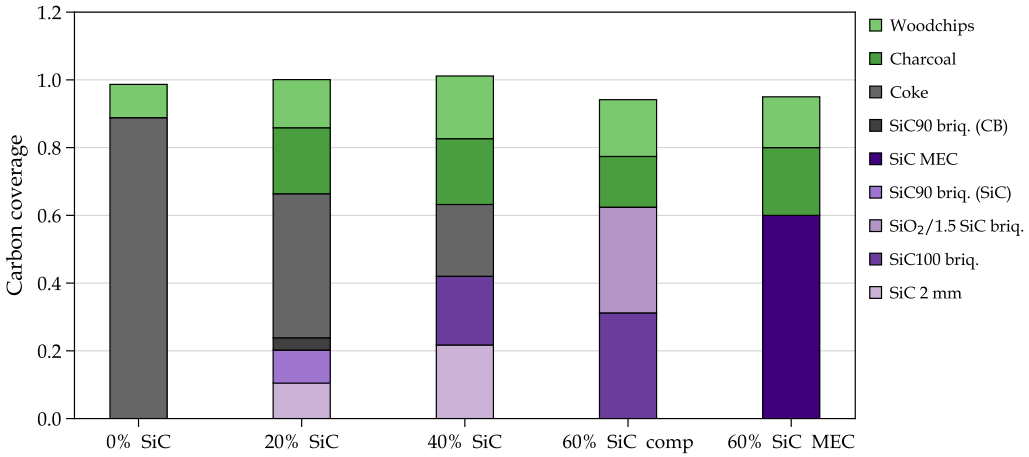

Figure 5: Nominal carbon coverage and SiC contribution in the test charge for the five pilot campaigns.

4.2 Operating procedure

The pilot campaigns consisted of the following operational phases:

1. **Baking (16–24 hours):** Baking of the lining.
2. **Charge filling (8–24 hours):** Gradual filling of the furnace with a start charge, with the aim of achieving stable furnace operation by the end of the period.
3. **Charge transition (8 hours):** Transition to the test charge. At the end of this period, the furnace was assumed to be completely filled with the test charge.
4. **Data collection (48–56 hours):** Stable operation with the test charge and collection of process data.
5. **Termination:** The campaign was terminated 20–30 min after the final tapping and charging, followed by cooling over three days without any mechanical movement.

The furnace was tapped every 60–75 minutes and stoking and charging of raw materials were carried out two to three times during each tapping cycle.

4.3 Material balance

Simplified stoichiometric balances were estimated for the data collection period of each campaign by assuming that (i) the electrode material is pure carbon, (ii) all tapped metal is silicon, (iii) all filter dust is SiO_2, and (iv) the oxygen in the SiO_2 input is converted to either SiO or CO.

Figure 6 illustrates the carbon balances. The carbon input per mole of SiO_2 is shown in the first column and the carbon participating in furnace reactions per mole of SiO_2 is shown in the second column for each campaign. The first column is equal to 2·FC plus the electrode consumption, while the second column is equal to 2·fc, corresponding to the amount of carbon leaving the process as CO gas. The difference between the two columns is the sum of carbon lost due to combustion at the charge top and carbon accumulated in the furnace in the form of SiC. The electrode consumption varies significantly between the campaigns, indicating overcoking and undercoking with low and high electrode consumption, respectively. The ratio of carbon participating in furnace reactions to total carbon input was lower in the first campaign (62%) and then remained relatively constant in the remaining campaigns (71–75%).

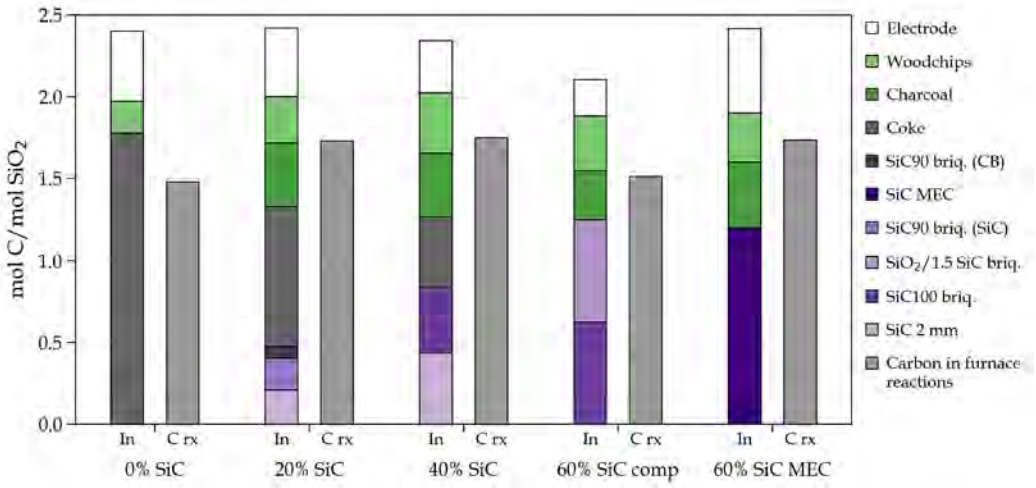

Figure 6: Molar carbon input and carbon participating in furnace reactions per mole of SiO_2 input.

Figure 7 illustrates the silicon balances. The various forms of silicon input per mole of SiO_2 are shown in the first column, while the silicon output in the form of liquid metal and dust is shown in the second column for each campaign. It is evident that in the second, third, and fourth campaigns, less silicon left the furnace than entered, indicating accumulation of silicon in the form of Si or SiC within the furnace. In contrast, the fifth campaign showed slightly higher silicon output than input, indicating that some silicon accumulated in the charge filling and charge transition periods was drained during the data collection period.

Silicon yields estimated on the basis of tapped silicon and on filter dust are presented in Table V. For the third and fourth campaigns, yields based on tapped silicon are significantly lower than those estimated from filter dust, indicating accumulation of silicon inside the furnace.

The first campaign resulted in a very low silicon yield of 48%. At this stage, the stoking and charging procedures were not yet optimised, and breakdowns in dust and NO_x measurements

made it difficult to predict and control blowing. The yields based on dust improved in the second and third campaigns, most likely due to improved stoking and charging procedures. In the fourth campaign, the dust-based yield decreased, before increasing again in the fifth campaign.

The increasing accumulation of silicon in the furnace from the second to the fourth campaign led to a stronger focus on tapping and draining performance. The fifth campaign was therefore extended by one day and included a longer charge-filling period to establish stable tapping conditions before switching to the test charge. Additional emphasis was also placed on maintaining high temperatures in the lower part of the charge. The fifth campaign achieved a high silicon yield: 92% based on tapped metal and 88% based on dust.

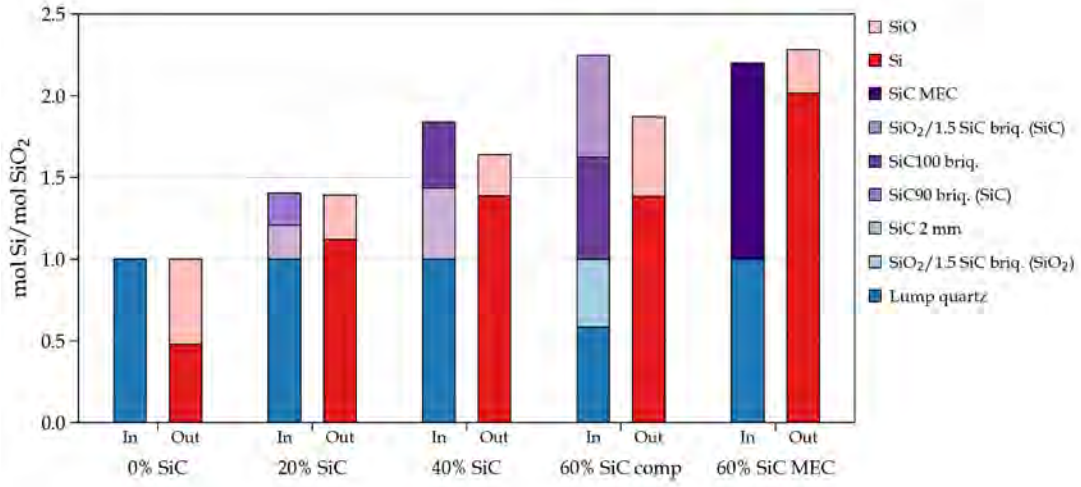

Figure 7: Molar silicon input and output per mole of SiO_2 input.

Table V: Estimated silicon yields.

Estimate basis	0% SiC (#1)	20% SiC (#2)	40% SiC (#3)	60% SiC comp (#4)	60% SiC MEC (#5)
Silicon tapped	48%	80%	75%	62%	92%
Filter dust	48%	81%	86%	78%	88%

4.4 Furnace excavation

After the termination of each campaign, the furnace was excavated, the cavities were measured, and the different types of materials were mapped and weighed. A certain amount of silicon material containing a mixture of Si and SiC (Si·SiC) is expected and was observed after all campaigns. The approximate mass of Si·SiC materials in the furnace is summarised in Table VI. The amount increased from 36 kg after the reference campaign to 135 kg after the fourth campaign, before decreasing to 37 kg after the fifth campaign. This is consistent with the material-balance observations and indicates that improved tapping and draining conditions in the fifth campaign substantially reduced the amount of material retained in the furnace.

Table VI: Approximate mass of Si·SiC material in the furnace after each campaign.

Quantity	0% SiC (#1)	20% SiC (#2)	40% SiC (#3)	60% SiC comp (#4)	60% SiC MEC (#5)
Mass of Si·SiC	36 kg	70 kg	87 kg	135 kg	37 kg

An illustration of the cavity mapped after the fifth campaign is given in Figure 8. The cavity was oval, with diameters of approximately 50 cm in the east–west direction and 25 cm in the north–south direction. The accumulation of Si·SiC was higher on the north and south sides of the furnace. This is likely related to the location of the two stoking and charging hatches in the east and west and suggests that the stoking and charging procedures can be further optimised to obtain more favourable cavity conditions.

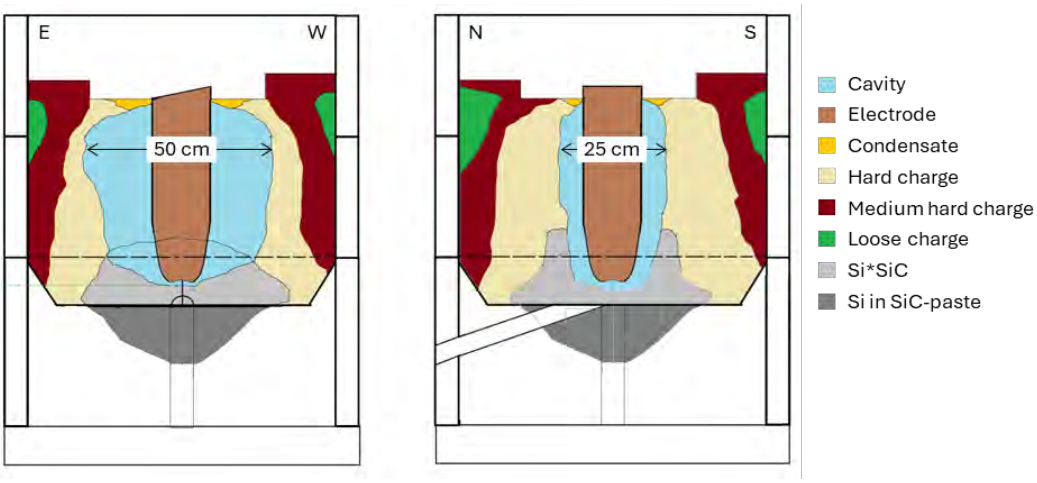

Figure 8: Illustration of the cavity mapped during excavation of the furnace after the fifth campaign. The left figure shows the cross section from east to west, and the right figure shows the cross section from north to south.

4.5 Specific energy consumption

The specific energy consumption and thermal efficiencies of the furnace during the five campaigns are presented in Table VII. The thermal efficiency of the furnace was around 50% during the first three campaigns, with a drop to 43% and 45% for the fourth and fifth campaigns. The lower value in the fourth campaign can be explained by the lower silicon yield, whereas for the fifth campaign the reason may be higher thermal losses associated with higher temperatures in the tapping zone. Thermal efficiencies in the range of 40–50% are as expected for pilot furnaces of this size.

Table VII: Specific energy consumption (SEC) and furnace thermal efficiency for the five campaigns.

Metric	**0% SiC (#1)**	**20% SiC (#2)**	**40% SiC (#3)**	**60% SiC comp (#4)**	**60% SiC MEC (#5)**
SEC (MWh/tonne)	34.0	16.4	12.6	13.8	11.8
Furnace thermal efficiency	49%	48%	49%	43%	45%

Figure 9 shows SEC as a function of effective carbon coverage at 50% thermal efficiency for varying amounts of SiC in the reduction material, with the five campaigns plotted. The colours of the dots indicate SiC content and are consistent with those of the lines. The first three campaigns are close to the theoretical curves calculated for 50% furnace thermal efficiency, whereas campaigns #4 and #5 plot above the corresponding curves because their measured thermal efficiencies were lower than 50%, at 43% and 45%, respectively.

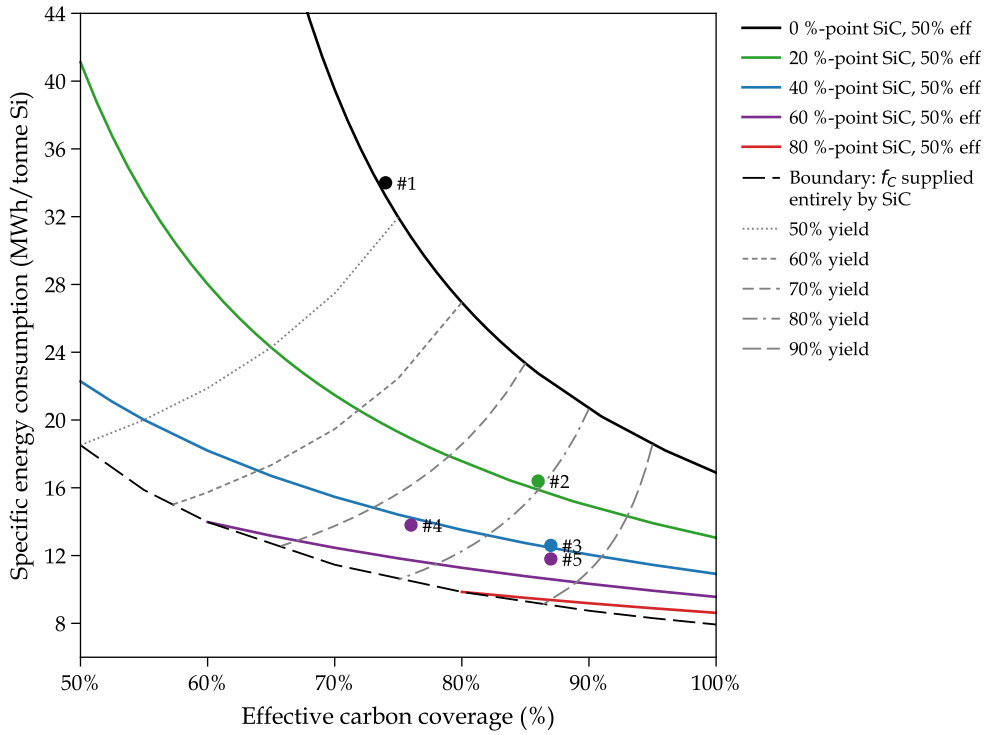

Figure 9: Measured specific energy consumption for the five pilot campaigns compared with theoretical SEC curves calculated at 50% furnace thermal efficiency as a function of effective carbon coverage and SiC contribution. Grey lines indicate constant calculated silicon yield.

5. CONCLUSION

This work presents the design of a pilot-scale submerged-arc furnace and results from five pilot campaigns carried out to establish an operating strategy for silicon production with a high SiC fraction in the reduction material. The campaigns were performed with progressively increasing SiC fractions, ranging from a reference case without SiC to approximately 60 percentage points SiC in the carbon coverage. The best campaign achieved a silicon yield of 92% based on tapped metal and 88% based on filter dust, with a specific energy consumption of 11.8 MWh per tonne Si. The results provide an experimental basis for subsequent demonstration campaigns and further development of the two-stage silicon production process and the Elkem Sicalo® concept.

6. ACKNOWLEDGEMENTS

This paper is published with permission of Elkem ASA. The contributions of our colleagues are gratefully acknowledged. The paper presents results from Elkem's Sicalo project. The project is funded directly by Elkem ASA, through the Enova pilot project "24/8481 Elkem Sicalo Phase 2 - Pilottesting av subprosesser", the Green Platform project GreenBox with financial support from SIVA, Innovation Norway, and RCN, and the Horizon Europe project MECALO. The MECALO project has received funding from the European Union's Horizon Europe Research and Innovation Programme under Grant Agreement No. 101122101. However, the views and opinions expressed are those of the author(s) only and do not necessarily reflect those of the European Union. Neither the European Union nor the granting authority can be held responsible for them.

7. REFERENCES

Dosaj, V. D., Rauchholz, A. W., Young, M. D. & Bokerman, G. N., 1991. *Silicon carbide as a raw material for silicon production.* United States, Patent No. 4981668.

Enova, 2023. *Eramet Norway får 132 millioner kroner til energi- og klimaprosjekter i Sauda.* Press release, March 30, 2023. NTB.

Kvande, R., 2011. *Solar Cells Manufactured from Silicon Made by the Solsilc Process.* Solar Energy Seminar, June 1, 2011, University of Agder.

Nygaard, L., 2008. *The Solsilc Process.* Oslo, Silicon for the Chemical and Solar Industry IX, June 23-26, 2008.

Øvrelid, E. & Pizzini, S., 2016. The MG Silicon Route. In: B. Ceccaroli, E. J. Øvrelid & S. Pizzini, eds. *Solar Silicon Processes: Technologies, Challenges, and Opportunities.* CRC Press, pp. 74-79.

Harald Wegge
R&D Scientist, ELKEM ASA

Harald Wegge holds an M.Sc. in Process Metallurgy from NTH and has over 40 years of experience in metallurgical process development. He has worked extensively with silicon and ferrosilicon processes in industrial and pilot-scale environments. He is currently leading the development of the silicon reactor step in the Elkem Sicalo® project.

Stabbforsmo, T., and M. Tangstad. 2026. Hot Strength of β-SiC Produced from Biocarbon. In *Silicon for the chemical and solar industry XVIII*, edited by M. Tangstad, H. Rong, A. Valderhaug, B. Andresen, H. Dalaker, and I. G. Page. Kristiansand, Norway, September 7–10, 2026.
https://doi.org/10.55669/oa900809

Hot Strength of β-SiC Produced from Biocarbon

T. Stabbforsmo[1], and M. Tangstad[1]
[1] Norwegian University of Science and Technology, Department of Materials Science and Engineering, Norway, thea.stabbforsmo@ntnu.no

Keywords: biocarbon, charcoal, hot strength, SiC

Abstract - In the production of silicon metal, β-SiC is produced as a crucial intermediate product which occupy a significant part of the interior of the submerged arc furnace (SAF). β-SiC is produced by the reaction between carbon and SiO gas. This work investigates how the compressive hot strength of β-SiC is affected by the carbon precursors coal and charcoal. The compressive hot strength is measured indirectly by change in particle size distribution after being exposed to compressive forces at room temperature, 400 °C, 800 °C and 1000 °C in a Spark Plasma Sintering (SPS) machine. The strength of SiC from charcoal is found to be up to 50 % lower than calcined charcoal, while there is no significant difference between SiC from coal and calcined coal. This is suggested to be caused by the deterioration of the organized cell wall structure when reacting from charcoal to SiC, while the coal has thicker cell walls and is not affected by SiC conversion in the same degree. It is also found that the strength of SiC from charcoal is more temperature dependent than SiC from coal, with an increase in strength at 800 °C and 1000 °C, while SiC from coal shows approximately the same strength for all temperatures. As expected, the strength of SiC from coal is significantly higher than of SiC from charcoal.

1. INTRODUCTION

A potential approach to reduce the carbon footprint of the silicon industry is to exchange some of the fossil carbon material with renewable biocarbon in the charge, as this can reduce the CO_2 emission factor (Monsen, Lindstad and Tuset, 1998). Silicon metal production is a carbothermic process where a mix of various carbon materials reduce quartz (SiO_2) in a submerged arc furnace (SAF). The process involves a series of reactions leading to the total mass balance described in Equation 1.

$$SiO_2\ (s) + 2C\ (s) = Si\ (l) + 2CO\ (g) \quad [1]$$

One of the reactions leading to the mass balance in Equation 1 is the reaction between SiO gas from the inner zone in the SAF rising to the outer zone where it reacts with the carbon material to form silicon carbide (SiC) and CO gas, as described in Equation 2.

$$SiO\ (g) + 2C\ (s) = SiC\ (s) + CO\ (g) \quad [2]$$

The SiC produced by Equation 2 is essential for the production of Si metal, as it is the intermediate SiC which reacts with SiO gas to form molten Si and CO gas in the inner part of the furnace, as described in Equation 3.

$$SiO\ (g) + SiC\ (s) = 2Si\ (l) + CO\ (g) \quad [3]$$

It is well established that biocarbon materials such as charcoal generally have has lower mechanical strength than fossil carbon materials such as coal and coke. It is less established how the SiC strength is compared to the carbon materials, and how the strength is affected by the carbon precursor, especially at the high temperature inside the SAF. The SiC produced by Equation 2 is β-SiC if the temperatures are below 2000 °C, but it has been observed that with

This work is licensed under the Creative Commons Attribution 4.0 International License. To view a copy of this license, visit https://creativecommons.org/licenses/by/4.0/

exposure to temperatures above >~2000 ℃ β-SiC will convert to α-SiC (Ringdalen, 2018; Jayakumari and Tangstad, 2020). During excavation of five different Si furnaces, SiC was found in all furnaces (Ksiazek, Tangstad and Ringdalen, 2016). Ringdalen looked into the formation of α-SiC and β-SiC in industrial furnaces and found the loose charge at the top of Si furnaces to contain only β-SiC, while the SiC crust from further down in the furnaces contained a higher amount of α-SiC, with only small amounts of β-SiC or no β-SiC at all (Ringdalen, 2018). A crust of SiC was found to occupy up to almost half the interior of a 40 MW SAF at Elkem Thamshavn, although this is a more extreme case, it emphasizes the importance of knowledge of how this material is affected by the charge materials (Ksiazek, Tangstad and Ringdalen, 2016).

SiC is widely known for its many desirable properties, including high strength and chemical stability, making it suitable for a wide range of applications, especially as an abrasive medium. It is commonly produced through the Acheson process, but it can also occur naturally, then known as Moissanite. There are several polytypes of SiC, which can be classified as β-SiC or α-SiC, the latter being the most commercially used. Polytypes are named by a number and a letter, such as the cubic 3C β-SiC polytype. Other common polytypes include the hexagonal 4H, 6H and 8H as well as the rhombohedral 15R, which are all α-SiC polytypes. It has been suggested that β-SiC is the non-equilibrium product, existing up to 2750 ℃, while 2H and 6H are the main polytypes at temperatures lower than 2750 ℃ when the system is in equilibrium, which is in accordance with the findings of Jayakumari (Jayakumari and Tangstad, 2018; Jayakumari, 2020).

Kim et al. looked into how mechanical properties of porous SiC ceramics are affected by the Si/C content (Kim *et al.*, 2020). The SiC ceramics they used were made from β-SiC and carbon black, forming a SiC ceramic consisting of the β-SiC polytype 3C and α-SiC polytypes 6H and 4H, as well as some Si at the highest Si content (30 wt%). Their results indicate that a higher carbon content increases strength in porous SiC ceramics up to 5 wt% carbon, with a decrease in strength with further increased carbon content. A compressive strength of 100 MPa at 0% carbon with an increase to 106.4 MPa at 5 wt% carbon was measured, followed by a decrease in compressive strength with higher wt% C, to 12.5 MPa with 30 wt% C addition. The opposite was observed for addition of Si, where it increased from 7.7 MPa at 0 wt% Si addition to 24.6 MPa after addition of 30 wt% Si. This indicates that a higher Si/C ratio can increase the strength of porous SiC ceramics, and is in line with the findings of Hoover (Hoover, 2023). Hoover tested the cold compressive strength of SiC from coal with different degrees of conversion, and found that the strength of coal slightly decreased with increasing SiC amount, until Si started to form, also indicating that a higher Si/C ration can increase the strength in more disordered SiC materials (Hoover, 2023).

There are concerns related to the higher friability of biocarbon than fossil carbon, particularly due to issues related to the generation of fines (Ramos *et al.*, 2019; Jahrsengene *et al.*, 2023). Higher friability can lead to a larger generation of fines, which can cause a series of problems such as mass loss, HSE issues related to inhalation and the risk of dust explosions, as well as negative effects on furnace operation and limited gas flow (Jahrsengene *et al.*, 2023). When charcoal reacts with SiO gas to form SiC, it is a topochemical reaction following the shrinking unreacted core model, i.e. SiO gas reacts on the surface of the pores and diffuses into the material, first transforming the pore walls to SiC (Jayakumari, 2020). The mechanical strength of carbon materials is dependent on the porosity and cell wall thickness, as it is the cell walls which are load bearing. The higher porosity and thinner cell walls in charcoal are therefore key factors contributing to charcoals lower strength compared to coal and coke. The literature on the extent of precursor effect on strength and friability of SiC in Si production is limited.

However, Hoover looked into the compressive strength of SiC made from coal and char, where the strength of SiC from coal slightly decreased with increasing SiC content, while the opposite trend was observed for SiC from char (Hoover, 2023). The strength of SiC from both coal and char were measured to be significantly lower than reported for commercial β-SiC.

As there is a knowledge gap in the hot strength of β-SiC as an intermediate product from biocarbon in Si production, it must be examined before charcoal is implemented on a larger scale. In this work the hot strength of SiC from coal and charcoal is investigated by the application of a Spark Plasma Sintering (SPS) machine, which can both heat samples and apply force. The effect of conversion to SiC is examined by density and porosity measurements, Scanning Electron Microscope (SEM) and Energy-Dispersive X-ray Spectroscopy (EDS), X-ray Diffraction (XRD), as well as μ-Computed Tomography (μ-CT).

2. METHOD

SiC was produced from calcined (1200 ℃ for 20 minutes) coal and charcoal, with the proximate composition shown in Table I, with calcined coal having a slightly higher fix-C than calcined charcoal.

Table I: Proximate analysis of calcined coal and charcoal (1200 ℃ for 20 minutes) on a dry basis, used for production of SiC.

	Fix-C (%)	Volatiles (%)	Ash (%)
Charcoal	93.1	3.2	3.7
Coal	97.8	0.8	1.3

With inspiration from the work of Jayakumari, the SiC was produced in a setup in an Inductotherm 75 kW furnace (Jayakumari, 2020). The setup was based on an BN coated graphite crucible (150 x 114 x 400 mm). The bottom of the crucible contained a mixture of Si and SiO_2. Three BN coated graphite pillars were also placed in the bottom of the crucible as a fundament for the graphite sieve separating the SiO producing materials from the carbon material, as shown in Figure 1a. The graphite sieve was 5 mm thick and approximately 110 mm in diameter. To allow for high gas flow upwards in the crucible the sieve was covered in holes as shown in Figure 1b. The carbon material was placed above the sieve together with a BN coated graphite tube (20 x 8 x 500 mm) which contained an alumina tube with a C-type thermocouple which measured the temperature inside the crucible during the process, as seen in Figure 1c.

a) b) c)

Figure 1: The different layers in the SiC formation set-up in the BN coated graphite crucible. Showing a) Si + SiO_2 mix and BN coated graphite pillars. b) The BN coated graphite sieve separating the Si + SiO_2 mix from the carbon material. c) Charcoal on top of the sieve and the BN coated closed-end graphite tube for the thermocouple.

The process was based on the reaction between SiO_2 and Si in the bottom of the crucible, which produce SiO gas, according to Equation 4.

$$SiO_2 + Si = 2SiO\ (g) \qquad [4]$$

The SiO gas produced in the bottom of the crucible rose through the sieve, to the carbon material where it reacted to form SiC and CO gas, as described in Equation 2. The process was carried out at ~1800 ℃ with a holding time of 60 minutes, and a heating rate of approximately 50 ℃/min. The amount of coal and charcoal differed between 200 g and 400 g. After cooling, the materials above the sieve were manually sorted according to conversion degree based on colour as shown in Figure 2, where the greenest material is the most converted. All materials from the same carbon material categorized as the most converted were mixed, and the most converted materials were further investigated and hot strength tested.

Figure 2: Sorting degree of SiC conversion from charcoal/coal manually by colour. The green/grey material closest to the camera is the most converted SiC.

Chemical analysis was carried out at Degerfors Laboratorium, where the amount of SiC in the samples was calculated based on Si detected in the samples, assuming that the amount of elemental Si present is negligible. The conversion degree of the most converted SiC from charcoal and coal was found to be 99 % and 52 %, respectively. Powder X-ray Diffraction (XRD) with Rietveld refinement for phase quantification of the SiC samples was also carried out using the software TOPAS. How well the refinement fit the XRD diffractogram is quantified by the "Goodness of fit" (GOF), where a lower GOF equals a better fit. Before XRD the samples were crushed and sieved through a 44 μm sieve. Cu-Kα radiation (λ = 1.5406) was applied in Bragg-Brentano geometry, with a measurement time of 120 minutes between 2θ = 20-80°.

Hot strength was measured with the application of a Spark Plasma Sintering (SPS) machine, which can steadily heat a sample and apply force. The procedure is the same as described in greater detail in (Stabbforsmo and Tangstad, to be published). The batch of material for the most converted SiC was split with a splitter to ensure representative samples. A material bed of approximately 1.5 g 4-6.3 mm SiC particles was placed in the 28.4 mm graphite die between two graphite punches. The inside of the graphite die is covered by graphite paper, as well as the ends of the graphite punches in which the sample is placed between. The

punches were secured by a manual press before it was placed in the SPS. The graphite setup was covered in graphite wool before hot strength testing. The testing temperatures were 25 ℃, 400 ℃, 800 ℃ and 1000 ℃, and a K-type thermocouple was used. The heating rate was 25 ℃/min up to 400 ℃ and 15 ℃/min above 400 ℃ to minimize rapid expansion of crucible causing premature compression of the sample. The minimum constant force during heating was 2 kN, and a total force of 4 kN with a rate of 0.65 kN/min was applied to the sample when the goal temperature was reached. Two parallels were carried out per sample at each temperature. After the samples had been subjected to compression at the various temperatures, the particle size distribution was measured by sieving. The particle size distribution after compression at elevated temperatures was used to evaluate the hot strength of the material. The same method was also used to measure the hot strength of calcined coal and charcoal as also presented in (Stabbforsmo and Tangstad, 2026).

Absolute density, also known as material density or particle density, was measured by helium pycnometry with the use of an Accupyc 1340. The apparent density was measured by SINTEF Industry by sand with the use of a Geopyc 1360. Porosity was calculated by Equation 5.

$$Porosity\ (\%) = 1 - \frac{Apparent\ density}{Absolute\ density} \quad [5]$$

Scanning electron microscopy (SEM) and energy dispersive spectroscopy (EDS) was carried out on the samples with the use of a Jeol IT800 to examine the morphology of the samples, as well as the extent and way of reaction to SiC. SEM images were also used to measure the cell wall thickness of samples of calcined charcoal and SiC from charcoal.

The interior of SiC from charcoal and coal was investigated by μ-CT, with the use of a Nikon XTH 225 ST Microfocus CT in reflection mode with Tungsten target.

3. RESULTS AND DISCUSSION

The ability to withstand compressive forces without breaking can be related to the strength of the material. The results in Figure 3 and Figure 4 show a larger amount of small particles after hot strength testing of SiC from charcoal than calcined charcoal. This indicate that SiC from charcoal has significantly lower hot strength than calcined charcoal at all testing temperatures. The hot strength decreases by ~50 % when calcined charcoal is converted to SiC, when comparing the mass of particles >3.15 mm at 1000 ℃. Both calcined charcoal and SiC from charcoal increase in strength at 800 ℃ and 1000 ℃, indicating that the strength increases with increasing temperature.

Figure 3 and Figure 4 show that the particle size distribution after compression at the elevated temperatures SiC from coal is approximately the same as for calcined coal at all temperatures, but it does not increase in strength at 1000 ℃ unlike calcined coal. This indicates no significant change in strength from calcined coal to 52 % SiC from coal. Though Hoover claimed a small difference in strength, this seems to be within the uncertainty of the measurements and in line with these findings (Hoover, 2023). The hot strength of SiC from coal is significantly higher than of SiC from charcoal at all temperatures, as expected.

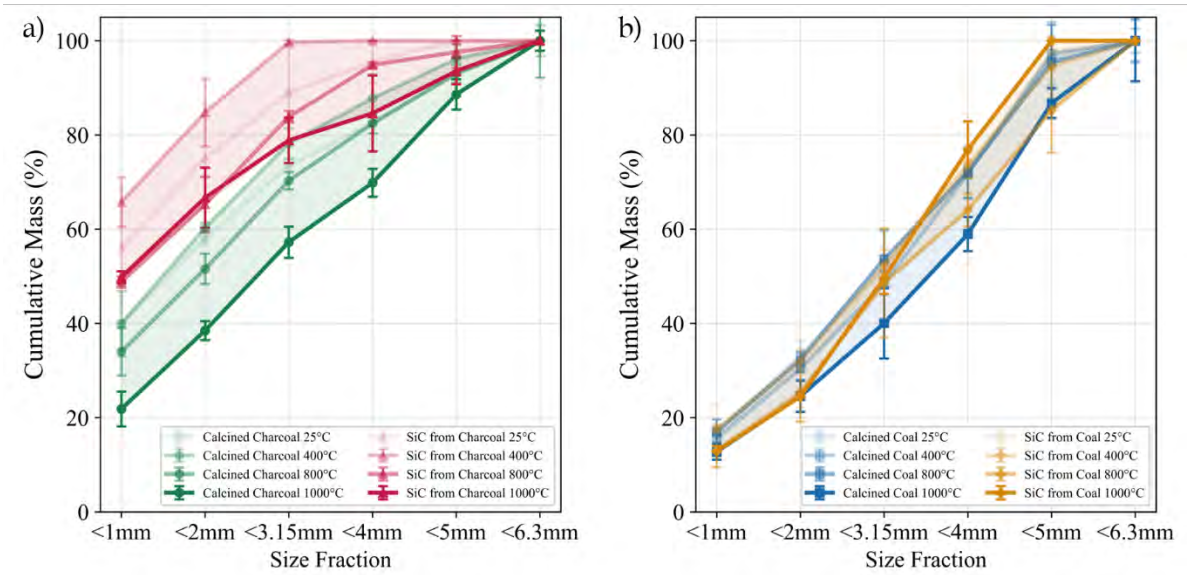

Figure 3: Cumulative mass for a) SiC from charcoal (red) and calcined charcoal (green) and b) SiC from coal (orange) and calcined coal (blue) after hot strength testing in the SPS.

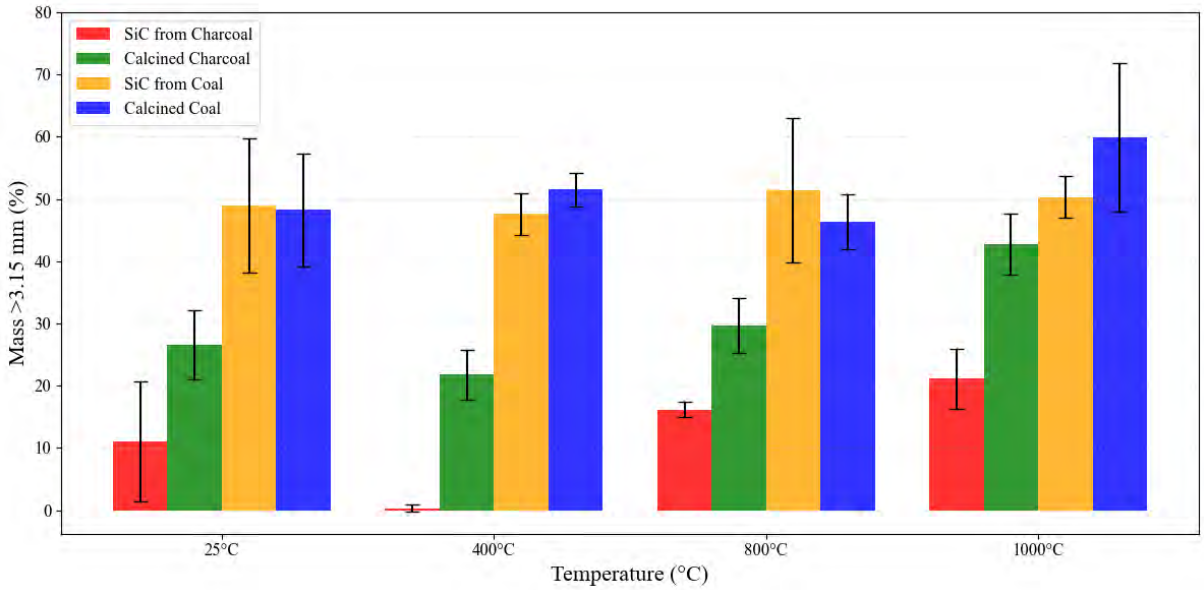

Figure 4: Total mass of particles >3.15 mm after hot strength testing in SPS, showing the difference in strength in SiC from coal and charcoal and calcined coal and charcoal. Values for calcined coal and charcoal also found in (Stabbforsmo and Tangstad, 2026).

The significant decrease in strength with the transformation from charcoal to SiC is likely linked to thinning of cell walls and decrease in structural integrity when charcoal reacts with SiO gas to form SiC, as seen in the SEM images in Figure 5. Measurements of cell wall thickness indicate a slight decrease in cell wall thickness with the transformation to SiC from calcined charcoal, with an average of 1.7 ± 0.5 µm cell wall thickness for calcined charcoal and 1.2 ± 0.3 µm for SiC from charcoal. It is mainly the cell walls that are load bearing, and when they lose their integrity the strength decreases. Figure 5a also show that some of the SiC produced deposits inside the pores. The SiC crystals appear to be loosely packed, which in combination with thinning of cell walls likely contributes to the decrease in mechanical strength with the conversion of charcoal to SiC.

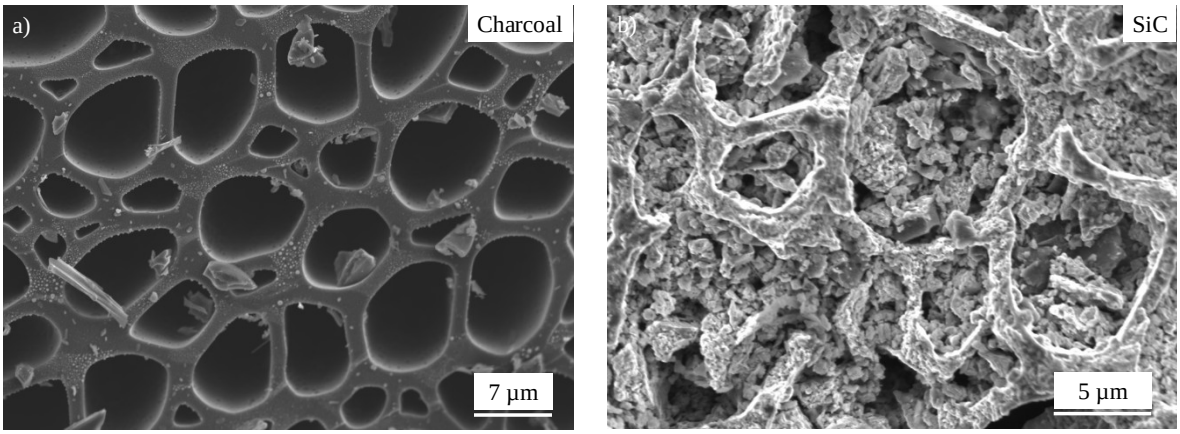

Figure 5: SEM images of a) SiC from charcoal showing the SiC crystals formed from the pore walls and b) calcined charcoal.

The strength of the materials is also usually also related to the porosity. As shown in Figure 6a, the average porosity of SiC from charcoal is found to be slightly lower than for calcined charcoal (81 % to 77 %), but as the margin of error is large the change is not considered to be significant and does likely not have a big effect on the strength of the material. The change in porosity with the reaction to SiC from coal is slightly more significant (61 % to 66 %) as the margin of error is smaller, but it is likely too small to contribute to a decrease in strength as this is not observed. A decrease in porosity with reaction to SiC is expected due to SiC having a larger molar volume than C, thus occupying more space. This is the opposite as observed for SiC from coal, but it can possibly be explained by the formation of CO gas from the reaction between SiO and C to SiC. CO generation can create a local increase in partial pressure if it cannot escape easily. Calcined coal is denser than charcoal, which can cause a local pressure build up leading to the growth of pores before it diffuses out of the material. Calcined charcoal already has a lower density and higher porosity which enable rapid gas escape and prevents pressure build up, thus also further porosity development. As expected, the absolute density of the material from both coal and charcoal increases with the conversion to SiC, as seen in Figure 6b. The theoretical density of 3C SiC is 3.2 g/cm^3 (Gavrilov, 1978), while the absolute density of 99 % SiC from charcoal is measured to be 3.0 g/cm^3.

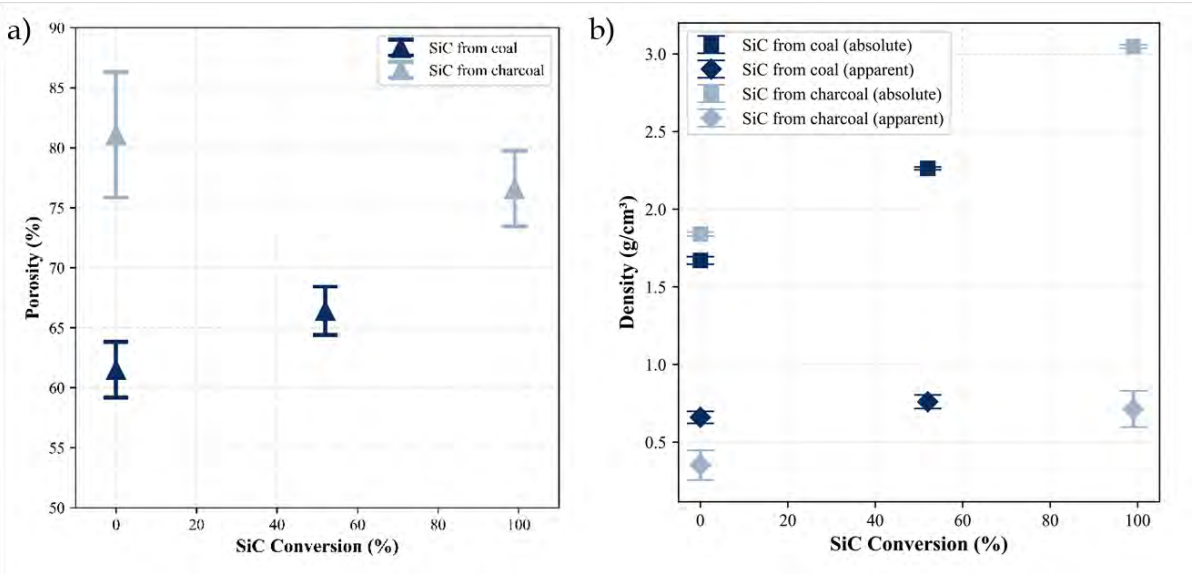

Figure 6: Measured a) porosity, and b) apparent density and absolute density of calcined coal and charcoal, as well as SiC from coal and charcoal. Values for calcined coal and charcoal from (Stabbforsmo and Tangstad, 2026).

The reaction between carbon particles and SiO gas to form SiC is observed to be topochemical, following the shrinking unreacted core model as seen in the image of a partly converted SiC particle from charcoal in Figure 7. The image shows a black core of charcoal and an outer layer of SiC, as expected. The composition of the layers was confirmed by EDS mapping as shown in Figure 8b. The reaction is also seen to occur in the large, open pores first, as green/grey dots are observed in the outer area of the charcoal core in Figure 7.

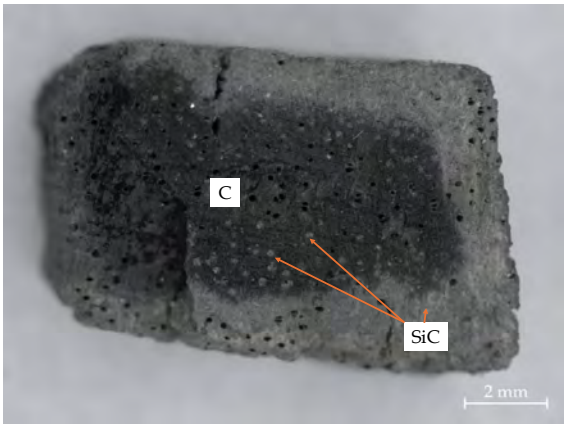

Figure 7: Image of the fracture surface of the interior cross-section of a partly converted SiC particle from charcoal. The particle reacts from the outer surface towards the centre, following the shrinking unreacted core model. Orange arrows indicating SiC as an outer layer as well as in pores in the carbon core.

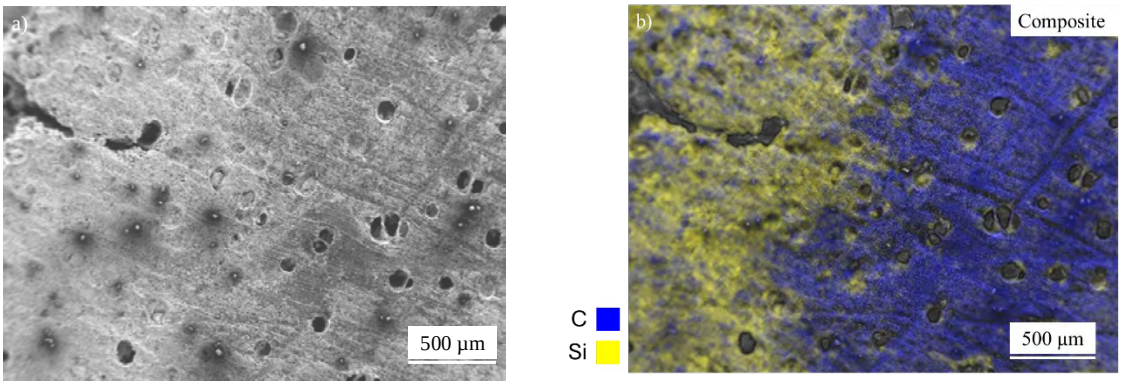

Figure 8: a) SEM image of the cross-section of a partly converted charcoal sample. b) EDS composite map of the area of transition from C to SiC showing carbon and silicon. The overlapping yellow and blue on the left indicates SiC and the blue is carbon (charcoal) on the right.

SiC crystals and whiskers were observed on the surface of particles of SiC from coal as seen in Figure 9a, b and c. This is confirmed by EDS point analysis carried out at the three points marked in Figure 9c, indicating approximately 50 at% carbon and 50 at% Si as listed in Table II. This is in line with the observations of others when converting carbon materials to SiC (Jayakumari and Tangstad, 2020; Hoover, 2023). Figure 9d shows the unreacted core of a sample of SiC from coal.

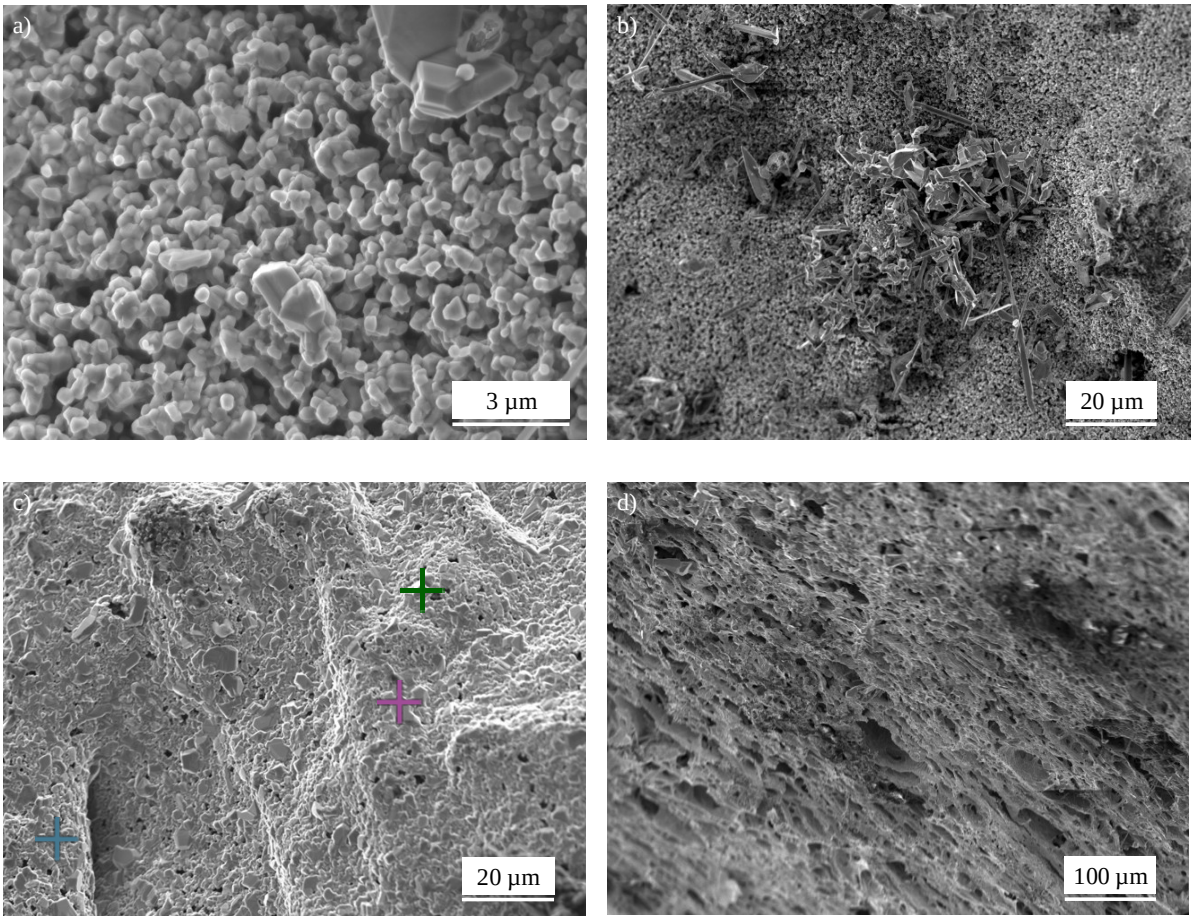

Figure 9: a) b) and c) shows the surface of a sample of SiC from coal with SiC crystals at different scale. b) shows SiC crystals and whiskers. In c) the green, pink and blue marks shows the spots for EDS point analysis and d) interior fraction surface of SiC from coal showing significant porosity and not small SiC crystals as on the surface.

Table II: Average atomic percent of C and Si detected by EDS point analysis at the three points shown in Figure 9c, indicating SiC.

	Average C (at%)	**Average Si (at%)**
SiC from coal	49.99 ± 2.57	50.01 ± 2.57

The XRD analysis shown in Figure 10 and Table III indicates a larger presence of amorphous graphite in the SiC from coal and very small amounts in the SiC from charcoal, in line with the chemical analysis. The main SiC polymorph is β-SiC, but there are also small amounts of an uncertain α-SiC polytype (2H was used in the refinement), along with ~1 % elemental Si in the SiC from charcoal, as presented in Table III. This is in line with the findings from SEM and EDS, as well as inside the margins of uncertainty of the chemical analysis.

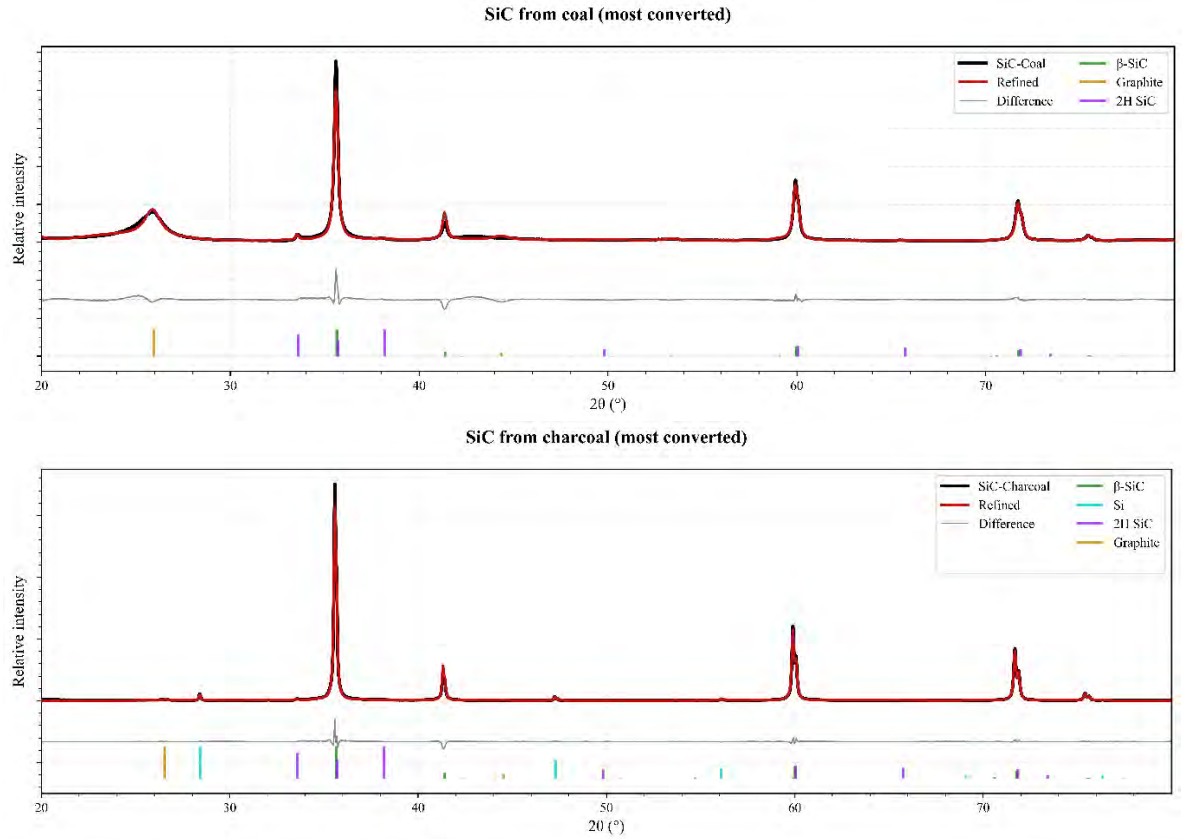

Figure 10: XRD diffractogram with Rietveld refinement for SiC from coal and charcoal, including the difference between the scan and refinement and bars for present structures. GOF for refinement is 7.97 for SiC from coal and 4.76 for SiC from charcoal. The present phases are indicated by the bars below the diffraction lines, they are β-SiC (green, PDF 04-008-4949, (Gavrilov, 1978)), graphite (orange, PDF 04-015-2407, (He *et al.*, 2007)) and 2H (purple, PDF 04-008-2392, (Sokhor and Glukhov, 1965)) for the most converted SiC from coal and β-SiC (green, PDF 01-075-0254, (Burdick and Owen, 1918)), Si (cyan, PDF 04-006-2527, (Steele and Rosi, 1958)), 2H (purple, PDF 04-008-2392, (Sokhor and Glukhov, 1965)) and amorphous graphite (orange, PDF 04-006-5764, (Zhao and Spain, 1989))

Table III: Quantitative analysis of phase content in the most converted SiC from coal and charcoal by Rietveld refinement from XRD. GOF for SiC from coal is 7.97 and 4.76 for SiC from charcoal.

	β-SiC (wt%)	**α-SiC (wt%)**	**Amorphous graphite (wt%)**	**Si (wt%)**
SiC from coal	47	<1	53	-
SiC from charcoal	97	<1	1	2

The μ-CT images in Figure 11 shows areas of different brightness. The lighter areas are of higher density and most likely consist of SiC, while the darker areas of lower density are unreacted carbon. The brightness and contrast of the images have been adjusted to make the particles the most visible. As the images are comparable with these adjustments, it indicates that the most converted samples have a higher density as they are significantly lighter. The lighter areas around the edge of the sample seen in Figure 11a likely consist of SiC while most of the samples in Figure 11b are converted to SiC. The findings of SiC around the edge of the material is in line with previous findings on SiC formation from carbon and SiO gas (Jayakumari and Tangstad, 2020), as well as the SEM and EDS shown in Figure 7 and Figure 8. Figure 11b also shows some smaller areas that are even lighter in some of the samples, especially in or around the pores, which could be Si as found by XRD.

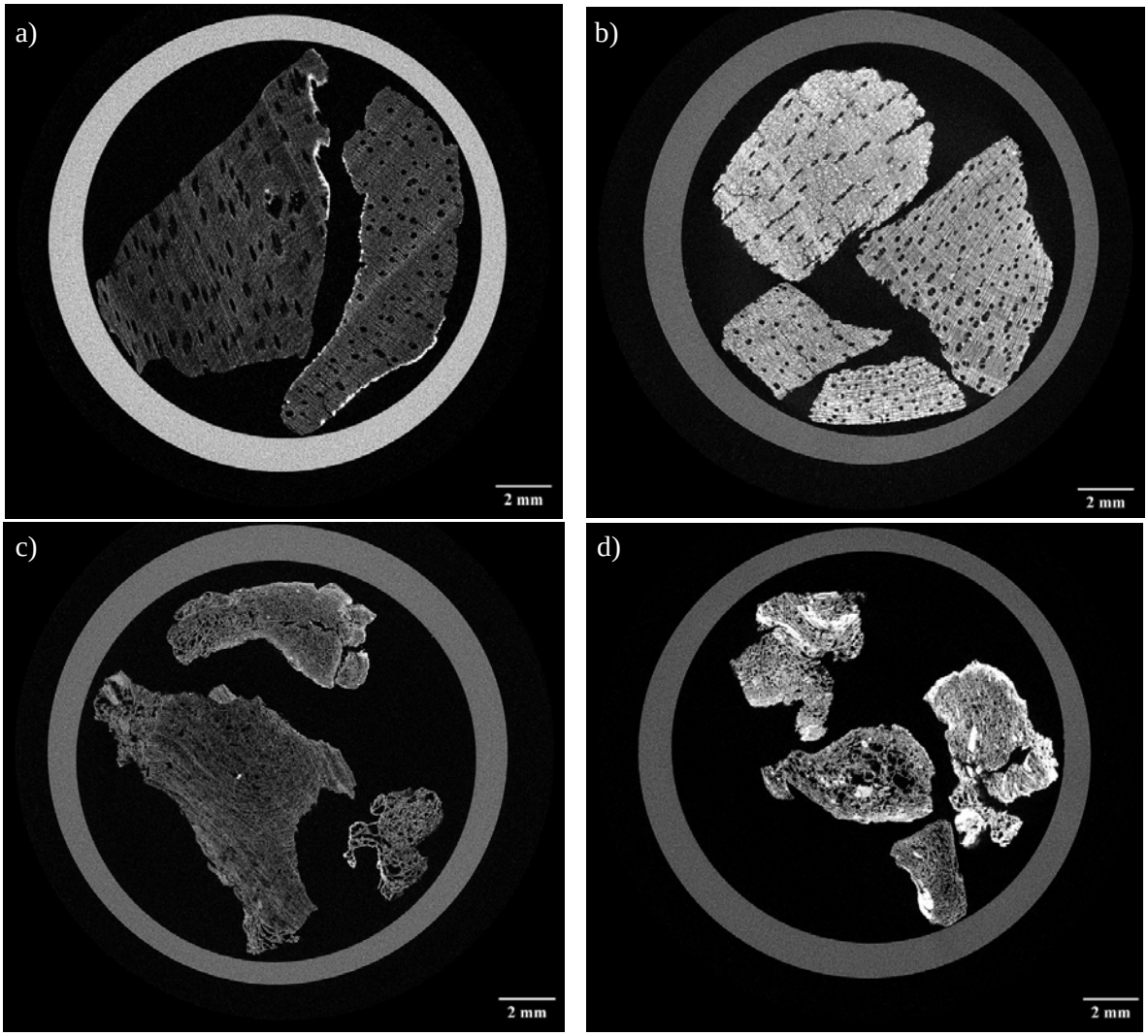

Figure 11: μ-CT images of a) 26 % SiC from charcoal, b) 99 % SiC from charcoal, c) 6 % SiC from coal and d) 52 % SiC from coal. Lighter areas have higher density and darker areas have lower density.

4. CONCLUSION

1. The hot strength of SiC from charcoal is significantly lower than of calcined charcoal, with ~50 % decrease in the distribution of particles >3.15 mm at 1000 °C. Likely due to the structural integrity of the material being compromised when the carbon from the cell walls react to form SiC. Both calcined charcoal and SiC from charcoal shows higher mechanical strength at 800 °C and 1000 °C than at lower temperatures.
2. The strength of SiC from coal is approximately the same as for calcined coal. For SiC from coal, the strength is found to be approximately the same at all temperatures, while calcined coal shows slightly higher strength at 1000 °C.
3. SiC from coal has, as expected, a significantly higher hot strength than SiC from charcoal at all temperatures. The difference in effect of SiC conversion on strength in charcoal and coal is likely to be affected by the difference in degree of conversion. The most converted SiC from coal contains 52 % SiC, while the most converted SiC from charcoal contains 99 % SiC. An important factor may also be the structure of the carbon precursor. Charcoal consists of an ordered structure of pores and thin cell walls, which the strength is highly dependent on. Coal on the other hand has lower porosity, higher density and thicker cell walls. This likely makes the integrity and strength of the coal less affected by the conversion to SiC than charcoal.

5. ACKNOWLEDGEMENT

This project has been financially supported by the Research Council of Norway through FME ZeMe, project number 350325.

6. REFERENCES

Burdick, C.L. and Owen, E.A., 1918. The atomic structure of carborundum determined by X-rays. *Journal of the American Chemical Society*, Vol.40, Issue 12, pp.1749–1759. https://doi.org/10.1021/ja02245a001.

Gavrilov, K.I., 1978. Variation of tetragonal bonds deformation in silicon carbide crystals with their hexagonality and degree of doping with nitrogen. *Sov. Phys. Crystallogr.*, Vol.23, Issue 6, pp.691–693.

He, J.L., Shen, Z.Q., Wu, E., Liu, Z.Y., He, L.L., Yu, D.L., Guo, L.C., Wu, Q.H., Luo, X.G. and Hu, Q.K., 2007. Carbon-rich boron carbide in the eutectic product synthesized by resistance heating of B2CN in graphite. *Journal of alloys and compounds*, Vol.437, Issue 1, pp.238–246.

Hoover, H., 2023. *Electrical Resistivity of Materials in the Silicon Furnace*. Doctoral thesis. NTNU.

Jahrsengene, G., Jayakumari, S., Kero, I.T. and Ringdalen, E., 2023. Sustainable Metal Production: Use of Biocarbon and the Concern of Dusting, COM 2023, *The 62nd Conference of Metallurgists*, Toronto, Canada, 21-24 August 2023, pp.1001-1007. https://doi.org/10.1007/978-3-031-38141-6_126.

Jayakumari, S., 2020. *Formation and characterization of β-and a-Silicon Carbide produced during Silicon/Ferrosilicon process*. Doctoral thesis. NTNU.

Jayakumari, S. and Tangstad, M., 2018. Formation of elemental silicon in β-SiC particles, *Silicon for the Chemical and Solar Industry XIV*, Svolvær, Norway, 11-14 June 2018, pp.125–138.

Jayakumari, S. and Tangstad, M., 2020. Transformation of β-SiC from Charcoal, Coal, and Petroleum Coke to α-SiC at Higher Temperatures. *Metallurgical and Materials Transactions B*, Vol.51, Issue 6, pp.2673–2688. https://doi.org/10.1007/s11663-020-01970-1.

Kim, G.-D., Kim, Y.-W., Song, I.-H. and Kim, K.J., 2020. Effects of carbon and silicon on electrical, thermal, and mechanical properties of porous silicon carbide ceramics. *Ceramics International*, Vol.46, Issue 10, pp.15594–15603. https://doi.org/10.1016/j.ceramint.2020.03.106.

Ksiazek, M., Tangstad, M. and Ringdalen, E., 2016. Five furnaces five different stories, *Silicon for the Chemical and Solar Industry XIII*, Kristiansand, Norway, 13-16 June 2016, pp.33-42.

Monsen, B., Lindstad, T. and Tuset, J., 1998. CO2 Emissions from the Production of Ferrosilicon and Silicon Metal in Norway, *56th Electric Furnace Conference*, New Orleans, United States of America, pp.371–378.

Ramos, D.C., Carneiro, A.D.C.O., Tangstad, M., Saadieh, R. and Pereira, B.L.C., 2019. Quality of Wood and Charcoal from Eucalyptus Clones for Metallurgical Use. *Floresta e Ambiente*, Vol.26, Special Issue 2. https://doi.org/10.1590/2179-8087.043518.

Ringdalen, E., 2018. SiC structures and SiC transformations in industrial Si- production. *Silicon for the Chemical and Solar Industry XIV*, Svolvær, Norway, 11-14 June 2018.

Sokhor, M.I. and Glukhov, V.P., 1965. Silicon Carbides with the Wurtzite Structure. *Sov. Phys. Crystallogr.*, Vol.10, pp.238–246.

Stabbforsmo, T. and Tangstad, M., 2026. Hot Strength of Coal and Charcoal by Spark Plasma Sintering Machine (To be published). *JOM*.

Steele, M.C. and Rosi, F.D., 1958. Thermal Conductivity and Thermoelectric Power of Germanium-Silicon Alloys. *Journal of Applied Physics*, Vol.29, Issue 11, pp.1517–1520. https://doi.org/10.1063/1.1722984.

Zhao, Y.X. and Spain, I.L., 1989. X-ray diffraction data for graphite to 20 GPa. *Physical Review B*, Vol.40, Issue 2, pp.993–997. https://doi.org/10.1103/PhysRevB.40.993.

Thea Stabbforsmo
PhD candidate, Norwegian University of Science and Technology

Thea Stabbforsmo is a PhD candidate at the Norwegian University of Science and Technology working with biocarbon in silicon production as a part of FME ZeMe. She holds a MSc in chemistry from NTNU.

Jahrsengene, G., A. A. Lindholm, I. Opstad, and S. Jayakumari. 2026. Dustiness of Various Carbon Materials for Metallurgical Industries. In *Silicon for the chemical and solar industry XVIII,* edited by M. Tangstad, H. Rong, A. Valderhaug, B. Andresen, H. Dalaker, and I. G. Page. Kristiansand, Norway, September 7–10, 2026. https://doi.org/10.55669/oa900811

Dustiness of Various Carbon Materials for Metallurgical Industries

G. Jahrsengene[1], A.A. Lindholm[2], I. Opstad[2], and S. Jayakumari[2]
[1]SINTEF, Norway, goril.jahrsengene@sintef.no
[2]SINTEF, Norway

Keywords: Carbon materials, Dustiness, Heubach dustmeter, Strength

Abstract – Due to the fragility of traditional biocarbon materials, high amount of dust and fines may be generated during transport and handling when replacing fossil carbon with biocarbon in metallurgical industries as part of their decarbonization strategies. Although carbon losses and effect on furnace performance are important, the health and safety of workers are of the highest importance. Inhalable and respirable dust is a direct safety concern, and the increased risk of dust explosions are also present. As such, being able to easily predict the airborne dust formed under typical conditions is necessary. In this work, the aim is to compare one of the most common strength tests, the tumble abrasion test, to a standardized dustiness evaluation called the Heubach Dustmeter Type I analysis, which has previously not been used on these types of materials.

1. INTRODUCTION

Utilizing renewable carbon reductants in metallurgical industries as a replacement of fossil carbon is a goal for industries spanning silicon, ferromanganese and other ferroalloys, steel, as well as for aluminium production. For charcoal, the main challenge is the fragility of the material, producing significant amounts of fines and dust during transport, storage and handling. This results in mass losses, affects furnace performance, and raises health and safety concerns due to the airborne dust (Jahrsengene et al., 2023; Jayakumari and Ksiazek, 2023). Related to health and safety, being able to predict the presence of airborne dust is an important step for choosing materials, and strategies related to agglomeration techniques which typically makes the biocarbon stronger.

Figure 1: Example of what occurs when dropping a fragile charcoal material after tumbling.

This work is licensed under the Creative Commons Attribution 4.0 International License. To view a copy of this license, visit https://creativecommons.org/licenses/by/4.0/

Tumble abrasion strength method, where a sample of known particle size distribution is tumbled in a drum for a set speed and time before sieving, is the main method used to estimate the mechanical strength as it attempts to replicate the mechanical degradation that occurs when the material is transported and charged into the furnace. The results are often reported as the tumble index and the abrasion index after sieving after the test. ISO 3271 (Iron ores for blast furnace and direct reduction feedstocks — Determination of the tumble and abrasion indices (ISO Standard, 2015)) defines these as amount over wt% >6.3 mm and wt%<0.5 mm respectively.

To evaluate if a specific material is likely to generate a lot of airborne dust, it has been suggested to further analyse the smallest fraction after the abrasion test. By including smaller sieves than 0.5 mm during the analysis, the airborne dust generated in the strength test could possibly be better identified. For this approach, representative sieves must be included in the analysis.

Airborne particles are most often defined as particular matter (PM) with an aerodynamic diameter (considering the combined effect of shape, density, porosity, surface roughness) rather than the actual diameter of the particles. The resulting aerodynamic diameter is equivalent to how a smooth, spherical particle with 1 g/cm^3 density would behave. Although airborne particles often are defined as having an aerodynamic diameter of 100 µm or less (PM_{100}), a 100 µm sieve will likely not capture the airborne dust due to the particles possibly having a higher measured diameter. Also, losses can be expected during transfer of materials to sieves and during sieving due to the aerodynamic properties. Small carbon dust is typically also electrostatic and can get stuck to other particles or equipment. In addition, the properties of the material have an influence on the sieving process; is the material fragile the sieving process itself may give rise to more dust and possible different fractions than what was initially produced by the drum.

Heubach Dustmeter is a standardized instrument designed to measure the dustiness of bulk solid materials, particularly powders and granulates (Delft Solids Solutions, 2025). It is used in various industries to assess how much dust a material release during handling by use of a rotating drum, a coarse particle separator, a well-controlled air stream and a filter. As such, the method follows the principle of the gravimetric filter method in a standardized, closed lab environment, reporting total airborne dust (in mg/kg) under certain conditions of material, drum speed and airflow, drawing airborne particles onto the filter. The result reported reflects the dust present in the bulk material, and those formed during the tumbling. The method is extensively used on seeds (Euroseeds, 2026) and powders (Bach and Schmidt, 2008) with well, pre-defined parameters for the standard test.

Heubach dustmeter measurements have currently not been reported for evaluating dustiness on materials for metallurgical industries. The methodology is similar as the abrasion tumble strength test but will avoid losses and influence of sieving due to the closed environment, and capture of dust using an airstream. Finding appropriate parameters and standardizing the method would be crucial for this to be a developed method for the metallurgical industries. Initial investigations are necessary to understand the major limitations of the equipment and identify important parameter effects when using these types of materials in this type of test.

In this work, metallurgical coke, coal, charcoals, and agglomerated biocarbon in the form of pellets have been assessed by rotating drum tests to determine the smallest airborne fractions. Heubach Dustmeter Type I measurements were done with standardized parameters for drum speed, time and airflow. One charcoal was investigated in more detail related to the effect of

drying, as well as variation in drum speed and time. The results were compared to more conventional tumble abrasion strength analysis using a Hanover drum followed by sieving. To investigate the airborne dust fractions further, particle size distribution analysis was performed on the airborne materials collected by the filter during the Heubach Dustmeter measurements.

2. EXPERIMENTAL

2.1 Materials

In this work, three different industrial charcoals (Charcoal 1, 2 and 3) were considered and included for different parts of the work. Reference materials of metallurgical coke and coal was included in most of the study. Two biocarbon pellets (Pellet 1 and 2, no further details on production available due to confidentiality) were also investigated to show how this important step of biocarbon agglomeration affects the strength and airborne dust generation. Pictures of the materials is given in Figure 2.

Charcoal 3 was investigated in more detail after drying for 24 h at 110 °C, to see how this would affect the results (as a possible pre-treatment to normalize the material before the test) and briefly evaluate the effect of moisture.

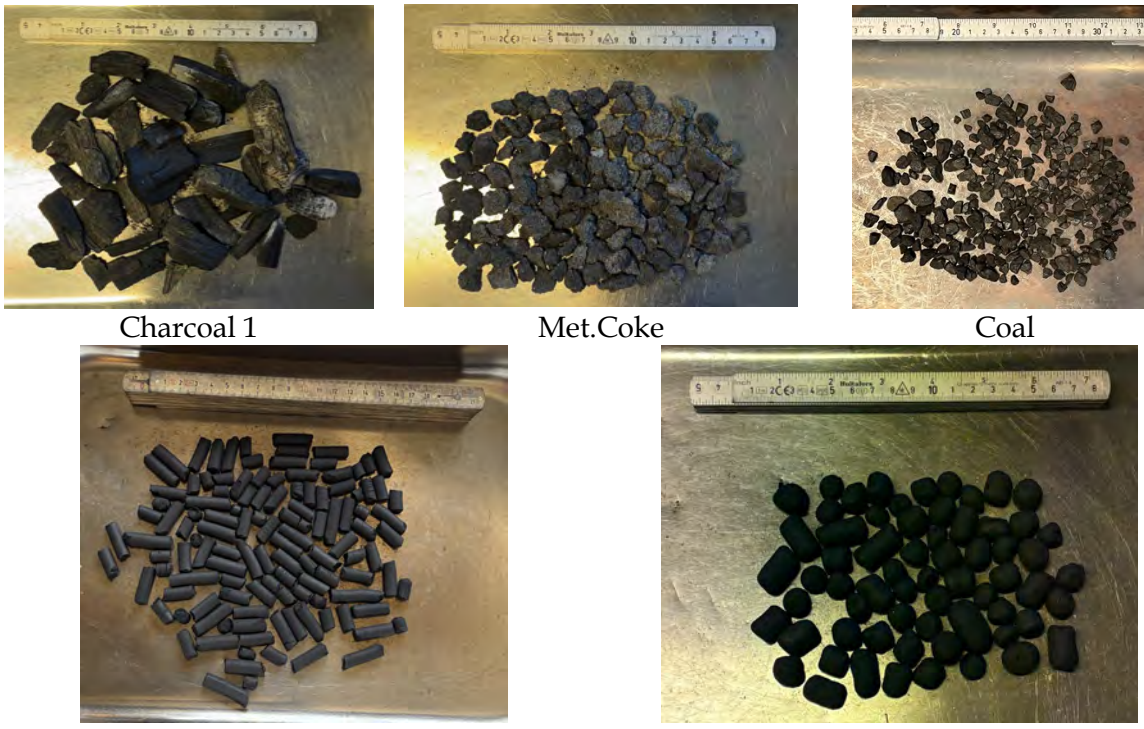

Figure 2: Materials used in the study (except charcoals 2 and 3).

2.2 Cold strength tumble test

Tumble abrasion strength was evaluated for the carbon materials in a lab setting using a Hanover drum. The carbon material was placed in the steel drum measuring 30 cm in diameter that contained 4 raisers spaced 90 degrees apart. The standard test was run with 100 g samples; however, some tests with Charcoal 3 also utilized 200 g (to see difference in the weight). The sample was tumbled 5-30 minutes at 30 or 40 rpm. For all samples, materials of size smaller than 1.25 mm was removed before start, and for the charcoal, coal and metallurgical coke

samples, 90-100 % of the material was above 6.7 mm (the rest above 4.75 mm). The pellets were used in the shape they were produced.

After the test, the material was sieved in 9 different fractions (+10 mm, +6.7 mm, +4.75 mm, +3.35 mm, +1.25 mm, +0.5 mm, +0.25 mm, +0.125 mm, and -0.125 mm). The expectation is that the fraction smaller than 0.125 mm is close to the airborne dust fraction and is the focus of this work, while there are also losses present that could be lost e.g. in the ventilation in the workspace. Only one parallel was done for each material.

2.3 Dustiness - Heubach Dustmeter type I measurements

The standard Heubach Dustmeter type I was used for the dustiness measurements; the standard settings utilize a rotary speed of 30 rpm for 5 minutes with an airflow of 20 L/min (DIN 55992-1). During the first campaign, the reference materials, pellets and Charcoal 1 were run as received and already generated dust is included in the analysis. Each material was run in triplicate. A second campaign, run with duplicate measurements, used Charcoal 3; both 30 and 40 rpm was used as rotation speed, and the time was increased to 10 minutes with the filter being changed and weighed at several points during the tumbling. This was partly done due to the generation of large amounts of dust for this sample; the dust blocks the filter, and the well-controlled air flow will be affected as a result of which the measurement clearly will lose accuracy. Charcoal 3 was also run at 30 rpm after drying overnight.

2.4 Particle size distribution

Laser diffraction (LD) is an instrumental method for the characterization of particle size distributions (PSD) of dry powders, suspensions and emulsions. The dust of the filters from the Heubach Dustmeter measurements was collected, split in two parallels (except for the least dusty material where all was combined to one parallel), and was placed in the sample unit of the laser diffraction instrument. A Malvern Mastersizer 3000 was used in combination with the Aero S sample dispersion unit for measuring in air. This configuration has a measuring range from 0.1 µm up to 3500 µm. The used optical model is Lorentz-Mie taking into account the optical characteristics of the particles, all in accordance with ISO 13320-1:2020. The applied optical model has a Particle Refractive Index [n] of 1.52, which is a commonly used value and among the range given for charcoal like materials. The validity of the optical characteristics is verified by the quality of the fit. The fit is a comparison of the actual measured diffraction pattern and the calculated deconvoluted diffraction pattern.

The principal result of the LD technique is a volume-based PSD for a collective of *spheres* having defined optical properties, for which the calculated scattering behaviour gives an optimum match with the measured pattern. As such, with non-spherical dust, the model may be less accurate. The definitions of the key numbers are given below.

- D_0: The minimum particle size.
- D_{10}: Distribution Percentile, 10% of the particle volume is smaller than the value.
- D_{50}: Distribution Percentile, median particle size.
- D_{90}: Distribution Percentile, 90% of the particle volume is smaller than the value.
- D_{100}: Distribution Percentile, 100% of the particle volume is smaller than the value, the end of the distribution.
- D [4,3]: Volume weighted mean diameter $(\Sigma n_i D_i^4)/(\Sigma n_i D_i^3)$.
- Span: Distribution width, calculated as $(D_{90} - D_{10})/ D_{50}$.
- Mode: Modal size, particle diameter present with the highest frequency

3. RESULTS AND DISCUSSION

3.1 Cold strength tumble test

The results of the smallest fractions of the cold strength tumble test after running the 100 g samples for the majority of the materials in the study is presented in Figure 3. The results show that when evaluating the more traditional abrasion index, the fraction below 0.5 mm, the trend between the different materials is slightly different than when evaluating the fraction only below 0.125 mm. Especially when evaluating the three charcoals this is evident; Charcoal 2, which had 14 wt% of material under 0.5 mm, had less than 2 wt% being below 0.125 mm. When evaluating Pellet 2, all the material below 0.5 mm is also below 0.125 mm, but in the other cases there is usually a difference (although much less than for Charcoal 2). These results show that the abrasion index is not sufficient to compare material trends related to the airborne dust, since the distribution within this fraction varies greatly between different materials.

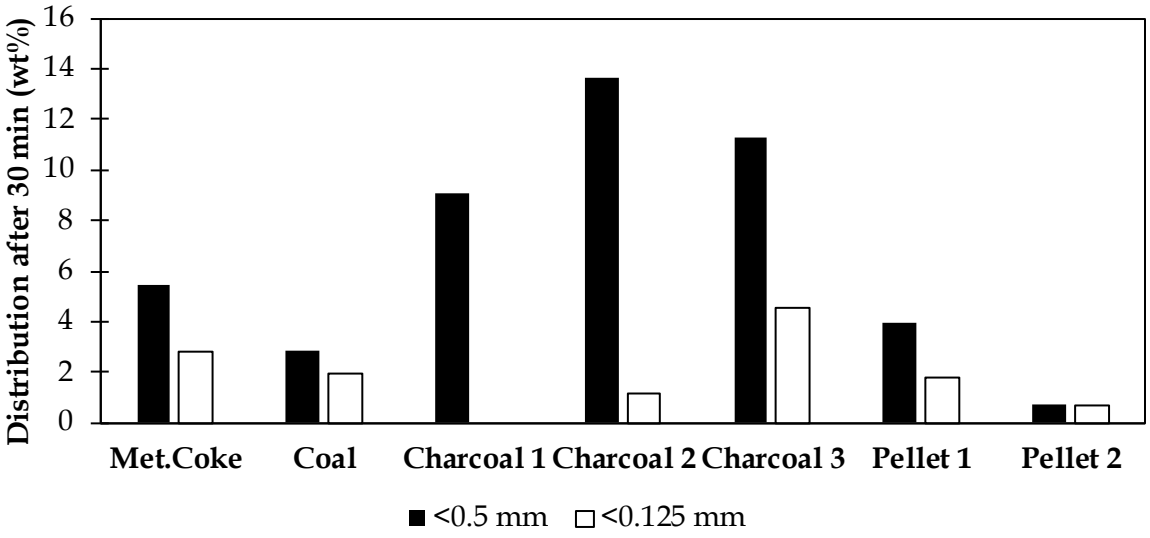

Figure 3: The weight distribution of the smallest fractions after 30 minutes tumbling at 40 rpm with the Hanover drum.

In these types of experiments, the final distribution most often disregards the material losses. 100 % typically sums up what is measured in the different fractions but depending on the properties of the material there are some carbon not found when weighing the resulting separated fractions. For the above materials, after 30 minutes, the charcoal materials had ca. 2.7-2.8 wt% loss, the metallurgical coke and coal about half at 1.4 wt%, while the pellets had only about 0.7 wt%.

It is observed that the losses are mainly due to the smaller particles, which is observed during the experiment to more easily get stuck to the smallest sieves as well as the tumbler, or small material that vanish into the ventilation when opening the drum, transferring from drum to the sieves, or from the sieves to the scale. Some of the carbon was also shown to be more electrostatic than others, and may both get stuck to other larger carbon particles, agglomerate together, and get stuck in the sieve. The small, airborne particles that ends up dispersed for longer time air during transfer between equipment may easily get removed with a normal lab ventilation suction, which is necessary to use for safety and could otherwise also spread out over the working area. As such, it can be assumed that large part of the losses is airborne dust, and the 0.125 mm fraction is not an exact measure of this fraction.

Charcoal 3 was investigated in more detail to get a better understanding of the losses, as well as some further information about moisture and rotation speed during the tumble test. After

drying the material overnight, it had lost 7 wt% which can be attributed to moisture. 200 g of the charcoal, both dried and as stored, was tumbled at 30 and 40 rpm, while the 100 g sample as presented above is also evaluated to see the effect of the sample amount.

The results related to the losses are presented in Figure 4. For the 100 g sample run at 40 rpm, it can be observed in Figure 4a that after 5 and 10 minutes, the material loss is of the range of what is measured in the 0.125 mm fraction. After an additional 20 minutes (the previously separated fine fractions below 0.5 mm was not re-introduced to the tumbler after mid-sieving), the total loss does not continue in a linear fashion. This indicates that some of the small dust could more easily attach to larger particles over time, or that the material itself is reaching a type of steady state.

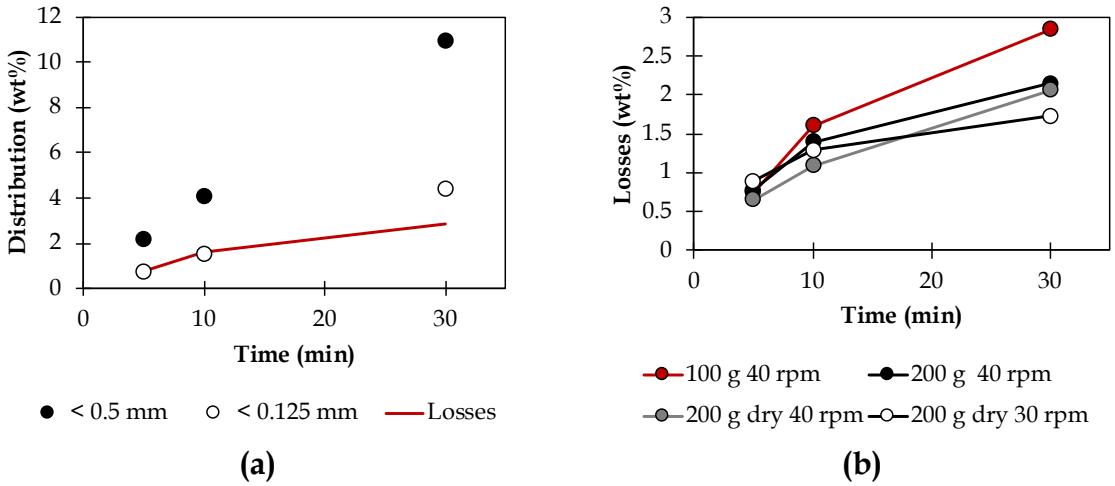

Figure 4: The distribution of the smallest fractions with the losses included after 5, 10 and 30 minutes tumbling. (a) 100 g, 40 rpm, and (b) variations specified for losses only.

Comparing only the losses in Figure 4b including most of the 200 g samples, the exact same trend is observed as for the 100 g loss in Figure 4a. In addition, the mass loss seems independent of the amount, moisture and rotation speed for the first five minutes. The three examples of 200 g samples are otherwise very similar after all three times, while the 100 g sample had significantly more losses after the full 30 minutes. This shows the importance of comparing same sample sizes; a possible explanation could be that more of the dust is able to settle on larger charcoal pieces when more are present.

Finally, the measured <0.125 mm fraction (excluding the losses) for all these are compared in Figure 5. As expected, the same sample run at 40 rpm gave more of the smallest fraction than 30 rpm, although, in the case of the dried material, the difference was minimal until reaching 30 minutes (Figure 5a and 5b). However, when observing the difference between the dried and not dried material run with the same rotation speed in Figure 5c and 5d, the expectant behaviour of the dried giving more fines is not observed. At 40 rpm the dry material is always marginally lower than the not dried, while at 30 rpm the materials shift, also ending with the dried material giving less of the smallest fraction.

The behaviour related to the dried materials observed in Figure 5c and 5d was surprising and could not be explained by including the losses. Although not done in repeat, both rotation speeds gave the same trend and is an indication of the effect that the moisture in the charcoal when it is at these levels (7 wt% and below) have little effect on the smallest dust.

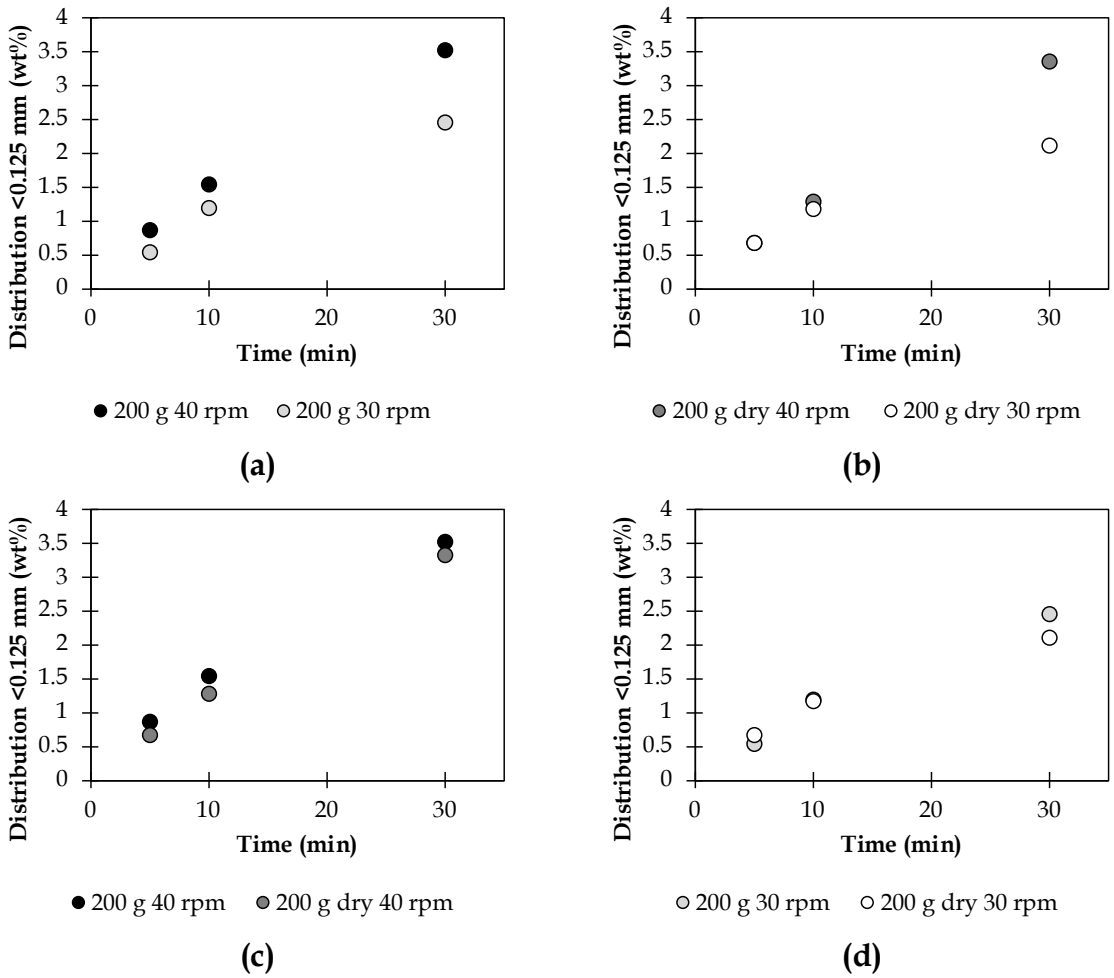

Figure 5: Comparison of the measured <0.125 mm fraction (excluding the losses) between the different parameters.

3.2 Heubach Dustmeter results

By use of the standard settings of the Heubach Dustmeter type I (DIN 55992-1: 30 rpm, 5 minutes, airflow 20 L/min), the average dustiness is reported as mg/kg (ppm, based on the weight loaded for the test) and is presented in Figure 6 (2 duplicates of Charcoal 3, 3 duplicates for all other samples). The relative standard deviation (RSD) is 5-13 % (well within the 17 % found by Round Robin testing). The dustiness is in the range of 400-2500 mg/kg for all but the charcoals, which have the highest dustiness potential, with Charcoal 3 (5600 mg/kg) more so than Charcoal 1 (4200 mg/kg).

The removal of moisture of Charcoal 3 by drying overnight, resulting in 8 wt% loss, have an expected increase in dustiness and ends up with the highest measured dustiness potential of 6800 mg/kg. By adjusting for the moisture initially included in the dried sample, the dustiness is estimated to 6300 mg/kg, which is closer to the non-dried material. When evaluating the uncertainties the adjusted number is within the uncertainty of the non-dried material. As the other samples does not have the final moisture level at time of measurement, it is not possible to compare them on dry basis, as the transport and storage have an effect (likely what is resulting in 8 wt% compared to the 7 wt% moisture loss before the Hanover drum test). The numbers reported from the test cannot be compared to previously reported numbers for other types of materials because they often investigate powders themselves more importantly their inherent dustiness, not dust that is formed during the test due to being a fragile material.

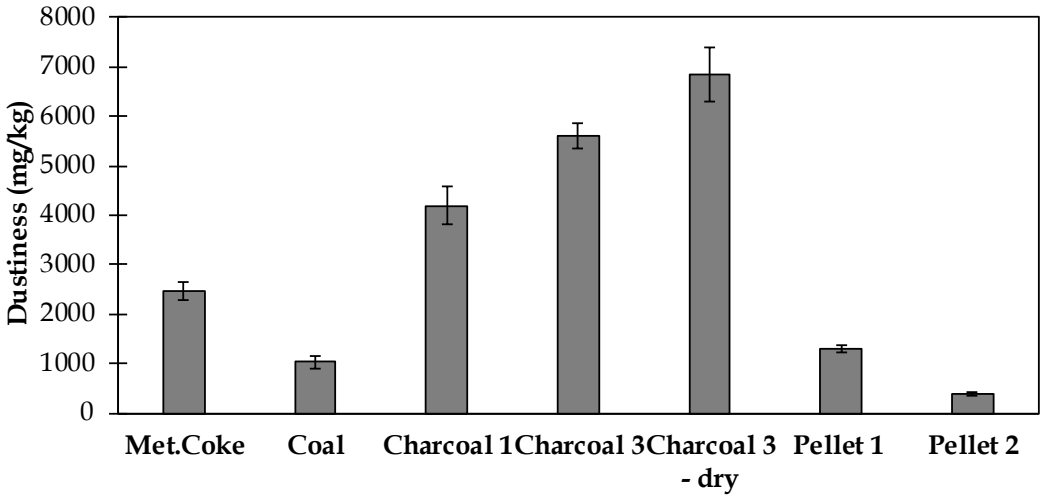

Figure 6. The dustiness as reported by standardized Heubach Dustmeter Type I for the different materials.

The results in Figure 6 also show that the agglomeration technique of pelletization is an effective way to improve biocarbon dustiness. The two pellets can be seen in Figure 2 to be different from each other, and the Hanover drum experiments also indicated a large difference (they are from different producers and as such not produced in the same way). Pellet 2 is the least dusty material, better than also the reference metallurgical coke and coal samples. Within the RSD, it is not possible to discern if Pellet 1 is any different than the coal, indicating this has not as good properties as Pellet 2, however, a large improvement from the typical charcoals can still be observed.

Charcoal 3 was investigated in more detail, running also at 40 rpm and for longer times. Although initially planned to go up to 30 minutes, to best compare with the Hanover drum test results, the high dustiness of the material made it necessary to either change the filter every few minutes or reduce the amount of material drastically. For this reason, the test was stopped after 10 minutes, keeping the initial amount around 100 g and the use of 3-6 filters per experiment. The results are presented in Figure 7, which summarize all filter measurements of the 2 parallel runs done for each set of parameters.

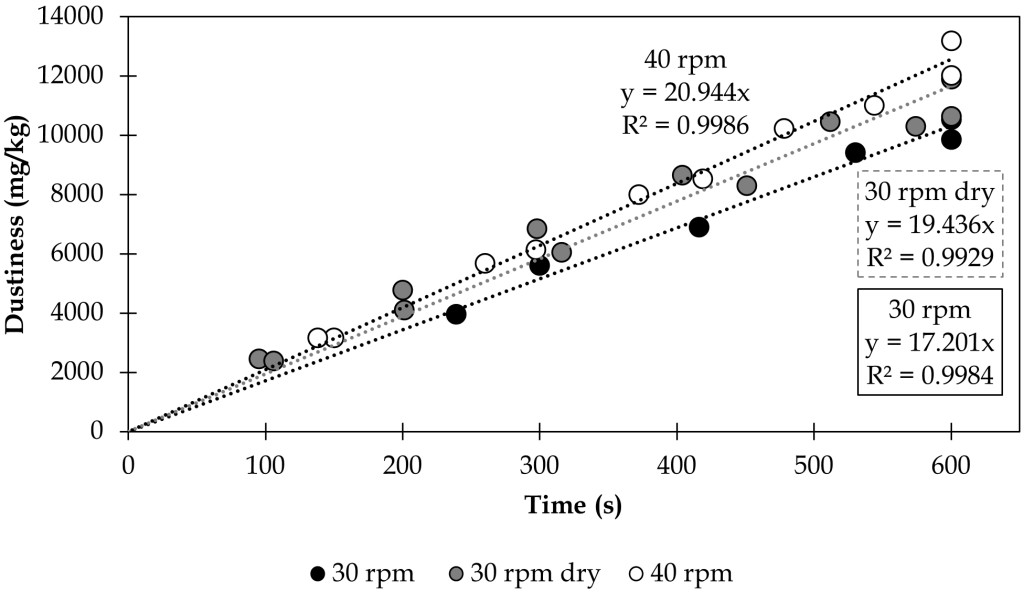

Figure 7: Dustiness behaviour of Charcoal 3 during 10 minutes of tumbling.

As expected, a linear increase with time is observed. The slope is higher for the higher rotation speed of 40 rpm, which is explained by the larger number of interactions with walls and other material that the material experience at higher rotation speed. The dry material also has an increased slope compared to the not dry material at 30 rpm. With more moisture in the sample, there is a possibility that this cause cohesive effects which prevent dust from becoming airborne, possibly by sticking it to larger particles. However, this change could also be explained by the lower sample mass when dried, as the sampling to 100 g was done before drying. Where the non-dried sample still has 8% weight in volatiles, these are not solids that can be caught by the filter. The dried sample did not contain these volatiles meaning a relatively higher possible dusting potential. The mass loss of 8% is also comparable to the relative difference of dusting potential between the samples of ~10% further strengthening this possibility; when adjusting for the 8 wt% the slope for the dried material is almost identical to the not dried material (17.88 mg/kg/s).

3.3 Particle size distribution of captured dust

The dust captured in the standardized Heubach Dustmeter type I measurements (except the Charcoal 3 variants), where collected from the different parallels and split into two for the LD analysis (for the least dusty material, Pellet 2, all the dust collected was used for one parallel LD measurement due to the low amount of dust for this sample). The results, in form of differential and cumulative volume, are presented in Figure 8, and the key numbers are presented in Table I.

In theory, for the Heubach type I method airborne particles with an aerodynamic diameter below 100 µm are caught on the filter as dust and larger particles settle in the coarse particle separator. For the samples, 97-99% of the volume of particles is below 100 µm in the LD analysis. The small volume of particles detected above 100 µm is likely due to the differences in equivalent sphere volume reported by laser diffraction and the aerodynamic diameter. In the latter also density, porosity, shape and potential surface roughness are considered.

Table I: The laser diffraction analysis key numbers.

	D_0 (µm)	D_{10} (µm)	D_{50} (µm)	D_{90} (µm)	D_{100} (µm)	D[4,3] (µm)	Span	Mode (µm)
Met.Coke	0.1	3.2	15.3	45.7	160.8	21.0	2.8	18.7
Coal	0.1	4.9	16.9	48.2	162.9	22.9	2.6	17.0
Charcoal 1	0.5	5.5	17.4	55.9	238.3	25.7	2.9	17.0
Pellet 1	0.2	5.5	13.5	32.5	183.0	17.7	2.0	13.6
Pellet 2	0.2	3.5	14.4	46.5	209.3	21.2	3.0	16.0

The results in Figure 8 show that the dust samples have similar particle size distributions with only nuanced differences. For all samples the particle size distribution of the dust is monomodal. The median particle size (D_{50}) was 13.5-17.4 µm, while the frequency that occurred the most (mode) was a bit higher, 13.6-18.7 µm. For the coal and Pellet 1 no difference is observed between these two values; metallurgical coke and Pellet 2 increased from median to modal while the charcoal was slightly lower. The volume weighted mean diameter was higher in all cases, 17.7-25.7 µm.

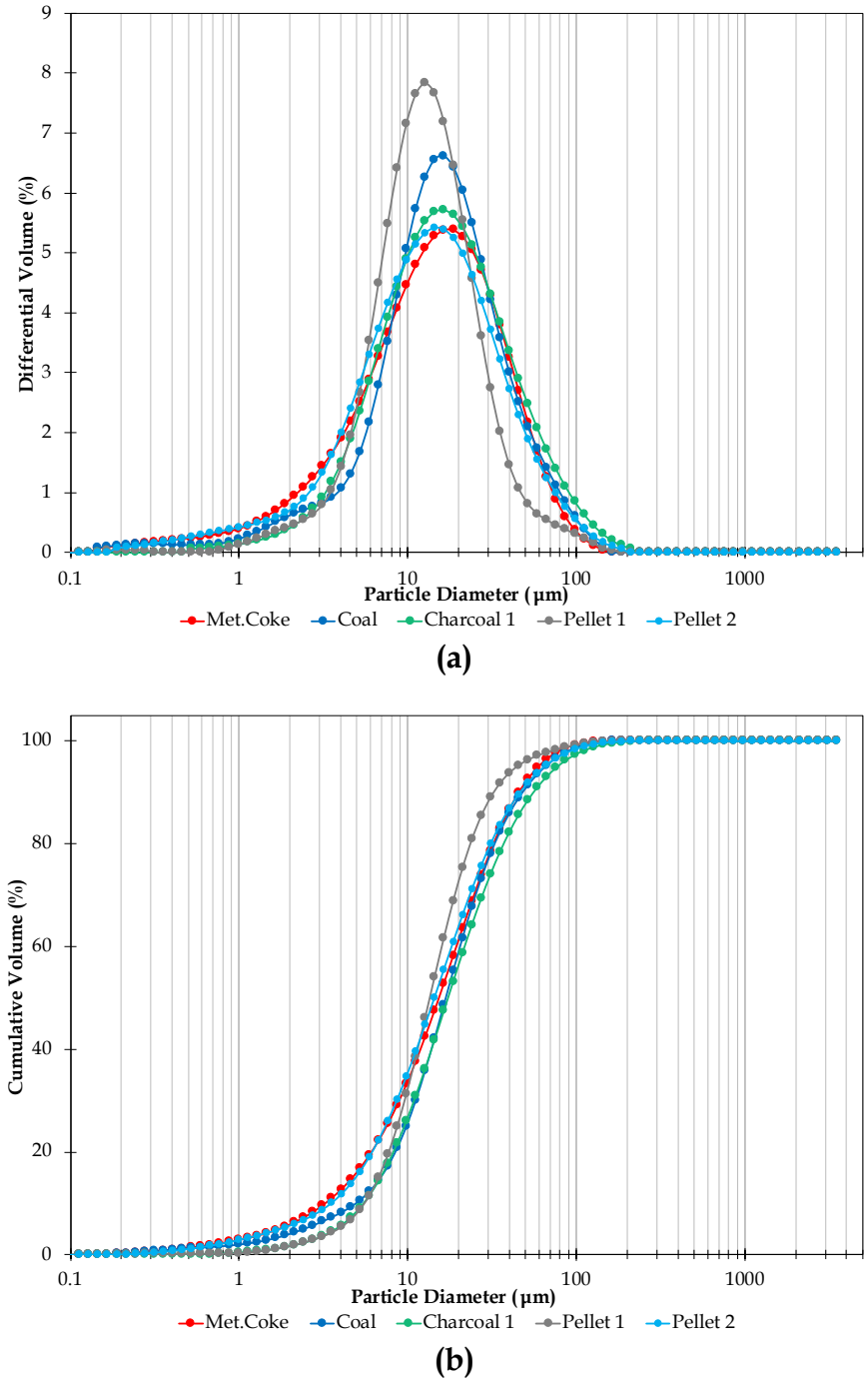

Figure 8. The particle size distribution of the captured dust in (a) differential and (b) cumulative volume.

Looking at the D_{90} values, metallurgical coke, coal and pellet 2 were all of similar values around 46-48 µm, but the charcoal was significantly higher with 56 µm and pellet 1 significantly lower, with 33 µm. Despite the difference, this mean that most of the dust captured is quite small. The test targets PM_{100} and as such 100 µm as the aerodynamic diameter, but small amounts of particles (1-3 vol%) were detected to have the spherical diameter above this value. The larger values detected can be due to the actual shape and the use of equivalent sphere volume used for the calculations. The largest particles captured by the test was close to 250 µm for charcoal, indicating that some dust of this size may still be airborne and as such with an aerodynamic diameter still below 100 µm, as previously mentioned likely due to density, porosity, shape and surface roughness of the particles.

4. HEALTH AND SAFETY

PM_{100} (dust with aerodynamic diameter of 100 µm or less) is expected to be airborne and cover both inhalable and respirable fractions upon handling scenarios (Heyder and Svartengren, 1999). Inhalable dust is often considered to only affect the upper respiratory system and is irritating for nose, mouth, eyes etc. Typically, one may sneeze, cough, or cry when subjected to this dust. This dust typically does not have the longest travel distance, and relatively quickly end up on surfaces (where it can be further disturbed and briefly be airborne again). However, the smaller dust, most typically defined as 10 µm and smaller (PM_{10}), can be airborne for a much longer time, and is defined as the respirable (or thoracic, or suspended) dust. This dust may penetrate the lungs and as such potentially cause very serious health issues.

The Heubach Dustmeter type I test aims to capture PM_{100}, but it is not possible to say if some of this is so small it is also respirable and PM_{10}. The LD results cannot be viewed as aerodynamic diameters and as such cannot properly differentiate between the amounts that is likely PM_{10}. However, the LD results may be presented as volume percentages in or below a certain size, similar as to how we divide different fractions in sieving tests, and as such give an indication if some can be expected to be in the PM_{10}. These results are presented in Figure 9 for the total fraction below 10 µm, 50 µm or 100 µm. It can be observed most of the material is below 50 µm, as indicated by the D_{90} value. However, the volume below 10 µm varies from 26-27 % for the coal and charcoal, to 32-34 % for the metallurgical coke and pellets, and this is the smallest dust most important to the respirable health issues. This may indicate that despite the pellet's good behaviour with total amount of fines, what little is produced could possibly be in a size fraction more prone to personal health.

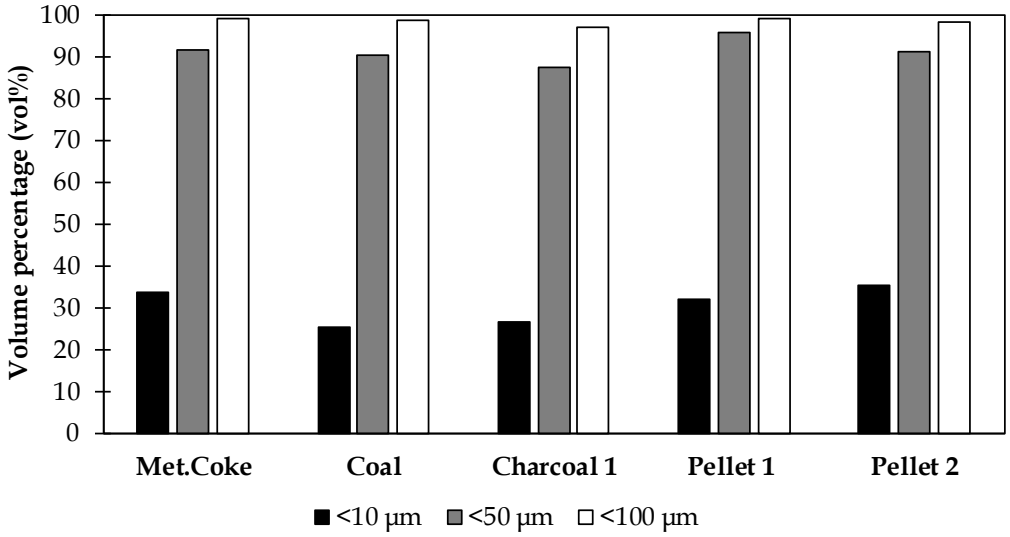

Figure 9. Volume percentages of differently chosen diameters of the dust captured in the filter during the Heubach Dustmeter type I measurements.

Different types of Heubach Dustmeters than the type I used in this study is further optimized to differentiate between inhalable and respirable dust. However, an exploratory exercise was done on the results, using the volume percentages obtained in the LD analysis to further normalize the total dust (in mg/kg) to attempt to get more information on the potential smallest <10 µm fraction (Figure 10). The trend is mainly kept with respect to the full dustiness in Figure 6, but when removing one and one fraction, the trend changes. For example, when only evaluating the fraction below 1 µm, the metallurgical coke appears to have the highest amount of this dust produced, while the charcoal has almost no dust below 1 µm despite

having the most under 10. As it is not known which carbon and biocarbon particle sizes that is of most importance related to especially the respirable dust, any of these might cause serious health issues. This exercise also demonstrates the need of more precise measurements to differentiate between the smallest fractions.

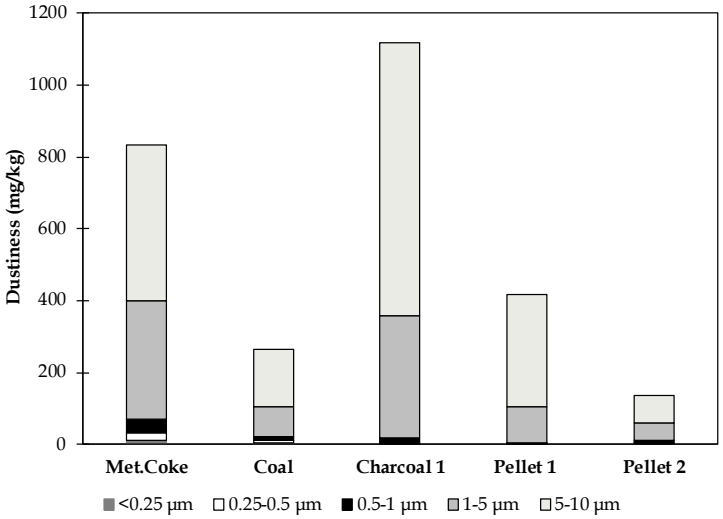

Figure 10: "Corrected" captured dustiness with the particle size analysis.

The risks related to dust explosions were not assessed as part of this study.

5. METHOD COMPARISONS AND LIMITATIONS

The study was conducted to investigate if a closed system like the Heubach Dustmeter type I could be used to better investigate airborne dust than adapting the already established tumble abrasion test. The relevant values from the tumble abrasion test, evaluating the <0.5 mm fraction after 30 minutes tumbling at 40 rpm, compared to the dustiness under standard conditions of 30 rpm, is presented in Figure 11. The numbers are not comparable in value, but the same linear trends related were observed in both tests over time (Figures 5 and 7), and now also when they are compared to each other. By further optimization and investigations of a larger number of samples it may be possible to predict the dustiness values of a material based on the tumble abrasion test without adjustments.

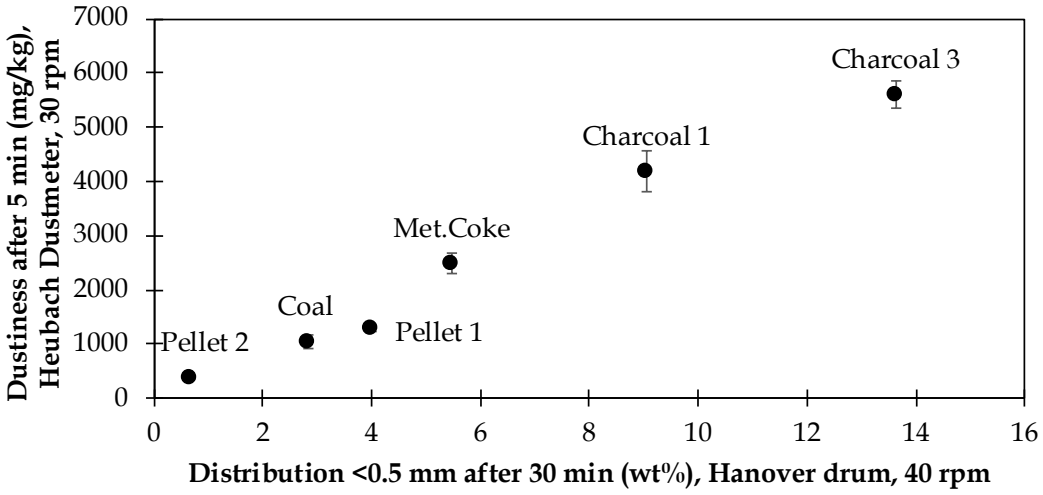

Figure 11: Comparison between the traditionally run <0.5 mm fraction after 30 minutes in the Hanover drum and the Heubach Dustmeter type I measurements.

Another option to get better comparisons of actual values are by including a smaller fraction during sieving, as was done in this study. As PM_{100} is a traditionally used value for airborne particles and the goal for the Heubach Dustmeter measurements, choosing 0.125 mm as the smallest sieve was suggested as a compromise to adjust for particles with larger diameter but still airborne due to e.g. shape and density, i.e. the aerodynamic diameter. The LD analysis in this study showed that among the captured dust, expected to be the PM_{100} fraction, most of the dust was significantly smaller than 100 µm, so it seems like a reasonable value for a sieve. Making the correlating graph as Figure 11 would not change the trend; the only difference is the order of Coal and Pellet 1 sample, which has already been identified as being too similar to differentiate. The 0.125 mm sieve could as such also give more similar values as in the Heubach Dustmeter measurements if both tests were run at the same time and rotation speed.

For Charcoal 3, measurements using 40 rpm for 5 minutes tumbling resulted in very similar values for the two tests. Heubach Dustmeter measurements gave 6100 mg/kg (0.61±0.04 wt%) and what was found after tumble testing and sieving <0.125 mm was 0.7 wt%. However, due to the large amount of loss in the tumble abrasion test (also around 0.7 wt% after the first 5 minutes), it is difficult to know how close the numbers are. Some, but not all, of the losses are likely also in the smallest fraction which is not captured in the open system. The closed Heubach Dustmeter method is superior evaluating this uncertainty, as such losses should be eliminated.

Despite the LD results indicating that most of the captured dust is significantly smaller than 100 µm, there might still be some material that is below 0.125 mm but not captured by the filter during the Heubach Dustmeter measurements. In the first campaign of the five materials included for LD analysis, an additional sieving of the non-captured material was introduced. The results showed that there were no additional materials in the <0.125 mm fraction for Pellet 1 and 2, and coal. This indicates that for these samples, all the airborne dust was captured and all the <0.125 mm fraction was airborne. However, for the charcoal and metallurgical coke, significant amount of material was observed for this fraction when sieving after the test, doubling the total value of material found to be below 0.125 mm in diameter. These are the two materials with the highest dustiness (Figure 6), and as such either have some material below 0.125 mm in diameter but not airborne, or some of the airborne particles was not captured in the filter.

In the second campaign it was discovered that Charcoal 3 clogged the filter and reduced the airflow before the first 5 minutes were done; the method was adjusted by replacing the filter to maintain the airflow. Instead of running the test with significantly less material, which is more often done with bulk powder testing, the filter was replaced anytime the flow was below 19.5 L/min. Although no notice was made related to reduced airflow during the first campaign, the sieving results indicate that this could be true due to the large number of fines found below 0.125 mm in these two materials when no changes in filter occurred. Likely, the airflow was reduced making some particles not captured by the filter. These results show the need of maintaining the airflow, and also indicates that the dustiness reported for these two materials may be underestimated in this study.

The study shows that the Heubach Dustmeter method is a promising tool for screening materials with respect to dustiness, but as the method is still undeveloped for materials for metallurgical industry and no limiting values exist related to health and safety, it will be no replacement for real workplace exposure measurements. The dustiness reported using the standard parameters of Heubach Dustmeter type I closely followed the trend when comparing the abrasion strength of the material, despite the method being superior in the view of losses.

However, the standard parameters like tumbling speed and time, and airflow, may need to be adjusted to best give an indication on the dustiness potential of these types of materials, and method sampling must be defined. As-received material is the most relevant for real handling exposure, but it might be more prudent to eliminate the small dust already formed during transport, especially since charcoal is so fragile. This approach would give information more closely resembling Hanover drum tumbling, and result in an understanding of the underlying material performance. Another parameter is drying; a drying step is often included in standards to get more similar material conditions and normalised conditions. However, moisture is so important for the dustiness behaviour that removing the water beforehand can change the results and the relevance towards real exposures. A more thorough material and parameter analysis should be conducted to best select standardized parameters, including a more thorough shape analysis of the captured powder to get a better understanding of the real diameters of the airborne dust.

Heubach Dustmeter measurements are no replacement of traditional cold strength testing, but, if optimized, may give better understanding of the airborne dust fraction which is more uncertain by only using sieving after a traditional abrasion tumble test. The type I measurements do not differentiate between the inhalable and respirable fraction of the airborne dust, but other Heubach Dustmeter types could be evaluated for this purpose.

6. CONCLUSIONS

The study explored the possibility of using the Heubach Dustmeter method to quantify the dustiness of carbon materials intended to use as carbon reductant in ferroalloy industry. This method is run with similar approach as the cold strength tumble test, but targets capturing the airborne dust by use of an airflow in the closed drum, eliminating any of the losses observed when using the Hanover drum and sieving. It was found that highly dusty charcoal resulted in clogging of the filter and possibly underestimating the dustiness unless airflow was maintained by changing the filter during the test. When this was optimized and the airflow maintained, a linear dustiness response was measured depending on the tumbling time.

Six different materials were tested under standard conditions, and the results showed a linear correlation between this test and the abrasion index (<0.5 mm fraction) of the material as found by tumbling in a Hanover drum, as well as towards the 0.125 mm fraction when this additional sieve was introduced. As most material was detected by laser diffraction to be below 50 µm in diameter, the 0.125 mm sieve can be assumed to be effective, further highlighted by no additional fines below 0.125 mm in the drum after the Heubach test when the airflow was maintained. Running one of the charcoals under identical tumbling speed and time in the two tests gave almost identical results for the measured fraction, however, the losses for the Hanover drum was significant and makes the measurements less ideal to compare. Since no second or third parallel were run in the Hanover drum, the uncertainty related to these results are larger than for the Heubach Dustmeter measurements.

Further optimization related to establishing a standard methodology is clearly needed, also establishing limits related to the numerical values of the dustiness. The method seems promising as a complementary method to the traditional cold strength methods to analyse materials as part of the screening process.

7. ACKNOWLEDGEMENTS

This research was funded by Research Council of Norway grant 336309 (BioCarbUpgrade). The authors also want to acknowledge Delft Solid Solutions Research Laboratory for running the Heubach Dustmeter analysis and particle size distribution.

8. REFERENCES

Bach, S., Schmidt, E., 2008. Determining the Dustiness of Powders—A Comparison of three Measuring Devices. *Ann Occup Hyg* 52, 717–725. https://doi.org/10.1093/annhyg/men062

Delft Solids Solutions, 2025. Heubach and EN 15051 dustiness analysis. https://www.solids-solutions.com/rd/bulk-solids-characterization-and-powder-testing/heubach-dustiness-analysis-rotating-drum-principle/

Euroseeds, 2026. euroseeds.eu/esta-the-european-seed-treatment-assurance-industry-scheme/dust-reference-values-heubach-test-method/

Heyder, J., Svartengren, M.U., 1999. Basic Principles of Particle Behavior in the Human Respiratory Tract, in: Drug Delivery to the Lung. CRC Press.

ISO Standard, 2015. ISO 3271:2015, Iron ores for blast furnace and direct reduction feedstocks—determination of the tumble and abrasion indices.

Jahrsengene, G., Jayakumari, S., Kero, I.T., Ringdalen, E., 2023. Sustainable Metal Production: Use of Biocarbon and the Concern of Dusting. *Proceedings of the 62nd Conference of Metallurgists*, COM 2023. Springer Nature Switzerland, Cham, pp. 1001–1007. https://doi.org/10.1007/978-3-031-38141-6_126

Jayakumari, S., Ksiazek, M., 2023. Fines Generation and Strength of Various Carbon Materials Used in the Ferroalloy Industries. *Proceedings of the Silicon for the Chemical and Solar Industry XVII*. https://papers.ssrn.com/sol3/papers.cfm?abstract_id=4942468

Gøril Jahrsengene
Research Scientist, SINTEF

The main author Gøril has a MSc (2015) and PhD (2019) degree in Materials Science from NTNU Norwegian University of Science and Technology (2019). She is currently working in metal production and recycling in SINTEF as a research scientist, focusing on electrolysis approaches. She also specializes in carbon for metallurgical processes, including the use of bio-carbon.

Amanda Andersson Lindholm
Engineer, SINTEF

The presenter Amanda holds a Master's degree in Materials Science from NTNU and has worked at SINTEF since completing her studies. She works at the intersection of laboratory experimentation and data processing, focusing on high-temperature furnace operations and parameter studies related to silicon production.

Jahrsengene, G., and K. S. Osen. 2026. Electrowinning of Silicon using SiO2 - Overview and Industrial Perspectives. In *Silicon for the chemical and solar industry XVIII*, edited by M. Tangstad, H. Rong, A. Valderhaug, B. Andresen, H. Dalaker, and I. G. Page. Kristiansand, Norway, September 7–10, 2026. https://doi.org/10.55669/oa900812

Electrowinning of Silicon using SiO_2 – Overview and Industrial Perspectives

G. Jahrsengene[1], and K.S. Osen[2]
[1]SINTEF, Norway, goril.jahrsengene@sintef.no
[2] SINTEF, Norway, karen.s.osen@sintef.no

Keywords: electrowinning of Si, FFC, molten oxide, molten salt, oxide dissolution

Abstract – Decarbonization of the silicon production process can be done by electrowinning from SiO_2 at high temperatures using molten salts or oxides producing O_2 as the anode product. Thermodynamics combined with knowledge of state-of-the-art electrowinning processes can provide an understanding of the possibilities and limitations of the approach, to best compare with today's submerged arc furnace (SAF) process. Carbon, if used in carbothermic reduction or as a consumable anode in an electrowinning process, provides energy that is not available when the carbon is eliminated from the process. The result is that an optimized electrowinning process is likely going to require more energy than by SAF, and renewable energy must be used to eliminate the CO_2 from the process. This work further details the knowledge needs related to dissolution behaviour of the SiO_2, electrode materials, cell design and upscaling for both solid and liquid Si production.

1. INTRODUCTION

Electrolytic production of silicon is the most direct way to electrify and decarbonise the silicon production process, especially when renewable energy is readily available. Electrolysis by use of carbon anode, like for aluminium in the Hall-Héroult process, still produce CO_2, but use of oxygen evolving (inert) electrodes in such a process will eliminate all process-related CO_2 emissions. By using quartz as the silicon raw material, O_2 may be produced at the same time as the silicon.

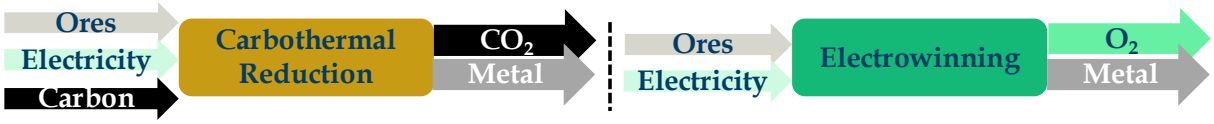

Figure 1: Comparison of today's process and a possible electrowinning process.

A lot of research has been done in relation to producing silicon by electrowinning and summarized in relevant reviews (Abramkin *et al.*, 2025; Tian *et al.*, 2023; Yasuda and Nohira, 2022). Historically, research focused on producing high purity Si to be used directly in photovoltaic (PV) production combined with a carbon anode. The production routes studied showed that although possible, they were not rendered cost effective enough to be industrially viable. However, the production of metallurgical grade silicon could be more promising as the impurity requirements are lower, especially when combined with O_2 evolving anode. As such, the product can be used as alloying elements in green steel and aluminium, making it possible to charge a premium.

In an electrolysis process for metal production there are two electrodes immersed in an electrolyte with dissolved metal cations and negative anions. The electrolyte should have high

This work is licensed under the Creative Commons Attribution 4.0 International License. To view a copy of this license, visit https://creativecommons.org/licenses/by/4.0/

mobility of the ions and high electrical conductivity. The positive metal cation is reduced at the negatively charged cathode where the metal is produced, and the negative anion is oxidised at the anode where another product, often a gas, is produced. For solid Si electrowinning producing O_2 at the anode, a typical lab setup and representative reactions (exact ions vary) are presented in Figure 2.

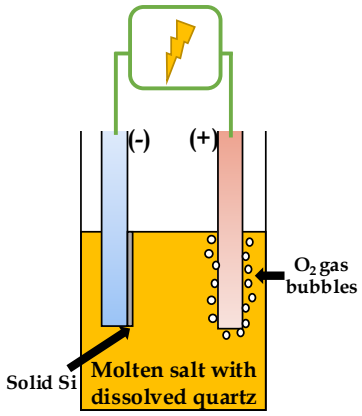

$Si^{4+} + 4e^- \rightarrow Si\ (s)$ $\quad 2O^{2-} \rightarrow O_2\ (g) + 4e^-$

Figure 2: Schematic Si electrowinning by dissolution of quartz and production of O_2.

Silicon cannot be produced by aqueous electrowinning, since the electrical reduction potential is much more negative than what is needed for electrochemically decomposition of water. Low temperature ionic liquids or organic solvents can allow for Si reduction, but the compounds are often expensive, the reduction rate very low, and quartz is not a suitable raw material. A high temperature electrowinning process with molten salts or molten oxides as electrolytes are the most promising to produce Si metal from quartz. Good overviews of the major electrolyte systems and electrochemical methods can be found in literature (Abramkin *et al.*, 2025; Yasuda and Nohira, 2022). More focus on general challenges can be found in another review (Tian *et al.*, 2023). Many excellent studies show the production of solid Si by use of K_2SiF_6 in combination with a CO_2-evolving anode, although recent studies (Padamata *et al.*, 2025) have demonstrated electrochemical production of Si through electrowinning using a SnO_2 oxygen evolving anode in molten salt with $CaCl_2$-NaCl-CaO-SiO_2.

Silicon is a semiconductor, resulting in low electrical conductivity of the metal and, when produced in solid form during an electrowinning process, will result in an electrode with low conductivity. This could potentially give rise to problems during an industrial electrowinning process.

Although there are good overviews of the different electrolyte options and many challenges have been identified, very few focus on some of the more practical aspects when using *quartz* as a raw material, and how this affects the possible industrialization. The goal of this paper is to show how the theoretical values that can be calculated by thermodynamics correlate to real electrochemical behaviour of an electrowinning cell for Si from quartz, and how limitations of different electrochemical systems will translate to business perspectives related to production rate, energy consumption, and cost.

2. SILICON ELECTROWINNING – ELECTROLYTE OPTIONS

Silicon can be produced as a solid or liquid product through the electrowinning process, depending on whether the process is carried out at a temperature higher or lower than the

melting point (1414 °C). Due to its high melting point, liquid Si production can only be carried out by molten oxide electrolysis (MOE), with stable oxides/slags used as the electrolyte. Molten salts, like chlorides and fluorides, can be used as electrolytes up to approximately 1000 °C producing a solid Si product.

Liquid production of metal is advantageous considering the potential of high throughput due to the kinetics allowing use of high current densities, no need to clean the product as it can be tapped directly, and the process can be done continuously through the feeding of raw materials. However, there are certain disadvantages to MOE, the major one being the typically low ohmic conductivity making the ohmic resistance (see section 3.2) high, influencing the real energy consumption (section 3.3). Due to the high temperature and corrosive nature of the oxides, materials challenges will occur. MOE is currently on a low technical readiness level (TRL) for silicon (Elwell and Rao, 1988; Mattei *et al.*, 1981) but is being carried out by Boston Metal for Fe at pilot scale (Boston Metal, 2025). Fe is easier to reduce than other typical metal oxides, but related to temperature the process on Fe must be carried out at even higher temperatures than for Si. However, Fe is denser than the oxide melt and the process can be similar as the Hall-Héroult process used for Al electrowinning, while Si is less dense and will end up floating on top. This requires a quite different design (section 6.2) than in the currently ongoing MOE process developement.

For production of solid Si product, the temperature could be done on significantly lower temperatures, enabling the use of molten salts which are typically thermally stable below 1000 °C. Besides the lower temperature, other advantages relate to the low viscosity (typically like water at the operating temperature) and high conductivity resulting in a low ohmic drop compared to the MOE system. The major drawbacks are that production of solid metal is very slow due to slow kinetics, as well as giving need of cleaning the electrolyte remains from the produced metal. Further advantages and disadvantages of chloride and fluoride melts are presented in Table I.

Electrodeoxidation, also known as the FFC Cambridge process (named after Fray, Farthing and Chen), is a different approach where the metal ion to be reduced is not dissolved in the melt. In Figure 3, the concept is shown compared to a more "conventional" electrowinning process. Si is reduced directly from a pellet of SiO_2 immersed in a molten $CaCl_2$ melt (850-900 °C) containing small amounts of CaO. As the reduction progresses, oxygen ions from the oxide are released into the melt and discharged at the anode as O_2 (when an inert anode is used). The reduction reaction takes place on the interface between the metal oxide pellet, molten electrolyte and cathode lead, and the Si phase propagates through the pellet until all the SiO_2 has been converted to Si. The FFC bypasses the problem of low SiO_2 solubility in chloride melts and was first suggested for the reduction of titanium from TiO_2 (Chen *et al.*, 2000). It has also been proven in laboratory scale for the reduction of other elements including silicon (Nohira *et al.*, 2003; Yasuda *et al.*, 2007). As suggested for TiO_2 by the OS method, the reduction mechanism is likely due to calciothermic reduction via Ca formation (Ono and Suzuki, 2002). Advantages and disadvantages are listed in Table I.

By use of a molten salt with both fluorides and chlorides, it may be possible to utilize the strengths of both systems. The better conductivity and oxide solubility of the fluorides can be combined with lower operating temperatures and easier cleaning of chlorides. From an industrial perspective, the KF-KCl melt is considered promising, and a lot of research has been conducted in this system.

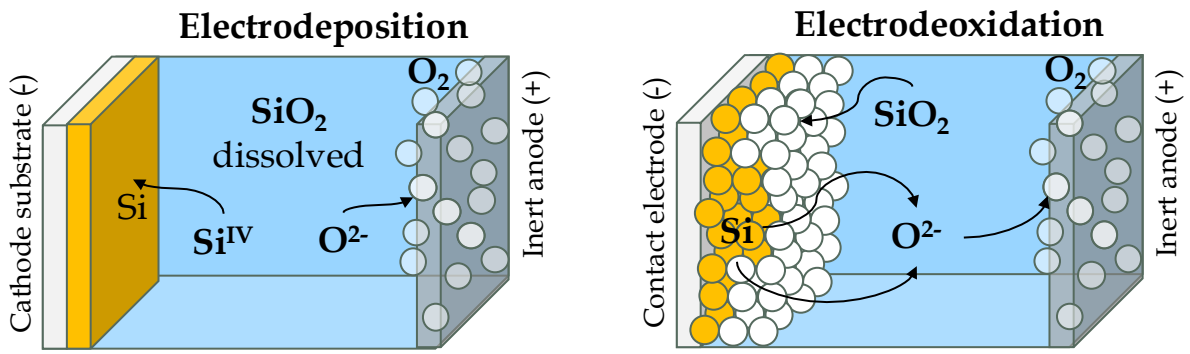

Figure 3: Electrodeposition of dissolved SiO_2 (left) and electrodeoxidation (FFC) of SiO_2 (right).

Table I: Advantages and disadvantages of electrolytic production of Si in different molten salt systems.

	Advantages	**Disadvantages**
Fluoride electrodeposition	• High electrical conductivity • High SiO_2 solubility • Demonstrated in pilot scale • Capitalize on Al electrolysis/Hall-Heroult • C anode possible (CO_2)	• Volatility: F emissions • Salt removal needs strong acids and/or high temperature • Very corrosive and might need frozen side ledge →Heat loss
Chloride electrodeposition	• Less corrosive electrolyte than fluorides • Salt removal possible with *water* • Does not require frozen side ledge → less heat loss and energy consumption	• Hygroscopic salt • Lower electrical conductivity than fluorides • Low SiO_2 solubility → Require need of additional oxide to enhance dissolution, and risk formation of Cl_2 • C anode not feasible (CO_3 formation → carbon reduction)
Chloride FFC	• Simple • Commercialised by Metalysis for Ta, Ti and high-entropy alloys • Many studies	• Very slow process and low current efficiency • Needs to inhibit SiO_2 dissolution → Cl_2 produced more easily than O_2 • Si is a semiconductor, difficulties with electrical conductivity of negative electrode

3. THERMODYNAMICS, ENERGY REQUIRERMENTS AND CO_2 FOOTPRINT

The energy use for today's production of silicon is typically in the 11-13 kWh/kg_{Si}, and direct carbon emissions from the process are ca. 5 $kgCO_2/\ kg_{Si}$ (Hoover *et al.*, 2024). Si and CO is produced in the reaction according to equation 1, via formation of SiC and SiO gas, with CO finally ending up as CO_2 after being oxidized by air.

$$SiO_2 + 2C \rightarrow Si + 2CO \quad [1]$$

By use of electrowinning processes to produce Si, equation 2 is the resulting electrochemical reaction when using a carbon anode. The electrochemical reaction on the anode can be assumed to result in CO_2, as for aluminium electrowinning, and not CO as in the carbothermal reduction process. When producing oxygen with an inert anode, the main driving force behind choosing this new technology, equation 3 represents the total electrochemical reaction.

$$SiO_2 + C \rightarrow Si + CO_2 \quad [2]$$
$$SiO_2 \rightarrow Si + O_2 \quad [3]$$

3.1 Standard potential

The fundamental thermodynamic relationship between the change in Gibbs free energy ($\Delta G°$) and the standard cell potential ($E°$) for an electrochemical reaction can be expressed with equation 4, where n is the number of electrons (4 in the case on Si), and F is Faraday's constant (96485 C/mol) representing the total electric charge carried by one mole of electrons. As can be deduced, using a negative sign in the equation ensures that for non-spontaneous reactions at standard states, $\Delta G°>0$, a negative cell potential is calculated since the electric cell requires an external power source to drive the reactions (Newman and Balsara, 2021).

$$E^o = -\frac{\Delta G^o}{nF} \quad [4]$$

In Figure 4 the traditional Ellingham diagram is shown together with the corresponding standard cell potential for an electrochemical reaction for a number of metal oxides per mol O_2. It can be observed that Fe and Mn will be produced electrochemically simultaneously with Si, since the $E°$ for these reactions are less negative than for Si. This means that if these more noble metal oxides have been introduced as an impurity in the quartz, co-reduction and production of a metal alloy or impure silicon product will be the resulting metal. It is not possible to eliminate these reactions if these oxides are present in the raw material, and therefore they should not be present as part of the electrolyte for molten oxide electrolytes for liquid Si production. The graph in Figure 4b also demonstrates that the MOE-process is most easily applicable to Fe, as other metals are not co-reduced, while for Mn, the presence of Fe in the oxide ore can prove problematic.

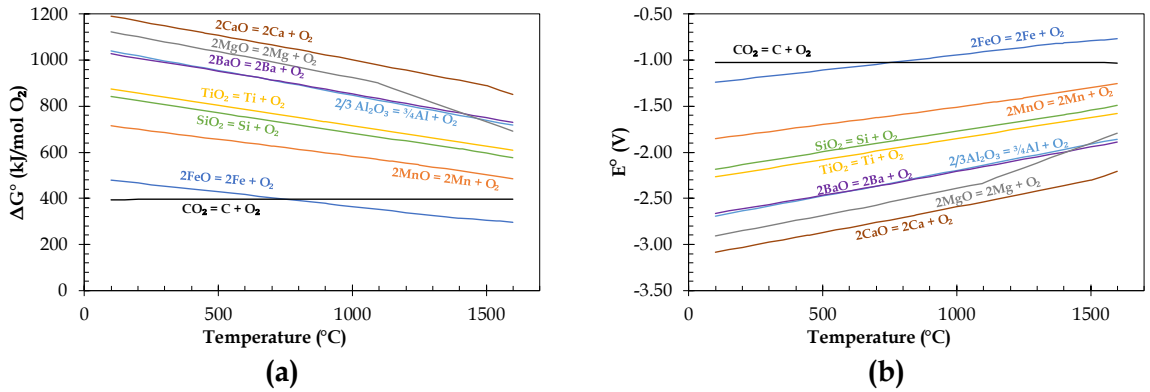

Figure 4: The (a) Ellingham diagram and (b) correlating standard cell potentials of a comparable electrowinning process of metal oxides, as found by FactSage 8.4 (Bale *et al.*, 2016).

Quartz, or the naturally occurring quartzite, typically has above 99 % of SiO_2. Typical impurities are Al, Fe, and Ti. Of these, Fe will always end up in the produced metal, while Al

and Ti should theoretically remain in the bath since they have a more negative cell voltage. However, metal reduction can also occur by forming alloys, which results in activities less than zero and the reduction happening at less negative potentials. This means that Al and Ti may potentially end up in the metal due to alloying with the produced Si, especially if it accumulates to high concentrations in the electrolyte. This accumulation may potentially require bleeding of the electrolyte, i.e. periodic removal of electrolyte, to ensure a pure product is produced at high efficiencies.

3.2 Cell voltage

The reversible, equilibrium cell voltage (E_{rev}), depends on temperature T (in Kelvin), and the reaction quotient Q (depending on activities of Si and SiO_2 and partial pressure of O_2 for the proposed reaction in equation 3). This is expressed by Nernst equation (equation 5).

$$E_{rev} = E^o - \frac{RT}{nF}\ln(Q) \quad [5]$$

The cell voltage (E_{cell}) needed for a reaction is always higher than E_{rev} (Newman and Balsara, 2021). The actual driving force for the reaction depends on kinetics and transport limitations, and these contributions are commonly denoted as overpotentials at each electrode. There is an activation energy barrier as reactions on a surface does not occur instantaneously, resulting in an activation overpotential (η_{act}). There is also a concentration overpotential (η_{con}) near each electrode in the case of limitation by mass transport, generating a concentration gradient of the electroactive species near the electrode. The sum of these on each cathode and anode is typically denoted η_c and η_a respectively.

Finally, an ohmic contribution to the cell voltage depends on the resistance (R) between the cathode and anode, and the current (I) through the system. This ohmic resistance depends on bath conductivity and anode-cathode distance. The ohmic contribution is as such strongly dependent on the geometry of cell, the chosen electrolyte and temperature, the total amperage and production rate of the system. In total, the cell voltage during the electrolysis can be expressed by equation 6. Small scale lab experiments typically have very low total current, and in some cases also very low current density, which can give a much lower IR contribution to the cell voltage than in an industrial cell.

$$E_{cell} = E_{rev} + \eta_a + |\eta_c| + I \cdot R \quad [6]$$

In practice, it is not possible to accomplish electrolysis at a reasonable rate without having considerable overvoltages and ohmic losses, and it is the total cell voltage which is important when evaluating the energy consumption of a proposed process, not the theoretically calculated values.

3.3 Energy consumption

The minimum energy needed is defined by the conditions in a hypothetical cell without loss in current efficiency, no side reactions, and without heat loss to the surroundings (i.e., adiabatic and isothermal conditions), and the energy needed to heat the raw material to the chosen reaction temperature (SiO_2). The isothermal cell voltage (E^{iso}) is the cell voltage needed to maintain electrolysis at these isothermal and adiabatic conditions, and it can be calculated by exchanging $\Delta G°$ with the change in enthalpy ($\Delta H°$) in equation 4. The theoretical energy related to the electrochemical reactions ($EC_{\text{theory,rx}}$) can then be calculated at a given temperature using the change in enthalpy ($\Delta H°$) and the molar mass (M) of the produced metal, by equation 7 (Helbæk and Kjelstrup, 2006).

$$EC_{theory,rx} = \frac{E^{iso} \cdot nF}{M \cdot 3600} = \frac{\Delta H^o}{M \cdot 3600} \quad (\frac{kWh}{kg}) \qquad [7]$$

Assuming an electrowinning process for silicon at 1000 °C, the energy of heating SiO_2 from 25 °C to 1000 °C is 0.62 kWh/kg_{Si}. For Si produced at 1000 °C using a carbon anode according to equation 2, the theoretical energy consumption for the electrochemical reaction is calculated to be 5.01 kWh/kg_{Si}, while using an inert anode as in equation 3 it requires more energy, 8.93 kWh/kg_{Si}. This correlates to a 1 V difference in standard potential of the relevant reactions. Summarizing, the resulting total theoretical energy consumption, assuming 100 % current efficiency, no heat losses, no overvoltages and no ohmic voltage drop, is 5.63 and 9.55 kWh/kg_{Si} for carbon anode and inert anode, respectively. The large difference between the two processes relates to the chemical energy in carbon, which needs to be replaced by electrical energy in the case of inert anodes.

Although the theoretical energy consumption is useful to evaluate the difference between a carbon and inert anode, the specific energy consumption of the reaction ($EC_{specific}$) is highly dependent on the cell voltage as described in equation 6, and not the isothermal cell voltage, in addition to the current efficiency. The formula for energy consumption for a given electrowinning process is given in equation 8, where the current efficiency (ε) is presented as the fraction (0-1) rather than the often-reported percentage. High cell voltage due to overvoltages and ohmic contribution can increase the specific energy consumption significantly compared to the theoretical values. Low current efficiency has the same effect, since this factor is reduced below 1 for not-ideal electrolysis (Newman and Balsara, 2021).

$$EC_{specific} = \frac{E_{cell} \cdot nF}{M \cdot \varepsilon \cdot 3600} \quad (\frac{kWh}{kg}) \qquad [8]$$

The current efficiency describes how much of the total current applied contributes to the wanted reaction (e.g. Si production). Deviations from 100 % current efficiency are typically resulting from re-oxidation of the metal (back-reaction), dissolution of the metal into the electrolyte (avoided by polarization of electrodes, which protects the metal), and parasitic reactions. The parasitic reactions can be due to co-deposition of other metals, which is strongly dependent on the quality of the raw material, but can also be loss of electrons used for reducing higher valency metals without producing the metal. The current efficiency of a metal *x* is given by Faraday's law for production rate ($\dot{m}$) in equation 9 (Newman and Balsara, 2021).

$$\dot{m}_x = \frac{I \cdot \varepsilon \cdot M_x}{nF} \quad (\frac{kg}{s}) \qquad [9]$$

Electrowinning of Al in a cryolite (fluoride) molten salt with a consumable carbon anode typically occurs around 4 V, significantly higher than the reversible voltage of 1.22 V. Much of this increase is due to the ohmic resistance in the bath. Si has a lower reversible voltage than aluminium, so assuming a cell voltage of 3 V (2 V is reported by use of carbon anode (Zou *et al.*, 2011), and 80 % current efficiency, the specific energy consumption would be ca. 14 kWh/kg_{Si}. Work with a fluoride system with SiO_2 and O_2-evolving anode gave 3.4-4.2 V cell voltage, and the energy consumption could also be a bit higher (Moudgal *et al.*, 2021). By comparison, MOE has a very high resistivity in the bath, typically resulting in much higher cell voltages than with molten salts. Previous work on Si MOE (Mattei *et al.*, 1981) gave 16 V cell voltage using 2 A (1 A/cm^2), and a very low current efficiency of 15-22 %, which results in an extremely high energy consumption above 300 kWh/kg_{Si}.

When evaluating values found in literature, it is important to confirm which anode reaction is occurring together with the Si production on the cathode, and relate this to the measured cell voltage in each specific experiment. Producing Si by electrowinning with carbon has in some cases been presented to give comparable, or even favourable improvements when comparing energy requirements to today's SAF-process. However, if the goal is to eliminate the CO_2 it is no longer comparable, since the theoretical energy consumption is higher with almost 4 kWh/kg_{Si}. Many experiments have not had any oxygen source in the experiment at all, using K_2SiF_6 as the raw material, and in these cases neither O_2 nor CO_2 is produced on the anode; typically, chlorine or fluorine/perfluorocarbon gases are the likely product depending on the melt and the resulting cell voltage depends on this reaction. Certain anodes may also react anodically at lower voltages than oxygen production potentials, giving a cell voltage significantly lower than when producing oxygen.

The theoretical values and what experience can be transferred from other electrowinning processes, like Al-production, shows that the energy consumption in a new electrowinning process for silicon is likely to have higher energy consumption than today's process with SAF.

3.4 CO_2 footprint

By use of an inert anode, the CO_2 produced in today's process, or in an alternative electrowinning process with consumable carbon anodes, can be eliminated completely as a process product. With the higher energy consumption compared to the SAF, this indicates that the energy mix used for the electrowinning will be detrimental to the associated CO_2-emissions per kg Si produced.

Calculations related to the change from carbon to inert anodes for aluminium production can be useful for the case of silicon. For aluminium, it is documented (Solheim, 2018) that the change from carbon anode to inert anode increases the minimum specific energy consumption from 6.24 to 9.16 kWh/kg_{Al}. By including the energy lost in the form of heat, the state-of-the-art Al electrowinning process ends up at 12.0 kWh/kg_{Al}, and the process with inert anodes at 14.9 kWh/kg_{Al}. Using a coal-fired powerplant operating at a 40 % efficiency, the total amount of CO_2/kg_{Al} is reported as 14.91 for the carbon anodes, and 16.10 for the inert anodes. This demonstrates that when using fossil energy sources, the positive result of producing O_2 instead of CO_2 is cancelled out, and electrowinning processes with oxygen evolving anode, due to its high energy requirement, must be done by use of renewable energy sources.

For silicon, the cell voltage for SiO_2 decomposition to Si and O_2 is less negative than for Al_2O_3 to Al and O_2 (Figure 4b), but due to the difference in electrons partaking in the reactions, the theoretical energy consumption ends up in the same range as for aluminium. Including heat losses the energy consumption, the total energy consumption is likely going to be higher than the 11-13 kWh/kg_{Si} today, and the CO_2 emissions are fully dependent on the energy source.

4. QUARTZ SOLUBILITY

In an MOE process the metal oxides are part of the electrolyte, and for Si the quartz would likely be present together with Al_2O_3, CaO and MgO (or other less noble metals). The basic oxides, CaO and MgO, dissociate easily into ionic forms, while the acidic oxides, SiO_2 and Al_2O_3, form networks and does not generally dissociate into their respective cat- and anions (Rosenqvist, 2004). For Si, this means that the three-dimensional polymerised network should be broken apart by basic oxides, enhancing the mobility of the electroactive species (SiO_x^{y-}), making them, as well as the oxygen species, available for the electrochemical reactions.

Oxygen can exist in different species depending on its basicity, but O^{2-} is probably the species being discharged at the anode (Park and Rhee, 2001).

In molten salts the electrolyte constituent helps to dissolve and make available the ions. As mentioned previously, a lot of Si electrowinning research in molten salts has focused on using K_2SiF_6 as the silicon source. This raw material may have its own challenges related to solubility and stability (SiF_4 can form as a gas), especially in chloride melts without any other fluorides present to stabilize dissolved ions, but if the raw material is going to be quartz, a good understanding of the dissolution of this oxide and formation of stable cations and anions needed for the electrochemical reaction is needed.

Looking again at the state-of-the-art aluminium electrowinning process in cryolite, alumina is added from the top of the cell into the bath. Well-dispersed alumina dissolves within just a few seconds, but because of the alumina is added cold and hits a very hot melt, the temperature difference can cause the electrolyte to freeze around the particles and forming hard to dissolve agglomerates. The natural stirring that occurs due to the CO_2 bubbles and electromagnetic forces helps to keep the powder dispersed and avoids agglomerated "sludge" forming at the bottom of the cell. In addition, the type and concentration of alumina are important for the dissolution process.

Very little work has been done on dissolving quartz in molten salts, and it is one of the major research questions that needs to be answered before approaching future electrowinning processes. As can be seen in Table I, chlorides have low solubility of SiO_2 and typically require a helping oxide, e.g. $CaCl_2$ with 10 wt% CaO can dissolve at least 6 wt% SiO_2 (Olsen, 2002). The recent demonstration from Icelandic researchers (Padamata *et al.*, 2025) demonstrated electrowinning of Si with 90 mol% $CaCl_2$-10 mol% NaCl, adding 2 wt% CaO and 2.2 wt% SiO_2 (1:1 molar ratio CaO:SiO_2), showing that oxygen was possible to produce on the anode with only a few wt% of total oxide in the melt (avoiding chlorine). For the FFC-process, it is important that the SiO_2 electrode does not dissolve, and the electrolyte should only transport the O^{2-} discharged to the anode to produce O_2 (Figure 3). As this is always done in a chloride melt, one should avoid the dissolution-enabling oxide as it increases SiO_2 solubility, but given the slow process and very low concentrations of O^{2-} there is a high chance of producing Cl_2 instead of O_2 at the anode. Fluorides can dissolve SiO_2 without any other oxides present; the F^- have an important role in breaking the Si-O-Si bridges, replacing the oxygen ion in the silicate tetrahedron with a fluoride anion (Zaykov *et al.*, 2014).

Pure chloride or fluoride melts have their advantages and disadvantages (Table I), which is why the focus typically has been on mixed systems. A study including quartz looking into dissolution was done in Russia in the years 2013-2017. The system studied was molten KF-KCl, mainly also with 10 mol% K_2SiF_6, changing the KF:KCl ratio and temperature (Zaikov *et al.*, 2013). The results showed a linear increase in SiO_2 solubility with increasing KF:KCl ratio, demonstrating the role of F^- in breaking Si-O-Si bridges and that, on a given melt, the liquidus increases with greater SiO_2 dissolved. The SiO_2 solubility was also dependent on the presence of K_2SiF_6, with a 2:1 KF:KCl ratio the solubility of SiO_2 increased from 6.6 to 7.4 wt% when going from 0 to 10 mol% K_2SiF_6. Too high concentration of K_2SiF_6 reduced the SiO_2 solubility. This work shows that it might be fully possible to dissolve SiO_2 to suitable concentrations without K_2SiF_6, but further research must be conducted. Electrowinning trials always had K_2SiF_6 present together with the SiO_2, changing the solid coatings of Si when only K_2SiF_6 was present to nanowires when including quartz (Zaykov *et al.*, 2013), and no research on electrowinning has been reported in literature in this system with only SiO_2 in the melt. Finally, the same group also showed that the dissolution rate of SiO_2 was very slow and

electrochemical signals related to the Si-reaction increased over time (several hours) after SiO_2 addition to the melt (Zhuk *et al.*, 2017).

For an industrial process, a good understanding of quartz solubility in suitable systems is needed. This includes dissolution limits and rates, effect of stirring (bubbles), quartz quality and particle size, and effect on resulting Si produced.

5. ELECTRODE MATERIALS

5.1 Oxygen evolving anode

The material development for the oxygen evolving anode, often called an inert anode, is crucial for the proposed electrowinning process. Such an anode must be mechanically stable at elevated temperatures, and it must be electrically conductive with reliable electrical connections to the external circuit. The anode is not likely to be fully inert, but it needs to have slow enough corrosion rate/anodic dissolution so that regular anode changes become obsolete (i.e. several months between each anode change). The limiting factor is the required purity of the metal; the anode must have slow enough dissolution rate to avoid significant contamination of the metal. The anode must withstand oxidizing conditions on the surface, the O_2 (and possibly Cl_2) gas produced and a high electrical potential. The anodes should be easily fabricated by non-polluting methods (manufacture and disposal included), and economically attractive. Different electrolyte chemistries are likely to require different anode materials.

Inert anodes for aluminium electrolysis are typically divided into three (He *et al.*, 2021).

- Ceramic anodes. Especially SnO_2 anodes have been investigated on lab and bench scale, with Sb_2O_3 and CuO to improve properties. They typically have high corrosion resistance and stability.
- Metal anodes, often Cu-Ni-Fe based. They form a protective layer of oxides during electrolysis but also dissolve. They have high electric conductivity, strength and toughness.
- Cermet anodes. A mixture of ceramic and metal, also with a protective oxide layer but less dissolution, resulting in a long service life with small consumption.

For silicon electrowinning with fluoride melts, the same strategies as for aluminium would likely be suitable, however, the temperature could potentially be a bit lower than for aluminium electrolysis giving more options. However, most developers do not specify what type of inert anode they are targeting in their development of a CO_2-free aluminium process. For Si produced in chlorides, some work have been done using ceramic SnO_2, but there might be issues with formation of insulating $CaSnO_3$ over time (Lomax *et al.*, 2020) as well as dissolution and contaminating the product (Padamata *et al.*, 2025). Other oxides anodes for silicon electrowinning have been done with very expensive materials including ruthenium (Hu *et al.*, 2015). Use of titanium-based anodes have also been demonstrated (McGregor *et al.*, 2006). The long-term behaviour has not been investigated for Si electrowinning. In MOE, research have been done on metallic anodes, e.g. CrFe-anodes (Allanore, 2013).

If both O^{2-} and Cl^- are present, as when using a chloride melt, the oxygen and chlorine evolution reactions compete on the anode. This makes it important to ensure that the anode chosen results in a low overvoltage for the oxygen reaction compared to the chlorine reaction. This is especially important if the O^{2-} concentration is low compared to the Cl^-.

5.2 Metal producing cathode

The choice of metal producing cathode is also difficult and depends on the targeted silicon morphology. In lab scale, Si product typically varies from coherent films, dendritic films, grains, powders, particles, alloys with other metals, or porous sponges and nanowires. The result depends on a variation of electrochemical parameters (e.g. temperature and current efficiency), including the cathode where the metal is produced. When producing solid silicon in molten salts, research typically focus on use of metals like Ag, Fe, Al, W and Mo, carbon materials like glassy carbon and graphite, single- or polycrystalline Si, or even metallurgical grade Si (Yasuda and Nohira, 2022). After the initial Si deposition, the produced Si continues to act like the cathode. After electrolysis, the produced Si must be separated from the cathode material and the bath remains; in the case of films these can often adhere very well to the substrate making them difficult to extract.

In MOE systems, little is typically specified on the cathode material; for electrowinning processes where the metal is produced at the bottom, a starting pool of the metal to be produced is typical. For Si, due to the density vs the slag electrolyte, this could be done only if it is alloyed with another metal, resulting in the alloy staying at the bottom. A vertical approach using inert cathodes could be applied, e.g. by use of TiB_2, which should have good wetting behaviour towards liquid slag and metal.

6. UPSCALING

Solid Si electrowinning has been demonstrated in pilot scale using cryolite (as for aluminium) in the 60s (summarized by Elwell and Rao, 1988), SiO_2 raw materials and carbon anodes at 0.8 A/cm^2, but the process was not commercial at the time due to the slow deposition rates (despite 0.8 A/cm^2 being quite high for solid deposition rates). Alloying with Al has also been demonstrated at 0.027-0.053 A/cm^2 (Stubergh, 2002). Solid Si-nanowires have been produced at pilot scale via the FFC-method in chlorides (Yu *et al.*, 2020), running for 14 months at 2.7 V. Pilot scale production of Si with MOE has been demonstrated up to 1 A/cm^2, but at these values the cell voltage was very high and current efficiency very low, resulting in very high energy consumption (as mentioned in section 3.3).

6. 1 Dimensions and capacity

The size of an electrowinning plant is fully dependent on the current density; by finding the optimal current density, the production rate of the process is scalable since it depends on the total current (equation 9). More total current results in more produced metal and simply needs more area, resulting in a final area footprint for the production. Liquid aluminium is produced at 1 A/cm^2, resulting in 3 kg/h/m^2 electrode area while liquid rare earth metals alloys can be produced at 5 A/cm^2 and 63 kg/h/m^2.

For carbothermal reduction of Si, one furnace with approximately 7 m in diameter, area 38 m^2 and a power of 20 MW can produce 40-60 tonne Si/day. For Al electrowinning, one cell, e.g. at Hydro Sunndalsøra, has size around 48 m^2, run on 1.2 MW and produce ca. 2.2 tonne Al/day. As such, the production is scaled by increasing the area footprint; Sunndalsøra have 340 cells (area for cells: 16320 m^2) running a total of 420 MW and produces around 1000 tons Al/day. The area needed for an Si electrowinning plant will have to be much higher than for today's process, despite not targeting the same amount of metal produced as in aluminium.

6.2 Materials and cell design

Outside of choosing suitable anode and cathode material, everything else for use in the cell must withstand the high temperatures and conditions of the electrowinning process. The cell

typically consists of refractories and insulation material as lining, covers and shells, and current collector bars. A lot of materials from the aluminium electrolysis process are likely also suitable for Si electrowinning, especially for fluoride molten salts and possibly also molten oxides, despite the large difference in temperature. Chamotte, a silica/alumina ceramic, is typically used as a refractory material in aluminium electrolysis. Also, steel is typically part of electronic connections for the electrodes, but these are important to protect due to the corrosive environment. This can be done with a frozen side ledge (frozen electrolyte), and protective coatings can be helpful.

For solid state Si electrowinning, a setup with vertical electrodes alternating anode and cathode will be the most effective cell design with respect to area footprint. The gas produced must be collected with a ventilation system, and the gas needs a scrubbing system to remove fluoride traces (for fluoride melts), and/or should scrub any unwanted chlorine gas.

For MOE, the liquid Si is less dense than the electrolyte and will float on the top. This requires a very different design than for aluminium electrowinning, or MOE producing Fe or Mn, as the metal cannot short circuit the cell by touching both cathode and anode. Modifying known design for electrowinning of magnesium or sodium (the Down's cell) could be a suitable approach, with anodes coming vertically from the bottom and cathodes either from the sides or vertically from the top. The electrodes should ideally be separated with a diaphragm, to limit the back reaction. To protect the silicon floating on top of the cell from oxidizing before collection, an inert atmosphere is required. The inert gas is going to be costly but may be recycled if separated from the other gases, including the produced O_2. Another option is a type of double cell with two compartments, alloying Si with a heavier metal like Cu (having the metal production on the bottom again). The other compartment will have a refining process (Johansen *et al.*, 2007).

6.3 Cost

The economic viability of a process depends on factors such as the number of process steps, specific energy consumption and production footprint (Humbert *et al.*, 2024).

The operational costs (OPEX) correlate with the costs of labour, energy, and raw materials. Compared to carbothermic processes, there will be no need for coke, and the sole raw material is SiO_2. The high purity of quartz is a large advantage for the operational costs of an electrolysis cell, as it requires little front-end processing, and allows feeding the raw material continuously with a speed matching the metal production rate. If the raw material contains other elements that does not co-deposit with Si it will alter the electrolyte chemistry with time. This will eventually causing operational problems and need for adjustment of electrolyte amounts and composition, increasing complexity and labour demand. The cell voltage and thus the energy consumption unavoidably increases with increasing current density, so a trade-off between production rate and energy costs must be made. Likewise, as high current efficiency as possible is essential to keep down the energy costs per unit metal produced. Another cost driving factor is the complexity of the harvesting and post processing of the metal. If Si is deposited in solid state, it can require acid leaching or vacuum distillation to separate the product from the electrolyte. This is avoided if Si is produced in its molten state.

Predicting the capital costs (CAPEX) for a new electrowinning process can be quite challenging and requires a different methodology than the chemical engineering procedures for upscaling and industrialization of conventional chemical processes. Stinn and Allanore developed a new, electrochemical engineering scaling law to predict the capital cost of electrochemical facilities (Stinn and Allanore, 2020). According to their work, an important main CAPEX driver

for an electrolyzer is the temperature (material cost), however this is compensated by the fact that the current density will be higher (higher production rate per area footprint).

The work of Stinn has been used to carry out techno-economic modelling of a 160 000 tonne/year solar silicon molten salt electrolysis process with inert anode (Moudgal *et al.*, 2021). The system studied was a CaF_2-MgF_2-CaO electrolyte with quartz as raw material, and vertical electrode set up with 0.2-0.3 A/cm^2 cathodic current density, giving a slightly lower area footprint than Hall-Heroult aluminium smelting. The Si is produced in solid state in the temperature region 980-1100 °C. The energy balance indicated that a self-heating cell at 1100 °C would require 14.3 kWh/kg Si produced, giving OPEX 1.74 \$/kg$_{Si}$ and CAPEX: \$10 500 /tonne/year.

7. CONCLUSIONS AND OUTLOOK

When evaluating technologies to eliminate CO_2 from today's carbothermic reduction process for Si production, electrowinning from the use of SiO_2 is a very strong contender. It is important to be aware of the higher energy consumption compared to today's SAF process related to removing the carbon from the reactions. The low productivity rates related to the low current density of solid silicon production will result in high area footprint for an electrowinning plant, while the high resistivity in molten oxide melts might result in high cell voltages and high energy consumption when producing liquid Si at higher production rates. The choice of melt is not trivial, especially related to the processes that may affect cost, the complexity of gas atmosphere, gas cleaning and post processing.

High purity Si has previously been demonstrated at pilot scale using carbon anodes, but the TRL level related to the oxygen evolving reaction is low. Choosing a suitable anode material is important, as it needs to facilitate the oxygen evolving reaction in the specific system. It will not be fully inert, and the slow corrosion will influence the silicon purity. This is one of the most important knowledge needs related to an industrial process, together with the need for a better understanding of solubility of quartz in suitable systems.

8. ACKNOWLEDGEMENTS

This project has received funding from The Research Council of Norway: Contract number 344259 (ZeSiM). Partners in the project are SINTEF, NTNU, Elkem ASA, Eramet Norway AS, Finnfjord AS and Wacker Chemicals Norway. A special thanks to Zhaohui Wang from SINTEF, confirming the thermodynamic data calculations.

9. REFERENCES

Abramkin, G., Stopic, S., Yasinskiy, A., Birich, A., Friedrich, B., 2025. Electrochemical Deposition of Silicon: A Critical Review of Electrolyte Systems for Industrial Implementation. *Materials* 18, 4009. https://doi.org/10.3390/ma18174009

Allanore, A., 2013. Electrochemical engineering of anodic oxygen evolution in molten oxides. *Electrochimica Acta*, ELECTROCHEMISTRY FOR ADVANCED MATERIALS, TECHNOLOGIES AND INSTRUMENTATION 110, 587–592. https://doi.org/10.1016/j.electacta.2013.04.095

Bale, C. W., Bélisle, E., Chartrand, P., Decterov, S.A., Eriksson, G., Gheribi, A.E., Hack, K., Jung, I.-H., Kang, Y.-B., Melançon, J., Pelton, A.D., Petersen, S., Robelin, C., Sangster, J., Spencer, P., Van Ende, M.-A., 2016. FactSage thermochemical software and databases, 2010–2016. Calphad 54, 35–53. https://doi.org/10.1016/j.calphad.2016.05.002

Boston Metal, 2025. Innovative metals processing [WWW Document]. Boston Metal. URL https://www.bostonmetal.com/ (accessed 8.12.25).

Chen, G.Z., Fray, D.J., Farthing, T.W., 2000. Direct electrochemical reduction of titanium dioxide to titanium in molten calcium chloride. *Nature* 407, 361–364. https://doi.org/10.1038/35030069
Elwell, D., Rao, G.M., 1988. Electrolytic production of silicon. *J Appl Electrochem* 18, 15–22. https://doi.org/10.1007/BF01016199
He, Y., Zhou, K., Zhang, Y., Xiong, H., Zhang, L., 2021. Recent progress of inert anodes for carbon-free aluminium electrolysis: a review and outlook. *J. Mater. Chem. A* 9, 25272–25285. https://doi.org/10.1039/D1TA07198J
Helbæk, M., Kjelstrup, S., 2006. *Fysikalsk kjemi*, 2nd ed. Fagbokforlaget.
Hoover, H., Bell, R., Rippy, K., 2024. Emerging Technologies for Decarbonizing Silicon Production. *J. Sustain. Metall.* 10, 1921–1932. https://doi.org/10.1007/s40831-024-00913-3
Hu, L., Song, Y., Ge, J., Jiao, S., Cheng, J., 2015. Electrochemical Metallurgy in CaCl2-CaO Melts on the Basis of TiO2 ·RuO2 Inert Anode. *J. Electrochem. Soc.* 163, E33. https://doi.org/10.1149/2.0131603jes
Humbert, M.S., Brooks, G.A., Duffy, A.R., Hargrave, C., Rhamdhani, M.A., 2024. Economics of Electrowinning Iron from Ore for Green Steel Production. *J. Sustain. Metall.* 10, 1679–1701. https://doi.org/10.1007/s40831-024-00878-3
Johansen, K., Sadoway, D.R., MYHRE, B., ENGVOLL, M., ENGVOLL, K., 2007. Method for electrolytic production and refining of metals. US20070215483A1.
Lomax, B.A., Conti, M., Khan, N., Bennett, N.S., Ganin, A.Y., Symes, M.D., 2020. Proving the viability of an electrochemical process for the simultaneous extraction of oxygen and production of metal alloys from lunar regolith. *Planetary and Space Science* 180, 104748. https://doi.org/10.1016/j.pss.2019.104748
Mattei, R.C.D., Elwell, D., Feigelson, R.S., 1981. Electrodeposition of Silicon at Temperatures above Its Melting Point. *J. Electrochem. Soc.* 128, 1712. https://doi.org/10.1149/1.2127716
McGregor, K., Frazer, E., Urban, A., Pownceby, M., Deutscher, R., 2006. Development of Inert Anode Materials for Electrowinning in Calcium Chloride Melts. *ECS Trans.* 2, 369. https://doi.org/10.1149/1.2196026
Moudgal, A., Buasai, S., Wu, Y.J., McMahon, A., Hazerjian, J.M., Luu, V., Ly, A., Asadikiya, M., Powell, A., Pal, U., Zhong, Y., 2021. Finite Element Analysis and Techno-economic Modeling of Solar Silicon Molten Salt Electrolysis. *JOM* 73, 233–243. https://doi.org/10.1007/s11837-020-04468-y
Newman, J., Balsara, N.P., 2021. *Electrochemical Systems*, 4th ed. John Wiley & Sons, Ltd.
Nohira, T., Yasuda, K., Ito, Y., 2003. Pinpoint and bulk electrochemical reduction of insulating silicon dioxide to silicon. *Nat Mater* 2, 397–401. https://doi.org/10.1038/nmat900
Olsen, E., 2002. Electrolyte and method for manufacturing and/or refining of silicon. WO2002099166A1.
Ono, K., Suzuki, R.O., 2002. A new concept for producing Ti sponge: Calciothermic reduction. *JOM* 54, 59–61. https://doi.org/10.1007/BF02701078
Padamata, S.K., Haarberg, G.M., Saevarsdottir, G., 2025. Electrochemical Production of Silicon Using an Oxygen-Evolving SnO2 Anode in Molten CaCl2-NaCl. *Ceramics* 8, 150. https://doi.org/10.3390/ceramics8040150
Park, J.-H., Rhee, P.C.-H., 2001. Ionic properties of oxygen in slag. *Journal of Non-Crystalline Solids*, 6th Int. Conf. on Molten Slags, Fluxes and Salts 282, 7–14. https://doi.org/10.1016/S0022-3093(01)00323-4
Rosenqvist, T., 2004. *Principles of Extractive Metallurgy*. Tapir Academic Press.
Solheim, A., 2018. Inert Anodes—the Blind Alley to Environmental Friendliness?, in: Martin, O. (Ed.), *Light Metals 2018*. Springer International Publishing, Cham, pp. 1253–1260. https://doi.org/10.1007/978-3-319-72284-9_164
Stinn, C., Allanore, A., 2020. Estimating the Capital Costs of Electrowinning Processes. *Electrochem. Soc. Interface* 29, 44. https://doi.org/10.1149/2.F06202IF
Stubergh, J.R., 2002. Process for preparing silicon and optionally aluminum and silumin(aluminum-silicon alloy). WO2002077325A1.
Tian, F., Pang, Z., Hu, S., Zhang, X., Wang, F., Nie, W., Xia, X., Li, G., Hsu, H.-Y., Xu, Q., Zou, X., Ji, L., Lu, X., 2023. Recent Advances in Electrochemical-Based Silicon Production Technologies with Reduced Carbon Emission. *Research* 6, 0142. https://doi.org/10.34133/research.0142
Yasuda, K., Nohira, T., 2022. Electrochemical production of silicon. *High Temperature Materials and Processes* 41, 247–278. https://doi.org/10.1515/htmp-2022-0033
Yasuda, K., Nohira, T., Hagiwara, R., Ogata, Y.H., 2007. Direct electrolytic reduction of solid SiO2 in molten CaCl2 for the production of solar grade silicon. *Electrochimica Acta*, ELECTROCHEMICAL PROCESSING OF TAILORED MATERIALS Selection of papers from the 4th International Symposium (EPTM 2005) 3-5 October 2005, Kyoto, Japan 53, 106–110. https://doi.org/10.1016/j.electacta.2007.01.024
Yu, Z., Wang, N., Fang, S., Qi, X., Gao, Z., Yang, J., Lu, S., 2020. Pilot-Plant Production of High-Performance Silicon Nanowires by Molten Salt Electrolysis of Silica. *Ind. Eng. Chem. Res.* 59, 1–8. https://doi.org/10.1021/acs.iecr.9b04430
Zaikov, Y.P., Redkin, A.A., Apisarov, A.A., Korzun, I.V., Kulik, N.P., Isakov, A.V., Kataev, A.A., Chemezov, O.V., 2013. Silica Solubility in Molten Fluoride–Chloride Electrolytes and Density of KF–KCl–K2SiF6–SiO2 Melts. *J. Chem. Eng. Data* 58, 932–937. https://doi.org/10.1021/je301195x
Zaykov, Y., Isakov, A., Apisarov, A., Chemezov, O., 2013. Production of silicon by electrolysis of halide and oxide-halide melts. *Non-ferrous Metals* 12, 58–62.

Zaykov, Y.P., Isakov, A.V., Zakiryanova, I.D., Reznitskikh, O.G., Chemezov, O.V., Redkin, A.A., 2014. Interaction between SiO2 and a KF–KCl–K2SiF6 Melt. *J. Phys. Chem. B* 118, 1584–1588. https://doi.org/10.1021/jp4086816

Zhuk, S.I., Isaev, V.A., Grishenkova, O.V., Isakov, A.V., Apisarov, A.P., Zaykov, Y.P., 2017. Silicon electrodeposition from chloride-fluoride melts containing K2SiF6 and SiO2. *Journal of the Serbian Chemical Society* 82, 51–62.

Zou, X., Xie, H., Zhai, Y., Lang, X., Zhang, J., 2011. Electrolysis Process for Preparation of Solar Grade Silicon. *Advanced Materials Research* 391–392, 697–702. https://doi.org/10.4028/www.scientific.net/AMR.391-392.697

Gøril Jahrsengene
Research Scientist, SINTEF

The main author Gøril has a MSc (2015) and PhD (2019) degree in Materials Science from NTNU Norwegian University of Science and Technology (2019). She is currently working in metal production and recycling in SINTEF as a research scientist, focusing on electrolysis approaches, including production of Si and Mn by electrowinning.

Sindland, C., V. Andersen, and M. Tangstad. 2026. Silicon Carbide Reactivity: Experimental study of the reaction between SiC and SiO gas. In *Silicon for the chemical and solar industry XVIII,* edited by M. Tangstad, H. Rong, A. Valderhaug, B. Andresen, H. Dalaker, and I. G. Page. Kristiansand, Norway, September 7–10, 2026. https://doi.org/10.55669/oa900813

Silicon Carbide Reactivity:
Experimental study of the reaction between SiC and SiO gas

C. Sindland[1,2], V. Andersen[1], and M. Tangstad[2]
[1]Elkem ASA, Norway, caroline.sindland@elkem.com. [2]Norwegian University of Science and Technology, Norway

Keywords: Silicon carbide, SiO gas, reactivity, reaction kinetics, experiments

Abstract – Silicon carbide (SiC) is an important intermediate material in silicon production. SiC is produced from reaction between carbon and SiO gas, and if it does not react further to silicon, it may accumulate in the furnace and affect material flow, gas flow and electrical conditions. This work presents a new experimental setup for studying the reaction between SiC and SiO gas in a resistance-heated furnace. SiO gas is generated in the lower part of the chamber and passes upward to react with SiC held at a higher temperature. The reactivity of three SiC materials was compared: β-SiC from charcoal, accumulated α-SiC from a silicon furnace, and α-SiC from an Acheson furnace. Degree of reaction was evaluated from mass change and silicon content measured by SEM and XRD.

The results show that the method can distinguish between SiC materials with different reactivity. Under the tested conditions, β-SiC from charcoal showed higher reactivity than accumulated α-SiC from a silicon furnace and α-SiC from an Acheson furnace. A simple diffusion-based model gave a reasonable fit to the data and BET analysis suggests that surface area may be important for the observed differences. The results indicate that SiC reactivity is in important factor when the overall efficiency of a furnace is considered.

1. INTRODUCTION

Silicon is produced by carbothermic reduction of quartz in a submerged arc furnace, through several reactions. In the hot lower part of the furnace, SiO gas is formed and may then react with carbon to form SiC or with SiC to form silicon, as illustrated in Figure 1.

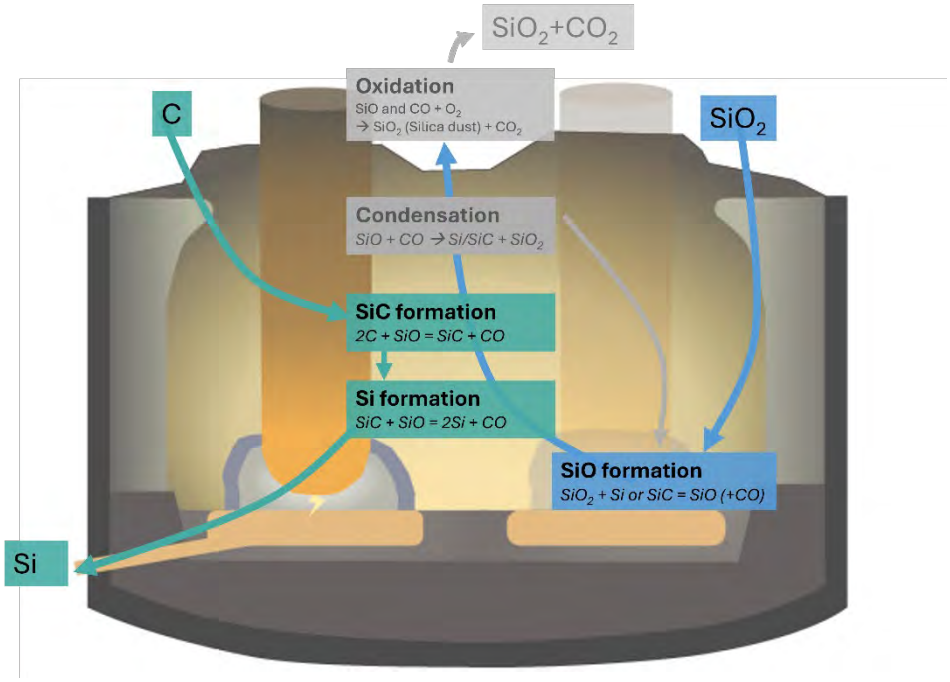

Figure 1: Illustration of the main reactions in a silicon furnace.

This work is licensed under the Creative Commons Attribution 4.0 International License. To view a copy of this license, visit https://creativecommons.org/licenses/by/4.0/

There should be a balance between SiC formation and SiC consumption. Accumulated SiC reduces the available reaction volume in the furnace and may also disturb electrical conditions (Haraldsson et al., 2024; Risinggård et al., 2022; Sindland et al., 2026; Tesfahunegn et al., 2018). While carbon reactivity towards SiO has been studied in detail (Lindstad et al.,2007; Myrhaug, 2003; Myrvågnes, 2008), there is limited published work on the reaction between SiC and SiO as described by Equation 1. In process models such as the two-zone model (Schei, Tuset and Tveit, 1998), this reaction is often assumed to reach equilibrium. In this work, we test whether SiC reactivity differs between materials and whether this difference can be measured experimentally.

$$SiC + SiO = 2Si + CO_{(g)} \qquad [1]$$

In the two-zone model (Schei, Tuset and Tveit, 1998), silicon formation from SiO and SiC takes place in the inner zone of the furnace. The partial pressure of SiO leaving the inner zone is described as the S-factor in this model. This factor is about 0.5 at 1970 °C if the reaction between SiC and SiO is significantly faster than the SiO formation rate, and it increases as the rate of SiO consumption decreases relative to SiO formation, as shown in Figure 2. The SiO leaving the inner zone must either react with carbon higher in the furnace or condense to maintain a high silicon yield. There must be a balance between SiC formation and SiC consumption over time to maintain stable operation, which implies that an increased S-factor will lead to increased condensation or formation of silica fume and thereby reduce yield. Condensation will move energy from the inner zone to the outer zone, since SiO formation is endothermic while condensation is exothermic, and it will form a highly viscous phase that prevents even gas and material flow, reducing overall efficiency. This makes SiC reactivity very relevant for process efficiency and stability by contributing to a low S-factor.

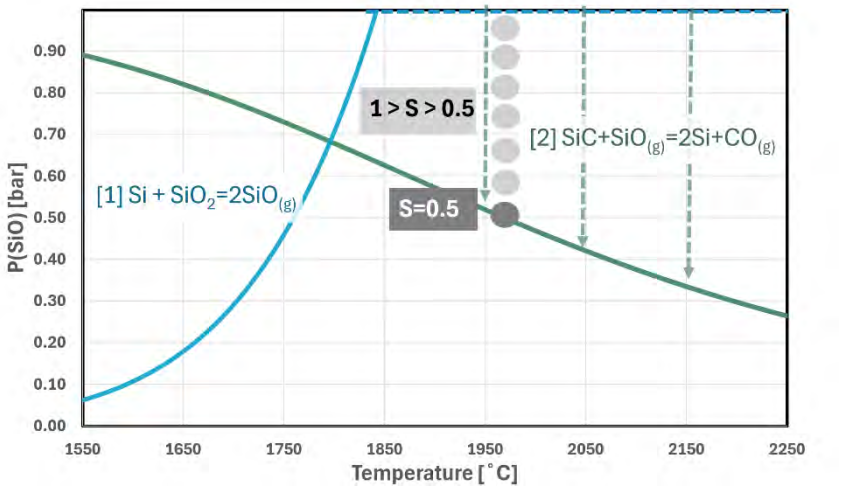

Figure 2: The equilibrium partial pressure of SiO for SiO formation [1] and silicon formation [2], given an activity of 1 for silicon. The dotted lines indicate the produced SiO pressure in the experimental setup of this paper and the driving force for silicon production at three temperatures. The figure illustrates how a lower rate of reaction [2] would increase the S-factor.

Silicon carbide (SiC) exists in several crystal structures, referred to as polytypes. In this work, β-SiC refers to the cubic 3C polytype, while α-SiC refers to the hexagonal and rhombohedral polytypes, which are commonly associated with higher formation temperatures (Jepps and Page, 1983). In silicon furnaces, β-SiC is typically formed first and may transform to α-SiC at higher temperatures (Jayakumari, 2020).

2. SiC reactivity test: Methodology and results

A method has been developed for testing relative SiC reactivity, and the setup has been used to compare β-SiC from charcoal, accumulated α-SiC from a silicon furnace, and α-SiC from an Acheson furnace. In this section, the setup and the basis for calculating degree of reaction are presented. Modelling of the SiC + SiO reaction rate based on these results is discussed in Section 3.

2.1 The SiC reactivity setup and raw materials

The SiC reactivity setup is illustrated in Figure 3. A total of 30 g of SiO granules are placed in a lower graphite crucible, while 10 g of SiC is placed in a perforated upper crucible. Because the lower part of the setup is colder than the upper part, SiO is generated below and passes upward to react with the hotter SiC. This design reduces premature condensation and allows the SiC to reach reaction temperature before significant SiO production starts.

Some SiO also reacts with graphite in the setup. This affects the CO content in the off-gas and is considered when interpreting the experiments and modelling the SiC + SiO reaction rate.

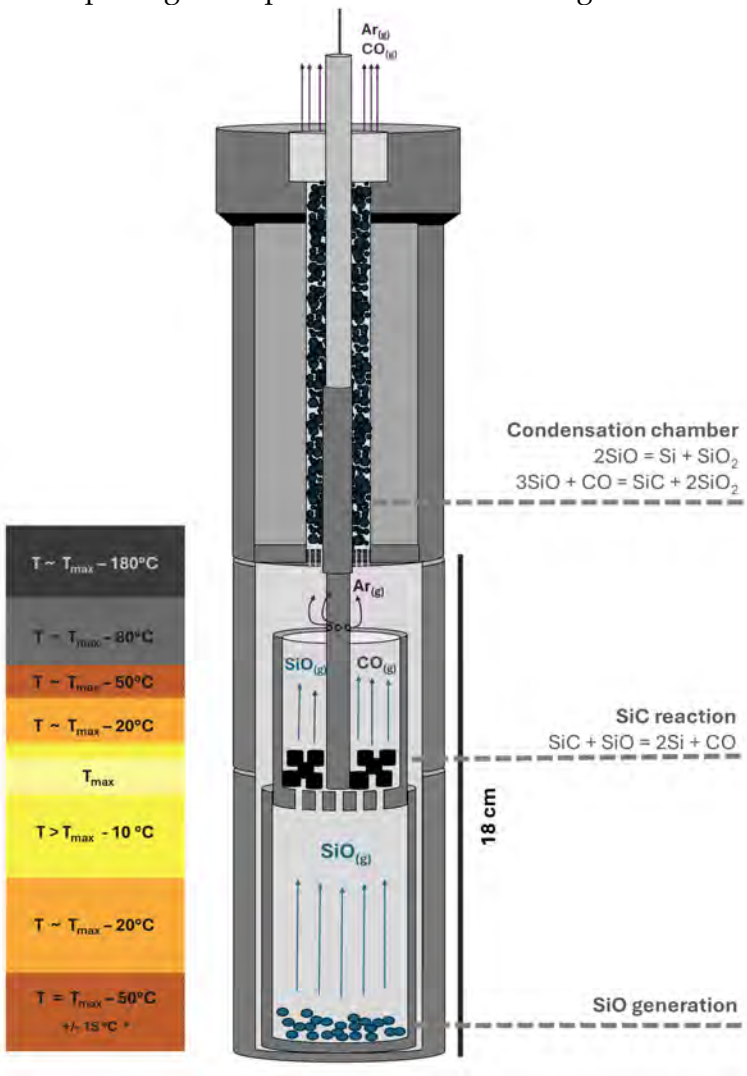

Figure 3: SiC reactivity setup with a lower chamber for SiO generation and an upper chamber for SiC reaction. The figure is adapted from Straum (2026).

Three types of SiC materials were tested: β-SiC from charcoal, accumulated α-SiC from a silicon furnace (same as investigated by Sindland et al., 2026), and α-SiC from an Acheson

furnace. The charcoal SiC was produced by calcining charcoal at 1200 °C for 20 minutes before exposing it to SiO gas for 1 h at 1800 °C. Before testing, the materials were crushed, sieved, and split into 10 g samples. The raw materials were analysed by scanning electron microscope (SEM) and X-ray diffraction (XRD) before reactivity testing.

Figure 4 shows the morphology of the three materials before reaction and their phase distribution before and after reaction with SiO, based on SEM images of cross section. The materials differ in morphology and porosity, and a clear increase in silicon content is observed after reaction. The silicon content, determined by SEM image analysis, and particle size of the raw materials is included in the figure.

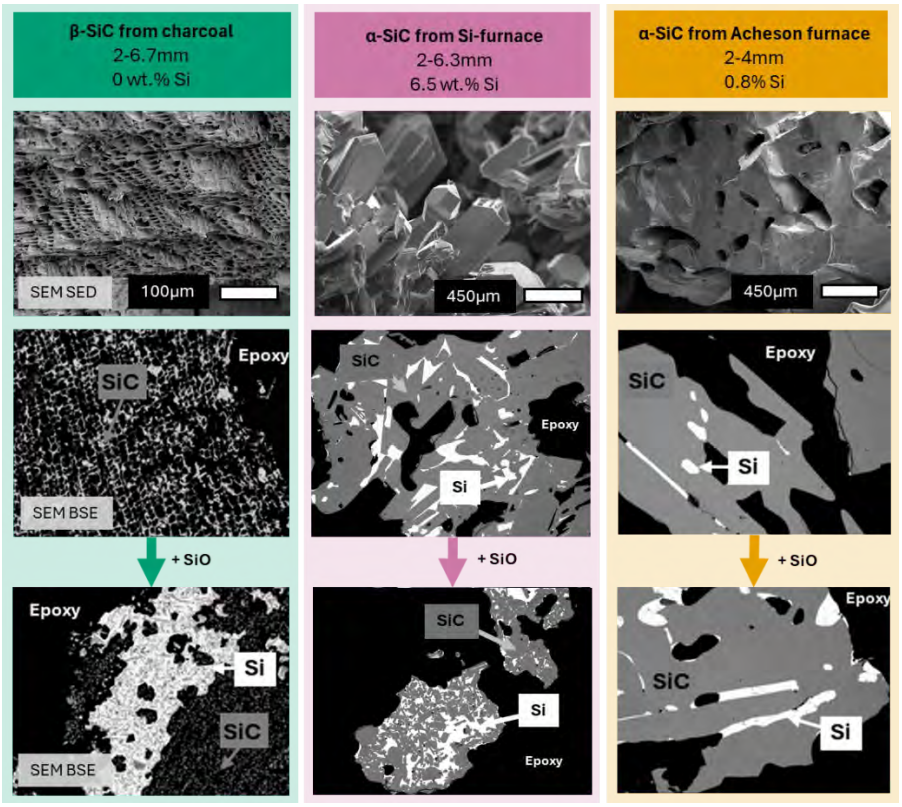

Figure 4: SEM images of the different SiC materials before and after reaction with SiO.

The materials were heated to temperatures from 1840 to 2140 °C and held for 5 to 60 minutes, as shown in Figure 5. CO in the off-gas reflects CO formation through both the SiO + SiC and SiO + C reactions, as well as CO consumption by condensation of SiO and CO. The CO content in the off-gas therefore cannot be used directly as a measure of SiC reactivity, in difference to the SINTEF SiO-reactivity test for carbon materials (Lindstad et al., 2007). The CO measurements are, however, useful for identifying when gas-phase reactions occur.

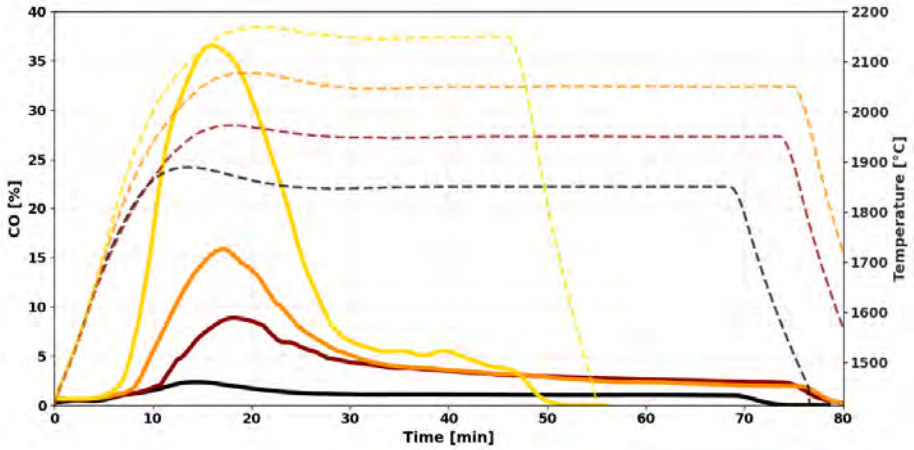

Figure 5: Heating program and CO evolution for typical experiments at four temperatures. CO concentration (%) in the off-gas is plotted as solid lines (left axis) while temperature is shown as dashed lines (right axis). The same colour is used for the corresponding CO and temperature curves.

Figure 6 shows that the SiO-generation data from Sindland and Tangstad (2020), Sindland (2026), and Kyaw (2024a and b) can all be described reasonably well by the same model structure proposed by Sindland (2020), $d\alpha/dt = A \cdot k \cdot \exp(-Q/RT)$, with relatively small deviations from the fitted curves within each dataset. The difference in reaction rates between the datasets of Sindland (2020) and Sindland (2026) is likely related to differences in available reaction area arising from the use of 1–8 mm particles and 2–4 mm granules, respectively. In particular, the external granule size cannot be directly compared with particle size, as the granules consist of finely distributed Si and SiO_2, resulting in a larger effective reaction area. However, the substantially higher reaction rates reported by Kyaw (2024a and b), from experiments where argon was purged through the SiO-forming chamber, suggest that gas flow conditions may also influence the observed SiO generation. Consequently, SiO generation should not be considered a function solely of temperature, time, and particle size, but also of material morphology and experimental design.

For the present study, all experiments were conducted using the same granule size fraction and gas flow conditions. Therefore, relative differences in SiC reactivity can be compared without accounting for variations in SiO generation. However, potential differences in SiO generation should be considered when experimental conditions are changed or when results are compared with data obtained using different experimental setups.

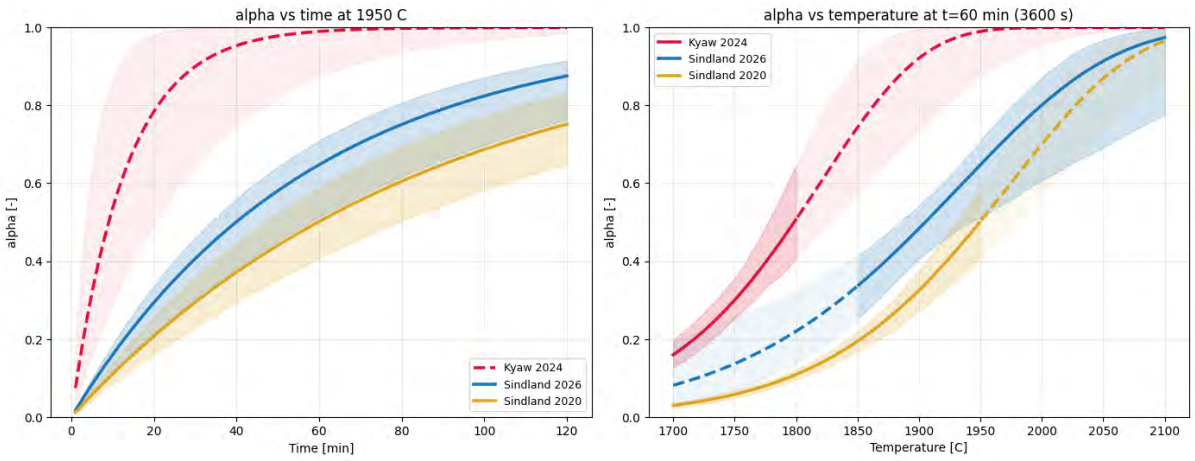

Figure 6: Modelled degree of reaction for the Si + SiO_2 = 2SiO reaction for three experimental setups using the equation proposed by Sindland (2020). Dashed lines indicate extrapolation beyond the measured temperature range. The shaded area represent the 95% confidence intervals.

2.2 Degree of reaction (SiC conversion to Si)

Degree of reaction is calculated as the amount of silicon carbide that has reacted, as described by Equation [2]. The initial and final amount of SiC ($SiC_{initial}$ and SiC_{final}) is given by the particle mass before and after the test ($m_{initial}$ and m_{final}) and their SiC content. The particles consist of SiC with some silicon, meaning that the SiC content can be calculated from the silicon content (%SiC = 100 - %Si).

$$\alpha = \frac{SiC_{initial} - SiC_{final}}{SiC_{inital}} = \frac{m_{initial} \cdot (100 - \%Si_{initial}) - m_{final} \cdot (100 - \%Si_{final})}{m_{initial} \cdot \%SiC} \qquad [2]$$

The silicon content was measured by XRD and SEM image analysis. For XRD, the material was milled and prepared for analysis on a Bruker D8 ADVANCE by back loading to reduce preferred orientation. Quantitative phase analysis was performed by Rietveld refinement in TOPAS v6. For SEM image analysis, approximately 10 grayscale images from each sample were segmented into epoxy, SiC, and silicon using fixed threshold values. A 3-point smoothed image was used to reduce misclassification caused by image resolution, and the bottom part of each image containing SEM parameters was excluded. A visualization of the process is included in Figure 7. The area fraction of silicon measured by SEM, relative to the combined Si and SiC content, was assumed to be equal to the volume fraction and was then converted to weight percent using the densities of Si and SiC.

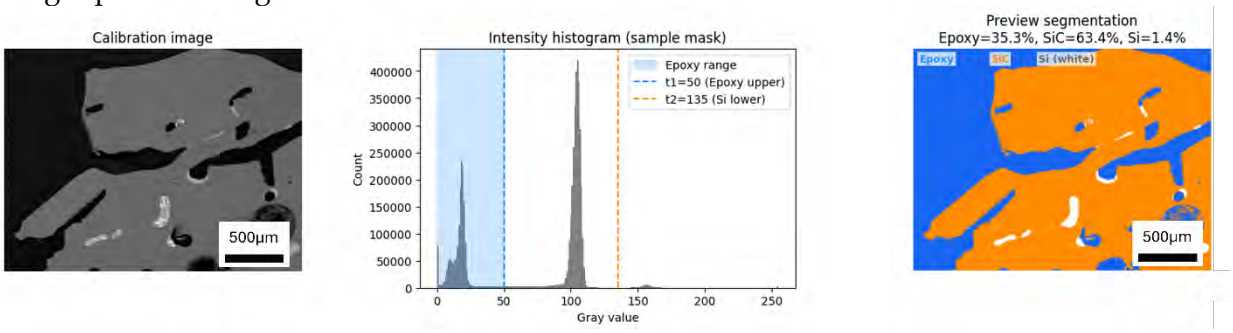

Figure 7: SEM image analysis method used to classify epoxy, SiC, and silicon from grayscale SEM images (50x).

A comparison of silicon content measured by XRD and SEM image analysis is presented in Figure 8. The two methods show the same main trend, but silicon content based on image analysis tends to be somewhat higher. The choice of SiC polytypes and parameters in the XRD refinement can influence the estimated silicon content, while for SEM image analysis there is uncertainty related to which particles are captured by the images. In the present work, the SEM results are used together with the mass change to estimate the degree of reaction.

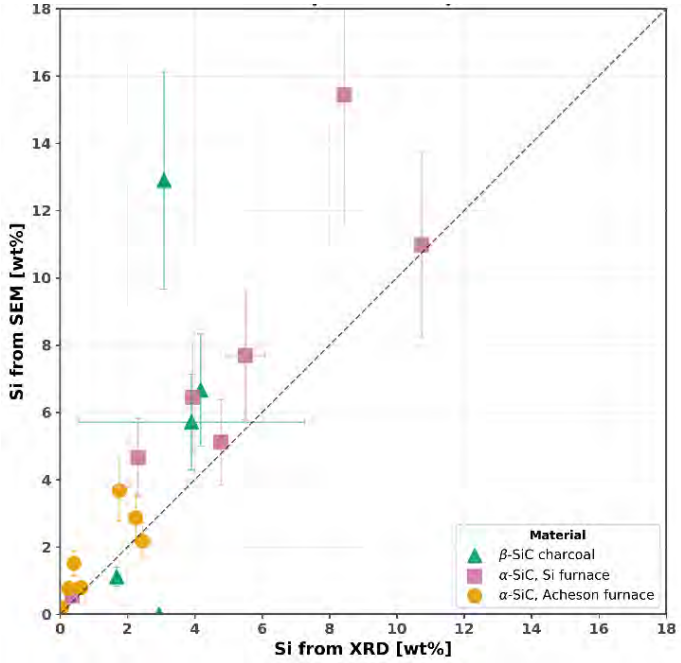

Figure 8: Silicon content determined by SEM image analysis and XRD.

Table I summarizes the experimental conditions and the calculated degree of reaction for the experiments used in the modelling.

Table I: Experimental conditions and degree of reaction for the experiments used in the modelling of SiC reactivity. *Negative degree of reaction is possible due to uncertainty in the measurement of silicon content.

Material	Run #	Temperature SiC [˚C]	Time [min]	SiC weight change [%]	Silicon after reaction [wt.%]	Degree of reaction (α)
β-SiC Charcoal	8	1940	60	+0.60	1.1	0.01
	17	2040	5	-1.11	5.7	0.10
	15	2040	60	+1.90	12.9	0.15
	19	2140	5	+8.96	6.7	0.12
α-SiC Si furnace	5	1840	60		0.54	
	7	1940	60	-1.70	5.1	0.00
	9	1940	60	-1.50	4.7	-0.01*
	14	2040	60	+2.00	7.7	0.00
	18	2090	30	-3.00	11.0	0.09
	12	2140	30	+3.01	15.4	0.10
α-SiC Acheson furnace	4	1840	60		0.2	
	6	1940	60	-1.20	2.2	0.03
	16	1990	60	+0.80	2.9	0.02
	10	2040	60	+0.90	3.7	0.03

Figure 9 shows CO content in the off-gas as a function of time for all experiments performed at 1940 °C. There is a large variation in the total amount of CO produced, and the amount of CO is not necessarily lower when there is no SiC in the system. This confirms that the CO measurements cannot be used as a measure of degree of reaction, as discussed previously.

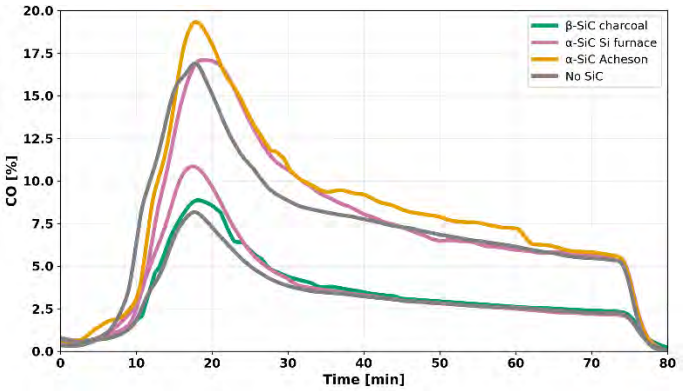

Figure 9: CO in the off-gas for all experiments at 1940 °C, including experiments without silicon carbide.

The silicon carbide produced from charcoal is initially β-SiC, while it transforms into α-SiC when exposed to temperatures above 2000 °C, as presented in Figure 10. Most of the results follow the trend where degree of transformation increases with temperature above 2000 °C, as discussed by Jayakumari (2020). However, the results at 2040 °C are unexpected regarding effect of time and more results are needed to indicate any clear trend and mechanism behind the transformation from β to α-SiC under exposure to SiO gas.

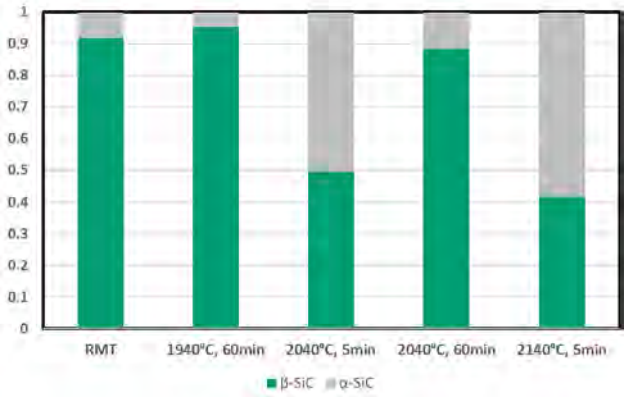

Figure 10: Content of β- and α-SiC in charcoal SiC before and after exposure to SiO gas at elevated temperatures.

3 Modelling of SiC reactivity

The purpose of the modelling is to describe how the degree of reaction depends on time and temperature, and to compare the relative reactivity of the tested SiC materials.

A simple diffusion-based expression (D1, Equation 3) was used as a framework to describe the dependence of the calculated degree of reaction on time and temperature (Khawam and Flanagan, 2006). The present dataset is limited, with only a few experiments for each material, and is therefore not sufficient to identify the controlling reaction mechanism or to validate one kinetic model over another. The model should consequently be regarded as a preliminary and comparative description of the data, rather than a mechanistic fit. Its purpose is to provide an initial basis for comparing apparent SiC reactivity between materials and for comparing the relative rate of the SiC + SiO reaction with other furnace reactions. More experiments are needed to determine whether the selected model form is physically representative.

$$\alpha = k_{material} \cdot \sqrt{t} \cdot \exp\left(-\frac{Q}{RT}\right) \qquad [3]$$

In this model, the degree of reaction (α) depends on time (t), temperature (T), activation energy (Q), the gas constant (R), and a material-specific mass transfer constant (k). Differences between the tested materials are therefore represented by different fitted values of k, listed in Table II. A comparison of modelled and measured degree of reaction is presented in Figure 11.

Table II: Constants for the diffusion-based model used to describe SiC reactivity.

Constant	Value	Unit
$k_{material}$ (α-SiC Si furnace)	$1.5 \cdot 10^9$	$1/s^{0.5}$
$k_{material}$ (α-SiC Acheson furnace)	$1.6 \cdot 10^9$	$1/s^{0.5}$
$k_{material}$ (β-SiC charcoal)	$4.1 \cdot 10^9$	$1/s^{0.5}$
Q	545	kJ/mol

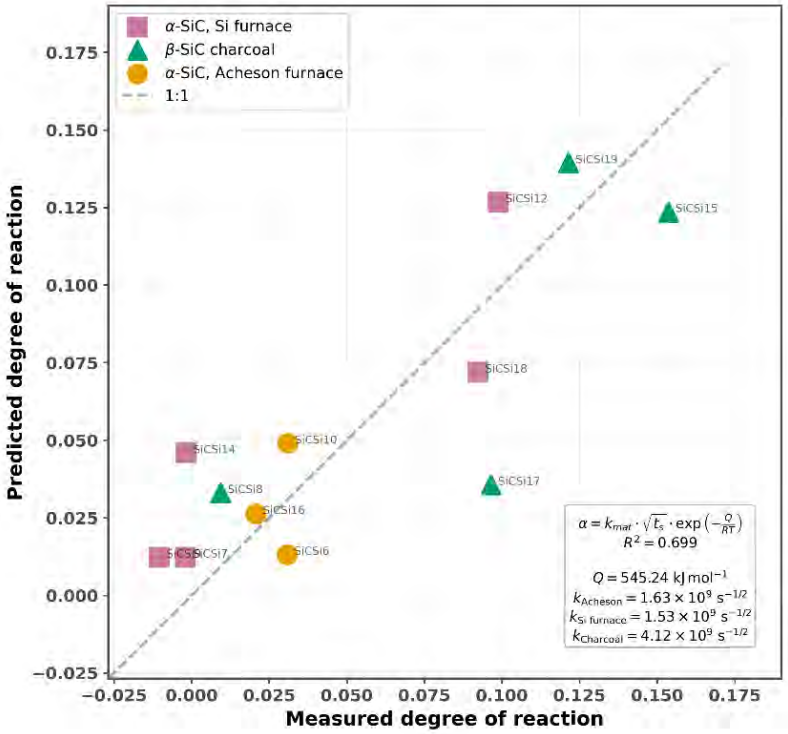

Figure 11: A comparison of predicted and measured degree of reaction for all experiments.

The fitted model gives an approximate description of the measured degree of reaction, but the limited number of data points and the uncertainty in the calculated degree of reaction mean that the fitted parameters should be interpreted with caution. Within these limitations, the results indicate that the apparent degree of reaction increases with temperature and time, as illustrated in Figures 12 and 13. The fitted material constants suggest that SiC from charcoal is more reactive than the two α-SiC materials under the tested conditions, while the two α-SiC materials behave similarly. The predicted reaction rate of charcoal SiC at 1950 °C is comparable to that of the α-SiC materials at about 2050 °C, illustrating the combined effect of material type and temperature.

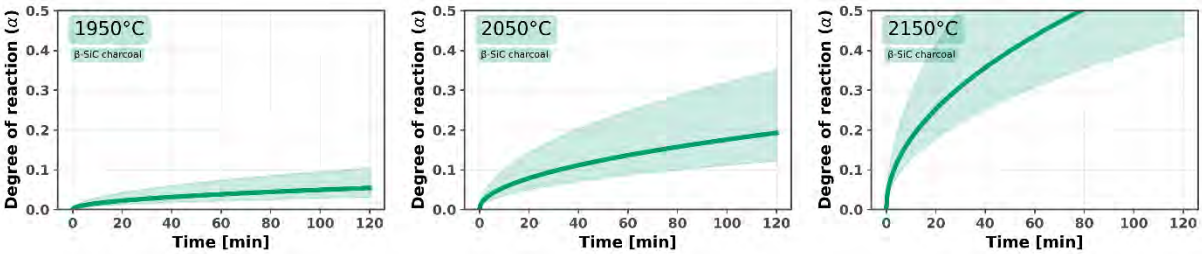

Figure 12: Model prediction of how the degree of reaction changes with time for β-SiC from charcoal at different temperatures. The shaded bands represent 50% confidence intervals from bootstrapping.

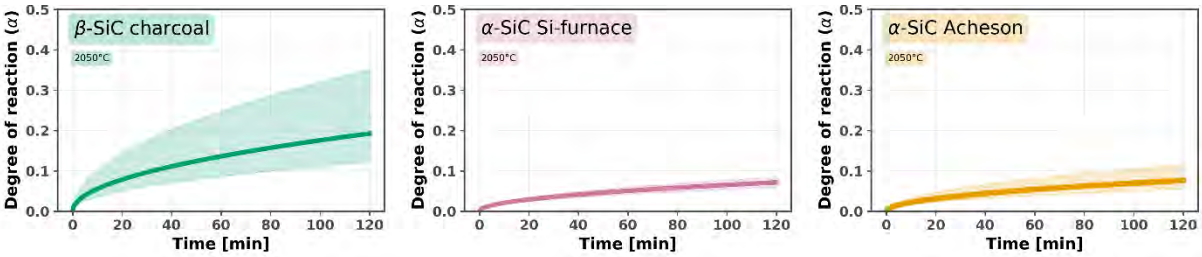

Figure 13: Model prediction of how the degree of reaction changes with time for the tested materials at 2050 °C. The shaded bands represent 50% confidence intervals from bootstrapping.

A comparison of BET surface area and the fitted material constant (mass transfer constant) in Figure 14 suggests that available surface area may be an important factor for SiC reactivity. The present results therefore indicate that surface area may be more important than polytype alone, but this cannot be concluded from the current dataset. This will be investigated further by testing α-SiC materials with higher specific surface area. We also aim to test various particle sizes in the future, as we expect that the rate of reaction increases with decreasing particle size.

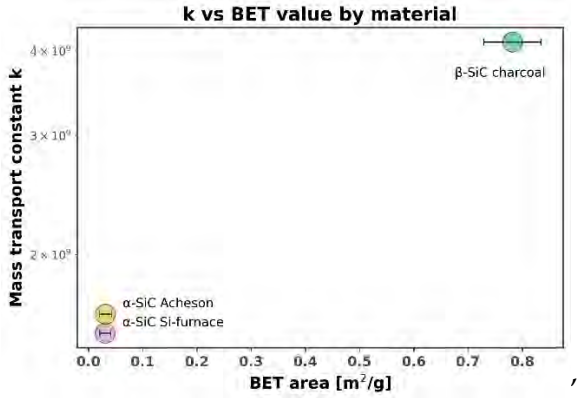

Figure 14: BET analysis of the three SiC materials before reactivity testing and their reactivity constants. The BET values for the α-SiC materials are outside the normal range for BET analysis due to their low specific area and should be considered approximate.

3.1 Comparison with other reactions and industrial implications

To explore the possible industrial relevance of the measured SiC reactivity, the newly developed model for the SiC + SiO = 2Si + CO reaction was combined with published models for SiO + 2C = SiC + CO, Si + SiO_2 = 2SiO, and SiC + $2SiO_2$ = 3SiO + CO (Myrhaug, 2003; Sindland, 2020; Tangstad, 2019). This makes it possible to compare the relative rates of important SiC-forming, SiO-forming, and Si-producing reactions under the same conditions.

Figure 15 compares the modelled degree of reaction as a function of time for several important furnace reactions at different temperatures and fixed particle sizes. The conversion of 4 mm

carbon particles to SiC is clearly the fastest reaction, which is consistent with furnace excavations showing SiC formation already in the upper part of the furnace (Ksiazek, Tangstad and Ringdalen, 2016). At 1850 °C, the SiO-forming reaction between 1–8 mm silicon and quartz proceeds only to a limited extent, whereas at 2050 °C significant SiO formation is predicted for both Si + SiO_2 and 3 mm SiC + SiO_2. In contrast, the predicted degree of reaction for SiC + SiO remains relatively low, indicating that SiC consumption may be slower than the competing SiO-forming reactions. The combined modelling should be regarded as indicative rather than conclusive, since some of the models were applied outside their original experimental ranges.

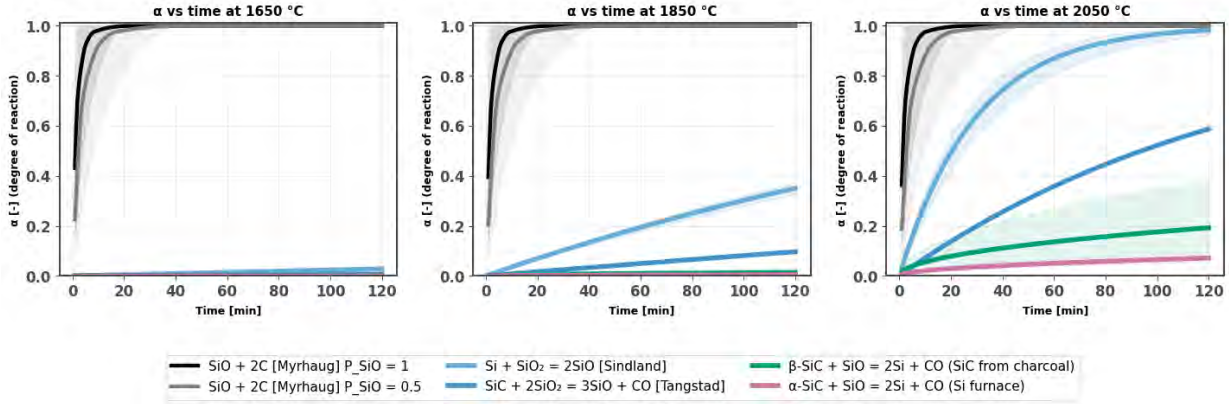

Figure 15: Modelled degree of reaction as a function of time for several furnace reactions at three temperatures.

The results indicate that SiC reactivity may be important for furnace operation. Accumulated SiC from a silicon furnace reacted more slowly with SiO than SiC produced from charcoal, and the combined modelling suggests that SiC consumption may be slower than some of the competing SiO-forming reactions. This means that low SiC reactivity may contribute to a higher SiO pressure leaving the inner zone, thereby increasing the need for SiO consumption by carbon or condensation higher in the furnace. If this consumption is insufficient, the probability of SiO loss as silica fume increases. The results therefore suggest that SiC reactivity should be considered alongside carbon reactivity in further discussion and modelling of furnace efficiency and yield.

4. CONCLUSIONS

The developed setup shows potential for comparing SiC reactivity of different materials under controlled conditions. The results indicate that β-SiC from charcoal reacts faster with SiO than the two tested α-SiC materials, although additional experiments are needed to confirm the trend and determine whether the fitted reaction model is physically representative. The results also suggest that specific surface area may contribute to the observed differences between the materials, but more data are needed before this can be concluded.

The comparison with published reaction models indicate that the SiC + SiO reaction is slower than several competing SiO-forming reactions, meaning that SiC reactivity is relevant for SiO consumption in the inner zone of the furnace. This means that SiC reactivity should be considered in further modelling and discussion of furnace operation.

5. ACKNOWLEDGEMENTS

The authors gratefully acknowledge the financial support from the Research Council of Norway (project number 354123) and Elkem ASA.

6. REFERENCES

Filsinger, D.H. and Bourrie, D.B., 1990. Silica to Silicon: Key Carbothermic Reactions and Kinetics. Journal of t*he American Ceramic Society*, 73, pp.1726–1732.

Haraldsson, H.V., Traustason, H., Tesfahunegn, Y.A., Tangstad M. and Sævarsdottir G., 2024. Modeling and Comparison Study of Industrial AC-Arcs. *Metallurgical and Materials Transactions B*, 55, pp.3750–3760.

Jayakumari, S., 2020. *Formation and Characterization of β- and α-Silicon Carbide Produced During Silicon/Ferrosilicon Process*. Doctoral theses at NTNU, 2020:252.

Jepps, N.W. and Page, T.F., 1983. Prog. Cryst. Growth Charact., 7, p.259.

Khawam, A. and Flanagan, D.R., 2006. Basics and applications of solid-state kinetics: A pharmaceutical perspective. *Journal of Pharmaceutical Sciences*, 95, pp.472–498.

Lindstad, T., Gaal, S., Hansen, S. and Prytz, S., 2007. Improved SINTEF SiO-reactivity test. In: *INFACON XI: Innovations in the Ferro Alloy Industry*, Vol. 1, pp. 414–423.

Ksiazek, M., Tangstad, M. and Ringdalen, E., 2016. Five furnaces five different stories. In: *Silicon for the chemical and solar industry XIII*, Kristiansand, Norway, 13 June 2016.

Kyaw, T.T. and Tangstad, M., 2024a. SiC formation in charcoal briquettes versus bulk material. In: *INFACON XVII*, Beijing, China, 13–22 September 2024.

Kyaw, T.T. and Tangstad, M., 2024b. Use of Agglomerates in Silicon Production. In: *Silicon for the Chemical and Solar Industry XVII*, Trondheim, September 2024.

Myrhaug, E.H., 2003. *Non-fossil reduction materials in the silicon process - properties and behaviour*. PhD thesis. Norwegian University of Science and Technology, Trondheim.

Myrvågnes, V., 2008. *Analyses and Characterization of Fossil Carbonaceous Materials for Silicon Production*. PhD thesis. Norwegian University of Science and Technology, Trondheim.

Risinggård, V.K., Sparta, M., Fromreide, M. and Halvorsen, S.A., 2022. Large electrode movements: Realistic electrical crater models. In: *Silicon for the Chemical and Solar Industry XVI*, Trondheim, Norway, 14–16 June 2022.

Schei, A., Tuset, J.K. and Tveit, H., 1998. *Production of High Silicon Alloys*. Trondheim: Tapir.

Sindland, C. and Tangstad, M., 2021. Production Rate of SiO Gas from Industrial Quartz and Silicon. *Metallurgical and Materials Transactions B*, 52B.

Sindland, C., Tangstad, M. and Andersen, V., 2026. Formation of α-SiC in the Low-Temperature Zone of Silicon Furnaces. *JOM*.

Straum, I., Behaviour of Quartz–Charcoal Agglomerates in Silicon Production 2026. *Master thesis*. June 2026.

Tangstad, M., Safarian, J., Bao, S., Ringdalen, E. and Valderhaug, A., 2019. Effect of Different SiO2 Polymorphs on the Reaction Between SiO2 and SiC in Si Production. *Aspects in Mining & Mineral Science*, 3, p.2.

Tesfahunegn, Y.A., Magnusson, T., Tangstad, M. and Saevarsdottir, G., 2018. Effect of Carbide Configuration on the Current Distribution in Submerged Arc Furnaces for Silicon Production—A Modelling Approach. In: Nastac, L., Pericleous, K., Sabau, A., Zhang, L., Thomas, B. (eds) CFD Modeling and Simulation in Materials Processing 2018. TMS 2018. The Minerals, Metals & Materials Series. Springer, Cham. https://doi.org/10.1007/978-3-319-72059-3_17

Caroline Sindland

Industrial PhD candidate and Research Engineer, Elkem ASA

Caroline Sindland is an Industrial PhD candidate and Research Engineer at Elkem ASA. She began her career as an apprentice in chemical analysis at Elkem, before completing an MSc in Materials Science and Engineering at NTNU. She later returned to Elkem as a Process Engineer. Since January 2025, she has been pursuing an industrial PhD on silicon carbide behaviour in silicon furnaces, in collaboration with NTNU.

Gryshan, D., M. Wallin, M. Yermolov, J. Legemza, N. Korol, and G. M. Tranell. 2026. Industrial experience of using biocarbon briquettes in FeSi production process. In *Silicon for the chemical and solar industry XVIII*, edited by M. Tangstad, H. Rong, A. Valderhaug, B. Andresen, H. Dalaker, and I. G. Page. Kristiansand, Norway, September 7–10, 2026. https://doi.org/10.55669/oa900814

Industrial experience of using biocarbon briquettes in FeSi production process

Denys Gryshan[1,2], Maria Wallin[2], Mykola Yermolov[1], Jaroslav Legemza[3], Nataliya Korol[4], and Gabriella M. Tranell[2]

[1]OFZ, a.s., Široká 381, 027 41, Oravský Podzámok, Slovakia, gryshan@ofz.sk
[2]Department of Materials Science and Engineering, Faculty of Natural Sciences, Norwegian University of Science and Technology, Trondheim 7491, Norway, gryshan.denys@ntnu.no
[3]Faculty of Materials, Metallurgy and Recycling, Technical University of Košice, Letná 1/9, 042 00 Košice, Slovakia, jaroslav.legemza@tuke.sk
[4]Perechin timber and chemical plant, 25, Uzhans'ka st., Perechin, Zakarpatska region, Ukraine, korolni@lxk.com.ua

Keywords: ferroalloys, ferrosilicon, FeSi, charcoal, biocarbon

Abstract – Substitution of fossil carbon by bio reductants such as charcoal is one of the prioritized directions for sustainable development of the high silicon alloy (MG-Si and FeSi) production process. The fines fraction created during the production of charcoal could potentially be effectively utilized in a traditional metallurgical submerged arc furnace (SAF) in the form of agglomerates. Compared with lumpy charcoal, agglomerates such as pellets and briquettes show several advantages, including lower moisture absorption and lower fragility which means reduced dust formation. In addition, their higher density improves logistics and utilization efficiency. Additional costs brought by the use- and processing of bio-reductants may be compensated by a decreased CO_2 emission cost.

Based on available laboratory-scale data, the differences in properties between agglomerates and lumpy materials are not expected to significantly affect the SiO reactivity of the carbon charge. Accordingly, potential deviations in furnace operation and energy consumption may be due to other factors such as thermal stability, charge density etc.

The aim of this work was to analyze available operational data of the behavior of an industrial 23MVA submerged arc furnace producing FeSi75 at OFZ during a 20-shift trial, using biocarbon charcoal briquettes as a partial replacement for fossil reductant. The briquettes were produced by the Perechin plant, using cornstarch as binder. Results indicated similar Si-yield, energy consumption and product composition for the charcoal briquettes as with a typical carbon mix, thereby opening the path towards an increased utilization of charcoal fines and a more robust approach towards cost-efficient carbon neutrality in FeSi production.

1. INTRODUCTION

OFZ, a. s., is manufacturer of ferroalloys based in Slovakia, with a history dating back to 1952. For over 70 years, the company has produced a wide range of alloys based on reduction smelting in submerged arc furnaces (SAF). These include chromium-based ferroalloys (FeCr LC, FeCr HC), manganese-based (FeMn HC, FeMn MC, FeSiMn), silicon-based (FeSi) and a wide range of other specific alloys (FeMo, FeW, FeSiAl, FeSiTi, FeTi, SiZr etc).

The production site has 7 submerged arc furnaces with a total capacity of more than 100, 000 tonnes of alloy per year. Current operation includes two furnaces for manganese-based alloys,

This work is licensed under the Creative Commons Attribution 4.0 International License. To view a copy of this license, visit https://creativecommons.org/licenses/by/4.0/

four for silicon-based alloys and one smaller furnace for refining and remelting of fines. In 2018, one of the SAF's was modernized for the possibility to produce Si metal.

Today, the most in-demand and competitive products for OFZ are concentrated around various types of FeSi, FeMn, FeSiMn, and FeSiCa alloys, as well as cored wires. OFZ is the last producer of FeSiCa in Europe due to the company's developed approach to switching the production process between FeSi and FeSiCa. However, the current situation in the local electricity market, compared to other production sites in the world, has not supported maintaining stable production volumes over the last few years. Nevertheless, development of long- and short-term solutions for improvement of production processes and decreasing Greenhouse Gas (GHG) emissions are part of the company's strategy. The use of biocarbon as a substitute for the fossil reductant is one of the promising short-term paths to reduce direct emission from ferroalloy production processes.

The specific ferroalloy production process is typically tuned towards different mechanical, thermal, chemical and electrical properties of the reductants and to some extent oxidic raw materials. Plant metallurgists evaluate the effects of different raw materials on the production process by analysis of available data from the furnace management system and the company's ERP (Enterprise Resource Planning) system Karat.

The traditional charge for MG-Si and FeSi alloy SAF operation is lumpy material (Schei et al., 1998). Permeability of the charge mix (Tranell et al., 2010), is a significant aspect both for the silicon-producing reactions and furnace safety.

The selection of reducing agents for the ferrosilicon production process requires consideration of several criteria, such as economic considerations, appropriate chemical composition (low ash, high reactivity, low volatile substances, high fixed carbon, etc.), high electrical resistance, appropriate granulation, and high mechanical strength. Compared to coke, semi-coke, and industrial coal, charcoal has lower thermal abrasion strength, low sulfur, and phosphorus content, high moisture content, low mechanical strength, higher reactivity and higher electrical resistivity (Etemadi et al., 2023). Higher SiO-reactivities (Myrhaug et al., 2004) of bio reductants in Si/FeSi process compared to fossil reductants may also decrease the power consumption (Junru et al., 2018) in addition to decreasing direct CO_2 emissions (Smith-Hanssen et al., 2023).

In the current work, a twenty-shift trial period producing FeSi75, using up to 38% Cfix equivalent of charcoal briquettes in the charge mix will be compared with two typical periods using only fossil reductants. Performance indicators such as silicon yield, specific energy consumption and product composition will be evaluated along with effects on furnace operation. Results from this work create a baseline for the use of composites/agglomerates in SAF production process, which will be further explored together with partners in the EU Horizon Europe project QUEEN (Quartz Enrichment Enabling Near-Zero Silicon).

2. PRODUCTION AND TESTING OF BIO-C BRIQUETTES In FeSi75 PRODUCTION

The main practical aspect of using agglomerated materials in the ferroalloy furnace is the possible disintegration of the briquettes before reaching the main reaction zone. Such disintegration decreases the Si yield, loses unreacted carbon to the off-gas dust and may affect the silica fume quality. Low temperature decomposition of an organic binder could affect reactivity of the charge and strength of lumps. Fines generation related with high temperature properties of agglomerates can affect furnace gas flow and pressure drop in charge (Ringdalen

et al., 2022). Performance of the agglomerates in the charge and their effect for furnace performance in the case of partial replacement of fossil carbon was subject for investigation with assumption overall permeability of the charge could be maintained by other components of the charge, primarily quartzite and wood chips.

2.1 SAF

The trials were performed in furnace No 23 for production of silicon-based alloys (Klocok et al., 2021). This SAF has a semi-open construction and self-baking electrodes. The annual capacity is 15, 000 tonnes of FeSi. The parameters of the furnace are presented in Table 1 below.

Table 1. SAF parameters

Installed capacity, MVA	Diameter of electrodes, mm	Pitch Circle Diameter, mm	Diameter of bath, mm	Bath depth, mm
22,8	1200	2900	6000	2400

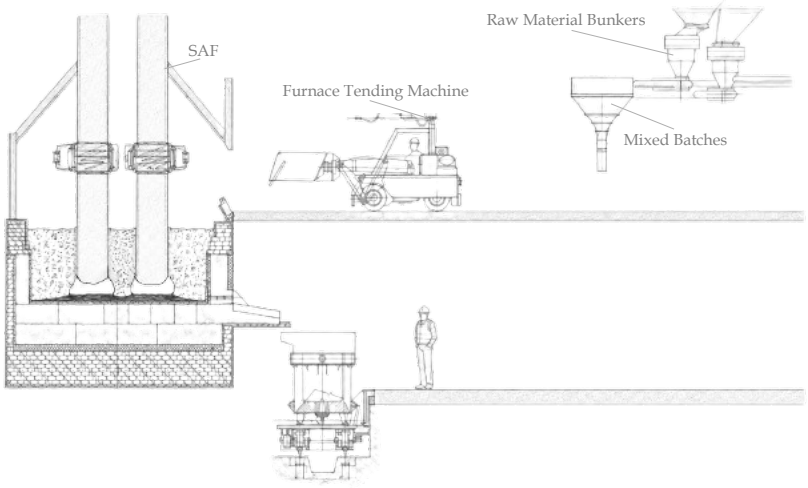

Figure 1. Schematic overview of furnace charging system

The furnace charging (Figure 1) is done batchwise by using a furnace tending machine. The different raw materials have separate bunkers above the loading area. Based on required recipe, a specific volume of each raw material is moved to the mixed batches bunker situated close to the uploading area. A furnace tending machine moves batches into the furnace.

2.2 Raw materials properties

The types and composition of the main charge components to produce FeSi in the studied periods are shown in Figure 2, Table 2 and Table 3.

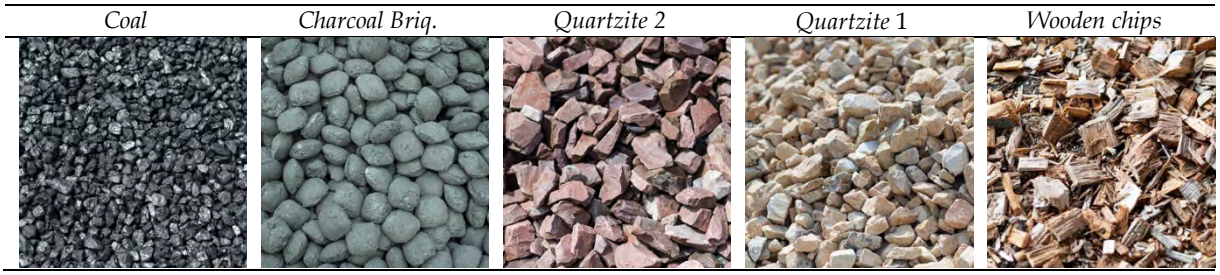

Figure 2. Main raw materials for FeSi production

Table 2. Chemical composition of quartzite sources (wt%)

Name	SiO_2	P	FeO	Al_2O_3	CaO	TiO_2	MgO	LOI
Quartzite 1	98.92	0.024	0.09	0.42	0.08	0.05	0.001	0.22
Quartzite 2	98.08	0.013	0.11	1.06	0.08	0.064	0.007	0.44

Table 3. Chemical composition of different carbon sources (wt%)

Name	Ad	Va	P	Al_2O_3	Cl	S	SiO_2	CaO	MgO	FeO
Coal	4.25	33.2	0.004	0.56	0.13	0.46	1.57	0.62	0.040	0.57
Charcoal 0-6 mm	4.00	12.63	0.052	0.50	0.06	0.03	0.2	0.7	0.019	0.08
Charcoal briq.	4.67	16.79	0.077	0.06	0.006	0.03	0.34	2.08	0.019	0.07

Va - Volatile matter content, air-dried basis
Ad - Ash content, air-dry basis

The measured SiO-reactivities of the carbon materials are listed in Table 4. As seen from the table, coal demonstrated lower reactivity than the charcoal, which is in agreement with published data (Jayakumari and Ringdalen, 2022) and practical experience of the authors.

Table 4. SiO-Reactivity of used carbon materials

Name	Coal	Charcoal (prior to briq.)	Charcoal briq.
SiO-Reactivity, ml SiO (SINTEF test)	771	530	534

2.3 Production of Charcoal Briquettes

Charcoal is a solid product of the high temperature pyrolysis of wood biomass. The Cfix content of charcoal, which depends on the pyrolysis temperature and is affected by the physical properties of the wood, typically ranges from 80 to 85 wt%. The volatile content in charcoal is typically 5–20 wt%, and ash content, which depends on the content of minerals in the wood material, is approximately 0.2 to 5 % (Legemza et al., 2019)

Briquetting an agglomeration and densification technology, is one of the technologies used to improve the quality of biomaterials (Lomunyak et al., 2024). Charcoal fines briquetting is a sustainability-oriented approach that allows transforming small charcoal fractions, which are difficult to use efficiently in loose form, into a stable, valuable, and marketable biocarbon material. As such, briquette production reduces raw material losses, improving resource efficiency, and creating added value from side stream of charcoal production.

The quality of a charcoal briquette depends on a combination of factors. These include the particle-size distribution of the charcoal, the type and concentration of binder, the moisture content of the mixture, the pressing method, and the drying regime. A key element of briquette production is the binder system. The binder must hold the charcoal particles together, but at the same time it should not significantly increase ash content or make the product too expensive. Available research (Pahnila et al., 2026) shows that starch-based binders are promising based on their properties and possible scalability. As outlined above, agglomeration could significantly increase the value of fine charcoal fractions which will allow its use in standard SAF operation. At the same time, agglomerated material could reduce fines generation during handling, packaging, transport and storage. This is especially important for a plant with an internal logistics line which was built for the more mechanically durable coal.

Figure 3. Charcoal briquettes with cornstarch binder used in trials

The briquettes in the study, illustrated in Figure 3, used cornstarch as binder and were produced by Perechin timber and chemical plant in the Ukraine. Cornstarch was chosen as a binder due to its cold strength characteristics and market availability (Yankovych and Korol, 2025). Charcoal fines with a particle size of 0-6 mm were used to produce the targeted briquette size of 52 × 52 × 30 mm. A mixture of charcoal, hot water, and 10 % binder is fed to the briquette press. The amount of added water depends on the initial moisture of both the charcoal and the binder. Briquettes are formed in industrial roller compactor with 300 mm patterned rollers and working pressure of 100 MPa. After compaction, the briquettes are transferred to the drying system. The drying unit contains three sequential temperature zones, with temperatures gradually decreasing from 120°C to 70°C. Gradual cooling prevents cracking and ensures stable mechanical strength of the final briquettes.

2.4 Trial Procedure

The approach for testing of briquettes in FeSi75 production was based on previous experience using lumpy biocarbon (20-70 mm) in the same production process. Stable operation with up to 38% lumpy charcoal of total Cfix in the charge mix had been achieved and hence, for the current trials, we set the same level of substitution. Trials were started with a base mix (only fossil reductant) in both reference periods (Ref.1 and Ref.2) as well as in the briquette trial period. The briquette fraction in the trial period was increased with each shift until achieving a Cfix fraction from briquettes of 20, 30 and 38% accordingly.

3. RESULTS AND DISCUSSION

The furnace performance and the operation during the reference and trial periods were assessed from several points of view;

- Furnace productivity
- Metal and silica fume quality
- Si yield
- Cost-effectiveness including effects of CO_2 pricing

3.1 Productivity

The SAF productivity for each of the three production periods with equal duration – 20 shifts, is presented in Figure 4. The average performances (MWh/tonne alloy) for each period are illustrated with dotted lines for comparison. The absolute difference between highest and lowest average performance in the different periods is around 3.1 %. It should be noted that reference periods Ref. 1 and Ref. 2 were monitored after a long interruption of the furnace,

which could have affected the productivity in those periods. There were also several short-term interruptions due to maintenance. However, as seen from the figure, the productivity in the period using a mixed briquette/fossil charge is not significantly different to a pure fossil charge.

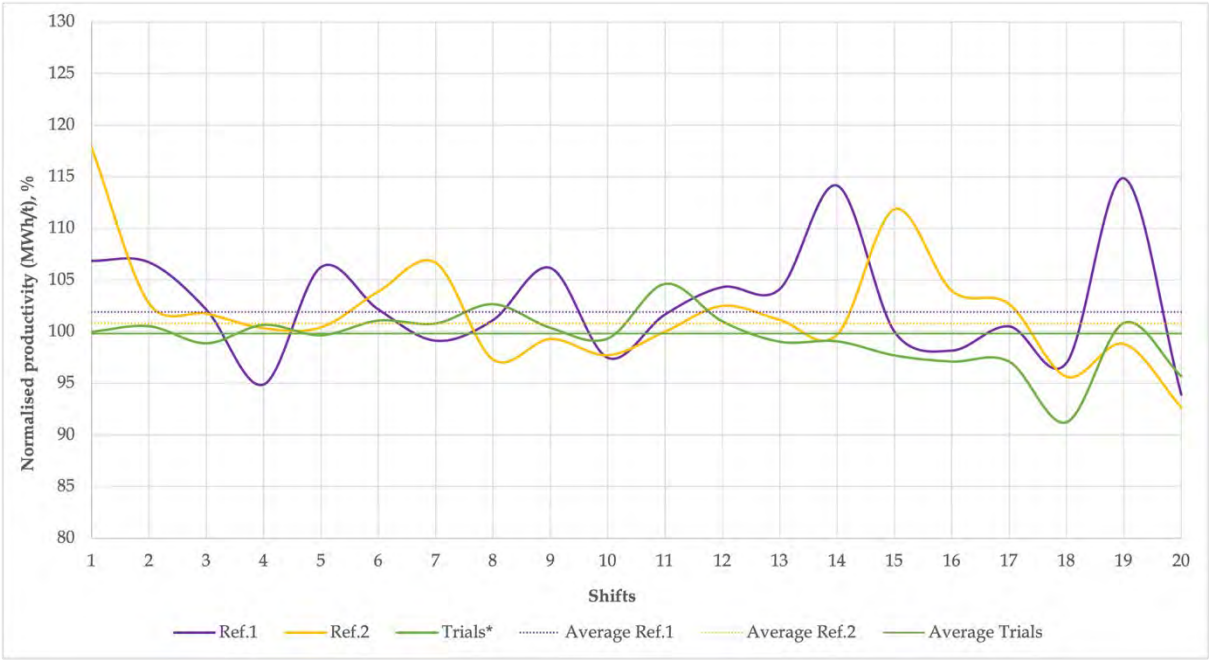

Figure 4. Normalised productivities of the SAF 23 during reference periods and trials with briquettes

During each period, 89 to 99 samples of the FeSi metal were analysed, results plotted in Figure 5. The standard deviation (σ) in average quality of FeSi (Si content 75 wt%) across all periods is 1.04 wt.%, and without any consistent difference between a fully fossil and a mixed bio-C/fossil charge.

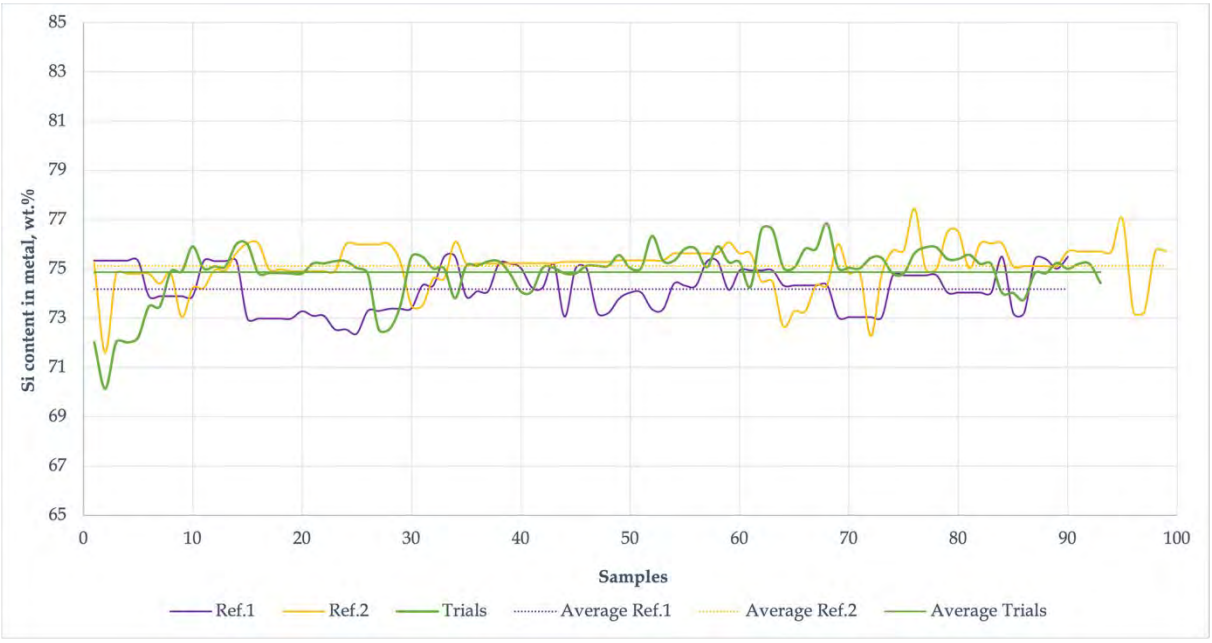

Figure 5. Variation in quality of the FeSi with average lines during investigated periods based on analysis of 89-99 samples in each period.

3.3 Metal and fume quality

The average quality of the FeSi metal for each period is presented below in Table 5.

Table 5. Average quality of the metal during investigated periods (in wt.%)

Period	Al	C	Ca	Cr	Fe	Mn	P	Si	Ti
Ref.1	1.52	0.20	0.68	0.10	22.65	0.23	0.03	74.18	0.11
Ref.2	1.12	0.08	0.54	0.09	22.25	0.21	0.03	75.11	0.12
Trials	0.72	0.07	0.25	0.09	23.02	0.24	0.03	74.88	0.11
Typical tolerance [OFZ, FeSi]	1.60						0.035	73.50	

The average quality of silica fume for each period is presented below in Table 6. There is no continuous measurement of the off-gas dust volume and quality in the furnace. Silica fume is collected in silos, densified, and then analyzed during packing. During each comparative period, from 5 to 7 samples of the fume were analyzed.

Based on the silica fume composition achieved for the different trial periods, we conclude that they all fulfill the requirements of both certified qualities of silica fume (Class 1-2 and Microxil) mentioned in Table 6 below.

Table 6. Average quality of the off-gas dust silica fume during investigated periods (in wt.%)

Period	Al_2O_3	C	Cl	Fe_2O_3	K_2O	Na_2O	MgO	SiO_2	CaO	Na_2Oeq
Ref.1	0.78	2.33	0.18	3.01	0.70	0.11	1.46	88.21	0.93	0.57
Ref.2	0.39	2.61	0.20	1.41	0.69	0.14	1.62	91.19	0.70	0.59
Trials	0.25	2.47	0.27	1.69	0.80	0.16	1.65	89.92	1.16	0.69
Typ. tolerance [OFZ, by-products] Class 1-2			0.30					85.00	1.00	6.00
Typ. tolerance[OFZ, by-products] Microxil			1.80					80.00	3.50	8.00

3.3 Si yield

The Si yield during the trial period has been analyzed by mass balance to recognize possible C-losses and for comparing average numbers from other periods. The amount of SiO_2 contained in the ash of the carbon materials was also taken into consideration in the mass balance. We can see somewhat lower average yield during the trials compared with the two reference periods in Table 7. At the same time, inside the trial period the Si-yield was increasing gradually from 84.3 in the beginning of the trial to 89.4 % at the end. The lower yield in the beginning of the trial period could be a consequence of adjustments to the furnace operation. The off-gas dust amount did not increase during the trials. The Si yield numbers do not include metal retained in the sculls. This middle-product can be used as raw material in the production of FeSiMn or alternatively, metal from the sculls could be separated from slag through different technologies (Gryshan and Kulish, 2015) for more efficient usage.

Table 7. Si-yield during investigated periods

Period	Ref.1	Ref.2	Trials
Si-yield, %	87.46	86.91	85.30

3.4 Cost-effectiveness

To estimate relevant production costs for different charge combinations, we have calculated the amount of all raw material consumed during each production period. These volumes have been connected to actual furnace productivity and prices of raw materials. Cumulative charge mixes used in each period are presented in Figure 6. The ratio of different carbon materials in the charge is presented in Figure 7.

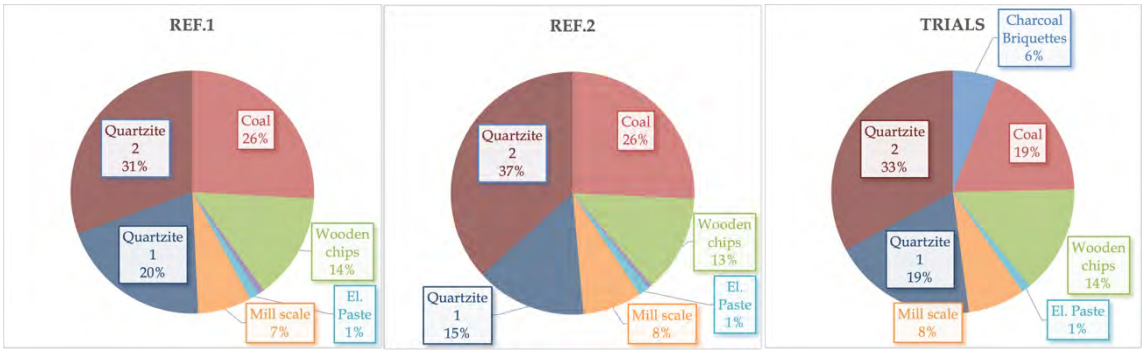

Figure 6. Cumulative charge raw material composition during investigated periods (in wt%)

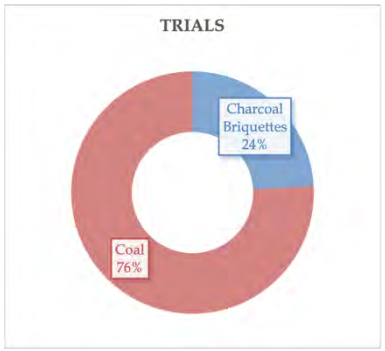

Figure 7. Average wt.% of biocarbon usage during trials

Direct emissions (scope 1) were calculated based on the consumed raw materials and their respective emission factors, following the company procedure in accordance with regulation (EU) 2018/2066. During the substitution trials, direct emissions have decreased 25.8 % compared to periods using fossil reductants as shown in Table 8.

Table 8. Calculated direct CO_2 emissions during investigated periods

Period	Ref.1	Ref.2	Trials
Direct production emissions, tCO_2e	3.02	3.03	2.24

The relative production cost per unit metal is compared in Figure 8. As shown in the figure, the total cost stayed almost the same for the part-briquette charge as for the fully fossil charge, using the price of carbon permits at a current level of 75 €/t (Trading Economics. EU Carbon permits). For instance, extrapolating the calculations to a hypothetical scenario in which 50 wt.% of the fossil reductant is replaced with biocarbon indicates that the raw material cost per tonne of alloy would increase by approximately 10%. However, the total unit production cost, including carbon permit costs, would increase by only about 2% compared with the reference case. Furthermore, the share of carbon permit costs in the total production cost would decrease to approximately 7%.

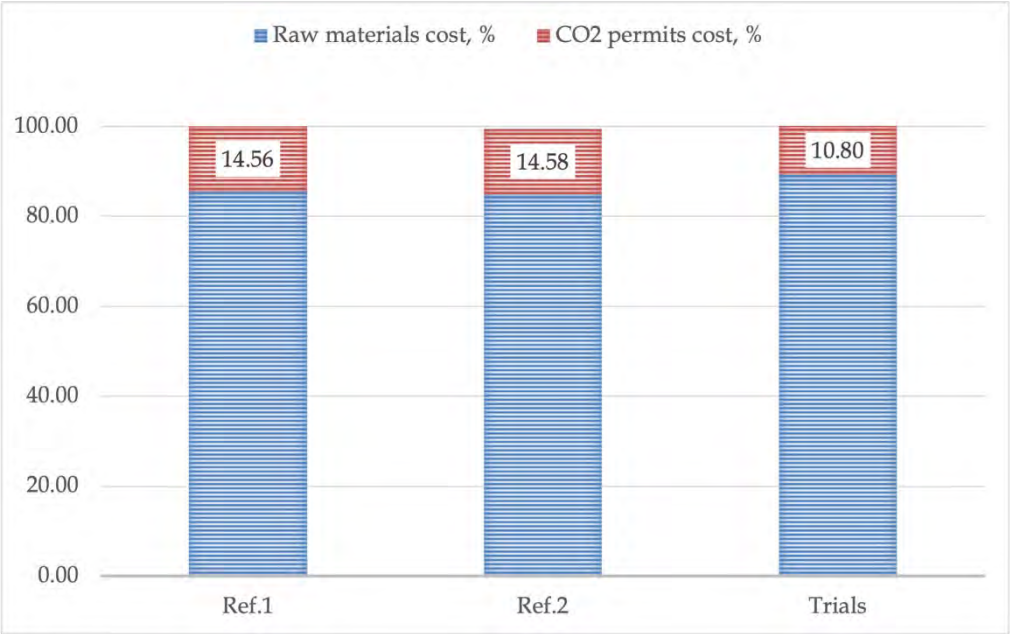

Figure 8. Relative unit production cost and CO_2 in cost structure

The main reason for these results is the significant difference in price of fixed carbon in bio- and fossil reductants, as indicated in Figure 9.

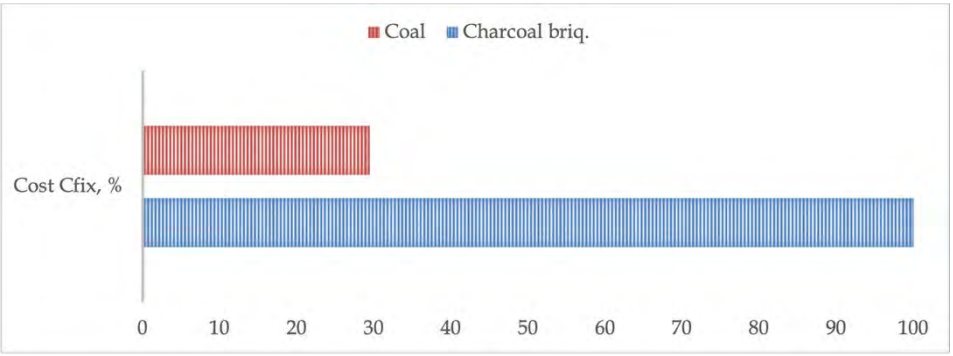

Figure 9. Normalised Cfix cost in coal and charcoal materials

The wider implementation of biocarbon materials in Europe will be driven mostly by price, availability of the required volumes, stability of the quality of reductants, as well as emission restrictions. CO_2 permit quotas will likely be reduced for most European companies using bio reductant. This is unfortunate as it does not stimulate producers to use the more expensive biocarbon reductants.

4. CONCLUSIONS

The trials described in the current work show that biocarbon briquettes, made from bio-carbon fines, meet the requirements of quality for use in the SAF at OFZ producing FeSi75.

The silicon yield during briquette trials have been recorded at a level of 84.3-89.4 % with an average of 85.3 %, which generally corresponds with the yield in production periods with fossil carbon usage. For more precise analyses of C-losses in the off-gas, real-time measurements should be carried out.

The difference in average furnace productivity (MWh/tonne alloy) across the studied reference- and trial periods is 3.1%. The total number of quality control samples can be considered statistically sufficient to assess the process deviation. The results indicate that productivity variations in the briquette period are similar to those of the fossil periods. The metal and silica fume qualities both pass the requirements of OFZ´s product specifications. Additionally, the production cost, taking into account CO_2 cost, are similar for a fully fossil charge and a partly substituted briquette charge. In addition to other parameters measured during the trials, the off-gas should be further investigated to determine the composition of volatiles and their interaction with the charge during a longer time period

Logistic adaptions may become important for the use of biocarbon at scale. Charcoal is more fragile than coal/coke, which can affect the generation of the fines and an increasing possibility of self-ignition. Ideally, biocarbon/charcoal should hence be minimally handled/transported before entering the SAF. Whether this fragility applies to the same extent to briquettes is still unknown as briquettes showed better cold strength/durability compared to charcoal lumps. Hence, these materials may better suit the standard logistic scheme built for fossil carbon materials.

5. ACKNOWLEDGMENTS

The authors gratefully acknowledge financial support from the European Union's Horizon Europe program Queen project under the grant N° 101178144

6. REFERENCES

Etemadi, A., Koohestani, H. and Tajally, M. (2023) The effect of different carbon reductants on the production of ferrosilicon 75% on an industrial scale in an electric arc furnace. Heliyon, 2023; 9
Available at: https://doi.org/10.1016/j.heliyon.2023.e13956.

European Commission (n.d.) Guidance Document No. 1
Available at: https://climate.ec.europa.eu/document/download/d5276f6c-4355-438a-a0ef-0c03a9b34a39_en?filename=1_gd1_general_guidance_en.pdf (Accessed: 26 May 2026)

Gryshan, D. and Kulish, A. (2015) Sensor-based technology for ore and slag sorting, Infacon XIV - The Fourteenth International Ferro-Alloys Congress, Kiev, 31 May–4 June.
Available at: https://www.pyro.co.za/InfaconXIV/184-Gryshan.pdf

Jayakumari, S. and Ringdalen, E. (2022) Effect of varying SiO contents on Si and FeSi production, Silicon for the Chemical and Solar Industry XVI, Trondheim, Norway, 14–16 June 2022
Available at: https://doi.org/10.2139/ssrn.4118642

Klocok, B., Kuzmenko, S., Suroviak, M., Lorinc, J. and Denys, G. (2021) Features of regulation of the electric regime of electro arc furnaces in the production of ferroalloys with high silicon content, Infacon XVI: International Ferro-Alloys Congress, Trondheim, Norway, 27–29 September
Available at: https://dx.doi.org/10.2139/ssrn.3922145

Legemza, J., Fröhlichová, M. and Findorák, R. (2019) Biomass and carbon fuels in metallurgy (1st ed) CRC Press
Available at: https://doi.org/10.1201/9780429274039

Liu, J., Chen, Z., Ma, W., Wei, K. and Ding, W. (2018) Application of a waste carbon material as the carbonaceous reductant during silicon production, Silicon, 10, pp. 2409–2417
Available at: https://doi.org/10.1007/s12633-018-9772-9

Lomunyak, G., Osodo, B., Njoka, F. and Kombe, E. (2024) Characterization, optimization and emission analysis of manually-made charcoal dust briquettes with starch, paper and algae binders, Heliyon, 10(24), e40991
Available at: https://doi.org/10.1016/j.heliyon.2024.e40991

Myrhaug, E., Tuset, J. and Tveit, H. (2004) Reaction mechanisms of charcoal and coke in the silicon process, Tenth International Ferroalloys Congress Proceedings

OFZ, a.s. (n.d.) By-products
Available at: https://siroka.ofz.company/en/by-products.html (Accessed: 26 May 2026)

OFZ, a.s. (n.d.) Ferrosilicon (FeSi)
Available at: https://siroka.ofz.company/en/ferosilicon-fesi.html (Accessed: Accessed: 26 May 2026)

Pahnila, M., Koskela, A., Uusitalo, J. et al. The Effect of Binders on the Behavior of Biocarbon Briquettes Under the Stresses of a Submerged Arc Furnace. J. Sustain. Metall. 12, 839–852 (2026)
Available at: https://doi.org/10.1007/s40831-025-01367-x

QUEEN Project (n.d.) Quartz Enrichment Enabling Near-Zero Silicon
Available at: https://queenproject.eu (Accessed: 26 May 2026)

Ringdalen, E., Einarsrud, K.E. & Nordhus, A. Gas Flow and Pressure Drop in Charge Material in Silicon Production. JOM 74, 3971–3979 (2022)
Available at: https://doi.org/10.1007/s11837-022-05431-9

Schei, A., Tuset, J.K. and Tveit, H. (1998) Production of high silicon alloys. Trondheim: Tapir Academic Press.

Smith-Hanssen, N., Jahrsengene, G. and Ringdalen, E. (2023) Biocarbon materials in metallurgical processes—investigation of critical properties, in Fleuriault, C. et al. (eds.) Advances in Pyrometallurgy. Cham: Springer.
Available at: https://doi.org/10.1007/978-3-031-22634-2_16

Sommerfeld M, Friedrich B. Replacing Fossil Carbon in the Production of Ferroalloys with a Focus on Bio-Based Carbon: A Review. Minerals. 2021; 11(11):1286.
https://doi.org/10.3390/min11111286

Trading Economics (n.d.) EU carbon permits
Available at: https://tradingeconomics.com/commodity/carbon (Accessed: 26 May 2026)

Tranell, G., Andersson, M., Ringdalen, E., Ostrovski, O. and Steinmo, J.J. (2010) Reaction zones in FeSi75 furnace: Results from an industrial excavation, Infacon XII: International Ferro-Alloys Congress, Helsinki, 6–9 June, pp. 709–716.
Available at: https://www.pyro.co.za/InfaconXII/709-Tranell.pdf

Yankovych, V. and Korol, N. (2025) Mechanochemical and molecular analysis of organic binders in charcoal briquetting for enhanced cold mechanical strength, Cleaner Engineering and Technology, 29, 101113
Available at: https://doi.org/10.1016/j.clet.2025.101113

Denys Gryshan
Innovation Project Manager, OFZ, Slovakia
PhD Candidate, NTNU, Norway

Hold an M.Sc. from KTU, Kryvyi Rih. With 15+ years of experience in the ferroalloys industry. Expertise includes realization of investment projects, ore beneficiation, sensor-based sorting technologies, by-products valorization and REACH. Actively involved in innovation projects for manganese and silicon alloys under Horizon Europe Programme.

Acker, J., T. Sieber, and V. Hoffmann. 2026. Copper Impurities in Silicon Kerf. In *Silicon for the chemical and solar industry XVIII*, edited by M. Tangstad, H. Rong, A. Valderhaug, B. Andresen, H. Dalaker, and I. G. Page. Kristiansand, Norway, September 7–10, 2026.
https://doi.org/10.55669/oa900815

Copper Impurities in Silicon Kerf

J. Acker, T. Sieber, and V. Hoffmann
Brandenburg Technical University Cottbus-Senftenberg,
Department of Physical Chemistry, D-01968 Senftenberg, Germany,
joerg.acker@b-tu.de

Keywords: kerf, copper, GD-OES, acidic treatment

Abstract Silicon wafers are manufactured using wire sawing processes, during which a significant portion—approximately 35–40%—of the high-purity silicon is lost in the form of very fine particles known as "Kerf." An economically meaningful use of kerf is only possible if the metallic impurities introduced during sawing can be efficiently removed. Copper poses a particular challenge in this context, as it creates deep defects in silicon, preventing it from being reused as a semiconductor material without additional processing steps. This study examines the mechanism by which copper is introduced into the kerf and outlines the challenges involved when attempting to reduce the concentration of copper in the kerf through wet chemical etching processes.

1. INTRODUCTION

Sawing silicon wafers results in significant material loss, which is referred to as "kerf loss" or simply "kerf." The kerf is a material of economic importance, particularly in the photovoltaic and semiconductor industries, since wire sawing typically results in the loss of about 35–40% of the original silicon ingot made of high-purity silicon as sawing slurry (Würzner *et al.*, 2014).

A method of wafer sawing is the slurry process, in which a steel wire is used together with a suspension of abrasive silicon carbide particles (loose abrasive slurry sawing). Material removal from the silicon is achieved through fracture formation processes, whereby the steel wire presses sharp-edged silicon carbide particles onto the silicon block (Möller, 2004). The kerf consists of fine silicon particles with particle sizes mostly under 10 µm and contains the more or less ground-down and fractured SiC particles, furthermore steel particles resulting from direct abrasion of the steel wire as well as adhering residues of coolants and lubricants.

Modern solar wafer production lines predominantly use diamond wire saws in which diamond grains are permanently bonded to a wire (fixed abrasive diamond wire sawing). This technology enables higher cutting speeds and lower material loss (Kumar and Melkote, 2018; *Li et al.*, 2023). In this technology, it is the diamond particles adhering directly to the wire that transfer the mechanical forces exerted by the wire to the silicon, thereby triggering the fracture processes in the silicon block. Consequently, the kerf contains nickel and iron contaminants from the abraded steel particles. The diamond particles can be fixed to the steel wire using organic resins or brass or nickel alloys, and latter leads to the introduction of copper, zinc and nickel into the kerf. Consequently, the type and concentration of metallic contaminants in the kerf depend heavily on the saw wire used and can range from a few ppm to several thousand ppm of total metallic impurity (Lottspeich *et al.*, 2018; Kong *et al.*, 2019; Xiong *et al.*, 2024).

A variety of process variants have been developed for silicon recovery; details of these can be found in the relevant literature (Li *et al.*, 2021; Xiong *et al.*, 2024). The core element of every

This work is licensed under the Creative Commons Attribution 4.0 International License. To view a copy of this license, visit https://creativecommons.org/licenses/by/4.0/

processing method is the removal of metallic contaminants using inorganic acids, such as sulfuric acid (H_2SO_4), hydrochloric acid (HCl), nitric acid (HNO_3), and hydrofluoric acid (HF), which may be followed by various further processing steps.

2. RESULTS

2.1 Experimental

Table 1 shows the composition of the used kerf and silicon purity calculated from the impurity elements listed in the table. Other impurities include: Cr < 0.4 ppm, Mn < 0.5 ppm, Co < 0.6 ppm, as well as B at 1.65 ppm and P at 16.16 ppm, which are insignificant in the chemical treatment (Cr, Mn, Co) or undergo no significant change (B, P). Iron, nickel, copper, and zinc are the most significant impurities and represent the abrasion on both the steel wire and the brass alloy. Impurities from aluminum, calcium, and magnesium are primarily introduced by the process media during sawing and in the post-treatment of the kerf in the collection tanks.

For chemical treatment, several grams of kerf were suspended in the respective acid or acid mixture at room temperature and stirred continuously for 60 minutes at a stirring speed of approximately 500 rpm. In all experiments, a mass-based solid-to-liquid ratio of 20% was selected, with a typical solution volume of approximately 50 mL. The treated kerf was separated by vacuum filtration, washed several times with deionized water, and gently dried. The initial samples as well as the purified samples were dissolved in a mixture of HF-HNO_3 and subsequently analyzed by ICP-OES (Rietig and Acker, 2017).

All impurity concentrations are expressed in mass ppm, based on the initial weight of the sample. The acid concentrations in mass percent (% (m/m)) are based on the proportions of concentrated acid prepared from the respective concentrated acids (HNO_3 65% (v/v), HF 40% (v/v), and HCl 30% (v/v), all acids are Suprapur).

Table I: Composition of the kerf as starting material and at the maximum purity achieved after a three-step treatment process in the sequence 30% HNO_3 – 4% HF – 30% HCl.

	Element impurity content [ppm]									silicon content [%]
	Al	Fe	Ca	Mg	Cu	Ni	Zn	Ti	sum	
kerf as-received	4813.5	94.6	158.9	39.2	11.3	415.1	13.71	1.3	5547.5	99.445
kerf leached	9.5	13.1	1.2	5.4	5.0	6.0	0.8	0.3	41.3	99.996

ICP-OES measurements were performed using an iCap 6500 DUO (Thermo Scientifc, Germany) with a dual-view option and equipped with an HF-resistant sample introduction system with a parallel path nebuliser made of PEEK (MiraMist, Burgener Inc.), a cyclonic chamber made of PTFE (Glass Expansion) and a ceramic injector tube (Glass Expansion).

A commercial GD-OES instrument GDS 750 (Spectruma, Hof, Germany) with PMT detection was used in HF mode. This instrument is also equipped with a monochromator (DigiKröm 480, Spectral Products, Albuquerque, USA) with a range of 200–750 nm.

2.2 Selection of an Etching Regime

Three different acids were selected for treating the kerf. Due to its high oxidation potential, nitric acid is capable of dissolving most metallic impurities, including copper; however, it causes surface passivation, particularly on steel alloys. Hydrochloric acid, as a non-oxidizing acid, also dissolves many metallic impurities and does not cause passivation. It can be assumed that the kerf particles are surrounded by a thin oxide layer, which under sawing conditions (aqueous medium, metallic impurities, oxygen) can reach a higher thickness than the known native oxide layer of silicon. Metallic impurities are usually protected from attack by HCl and HNO_3 as long as they are located within or below the oxide layer and as long as the oxide layer does not exhibit particularly high porosity. To remove this oxide layer, treatment with hydrofluoric acid (HF) solutions is required. In addition, hydrofluoric acid-hydrochloric acid mixtures (HF/HCl) were tested to combine the removal of the oxide layer from the kerf particles with the high solubility for metals. Hydrofluoric acid-nitric acid mixtures were not used, as these lead to the complete dissolution of the silicon particles.

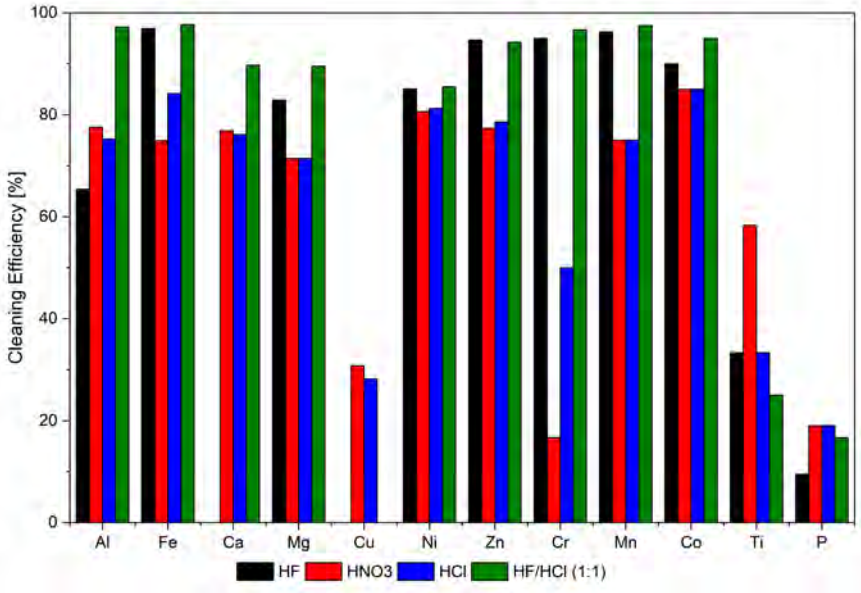

Figure 1: Kerf cleaning efficiency using four different etching regimens.

As Figure 1 shows, the HF-HCl mixture results in the highest removal of metallic impurities when considering all elements, which is significantly higher than what could be achieved with HNO_3 or HCl alone. This suggests that a certain amount of the impurities is protected within or beneath the oxide layer and is largely shielded from surface acid attack. Further investigations show that this dissolution behavior can be further optimized by varying the HF-to-HCl mixing ratios and by adjusting the total concentration of the acids. However, these positive findings do not apply to copper. Only HNO_3 and HCl (when the solution is stirred, allowing atmospheric oxygen to enter) are capable of reducing the copper content at all. It should be noted, that in all studies in which HF/HCl mixtures were used, the final copper content corresponded to the initial value or even slightly exceeded it. This effect of re-deposition will be discussed later.

2.3 On the interaction between copper and silicon

The behavior of copper raises questions about its presence in the kerf and its fate in the acid solution. Because some of the copper can be dissolved by HNO_3, it can be assumed that only individual copper particles or copper adhering to the surface of the silicon particles is accessible to the acid. It cannot be determined whether this copper consists exclusively of

metallic copper or also includes partially oxidized copper particles. Even in an HCl-acid solution, metallic copper can dissolve in small quantities if sufficient atmospheric oxygen is introduced into the solution, for example during stirring. Furthermore, if hydrofluoric acid enables the dissolution and complexation of silicon, this opens the reaction pathway for the electrochemical deposition of copper on the silicon as $[SiF_6^{2-}]$-ions, a process widely known as metal-assisted etching (Schönekerl and Acker 2020). Deposition can only be prevented in presence of a strong oxidizing agent (e.g., hydrogen peroxide, potassium peroxodisulfate), however, the use of which was not planned within the scope of this work.

Of greater importance is the fraction of copper that cannot be removed by the acid treatment. In this respect, a hypothesis was developed that the high mechanical forces generated during diamond wire sawing—specifically at the points of contact between the brass-coated sections of the wire and the silicon surface, or with already abraded silicon particles, lead to the penetration of copper into the silicon.

To verify these hypotheses, the surfaces of polished single-crystal wafer pieces were treated once using a diamond grinder, in which the diamond particles were bound to the steel wheel with an organic resin adhesive, and once with a brass grinding attachment. These mechanical treatments were performed once dry and once with an aqueous, diluted $CuSO_4$ solution. In parallel, wafer pieces were immersed in an aqueous, HF-free, diluted $CuSO_4$ solution to simulate copper penetration without mechanical stress. After completion, all wafer pieces were treated with an aqueous ammonium peroxodisulfate solution, to dissolving metallic copper particles and copper silicide phases; copper diffused into the silicon is not dissolved.

Using GD-OES (glow discharge optical emission spectroscopy), the depth profile of copper penetration into the silicon can be determined. In GD-OES the measured intensity of an element emission line is proportional to the partial pressure of the element in the plasma, and under stable plasma conditions this is proportional to the element concentration in the solid. However, the calibration of the copper emission intensity was omitted, so that quantification of the copper content is not possible. Calibration of the erosion depth was also omitted, and the depth of erosion is instead specified as time of sputtering. For a qualitative assessment, it is entirely sufficient to examine the profile of copper emission intensity in relation to the profile of silicon emission intensity as the main component. GD-OES spectra are characterized by a "start-up effect" of the plasma lasting several milliseconds, during which the intensities of the sputtered elements initially build up over time. Surfaces of solids are always contaminated by thin oxide layers, organic deposits, and adsorbed water and CO_2, these are abruptly released upon plasma ignition. Since the emission intensities of any elements are proportional to their corresponding partial pressure in the sputtering chamber including the elements released from the desorbed surface impurities, a quantification of the analyte elements is not possible during this "start-up" period.

The analyses show that a simple immersion of silicon wafers in a HF free, diluted copper salt solution does not lead to a diffusion of copper into silicon; no copper signal is detectable by GD-OES. If the surface is treated with a resin-bonded diamond disc in the presence of a copper salt solution, only a larger fluctuation in the very low copper signal is observed, which also does not account for a significant diffusion of copper into the silicon.

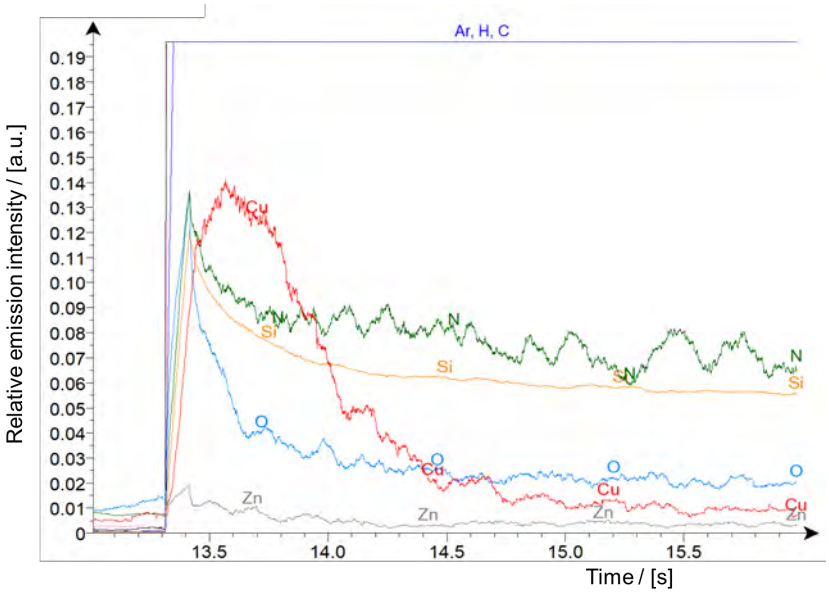

Figure 2: GD-OES depth profile analysis for a Si wafer that was dry-polished using a brass polishing wheel.

Figure 2 shows the depth profile of copper in silicon (along with Zn, O, N, and Si) following dry polishing with a brass polishing wheel. The profile of copper emission intensity shows a high emission intensity that decrease only slowly with increasing depth, i.e., over long erosion times of approximately 1.5 seconds. Zinc is also present in the near-surface region, and elevated levels of oxygen are detectable, indicating oxidation in the nearby surface area. This clearly demonstrates that copper has penetrated into the silicon under mechanical stress.

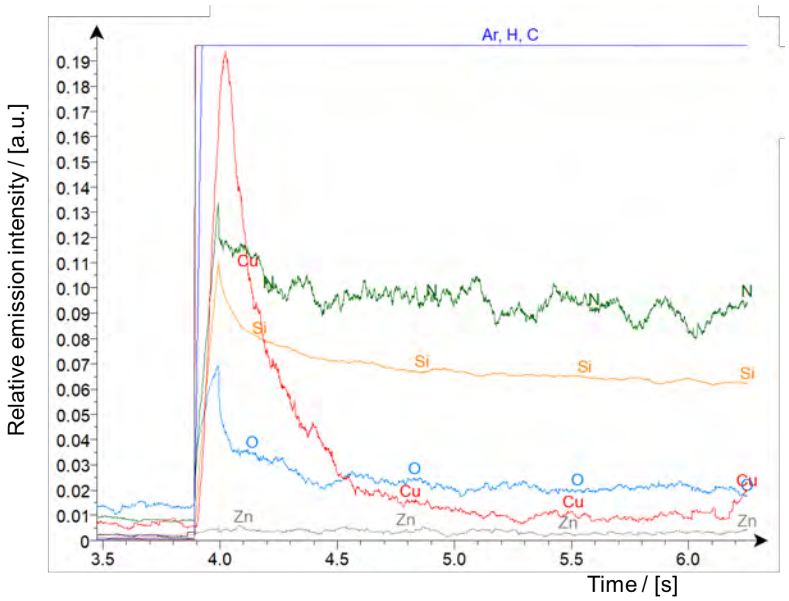

Figure 3: GD-OES depth profile analysis for a Si wafer treated with a brass polishing wheel in a $CuSO_4$ solution.

Figure 3 shows the depth profile after treatment the silicon surface with the brass polishing wheel immersed in a copper solution. Although the profile of the copper emission intensity also shows a very strong surface enrichment of copper, the drop over the erosion time occurs much more rapidly than in Figure 2 indicating a lower penetration depth. No significant enrichment of zinc is observed, and the presence of oxygen appears to be concentrated very close to the surface. The differences between Figure 2 and Figure 3 indicate that, in the presence of the aqueous solution, the copper penetrates less deeply into the silicon and less oxidation

in the topmost surface region only. This suggests that the aqueous solution leads to better heat distribution during the mechanical treatment, which attenuates the local temperature rise. Thus, in addition to mechanical pressure, the influence of temperature is particularly decisive for the penetration and diffusion of the copper.

In conclusion, the presence of metallic copper and significant mechanical stress load is necessary for the diffusion of copper into silicon. In order to determine the penetration depth of the copper within the silicon particles, the kerf was partially etched stepwise using a very slow-etching HF-HNO_3 mixture. A after washing and drying, the material was cleaned again with concentrated HNO_3 to remove metallic copper deposited from the surface. After washing and drying again, the material was completely dissolved in an HF/HNO_3 mixture and analyzed by ICP-OES (Rietig and Acker, 2017). The quantitatively determined silicon content was used to calculate the amount of silicon removed. A total of 6 etching steps were performed, and 7%, 15%, 20%, 23%, 34%, and 49% of the silicon was dissolved.

The black dotted curve in Figure 4a shows the particle size distribution of the as-received kerf. Based on that curve, the volume loss of total silicon by stepwise etching was converted, in average, into a uniform thickness removal for silicon particles of all sizes resulting in particles of lesser diameter. The calculated solid curves in Figure 4a represent the loss of volume in each particle size fraction and in each etching step; which is more instructive than a plot of the obtained particle size distribution after each etching step. Figure 4a shows that particles smaller than 2 µm faces the highest volume loss, while particles larger than 5 µm show virtually no loss in volume.

Figure 4b shows the copper concentrations in the etched kerf samples with increasing averaged removal. The trend follows a typical concentration profile of solid-state diffusion according to the square root law (Ward *et al.*, 1982; Hong *et al.*, 1991). Clearly, the top 50 nm layer of the silicon particles contains the most copper. This value is halved within a further 50–100 nm of removal. A minimum of 1 ppm can be achieved removing of 350 nm silicon. However, such a procedure cannot be recommended, because the silicon loss amounts to nearly 50%.

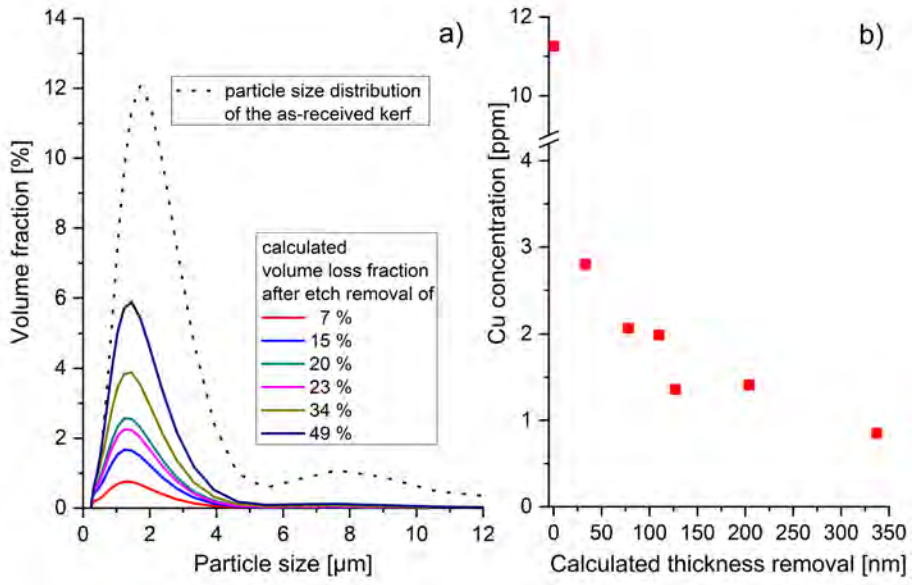

Figure 4: a) Particle size distribution calculated from the measured particle size distribution (black curve) as etching removal increases. b) Copper content in the kerf after layer-by-layer dissolution of the silicon.

2.4 Development of a multi-stage acid treatment process

Preliminary studies show that the efficient removal of metallic impurities requires a multi-step treatment. This has led to a sequence of acid treatments that has proven to be particularly effective. The first step involves treatment with nitric acid to remove surface metal impurities, particularly copper, without causing redeposition. The second step involves treatment with a low-concentration hydrofluoric acid solution to primarily remove oxide layers on the silicon particles. The third step involves treatment with hydrochloric acid to remove residual metals located within or beneath the oxide layer on the silicon particles that have not yet been completely dissolved by nitric and hydrofluoric acid. Three concentrations were selected for each acid: 5, 15, and 30% (w/w) for nitric acid; 1, 2, and 4% (w/w) for hydrofluoric acid; and 5, 15, and 30% (w/w) for hydrochloric acid. The concentration of hydrofluoric acid was set very low to minimize silicon loss as much as possible.

Figures 5 and 6 provide examples comparing the final removal efficiency of three consecutive treatment steps, which differ in the concentration of HNO_3 in the first treatment step at 15% (Figure 5) and 30% (Figure 6). It should be noted that the impurity elements are present in very different initial concentrations (Table I).

All results show (even with an initial treatment step using 5% HNO_3) that the elements Al, Ca, Ni, and Zn are removed almost completely. The removal of Mg always requires the highest acid concentrations to achieve a removal of more than 85%. The reason for the difference between Ca and Mg—namely, that Mg is not nearly completely removed under the same conditions—is unknown. In contrast, a clear trend can be observed for iron. Removal reaches its respective maximum value when the highest HCl concentration is used in the final step. The residual iron levels range from 81 ppm (5% HNO_3, 1% HF, 5% HCl) to 6 ppm (5% HNO_3, 4% HF, 30% HCl), making it the second most significant impurity in the leached kerf.

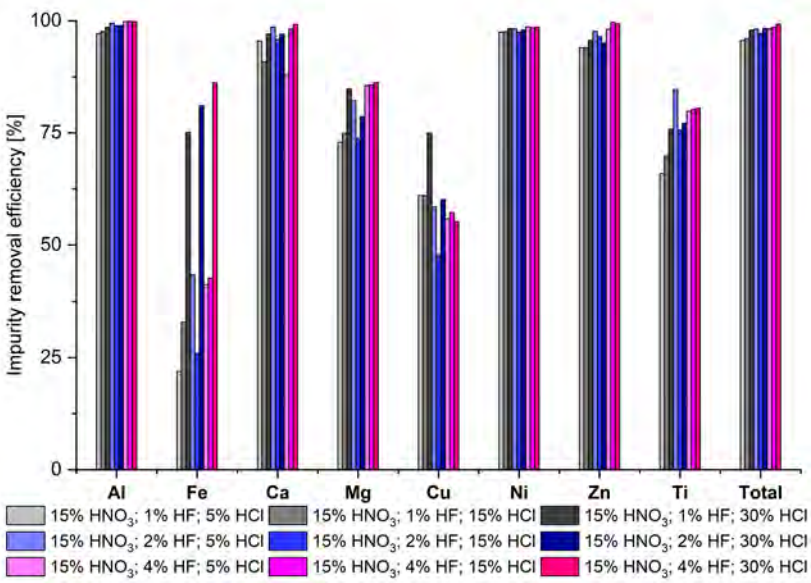

Figure 5: Cleaning efficiency following treatment with 15% HNO_3 in the first step, followed by 1% to 4% HF in the second step and 5% to 30% HCl in the third step.

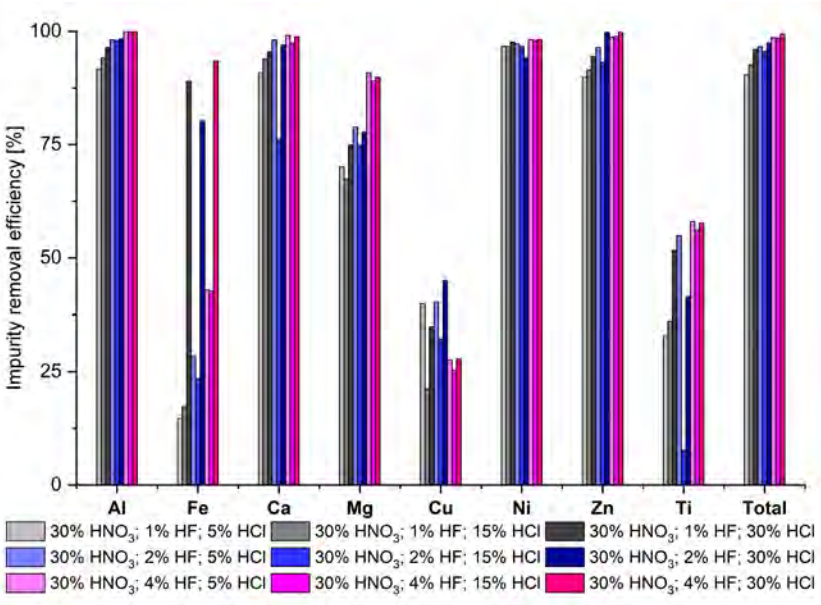

Figure 6: Cleaning efficiency following treatment with 30% HNO_3 in the first step, followed by 1% to 4% HF in the second step and 5% to 30% HCl in the third step.

Titanium is present in the kerf only at a very low initial concentration of 1.3 ppm. The higher the acid concentrations, the more titanium dissolves, which results in the lowest residual levels—between 0.2 ppm and 0.4 ppm—in the series using 30% HNO_3 in the first treatment step. Thus, titanium contributes only minimally to the remaining impurities in the treated kerf.

Copper, on the other hand, exhibits more complex behavior. The treatment series using 5% HNO_3 in the first treatment step achieve a reduction of between 20% and 45%. Removal efficiency increases with acid concentration and, with 30% HNO_3 in the first treatment step, reaches values between 47% and 75%, resulting in final copper levels between 4.4 ppm and 5.9 ppm. Copper and nickel thus rank third in terms of their contribution to contamination.

To further illustrate the purification effect of the acid combinations, Figure 7 shows the absolute concentrations of several selected elements—nickel, iron, and copper—for each individual step of treatment, including the results from the series using 5% HNO_3 in the first treatment step.

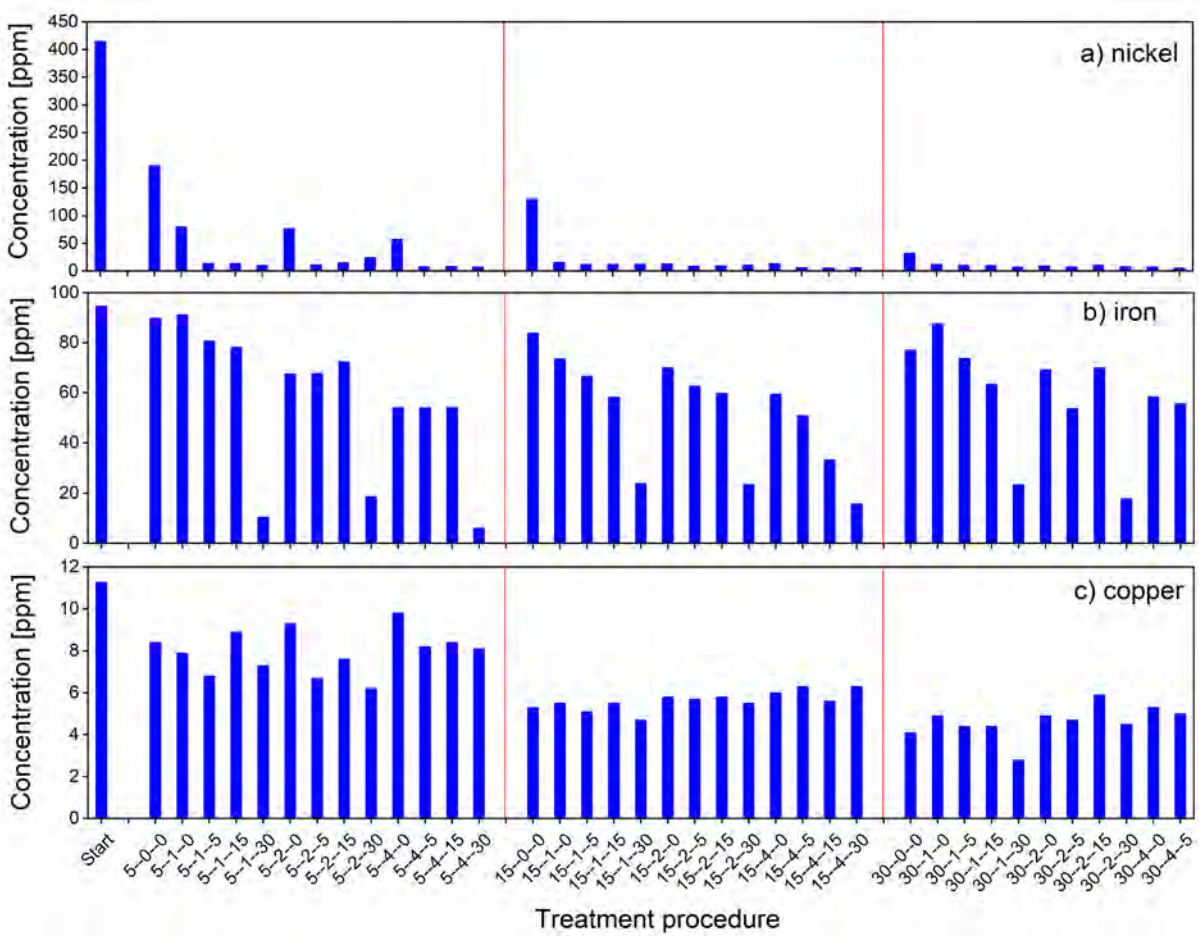

Figure 7. Element contents for a) nickel, b) iron, and c) copper according to the respective treatment steps. The first number indicates the concentration of HNO_3 (in %(m/m)) in the first treatment step, the second number indicates the concentration of HF (in %(m/m)) in the second treatment step, and the third number indicates the concentration of HCl (in %(m/m)) in the third treatment step.

Nickel (Figure 7a) exhibits the ideal typical trend of decreasing concentrations with each treatment step. HNO_3 in the first step of treatment and with increasing concentration removes always the majority of the present nickel contaminations. Only for 5% HNO_3 the subsequent acid treatments still play a role in nickel removal; however, their effect diminishes starting at 15% HNO_3. In fact, HNO_3 is thus the most important acid component for the removal of nickel.

In the case of iron (Figure 7b), the highest purifying effect comes from HCl, whereas high-concentration hydrochloric acid has the highest removal effect. Treatment with HNO_3 in the first step does not lead to a significant reduction in the iron concentration. However, as higher the HNO_3 as lower is the removal efficiency. It is interesting to note, that the removal by hydrochloric acid is less effective with higher the concentration of HNO_3 in the first treatment step. It can be assumed that HNO_3 leads to passivation of the iron, which is less pronounced at low HNO_3 concentrations. Hydrofluoric acid treatment does not appear to have any significant effect.

The most interesting behavior shows copper (Figure 7c). The concentration of HNO_3 in the first treatment step plays the most significant role in copper removal; the higher the concentration, the lower the residual copper content. HNO_3 treatment dissolves the copper impurities that are accessible to the acid. The subsequent treatment steps show only a marginal effect, because the remaining copper has diffused into the silicon. Copper shows an interesting effect that is also seen for the chemical cleaning of other materials for elements in low

concentrations. When kerf is treated with HF, the copper concentration remains virtually unchanged or even increases slightly, whereby the increase corresponds to an increase of the HF concentration. HF treatment leads to the removal of the oxide layer from the silicon particles that therefore lowers the mass of the remaining silicon; i.e. the total mass of the sample after HNO_3 treatment is higher than after HF treatment due to oxide removal. After complete digestion with HF/HNO_3 the quantified amount of copper is divided by a lower value for the mass of silicon resulting in a slightly higher Cu concentration after HF treatment compared to that after HNO_3 treatment. However, it cannot be ruled out that a fraction of copper may be trapped within the oxide layer and partially dissolved by HF—may have been redeposited.

Overall, it can be stated that, the treatment steps examined achieved a silicon purity of 99.947% for the sequence 5% HNO_3 - 1% HF - 5% HCl and in the best-case scenario, 99.996% for the sequence 30% HNO_3 - 4% HF - 30% HCl (Table I).

3. CONCLUSIONS

The use of diamond wire saws with brass-bonded diamond particles leads to the introduction of copper into the resulting silicon kerf during silicon sawing. The challenge with copper-containing kerf is finding a suitable use for it. Since copper in silicon leads to deep electronic defects, direct further processing—such as melting crystalline silicon for photovoltaic applications—is not recommended without prior pretreatment to remove the copper. Possible approaches could involve using it as a copper-containing feedstock for the production of methylchlorosilanes. What is interesting, however, is a potential application for producing anode material for lithium-ion batteries. Highly interconnected hollow Si–Cu alloy nanotubes can serve as high-capacity and self-conductive anode structures with robust mechanical support in lithium ion batteries (Song *et al.*, 2016).

To determine the cause of the copper content in the silicon, the process of mechanical force exerted by copper-containing material on a silicon surface was simulated under various conditions, and the penetration behavior of the copper into the silicon was determined using GD-OES depth profile analysis. The basic prerequisite for copper contamination is mechanical contact between the copper-containing material and the silicon; dissolved copper ions play no role. The layer-by-layer etching of the silicon particles indicates that the copper diffuses into the silicon, with its concentration decreasing with depth according to the square root law. It appears, that the driving force for copper diffusion is a local temperature increase at the silicon/copper interface initiated by the mechanical load and the resulting fracture formation. The presence of a cooling medium is able to dampen this effect, however, not able to prevent it. Copper diffusion into silicon is known to start at temperatures as low as 200 °C (Ward *et al.*, 1982; Hong *et al.*, 1991), however, the local temperatures are apparently not high enough to form copper silicide phases. Therefore, the copper that has penetrated is likely present as a solid solution of copper in silicon and is consequently not attacked by acids. As a result, a further reduction in the copper concentration can only be achieved by dissolving a significant portion of the silicon—approximately 50%.

The wet chemical treatment regimens examined demonstrate the contradictory behavior of the metallic impurities in the kerf when exposed to various acids, so that a combined approach using different acids is necessary if high purity is to be achieved through wet chemical treatment steps alone. If only acid treatment at room temperature is considered, a regime based on an HNO_3-HF-HCl treatment using moderate acid concentrations for both HNO_3 and HCl proves to be the most efficient of all tested variants. In the present investigations, it was

thus possible to achieve a purity of 99.996% Si with a final copper concentration of 5.0 ppm starting from a kerf with a silicon content of 99.443% Si.

4. REFERENCES

Hong S.Q., Comrie C.M., Russell S.W., and Mayer J.W. 1991. Phase formation in Cu-Si and Cu-Ge. *Journal of Applied Physics*, Vol.70, pp.3655-3360. https://doi.org/10.1063/1.349213

Kong J., Xing P., Liu Y., Wang J., Feng Z., and Luo X. 2019. An Economical Approach for the Recycling of High-Purity Silicon from Diamond-Wire Saw Kerf Slurry Waste. *Silicon*, Vol.11, pp.367–376. https://doi.org/10.1007/s12633-018-9889-x

Kumar A., and Melkote S.N. 2018. Diamond wire sawing of solar silicon wafers: A sustainable manufacturing alternative to loose abrasive slurry sawing. *Procedia Manufacturing*, Vol.21, pp. 549-566. https://doi.org/10.1016/j.promfg.2018.02.156

Li X., Lv G., Ma W., Li T., Zhang R., Zhang J., Li S., and Lei Y. 2022. Review of resource and recycling of silicon powder from diamond-wire sawing silicon waste. *Journal of Hazardous Materials*, Vol.424, p.127389. https://doi.org/10.1016/j.jhazmat.2021.127389

Li A., Hu S., Zhou Y., Wang H., Zhang Z., and Ming W. 2023. Recent advances in precisions diamond wire sawing monocrystalline silicon. *Micromachines*, Vol.14, Issue 8, p.1512. https://doi.org/10.3390/mi14081512

Lottspeich L., Müller P., and Kaden T. 2018. Metal contamination of silicon wafers in diamond wire sawing processes depending on the sawing parameters. *AIP Conference Proceedings*, Vol.1999, 140003. https://doi.org/10.1063/1.5049342

Möller H. J. 2004. Basic mechanisms and models of multi-wire sawing. *Advanced Engineering Materials*, Vol.6, pp.501–513. https://doi.org/10.1002/pssa.200564508

Rietig A., and Acker J. 2017. Development and validation of a new method for the precise and accurate determination of trace elements in silicon by ICP-OES in high silicon matrices. *Journal of Analytical Atomic Spectrometry*, Vol. 32, pp.322–333. http://dx.doi.org/10.1039/C6JA00241B

Schönekerl S., and Acker J. 2020. The kinetics and stoichiometry of metal cation reduction on multi-crystalline silicon in a dilute hydrofluoric acid matrix. *Nanomaterials*, Vol.10, Issue 12, p.2545. https://doi.org/10.3390/nano10122545

Song H., Wang H.X., Lin Z., Jiang X., Yu L., Xu J., Yu Z., Zhang X., Liu Y., He P., Pan L., Shi Y., Zhou H., and Chen K. 2016. Highly Connected Silicon–Copper Alloy Mixture Nanotubes as High-Rate and Durable Anode Materials for Lithium-Ion Batteries. *Advanced Functional Materials*, Vol.26, pp. 524–531. https://doi.org/10.1002/adfm.201504014

Ward W.J., and Carroll K.M. 1982. Diffusion of Copper in the Copper-Silicon System. *Journal of the Electrochemical Society*, Vol.129, pp.227-229. https://doi.org/10.1149/1.2123764

Würzner S., Herms M., Kaden Th., Möller H.-J., and Wagner M. 2017. Characterization of the diamond wire sawing process for monocrystalline silicon by Raman spectroscopy and SIREX polarimetry. *Energies*, Vol. 10, 414. https://doi.org/10.3390/en10040414

Xiong, B., Han, S., Yang, S., Xie, K., Wei, K., and Ma, W. 2024. Review of silicon recovery from diamond wire saw silicon powder waste based on hydrometallurgical process. *Molecules*, Vol.29, p.5645. https://doi.org/10.3390/molecules29235645

Jörg Acker

Professor, Chair and Head of Department of Physical Chemistry, Brandenburg University of Technology Cottbus-Senftenberg, Germany

He earned his Ph.D. (1999) and completed his habilitation (2004) at the Technical University of Freiberg, focusing on metal-catalyzed reactions of chloro- and methylchlorosilanes. After holding positions at Princeton University and the Leibniz Institute for Solid State and Materials Research in Dresden, he became a full professor of physical chemistry at the Brandenburg University of Technology. He continues to work in various areas of silicon chemistry, although for the past 14 years his main research topics have been lithium-ion battery recycling, spectroscopy, microscopy, and chemical analytics.

Abo-Hamad, A., M. Phadatare, and J. Örtegren. 2026. Urea-Assisted Porosification of Silicon Microparticles. In *Silicon for the chemical and solar industry XVIII,* edited by M. Tangstad, H. Rong, A. Valderhaug, B. Andresen, H. Dalaker, and I. G. Page. Kristiansand, Norway, September 7–10, 2026. https://doi.org/10.55669/oa900816

Urea-Assisted Porosification of Silicon Microparticles

Ali Abo-Hamad[1], Manisha Phadatare[1], and Jonas Örtegren[1]
[1]Department of Engineering, Mathematics and Science Education (IMD), Mid Sweden University, Sundsvall, SE-851 70, Sweden, jonas.ortegren@miun.se

Keywords: Porous silicon, Urea etching, Mesoporosity, Surface chemistry

Abstract – Fluorine-free routes for producing porous silicon are attractive for safer and more scalable silicon processing. In this work, urea-assisted thermochemical porosification of polycrystalline silicon microparticles was investigated at 400 °C, with emphasis on urea loading and the thermal sequence leading to pore formation. Silicon microparticles were blended with urea at urea-to-silicon (Urea:Si) mass ratios of 0.5:1, 1:1, 2:1, and 4:1, followed by a staged thermal protocol involving urea melting at 135 °C and subsequent treatment at 400 °C. Urea loading was evaluated using nitrogen sorption, BJH pore-size analysis, SEM, and EDS. The 2:1 Urea:Si blend produced a sharp increase in porosity, reaching a BET surface area of 25.7 $m^2 g^{-1}$ and a pore volume of 0.039 $cm^3 g^{-1}$, while further increasing the ratio to 4:1 gave only minor additional improvement. The 2:1 blend was selected and further examined using mercury porosimetry and TG/DSC. TG/DSC showed that pristine silicon remains mass-stable, whereas the Urea:Si mixture undergoes substantial mass loss during the 135 °C hold and displays lower-temperature DSC events than pure urea. These results suggest coupled gas-solid surface modification and stress-assisted pore formation during heating to 400 °C.

1. INTRODUCTION

Porous silicon has evolved into a versatile silicon-based platform because its high internal surface area, tuneable pore architecture, versatile surface chemistry, photonic response, and structural void space can be tailored for different functions. These characteristics enable refractive-index and photoluminescence-based transduction in optical biosensing (Moretta et al., 2021), improved stability and functionality in polymer-modified porous silicon sensors (Nocerino et al., 2024), enhanced biomolecule loading and sensitivity in point-of-care, wearable, and implantable biosensors (Sánchez-Salcedo et al., 2025), and support drug delivery, tissue engineering, and implant-related applications in biomedical systems (Kang et al., 2025) In energy-related applications, the combination of accessible active sites, short diffusion distances, and internal void space is advantageous for electrocatalysis and supercapacitors (M. Wang et al., 2025), while in Li-ion batteries porous silicon architectures can partially accommodate silicon volume expansion and improve electrochemical accessibility compared with bulk silicon (Cheng et al., 2023). More broadly, porous silicon is regarded as a structure-sensitive material platform whose performance depends on coupled control of pore geometry, crystallinity, connectivity, and surface termination (Y. Wang & Wang, 2026).

Despite this broad potential, the preparation of porous silicon remains strongly linked to wet-chemical dissolution routes that can complicate scalability, safety, and feedstock flexibility. Electrochemical anodization is still regarded as a cornerstone method because it enables precise control over pore morphology through current density, electrolyte composition, and etching time; however, it commonly relies on hydrofluoric acid (HF)-based electrolytes and is

This work is licensed under the Creative Commons Attribution 4.0 International License. To view a copy of this license, visit https://creativecommons.org/licenses/by/4.0/

most naturally suited to wafer-based processing (Y. Wang & Wang, 2026). Similarly, many biosensing-oriented porous silicon structures are fabricated by electrochemical etching in HF-based media, where pore size and film thickness must be optimized for analyte infiltration and sensor performance (Sánchez-Salcedo et al., 2025). In biomedical porous silicon fabrication, electrochemical etching also remains the dominant route, with HF-based electrolytes used to dissolve silicon into hexafluorosilicate species and generate the porous matrix (Kang et al., 2025). Although such methods are highly effective, the need for hazardous fluorine-containing chemistry, wafer-based configurations, and careful post-processing creates limitations for large-scale or powder-compatible production. In energy-storage applications, additional challenges arise because many porous silicon routes involve high temperatures, expensive precursors, complex procedures, or hazardous chemicals, which can limit practical scalability (Abo-Hamad et al., 2026). Recent reviews also note that porous silicon obtained through electrochemical corrosion or high-temperature processing can show complex, difficult-to-control pore structures, affecting surface utilization and mass transport (M. Wang et al., 2025). These limitations motivate the development of fluorine-free, powder-compatible, and thermochemically tuneable routes that can generate accessible porosity while preserving the crystalline silicon framework and enabling controllable surface modification. Such powder-compatible approaches may also offer advantages for future integration with existing silicon powder-processing workflows, although their practical scalability depends on heat and mass transfer, reagent utilization, energy demand, and process configuration.

Urea offers an attractive chemical entry point into fluorine-free silicon porosification because it is inexpensive, widely available, and thermally active over a temperature range compatible with low-temperature silicon processing. Its decomposition, however, is not a single-step release of gaseous products. Urea first melts near 133 °C and then undergoes a temperature-dependent sequence of evaporation, decomposition, condensation, and secondary reactions. The primary thermolysis pathway is commonly described as:

$$(H_2N)_2CO \rightarrow NH_3 + HNCO \quad (1)$$

followed by hydrolysis of isocyanic acid:

$$HNCO + H_2O \rightarrow NH_3 + CO_2 \quad (2)$$

and by secondary reactions that generate condensed intermediates such as biuret and cyanuric acid:

$$(H_2N)_2CO + HNCO \rightarrow (H_2NCO)_2NH \quad (3)$$

$$(H_2NCO)_2NH + HNCO \rightarrow CYA + NH_3 \quad (4)$$

$$3HNCO \rightarrow CYA \quad (5)$$

where CYA denotes cyanuric acid. Further reactions can form ammelide and ammeline through NH_3-containing pathways, indicating that urea decomposition generates not only volatile species but also transient condensed phases (Zhu et al., 2021).

The temperature dependence of these reactions is central to the present process. Thermogravimetric and mass-spectrometric studies have shown that below 160 °C, urea decomposition is limited and the dominant process is slow evaporation of molten urea, whereas between 180 and 200 °C biuret formation becomes significant. Above 200 °C, urea and biuret decompose more rapidly, while cyanuric-acid-type residues become increasingly important and later decompose at higher temperature, particularly above approximately 330 °C (Zhu et al., 2021). Schaber and co-workers (Schaber et al., 2004) further showed that urea pyrolysis in an open vessel proceeds through competing temperature-dependent pathways, with HNCO reacting with intact urea to form biuret, followed by formation of cyanuric acid, ammelide, and ammeline; Tischer and co-workers (Tischer et al., 2019) later emphasized the role of equilibrium processes and explained the liquefaction and re-solidification of biuret in the 193-230 °C range through eutectic behavior with urea. These studies imply that, during urea-assisted silicon treatment, the active chemical environment is likely produced

progressively through melting, redistribution, gas evolution, and transient solid or viscous intermediate formation rather than by a single decomposition event at the final treatment temperature.

The relevance of urea-derived species to silicon porosification is supported by the broader chemistry of silicon in ammonia-containing environments. Ammonium hydroxide-based etchants have long been used in silicon micromachining, where $NH_4OH–H_2O$ solutions can anisotropically etch monocrystalline silicon while showing high selectivity toward SiO_2, Si_3N_4, and highly boron-doped silicon (Schnakenberg et al., 1990). Selective etching of silicon in aqueous ammonia has also been demonstrated under electrochemical bias, where the formation of passivating oxide films and the relative behavior of n- and p-type regions depend sensitively on the applied potential (Chen et al., 1995). In NH_3 solution, Si(111) etching has been monitored through hydrogen evolution, indicating that alkaline silicon dissolution is coupled to surface oxidation/reduction processes, represented in that study in simplified form by:

$$Si + 4H_2O \rightarrow Si^{4+} + 4OH^- + 2H_2 \quad (6)$$

with dissolved oxygen found to alter both surface morphology and etching rate. High dissolved oxygen concentrations produced etch pits, whereas oxygen removal led to flatter hydrogen-terminated Si(111) surfaces; the etching rate decreased from 25 ± 1 to 19 ± 1 nm min^{-1} in the presence of dissolved oxygen (Fukidome & Matsumura, 2000). Ammonia–peroxide mixtures used in Radio Corporation of America (RCA) cleaning further illustrate the coupled nature of oxidation and dissolution: silicon can be oxidized to a thin chemical oxide while ammonia participates in oxide redissolution, and deviations in oxidant concentration can produce localized alkaline etching and roughening (Knotter et al., 2000; Lee & Raghavan, 1999). At the molecular scale, reactions between SiO_2 and NH_3 have also been reported to form $SiO_2–NH_3$ complexes and $H_2NSiOOH$-type species, suggesting that ammonia can interact not only with elemental silicon but also with oxidized silicon surfaces (Zhou & Chen, 2001).

These observations are particularly relevant because urea decomposition can supply NH_3 and HNCO locally within a silicon powder bed, while oxygen and residual moisture can simultaneously influence surface oxidation, oxide dissolution, and nitrogen incorporation. In this context, urea is not simply a gas precursor; it is a thermally evolving chemical medium that can wet silicon particles, generate volatile species, form condensed intermediates, and create localized pressure or stress as those intermediates expand, crystallize, or decompose. This combination provides a plausible basis for a dual porosification pathway in which chemical surface modification and mechanically assisted disruption occur together (Abo-Hamad et al., 2026). Such a view is consistent with the known behavior of urea-derived phases and with ammonia-based silicon surface chemistry, although the actual chemistry within the powder bed is likely more complex and may also involve local variations in oxygen partial pressure and moisture content, HNCO adsorption, oxide transformation, and transient Si–O–N-type surface environments. These possibilities are regarded here as potential secondary pathways rather than experimentally established reactions. It remains important to resolve how these processes unfold under the specific staged heating program used for silicon microparticle treatment.

In our previous work (Abo-Hamad et al., 2025), we introduced urea-assisted thermochemical treatment as a fluorine-free route for producing porous silicon microparticles from metallurgical-grade polycrystalline silicon. That study evaluated temperature and container environment and showed that urea treatment transformed dense pristine silicon microparticles with a Brunauer-Emmett-Teller (BET) surface area of 2.3 $m^2 g^{-1}$ into porous silicon with surface areas as high as 26.7 $m^2 g^{-1}$. Under atmospheric conditions, the most

pronounced porosity was obtained at 400 °C, where the surface area reached 25.7 $m^2\ g^{-1}$ and the pore volume reached 0.039 $cm^3\ g^{-1}$, with an etching yield of 17.5%, an average etching rate of 14.6 mg h^{-1}, and a pore formation efficiency of about 43%. In contrast, treatments at 600 and 800 °C produced porosity close to that of pristine silicon, which was attributed to rapid and intense urea decomposition that limited sustained gas-solid interaction. That study also showed that urea treatment produced temperature- and environment-dependent oxidation and nitrogen incorporation, with Si–N, NH_2/NH_3^+, and NO_x-type species detected under selected conditions. More detailed surface-sensitive characterization combining X-ray photoelectron spectroscopy (XPS) with complementary techniques such as Fourier-transform infrared spectroscopy (FTIR), Raman spectroscopy, and time-of-flight secondary ion mass spectrometry (ToF-SIMS) could further resolve Si–O, Si–N, Si–O–N, and NH_x-type surface environments in future studies.

A subsequent study extended this strategy to porous silicon microparticles for Li-ion battery anodes and provided more direct support for a coupled porosification mechanism (Abo-Hamad et al., 2026). Therein, urea-assisted treatment produced particles with open pores and cavities, increased oxygen content, nitrogen-containing surface functionalities, and a substantial increase in BET surface area from 2.3 to 26.7 $m^2\ g^{-1}$. The observed morphology was interpreted as arising from both mechanical effects, associated with gas evolution and transient urea-derived phases, and chemical effects, associated with NH_3/HNCO-mediated surface modification, oxidation, and possible oxide transformation. Control experiments further showed that thermal exposure alone did not reproduce the porosity, while chemically minimized and mechanically minimized conditions generated only partial features; the full urea-assisted treatment produced the strongest mesoporosity, supporting a dual-effect mechanism in which chemically driven surface modification and stress-assisted structural disruption act together.

Despite these advantages, two mechanistic questions remain open for the 400 °C condition. First, the influence of urea loading has not been isolated at this selected temperature, even though the amount of urea should govern the balance between molten-phase redistribution, gas generation, intermediate formation, and silicon surface accessibility. Too little urea may provide insufficient chemical and mechanical driving force, whereas excessive urea may promote rapid mass loss, shielding, agglomeration, or inefficient gas-solid contact. Second, the thermal pathway of urea in direct contact with pristine silicon under the exact staged heating protocol remains unresolved. This distinction is important because urea alone is known to decompose through multistep pathways, but the silicon powder bed may modify the apparent onset, extent, and stability of urea-derived events by dispersing molten urea over particle surfaces and confining intermediate phases within interparticle voids.

In this work, we address these questions by fixing the treatment temperature at 400 °C and varying the Urea:Si mass ratio from 0.5:1 to 4:1. The effect of urea loading is evaluated using nitrogen sorption, Barrett-Joyner-Halenda (BJH) pore-size analysis, scanning electron microscopy (SEM), and energy-dispersive X-ray spectroscopy (EDS) to determine how urea amount controls porosity development and surface composition. The Urea:Si (2:1 mass ratio) blend is then selected for further analysis using mercury porosimetry and thermogravimetry/differential scanning calorimetry (TG/DSC) to connect pore-network accessibility with the staged thermal evolution of urea in contact with silicon. By comparing pristine silicon, pure urea, and the Urea:Si mixture under the same heating protocol, this work aims to identify when the active chemical and mechanical events occur and how they relate to pore formation. The purpose is therefore not to re-establish the general feasibility of urea-

assisted silicon etching, but to clarify how urea loading and staged thermal decomposition govern fluorine-free porosification at 400 °C.

2. Materials and Methods

2.1 Materials

Metallurgical-grade polycrystalline silicon microparticles were used as the silicon feedstock. The powder was commercially supplied as SicoMill Grade 2E by Vesta Si Sweden AB (SKF Group Company, Sweden), batch drum no. 35512, with a reported purity of 98 to 99% and an average particle size of approximately 4.6 to 5 µm. The silicon powder was used as received without further purification or pretreatment. Urea (ACS reagent grade, ≥99.5%) was purchased from Sigma-Aldrich and used as the thermochemical porosification agent. Deionized water and ethanol were used for cleaning and post-treatment washing.

2.2 Synthesis of porous silicon

Silicon microparticles were blended with urea at Urea:Si mass ratios of 0.5:1, 1:1, 2:1, and 4:1. The powders were mixed manually using an agate mortar and pestle for 10 min to promote homogeneous distribution of urea throughout the silicon powder bed. Before use, all tools and containers were rinsed with deionized water and ethanol and dried. The untreated pristine silicon powder is denoted as PrSi, while the porous silicon obtained from the selected Urea:Si (2:1 mass ratio) mixture is denoted as PoSi.

The blended powders were thermally treated under ambient laboratory air at atmospheric pressure in ceramic crucibles using a programmable Nabertherm furnace. The heating program consisted of two stages. First, the mixture was heated to 135 °C at 5 °C min^{-1} and held for 1 h to melt urea and promote redistribution within the silicon powder bed. Second, the temperature was increased to 400 °C at 10 °C min^{-1} and maintained for 12 h. This temperature was selected based on previous optimization of urea-assisted silicon porosification, where 400 °C under atmospheric conditions produced the most pronounced mesoporosity (Abo-Hamad et al., 2025).

After thermal treatment, the powders were allowed to cool to room temperature and were washed repeatedly with boiling deionized water to remove residual urea and soluble urea-derived by-products. The powders were then filtered and dried prior to characterization.

2.3 Characterization

Nitrogen adsorption-desorption measurements were performed using a TriStar II Plus analyzer (Micromeritics) to determine the textural properties of PrSi and the treated samples. Before analysis, the powders were degassed under nitrogen flow at 300 °C for 1 h. The specific surface area was calculated using the Brunauer-Emmett-Teller (BET) method, and the pore-size distribution was estimated using the Barrett-Joyner-Halenda (BJH) model. Measurements were performed in triplicate, and the reported BET surface area and pore volume values represent the mean of three measurements, with error bars indicating the standard deviation.

Surface morphology and elemental composition were analyzed by scanning electron microscopy (SEM) and energy-dispersive X-ray spectroscopy (EDS) using a TESCAN MAIA3 Triglav™ SEM equipped with EDS. SEM was used to examine changes in particle morphology, surface roughness, and pore formation as a function of urea loading, while EDS was used to evaluate changes in elemental composition after treatment.

Thermogravimetric and differential scanning calorimetry analysis was performed using a NETZSCH STA 449 F1 instrument in simultaneous TG/DSC mode. Measurements were

carried out for PrSi, pure urea, and the selected Urea:Si (2:1 mass ratio) mixture using alumina crucibles. The applied program followed the synthesis sequence: heating from room temperature to 135 °C at 5 °C min^{-1}, holding at 135 °C for 1 h, heating to 400 °C at 10 °C min^{-1}, and holding at 400 °C for 2 h for analytical tracking of the main thermal events. The measurements were conducted under an N_2/O_2 flow of 50 mL min^{-1}, together with N_2 protective gas at 20 mL min^{-1}, to mimic the oxidizing air-containing environment used during the atmospheric thermal treatment. The TG signal was used to follow mass changes, while the DSC signal was used to identify thermal events associated with urea melting, decomposition, and removal of urea-derived intermediates.

Mercury intrusion porosimetry was performed using a Micromeritics AutoPore IV 9500 instrument to assess pore-network accessibility in PrSi and PoSi. Measurements were carried out using a powder penetrometer with a 3 mL cup volume and 0.412 mL stem/internal volume, and the intrusion data were used to compare accessible pore volume and pore-size distribution beyond the mesopore range probed by nitrogen sorption.

2.4 Data analysis

The influence of urea loading was evaluated by comparing BET surface area, BJH pore-size distribution, SEM morphology, and EDS elemental composition across the Urea:Si series. The 2:1 Urea:Si sample was selected for additional mechanistic analysis because it produced nearly the full porosity enhancement observed at higher urea loading while avoiding excess reagent. TG/DSC data were used to compare the thermal behavior of PrSi, pure urea, and the Urea:Si mixture under the same staged heating program, while mercury intrusion porosimetry was used to complement nitrogen sorption by probing larger-scale accessible pore features.

3. Results and Discussion

Our previous work (Abo-Hamad et al., 2025) established urea-assisted thermochemical treatment as a fluorine-free route for porosifying polycrystalline silicon microparticles and identified two particularly informative processing conditions: confined treatment at 220 °C and atmospheric treatment at 400 °C. The confined 220 °C route was later examined through control experiments, supporting a dual-effect mechanism involving chemical surface modification and stress-assisted structural disruption (Abo-Hamad et al., 2026). The present work focuses on the other key condition, namely the 400 °C atmospheric treatment, and examines how urea content controls pore development. Urea:Si mass ratios of 0.5:1, 1:1, 2:1, and 4:1 were compared by nitrogen sorption, BJH analysis, SEM, and EDS, while the selected 2:1 composition was further studied by mercury intrusion porosimetry and TG/DSC.

3.1 Urea-content dependence of mesopore development at 400 °C

Nitrogen sorption was first used to evaluate how the initial urea content influences pore formation during atmospheric treatment at 400 °C. PrSi microparticles showed only limited nitrogen uptake across the full relative-pressure range, consistent with the dense and weakly porous nature of the starting material (Figure 1a). The BJH pore-size distribution of PrSi was also weak and poorly defined, confirming that the untreated powder does not contain a developed mesopore network in the range probed by nitrogen sorption (Figure 1b). Consistently, PrSi exhibited a low BET surface area of 2.4 m^2 g^{-1} and a total pore volume of only 0.0031 cm^3 g^{-1} (Figure 1c).

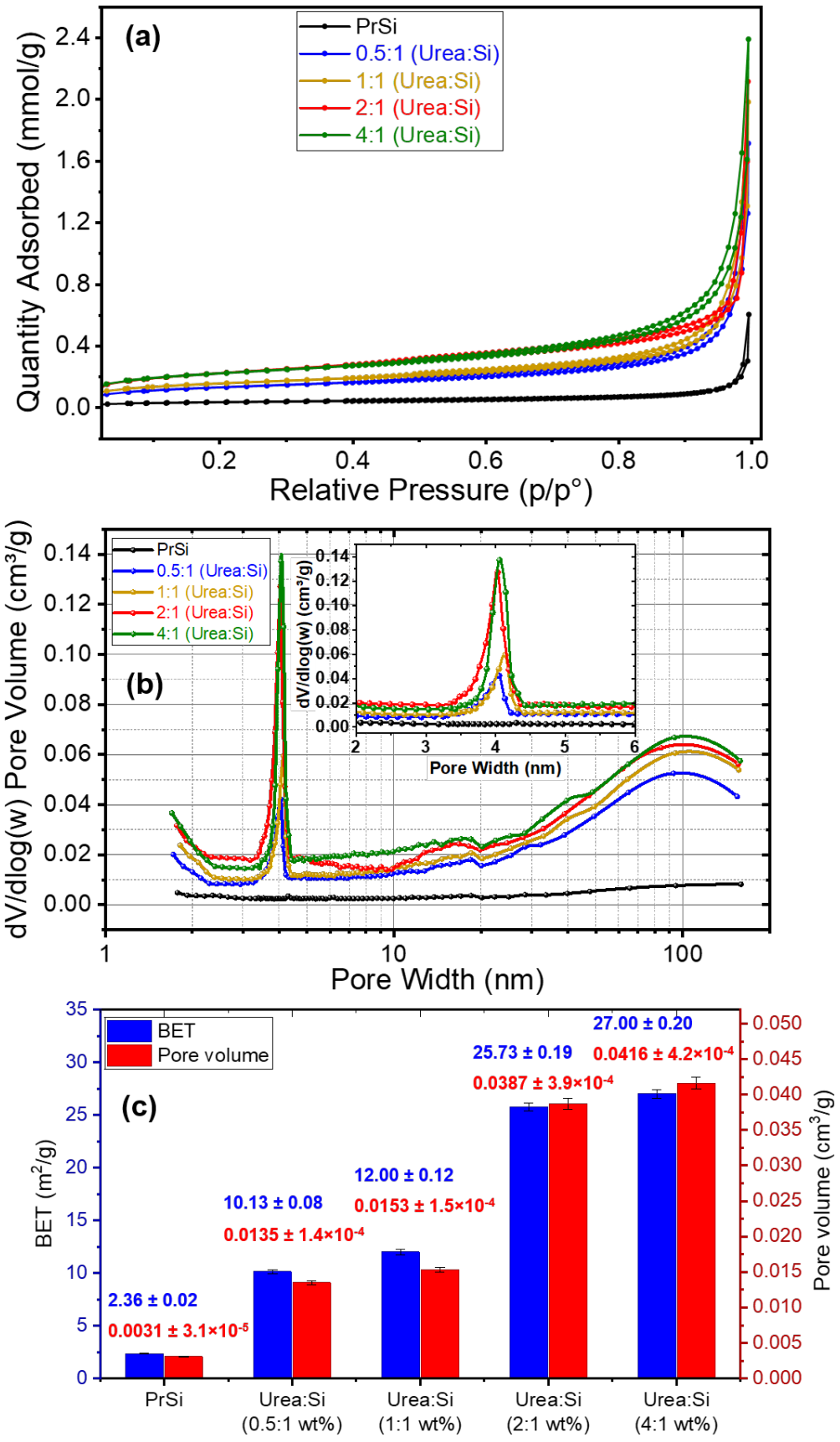

Figure 1. Effect of urea content on pore development in silicon microparticles treated at 400 °C. (a) Nitrogen adsorption-desorption isotherms, (b) BJH pore-size distributions, with inset highlighting the dominant ~4 nm mesopore population, and (c) BET surface area and pore volume of PrSi and Urea:Si-treated samples. Values in (c) are presented as mean ± standard deviation (n = 3).

After urea-assisted treatment, the adsorption capacity increased for all Urea:Si ratios, demonstrating that the 400 °C treatment generates additional accessible porosity. Even the lowest urea loading, 0.5:1 Urea:Si, increased the BET surface area to 10.1 $m^2 g^{-1}$ and the pore volume to 0.014 $cm^3 g^{-1}$, corresponding to roughly a fourfold increase relative to PrSi. Increasing the urea content to 1:1 produced a further but moderate increase, with a BET surface area of 12.0 $m^2 g^{-1}$ and pore volume of 0.015 $cm^3 g^{-1}$. This indicates that low urea loadings are sufficient to initiate porosity formation, but not enough to fully develop the accessible pore network.

A more pronounced transition occurred when the Urea:Si ratio was increased to 2:1. At this composition, the BET surface area rose sharply to 25.7 $m^2 g^{-1}$, while the pore volume increased to 0.039 $cm^3 g^{-1}$. Compared with PrSi, this corresponds to an approximately 11-fold increase in surface area and a 12.5-fold increase in pore volume. The adsorption isotherm also showed substantially higher nitrogen uptake, particularly at elevated relative pressures, indicating a much larger accessible void volume after treatment. This sharp increase suggests that a critical urea content is required to generate sufficient volatile and transient urea-derived species for effective pore development.

Further increasing the urea loading to 4:1 gave the highest numerical BET surface area and pore volume, 27.0 $m^2 g^{-1}$ and 0.042 $cm^3 g^{-1}$, respectively. However, the gain relative to the 2:1 sample was small, only about 5% in surface area and 8% in pore volume. Thus, the porosity development does not scale linearly with urea content. Instead, the sorption data indicate that the system approaches a near-saturation regime after the 2:1 ratio, where additional urea provides only a limited improvement in accessible porosity. This plateau may indicate that, beyond the 2:1 ratio, additional urea provides little further benefit because gas transport becomes more restricted and urea-derived intermediates may accumulate, reducing access to fresh Si surface.

The BJH pore-size distributions provide further insight into this behavior (Figure 1b). All urea-treated samples show a distinct mesopore population centered at approximately 4.0-4.1 nm, whereas PrSi exhibits only a weak background response. This dominant feature is highlighted in the inset of Figure 1b. Increasing the urea content does not substantially shift the position of this main peak; instead, its intensity increases strongly from 0.5:1 to 2:1 and then changes only modestly at 4:1. This indicates that urea loading primarily controls the extent and accessibility of this dominant mesopore population, rather than changing its characteristic pore width. In addition, the distributions show a broader, less-defined contribution at larger pore widths, extending toward ~100 nm, particularly for the urea-treated samples. This feature should be interpreted cautiously because BJH analysis above the mesopore range is sensitive to near-saturation adsorption and may include interparticle or packing-related contributions. Nevertheless, it agrees with previous control experiments showing that full urea-assisted treatment can combine a dominant ~4 nm mesopore population with secondary larger pore/void features, whereas crack- and void-dominated conditions give stronger large-pore responses (Abo-Hamad et al., 2026).

Taken together, the nitrogen sorption results show that urea content is a decisive parameter in the atmospheric 400 °C porosification route. Low urea loadings initiate surface and pore development, while the transition from 1:1 to 2:1 marks the major increase in accessible mesoporosity. The small additional gain at 4:1 indicates that excessive urea is not proportionally beneficial, likely because pore formation becomes limited by silicon surface accessibility, gas-solid contact, or the removal of urea-derived intermediates rather than by urea availability alone. Therefore, the 2:1 Urea:Si composition represents a practical high-

porosity condition, providing nearly the full porosity enhancement observed at higher urea loading while avoiding unnecessary excess reagent.

3.2 Morphological and compositional evolution with urea content

SEM and EDS analyses were used to examine whether the textural changes identified by nitrogen sorption are reflected in the particle morphology and surface composition. PrSi consists of angular microparticles with compact, faceted surfaces and no clear open-pore network at the SEM scale (Figure 2). The higher-magnification images show mostly smooth surface regions with only minor surface debris or native roughness, consistent with the low nitrogen uptake, weak BJH response, and low BET surface area discussed above.

After urea-assisted treatment at 400 °C, all Urea:Si compositions exhibit pronounced morphological modification relative to PrSi. At the lowest urea content, 0.5:1 Urea:Si, the particles already show a roughened and granular surface, together with visible cracks and local voids. Increasing the ratio to 1:1 and 2:1 produces more extensive surface disruption, with roughened domains, open cavities, and pore-like features distributed across the particle surfaces. At 4:1, the surface remains highly roughened and porous-looking, although the morphology does not show a simple linear increase in pore development compared with the 2:1 sample. This agrees with the nitrogen sorption data, where increasing the urea loading from 2:1 to 4:1 resulted only in a modest additional increase in BET surface area and pore volume.

The treated morphologies are consistent with the dual chemical-mechanical mechanism proposed in our earlier work (Abo-Hamad et al., 2025), where urea-derived species contribute to chemical surface modification while gas evolution and transient condensed phases may generate local stresses within defects, interparticle spaces, or pre-existing voids. Control experiments previously showed that thermal treatment alone retained a dense PrSi-like morphology, whereas the full urea-assisted process produced the strongest surface disruption and nanoscale void formation (Abo-Hamad et al., 2026). The present SEM images therefore support the same picture for the 400 °C atmospheric route, showing surface roughening, cracking, and pore opening across all urea-containing samples.

Because SEM probes only selected local regions, it should be used qualitatively rather than as a direct ranking of porosity among the treated samples. Individual particles can differ in crystal facets, defect density, local urea contact, and gas-escape pathways. Thus, SEM confirms the morphological transformation from compact PrSi to roughened, cracked, and void-containing particles, while the quantitative urea-content trend is more reliably determined from nitrogen sorption.

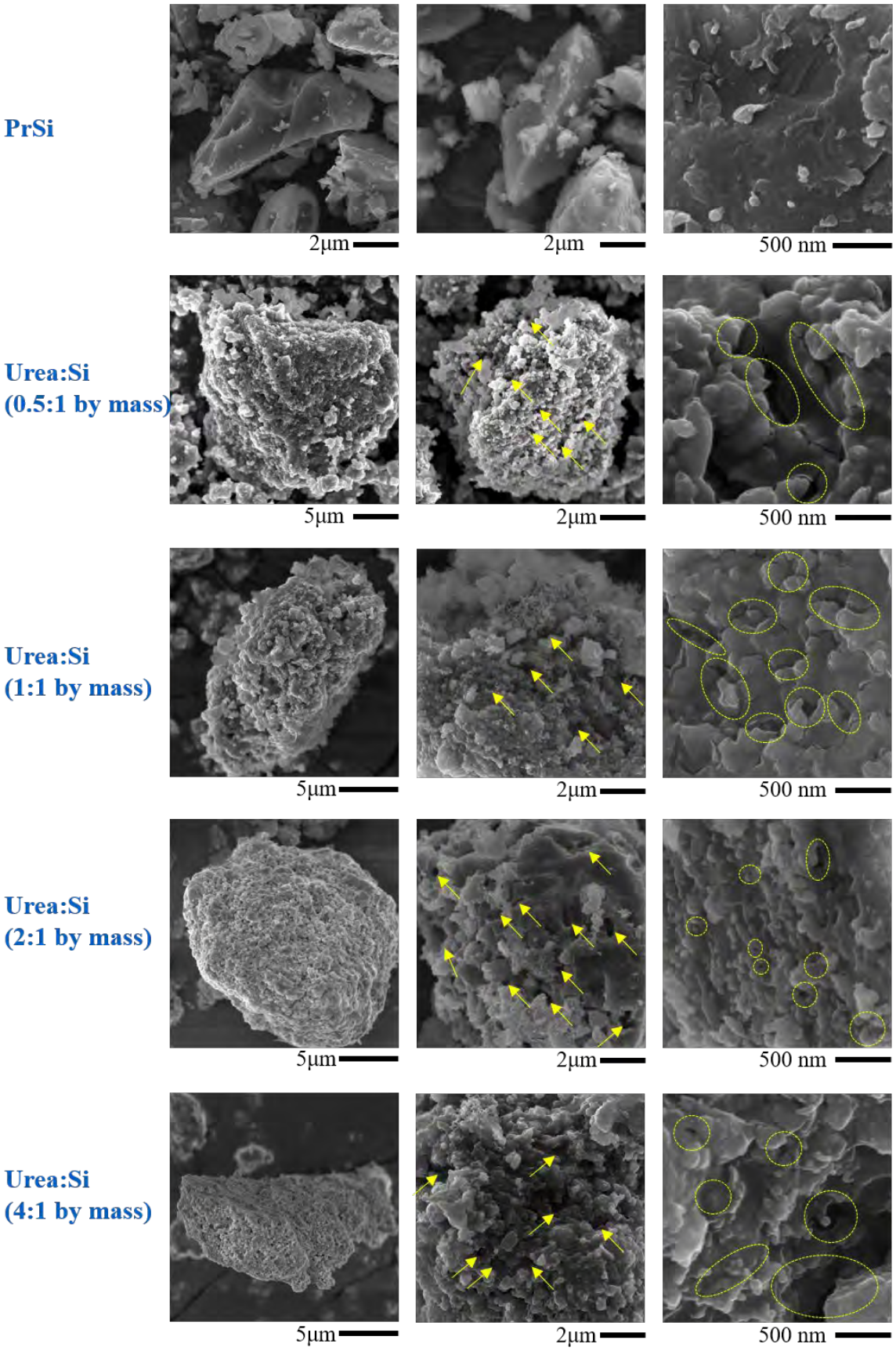

Figure 2. SEM morphology of PrSi and Urea:Si-treated samples. Arrows and dashed outlines highlight representative cavity- and pore-like features visible at higher magnification.

EDS mapping further confirms that the urea treatment modifies the surface composition (Figure 3). In PrSi, the EDS scan shows a dominant Si signal with only 2.5 wt% O, consistent with a native oxide layer on the untreated silicon surface. After treatment, the oxygen signal increases systematically with urea content: 5.5 wt% for 0.5:1, 8.2 wt% for 1:1, 11.4 wt% for 2:1, and 11.8 wt% for 4:1 Urea:Si. The corresponding Si signal decreases from 97.5 wt% in PrSi to 94.5, 91.8, 88.6, and 88.2 wt%, respectively. This progressive increase in oxygen is consistent with greater oxygen-containing surface modification during the 400 °C treatment; however, EDS does not provide chemical-state information and therefore cannot distinguish specific Si–O or related bonding environments.

The oxygen maps show that O is not distributed as a uniform bulk component but is more visible at particle edges, roughened surfaces, cracks, and boundary regions. Such spatial localization is consistent with preferential oxygen enrichment at more exposed and structurally disrupted regions, where edges and pore walls provide greater accessible surface area than smooth facets. The increase in oxygen content therefore likely reflects both chemical modification and the increased surface area generated during porosification. This interpretation is consistent with our previous temperature-screening study, where the 400 °C atmospheric sample showed both high porosity and strong oxygen incorporation; the increased oxygen content was attributed to enhanced surface exposure together with sufficient residence of urea-derived reactive species to interact with the silicon surface (Abo-Hamad et al., 2025).

Importantly, the oxygen increase follows the same general trend as the nitrogen sorption data. The largest compositional shift occurs as the urea content is increased toward the 2:1 ratio, whereas the difference between 2:1 and 4:1 is small. This plateau-like behavior suggests that beyond a certain urea loading, the accessible silicon surface and the efficiency of gas-solid interaction become limiting factors. Additional urea may generate more volatile products, but it does not proportionally increase the accessible oxidized or porous surface. Thus, the SEM/EDS results support the conclusion from nitrogen sorption: the 2:1 Urea:Si composition provides a high degree of surface modification and pore development, while further increasing urea content gives only limited additional benefit.

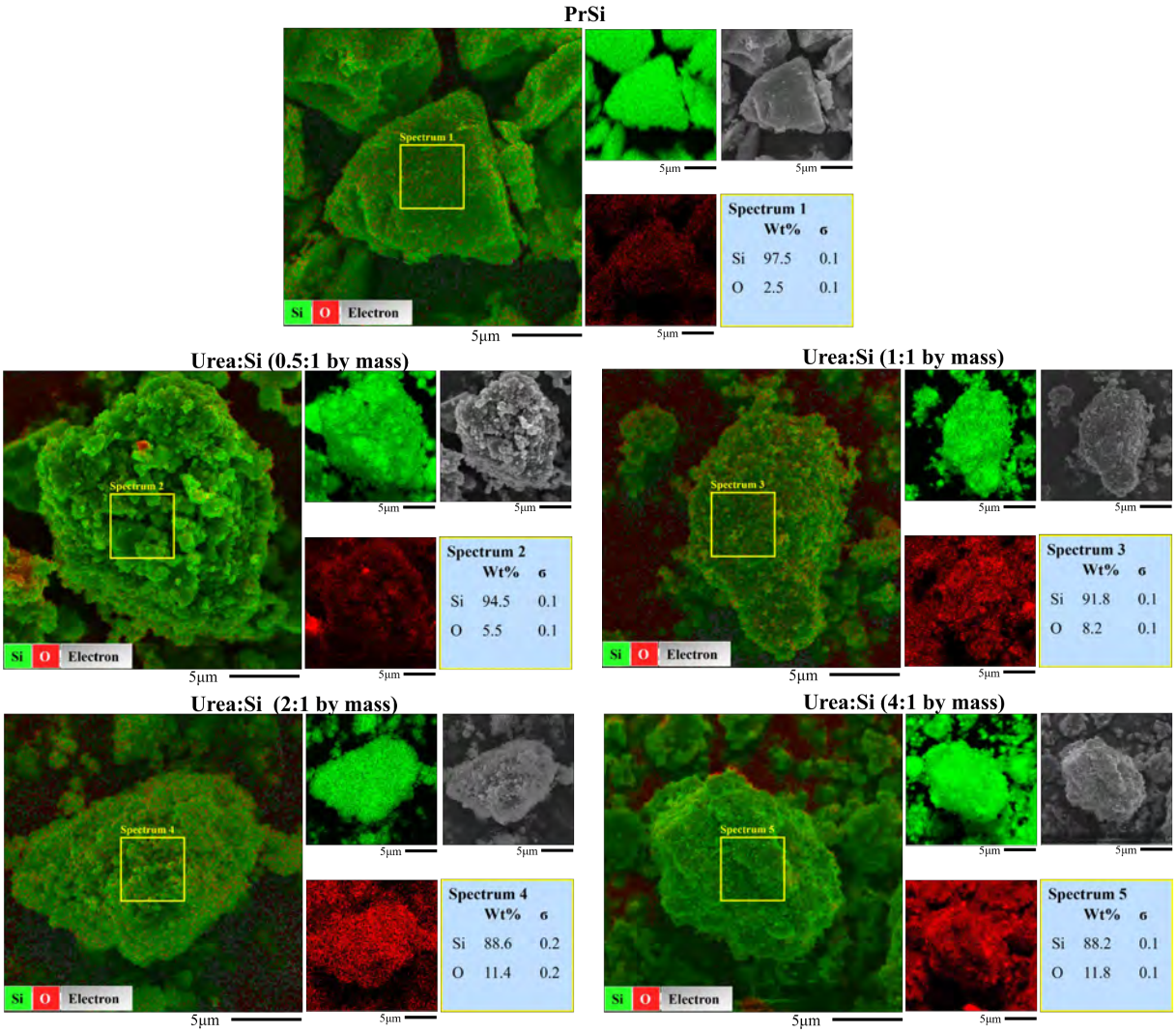

Figure 3. EDS elemental mapping of PrSi and Urea:Si-treated samples. For each sample, the merged Si/O map is shown on the left, with Si in green and O in red. The right-side panels show the separated Si signal and SEM image above, and the separated O signal with local Si/O quantification below. Boxed regions indicate the areas used for EDS quantification.

3.3 Pore-network accessibility of the selected 2:1 Urea:Si-derived PoSi

Mercury intrusion porosimetry was used to complement nitrogen sorption by probing larger accessible pore-throat features in PrSi and the PoSi obtained from the 2:1 Urea:Si treatment. While nitrogen sorption is most sensitive to the mesopore range, mercury intrusion provides information on larger accessible voids, cracks, cavities, and pore throats. For powder samples, the response may also include interparticle voids associated with particle packing; therefore, the data are interpreted here as a comparison of larger-scale pore-network accessibility rather than solely as internal particle porosity. Accordingly, the absolute intrusion volumes and larger pore-size features should not be interpreted exclusively as intraparticle porosity.

PrSi shows a limited intrusion response, with a cumulative intrusion of approximately 0.32 mL g^{-1} and a main differential feature centered near 1 µm (Figure 4). Since PrSi appears compact and non-porous in SEM and exhibits only weak nitrogen uptake, this micron-scale intrusion is most likely dominated by packing-related voids between irregularly shaped silicon particles rather than by a developed internal pore network.

PoSi, however, exhibits a substantially stronger intrusion response. The cumulative intrusion increases to approximately 0.84 mL g^{-1}, corresponding to about 2.6 times the value measured for PrSi (Figure 4). The differential intrusion curve shows a dominant feature near 0.84 µm, together with an additional contribution extending roughly from 150 to 600 nm, which is largely absent in PrSi. This indicates that the 2:1 Urea:Si treatment introduces new accessible pore/void features at submicron length scales, in addition to the larger interparticle void contribution common to powders.

Together with the nitrogen sorption data, the mercury intrusion results suggest that PoSi develops a hierarchical pore structure. Nitrogen sorption resolves a dominant mesopore population near 4 nm, and a broader, less-defined contribution in the ~80-100 nm range, while mercury intrusion reveals larger accessible features from roughly 0.15 to 1 µm. This multiscale pore response is consistent with the SEM observations of roughened surfaces, cracks, and open voids, and is also consistent with previous control experiments suggesting that urea-derived chemical surface modification and gas/intermediate-driven structural disruption may act together during porosification (Abo-Hamad et al., 2026).

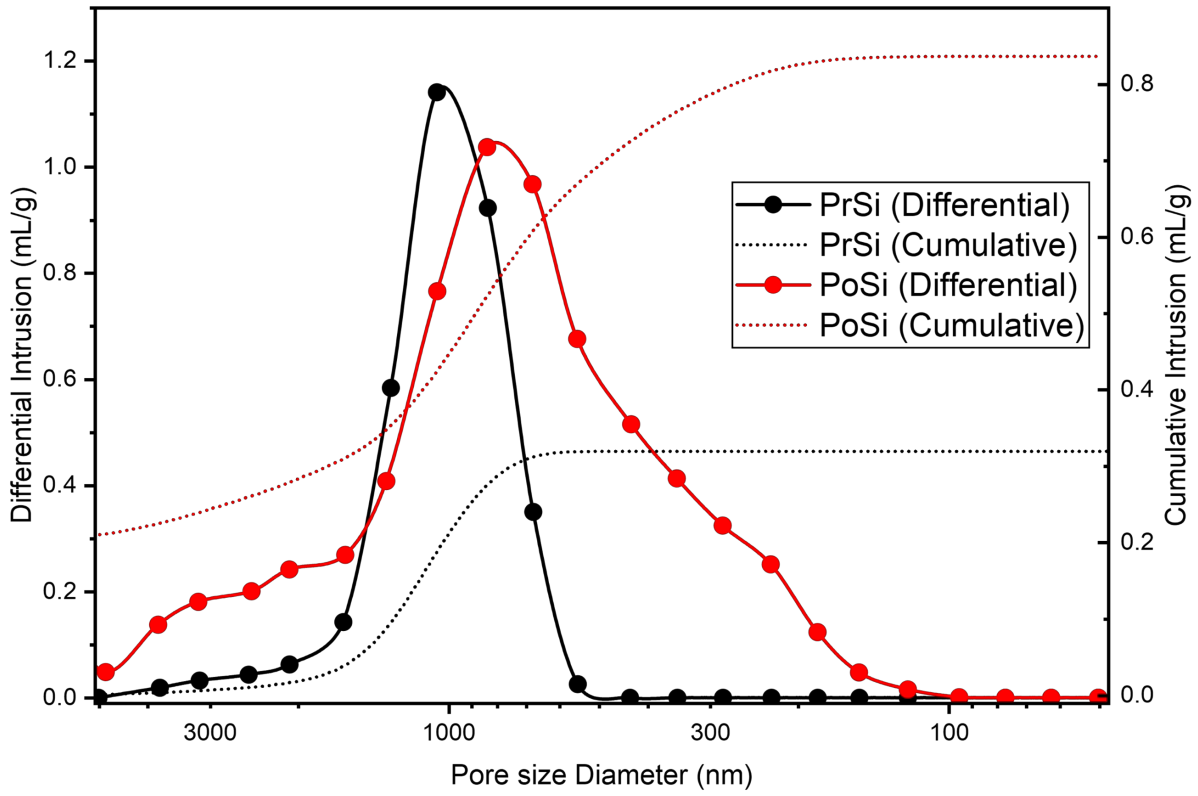

Figure 4. Differential and cumulative mercury intrusion curves comparing PrSi and PoSi obtained from the 2:1 Urea:Si treatment.

3.4 Thermal sequence of urea transformation in contact with silicon

TG/DSC analysis was used to resolve how urea evolves during the staged thermal treatment and how this behavior changes when urea is mixed with PrSi. The full TG response and temperature profile are shown in Figure 5a, the corresponding DSC traces as a function of time are shown in Figure 5b, and the dynamic region between 135 and 400 °C, where the main decomposition events occur, is enlarged in Figure 5c. The main mass changes and DSC features are summarized in Table I.

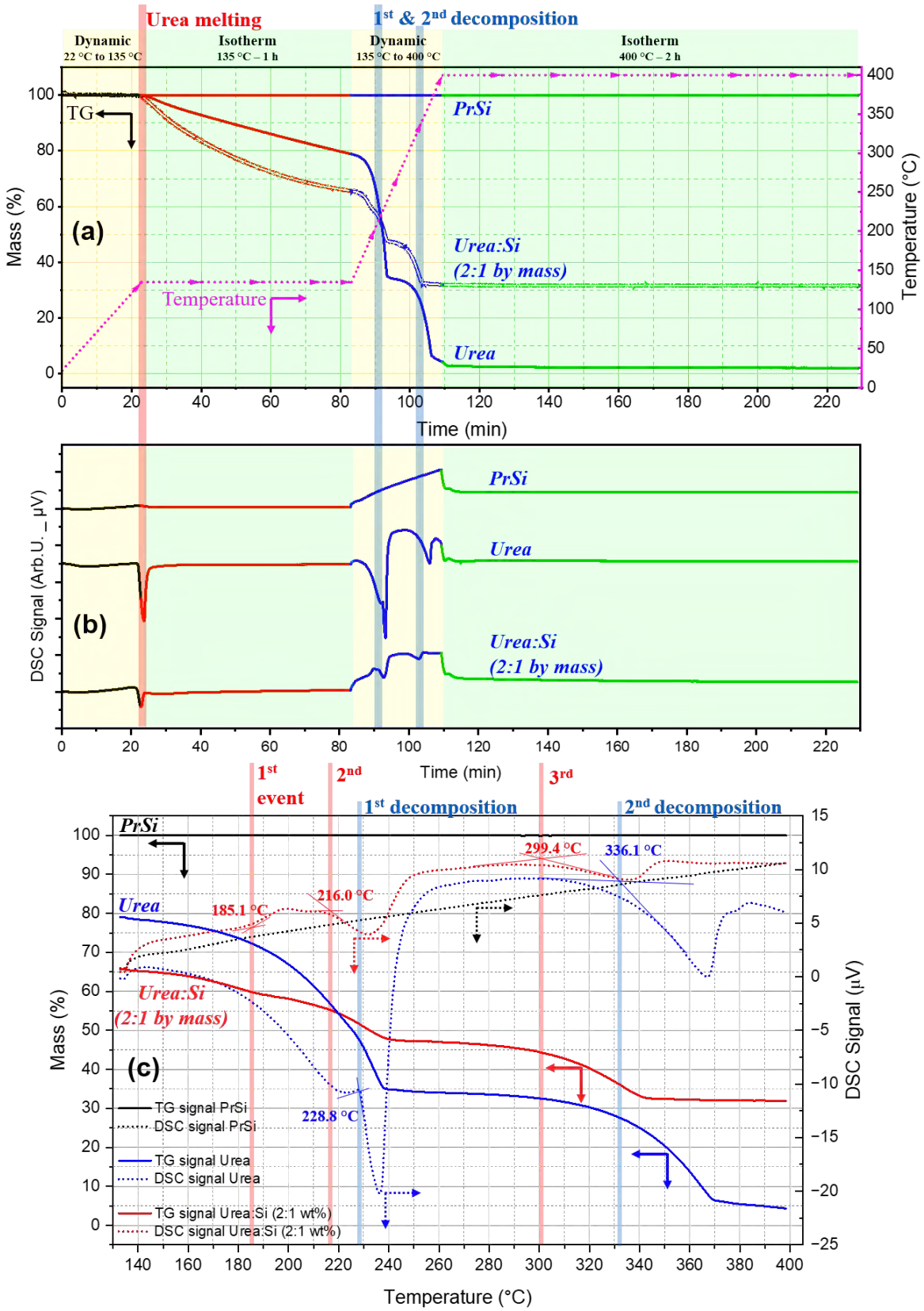

Figure 5. TG/DSC response of PrSi, urea, and Urea:Si (2:1 mass ratio). (a) TG curves and temperature profile during the full staged thermal program, (b) DSC traces versus time, and (c) enlarged TG/DSC comparison during the dynamic 135-400 °C region, showing shifted urea-derived thermal events in the Urea:Si mixture.

Table I: Summary of TG mass changes and DSC features during the staged thermal program

Sample	Thermal segment	Mass change (%)	Residual mass (%)	Main DSC feature
PrSi	1, Dynamic, 22 to 135 °C at 5 °C/min	-0.03	99.97	-
	2, Isothermal, 135 °C for 1 h	-0.01	99.96	-
	3, Dynamic, 135 to 400 °C at 10 °C/min	-0.02	99.94	-
	4, Isothermal, 400 °C for 2 h	+0.07	100.01	-
Urea	1, Dynamic, 22 to 135 °C at 5 °C/min	-0.09	99.91	Melting, ~133 to 135 °C
	2, Isothermal, 135 °C for 1 h	-20.87	79.04	Weak
	3, Dynamic, 135 to 400 °C at 10 °C/min	-44.78 -29.92	34.26 4.34	Onset: 228.8 °C Onset: 336.1 °C
	4, Isothermal, 400 °C for 2 h	-0.63	3.71	Weak
Urea:Si (2:1 by mass)	1, Dynamic, 22 to 135 °C at 5 °C/min	-0.56	99.44	Melting ~133 to 135 °C
	2, Isothermal, 135 °C for 1 h	-33.77	65.67	Weak
	3, Dynamic, 135 to 400 °C at 10 °C/min	-18.38 -15.35	47.29 31.94	Onsets: 185.1 & 216.0 °C Onset: 299.4 °C
	4, Isothermal, 400 °C for 2 h	-0.41	31.53	Weak

PrSi remains essentially mass-stable throughout the full program, with no distinct DSC event (Figure 5a-c, Table I). This shows that PrSi undergoes no measurable mass loss or distinct thermal event under the applied conditions. Therefore, the mass-loss events observed for Urea:Si can be assigned primarily to urea-derived processes rather than degradation or volatilization of silicon.

Pure urea shows a multistep thermal response. During the initial heating to 135 °C, only negligible mass loss occurs, while the DSC trace displays the melting region near 133-135 °C (Figure 5b, Table I). During the subsequent 135 °C isothermal hold, however, urea loses ~20.9% of its initial mass. This shows that molten urea is not fully retained under the applied gas flow, even near its melting temperature. Such behavior is consistent with previous TG-MS studies

showing that below approximately 160 °C, urea decomposition is limited, but molten urea can evaporate slowly. At higher temperatures, urea decomposition becomes progressively more complex, involving NH_3, HNCO, biuret, cyanuric acid, and related condensed intermediates(Zhu et al., 2021).

The dynamic region in Figure 5c highlights the main difference between pure urea and the Urea:Si mixture. Pure urea undergoes two major mass-loss steps during heating from 135 to 400 °C. These are associated with DSC onsets at 228.8 °C and 336.1 °C and correspond to mass losses of ~44.8% and 29.9%, respectively (Table I). The first event is consistent with the main urea decomposition and volatilization stage, while the second is consistent with decomposition or removal of more stable condensed urea-derived residues. This assignment agrees with reported urea decomposition studies, where the first major mass-loss region occurs between roughly 140 and 250 °C, followed by further residue decomposition up to approximately 360-410 °C; cyanuric-acid-type species are especially relevant to the higher-temperature event, with rapid mass loss reported above approximately 330 °C (Tischer et al., 2019; Zhu et al., 2021).

In contrast, the Urea:Si mixture displays a shifted and redistributed thermal response. During the 135 °C isothermal stage, the mixture loses ~33.8% of its total mass, which corresponds to approximately half of the original urea fraction in the 2:1 Urea:Si mixture. This loss is substantially larger than for pure urea, indicating that the presence of silicon microparticles changes the physical state and retention of molten urea. A likely explanation is that molten urea spreads across the silicon particle surfaces and interparticle spaces, increasing its exposed area and accelerating evaporation or early transformation.

The DSC response in Figure 5c further supports this interpretation. Instead of the pure-urea onsets at 228.8 °C and 336.1 °C, the Urea:Si mixture shows features at 185.1 °C, 216.0 °C, and 299.4 °C. The corresponding TG losses during the dynamic ramp are ~18.4% and 15.4% (Table I). The lower-temperature events at 185.1 and 216.0 °C are consistent with decomposition or removal of remaining dispersed urea and early urea-derived intermediates. The later event at 299.4 °C is consistent with removal of more condensed urea-derived residues. Compared with pure urea, the shift to lower temperature indicates that these processes occur more readily when urea is distributed within the silicon powder bed. This may arise from thinner urea domains, greater gas exposure, stronger contact with silicon/native oxide surfaces, or reduced stability of condensed intermediates when formed in a dispersed state.

After the full program, the Urea:Si mixture retains ~31.5% of its initial mass, close to the theoretical silicon fraction of 33.3 wt% expected after complete removal of the urea-derived component from a 2:1 Urea:Si mixture. This agreement indicates that most of the urea-derived mass is removed by the end of the treatment, leaving silicon as the dominant solid residue. The small deviation from the theoretical value may reflect local mixture inhomogeneity, baseline correction, or minor physical loss during gas evolution.

Overall, the TG/DSC results show that urea-assisted porosification at 400 °C is not governed by a single decomposition event at the final temperature. Instead, the process begins during the 135 °C hold, where molten urea is partially lost or transformed, and continues through a shifted series of decomposition events between approximately 185 and 300 °C when urea is in contact with silicon. This observation also clarifies the role of the 400 °C condition identified in the previous temperature-screening study. That study compared atmospheric treatments at 220, 400, 600, and 800 °C and did not include an intermediate temperature between 300 and 400 °C. Thus, the present TG/DSC results do not imply that pore formation begins only at 400

°C; rather, they indicate that the principal urea-derived transformations occur during heating toward the final treatment temperature. The 400 °C condition should therefore be regarded as the previously identified processing endpoint at which the strongest atmospheric mesoporosity was obtained, while the active thermal sequence develops substantially below this temperature. This staged behavior is consistent with the strong influence of urea content on pore development, because the amount of urea controls not only the quantity of volatile species generated, but also the extent of molten-phase redistribution, intermediate formation, and removal within the silicon powder bed. Direct evolved-gas analysis, for example by TG-MS, gas-phase FTIR, or GC-MS, would be valuable in future work to verify the identities and temperature-dependent evolution of NH_3, HNCO, and other proposed urea-derived species.

3.5 Proposed mechanism of urea-assisted silicon porosification at 400 °C

The combined data suggest that porosification at 400 °C proceeds through a coupled thermal, chemical, and mechanical corrosion pathway. The process begins when molten urea redistributes through the Si powder bed during the 135 °C hold. In the Urea:Si mixture, this stage already removes a large fraction of the urea component, which is consistent with redistribution of the molten phase over Si surfaces and interparticle voids rather than its retention solely as a bulk urea pool. This redistribution is important because it may place urea-derived species directly at Si/SiO_x surfaces, grain boundaries, defects, and particle contacts, where pore formation is most likely to initiate.

Upon further heating, dispersed urea decomposes and produces NH_3 and HNCO, while secondary reactions generate biuret, cyanuric-acid-type species, and other condensed intermediates, as described by Reactions 1-5 in the Introduction.

These reactions are relevant because the intermediate region around 180-300 °C coincides with the temperature window where the Urea:Si mixture shows shifted DSC events and where the first major pore-opening processes are likely to occur. Previous studies of urea decomposition show that biuret, cyanuric acid, ammelide, and ammeline form through competing temperature-dependent pathways, and that biuret/urea-derived phases can pass through liquid, viscous, foam-like, or re-solidified states in the approximate 190-230 °C region (Schaber et al., 2004; Tischer et al., 2019; Zhu et al., 2021). In a powder bed, such transient phases can fill surface defects and interparticle constrictions, then expand, crystallize, decompose, or volatilize. This provides a plausible source of local stress, cracking, and cavity opening, consistent with the SEM and mercury intrusion observations.

The proposed chemical etching contribution may involve a local ammonia-water-oxygen-silicon oxide cycle. Although the present system is not an aqueous NH_4OH bath, it contains NH_3 from urea decomposition, oxygen from the air-containing atmosphere, and possible water from adsorbed moisture or urea-derived reactions. In such a microenvironment, NH_3 can act as a weak base:

$$NH_3 + H_2O \rightleftharpoons NH_4^+ + OH^- \quad (7)$$

The generated OH^- may then participate in alkaline attack of oxidized or hydroxylated silicon sites. A simplified alkaline silicon dissolution pathway can be written as:

$$Si + 2OH^- + 2H_2O \rightarrow Si(OH)_4 + 2e^- + H_2 \quad (8)$$

This type of reaction is consistent with ammonia-based silicon etching literature, where hydrogen evolution is used to quantify Si etch rates in NH_3 solutions and where dissolved oxygen strongly affects pit formation, surface roughness, and etching rate (Fukidome & Matsumura, 2000). Ammonia-peroxide cleaning studies also describe Si surface evolution as a competition between oxidation of Si and dissolution of the resulting oxide in alkaline media,

producing roughening when the formation and dissolution of hydrous silicon oxides are locally imbalanced (Knotter et al., 2000; Lee & Raghavan, 1999).

In the present process, we propose that O_2 does not simply passivate the surface. Instead, it may help generate oxidized or hydroxylated Si sites on freshly exposed surfaces, especially at defects, edges, cracks, and grain boundaries. These oxidized regions may then be destabilized or partially removed in the local NH_3/H_2O environment. Repetition of this oxidation-hydroxylation-dissolution cycle could preferentially attack high-energy regions rather than uniformly removing the whole particle. This is consistent with the EDS maps, where oxygen is enriched at edges and roughened regions, and with the progressive increase in O content as the urea loading increases. It may also help explain why pore formation is accompanied by oxygen incorporation rather than by clean removal of Si.

The role of the polycrystalline feedstock is also important. Polycrystalline Si contains grain boundaries, defects, and impurity-rich regions that are more chemically and mechanically vulnerable than ideal crystalline facets. Alkaline etching studies on polycrystalline Si have shown that grain boundaries and different crystal planes can etch preferentially, leading to interconnected porous structures (Yan et al., 2022). Therefore, in the Urea:Si system, urea-derived species likely exploit pre-existing heterogeneity in the metallurgical-grade Si. Initial cracking and oxide/hydroxide attack could expose fresh defect-rich surfaces, which may then undergo further localized modification. This could establish a reinforcing process in which cracking exposes new surface, newly exposed surface undergoes oxidation or hydroxylation, and chemically weakened regions become more susceptible to further opening.

Nitrogen incorporation may occur through surface reactions rather than bulk nitridation. NH_3 can interact with hydroxylated or oxidized Si surfaces through hydrogen bonding, acid-base interactions, or formation of aminosilicon/oxynitride-like surface motifs. Studies of SiO_2 and NH_3 show that NH_3 can form SiO_2–NH_3 complexes and $H_2NSiOOH$-type species, supporting the possibility of ammonia-derived modification of silica-like surface sites (Zhou & Chen, 2001). However, crystalline or stoichiometric Si_3N_4 formation generally requires much higher-temperature NH_3 treatments than used here; porous Si nitridation studies typically use NH_3 annealing above ~860 °C (Mei et al., 2022). Thus, the nitrogen-containing species reported previously for urea-treated Si are more plausibly assigned to surface-bound Si–N/Si–O–N-like environments, adsorbed or reacted urea fragments, NH_x-containing groups, or defect-associated nitrogen species rather than bulk silicon nitride formation.

The final pore architecture is therefore interpreted in terms of two cooperating contributions, consistent with our previous control experiments. The first contribution is chemical porosification, where $NH_3/H_2O/O_2$-derived local chemistry may modify, oxidize, hydroxylate, and partially dissolve vulnerable Si/SiO_x regions. This contribution is consistent with the BJH-resolved mesopore population near 4 nm and the oxygen-rich surfaces. The second contribution is mechanical pore opening, where gas evolution and transient urea-derived condensed phases may generate local pressure, swelling, cracking, and cavity formation. This contribution is consistent with the SEM-visible cracks and voids, the broader BJH feature in the ~80-100 nm range, and with the mercury-intrusion features in the 0.15 to 1 µm range. Together, these chemically and mechanically assisted processes provide a plausible explanation for the hierarchical structure observed in the present work, while the stronger experimental basis for separating these effects comes from the previous control study (Abo-Hamad et al., 2026).

This proposed mechanism is also consistent with the urea-loading dependence. At 0.5:1 and 1:1 Urea:Si, urea is sufficient to initiate surface roughening and mesopore formation, but the amount of molten phase and decomposition products is limited. At 2:1, urea appears sufficient to wet a large fraction of the powder bed and generate sustained local chemical and mechanical interactions, producing the large increase in BET surface area, pore volume, oxygen incorporation, and pore-network accessibility. Increasing the ratio to 4:1 gives only limited additional benefit, suggesting that the process becomes limited by Si surface accessibility, gas escape, intermediate removal, or local saturation of reactive sites rather than by urea availability alone. Excess urea may also decompose away from the Si surface or form transient condensed phases that do not contribute efficiently to pore generation.

Thus, the proposed 400 °C pathway is not simply a case of "urea decomposes and etches Si". A plausible interpretation is that molten urea first infiltrates and coats the Si powder bed; then NH_3/HNCO and condensed intermediates develop locally; oxygen and water may contribute to an oxide/hydroxide-mediated surface corrosion cycle; and simultaneous gas evolution plus intermediate expansion may assist the opening of cracks and cavities. The outcome is a porous, oxygen-enriched Si material in which mesopores and larger accessible pore/void features are consistent with contributions from the same coupled chemical-mechanical process.

From an implementation perspective, the use of commercially available Si powder, inexpensive urea, atmospheric-pressure processing, and a fluorine-free chemistry is favorable for future scale-up. The present process, however, remains a laboratory-scale batch treatment, and translation toward continuous processing would require further optimization of heat and mass transfer, gas handling, reagent utilization or recovery, and overall energy demand. Quantitative assessment of process economics and environmental impact will therefore be required before industrial deployment, and the present work should be regarded as an early-stage laboratory demonstration rather than an industrially validated process. The multiscale pore structure identified here may also be relevant to applications where accessible surface area, mass transport, and internal void space are important. In particular, these characteristics could be beneficial for Si-based battery electrodes and Si-carbon composites, as well as catalytic or other surface-driven applications. Application-specific performance, however, was not evaluated in the present study and requires dedicated investigation.

4. CONCLUSIONS

This study clarifies how urea content and staged thermal evolution govern fluorine-free porosification of polycrystalline Si microparticles at 400 °C. Increasing the Urea:Si ratio enhanced mesopore development up to 2:1, where the BET surface area reached 25.7 $m^2\ g^{-1}$ and the pore volume reached 0.039 $cm^3\ g^{-1}$. Further increasing the urea content to 4:1 gave only minor additional improvement, suggesting that pore formation may become limited by surface accessibility, gas transport, or intermediate removal rather than by urea availability alone.

The resulting porous Si is best described as a hierarchical, chemically modified structure rather than a simply etched powder. Nitrogen sorption revealed a dominant mesopore population near 4 nm together with a broader, less-defined contribution in the ~80-100 nm range, while mercury intrusion showed additional accessible pore/void features from approximately 0.15 µm to 1 µm. SEM and EDS further indicated that porosification is accompanied by surface roughening, cracking, cavity formation, and oxygen enrichment.

TG/DSC showed that the active transformation begins before the final 400 °C hold. In contact with Si, urea undergoes substantial loss during the 135 °C stage and displays decomposition

events shifted to lower temperatures than bulk urea. These findings are consistent with a proposed mechanism in which molten urea first redistributes through the powder bed, followed by localized generation of urea-derived species that may chemically modify Si/SiO_x surfaces while gas evolution and transient condensed phases may assist crack opening and pore formation.

Overall, the 400 °C route is not a single-temperature etching step, but a multistage porosification process controlled by the local contact between urea-derived phases and Si. The 2:1 Urea:Si condition provides a practical balance between reactivity and accessibility, providing a basis for further development toward scalable, fluorine-free production of porous silicon microparticles. Future work should focus on treatment-atmosphere optimization, particle-size and Si-purity effects, direct evolved-gas analysis, continuous processing and scale-up, and evaluation of electrochemical performance and long-term structural stability.

5. ACKNOWLEDGEMENTS

The authors gratefully acknowledge Vesta Si Sweden AB for providing the silicon microparticles and for access to facilities used for nitrogen sorption analysis. We also thank Pedro Berastegui at the Department of Chemistry, Ångström Laboratory, Uppsala University, for performing the TG/DSC measurements. Financial support from the Swedish Agency for Economic and Regional Growth and Region Västernorrland through the IMPHET project is gratefully acknowledged.

6. REFERENCES

Abo-Hamad, A., Phadatare, M., Brandell, D., Hahlin, M., & Örtegren, J. (2026). Porous Structuring of Si Microparticles for Li-Ion Battery Anodes by Urea-Assisted Etching. *ACS Omega*, *11*(8), 13902–13921. https://doi.org/10.1021/acsomega.5c12477

Abo-Hamad, A., Phadatare, M., Lindgren, F., Brandell, D., Hahlin, M., & Örtegren, J. (2025). Safe and cost-effective synthesis of porous silicon using Urea: Structural, morphological, and porosity analysis. *Microporous and Mesoporous Materials*, *397*, 113773. https://doi.org/10.1016/j.micromeso.2025.113773

Chen, L.-C., Chen, M., Tsaur, T.-H., Lien, C., & Wan, C.-C. (1995). Selective etching of silicon in aqueous ammonia solution. *Sensors and Actuators A: Physical*, *49*(1), 115–121. https://doi.org/10.1016/0924-4247(95)01007-N

Cheng, Z., Jiang, H., Zhang, X., Cheng, F., Wu, M., & Zhang, H. (2023). Fundamental Understanding and Facing Challenges in Structural Design of Porous Si-Based Anodes for Lithium-Ion Batteries. *Advanced Functional Materials*, *33*(26), 2301109. https://doi.org/10.1002/adfm.202301109

Fukidome, H., & Matsumura, M. (2000). Effect of dissolved oxygen on etching process of Si(111) in 2.5% NH3 solution. *Surface Science*, *463*(3), L649–L653. https://doi.org/10.1016/S0039-6028(00)00688-9

Kang, R. H., Baek, S. W., Oh, C.-K., Kim, Y. H., & Kim, D. (2025). Recent Advances of Macrostructural Porous Silicon for Biomedical Applications. *ACS Applied Materials & Interfaces*, *17*(4), 5609–5626. https://doi.org/10.1021/acsami.4c18296

Knotter, D. M., de Gendt, S., Mertens, P. W., & Heyns, M. M. (2000). Silicon Surface Roughening Mechanisms in Ammonia Hydrogen Peroxide Mixtures. *Journal of The Electrochemical Society*, *147*(2), 736. https://doi.org/10.1149/1.1393261

Lee, K. T., & Raghavan, S. (1999). Etch Rate of Silicon and Silicon Dioxide in Ammonia-Peroxide Solutions Measured by Quartz Xrystal Microbalance Technique. *Electrochemical and Solid-State Letters*, *2*(4), 172. https://doi.org/10.1149/1.1390773

Mei, S., Guo, S., Xiang, B., Deng, J., Fu, J., Zhang, X., Zheng, Y., Gao, B., Chu, P. K., & Huo, K. (2022). Enhanced ion conductivity and electrode–electrolyte interphase stability of porous Si anodes enabled by silicon nitride nanocoating for high-performance Li-ion batteries. *Journal of Energy Chemistry*, *69*, 616–625. https://doi.org/10.1016/j.jechem.2022.02.002

Moretta, R., De Stefano, L., Terracciano, M., & Rea, I. (2021). Porous Silicon Optical Devices: Recent Advances in Biosensing Applications. *Sensors*, *21*(4), 1336. https://doi.org/10.3390/s21041336

Nocerino, V., Rea, I., Siciliano, G., De Stefano, L., & Primiceri, E. (2024). Polymers modified porous silicon optical (bio)sensors. *TrAC Trends in Analytical Chemistry*, *177*, 117811. https://doi.org/10.1016/j.trac.2024.117811

Sánchez-Salcedo, R., Sharma, P., & Voelcker, N. H. (2025). Advancements in Porous Silicon Biosensors for Point of Care, Wearable, and Implantable Applications. *ACS Applied Materials & Interfaces*, *17*(2), 2814–2843. https://doi.org/10.1021/acsami.4c18273

Schaber, P. M., Colson, J., Higgins, S., Thielen, D., Anspach, B., & Brauer, J. (2004). Thermal decomposition (pyrolysis) of urea in an open reaction vessel. *Thermochimica Acta*, *424*(1), 131–142. https://doi.org/10.1016/j.tca.2004.05.018

Schnakenberg, U., Benecke, W., & Löchel, D. (1990). NH4OH-based etchants for silicon micromachining. *Proceedings of the 5th International Conference on Solid-State Sensors and Actuators and Eurosensors III*, *23*(1), 1031–1035. https://doi.org/10.1016/0924-4247(90)87084-V

Tischer, S., Börnhorst, M., Amsler, J., Schoch, G., & Deutschmann, O. (2019). Thermodynamics and reaction mechanism of urea decomposition. *Physical Chemistry Chemical Physics*, *21*(30), 16785–16797. https://doi.org/10.1039/C9CP01529A

Wang, M., Ou, W.-C., & Yu, Z.-T. (2025). Porous Silicon-Supported Catalytic Materials for Energy Conversion and Storage. *ChemSusChem*, *18*(3), e202401459. https://doi.org/10.1002/cssc.202401459

Wang, Y., & Wang, D. (2026). Advances in porous silicon materials for sensing, energy storage, and microelectronics. *Nanomaterials*, *16*(4), 257. https://doi.org/10.3390/nano16040257

Yan, Z., Jiang, J., Zhang, Y., Yang, D., & Du, N. (2022). Scalable and low-cost synthesis of porous silicon nanoparticles as high-performance lithium-ion battery anode. *Materials Today Nano*, *18*, 100175. https://doi.org/10.1016/j.mtnano.2022.100175

Zhou, M., & Chen, M. (2001). Reactions of silicon dioxide with ammonia molecules: Formation and characterization of the SiO2–NH3 complex and the H2NSiOOH molecule. *Chemical Physics Letters*, *349*(1), 64–70. https://doi.org/10.1016/S0009-2614(01)01192-7

Zhu, N., Qian, F., Xu, X., Wang, M., & Teng, Q. (2021). Thermogravimetric Experiment of Urea at Constant Temperatures. *Materials*, *14*(20). https://doi.org/10.3390/ma14206190

Ali Abo-Hamad
PhD Candidate, Engineering Physics, Mid Sweden University

Ali Abo-Hamad is a final-year PhD candidate in Engineering Physics at Mid Sweden University. He holds a Master of Engineering Science in Chemical Engineering and has previous industrial experience in the silicon sector. His research focuses on silicon-based materials, fluorine-free porous silicon synthesis, and surface/porosity engineering for functional applications. He has also worked on carbon nanomaterials, ionic liquids, deep eutectic solvents, and electrochemical sensor materials.

Søiland, A. K., K. Mørk, A. Muguruza, I. De Meatza, P. S. Ioannou, and Th. Kyratsi. 2026. Recycled silicon kerf-loss towards high-end applications. In *Silicon for the Chemical and Solar Industry XVIII*, edited by M. Tangstad, H. Rong, A. Valderhaug, B. Andresen, H. Dalaker, and I. G. Page. Kristiansand, Norway, September 7–10. https://doi.org/10.55669/oa900817

Recycled silicon kerf-loss towards high-end applications

A.K. Søiland[1], K. Mørk[1], A. Muguruza[2], I. De Meatza[2], P. S. Ioannou[3], Th. Kyratsi[3]

[1]ReSiTec AS, Kristiansand, Norway, aks@resitec.no
[2]CIDETEC, Basque Research and Technology Alliance (BRTA), 20014 Donostia-San Sebastian, Spain
[3]Department of Mechanical and Manufacturing Engineering, University of Cyprus, 1678 Nicosia, Cyprus

Keywords: secondary silicon, recycled silicon kerf-loss, lithium-ion batteries, thermoelectric modules

Abstract
ReSiTec has developed an industrial scale process for recycling silicon kerf-loss from the photovoltaic industry. Two high-end applications have been assessed for this material, as anode material for lithium-ion batteries (LIBs) and into silicides for thermoelectric modules (TEMs). The resulting product from the industrial process is a fine powder material of purity 3-4 N (excluding carbon and oxygen), mean particle size (d50) of 700 nm, carbon footprint of 1 kg CO_2 eq/kg, and a silicon oxide layer thickness of 1-2 nm, the latter considered critical for use into LIBs. A comparison study with commercially available primary silicon for LIBs showed comparable electrochemical results between the recycled silicon kerf-loss and the primary silicon with specific capacities from 706 mAh/g to 756 mAh/g and similar cycling stability. State-of-the-art cycling stability is demonstrated for the recycled silicon kerf-loss in a Si-C composite drop-in solution, with over 400 cycles above 80% State-of-Health (SoH) in 1 Ah pouch cell testing. The recycled silicon kerf-loss was tested into manganese- and magnesium silicides for TEMs. A 16-leg prototype was made exhibiting a high-power density. Accordingly, the recycled silicon kerf-loss derived from the industrial process proves its applicability in two high-end powder applications.

1. INTRODUCTION

Over the past decades solar power has grown exponentially. The cumulative capacity surpassed 2 TWp in 2025 and is growing approximately 25% per year [Solar Power Europe: Global Market Outlook for Solar Power 2025-2029, 2025, Ember: Global Electricity Review 2026]. Silicon kerf-loss which is generated during fixed abrasive sawing (FAS) of ingots for the photovoltaic industry (PV) constitutes a major secondary silicon source. In 2023 this secondary source amounted to more than 400 000 tonnes per annum [Yang *et al.*, 2025]. There are strong economic and environmental drivers to upcycle this silicon source, aiming at preserving the inherent value of the material. This has resulted in extensive research on process development and various applications areas have been explored, such as thermoelectric modules, silicon feedstock to PV, in alloying (Al-Si, Fe-Si), for hydrogen production, for silicon nitride production and as anode material in lithium-ion batteries (LIBs) [Mangelis *et al.*, 2024, Halvorsen *et al.*, 2017, Drouiche et al., 2014, Huang *et al.*, 2018, Wei *et al.*, 2020, Kao *et al.*, 2016, Jin *et al.*, 2019, Wagner *et al.*, 2019, Zheng *et al.*, 2022, Hengsong *et al.*, 2023, Ma *et al.*, 2020]. Particularly attractive from a circularity viewpoint is recycling back into silicon feedstock for the PV industry. This would however necessitate phase transformative process steps requiring high energy inputs, either through a metallurgical refining route or through a chemical vapour deposition route (CVD). Aiming to upcycle this side/waste stream towards high-end applications where the inherent powder properties of silicon kerf-loss are exploited directly would be beneficial as phase transformative steps can be avoided.

This work is licensed under the Creative Commons Attribution 4.0 International License. To view a copy of this license, visit https://creativecommons.org/licenses/by/4.0/

Both LIBs and thermoelectric modules (TEMs) represent advanced applications where a fine silicon powder can be exploited. Silicon is considered the next generation anode material for LIBs due to its high specific capacity (~10x that of graphite). During lithiation/de-lithiation silicon is subject to an expansion of 300% causing cracking of particles. This leads to a continuous capacity degradation due to new solid electrolyte interphase (SEI) formation, yielding poor cyclability. Today, concepts like nanosizing silicon particles, SiO_x and Si-C (composites) are solutions that can offer higher cycling stability. In 2023 around 30% of the anodes contained silicon in the form of SiO_x or Si-C (composites) [IEA: Global EV Outlook 2023]. The type of silicon typically used for Si-C composites is either milled metallurgical grade silicon or nano-sized silicon from a chemical vapour deposition. However, converting to already sub-micrometer sized recycled silicon kerf-loss can provide significant reductions in cost and carbon footprint. One crucial aspect for the performance as anode material is the surface properties of silicon particles. Especially the oxide layer thickness needs to be controlled or limited in the processing of the silicon kerf-loss filter cake material. The thickness of the silicon oxide layer is of importance for the transport of electrons and lithium-ions and lithium-ion storage capacity, where severe impacts on electrochemical performance have been observed for oxide layer thickness above 3 nm [Schnabel *et al.* (2020), Jiang *et al.* 2024].

Although thermoelectric generators (TEGs) have not yet reached a high level of commercial maturity, silicides are promising thermoelectric materials in terms of economy, sustainability and efficiency for intermediate temperature applications. Utilisation of recycled silicon instead of primary silicon for the manufacturing of the silicides could lower the cost and thereby aid the establishment of TEGs as a sustainable technology in future years [Mangelis *et al.*, 2024, Ioannou *et al.*, 2025, Mangelis *et al.*, 2026].

Resitec has developed a proprietary energy efficient industrial scale processing route for silicon kerf-loss filter cake material to a fine powder material targeted for high-end applications. The main characteristics of the material, including its carbon footprint, are reviewed and assessed with regards to its applicability as anode material for LIBs. Furthermore, electrochemical performance is evaluated through testing and comparison with commercially available nanosized silicon in coin cells and validated in 1 Ah pouch cells, providing new insight into industrially processed silicon kerf-loss as alternative silicon anode material for LIBs. Moreover, novel results, obtained from prototype thermoelectric devices based on p-type manganese silicides and n-type magnesium silicides respectively, are presented.

2. RECYCLED SILICON KERF-LOSS CHARACTERISTICS AND PERFORMANCE IN LIBS AND TEMS

2.1 Industrial route for silicon kerf-loss filter cake

ReSiTec has developed a proprietary low energy intensive industrial scale processing route for silicon kerf-loss filter cake material yielding a recycled silicon powder material targeted towards high-end applications (product and process patents granted). The processing route consists of three main steps (2-4), see fig 1, where step 2 pretreatment is a chemical purification of the silicon kerf filter cake for purification, step 3 is a drying step and in step 4 the post treatment the material is deagglomerated and classified to a fine-grained powder material. Incoming filter cake materials contain from 30-50 wt% moisture, typically 42-48 wt%, while

the resulting fine powder materials exhibit < 0.5 wt% moisture and with a purity of 3-4N (excluding carbon and oxygen).

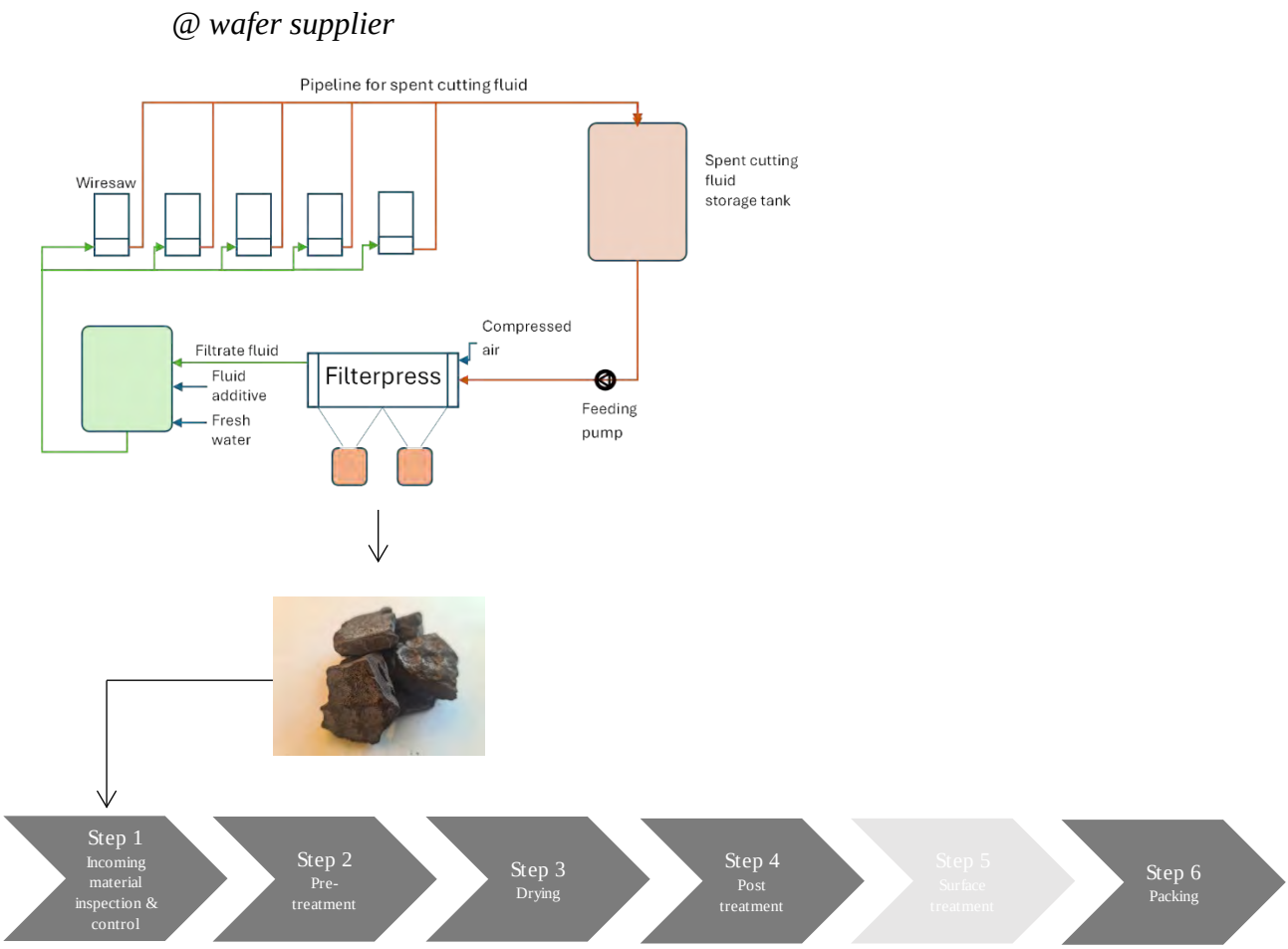

Figure 1: Process flow sheet for ReSiTec's industrial route for recycling of silicon kerf-loss, where step 5 is under development.

2.2 General characteristics of silicon kerf-loss

Silicon wafers for the photovoltaic industry are produced through cutting of high-purity monocrystalline ingots. In the FAS wafering process ultrathin high carbon steel wires of thickness ~60 µm is used. Diamonds of size 8-20 µm are attached to the wires with an electroplated nickel coating or resin bonded [Kumar and Melkote, 2018]. Silicon kerf-loss is the fine saw dust (waste/side stream) that is generated alongside the wafers. Due to the common sizing of the wires and diamonds between most wafer producers there are some general characteristics of the silicon kerf-loss particles. The particle size distribution of the silicon kerf-loss is one feature that is comparable between various sources showing a d50 ~ 700 nm, see figure 2 a). The specific surface area measured of the silicon kerf-loss sources ranges from 20 to 26 m^2/g [Søiland *et al.*, 2024]. Converting this surface area to spherical particles would represent a size of ~100 nm. However, the shape of the silicon kerf-loss particles is very distinct; flake-like in morphology and can extend up to several micrometres but with a thickness of only a few tens nanometres. In addition, it typically contains nanosized particles that exhibit lower anisotropy, see figure 2 a). Another common feature of these particles is their semi-amorphous structure. A thorough study of the crystallinity conducted

with X-ray powder diffraction (XRPD), nuclear magnetic resonance (NMR) and Raman spectroscopy of three different silicon kerf-loss filter cake sources from ReSiTec revealed that the silicon kerf-loss particles consist of ~50% amorphous phase and that the crystalline fraction is present as small nanosized crystals within an amorphous matrix [Heintz *et al*. 2023].

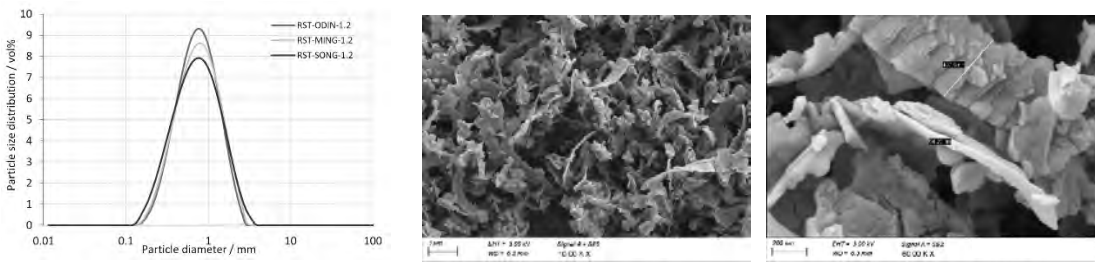

Figure 2: a) Particle size distribution of three different sources of silicon kerf-loss filter cake measured with laser diffraction (Malvern 2000), b) overview image with secondary electron image at 10 K X, c) detailing of silicon kerf-loss flake thickness and width with secondary electron image at 60 K X

2.3 Chemical- and surface characteristics of recycled silicon kerf-loss

The chemical composition of the silicon kerf-loss filter cakes shows more variations between suppliers than the sizing, morphology and structural characteristics which are directly linked to the wire thickness, diamond size and cutting speed. Influencing strongly the impurities is the sacrificial beam material, glue, cutting fluid, wire wear and dopant strategy. Some producers use beam material made from $Al(OH)_3$ in mix with for instance polymethylmethacrylate (PMMA) or similar poly resins while others use aluminium free beam materials. Therefore, the aluminium contents can vary strongly between suppliers, see figure 3. Nickel, an impurity originating from the nickel coating on the wire are more comparable between the producers. For iron there is larger variations, but this impurity is strongly linked to wear of the wires. While most of the impurities in silicon kerf-loss filter cake are present as separate particles the dopants are dissolved in the silicon bulk. The typical dopants in use today are boron, phosphorus, gallium and antimony (emerging). The most common is phosphorus due to the high share of n-type wafers (70%) [Fraunhofer ISE Photovoltaic Report, 2025]. For the LIB application the presence of dopants within the silicon bulk is beneficial since the electron conductivity will increase compared to high purity undoped silicon. The pretreatment step developed efficiently reduces particularly aluminum, nickel and iron, as seen in figure 3 below.

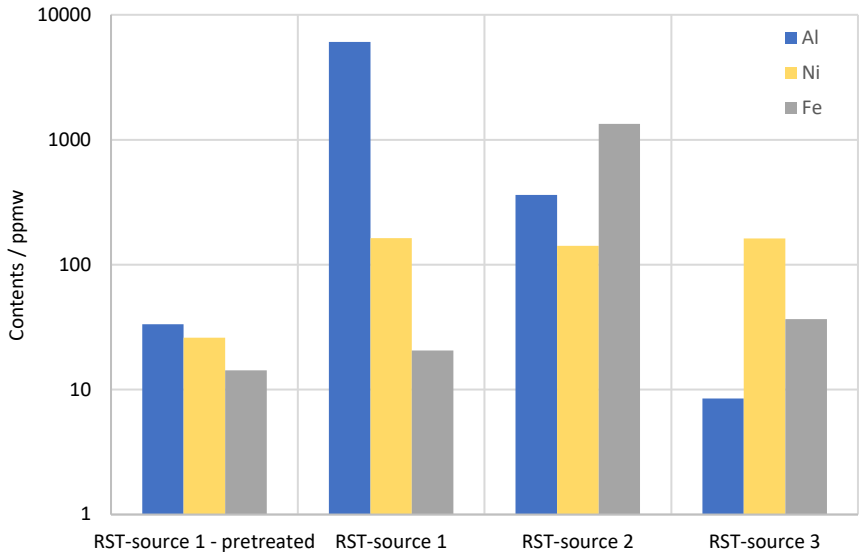

Figure 3: Main metallic impurities in three different sources of silicon kerf-loss and one pretreated source (source 1), measured with inductively coupled plasma mass spectrometry (ICP-MS)

The surface of the silicon kerf-loss particles gets readily oxidized due to the large surface area and the high stability of the Si-O bond [452 kJ/mol]. Furthermore, the numerous dangling bonds present after FAS increases the reactivity of the powder. Both water quality and the cutting fluid composition may influence the stability of the native oxide layer formed initially on the filter cake [Benayad *et al.*, 2016]. Increasing storage time is another parameter that similarly to larger sized silicon powder materials can reduce the reactivity towards water [Sunde, 2024]. The typical silicon kerf-loss filter cake materials from the wafer suppliers contains 40 – 50 wt% moisture and can therefore be subject to the following overall reactions:

$Si_{(s)} + H_2O_{(l)} = SiO_{2(s)} + H_{2(g)}$ ΔH_r^0= -339 kJ/mol at standard state conditions

$Si_{(s)} + H_2O_{(g)} = SiO_{2(s)} + H_{2(g)}$ ΔH_r^0= -427 kJ/mol at standard state conditions

$Si_{(s)} + O_{2(g)} = SiO_{2(s)}$ ΔH_r^0= -911 kJ/mol at standard state conditions

The exothermic nature of all reactions can create self-enhancing and propagating reactions under certain conditions leading to thermal runaways. Furthermore, the release of hydrogen accompanying the reactions with water poses serious safety risk and careful control of the drying process and understanding of variations in the reactivity of silicon kerf-loss from different sources is therefore necessary.

Controlling or limiting the silicon oxide layer thickness on the particles is crucial for the suitability of the recycled silicon in downstream applications like LIBs. The silicon oxide layer thickness will influence the transport of electrons and lithium-ions. A study of nanosized chemical vapour deposited silicon with a SiO_2 layer of 6.2 nm negative effects on the electrochemical performance was observed that was attributed to a slowing down of the lithium-ion transport at the silicon-oxide/silicon interface [Xun *et al.*, 2011]. In a study of SiO_2 coatings a thickness below 3 nm was found to be preferred to ensure high round-trip energy efficiency and high-rate capability [Schnabel *et al.*, 2020]. While the above-mentioned studies both worked with chemical vapour deposited silicon and monocrystalline silicon, in a recent

article the impact of oxidation on the electrochemical performance specifically for silicon kerf-loss was investigated [Jiang *et al.*, 2024]. They report a clear detrimental effect for increased SiO_x-layer thicknesses which is different to previously reported results on nanosized silicon. For the lowest oxygen contents (2.5 wt%) with a SiO_x thickness of 2.3 nm a good electrochemical performance and cycling stability is reported, while it deteriorates with increasing oxygen contents leading to a loss of Li-ion storage capacity at 35.8 wt% of oxygen. Furthermore, the expansion of the electrodes after 100 cycles showed increasing expansion with increasing oxygen contents. These findings highlight the importance of limiting the SiO_x layer thickness for recycled silicon kerf-loss targeted towards an application such as LIBs.

The SiO_x/SiO_2 layer in the recycled silicon kerf-loss has been characterised with both field-emission gun transmission electron microscopy (FEG-TEM) and X-ray photoelectron spectroscopy (XPS) [Søiland *et al.*, 2023, Stokkan *et al.* 2022]. A thickness of the uniform oxide layer from 1-2 nm is found by Scanning Transmission Electron Microscopy-Electron Energy Loss Spectroscopy (STEM-EELS), see figure 4 a). This correlates well with the thickness estimated from XPS. Furthermore, according to the XPS results this layer seems to be dominated by SiO_2. The total oxygen contents were measured to 4.2 wt% which is significantly higher for a narrower oxide layer than in the study of Jiang *et al.* This can be explained either by a smaller particle size distribution in the material investigated or higher oxygen contents in the silicon-oxide layer as the XPS result shows.

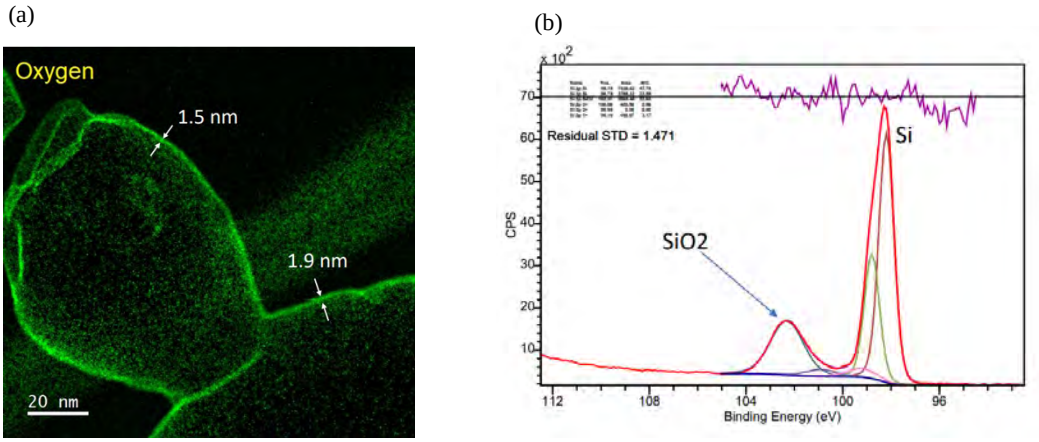

Figure 4: a) STEM-EELS characterization of the silicon particles, determination of oxide layer thickness. **b)** XPS spectra of the recycled silicon particles, showing the peaks Si 2p core electron for SiO_2 and Si respectively, estimated thickness of the oxide layer 1-2 nm [Søiland *et al.*, 2023, Stokkan *et al.*, 2022]

2.4 Life cycle assessment

A screening life cycle assessment has been conducted for the recycled silicon kerf-loss (ReSite™), this analysis is limited to greenhouse gas emissions (CO_2 equivalents). The functional unit for this screening LCA is production of 1 MT of recycled silicon kerf-loss powder, with purity 3-4 N (excl. C and O) and d50 < 1.5 µm, at factory gate. System boundaries for the analysis include greenhouse gas emissions from production of sources, transport and energy use for production of the recycled silicon kerf-loss. For the footprint of the source (silicon kerf-loss filtercake) an allocation method based on a financial basis has been employed. The screening LCA for the recycled silicon kerf-loss yields a carbon footprint of ~1 kg CO_2 eq/kg. A comparison to the carbon footprint of metallurgical-grade silicon, produced with

renewable and non-renewable energy, by use of data from the Ecoinvent database is shown in Figure 5.

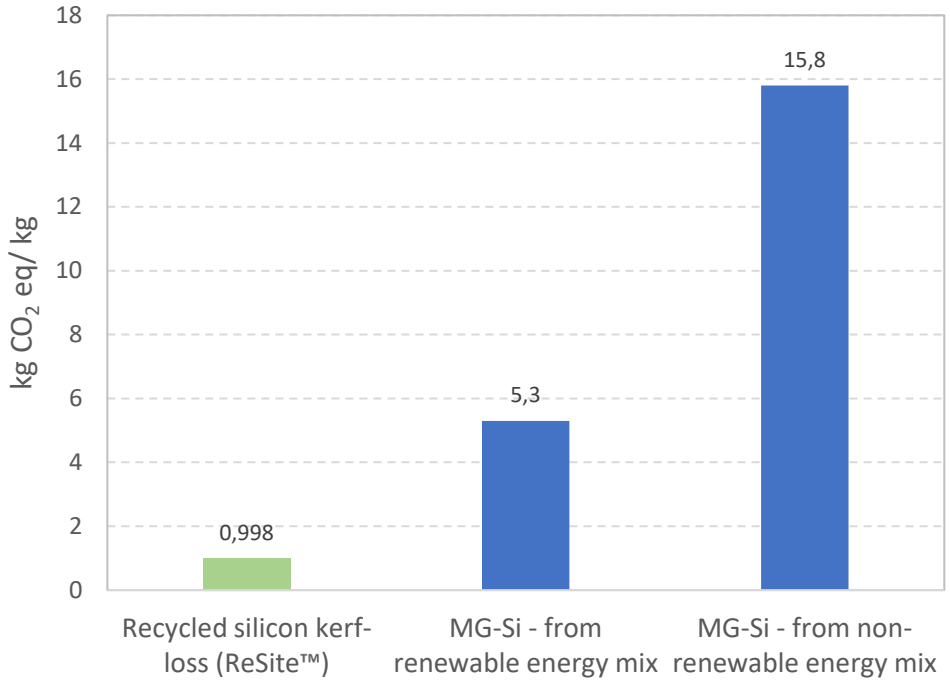

Figure 5: Carbon footprint from screening LCA for recycled silicon kerf-loss (ReSite™) compared to virgin MG-Si produced with renewable energy mix and with non-renewable energy mix with data from Ecoinvent database.

2.5 Recycled silicon kerf-loss as anode material in LIBs

Comparison study with commercial nano-sized silicon (half-cell testing)

The industrially processed recycled silicon kerf-loss has been tested as anode material directly in mix with graphite (on slurry level) and in a silicon-carbon composite. To evaluate the suitability of the recycled silicon kerf-loss in LIBs, half-cell testing comparing with commercially available nano-sized silicon (d50 ~ 40 nm and 100 nm) for LIBs was performed initially. The parameters for the half-cell testing are summarized in table I below.

Table I: Coin cell configuration and test conditions

Slurry formulation	Loading	Counter electrode & Separator	Electrolyte	Formation step	Cycling C-rate
12 wt% silicon /80 wt% graphite (Gr) /3 wt% sodium carboxymethyl cellulose (CMC) / 3 wt% styrene-butadiene-rubber (SBR) / 2 wt% carbon black (CB)	2.2 mAh/cm²	Lithium metal & Celgard 2400	1.2 M $LiPF_6$ in EC/EMC with 2% VC and 10% FEC	2xC/20 and 1xC/10 in the voltage range 0.05 V to 1 V	C/3

The average specific capacities from the first discharge range from 706 to 756 mAh/g-Si-Gr with the two recycled silicon kerf-loss samples exhibiting the lowest and highest specific capacities (figure 6 a). One recycled silicon kerf-loss sample received a surface treatment; this could be the reason for the slightly lower capacity observed. It also correlates with a higher first cycle efficiency (FCE) for this sample. The first cycle efficiencies of the recycled silicon kerf-loss samples are comparable to the reference samples which exhibit the lowest (86%) and highest (93.2%) FCE in this test.

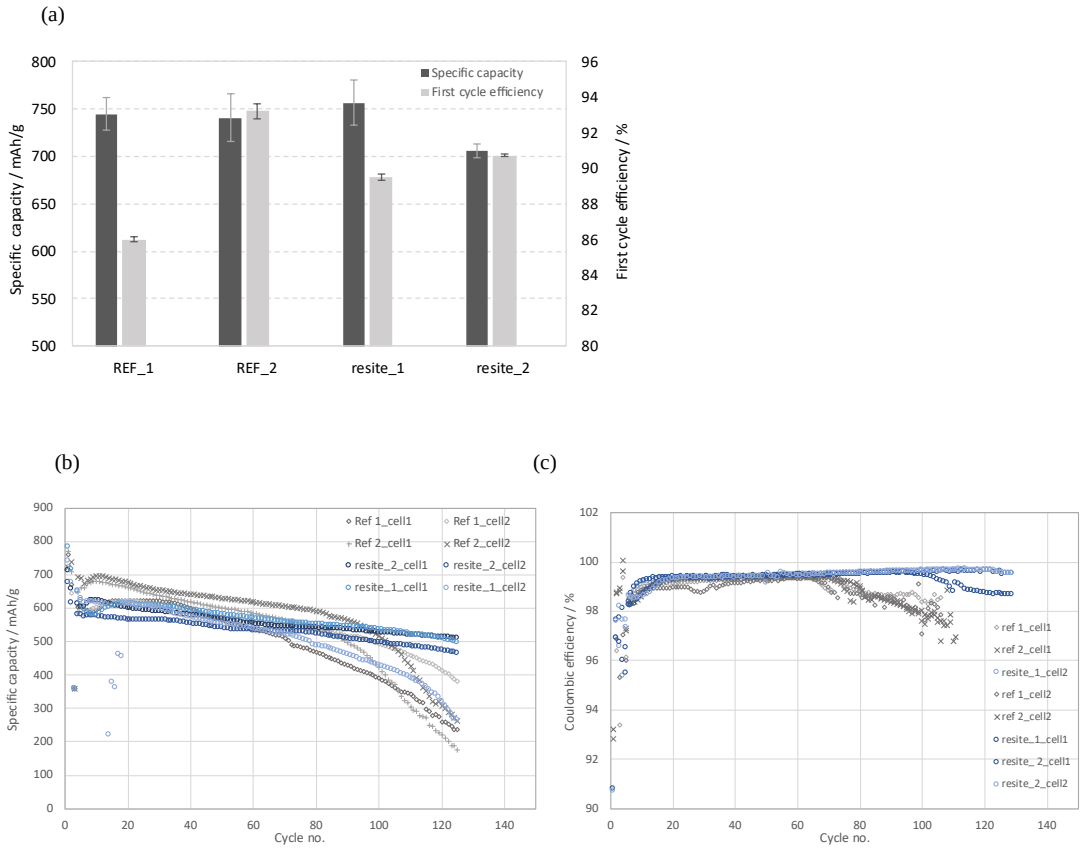

Figure 6: a) Average specific capacities after first discharge and first cycle efficiencies for half-cells with recycled silicon kerf-loss from the industrial processing line, where sample 2 received a surface treatment in addition, and reference commercially available nanosized silicon samples; b) Specific capacity for half-cells with processed silicon kerf and reference silicon samples as a function of cycle number, cycling rate after formation cycles is C/3 and 1.0 V to 50 mV vs. Li/Li$^+$; c) Coulombic efficiencies for the same half-cells.

The specific capacities and coulombic efficiencies of the half cells when cycled at C/3 and 1.0 V to 50 mV versus Li/Li$^+$ as function of cycle number are shown in figure 6 b) and c). Cycling stability on par with the reference materials is demonstrated for the recycled silicon kerf-loss samples (resite_1 and resite_2). Furthermore, detailed Differential Voltage Analysis (DVA) of the galvanostatic data reported previously showed that only the recycled silicon kerf-loss samples maintain some silicon activity beyond 120 cycles [Søiland *et al.* 2023].

Testing into 1 Ah pouch cells: recycled silicon kerf-loss directly into electrode (slurry mix) and in Si-C composite

Recycled silicon kerf-loss from the industrial processing route has been tested in 1 Ah pouch cells both directly into slurry mixing with graphite and as a silicon-carbon composite. The recycled silicon kerf-loss directly used into electrode preparation was subjected to a surface treatment after the industrial processing. Cell specific data for both types of materials tested are given in table II. After the formation protocol the cells were cycled at C/3 and at different applied pressures with a pressure plates and springs system.

Table II: Cell specific data for the materials tested into 1 Ah pouch cells

Type of active material (AM)	Slurry formulation	Loading	Cathode electrode and loading	Electrolyte	Formation protocol
Recycled kerf-loss in Si-C composite	94 wt% AM /2 wt% CMC / 2 wt% SBR / 2 wt% CB	3.3 mAh/cm^2 Specific capacity: 480 mAh/g	NMC622 (AM) 94 wt% AM /3 wt% CB / 3 wt% PVDF 3 mAh/cm^2	1 M $LiPF_6$ in EC:DMC 1:1 (vol/vol) + 10% FEC + 1%VC + 1% LiTFSI	0.05C CC-CV Charge / CC Discharge, 40 hrs
Recycled kerf-loss directly in electrode (slurry mixing)	10.2 wt% recycled silicon kerf-loss / 74.8 wt% graphite /5 wt% CMC / 5 wt% SBR / 5 wt% CB	3.52 mAh/cm^2 Specific capacity: 720 mAh/g-Si-Gr			

The initial discharge capacities of both materials provide the expected 1 Ah capacity with initial coulombic efficiency above 85%. However, the directly used recycled silicon kerf-loss shows a faster capacity decay when cycled at full operating window of 3.0-4.2 V (100% DoD, Depth of Discharge), as shown in Figure 7 a. The reduction of the DoD by using a higher discharge cut-off voltage, increases the cycling stability from ca. 75 to 250 cycles at 80% DoD (3.15 V) with less than 16% reduction of the discharged cell capacity (0.8 Ah vs 0.95 Ah).

However, for the recycled silicon kerf-loss incorporated in a Si-C composite drop-in solution, a high storage capacity and cycling stability competitive to state-of-the-art silicon for LIBs is obtained, with more than 400 cycles above 80% SoH (State-of-Health) or capacity retention at C/3, see figure 7 b. The composite solution has gained momentum the last years as a concept that can bring stability for a silicon-based anode and is dominating along with SiO_x for silicon containing anodes [Benchmark minerals]. These results show that recycled silicon kerf-loss is compatible with other primary silicon sources in a Si-C composite concept and that only the composite solution provides a high cycling stability at 100% DoD and without the need of high applied pressure.

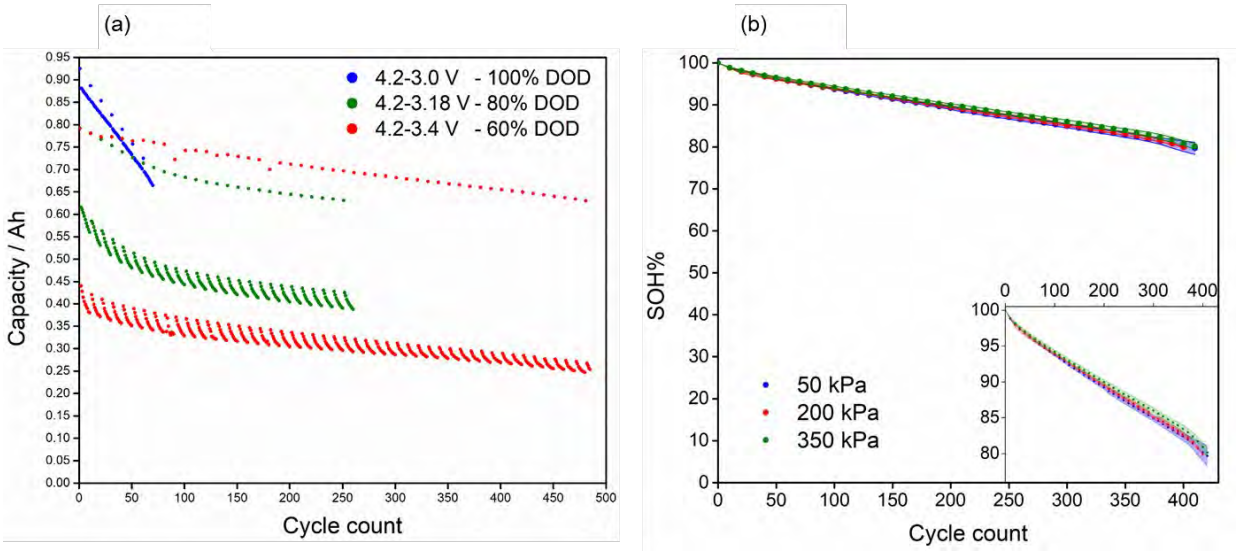

Figure 7: Cycling performance of pouch cells (1 Ah) with NMC cathode @ cycling rate C/3. **a)** Capacity as a function of cycle number for the recycled Si-kerf-loss anode at different discharge cut-off voltages (%DoD); **b)** Capacity retention or State-of-Health (SoH) for the Si-C composite anode at 100%DoD and different applied pressure.

2.6 Recycled silicon kerf-loss in thermoelectric modules

For testing into TEMs n-type magnesium silicides ($Mg_2(Si,Sn)$) and p-type higher manganese silicide have been manufactured with recycled silicon kerf-loss. Metallization was achieved using sputtered layers and Ni/Cu bilayers, while bonding was performed via pressure-assisted silver sintering. Prototype TEMs based on a 4 -leg proof-concept design was built with recycled silicon kerf-loss and also upscaled to 16-leg TEMs [Ioannou *et al.*, 2025]. Figure 8 a) shows the power density as a function of temperature, while b) shows the comparison between experimental and modeled results for the 16-leg and 4-leg variants. As the recycled silicon kerf-loss used in this study originates from a first processing iteration, there remains significant potential for further optimization of the recycled silicon material for this application. Nevertheless, the power density achieved with the 16-leg (8-couple) prototype appears to be the highest reported for a "traditional" (rigid) TEM based on silicides with more than 4-legs (2-couples). Thus, it shows another possible high-end application for the recycled silicon kerf-loss and suggests further room for improvements through optimization of contact resistance (r_c).

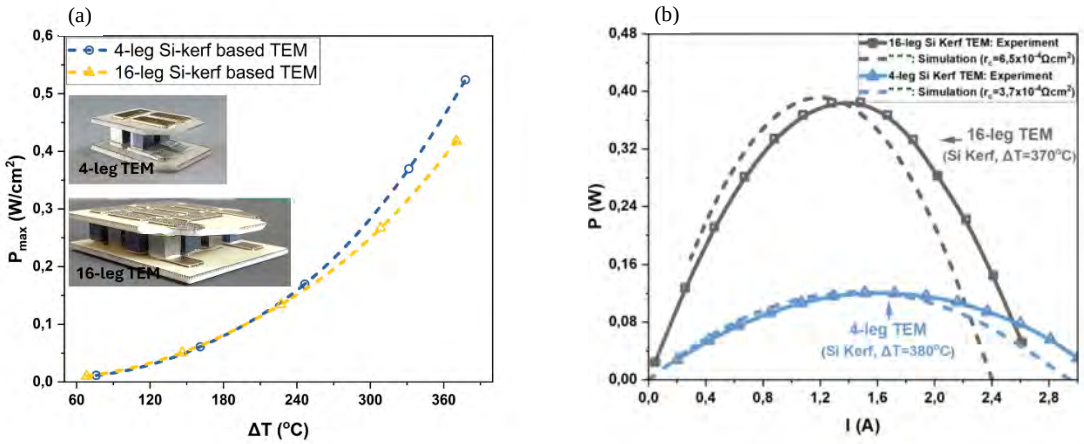

Figure 8 a) Power density as a function of temperature for TEMs manufactured from magnesium- and manganese- silicides based on recycled silicon kerf-loss **b)** Comparison between experimental and modeled power-current characteristics of 16-leg and 4-leg TEMs based on recycled Si-kerf TE materials at $\Delta T_{max} \approx 380$ °C and for simulated r_c values of 6.5×10^{-4} Ωcm² and 3.7×10^{-4} Ωcm² respectively [Ioannou *et al.*, 2025].

3. CONCLUSIONS

As a secondary silicon source, recycled silicon kerf-loss from the ReSiTec's industrial route has shown its applicability for integration into advanced powder applications. The material has a purity of 3-4N, is partially amorphous with a particle size of d50 ~ 700 nm, contains a silicon oxide layer thickness of 1-2 nm, and exhibits a carbon footprint of 1 kg CO_2 eq/kg. A comparison study in half-cells with commercially available nanosized silicon demonstrated comparable electrochemical performance and thus a potential upcycling path. State-of-the-art performance with over 400 cycles above 80% SoH is demonstrated for the recycled silicon kerf-loss tested in a Si-C composite in 1 Ah pouch cells. It could therefore be a viable alternative to primary sources currently being used, still ensuring comparable electrochemical performance and cycling stability. Furthermore, the recycled silicon kerf-loss shows its potential use in manganese- and magnesium silicides for thermoelectric modules yielding high power densities for a 16-leg device. The use of silicon in high-end applications as LIBs and TEMs can therefore be facilitated by converting into a secondary silicon source such as recycled silicon kerf-loss providing reductions in both cost and carbon footprint.

4. ACKNOWLEDGEMENTS

The authors cordially thank the ICARUS project (HORIZON 2020, Grant agreement number 958365).

5. REFERENCES

Solar Power Europe: Global Market Outlook for Solar Power 2025-2029, 2025, https://www.solarpowereurope.org/insights/outlooks/global-market-outlook-for-solar-power-2025-2029

Ember Energy: Global Electricity Review 2026, 2026,

https://ember-energy.org/latest-insights/global-electricity-review-2026/

F. Yang, W. Yu, Y. Chen, H. Yuan, W. Jiang, T. Xiong, Recovery of silicon from polysilicon kerf loss by employing Mg-Gd alloy scrap as deoxidation reagent during vacuum magnesium thermal reduction, *Separation and Purification Technology*, Vol. 373, 2025, DOI: 10.1016/j.seppur.2025.133633

P. Mangelis, A. Sousanis, G. Mesaritis, P.S. Ioannou, A-K Søiland, Y. Xu, Th. Kyratsi, Mg2Si0.4Sn0.6 and Mg2Si0.6Sn0.4 based on Recyclable Si Kerf Derived from PV Manufacturing, *ACS Appl. Electron. Mater.*, 6, 2988−2998, 2024, DOI: 10.1021/acsaelm.3c01802

Halvorsen, T., Moen, M., Mørk, K., Grosset-Bourbange, D., Rivat, P., Hajjaji, H., Brizé, V., Coustier, F., Cabriss Recycling of Si-kerf from PV, *33rd European Photovoltaic Solar Energy Conference and Exhibition*, 1524-1528, 2017

Drouiche, N., Cuellar, P., Kerkar, F., Medjahed, S., Boutouchent-Guerfi, N., Hamou, M.O., Recovery of solar grade silicon from kerf loss slurry waste, *Renewable and Sustainable Energy Reviews,* Vol. 32, 936-943, 2014, DOI: 10.1016/j.rser.2014.01.059

Huang, L., Chen J., Fang, M., Thomas, S., Danaei, A., Luo, X., Barati, M., Clean enhancing elimination of boron from silicon kerf using Na_2O-SiO_2 slag treatment, Journal of Cleaner Production, Vol 186, 718-725, 2018, DOI: 10.1016/j.jclepro.2018.03.152

Wei, D., Gao, S., Kong, J., Jin, X., Jiang, S., Zhou, S., Zhuang, Y., Yin, H., Xing, P., Recycling silicon from silicon waste by Al-Si alloying, *Journal of Cleaner Production*, Vol. 251, 2020, DOI: 10.1016/j.jclepro.2019.119647

Kao, T-L., Huang, W-H., Tuan, H-Y., Kerf-loss silicon as a cost-effective, high-365 efficiency, and convenient energy carrier: additive-mediated rapid hydrogen production and integrated systems for electricity generation and hydrogen storage, *J. Mater. Chem. A*, 4, 12921-12928, 2016, DOI: 10.1039/c6ta03657k

Jin, X., Kong, J., Zhou, X., Xing, P., Zhuang, Y., Recycling of silicon kerf loss derived from 369 diamond-wire saw cutting process to prepare silicon nitride, *Journal of Cleaner Production*, Vol. 247, 370, 2020, DOI: 10.1016/j.jclepro.2019.119163

Wagner, N.P., Tron A., Tolchard, J.R., Noia, G., Bellmann, M. P., Silicon anodes for lithium-ion batteries recovered kerf powders, *Journal of Power Sources* 414, 486-494, 2019, DOI: 10.1016/j.jpowsour.2019.01.035

S. Zheng, S. Cheng, Z. Fan, Z. Wang, Recycling of Si slurry as high performance anode materials for Lithium-ion batteries, *Silicon for the chemical and solar industry XVI*, ISBN 978-82-692919-0-2, 2022, DOI: 10.2139/ssrn.4117731

Hengsong, J., Z. Liu, X. Li, J. Li, Z. Jan, K. Tang, Recycling silicon waste from the photovoltaic industry to prepare yolk-shell Si@void@C anode materials for lithium-ion batteries, Processes, vol. 11, no. 6, 1764-1778, 2023, DOI: 10.3390/pr11061764

Ma, Q. , J. Qu, X. Chen, Z. Zhao, Y. Zhao, H. Zhao, H. Xie, P. Xing, H. Yin, Converting micro-sized kerf-loss silicon waste to high-performance hollow-structured silicon/carbon composite anodes for lithium-ion batteries, *Sustainable energy and fuels*, Issue 9, 2020, 10.1039/D0SE00831A

International Energy Agency (IEA): Global EV Outlook 2023 Catching up with climate ambitions, https://iea.blob.core.windows.net/assets/dacf14d2-eabc-498a-8263-9f97fd5dc327/GEVO2023.pdf

M. Schnabel, S.P. Harvey, E. Arca, C. Stetson, G. Teeter, C. Ban, P. Stradins, Surface SiO_2-thickness controls uniform-to-localized transition in silicon anodes for lithium-ion batteries, *ACS Appl. Mater.Interfaces*, 12, 24, 2020, DOI: 10.1021/acsami.0c03158

Y. Jiang , S. He, S. Ma, F. Xi, I.M. Gavrilin, Z. Tong, J. Lu, N. Wan, W. Ma, Y. Zhu, P. Wu and S. Li, Controlling Oxidation of Kerf Loss Silicon Waste Enabling Stable Battery Anode, *Processes*, 12, 1173, 2024, DOI: 10.3390/pr12061173

Søiland, A-K., Meatza, I., Muguruza, A., Xu, Y., Bellmann, M., Silicon kerf-loss as potential anode material in Lithium-ion batteries, Front. Photonics, Vol.5, 2024, DOI: 10.3389/fphot.2024.1332830

Søiland, A-K., Mørk, K., Heintz, M.C., Bellmann, M., Xu, Y., Recycled silicon as potential anode material in Lithium-ion batteries, *Poster at Advanced battery power conference in Aachen*, April 27-28, 2023

Heintz, M.C., J. Grins, A. Jaworski, G. Swensson, T. Thersleff, W. Brant, R. Lindblad, A. Naylor, K. Edström, G. Hernandez, Photovoltaic wafering silicon kerf loss as raw material: example of negative electrode for lithium-ion battery, *ChemElectroChem* Vol. 10, Issue 19, 2023, DOI: 10.1002/celc.202300331

G. Stokkan, Y. Xu, M. Bellmann, Waste inventory for a circular solar cell production, *ICARUS report*, 2022

Philipps, S. and Warmuth W., Fraunhofer ISE, *Photovoltaics Report*, 2025 https://www.ise.fraunhofer.de/en/publications/studies/photovoltaics-report.html

Ioannou, P.S., P. Mangelis, S. Hadjipanteli, M. Mina, A-K. Søiland, J. Giapintzakis, Th. Kyratsi, Development of silicide thermoelectric modules based on high purity Si and recycled Si-kerf: A contact resistance investigation, *Materials Today Energy*, 49, 2025, DOI: 10.1016/j.mtener.2025.101855

Mangelis, P., P. Ioannou, A-K. Søiland, T. Kyratsi, Structural and thermoelectric properties of Mn(Si1−xAlx)1.75: a commensurate phase mixture approximation, *Mater.Adv.*, 7, 898, 2026, DOI: 10.1039/D5MA00500K

Mangelis, P., A. Sousanis, G. Mesaritis, P.S. Ioannou, A-K Søiland, Y. Xu, Th. Kyratsi, Mg2Si0.4Sn0.6 and Mg2Si0.6Sn0.4 based on Recyclable Si Kerf Derived from PV Manufacturing, *ACS Appl. Electron. Mater.*, 6, 2988−2998, 2024, DOI: 10.1021/acsaelm.3c01802

Kumar, A. and S.N. Melkote, Diamond wire sawing of Solar Silicon Wafers: A sustainable manufacturing alternative to Loose Abrasive Slurry Sawing, *Procedia Manufacturing 21*, 549-566, 2018, DOI: 10.1016/j.promfg.2018.02.156

Beyanad, A., Hajjaji, Coustier, F., Benmansour, M., Chabli, A., Surface chemical-bonds analysis of silicon particles from diamond-wire cutting of crystalline silicon, *Journal of Applied Physics 120*, 2016, DOI: 10.1063/1.4972193

Sunde, M., Effect of Thermal Oxidation on Reactivity of Silicon Powder in Water, *Master Thesis*, 2024

Benchmark Minerals: https://source.benchmarkminerals.com/article/benchmark-launches-silicon-anode-forecast-report

Anne-Karin Søiland
Senior R&D Engineer, ReSiTec AS

Anne-Karin Søiland holds a cand scient degree from the University of Oslo in Physical Chemistry, and a PhD degree in Materials Technology from NTNU (2005) within silicon for solar cells. She worked for 15 years in R&D at Elkem Solar/REC Solar, with significant experience in product development, qualification processes and technical customer support. In 2021 she joined ReSiTec AS focusing on the development of recycled silicon products targeted for advanced powder applications.

Wang, L., J. Bakken, and S. Dahlbom. 2026. Characterization properties of biocarbon pellets for safe transportation and storage. In *Silicon for the Chemical and Solar Industry XVIII*, edited by M. Tangstad, H. Rong, A. Valderhaug, B. Andresen, H. Dalaker, and I. G. Page. Kristiansand, Norway, September 7–10. https://doi.org/10.55669/oa900819

Characterization properties of biocarbon pellets for safe transportation and storage

Liang Wang[1], Jorn Bakken[1], and Sixten Dahlbom[2]
[1]SINTEF Energy Research, Norway, liang.wang@sintef.no
[2]RISE Research Institutes of Sweden, Sweden, sixten.dahlbom@ri.se

Keywords: biocarbon, pellet, water immersion, self-heating, smouldering, safety

Abstract –Replacing the fossil carbon with biocarbon is a promising and effective way to reduce dependence of the metallurgical industry on the fossil carbon and increase sustainability as well. Densification is the process of compressing loose biocarbon into regularly shaped, dense products such as pellets and briquettes. Densification technology serves as a viable and efficient strategy to refine raw biocarbon into high-value forms such as pellets and briquettes, effectively improving its mechanical performance and boosting both mass density and energy density. Despite these improvements, densified biocarbon products remain susceptible to quality degradation when exposed to rainfall or high-humidity environments for short periods during transportation and storage. Systematic study on the thermal stability of densified biocarbon is important for safe transportation and storage of biocarbon, especially in large scale under different conditions. The objectives of this study are to evaluate the mechanical stability of biocarbon pellets upon water immersion treatment and investigate self-heating and self-ignition of biocarbon pellets through different measures. Water immersion and subsequent air-drying significantly degrade the durability of biocarbon pellets, with weight fluctuations returning to baseline but causing severe structural weakening after prolonged exposure. Thermal stability evaluation reveals that pellets undergo thermal runaway and smouldering combustion at temperatures above 145–160°C, accompanied by oxygen depletion and carbon oxide emissions. Consequently, a dual-monitoring approach combining temperature sensors with CO/CO_2 gas detection is recommended to manage self-heating and ignition risks during transport and storage.

1. INTRODUCTION

The global metallurgical industry has long relied mainly on fossil carbon feedstocks, predominantly metallurgical coal and coke. This heavy fossil dependence makes metal production one of the most carbon-intensive industrial sectors worldwide. To address growing global climate constraints, metallurgical facilities in Norway and across international markets are actively developing decarbonization strategies to renovate conventional production workflows and mitigate greenhouse gas (GHG) emissions (Werra, M., et al., 2021). For the short-to-medium term, the substitution of fossil-based metallurgical reductants with sustainably derived biocarbon represents the most technically and economically viable route toward low-carbon metallurgy. Produced via the pyrolysis of renewable biomass feedstocks, biocarbon qualifies as a biogenic, carbon-neutral material under mainstream carbon accounting frameworks (Makgobelele et al., 2021). The CO_2 released during biocarbon reduction is offset by the carbon previously sequestered by parental biomass during vegetative growth, enabling a closed carbon cycle for industrial metallurgical operations.

Despite its unique carbon-neutral advantage, the industrial-scale deployment of raw biocarbon is severely limited by scalability barriers and logistical constraints. Global metallurgical manufacturing consumes tens of millions of tons of coal and coke annually; even partial replacement of these fossil inputs requires a stable, high-volume supply chain that delivers biocarbon with consistent and controllable physicochemical properties (Wang and Skreiberg, 2023). Raw biocarbon typically pyrolyzed at 500–700 °C exhibits low bulk density, high porosity, and poor mechanical stability. Relative to conventional metallurgical coke, raw biocarbon readily fractures and collapses under mechanical stress, generating fine dust

This work is licensed under the Creative Commons Attribution 4.0 International License. To view a copy of this license, visit https://creativecommons.org/licenses/by/4.0/

particles during routine handling, transportation, and storage. This structural fragility causes substantial material loss and introduces critical operational safety hazards (Wang et al., 2018; Wang and Skreiberg, 2023). Mechanical densification of raw biochar into standardized pellets or briquettes provides an effective solution to these inherent deficiencies (Wang et al., 2018). This compaction process converts loose, low-density biocarbon into a high-performance energy and carbon carrier through three key improvements (Ngene et al., 2024). Densification drastically improves volumetric energy density of raw biocarbon, minimizing storage space requirements and reduces long-distance transportation costs (Riva et al., 2021). Densified biocarbon possesses enhanced mechanical durability, resisting physical abrasion and impact during transit and loading. This mechanical robustness effectively reduces material attrition, fine particle shedding, and associated spontaneous combustion risks (Riva et al., 2021). Even with these significant performance enhancements, densified biocarbon pellets remain vulnerable to structural degradation throughout logistical operations. Compressive force, surface abrasion, and high-energy impact—generated by material dropping from conveyors, chutes, and storage containers—progressively undermine the structural integrity of compacted biocarbon products (Ngene et al., 2024). Ambient environmental exposure further exacerbates pellet quality deterioration. Better water resistance is therefore an essential performance indicator that guarantees structural stability of biocarbon pellets under high-humidity conditions or intermittent rainfall during transportation and storage (García et al., 2021). Moisture infiltration not only lowers the calorific value of biocarbon pellets but also destroys internal bonding structures, leading to irreversible structural failure and performance degradation. Currently, there is a lack of systematic investigations into this moisture-induced degradation behaviour. Although Makgobelele et al. (2021) verified that increased binder content improves the water resistance of wood-derived charcoal briquettes, their evaluation was limited to a short-duration 2-hour immersion test. The long-term degradation kinetics and structural evolution of densified biocarbon under sustained moisture exposure remain poorly characterized.

The biocarbons with intrinsic properties such as high porosity and large specific surface area can pose substantial challenges for the large-scale handling, transportation and storage of biocarbon, owing to its high tendency toward self-heating and spontaneous ignition (Restuccia et al., 2019). Self-heating is a thermally hazardous phenomenon triggered by spontaneous exothermic reactions inside porous carbonaceous materials (Wang and Skreiberg, 2023). For biocarbon, this process is predominantly governed by surface oxygen chemisorption, during which gaseous oxygen reacts with active carbon sites to form stable carbon–oxygen surface complexes while continuously releasing thermal energy (Phounglamcheik et al., 2022). When internal heat generation surpasses the rate of ambient heat dissipation, accumulated thermal energy induces thermal runaway, potentially progressing into smouldering combustion or open flaming ignition. Existing studies have confirmed that low-temperature oxygen chemisorption serves as the dominant heat source responsible for the self-heating propensity of biocarbon materials (Restuccia et al., 2019). Beyond oxidative chemisorption, water vapor condensation represents a secondary exothermic mechanism that exacerbates biocarbon self-heating. The thermal interaction between biocarbon and moisture varies dynamically: water condensation releases heat, whereas water evaporation consumes thermal energy. Under humid storage conditions, biocarbon particles and fine residues readily adsorb atmospheric water vapor, and the subsequent condensation process generates instantaneous heat accumulation. This rapid thermal input elevates the baseline temperature of bulk biocarbon stockpiles, acting as a thermal precursor that reduces the energy barrier for intensified oxygen chemisorption and further accelerates self-heating progression. Additionally, humid environments facilitate microbial and fungal proliferation, triggering biological degradation of biocarbon during prolonged storage and transportation. This microbial activity also contributes to gradual temperature elevation and material performance

deterioration (Wang et al., 2017). Current experimental frameworks for evaluating biocarbon self-heating and autoignition risks primarily adopt oven-based assays and fixed-bed reactor systems. The oven basket method, established on the Frank-Kamenetskii critical thermal theory, is a standard static approach for determining the minimum ambient ignition temperature for a given biocarbon volume (Restuccia et al., 2019). Conventional safety assessments have heavily relied on this static testing strategy to define safe stacking and storage thresholds for bulk biocarbon (Van Blijderveen et al., 2013).

This study addresses these fundamental knowledge gaps by systematically investigating the water resistance and mechanical degradation behaviours of biocarbon pellets across various immersion timelines. Following water exposure, the pellets were evaluated for mechanical durability—a primary indicator of logistical viability and structural survival. The self-heating potential of the studied pellets are evaluated by conducting basket test and fixed bed tests. The insights gained from this work are critical for establishing reliable biocarbon value chains, preventing premature material degradation, and accelerating the widespread adoption of bio-based reductants in advanced metallurgical applications.

2. MATERIALS AND METHODS

2.1 Material

Biocarbon investigated in this study was manufactured from bamboo using a pilot-scale kiln reactor operated at approximately 600-650 °C. The as-produced biocarbon was ground into powder and subsequently densified into pellets.

2.2 Water immersion tests

Water immersion experiments were carried out by submerging individual biocarbon pellets in cold water. Two kinds of pellets were tested with different total immersion durations, including long pellets with length of 20-23 mm and short pellets with length of 10-12 mm. For water immersion test, each pellet was merged in cold water and retrieved for weighing at 15-minute intervals throughout the first hour. The same pellet was subsequently submerged for a further hour before undergoing another weight measurement and returned to the vessel for continued soaking. Following initial submersion, periodic weighing of the identical pellet was conducted at 12 h, 24 h and one week after the start of immersion. During every weighing procedure, each pellet was held above the vessel opening and shaken gently (fixed holding duration for 5 seconds and 5 of shakes) to remove surface water. Mass gain was calculated from the initial pellet mass and the measured mass recorded after each immersion interval. Structural evolution and physical integrity of each pellet were visually monitored continuously after submersion. Additionally, pellets subjected 1 week immersion test was further underwent ambient air-drying to characterise mass loss behaviour. A single saturated pellet was placed in a glass tube, with mass measurements collected at 10-minute intervals in the first hour, followed by subsequent measurements at 2 h, 12 h and 24 h. After that, the pellet was taken out the tube and place in a flat baker and dried one week. The weight of one pellet after each drying time scale was measured.

2.3 Durability of pellets

Mechanical durability (MD) measurements were performed using an ISO Tumbler 1000+ apparatus (Bioenergy Institute, Vienna, Austria) complying strictly with standard ISO 17831-1. These tests aimed to quantify how water immersion and subsequent air-drying alter the mechanical strength and structural integrity of biocarbon pellets. A defined initial mass of pellets (m_i) was introduced into the stainless-steel tumbling chamber. The chamber rotated continuously at 50 rpm over a 10 min testing period, corresponding to a total of 500 rotations to apply controlled mechanical abrasion and impact. Upon completion of tumbling, the

recovered material was sieved using a 3.15 mm round-hole sieve to isolate fine particles produced during the test. The residual mass of undamaged pellets (m_f) was then weighed, and this value was adopted to compute the mechanical durability index via the equation presented below□

MD = 100x mf/ mi

Where:

- mi represents the initial pre-test sample mass.
- mf represents the final mass of the pellets retained on the sieve post-test.

2.4 Fixed bed test

Self-heating and autoignition tests were performed in a fixed-bed reactor employing biocarbon particles with sizes between 0.5–1 mm. For each measurement, pre-dried biocarbon (around 70 g) was filled into a 78 mm-diameter, 100 mm-tall cylindrical mesh basket positioned at the reactor tube mid-section. A central thermocouple embedded in the sample bed recorded temperature profiles continuously. Air flowed upward through the bed after entering the reactor base. The reactor was heated at 10 K min^{-1} to target temperatures (180, 190, 200, 250 °C) and maintained isothermally for defined periods. Produced gases passed through a condenser and dual filters to remove particles and tar vapour. The treated gas stream was metered and analysed via a Varian CP-4900 Micro-Gas Chromatograph to quantify CO, CO_2 and O_2. Once each experiment concluded, the basket was cautiously removed from the reactor, and the remaining solids were photographed and visually characterised.

2.5 Crossing-point self-heating test

All crossing-point tests were implemented based on the standard N.4 test procedure using a 1 dm^3 wire mesh basket. Major deviations from the standard protocol included the adoption of multiple testing temperatures (120, 140, 160, and 180 °C), upgraded thick-wire thermocouple probes, and the incorporation of an additional thermocouple embedded within the sample matrix. Except for the 140 °C test, which lasted continuously for 24 h, all other experimental runs were terminated within 3–16 h, which was sufficient to capture the characteristic crossing-point behaviour for self-heating assessment. Experiments were conducted using a Binder FD 53 laboratory oven equipped with a double-layer stainless steel mesh basket assembly. Temperature monitoring was achieved using three 1 mm-diameter Type K thermocouples complying with the Class 1 accuracy requirements specified in the IEC 60584:2013 (IEC 60584-1, 2013) standard. The thermocouple tolerance was defined as the greater value between ±0.5 °C and ±0.004 × T (T in °C), with a valid operational temperature range of 40–1000 °C. Temperature data were logged at a constant sampling frequency of 0.5 Hz using a calibrated data acquisition system that undergoes annual recalibration to ensure measurement accuracy and traceability. For spatial temperature arrangement, the first thermocouple (TC1) was positioned at the geometric centre of the cubic sample volume, whereas the second thermocouple (TC2) was placed 10 mm away from TC1 along a direction perpendicular to one lateral surface of the cubic sample assembly.

3. RESULTS AND DISCUSSIONS

Figure 1 shows weight gain of tested long and short biocarbon pellets after water immersion test at different time interval. Both long and short pellets had weight increase already after 15 minute and reached approximately 33-35% after 10,080-minute (7-day) period. Weights of long single pellets increased from about 1.3 to 1.8 gram, while weights of the short pellets increased from about 0.6 to 0.9 gram. It is interesting to see more weight increase of short pellets after same water immersion time, in comparison to the long pellets. The weight increase of one biocarbon pellet in the water involves filling of water in surface pores and wetting of the

pellet's exterior. The initially adsorbed water might transfer to interior of the pellets, which can be trapped within the internal micro-pores. As accumulation of the water in the interior structure of the pellets, an equilibrium might be established, and the water might not be easy to enter into or escape from the pellets. However, with longer water immersion time, already adsorbed water might movers further into the deeper micro-porous structure of the biocarbon through slow capillary action and diffusion. This might cause swelling of the biocarbon with fibrous structure and possible break down of internal cell walls. This can cause physical expansion and cracks of biocarbon pellets, opening up previously inaccessible internal volume and allowing the pellet to hold more water. This can partially explain increase of pellet weight upon prolonged water immersion test.

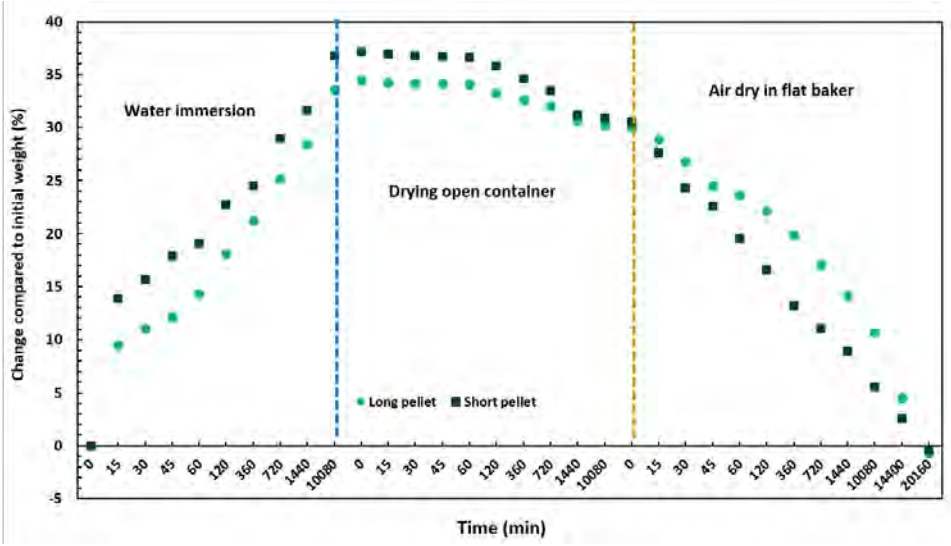

Figure 1: Weight gain of long and short biocarbon sample pellet after water immersion tests at different time interval

Figure 1 also shows different weight decrease behaviours of one test pellet as it was dried in a tube and a flat baker. The pellet was dried in a tube that has a diameter of 10 mm and length of 1 cm, which is placed on the bottom of the tube. It means there is almost no air flowing around of the pellet and adsorbed water is hardly evaporate. Therefore, only small weight losses were observed from the pellets as they were dried in the tube even after dried after 12 hours. However, as one pellet was taken out of the tube and place in a flat baker, it has more contact with surrounding air. Evident decrease of the pellet weight was monitored. During drying in open air in the flat baker, more weight loss was measured from the short pellet. The surface adsorbed water evaporates first, and internally trapped water will diffuse from internal structure. For the short pellets, the distance for water transferring from interior of pellet is shorter. It means more water can migrate and evaporate from the short pellets with given time.

Figure 2 shows that there were only slight decreases of durability of both long and short pellets after water immersion test with one week period. However, after two weeks water immersion test, more evident decreases of pellet durability were observed, indicating higher potential of formation of fines and reduction of mechanical properties of the pellet. During tumbling test, the pellets crush with internal surface of the tumbler, causing manifestation of pellet's surface and internal breaking down. Longer water immersion time leads to weaken binding force of the added binder that bonding biocarbon particle together. It causes reduction of binding forces, shredding of particles and production of fines from the pellet during tumbler test.

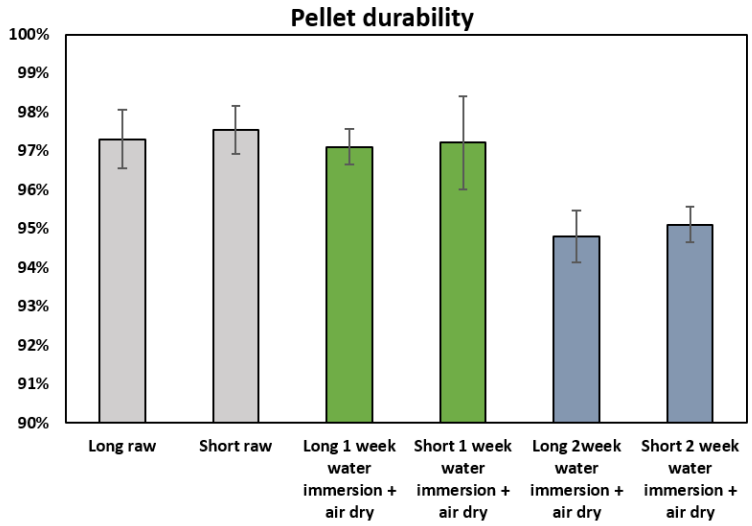

Figure 2: Durability of biocarbon pellet after water immersion test with different time periods and further air dry

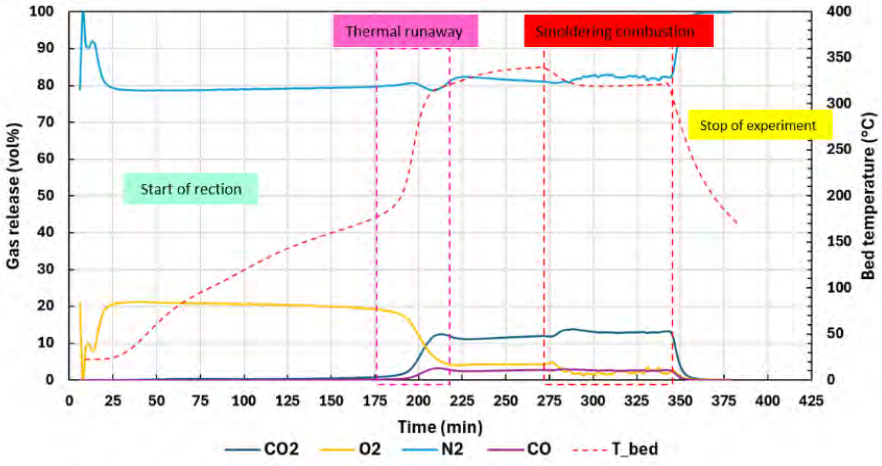

Figure 3: Temperature history of heating up the sample to 160°C with further holding time of 6 hours and change of supply of air

Figure 3 illustrates the temperature evolution and gas-release profiles measured during experiments conducted under a constant furnace set-point of 160 °C and a continuous air feed rate of 1 L/min. As sample temperature slowly reaches 160 °C, the outlet-gas O_2 concentration decreases marginally while CO_2 concentration increases. Once the sample attains 200 °C, CO and CO_2 emerge as indicator gases, denoting chemical-bond rupture and the transition from physical adsorption to active oxidation. After about 50 min of testing, sample temperature increases to 180 °C and then jumps steeply to nearly 330 °C within about 25 min. This temperature burst is accompanied by severe O_2 consumption, demonstrating intense internal reactions driven by high oxygen uptake of porous biocarbon. A major finding is that thermal runaway takes place at a furnace setting of 180 °C for biocarbon pellets. Post-runaway, sample temperature steadily rises and reaches 350 °C after 2 h. In this period, CO and CO_2 emissions stay at a high stable plateau, pointing to persistent smouldering combustion.

A total of five tests at temperatures from 120–160 °C were conducted using basket test. The recorded temperatures in the center of the sample are presented in Figure 4. As the preset temperature was 140 °C, there was a slight increase of temperature in the center of sample bed, which is over 150 °C. However, with further increase of testing time, the measured temperature decreased gradually and reached preset temperature 140 °C. The temperature measured from 140 °C indicates that there was heat accumulation in the center of the biocarbon

sample bed. However, the generated heat further dispatched with causing self-ignition of the sample. For basket tests conducted at temperature even at 145 °C, the measured temperature increase after the sample was loaded in the furnace after about 3.5 hours. After the temperature reached about 170 °C it increased sharply and reached 250 °C in about 20 minutes time, indicating combustion of the sample. With further increase of preset temperature of 150 °C and 160 °C, more evident increase of temperature took place in a shorter time, implying more intensive generation of heat.

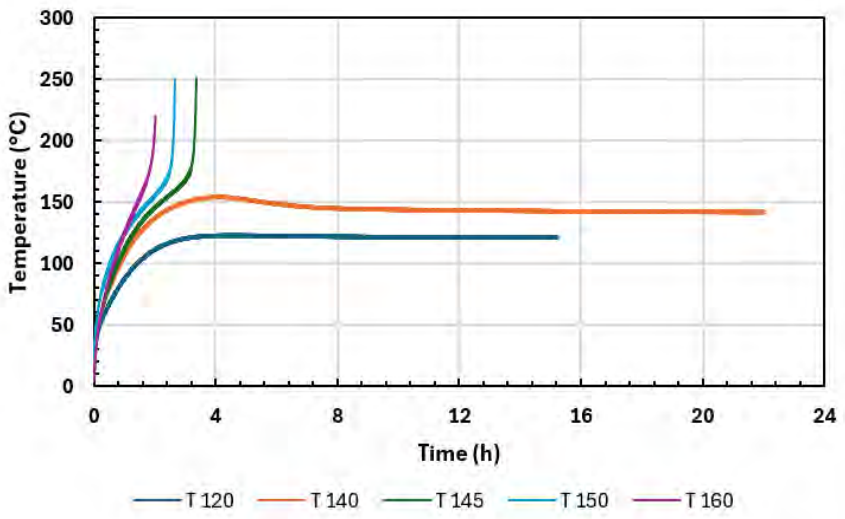

Figure 4: Recorded biocarbon sample bed centre temperatures at the different preset oven temperatures.

4. CONCLUSIONS

The comprehensive evaluation of biocarbon with different lengths reveals that moisture exposure and immersion duration are critical determinants of their structural integrity and logistical viability. Significant weight gains were monitored from the studied biocarbon pellets event after a short water immersion time. Prolonged immersion-extending to 7 days-results in substantial weight increases of approximately 33-35% for both short and long pellets. The further air-drying of water immersed pellets resulted in decline of weights, which eventually falls to their 'as received' state. However, the weight loss behaviours of pellets were considerably different as they dried in a semi open tube and a fully open flat baker. After water immersion and further air dry, the durability of pellets decreased, which are more evident after 2-week water immersion period compared to 1-week.

Self-heating and self-ignition behaviours of the studied biocarbon pellets were investigated by using fixed bed reactor and oven-basket test methods. The fixed bed reactor test results showed that at preset temperature of 160°C, the biocarbon become thermally unstable and further undergoes thermal runaway. This process was accompanied by reduction of O_2 and measurable appearance of CO_2 and CO in the gas exiting the furnace, indicating transition and occurring of biocarbon from self-heating to more intensive smouldering combustion. Oven-basket tests showed that thermal runaway of the studied biocarbon pellets took place as the oven temperature was preset at 145°C and a temperature higher than this value. The fixed bed and oven-basket test results indicate that a dual-monitoring approach - combining traditional temperature sensors with advanced gas detection for CO and CO_2 can be more sensitive and valuable to characterize properties of biocarbon related to self-heating and self-ignition during transportation and storage.

5. ACKNOWLEDGEMENTS

The authors acknowledge support from the project Improving energy production and safety in biocarbon value chains (EnergyProSafe). The supports are through the funding from the Research Council of Norway (grant no: 353147) and financial support from the EnergyProSafe project industry partners.

6. REFERENCES

Werra, M., Tørset, H.K.B., Hua, T., Hu, X., Joncourt, L., Cheisson, T., Watanabe, M.D.B., Skreiberg, Ø., Cherubini, F., 2026. Life-cycle assessment and sustainable supply potential of charcoal for low-emission silicomanganese production in Gabon. Resources, Conservation and Recycling 229, 108858.

Wang L, Buvarp F, Skreiberg Ø, Bartocci P, Fantozzi F., 2018, A study on densification and CO2 gasification of biocarbon. *Chemical Engineering Transaction*. 65: 145-150

Wang L., Skreiberg O., 2023, A Critical Review on Self-Heating and Self-Ignition of Biocarbon, *Chemical Engineering Transactions*, 105, 271-276

Ngene, G.I., Bouesso, B., González Martínez, M., Nzihou, A., 2024, A review on biochar briquetting: Common practices and recommendations to enhance mechanical properties and environmental performances. Journal of Cleaner Production 469, 143193.

Makgobelele, N.W., Mbaya, R.K.K., Bunt, J.R., Leokaoke, N.T., Neomagus, H.W.J.P., 2021, Evaluation of the mechanical properties of wood-derived charcoal briquettes for use as a reductant. J*ournal of the Southern African Institute of Mining and Metallurgy* 121, 187–192.

Riva L, Wang L, Ravenni G, Bartocci P, Buø T.V., Skreiberg Ø, Fantozzi F., Kofoed N. H. 2021, Considerations on factors affecting biochar densification behavior based on a multiparameter model. Energy. 221, 119893.

Riva L, Nielsen H. K., Skreiberg Ø, Wang L, Bartoccic P, Barbanera M, Bidini G, Fantozzi F. 2019, Analysis of optimal temperature, pressure and binder quantity for the production of biocarbon pellet to be used as a substitute for coke. *Applied Energy*. 256: 113933

Garcia Torrent, J., Fernandez Anez, N., Medic Pejic, L., Montenegro Mateos, L., 2015. Assessment of self-ignition risks of solid biofuels by thermal analysis. *Fuel* 143, 484–491.

Lohrer, C., Krause, U., Steinbach, J., 2005. Self-Ignition of Combustible Bulk Materials Under Various Ambient Conditions. *Process Safety and Environmental Protection* 83(B2), 145–150.

Phounglamcheik, A., Johnson, N., Kienzl, N., Strasser, C., Umeki, K., 2022. Self-Heating of Biochar during Postproduction Storage by O2 Chemisorption at Low Temperatures. *Energies* 15(1), 380.

Restuccia, F., Mašek, O., Hadden, R.M., Rein, G., 2019. Quantifying self-heating ignition of biochar as a function of feedstock and the pyrolysis reactor temperature. *Fuel* 236, 201–213.

Van Blijderveen, M., Bramer, E.A., Brem, G., 2013. Modelling spontaneous ignition of wood, char and RDF in a lab-scale packed bed. *Fuel* 108, 190–196.

Wang, L., Barta-Rajnai, E., Hu, K., Higashi, C., Skreiberg, Ø., Grønli, M., Czégény, Z., Jakab, E., Myrvågnes, V., Várhegyi, G., Antal, M.J., 2017. Biomass Charcoal Properties Changes During Storage. *Energy Procedia* 105, 830–835.

Liang Wang

Research Scientist, SINTEF Energy Research

Dr. Liang Wang is working as research scientist in SINTEF Energy Research. Dr. Wang has long experiences and active R&D activities on biomass & waste thermochemical conversion processes, the use of biobased material for low-emission metal production, and the production and utilization of biochar/biocarbon for various applications. Dr. Wang has over than 155 publications indexed in Scopus, with an h-index of 36. He has served as project manager and sub-project leader for more than 15 regional, national, EU, and international projects.

Windfeldt, M. K., V. Andersen, and G. Tranell. 2026. Exploring future flue gas conditions from silicon production through stochastic process simulation. In *Silicon for the chemical and solar industry XVIII,* edited by M. Tangstad, H. Rong, A. Valderhaug, B. Andresen, H. Dalaker, and I. G. Page. Kristiansand, Norway, September 7–10, 2026. https://doi.org/10.55669/oa900821

Exploring future flue gas conditions from silicon production through stochastic process simulation

M.K. Windfeldt[1*], V. Andersen[2], and G. Tranell[1]
[1]Norwegian University of Science and Technology, Norway, *magnus.k.windfeldt@ntnu.no
[2]Elkem ASA, Norway

Keywords: Flue gas, process modelling, charcoal, biocarbon, carbon capture

Abstract – Many industrial producers of metallurgical grade silicon (MG-Si) have a strategy for emission reduction involving biocarbon reductants in the near future, followed by carbon capture on the medium term. Technical and economic challenges in implementing carbon capture are related to flue gas conditions from the submerged arc furnace. This work takes a modelling approach to explore how these conditions will be affected by the upcoming transition to biocarbon.

Two different scenarios are studied, one investigating mixed fossil/bio-reductant charges with increasing use of charcoal, and one investigating selected charge parameters with biocarbon as the only reductant. Six different charcoals, treated at different temperatures and from various wood sources are used in the model. A Monte Carlo approach is taken for simulations, capturing variability and uncertainty in process and furnace parameters.

Results show the significance of volatiles on flue gas conditions. The charcoals contain less volatiles than coal, and thus produce flue gases with significantly lower heat content and temperatures, and with less water and CO_2. There is also a drastic reduction observed on the flue gas sulfur content, although this relies on a mechanism that requires verification. In general, the results indicate that conditions could become more favourable for carbon capture implementation when biocarbon is replacing fossil carbon sources in silicon production.

1. INTRODUCTION

The Norwegian silicon- and ferroalloy-producing industry is aiming at net zero greenhouse gas emissions from their operations by 2050. Current technology for silicon production relies on carbon for reduction of silica and thus inherently produces large amounts of CO_2, with direct emissions around 4.7-5 kg CO_2e/kg Si (Sævarsdottir *et al.*, 2021). While novel, carbon-free technologies are under development, it is necessary to make adaptations to the current processes in the very near future. The strategies shared by major industrial actors Elkem and Eramet (Ravary *et al.*, 2021) highlight both increased use of bio-based carbon materials and implementation of carbon capture (CC) from flue gases as the most viable pathway towards their climate goals.

The carbon capture system needs to be designed for the properties of the furnace flue gas, and some adaptations must likely be made to the furnace operations to make the conditions for carbon capture more economically favourable. Andersen investigated flue gas composition under different conditions for open and semi-closed furnaces, and proposed technology for increasing CO_2 concentration in the flue gas, thus reducing the necessary size and cost of implementing conventional carbon capture equipment (Andersen, 2023). On the other hand, Riboldi et al. has investigated the use of a more novel capture concept based on temperature swing adsorption in a rotary vessel for the conditions from ferroalloy production (Riboldi *et*

This work is licensed under the Creative Commons Attribution 4.0 International License. To view a copy of this license, visit https://creativecommons.org/licenses/by/4.0/

al., 2024). There is however a gap in knowledge on how flue gas conditions in silicon production will be impacted by the increasing use of biogenic carbon materials in the furnaces.

The carbon material mixes currently used in silicon producing furnaces can be quite varied, but typically consist mostly of coal together with some coke and woodchips (Myrvågnes, 2008). Reducing the use of fossil carbon entails replacing the coal and coke fractions, usually with woody charcoals and agglomerates thereof. Many technical challenges related to gas flow and reactivity derive from different structural/chemical and mechanical properties of the novel materials, but for flue gas conditions the most important differences are in the amount of fixed carbon, the chemical composition of the ash and volatile fractions, as well as the resulting heating value.

This work explores the impact of these differences through a modelling approach, using mass- and energy balances together with elemental distribution coefficients to relate changes in raw material mix parameters to changes in flue gas conditions. Two case studies are performed, varying both the amount of biocarbon used and specific properties of the biocarbon mix. Six different sets of charcoal analysis data are used, with variation both in pretreatment and wood source. Finally, the findings are discussed with regards to flue gas treatment in general and carbon capture in particular.

2. METHODOLOGY

In this study, a model of material and energy flows in a silicon producing submerged arc furnace was constructed using HSC Sim 10 (Roine, 2025). Distribution coefficients from furnace mass balances (Kamfjord, 2012) were used together with equilibrium calculations to solve the material flows. Heating value correlations and some select temperature specifications were used to solve the energy flows. Being a fully static model, it did not include any dynamics in gas evolution or any accumulation of material in the furnace. This is not to suggest that the furnaces operate in steady state, but rather to limit the scope to operational ranges for parameters instead of studying transients.

2.1 Model details

Starting with a quartz consumption of 2 tonnes/hour, a specified fixed carbon-based raw material mix and a set carbon coverage close to 95 % is used to determine the required carbon material input. Based on the raw material analysis data, these carbon materials are split into fixed carbon, volatile and ash fractions. The volatiles are simplified as N_2, O_2, H_2, and CH_4 or CO only, while all other elements go into the ash as oxides. These volatiles, any moisture, and a small percentage of the fixed carbon, representing carbon losses from fines, are sent to combustion calculations, while the ash, quartz and rest of the carbon is sent down into the furnace. This quartz is assumed to be pure SiO_2. Heating values, calculated from the Dulong formula (Hosokai, 2016), are used to correct the energy content of the volatiles, based on the elemental composition in dry basis. The lower heating values (LHV) are used, which assumes that the energy used for evaporation of water is not recovered through condensation.

$$LHV\ [kWh/kg] = 33.8m_C + 122.3\left(m_H - \frac{m_O}{8}\right) + 9.4m_S \quad [1]$$

The descending reactants are first heated by ascending process gases. Then, distribution coefficients are used on the elements in the ash to determine how much should enter the metal and slag phases. Any remaining material enters the rising process gas phase. To maintain the oxygen balance when elemental vapours form from the ash oxides, some of the SiO in the process gas reacts to SiO_2 and enters the oxide phase with the remaining ash. These oxides

then react to equilibrium at 2000 °C with the fixed carbon to form metal and slag, which is tapped, and the CO- and SiO-containing process gas. It is here assumed that all fixed carbon eventually reacts to CO. A small percentage of this gas, on CO basis with a set SiO/CO ratio, is removed as tapping gas at 1800 °C before the addition of vapours from the ash.

Power is supplied to the furnace based on the energy balance of the equilibrium reaction. A small but proportional amount of carbon is also added as electrode consumption. The degree of reactant heating and remaining energy flows are then determined by fixing the temperature of the process gas in both the lower and upper part of the furnace. Any difference in process gas heat content between the slag/metal equilibrium calculation and the lower part of the furnace is taken as diffuse heat loss.

The combustion step is also solved as an equilibrium. Here, process gas and volatiles combine with large amounts of air, and are allowed to react to form gaseous oxides. The temperature is controlled to maintain the energy balance. For simplicity, it is assumed that all particles combust to gases in this step. In the next step SiO_2(s) fumes are condensed and removed from the gas, and other elements also enter the solid fume phase according to their distribution coefficients. A simplification is made specifying only a single solid compound per element in the fumes, either an oxide, sulphide or hydroxide, according to predominance. The amount of sulfides formed determines how much SO_x(g) is left in the gas, and as such the distribution coefficient for sulfur is not used. An exception is made for calcium, which forms both CaO(s) and $CaSO_4$(s) depending on stoichiometry and availability of sulfur. Lastly, an equilibrium is solved in the remaining gas phase, allowing for the formation of CO and H_2 if conditions allow. The temperature is again controlled to maintain the energy balance, and the final flue gas conditions are obtained.

2.2 Simulation strategy

Any simplified model of complex systems like a silicon furnace will heavily depend on the values set for innate and operational parameters, such as electrode consumption, carbon coverage and the aforementioned process gas temperatures. Many of these are difficult to know accurately, and they will also vary between furnaces and with time. In order to capture this uncertainty and variability in the results, a Monte Carlo simulation strategy is adopted. Here, most parameters are given a probability distribution around a typical value, and results are aggregated from a large number of simulations where the actual parameter values are randomly drawn each time. The probabilities are distributed normally, with mean values and standard deviations derived both from open literature and discussion with industry. An illustration of the simulation framework is included in Figure 1, together with an overview of process parameters in Table 1.

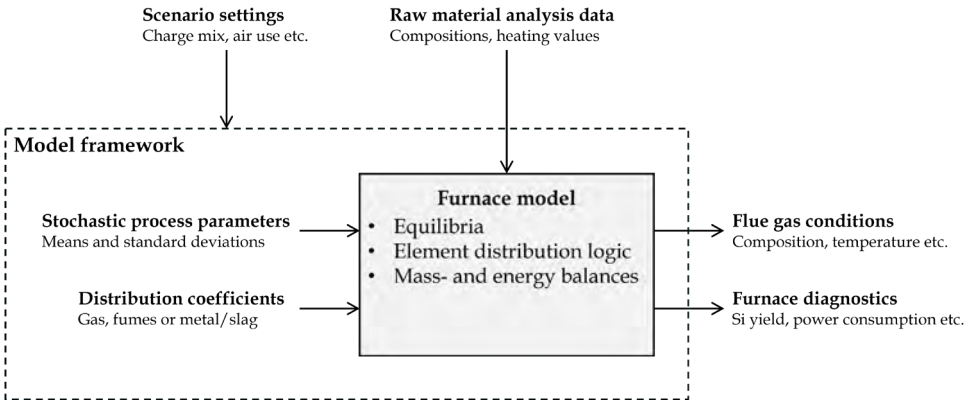

Figure 1: Illustration of model framework and boundaries.

Table 1: Model input parameters with their mean values and standard deviations. Parameters without st.d. values are kept constant in the current iteration of the model.

Process parameters in model	**Mean**	**St.d.**
Carbon coverage (%)	95	2
Carbon loss, all materials (% of fix. C)	2,5	1
Woodchips moisture content (wt %)	45	5
Charcoal moisture content (wt %)	25	8
Coke moisture content (wt %)	3	0,5
Coal moisture content (wt %)	25	5
Metal/slag equilibrium temperature (°C)	2000	-
Lower furnace gas temperature (°C)	1750	50
Tapping gas temperature (°C)	1800	-
Upper furnace gas temperature (°C)	1550	50
Ambient air temperature (°C)	15	5
Tapping gas amount (% of CO)	1	-
Tapping gas SiO content (vol %)	40	-
Electrode consumption (kg/MWh)	0,15	0,01
SO2 to SO3 conversion rate (%)	3	0,5
CaO to CaSO4 conversion rate (%, also limited by available sulfur)	50	-

Two case studies were conducted for this work, one investigating the impact of increasing the charcoal use, and one investigating the impact of selected charcoal parameters when using only biocarbon. For these studies, some parameters of interest were given uniform distributions over a wider range, while others were kept constant as listed in Table 2.

Table 2: Parameter specifications for simulation cases.

	Uniformly distributed parameters		**Constants**	
	Parameter	**Range**	**Parameter**	**Value**
Case 1	Charcoal use (% of fix.C)	0-85	Woodchips use (% of fix.C)	15
	Coke use (% of fossil fix.C)	0-34	Air flow (Nm^3/h)	36 000
Case 2	Woodchips use (% of fix.C)	5-25	Coke use (% of fix.C)	0
	Charcoal moisture (wt %)	5-45	Coal use (% of fix.C)	0
	Charcoal carbon loss (wt %)	2-15	Air flow (Nm^3/h)	36 000

Case 1 examines the effects of gradually removing the fossil reductants, a random mix of coal and coke, and replacing them with charcoal. This represents the path the industry is taking, and should reveal the main trends in flue gas conditions in the near future.

Case 2 examines a scenario where the fossil reductants are no longer in use. It studies the effects of woodchips/charcoal ratio in the charge, moisture content of the charcoal, and the amount of fixed carbon burning off at the top of the charge instead of contributing to reduction. The moisture content is of interest because while freshly produced charcoal contains very little of it, environmental conditions during storage can cause them to absorb large amounts. The carbon loss from charcoal is included in the study because it primarily depends on the strength of the material and how much fines it produces during charging. This is a known issue with charcoal specifically. Outside of case 2, this parameter is kept normally distributed around 2,5 % for all carbon materials.

2.3 Charcoal materials

Six different charcoal materials were used in the simulations. These were chosen simply due to availability of complete analysis data. Two were sourced from Wang et al., who produced charcoal at high temperatures specifically with the metal industry in mind (Wang *et al.*, 2024). Two were sourced from the Phyllis2 open database (TNO, 2026), originally uploaded by the Energy Research Centre of the Netherlands. The last two were unpublished analysis data on charcoals used by SINTEF and NTNU in pilot experiments, originally received from industry. Woodchips, coal and coke data was also sourced from materials used for pilot experiments. Table 3 below gives an overview of the charcoals used in this study.

Table 3: Data source, wood type and pyrolysis temperature for charcoal materials.

Charcoal material	Wood source	Pyrolysis temperature	Data source
Char O Char W	Oak Willow	400 °C 550 °C	Phyllis2 database
Char B Char S	Birch Spruce	1000 °C	Wang et al.
Char P Char Z	Unknown	Unknown	Unpublished analyses

The charcoals differ in their proximate analysis, showing a range of volatile and ash content. There is also variation in composition for some key elements such as sulphur and calcium. Heating values also differ, but this was derived from the composition for comparisons sake, even though it was included in some data sets. Figures 2-4 show these differences compared to the other carbon materials.

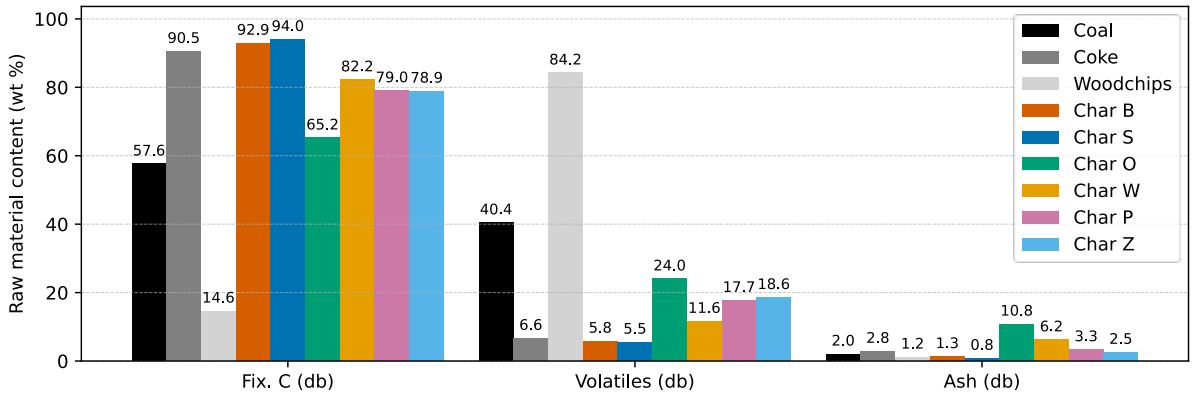

Figure 2: Proximate analysis data for the carbon materials in the study, on dry basis.

As could be expected, the proximate analysis data show less volatiles in the charcoals produced at higher temperatures. Seeing the same trend in the ash fraction is surprising, but this could be due to difference in wood source, or analysis method.

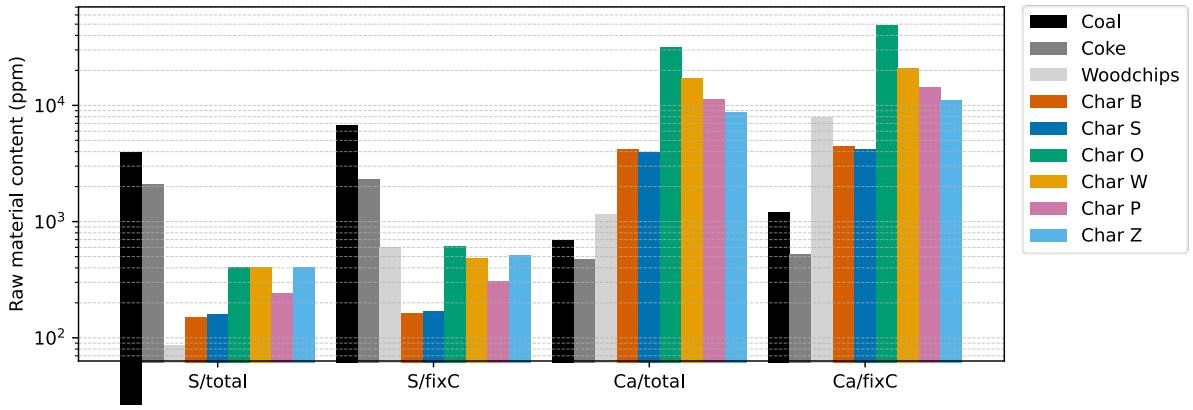

Figure 3: Content of sulphur and calcium in the carbon materials.

Compared to the fossil reductants, the charcoals contain less sulphur and more calcium by an order of magnitude. There is also significant differences between the charcoals, especially between those treated at high temperatures and the rest.

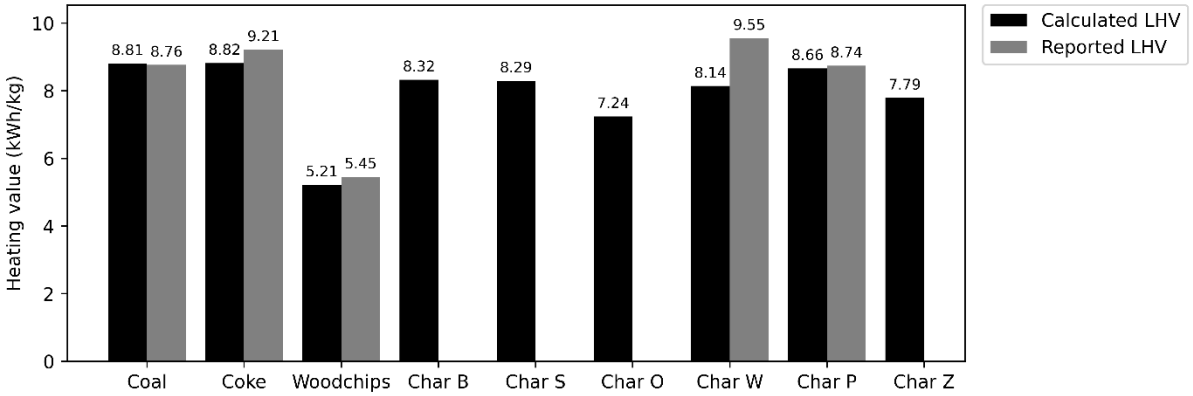

Figure 4: Lower heating values for the carbon materials. Calculated values were used for simulations, reported values from original data source shown for comparison.

With the calculated heating values used in this work, there is a slight decrease in energy input when using charcoal instead of fossil reductants. This is amplified by higher fix. C content, giving lower total amount of carbon material added. Using calculated values seem less

consistent for charcoals than for other materials, which motivates including calorimetric heating value determination in raw material analysis.

3. RESULTS

The simulation strategy produces one large dataset for each case, containing randomly drawn input parameters and resulting output parameters. They are made up of six subsets, one for each charcoal material. The following statistical methods are used to explore relations between parameters: First, locally weighted linear regression (Cleveland and Devlin, 1988) is performed on the entire dataset, giving a smooth trendline. This is plotted along with a shaded prediction interval capturing the variability of the data, calculated using conditional quantile regression with the same local weighting. Lastly, the same regression is performed on each subset. Subset quantiles are not included for visibility.

3.1 From fossil to biocarbon

As can be interpreted from the proximate analysis, replacing fossil carbon materials with charcoal primarily has the effect of reducing the amount of volatiles and ash added to the furnace. Figure 5 shows how this reduces the concentration of CO_x, SO_x and water in the flue gas. Both CO_2 and CO is included in the CO_x number, but the model predicts close to no CO after combustion. Due to the simulated formation of $CaSO_4$, additional Ca in the charcoals also contributes to a predicted reduced SO_x content.

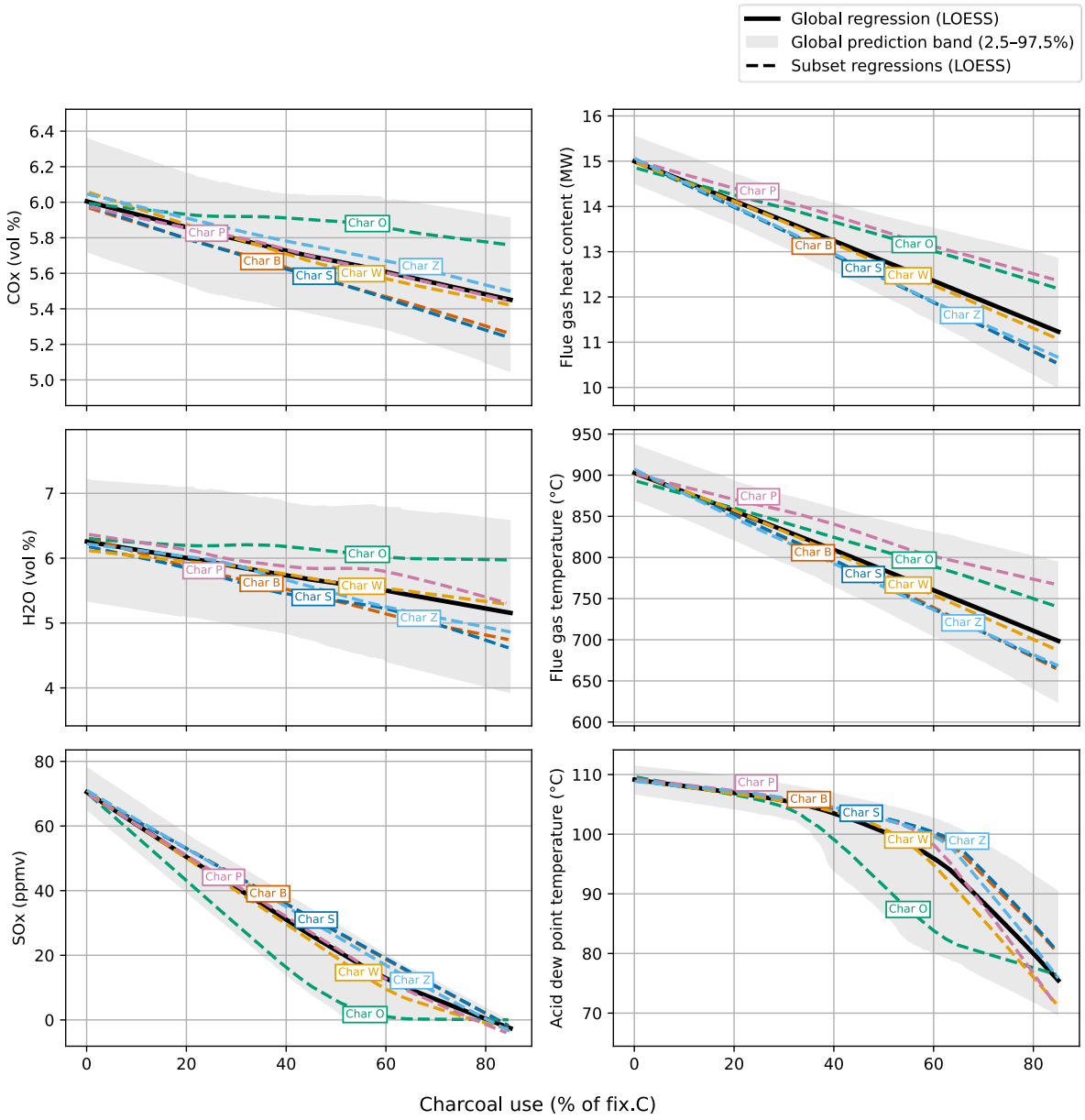

Figure 5: Effect of increased charcoal use on CO_x, water and SO_x content of the flue gas, along with temperature, heat content, and predicted sulfuric acid dew point temperature.

Also shown in Figure 5 is the effect on heat content and flue gas temperature. A reduced amount of combustible volatiles significantly reduces the energy of the flue gas, by around 15-30 %. With the amount of air used in these simulations, this corresponds to a temperature drop of around 200 °C.

Lastly, a drastic effect on the H_2SO_4 Acid Dew Point (ADP) temperature is observed, which is calculated using the following empirical correlation from Okkes (Okkes, 1987):

$$T_{ADP}[°C] = 203.25 + 27.6 \log_{10} p_{H_2O} + 10.83 \log_{10} p_{SO_3} + 1.06 (\log_{10} p_{SO_3} + 8)^{2.19} \quad [2]$$

The acid dew point depends both on the moisture content of the gas and the amount of SO_3 present. While the rate of reaction to form SO_3 from SO_2 is typically kinetically limited, this model instead has the SO_3/SO_x rate in the flue gas as a stochastic input parameter around 3 % for simplicity.

Both Char O and Char P behave noticeably different than the global trend. Char O contains more volatiles than the rest, thus adding more carbon, hydrogen and energy to the system. It also has more calcium, which explains the more rapid drop in SO_x. Char P has a slightly higher heating value than the other charcoals, giving a smaller drop in temperature and heat levels.

3.2 Biocarbon charge mix properties

This set of simulations studies the conditions at 100 % biocarbon more intently, and investigates the effect of woodchips use, moisture content, and carbon loss. These parameters are varied simultaneously, which increases the variability of results, but regression trends are still clearly identifiable.

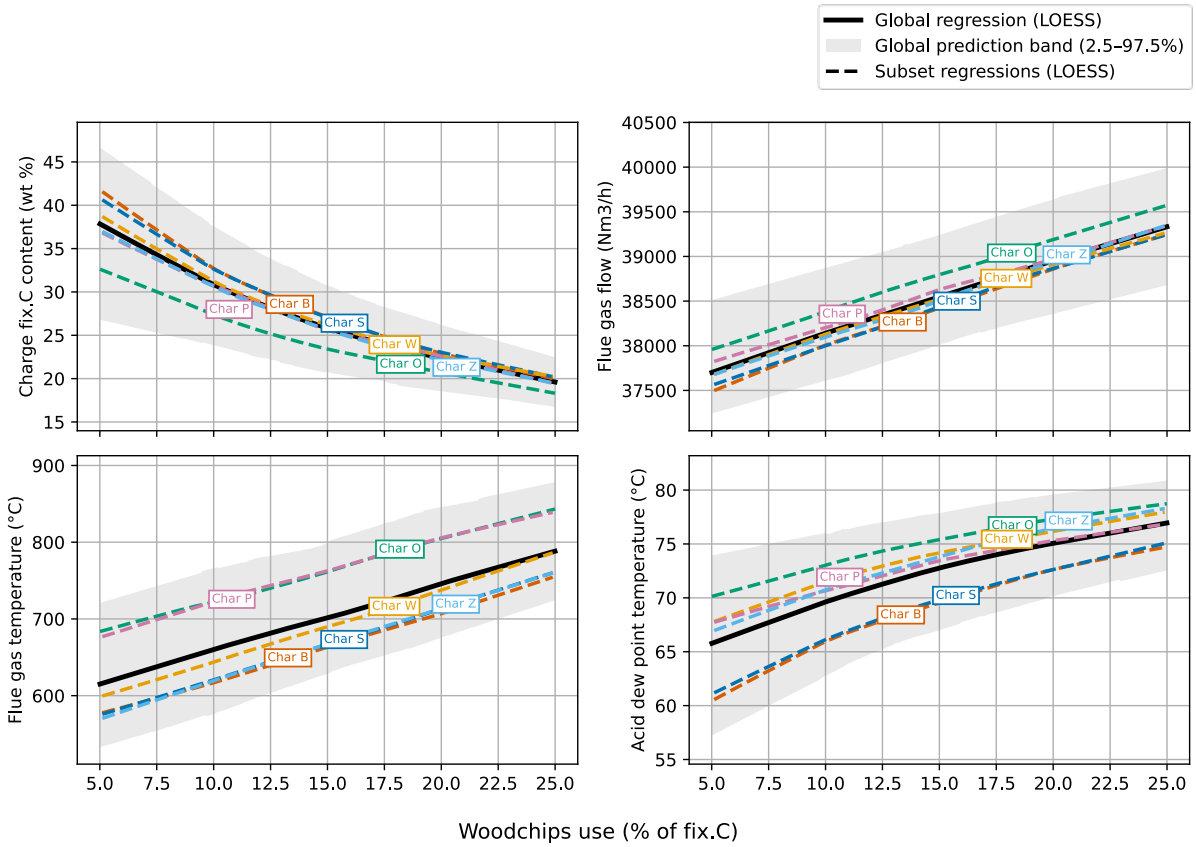

Figure 6: Effect of woodchips amount at 100 % biocarbon use on fixed carbon content in charge, flue gas production, temperature and acid dew point.

Figure 6 shows the effect of varying the woodchip amount at the cost of charcoal. More woodchips significantly increases the amount of volatiles in the charge, leading to more flue gas and higher flue gas temperatures at fixed air intake. There is also a clear increase in the acid dew point temperature. Woodchips has less sulphur than charcoal, but this could be explained by increased moisture content or the reduced fixed C content leading to more carbon material used overall. The dew point remains lower than when using fossil reductants, however.

Varying the charcoal moisture content has a less pronounced effect, as shown in Figure 7. The water content and acid dew point temperature both increase predictably, while the flue gas temperature decreases from the increased use of energy for vaporisation.

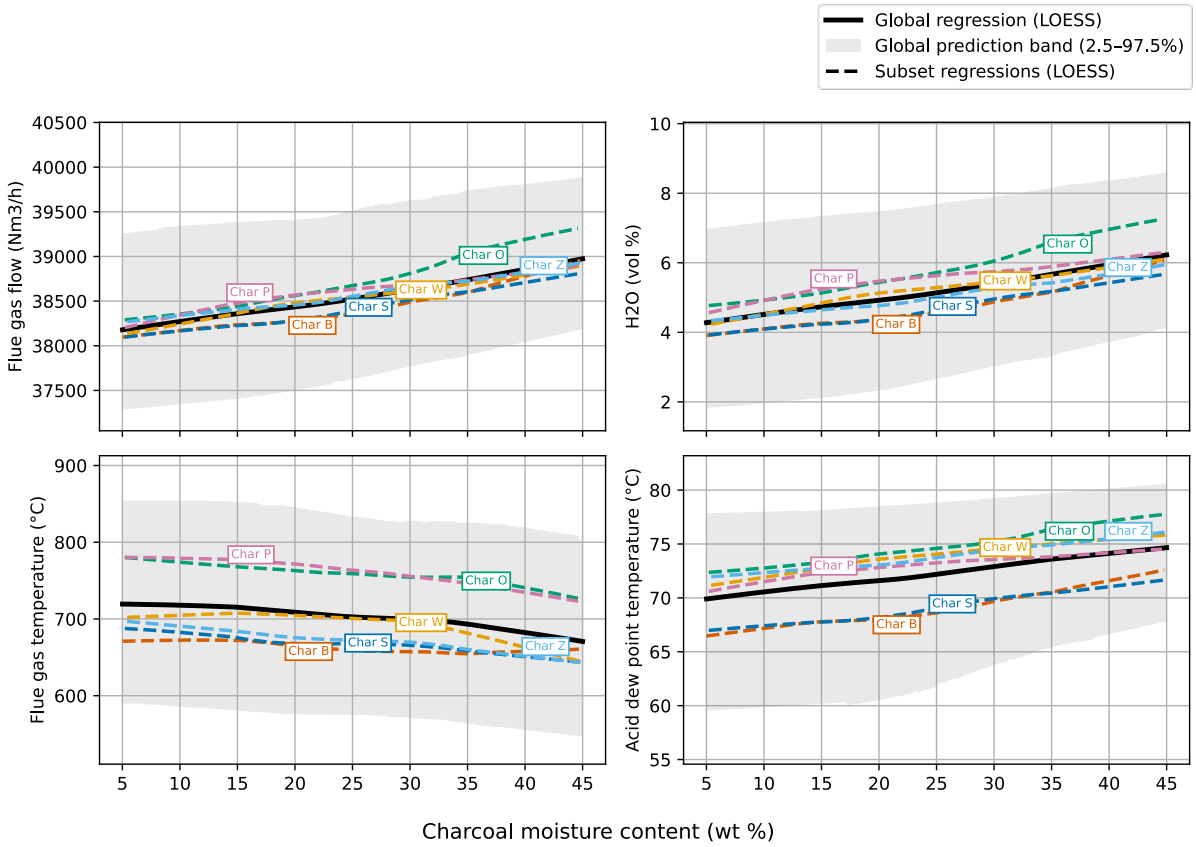

Figure 7: Effect of increasing moisture in charcoal at 100 % biocarbon use on flue gas production, water content, acid dew point, and temperature.

When the carbon loss was varied, the mean value for carbon coverage was also adjusted to maintain the silicon yield. This is shown in Figure 8. While this increases the carbon material need of the furnace, it also has the direct effect of increasing flue gas energy content, temperature and CO_2 content.

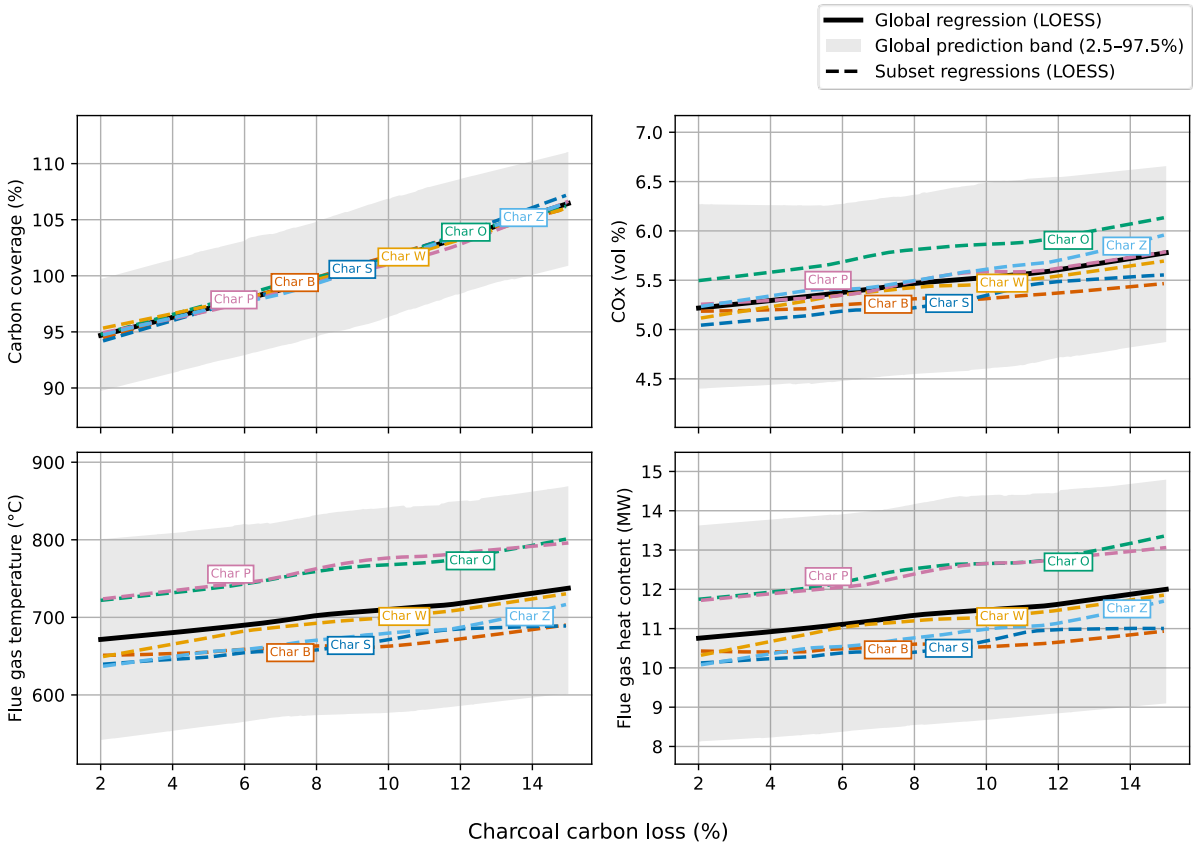

Figure 8: Effect of increasing carbon loss for charcoal at 100 % biocarbon use on required carbon coverage, flue gas CO_x concentration, temperature and heat content.

4. DISCUSSION

The simulations carried out in the current work show the importance of volatiles in the carbon materials for the characteristics of the flue gas. Charcoals contain less volatiles than fossil coal, and thus produce flue gas with drastically lower heat content and temperature. Woodchips contain more volatiles and has the opposite effect. Combustion products from charcoal volatiles such as water and CO_2 has their concentrations noticeably reduced. Further studies could verify if this holds true for more complex combustion products not included in this model, such as NO_x and PAHs.

Furthermore, the results indicate that the issues of SO_x and sulphuric acid in the flue gas system could be almost entirely removed. This relies heavily on the formation of $CaSO_4$ in the flue gas from CaO, originating from ash or mineral impurities in quartz, and as such the mechanisms behind this should be studied and verified experimentally. The potential for detrimental effects on silica fume quality should also be addressed.

There are significant differences between the charcoal materials used in this study, again mostly related to volatile content. Those pyrolysed at higher temperatures contain less volatiles, and thus behave most differently from the fossil reductants. With regards to heat content and temperature, these results heavily rely on the correlation for heating value, which was developed for coal and could be inconsistent depending on the actual volatile compounds present. Calorimetry should therefore be included in any analysis of carbon materials for use in furnaces if energy balance is of concern.

Considering how much the flue gas conditions are predicted to change when transitioning to biocarbon, there are some significant effects that should be taken into account should CC be implemented: Firstly, while the reduction in CO_2 concentration is bad for equipment sizing, it is a minor effect and could be compensated for by other means, such as the reduction in overall gas production. Next, sulphur removal might not be necessary, which could simplify the entire process. Lastly, the reduced heat content of the flue gas is unfortunate for energy recovery systems, and reduces the potential benefits of using thermally driven carbon capture processes. However, the reduced temperatures might also be beneficial, as this would reduce the need for air dilution on top of the furnace. This could increase the CO_2 concentration and reduce the gas volume significantly, which would benefit carbon capture implementation greatly.

While these simulations give good insights into how flue gas conditions are related to raw materials and process parameters, they are the result of a model that is yet to be validated. Verification of mechanisms and calibration of furnace parameters by use of actual furnace data is a necessary next step to enable trust in the findings. If successful, this modelling approach has potential for investigating even more scenarios and raw materials, or even other furnace systems besides silicon.

4. ACKNOWLEDGEMENTS

This work has received funding from FME ZeMe - Zero Emissions Metal Production, a Norwegian centre for environment-friendly energy research, supported by the Research Council of Norway under grant number 350325.

5. REFERENCES

Andersen, V. 2023. Flue Gas Recirculation for the Silicon Process. Doctoral Thesis, NTNU, Trondheim, Norway, 2023. https://ntnuopen.ntnu.no/ntnu-xmlui/handle/11250/3069034

Cleveland, W.S. and Devlin, S.J. 1988. Locally Weighted Regression: An Approach to Regression Analysis by Local Fitting. *Journal of the American Statistical Association.* Vol. 83, pp. 596-610. https://doi.org/10.1080/01621459.1988.10478639

Hosokai, S., Matsuoka, K., Kuramoto, K., and Suzuki, Y. 2016. Modification of Dulong's formula to estimate heating value of gas, liquid and solid fuels. *Fuel Processing Technology,* Vol. 152, pp. 399-405. https://doi.org/10.1016/j.fuproc.2016.06.040

Kamfjord, N.E. 2012. Mass and Energy Balances of the Silicon Process - Improved Emission Standards, Doctoral Thesis, NTNU, Trondheim, Norway, 2012. https://hdl.handle.net/11250/249043

Myrvågnes, V. 2008. Analyses and Characterization of Fossil Carbonaceous Materials for Silicon Production. Doctoral Thesis, NTNU, Trondheim, Norway, 2008. https://ntnuopen.ntnu.no/ntnu-xmlui/handle/11250/248717

Okkes, A.G. 1987. Get acid dew point of flue gas. *Hydrocarbon Processing*, Vol. 66:7. https://www.osti.gov/biblio/6450139

Ravary, B., Bjelland, K.B., Valderhaug, Aa., and Messenlien, A.G. 2021. Towards a climate-friendly ferroalloy industry in Norway, Infacon XVI: International Ferro-Alloys Congress, Trondheim, Norway 27-29 September 2021. https://dx.doi.org/10.2139/ssrn.3926062

Riboldi, L., Holm, S., Skjervold, V.T., and Subraveti, S.G. 2024. Process Evaluation of Temperature Swing Rotary Adsorber for Post-Combustion CO2 Capture in Ferroalloy Industry, 17th International Conference on Greenhouse Gas Control Technologies GHGT-17, Calgary, Canada, 20-24 October 2024. https://dx.doi.org/10.2139/ssrn.5062628

Roine, A. 2025. HSC Chemistry 10, Metso, Pori, 2025. Software available at https://www.metso.com/portfolio/hsc-chemistry/

Sævarsdottir, G., Kvande, H. and Magnusson, T. 2021. Greenhouse Gas Emissions from Silicon Production - Development of Carbon Footprint with Changing Energy Systems, Infacon XVI: International Ferro-Alloys Congress, Trondheim, Norway 27-29 September 2021. https://dx.doi.org/10.2139/ssrn.3926088

TNO Biobased and Circular Technologies. Phyllis2, database for (treated) biomass, algae, feedstocks for biogas production and biochar. https://phyllis.nl/

Wang, L., Khalil, R., Bakken, J., and Skreiberg, Ø. 2024. Production and characterization of biocarbon from woody biomasses produced at 1000 °C. *Fuel*, Vol. 370, Article 131667. https://doi.org/10.1016/j.fuel.2024.131667

Magnus K. Windfeldt
PhD Candidate, NTNU
Magnus is a PhD candidate at the department of Materials Science and Engineering at NTNU, and he holds a MSc from the same department. He also has 5 years of research experience from SINTEF, where he worked and published in the field of industrial energy efficiency and heat recovery. His work is part of the FME Zero Emission Metal Production research centre, and aims to facilitate efficient carbon capture from future silicon production.

Perrotin, A., A. Olivo, J. O. Odden, and M. Di Sabatino. 2026. Characterization of gas-atomized aluminium-silicides for laser powder bed fusion applications. In *Silicon for the chemical and solar industry XVIII*, edited by M. Tangstad, H. Rong, A. Valderhaug, B. Andresen, H. Dalaker, and I. G. Page. Kristiansand, Norway, September 7–10, 2026. https://doi.org/10.55669/oa900822

Characterization of gas-atomized aluminium-silicides for laser powder bed fusion applications

A. Perrotin[1], A. Olivo[2], J.O. Odden[2], M. Di Sabatino[1]
[1]NTNU, Norway, armel.perrotin@ntnu.no
[2]ELKEM, Norway

Keywords: Aluminium-silicides, powder characterization, additive manufacturing, atomized powders

ABSTRACT:

Additive manufacturing (AM) is a blooming field which could allow for a shift towards more sustainable manufacturing of products while maintaining industrial scalability. Laser powder bed fusion (L-PBF) is an AM technique that allows the production of components using powders as a feedstock. Aluminium-silicide powders produced by gas atomization (GA) emerge as prospects for AM applications thanks to their low number of defects, good flowability, and casting properties. Increasing the Si content of these powders would allow to build stronger parts and tailor the materials thermal expansion coefficient for specific uses (e.g. aerospace and automotive industry). In order to optimize the printing process, deep understanding of the feedstock is necessary and, therefore, extensive characterization is required. In this work, we establish a methodology to characterize these powders, which consists of several techniques. Three batches of aluminium silicide powders were characterized by glow discharge mass spectrometry (GD-MS), scanning electron microscopy (SEM) as well as laser diffraction particle size distribution (PSD) and image analysis using ImageJ. Altogether, these techniques generate informative data on the sample and establish a characterization routine for such alloy systems which should improve the understanding of the powders by trying to correlate the physicochemical properties and the morphology of the particles to the performance in powder production for L-PBF applications.

1. INTRODUCTION

In today's world the demand for manufactured parts remains strong for many fields such as the automotive and aerospace industry. The standards and the competition in these fields push for development of newer materials to achieve stronger, lighter and better performing parts whilst limiting the compromises.

Another important metric to consider is the environmental footprint of parts production. Traditionally, metallurgy and parts production have been notorious for their CO_2 emissions, although nowadays the processes are mostly optimized and are controlling the emissions not only for the casting part but the whole process chain.

Furthermore, additive manufacturing (AM) offers an alternative way to produce parts and components with higher production yield and low energy budget. Within AM, laser powder bed fusion (L-PBF) is a process which allows to fabricate pieces with high levels of detail and complex structures in one single body, which avoids post processing steps like welding and machining, good versatility for part design, as well as lower waste coming from the process and compared to traditional casting (DeBoer *et al.*, 2021).

Aluminium-silicides are alloys that could be used for these applications due to their good castability and thermal conductivity (*Aluminium AlSi10Mg Data sheet*, no date). The addition

This work is licensed under the Creative Commons Attribution 4.0 International License. To view a copy of this license, visit https://creativecommons.org/licenses/by/4.0/

of a higher fraction of silicon could help to tailor the stiffness and thermal properties of the alloy, silicon having high Young's modulus, high heat of fusion, and low coefficient of thermal expansion (CTE). Increasing the silicon content could, thus, be beneficial for aerospace applications where these properties are required. (Mueller *et al.*, 2019; Eberle *et al.*, 2019; Garrard *et al.*, 2022; Reutlinger *et al.*, 2023; Wilsnack *et al.*, 2023)

Typical aluminium-silicon alloys used for AM have a silicon concentration close to the eutectic point (12 wt. %). With close to 3000 publications in the last 15 years, the most published Al-Si alloy system for additive manufacturing is AlSi10Mg, which possesses good printing qualities as well as good mechanical properties. Introducing more silicon content would lead to hypereutectic Al-Si alloys which can be produced using rapid cooling technologies such as gas atomization. On top of the silicon content, introducing fractions of other elements like Mg in the AlSi10 could have beneficial effects, improving the mechanical strength, ductility and corrosion resistance of the alloys. (Tambing *et al.*, 2025; Pan *et al.*, 2026)

Gas atomization (GA) is a technique of powder production that consists of disintegration of a molten metal stream using high velocity gas jets to spray tiny and spherical droplets (Neikov, 2019). Additive manufacturing requires homogeneous particles with good flowability (usually coming from round particles) to ensure smoother printing process. GA produced powders could, therefore, be used as a feedstock for AM.

Defects in the powders such as satellites (smaller particles attached to larger ones) or shape defects can have detrimental effects on the printing quality, leading to uneven powder bed which can lead to inaccurate printing parameters. Therefore, feedstock characterization is a key step to improve the printing quality.

In order to better understand the feedstock for AM and therefore tailor the printing parameters, characterization is required to try to correlate the performance of the materials to their physicochemical properties. However, in the literature the characterization of the powder feedstock is often disregarded compared to the printing parameter design and printed parts characterization (Mueller *et al.*, 2019; Eberle *et al.*, 2019; Garrard *et al.*, 2022; Reutlinger *et al.*, 2023; Wilsnack *et al.*, 2023). In this work, a methodology for the characterization of gas atomized hypereutectic aluminium-silicide powders is proposed. The method is comprised of two components: one physicochemical part with chemical characterization using glow discharge mass spectrometry (GD-MS) as well as porosity measurements with N_2 physisorption, and a second part using micrographs analysis from scanning electron microscopy (SEM) and particle size distribution (PSD). These characterizations were performed to assess powders quality using different compositions of aluminium silicides with different morphologies.

2. EXPERIMENTAL WORK

2.1 Materials

The materials used for all the characterizations are aluminium-silicide powders produced by Elkem (for the AlSi40 and AlSi20) and an additional external provider (for the AlSi35-5Cr) using a gas atomizer, and are listed in Table I. The composition of the batches was chosen to have diversity in the silicon content, as well as to allow the possibility of adding different elements to the matrix. The batches were atomized using pre-alloyed materials. Pre-alloying allows for better homogeneity of the atomized powder as described by Garrard *et al.* (Garrard *et al.*, 2022).

Table I: List of the batches studied with their actual composition and size fraction

Batch name	**AlSi40**	**AlSi20**	**AlSi35-Cr5**
Actual alloy composition	60 % Al 40 % Si	80 % Al 20 % Si	60 % Al 35 % Si 5 % Cr
Size fraction	20-60 µm	20-60 µm	20-60 µm

2.2 Methods

2.2.1 GD-MS

The chemical characterization of the powders was performed on the Astrum glow discharge mass spectrometer from Nu Instruments. The analysis was targeted to have a mass resolution of 4000 and had integration time ranging from 80 to 160 seconds per element. A total of 14 elements were studied due to their potential presence as residues from the aluminium and silicon production steps, and are listed in Table II with the corresponding relative sensitivity factors (RSF) used. The RSFs used in this study were established by Paudel and Di Sabatino in (Paudel et Di Sabatino, 2020) for silicon powders samples. Each batch was analyzed 3 times, and each sample was scanned 5 times for a total of 15 measurements per batch to assess the homogeneity. +

Table II: List of the elements used for the GD-MS methodology and their associated RSF coefficients

	B	**Al**	**Si**	**P**	**Cr**	**Mn**	**Fe**	**Ni**	**Cu**	**Ga**	**As**	**Zr**	**Sb**	**Pb**
Isotope	11	27	28	31	52	55	56	58	63	69	75	90	121	208
RSF	1.22	1.39	1.96	3.51	2.23	1.48	1	1.54	4.96	4.45	3.1	0.64	3.9	2.19

2.2.2 Particle Size Distribution (PSD) analysis

The size distribution of the different batches was determined using the Partica LA-960 laser scattering particle size analyzer from Horiba. The experiment was performed in wet mode using ethanol as a medium. The refractive index chosen for the materials was 1.5 and the targeted transmittance value was 87 %. Each batch was analyzed 3 times by PSD, and each sample was measured 10 times to ensure homogeneity of the batch.

2.2.3 Scanning Electron Microscopy (SEM)

All the scanning electron microscopy from this work were performed on a JEOL IT800 Field emission gun scanning electron microscope (FEG-SEM). The samples were mounted on a sample holder which can gather 3 samples at a time. The samples were adhered to the pins using conductive carbon glue as it ensures stronger adhesion to the pins of the sample holder compared to traditional carbon tape. The micrographs were taken in backscattered mode, using 10 kV or 15 kV acceleration voltage and 250x magnification for the sake of standardization of the analyses.

For this study, a standardized procedure was established to gather as many micrographs as possible per sample. With this method, it is possible to ensure that the data obtained from it are relevant for the batch. Around 40 micrographs per batch were taken, which corresponds to around 700 particles studied for each batch.

2.2.4 ImageJ (IJ)

Micrographs obtained through the SEM have been analyzed using ImageJ software (Schneider, Rasband et Eliceiri, 2012). The roundness (Round) of a particle is established by measuring the aspect ratio of the particle's fitted ellipse (ratio of the minor axis by the major axis of a particle) and calculated using Equation [1].

$$\boldsymbol{Round} = \mathbf{4} \times \frac{[\boldsymbol{Area\ of\ the\ particle}]}{\boldsymbol{\pi} \times [\boldsymbol{Major\ Axis}]^2} \quad \textbf{[1]}$$

The particles Feret diameter can also be measured by ImageJ to assess the particles size. Feret diameter is obtained by measuring the longest distance between any two points along the selection boundary.

In order to gather relevant data, the 10 micrographs produced per sample by the SEM procedure are analyzed, and several samples from the same batch are investigated to get the largest possible study. A total of 648, 708, and 4452 particles were studied for the batches of AlSi40, AlSi20, and AlSi35-5Cr, respectively.

2.2.5 Porosity measurements using nitrogen physisorption

The powders porosity as well as their specific surface area were analyzed using nitrogen physisorption on a Micromeritics® Tristar II plus. The powders were outgassed at 300 °C overnight under vacuum (0.1 mTorr, 16 h) to ensure that the pores are clean from moisture as well as other gases and vapors that might have been adhered to the pores.

2.2.6 Flowability measurements

The flowability of the powders was measured using a hall flow meter and measured once the powders have been cooled and sieved after the atomization process. The measurements were done for 50 g of powders for each batch.

3. RESULTS AND DISCUSSION

In this work a methodology for the characterization of aluminium silicide powders is proposed, which can allow to gather extensive information about the sample (chemical composition, size distribution, imaging as well as porosity), as well as post processing methods to assess easily the quality of a batch before printing it, therefore reducing operational time and resources.

The methodology proposed involves two main core characterization, which aligns with previous literature for additive manufacturing feedstock characterization (Sutton *et al. 2016)*: i) a physicochemical characterization (which comprises both chemical composition analysis and the detection of pores within the material), and ii) particle characterization which involves imaging and measurement of the particle (SEM and PSD). This method is relatively quick, involving few instruments and fast operating times while still gathering important data on the samples.

Firstly, chemical composition of the batch is one of the most important parameters to gather accurate information in order to match the laser power accurately as variations in the traces and matrix elements will have an effect on the melting behavior of the alloy (melting temperature as well as surface tension). For this reason, GD-MS was used as this technique allows for great resolution and limits of detection (LoD) for trace elements up to the part per billion (ppb). (Di Sabatino, 2014)

Using GD-MS for chemical characterization of powders can be rather useful as the technique does not require extensive sample preparation compared to techniques like inductively coupled plasma coupled with mass spectrometry or optical emission spectroscopy (ICP-MS or ICP-OES) that require digestion of the samples which can be challenging for these materials requiring strong acids like hydrofluoric acid and poses HSE concerns. (Pisonero, Fernández et Günther, 2009)

The GD-MS measurements showed good homogeneity of the batch composition with good confidence in the results thanks to its low standard deviation (STD) as seen in Table III. The concentrations of the main elements present in the studied alloys are plotted in Figure 1. The Fe content in this figure was not displayed for the AlSi40 as the iron concentration was about 1 wt.% due to the presence of recycled Al in the feedstock for atomization, which would have been out of scale compared to the other two powders.

Table III: Average standard deviation for the AlSi35-Cr5 batch using GD-MS

	B	Al	Si	P	Cr	Mn	Fe	Ni	Cu	Ga	As	Zr	Sb	Pb
STD (ppmw)	0.18	10000	11000	41	3100	4.0	33	86	37	20	0.06	1.4	0.02	1.8

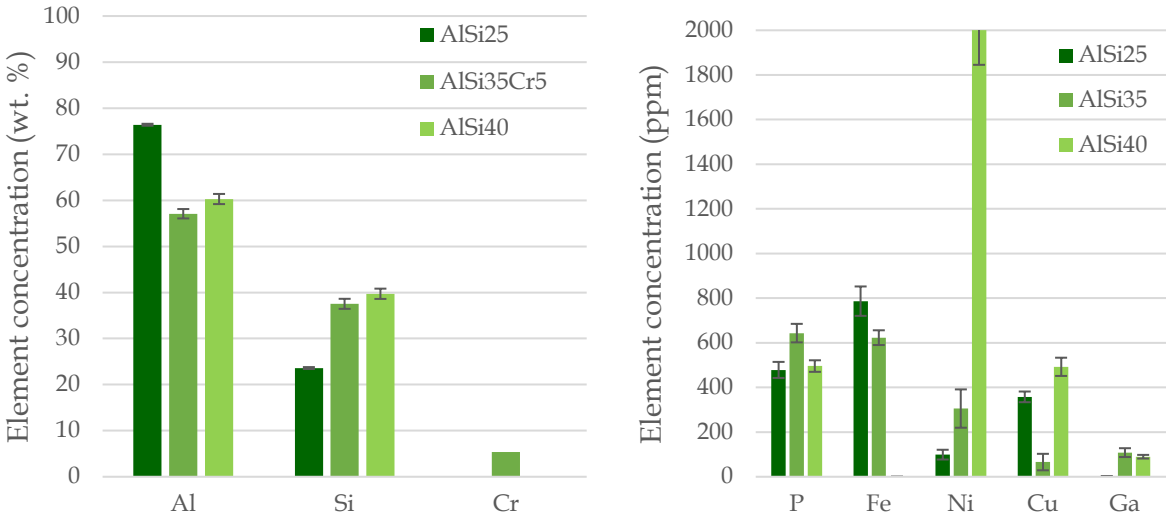

Figure 1: Chemical analysis by GD-MS of the main elements present in the alloys

GD-MS is a powerful technique which excels in the characterization of traces thanks to its low detection limits and good accuracy. However, it still has some limitations, especially for the precise quantification of the matrix, as even with low standard deviation (around 1 % wt.) the deviation is not negligible. Therefore, this technique should be paired with other analytical techniques such as inductively coupled plasma mass spectrometry (ICP-MS) to assess precisely the matrix content and serve as a validation pathway for this methodology.

The presence of pores in the feedstock is also an important parameter to monitor. As forementioned, pores are one of the typical defects found in the printed part, leading to crack formation and, thus, deteriorating the mechanical properties of the printed part. Assessing the presence of pores in the feedstock would, therefore, alert the user to the potential risk of having trapped gases in the melt pool and, thus, crack formation in the printed part.

To observe such pores, nitrogen physisorption measurements were performed on the powders to either guarantee the absence of pores or assess the types of pores (macro or micropores). The pore volume were 0.360 mm^3/g, 0.239 mm^3/g and 0.149 mm^3/g for the AlSi35-Cr5, AlSi20 and AlSi40 respectively, showcasing very little porosity across the three samples. Their specific surface area lower than 0.15 m^2/g were measured for all batches, which is considered as a very low surface area.

In order to produce powders for additive manufacturing, it is necessary to gather insight on the particle size distribution of the batches. As each additive manufacturing technique requires different size distribution, the characterization of the particle size processes a high value on an industrial perspective.

Typically for laser powder bed fusion, the size fraction of the powders should range from 20 to 60 micrometers, with a mean diameter comprised between 30 and 40 µm. It is necessary to know in detail the size distribution of the batch to ensure that the powder bed is homogeneous and maintains a similar height throughout the printing process to avoid any defects such as lack of fusion or keyhole formation which would occur in case of bad laser parameter due to unevenness of the bed.

For this work the PSD was measured using wet mode laser diffraction as the technique is a fast and user-friendly method that gathers accurate information about the whole size distribution of the batch. Considering that the powders are sieved right after the atomization process, it is possible that some particles could get through the mesh due to their elongated shape. Laser diffraction allows to detect not only the distribution and the mean size, but also to assess if many oversized particles have passed through the mesh.

The size distribution for all 3 batches was plotted in Figure 2, showing an even distribution with a single peak for each composition, while still being comprised mostly within the 20-60 µm range. The mean particle size (D_{50}) for each batch was 42, 40 and 33 µm for the AlSi40, AlSi20, and AlSi35-5Cr, respectively. A small fraction is also observed with larger particles than the expected one, which can be explained by the presence of elongated particles fitting through the mesh of the sieve.

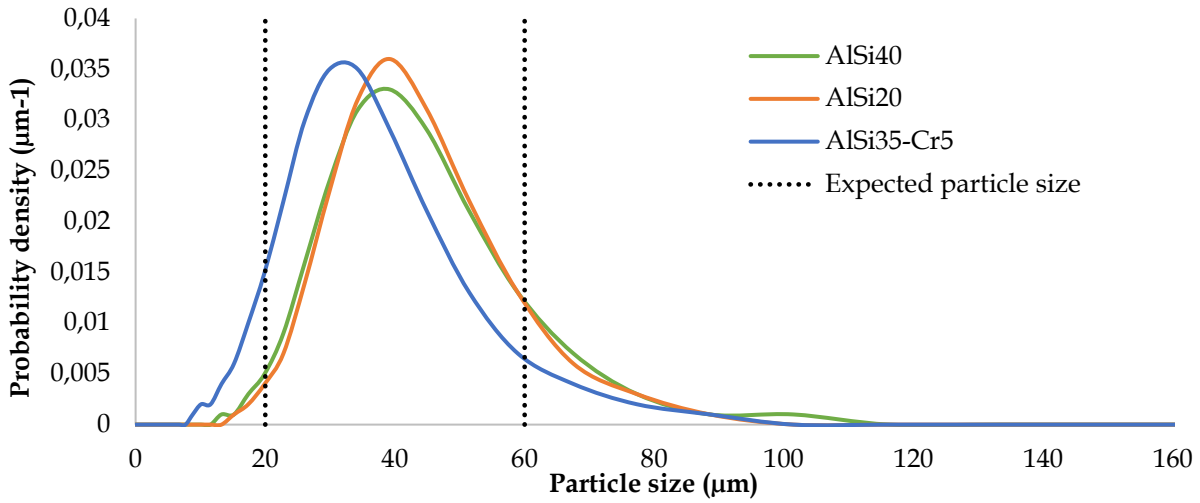

Figure 2: Particle size distribution of AlSi40, AlSi20 and AlSi35-5Cr

On top of the previous characterization, gathering information about the powders through imaging is of paramount importance to assess the batch quality. For this matter, scanning electron microscopy (SEM) is a reliable and powerful tool to use, allowing for high resolution imaging of the particles shape and the potential satellites.

The SEM micrographs allowed to observe the typical defects coming from the atomization process such as the satellite formation (both from particle collision and adhesion) as well as splashing (Figure 3). Splashing usually appears as a smoother phase on the surface of the

particles and was observed on every batch. Similarly, the satellites formed by particle adhesion were also found on all the batches and are the most common defect detected in this study.

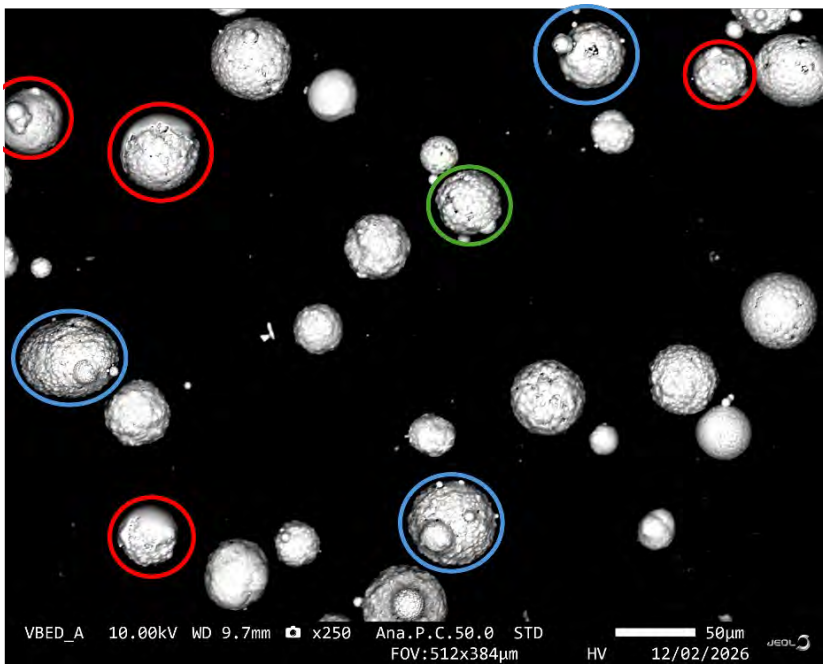

Figure 3: SEM Micrograph of AlSi40 showing the usual gas atomization defects. In red the splashing, blue the satellite adhesion and in green the satellite coming from particle collision

The typical morphologies from the three powders studied in this paper are shown in Figure 4. The morphology of the powders is relatively different for each composition, showing a smoother surface for the AlSi20, a very heterogeneous batch for the AlSi35-5Cr (different particle size, satellites on almost all particles) and homogeneous but textured particles (cotton balls-like) for the AlSi40 sample. These differences could be due to the silicon content. However, additional systemic studies are required to draw any conclusions on the role of silicon on the texture of the powders since these batches are not only differing in silicon content, but also in added elements (Cr), and were also manufactured by two different producers.

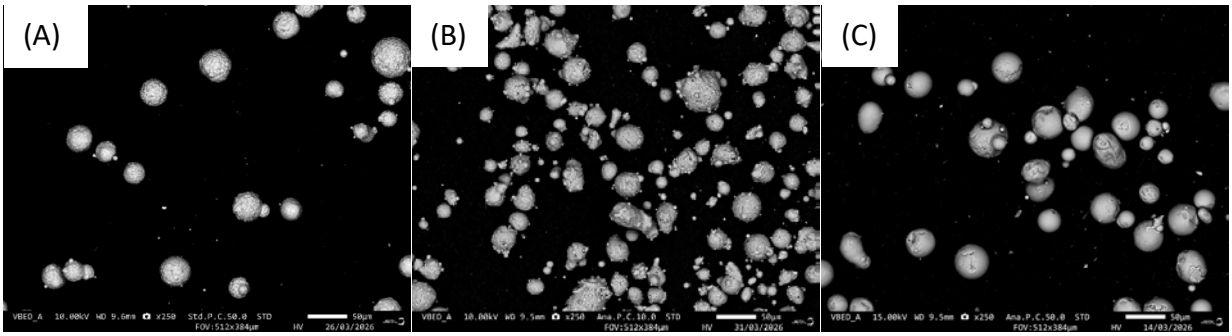

Figure 4: Typical micrographs for the studied powders. (A) AlSi40; (B) AlSi35-5Cr; (C) AlSi20

After gathering information on the particles by collecting micrographs, it is possible to go deeper in the understanding of the batch morphology and perform some post processing work on the micrographs. To do so, ImageJ was used as it is an open-source software which is designed specifically for image analysis. Through ImageJ it is possible to gather a wide range of information about the sample such as the area per particle, the particle's perimeter, the Feret diameter, and measure its roundness for instance.

In this work, the imaging characterization of the batches focuses on two of these parameters: i) the Feret diameter, and ii) the roundness. The Feret diameter on one hand was chosen as a particularly interesting data as it measures the particle's size (maximum distance between two points within the same particle), which could be used to perform a particle size distribution (PSD) using the SEM. On the other hand, the particle's roundness was chosen as an equally interesting data as it could be used to assess the batch homogeneity in terms of shape and could potentially be linked to the flowability of the sample. Suri and Patel (Suri et Patel, 2024) for example reported on the importance of sphericity of the particles to ensure good flowability as well as reduce friction

To do so, the different micrographs of the samples were processed through ImageJ, with a standardized procedure automatized using the macro function of the software. The macro command allowed to set the scale automatically thanks to the standardized SEM micrograph procedure, as well as the threshold for the image, filling the holes within the particles (which decreases the chances of the software considering shadows as particles) and lastly doing the particle analysis while showcasing the ellipses for each particle. The ellipses are used as quality control to verify that the macro functioned well and spot any incoherence in the counting of the particles (particles being split in two, round particles being counted as oval or satellites being counted as particles for example).

For this methodology a minimum threshold of area per particle was established at 150 μm^2 in order to only consider particles and omit the satellites as having a too little threshold would create incoherences with shadows and would therefore affect the overall roundness of the particles. Therefore, satellites are not considered for this study which consists in one of the limitations of this work. Further work on the characterization of satellites is required to assess their effects on the roundness of the batch, on the size distribution as well as other physical metrics such as the flowability for example.

The size distribution obtained from the micrographs was calculated by gathering the Feret diameter rounded to the nearest integer of every particle for each micrograph of the same batch, the standard deviation and the mean diameter were then extracted from this series, and a normal distribution was then performed on the data set. The normal distribution was then plotted as a function of the Feret diameter. The calculated size distribution from micrographs analysis was plotted on Figure 5 and compared to the PSD obtained from laser diffraction. On one hand, the size distributions show relatively similar behavior and match with the expected 20-60 distribution. On the other hand, it is noteworthy to say that there is a small mismatch (especially for the AlSi20), showing a difference between the size distribution of the same batch using the two different methods. Although this could be due to the batch size (AlSi20 being plotted with only 28 micrographs), this could also be due to lack of homogeneity in the batch. This methodology could be useful to monitor the number of elongated particles in the batch.

In order to compare the plotted data from the micrographs to the data obtained by laser diffraction, a Kolmogorov-Smirnov-test was performed. This technique was used in the literature by Vigneau et al. as a relevant approach to estimate if the batch size is statistically relevant for powder size distribution analysis (Vigneau et al. 2000). This test involves two parameters: p-value which is a measure to evaluate the mean, and the D value which is the largest vertical distance between the two cumulative curves, and it is a way to compare the width of normal size distribution.

Table IV: Kolmogorov-Smirnov statistical analysis of the size distribution experiments

	p-value	D
AlSi35-Cr5	0.998	0.100
AlSi40	0.902	0.132
AlSi20	$3.15 \cdot 10^{-15}$	0.352

From the values logged in Table IV, one can observe that 2 samples have p-values above 0.05 (more than 95 % of the distribution describes the average sample), while also having a D value inferior to 0.20, meaning that the width of the distribution is similar. This shows that the method could be relevant for the characterization of particle size. However, the AlSi20 sample showed that both the p-value and the D value are off the scope to be considered statistically relevant, and therefore more particles should be analyzed to refine the results from the micrograph analysis.

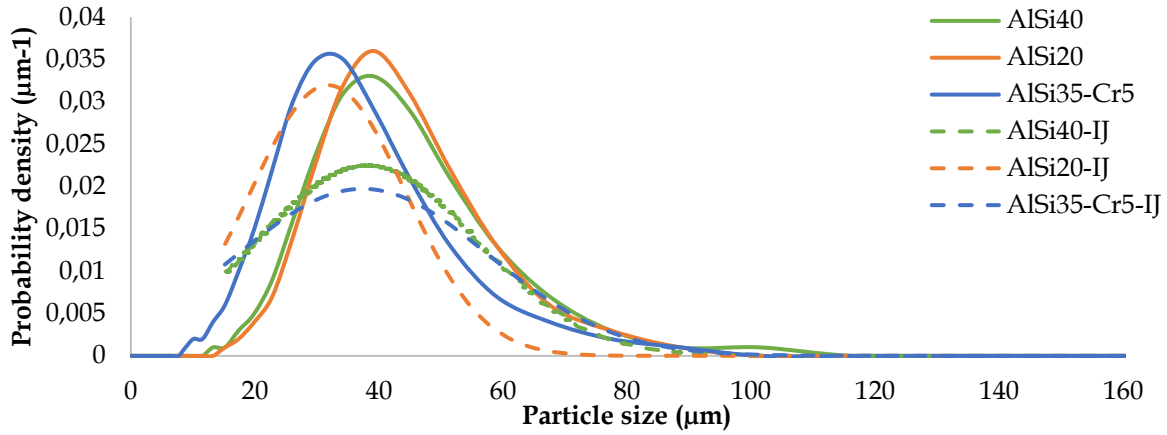

Figure 5: Comparison between the computed PSD using micrographs (dashed lines) and the PSD done with laser diffraction (continuous line)

The roundness was also measured using the same methodology as the size distribution previously mentioned and was plotted in Figure 6, and the results are equally in accordance with the expected behaviors. The AlSi40 and AlSi20 show similar roundness, while also showing similar printability and flowability (about 20.5 seconds per 50 grams of powder in a hall flow). The AlSi35-5Cr on the other hand shows a much lower roundness (10% lower) which could explain the lack of flowability observed (no flow was observed in the hall flow). Being able to quantify and potentially link the roundness of the particles to a measurable metric like the flowability would enhance the quality assessment of the powder production in order to evaluate the batch quality right after atomizing. Lower or lack of flowability being detrimental to the L-PBF process as it could totally hinder the recoating process and therefore abort the printing step.

On top of the characterizations presented in this work, more techniques could be used to better refine the understanding of the properties and characteristics of the aluminium-silicide feedstock. As suggested by Sutton *et al.* 2016 (Sutton *et al.* 2016), analyses such as energy dispersive spectroscopy (EDS) could be used to observe the dispersion of the elements in the particles. X-ray diffraction measurements could be performed to identify some phases present in the powders. X-ray photoelectron spectroscopy could also be used to gather important information about the surface composition and its oxidation, which on top of the forementioned techniques could help to enhance the printing parameters and better correlate the feedstock properties to parts performance.

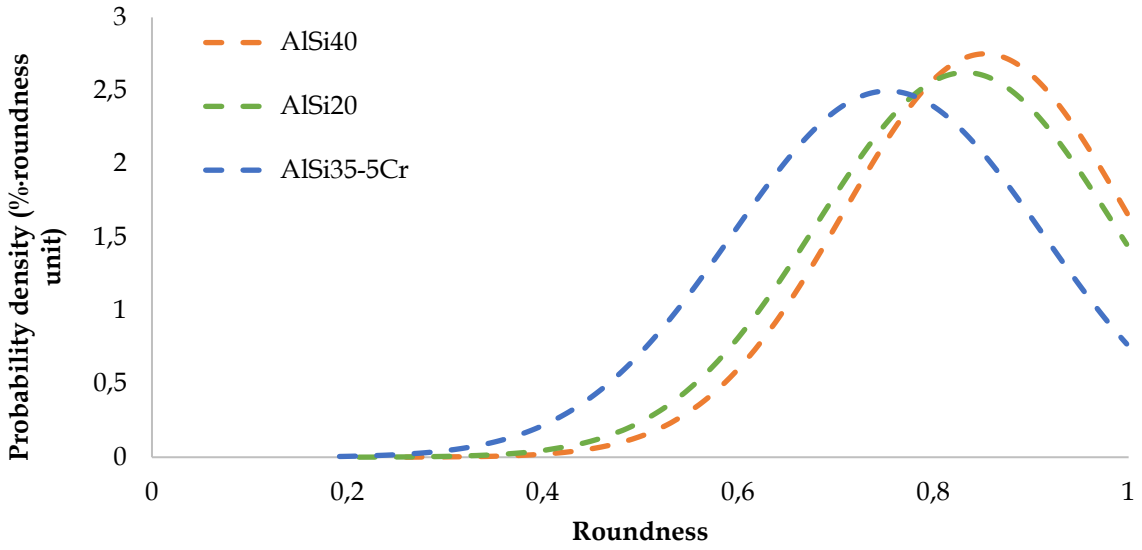

Figure 6: Particle's roundness distribution of the three batches studied

4. CONCLUSION AND PERSPECTIVES

Characterizing additive manufacturing feedstock can be relatively challenging as the feedstock can differ drastically based on powders producers (e.g. shape and composition). The lack of clear, easy-to-follow methodology for the characterization of such feedstock, especially for Al-Si alloys with high Si content pushes for a standardized procedure in order to compare powders before printing as part of the quality assessment.

In this study, a simple characterization methodology was proposed involving few techniques while still maintaining a high amount of data and good resolution in an effort to reduce operational time. The proposed method offers to not only visualize the defects and some physical properties using the SEM (quality control of the batch, satellites, shape, phases) but also begin a quantification of some of them (size distribution and roundness) which could be obtained by other techniques such as laser diffraction PSD or flowability measurements.

Reducing the number of tools necessary to assess the powder quality could have advantages both in academia and in industry, reducing the experimental costs (no need to print if the powder shows too many defects) as well as operational costs by having to maintain fewer equipment and using fewer operators.

This contribution aims to broaden the knowledge of the feedstock, especially for high Si content Al-Si alloys and propose easy routine analysis methodology to ensure batch quality before printing. The proposed approach allows for the characterization of powders using micrographs post processing with ImageJ and gather information such as the particle size distribution, or the roundness which could be linked to the flowability of the particles. Therefore, increasing the value from the SEM data gathered. Another way to valorize the SEM data acquisition would be to use the data set created in order to feed models to predict batch quality after production and therefore reduce operational costs.

More characterizations could be performed on the feedstock to be in accordance with the literature such as XPS, XRD or EDS for example. This could broaden the knowledge of the powders prior to the printing step, thus allowing to tailor the laser parameters and printing strategies, as well as offering ways to corroborate the feedstock quality to parts performance. At the academic level, it would certainly help to widen the range of characterization

techniques for deeper knowledge, while at the industry level time and resources are pivotal. Thus, the methodology that we have proposed is a good compromise between all these aspects.

5. ACKNOWLEDGEMENTS

Dr. Sergei Khromov from NTNU is gratefully acknowledged for his help on the method development of the GD-MS analyses. This work has been funded by Research Council of Norway (RCN) through SFI PhysMet – Centre for Sustainable and Competitive Metallurgical and Manufacturing Industry under the project number: 309584.

6. REFERENCES

Aluminium AlSi10Mg Data sheet (no date). Xometry. Last checked: 06-07-2026. https://xometry.pro/wp-content/uploads/2023/08/Aluminium-1706-1.pdf.

DeBoer, B. *et al.* (2021) « Additive, subtractive, and formative manufacturing of metal components: a life cycle assessment comparison », *The International Journal of Advanced Manufacturing Technology*, 115(1-2), p. 413-432. https://doi.org/10.1007/s00170-021-07173-5.

Di Sabatino, M. (2014) « Detection limits for glow discharge mass spectrometry (GDMS) analyses of impurities in solar cell silicon », *Measurement*, 50, p. 135-140. https://doi.org/10.1016/j.measurement.2013.12.024.

Eberle, S. *et al.* (2019) « Additive manufacturing of an AlSi40 mirror coated with electroless nickel for cryogenic space applications », in N. Karafolas, Z. Sodnik, et B. Cugny (éd.) *International Conference on Space Optics — ICSO 2018*. *International Conference on Space Optics - ICSO 2018*, Chania, Greece: SPIE, p. 40. https://doi.org/10.1117/12.2535960.

Garrard, R. *et al.* (2022) « Comparison of LPBF processing of AlSi40 alloy using blended and pre-alloyed powder », *Additive Manufacturing Letters*, 2, p. 100038. https://doi.org/10.1016/j.addlet.2022.100038.

Mueller, M. *et al.* (2019) « Microstructural, mechanical, and thermo-physical characterization of hypereutectic AlSi40 fabricated by selective laser melting », *Journal of Laser Applications*, 31(2), p. 022321. https://doi.org/10.2351/1.5096131.

Neikov, O.D. (2019) « Atomization and Granulation », *Handbook of Non-Ferrous Metal Powders*. Elsevier, p. 125-185. https://doi.org/10.1016/B978-0-08-100543-9.00004-X.

Pan, C. *et al.* (2026) « Effect of Mg Content on the Mechanical and Corrosion Behavior of AlSi10Mg *x* Alloys via Selective Laser Melting », *Materials and Corrosion*, 77(2), p. 268-279. https://doi.org/10.1002/maco.70051.

Paudel, G. et Di Sabatino, M. (2020) « Quantification of discharge gas to optimize discharge parameters for relative sensitivity factors (RSFs) determination by slow-flow glow discharge mass spectrometry (GDMS) », *Journal of Analytical Atomic Spectrometry*, 35(11), p. 2748-2757. https://doi.org/10.1039/D0JA00281J.

Pisonero, J., Fernández, B. et Günther, D. (2009) « Critical revision of GD-MS, LA-ICP-MS and SIMS as inorganic mass spectrometric techniques for direct solid analysis », *Journal of Analytical Atomic Spectrometry*, 24(9), p. 1145. https://doi.org/10.1039/b904698d.

Reutlinger, A. *et al.* (2023) « Printed Athermal Mirror (PAM) based on AlSi40 and NiP coating for space application », in K. Minoglou, N. Karafolas, et B. Cugny (éd.) *International Conference on Space Optics — ICSO 2022*. *International Conference on Space Optics — ICSO 2022*, Dubrovnik, Croatia: SPIE, p. 105. https://doi.org/10.1117/12.2690312.

Schneider, C.A., Rasband, W.S. et Eliceiri, K.W. (2012) « NIH Image to ImageJ: 25 years of image analysis », *Nature Methods*, 9(7), p. 671-675. https://doi.org/10.1038/nmeth.2089.

Suri, P. et Patel, S.A. (2024) « Particle shape matters: Flow and heat transfer characteristics of nonspherical particles », *Powder Technology*, 431, p. 119102. https://doi.org/10.1016/j.powtec.2023.119102.

Sutton, A. *et al.* (2016) "Powders for additive manufacturing processes: Characterization techniques and effects on part properties."

Tambing, E. *et al.* (2025) « The Effect of Magnesium Addition to Al-10Si Alloy Through Casting at 740℃ on Mechanical Properties: A Simulation Study », *Annales de Chimie - Science des Matériaux*, 49(4), p. 375-383. https://doi.org/10.18280/acsm.490405.

Vigneau, E. *et al.* (2000) « Number of particles for the determination of size distribution from microscopic images », *Powder Technology*, 107(3), p. 243-250. https://doi.org/10.1016/S0032-5910(99)00192-8.

Wilsnack, C. *et al.* (2023) « Fabrication of an athermal mirror from a hyper-eutectic AlSi alloy via LPBF ».

Armel Perrotin
PhD Candidate, NTNU (Trondheim, Norway)
Armel Perrotin holds a MSc in Green Chemistry from the university of Poitiers (France). His master thesis was on the preparation and characterization of catalysts for aircraft air purification. He is currently working on the characterization of feedstock for additive manufacturing as part of his PhD at the Dept. of Materials Sciences and Engineering at NTNU within the SFI PhysMet (Centre for Sustainable and Competitive Metallurgical and Manufacturing Industry).

Jayakumari, S., V. Canaguier, H. Dalaker, C. Van der Eijk, and M. Ksiazek. 2026. Developing Optimized Agglomerates for Silicon and Ferroalloys industries. In *Silicon for the Chemical and Solar Industry XVIII*, edited by M. Tangstad, H. Rong, A. Valderhaug, B. Andresen, H. Dalaker, and I. G. Page. Kristiansand, Norway, September 7–10. https://doi.org/10.55669/oa900823

Developing Optimized Agglomerates for Silicon and Ferroalloys industries

Sethulakshmy Jayakumari[1], Vincent Canaguier[1], Halvor Dalaker[1], Casper Van der Eijk[1] and Michal Ksiazek[1]

[1]SINTEF, Norway, Sethulakshmy.Jayakumari@sintef.no

Keywords: Bio-carbon agglomerates, Pellets, Briquettes, SiO-reactivity, CO_2-reactivity, Strength

Abstract – The ferroalloy industry aims to reduce CO_2 emissions and achieve carbon-neutral production by 2050 by replacing fossil carbon with renewable biocarbon and developing sustainable process technologies. Although charcoal is already used as a reductant in ferroalloy production, its lower mechanical strength and higher fines generation compared with fossil carbon materials limit its use in large, closed furnaces, particularly in Norway. Therefore, improved biocarbon materials are needed to enable wider industrial adoption. This study focuses on developing sustainable, high-performance biocarbon agglomerates derived from biomass and waste/byproducts for silicon and ferroalloy production. It also focuses on improving the mechanical durability of renewable reductants through agglomeration techniques such as extrusion and briquetting, enabling the production of biomass pellets and briquettes. Strength enhancement is essential to minimize fines formation during transportation, storage, and furnace operation, thereby ensuring predictable carbon availability and stable carbon balance in industrial processes.

The study systematically investigates key agglomeration parameters - including particle size distribution, binder selection, and applied compaction pressure - and their influence on pellet strength, porosity, and gas reactivity. Laboratory-scale testing evaluated the durability and gas reactivity of the developed agglomerates to identify optimal processing conditions. Overall, the results demonstrated that charcoal fines can be successfully agglomerated into mechanically robust and thermally stable materials with properties suitable for ferroalloy production processes. The outcomes supported the transition toward carbon neutral ferroalloy production by providing mechanically robust, reactive, and sustainable biocarbon-based reductants suitable for industrial furnace applications.

Graphical abstract

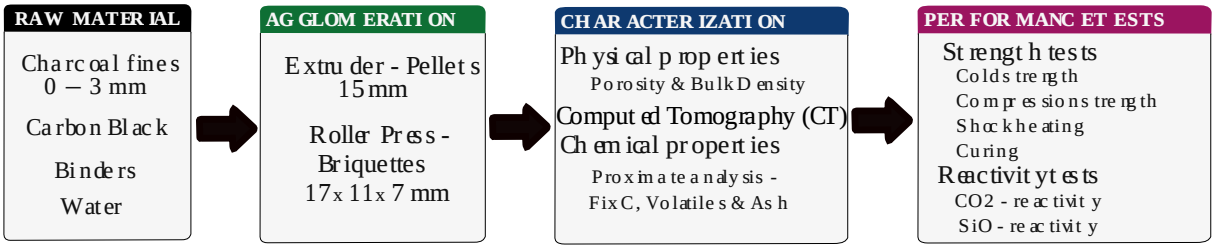

1. INTRODUCTION

Ferroalloys and silicon production play a vital role in modern industry and technologies, particularly in steel making, renewable energy systems and advanced electronic applications. These processes largely depend on carbonaceous reductants, to perform the carbothermic reduction of metal oxides in high temperature furnaces, traditionally using fossil based materials such as coal, coke and petroleum coke while also incorporating charcoal as part of the reductant mix in some operations. (Schei, Tuset and Tveit, 1998; Olsen, Tangstad and Lindstad, 2026). This significantly affects greenhouse gas emissions from metallurgical industries, thereby contributing to climate change (Lindstad et al., 2007a; Tangstad and Ringdalen, 2025). In response to the increasing environmental concerns and strict climate policies, there is a strong global commitment to achieve carbon neutrality by 2050. According

This work is licensed under the Creative Commons Attribution 4.0 International License. To view a copy of this license, visit https://creativecommons.org/licenses/by/4.0/

to Prosess21 report "New Process Technology for Reduced Carbon Footprint, including CCU", industrial greenhouse gas emissions especially in Norway are to be phased out by 2050 (Prosess21 ekspertgrupperapport, 2021). To achieve these ambitious targets, increased research and development of carbon neutral processes is essential. Although Norway already uses renewable hydropower making its production cleaner compared to many other countries, fossil carbon is still used in the furnaces, resulting in significant CO_2 emissions during metal production. The CO_2 footprint from the silicon and ferroalloy production is directly linked to the consumption of fossil reductants, with emissions of several tonnes of CO_2 per tonne of metal produced. Typical emissions range from 1.4 to 6.9 t CO_2 per tonne of ferroalloy and 2.5 to 4.8 t CO_2 per tonne of for ferrosilicon (FeSi) (Han and Tangstad, 2024). A promising solution is to replace fossil-based reductants with renewable carbon sources, in particularly with biocarbon derived from biomass. In response to these challenges, the ferroalloy industries aim to replace fossil carbon with biocarbon, targeting a 40–50% reduction in CO_2 emissions by 2030, and further progressing towards fully carbon neutral processes by 2050. (Sommerfeld and Friedrich, 2021; Han and Tangstad, 2024; Hoover, Bell and Rippy, 2024)

Biocarbon is a renewable and CO_2 neutral source of carbon, since the CO_2 released during its use is balanced by the CO_2 absorbed during the growth of biomass. Because of this, the use of biomass-based materials in metallurgical process has received increasing research attention. But despite known benefits, the industrial use of biocarbon is still limited due to its weaker physical and mechanical properties compared to conventional coal and coke. (Smith-Hanssen, Jahrsengene and Ringdalen, 2023a; Han and Tangstad, 2024). Some of the main limitations of biocarbon, particularly charcoal, are its low mechanical strength, high porosity, and poor structural integrity. These properties lead to significant degradation during handling, transportation, and furnace operation, resulting in the generation of fines. In industrial silicon production, it has been reported that more than 10% of charcoal can be lost as fines due to abrasion (Jayakumari and Ksiazek, 2024). The presence of these fines in submerged arc furnaces negatively affects burden permeability, gas flow distribution, and process stability, ultimately reducing furnace efficiency and operational reliability (Makgobelele et al., 2021; Han and Tangstad, 2024; Jayakumari and Ksiazek, 2024).

To address these challenges, agglomeration techniques such as extrusion, briquetting, and pelletizing have been proposed as effective solutions to improve the handling and performance of biocarbon materials. These techniques convert fine materials into compact, high-density agglomerates with uniform size and shape, enhancing their mechanical durability and suitability for industrial applications (Karunanithy et al., 2012).

Many ferroalloy and silicon plants possess significant quantities of underutilized carbon resources in the form of charcoal fines that cannot be directly add into the furnaces. With the growing demand for biocarbon in metallurgical applications, it becomes increasingly important to utilize all available biomass resources efficiently. In addition to the conventional lump charcoal, significant quantities of carbon rich residues are generated throughout the biomass value chain, including fines from pyrolysis process, sawdust from wood processing industries etc. The conversion of such residual biomass into useful products is a key element of circular bioeconomy strategies, where waste streams are valorised into high-value materials, reducing environmental impact and improving resource efficiency (Obi, Pecenka and Clifford, 2022; Olofsson, 2025). Although agglomeration through briquetting or pelletizing appears to be an intuitive solution to recover these materials, practical implementation often faces critical challenges. A common limitation in existing approaches is the emphasis on cold mechanical strength, which primarily addresses handling, storage, and transportation requirements. However, the performance of agglomerates under actual furnace conditions is governed by their thermal stability, or hot strength, so binder selection is crucial. In submerged arc furnace (SAF) operation, agglomerates are exposed to rapid temperature gradients and mechanical stresses within the reaction zone. If the binder system and curing conditions are

not properly optimized, agglomerates may undergo degradation due to thermal shock. This can result in the formation of fines within the furnace; Therefore, the design of biocarbon agglomerates must extend beyond cold strength considerations to ensure adequate performance under high-temperature process conditions.

Optimizing agglomerated biocarbon requires careful control on both mechanical and chemical properties. While increasing compaction pressure, binder content and addition of water can significantly affect strength and durability. Furthermore, different metallurgical processes impose distinct requirements on the properties of carbon reductants. Some processes require materials with high porosity and sufficient mechanical strength to ensure gas reactivity and permeability, on the other hand other processes may benefit from denser materials with low reactivity to achieve controlled and stable reduction behaviour (Kaffash, Surup and Tangstad, 2021). This highlights the need for process specific design of agglomerates, where the balance between mechanical strength, porosity, and reactivity must be carefully optimised (Jayakumari and Ksiazek, 2024).

Several key parameters govern the performance of agglomerated biocarbon, including particle size distribution, binder type and amount, moisture content, applied compaction pressure and curing conditions. These parameters significantly influence the internal structure, density, porosity, and gas reactivity of the final agglomerated product. Mechanical strength, thermal behaviour and performance under high temperature conditions are also affected (Olugbade, Ojo and Mohammed, 2019; Zhang et al., 2020). Although previous studies have investigated individual aspects of biomass densification, there remains a lack of systematic and application-specific research focused on optimizing agglomerates for silicon and ferroalloy production (Karunanithy et al., 2012).

The present study aims to develop sustainable and high-performance biocarbon agglomerates derived mainly from charcoal fines as well as carbon black. The work focuses on optimizing agglomeration techniques such as extrusion and briquetting to produce agglomerated pellets and briquettes with mechanical durability and controlled reactivity at high temperature conditions. Laboratory scale investigations are conducted to evaluate both the physical and chemical properties, mechanical strength, and gas reactivities and compare their performances with that of charcoal, coal and metallurgical coke, the latter being the coke (made form coking coal) typically used in the manganese ferroalloy production. The outcomes of this research are expected to provide valuable insights into the design of robust and sustainable carbon materials with optimal reactivity, thereby supporting the transition towards carbon neutral silicon and ferroalloy production.

2. MATERIALS AND METHODS

2.1 Materials

Charcoal fines (CC-17) in the particle range of 0–3 mm were used as the primary carbon source in this study. These materials were supplied by **OZEN Sp. Z o.o.**, a leading producer of certified charcoal. Regarding carbon black, the sources are anonymized for confidentiality reasons. To produce charcoal-based agglomerates, a range of binders was utilized including Ca-, Na- and NH_3- based lignosulphonates, wheat starch and solid pyrolytic lignin (SPL) (Narron, Wolken and Gargulak, 2020; Butler, Skrivan and Lotfi, 2023). These binders were provided by established industrial suppliers, namely **Borregard**, **Crespel & Deiters** and **BTG group**. In addition, commercially available bentonite was included in some of the binder mix. Microsilica, sourced from an industrial silicon production plant was also investigated as a potential binding agent in the production of extruded pellets to examine its influence on strength and high temperature behaviour. Furthermore, quartz-charcoal composite pellets were produced separately via extrusion to examine the feasibility of manufacturing such

composite materials using this technique. The carbon black pellets were produced using two carbon black types and bio binders. Due to confidentiality, the specific details regarding the composition and formulation of the binders cannot be disclosed. It should be noted that these pellets were not produced as part of present study, but these were developed as a part of the MECALO project by **ITPE** (Institute of Energy and Fuels Processing Technology, Zabrze, Poland).

The carbon source, binding agents and the produced pellets and briquettes are shown in figure 1. Table 1 presents the abbreviations used for the carbon and binder materials in the different pellet and briquette recipes. Charcoal (CC-16), coal (C-17) and coke (CK-009), acquired from ferroalloys industries, were used as reference materials.

Figure 1: Raw materials used for producing charcoal pellets and briquettes

Table I. Abbreviations used for carbon and binder materials

Charcoal - **CC**	Starch - **S**
Coal - **CL**	Solid Pyrolytic Lignin - **SPL**
Coke - **CK**	Bentonite - **B**
Carbon Black - **CB**	Quartz - **Qz**
Pellets - **PLT**	Microsilica - **M**
Briquettes - **BRQT**	**Ca, Na, NH_3** – Calcium-, Sodium-, Ammonium-Lignosulphonates

2.2 Extrusion and Briquetting

Prior to extrusion, all raw materials were thoroughly premixed using a laboratory mixer to ensure homogeneous distribution of biomass, binders, and moisture.

Extrusion of charcoal pellets was carried out using a laboratory-scale extruder (DEX Lab, Verdes). The extruder consists of an inlet hopper, a pre-compression unit equipped with

mixing knives, a vacuum chamber, and an extrusion body. The premixed material was fed through the hopper into the pre-compression unit, where it was further conditioned to facilitate smooth transport by the augers. The material was then conveyed into the next chamber and subsequently extruded into pellets.

A die size of 15 mm was used for all extrusion experiments to produce uniform pellets. The operating conditions were adjusted by varying the auger speed within a frequency range of 20–30 Hz. The extrusion parameters were optimized depending on material characteristics such as particle size, binder type, and moisture content to ensure stable pellet formation. A schematic illustration of the extrusion set up, including the pre-mixer, extruder and extrusion die is shown in figure 2 while the schematic illustration of the briquetting machine is shown in figure 3.

Charcoal fines briquettes were produced using a laboratory-scale roller press (B050), with a processing capacity of 1–45 kg/h depending on material properties and operating conditions. Prior to briquetting, the raw materials including charcoal fines, binders, and water were thoroughly premixed in a separate mixer to ensure homogeneity. The prepared mixture was fed into the briquetting machine through the feed hopper, from where it was transported via vertical and horizontal screw feeders into the nip zone. Briquetting was achieved by compressing the material between two counter-rotating rolls under applied hydraulic pressure. The operating parameters, including screw and roll speeds, were adjusted using variable speed drives to ensure stable briquette formation. The briquettes produced had approximate dimensions of 17×11×7 mm, using rolls with a diameter of 100 mm and a width of 20 mm.

It should be noted that carbon black (CB) pellets were not produced using the same methodology as in the present study, and detailed information regarding their production process is not disclosed.

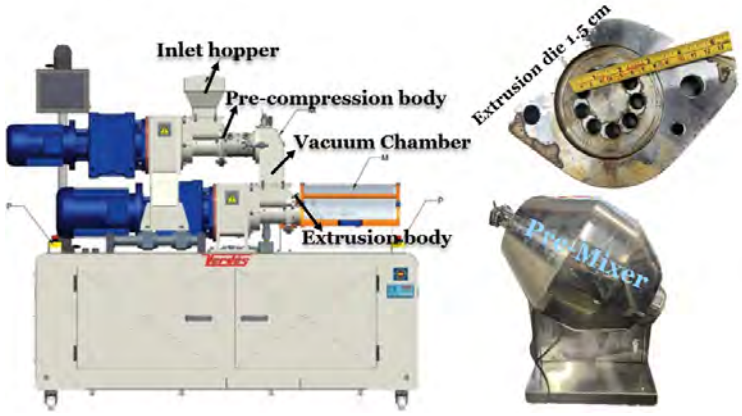

Figure 2. Schematic illustration of the extrusion set up, including the pre-mixer, extruder and extrusion die.

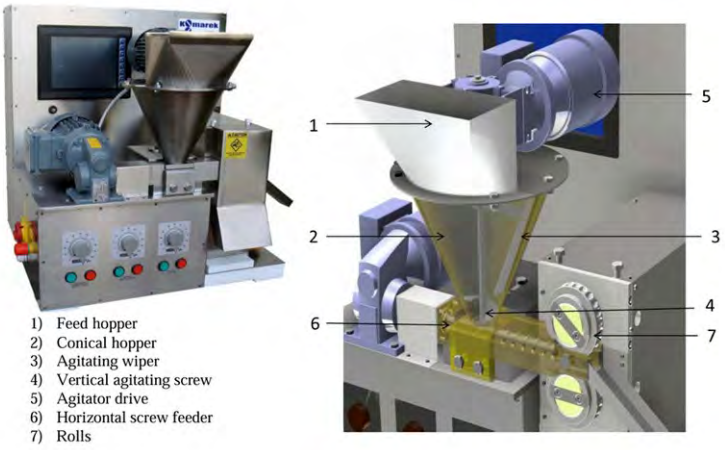

Figure 3. Schematic illustration of the briquetting machine

A stage-gate approach was used to evaluate carbon materials for Mn and Si processes (Smith-Hanssen, Jahrsengene and Ringdalen, 2023a). Mechanical properties were assessed first to exclude unsuitable materials, followed by reactivity testing for the selected materials. Materials were characterised under process relevant conditions using experimental procedures developed at SINTEF and NTNU. This approach enables systematic evaluation of carbon materials considering their multiple roles in metallurgical process.

Porosity was determined by combining skeletal and envelope density measurements using an AccuPyc gas pycnometer using helium gas displacement and a GeoPyc displacement pycnometer respectively.
Figure 4 shows the porosity measured for one briquette (BRQT), five different charcoal pellets (PLT) produced using different binder compositions, three selected silicon carbide (SiC) pellets after the SiO reactivity test, two carbon black (CB) pellets, two types of charcoal (CC), one coal (CL) and one coke (CK-009). Interestingly, the porosity of all pellets, the briquette and the SiC converted pellet samples fall within the value observed for coal. However, the conventional carbon materials show a clear difference in porosity, with charcoal exhibiting the highest porosity followed by coal and then coke.

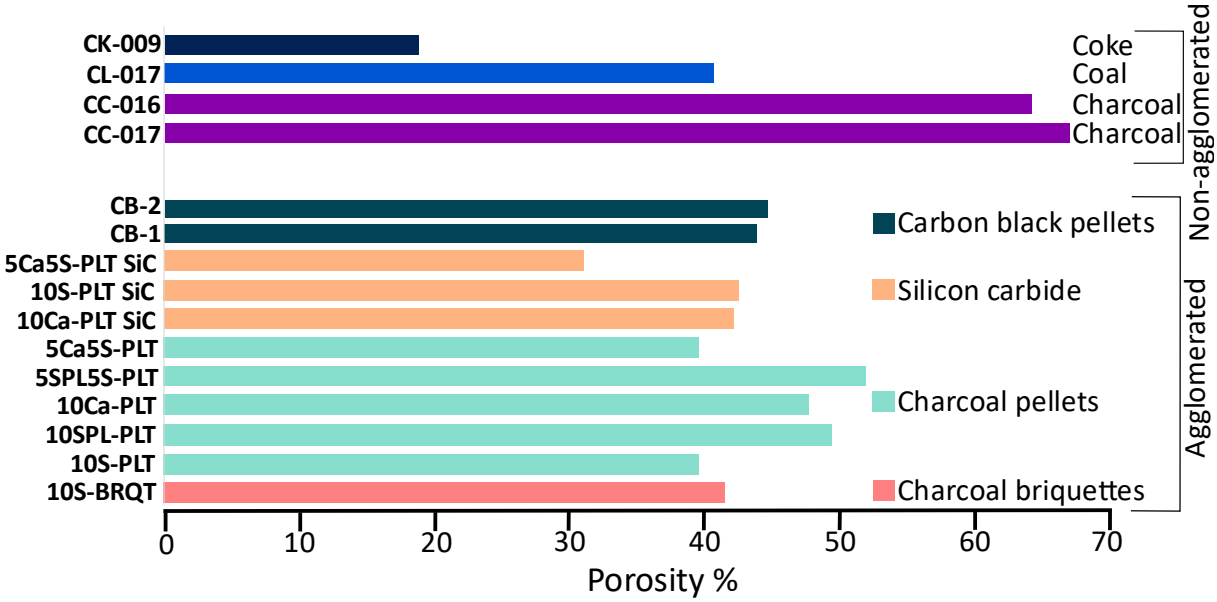

Figure 4. Porosity values for the agglomerated charcoal materials, carbon pellet converted SiC samples (after the SiO reactivity test), carbon black pellet sand the conventional carbon materials.

Bulk density was measured by filling a 100 mL beaker with the sample and determining its mass. The bulk density was then calculated as the ratio of sample mass to the known volume of the beaker. Figure 5 presents the measured bulk densities of the pellets, briquettes and conventional carbon materials. The agglomerated pellets and briquettes exhibit relatively higher bulk densities in the range of 0.30–0.40 g/cm^3, which is comparable to that of coal. Among the agglomerated samples, the carbon black pellet (CB-2) shows the highest bulk density, exceedingly even that of coke. In contrast, both charcoal samples display lower bulk densities, with noticeable variation in both.

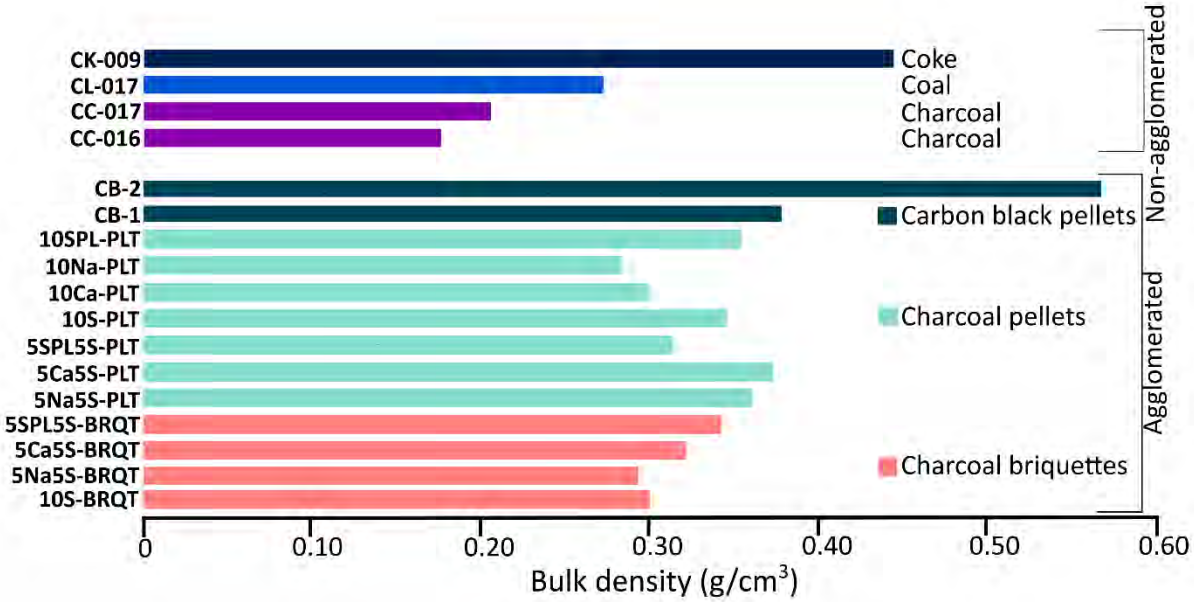

Figure 5. The measured bulk densities of the pellets, briquettes and conventional carbon materials.

Bulk density and porosity show an inverse relationship, where higher porosity generally results in lower bulk density (Jayakumari and Ringdalen, 2022). The agglomerated pellets and briquettes exhibit moderate porosity and relatively higher bulk densities similar to coal. In contrast charcoal samples display higher porosity which corresponds to their lower bulk densities. The carbon black pellet (CB-1) shows higher bulk density indicating a more compact structure with reduced pore volume. Overall, these trends confirm that variations in porosity strongly influence the bulk density of the materials.

A micro-X-ray computed tomography (µCT) analysis was conducted to evaluate the internal structure of the pellets such as the distribution and incorporation of the binder and the particle size distribution within the pellets. Figure 6 presents CT-images of charcoal and coal, figure 7 shows different agglomerated pellets and figure 8 shows pellets produced using charcoal-microsilica and charcoal-quartz mixtures. The pores in charcoal are relatively large and uniformly distributed, whereas coal exhibits a more heterogeneous pore structure with regions of both large pores and dense areas. In the agglomerated pellets, both pores and particles of varying sizes are more homogeneously distributed, resulting a dense structure. A clear influence of the binder on pellets structure is observed. The use of SPL as a binder made pellet production more challenging, leading to the development of cracks in the final pellets. Additionally, pellets containing microsilica and quartz demonstrate that such composite materials can be successfully produced using extrusion process.

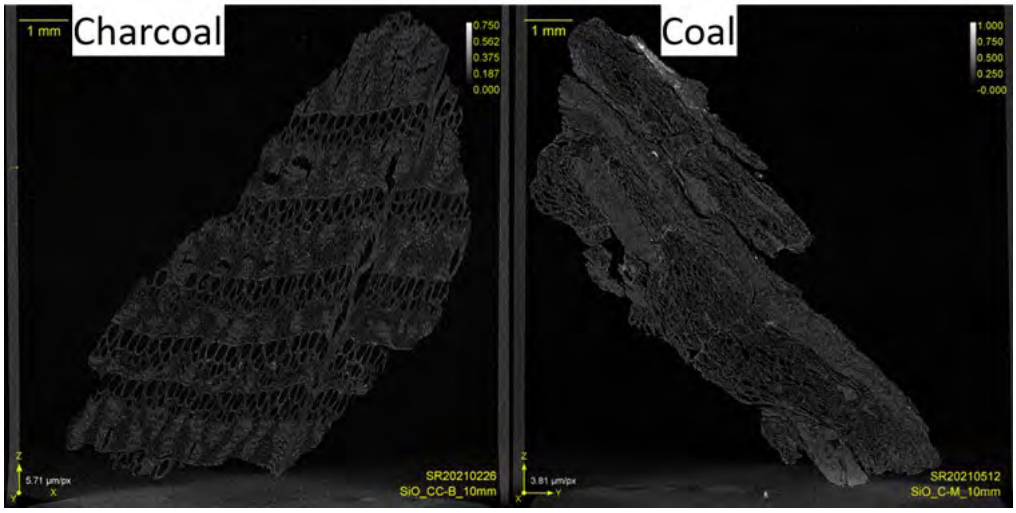

Figure 6. CT-images of charcoal and coal

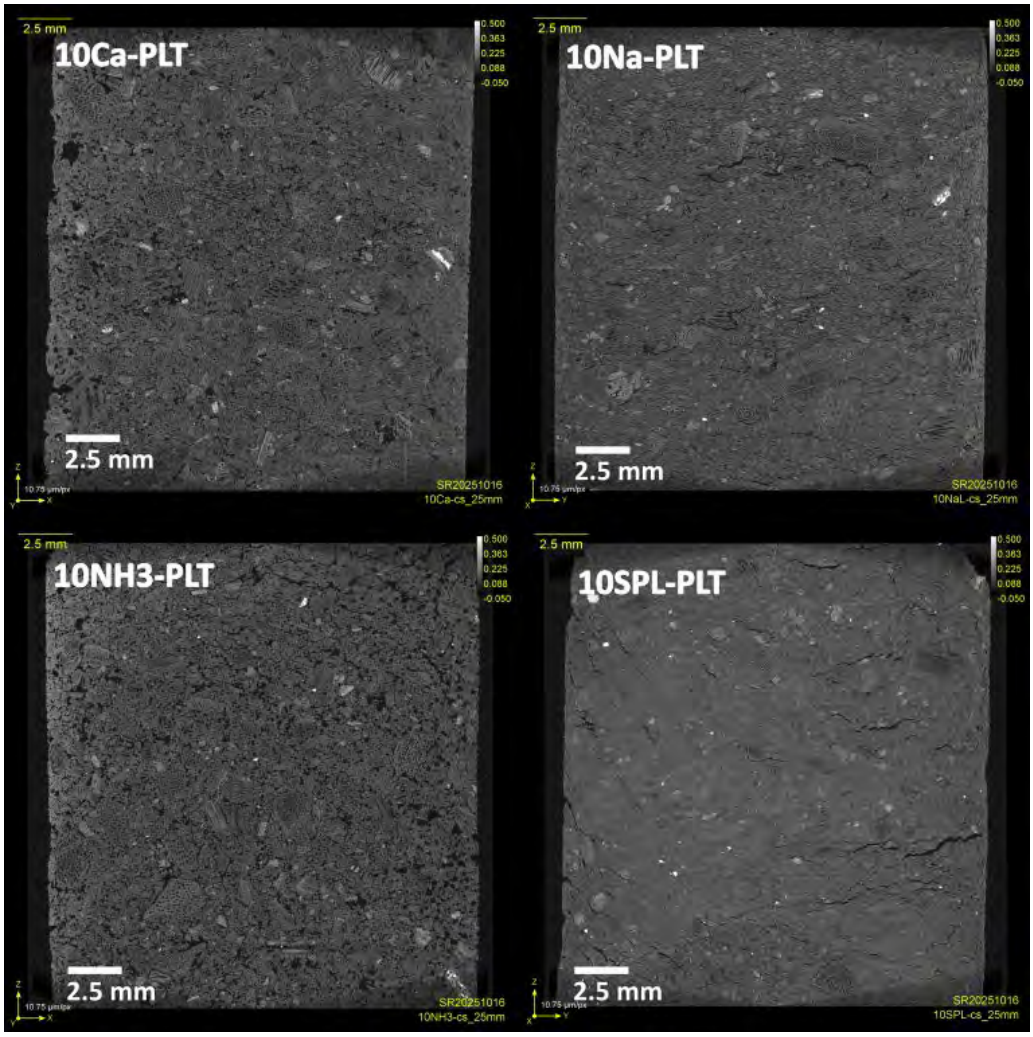

Figure 7. Extruded pellets with different binders

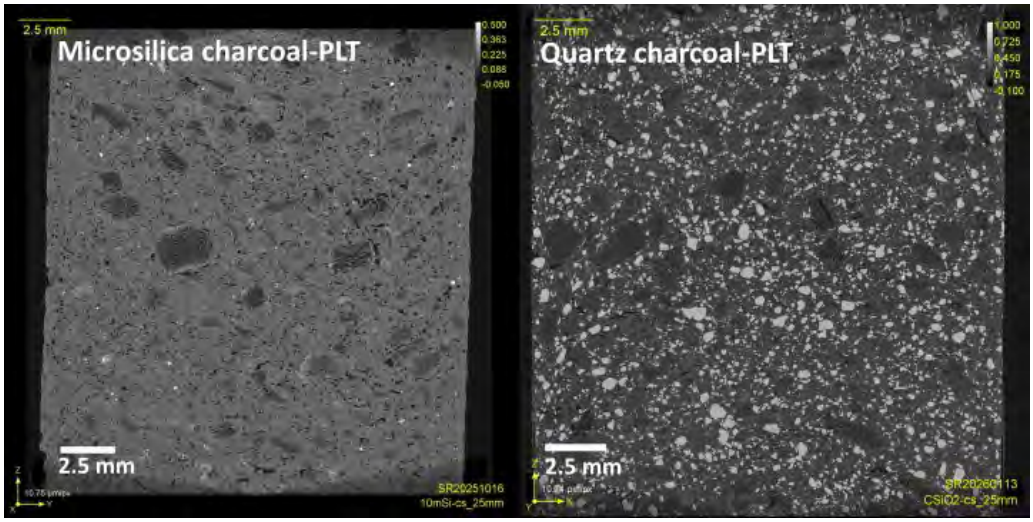

Figure 8. Extruded microsilica-carbon pellets and quartz-carbon pellets

Proximate analysis of the extruded pellets was performed at an accredited laboratory to determine the total fixed carbon (Fix-C), volatile matters and ash.

Table II: Proximate analysis of both the conventional carbon materials and the various agglomerated pellets.

Sample name	Fix-C (wt.%)	Volatiles (wt.%)	Ash (wt.%)	Moisture (wt.%)
Conventional carbon materials				
CK-009	87.08	0.61	11	4.5
CL-017	97.8	0.83	1.31	0.02
CC-016	91.9	3.18	3.67	1.27
CC-017	86.37	11.74	1.89	2.49
Agglomerated pellets				
10S-PLT	81.30	16.78	1.92	16.78
10SPL-PLT	75.69	12.71	11.6	1.01
10Ca-PLT	81.42	15.05	3.53	1.43
10Na-PLT	81.82	14.55	3.63	1.52
7SPL3S-PLT	81.91	15.85	2.24	0.91
7Ca3S-PLT	81.45	15.39	3.16	1.14
5SPL5S-PLT	81.42	16.24	2.34	0.90
5Ca5S-PLT	80.45	16.98	2.57	1.07
5Na5S-PLT	81.12	16.38	2.50	1.11

**CL-017, CC-016 and CC-017 proximate analysis measured after calcinated samples at 1200 °C.

2.3 Evaluating Mechanical Strength

Industrial furnaces are typically large and contain substantial amounts of raw materials. The production of dust and fines is closely correlated with the mechanical strength of these materials. Evaluating the cold strength is of importance as it both influences fines generation during transportation but also denotes the material's capacity to withstand the weight above it without undergoing crushing. Similarly, the interaction of carbon materials with gas and sudden temperature change upon entering the furnace can lead to a change in its strength (Monsen et al., 2007). The warm strength is the ability of the material to withstand the burden load of the descending charge materials and is measured through shock heating tests at the laboratory scale.

Cold Strength

The cold strength of carbon materials is a critical factor for various industries and currently represents a significant challenge in increasing the use of biocarbon. Studies have shown that up to 25% of charcoal can be lost during transport from the pyrolysis plant to the furnace, leading to substantial cost implications and potential environmental impacts due to the dispersal of fine particles **(Jahrsengene et al., 2023)**. Mechanical strength can be evaluated through multiple methods, each measuring different types of strength relevant to various stages of handling and processing. These methods include:

1. **Tumble/Drum test**: This measures resistance to abrasion and is the primary method used to estimate the degradation occurring during transport and furnace charging.
2. **Compression test**: This evaluates the breakage of materials under high loads, similar to those experienced in the lower parts of the furnace.

Tumble/Drum test

The strength of the sample was estimated by tumbling it in a rotating drum. Samples of approximately 100 g of either extruded pellets (maximum length 30–40 mm) or briquettes were tested separately in their original form without crushing. The selected sample was then placed in a steel drum with an inner diameter of 200 mm, equipped with four raisers spaced 90 degrees apart. A schematic illustration of the rotating drum used to evaluate the generation of fines is shown in Figure 9. The sample tumbled for a total of 30 min in two steps. In step 1, the sample tumbled for 10 min at 40 rpm. Then the sample was removed, sieved into size fractions of 10 mm, 6.3 mm, 4.75 mm, 3.35 mm, 1.25 mm, 0.5 mm, 0.25 mm, and 0.125 mm and the size distribution was measured. The entire sample was then placed back in the drum and tumbled for an additional 20 min at 40 rpm. After this second tumbling, the sample was removed and re-sieved. The fraction of fines, defined as any material under 3.35 mm, was used to determine the mechanical strength of the material. These methods ensure a comprehensive understanding of the mechanical durability of carbon materials, which is essential for optimizing its use in industrial processes and minimizing material losses and environmental impacts.

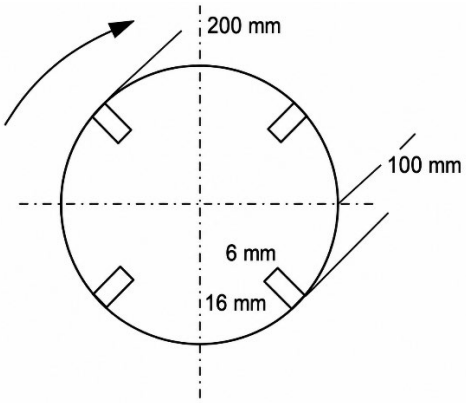

Figure 9. Schematic illustration of the rotating drum.

Compression Tests

Compression tests were conducted using a Zwick Roell compression tester with a maximum load capacity of 2500 N (Jayakumari and Ksiazek, 2024). Extruded pellets of 10 mm length were subjected to an increasing compression load until failure. The compression tester's head moved at a fixed rate of 2 mm/min, and the applied load was recorded. The test continued until either failure occurred or the original sample height was reduced by at least 4 mm. For

each carbon type (extruded pellets or briquettes), 10 tests were performed: 5 tests parallel to the extrusion direction and 5 perpendicular. The average, minimum, and maximum peak load for each direction were calculated.

Warm Strength (Thermal Shock Heating)

In industrial silicon furnaces, raw materials are subjected to rapid heating as the furnace's top typically reaches temperatures of 800–1000 °C. This rapid temperature change can induce significant thermal stresses, leading to the fracturing of the material. The ability of a carbon reductant to withstand this rapid heating is crucial for maintaining its integrity and performance in the furnace (Smith-Hanssen, Jahrsengene and Ringdalen, 2023b). This can be assessed using the Thermal Shock Heating test.

In this method, 100 g of a sample with a known particle size is dropped into a crucible preheated to 1000 °C and held at this temperature for 10 min. This test simulates the conditions for Si-production in a submerged arc furnace where cold fresh charge is introduced on top of the hot burden. The change in particle size distribution after exposure provides an indication of the material's thermal shock resistance. Following the test, the sample is sieved into the following size fractions: 10, 6.7, 4.75, 3.35, 1.25, 0.5, 0.25, and 0.125 mm. The aim of this task was to investigate the effect of fines generation in different reduction materials at temperature relevant to different furnace operations. Temperatures in the upper burden region of Mn alloys furnaces are typically below 500 °C, contrasting with temperature up to 1000 °C for Si furnaces (Ringdalen, 2014; Jusnes, 2020; Aasly Kurt , 2016). Therefore, the samples were subjected to thermal shock at both 500 °C and 1000 °C for 10 minutes to evaluate the influence of thermal shock under different temperature conditions. The resulting particle size distributions were then determined and compared to identify differences in material behaviour and test temperature.

Curing

The effect of curing was investigated on pellets samples made with two different recipes, one with only starch as the binder and another with a combination of Ca-lignosulphonate and starch. A muffle furnace capable of operating under argon atmosphere was used and the samples were heated to 200, 250 and 300 °C separately, with a holding time of 30 minutes at the final target temperature. After curing and for each temperature program, one pellet was immersed in water to assess the resistance to degradation, while the remaining samples were subjected to an abrasion (cold strength) test to evaluate the effect of curing on the generation of fines.

2.4 Reactivity with furnace gas at high temperatures

In silicon and ferroalloys production processes reactivity of carbon materials strongly influences both energy consumption and final metal yield. In the silicon process, reactivity refers to the ability of carbon materials to react with silicon monoxide (SiO) gas to form silicon carbide (SiC) which is the main intermediate compound in the final silicon forming reaction. Therefore, a carbon reductant with sufficiently high reactivity is required. In contrast, in the manganese process, the reactivity of carbon towards carbon dioxide (CO_2) gas is critical and undesired, as it affects the carbon balance and energy efficiency. In this case, a lower reactivity is preferred to minimize excessive carbon consumption (Schei, Tuset and Tveit, 1998; Olsen, Tangstad and Lindstad, 2026).

CO_2 – Reactivity test

The CO_2 reactivity test was performed using a thermogravimetric furnace (Figure 10), by a method developed by NTNU/SINTEF specifically for Mn alloy production. In the industrial manganese process, the CO_2 concentration ranges from 0 to 50%, and the temperature increases from the top of the charge towards the top of the coke bed where the liquid slag is formed (Olsen, Tangstad and Lindstad, 2026). The tests are conducted in an atmosphere that consists of either 75% CO and 25% CO_2 or 50% CO and 50% CO_2, simulating the conditions in the furnace, at temperatures ranging from 800 to 1100 °C (Jayakumari et al., 2023). In this work, a 50:50 ratio of CO:CO_2 and a temperature of 1100 °C were selected.

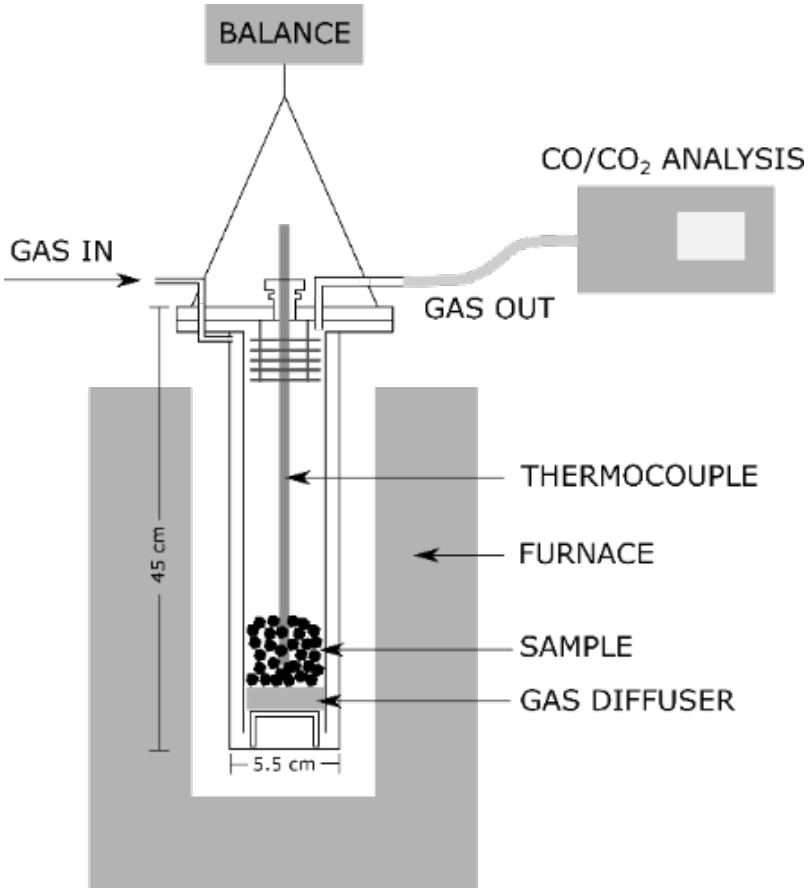

Figure 10. TGA furnace setup is used to measure the CO_2 reactivity (Jayakumari et al., 2023).

The test involves heating approximately 100 g of 5–10 mm carbon samples at a rate of 10 °C/min to reach a temperature of 1100 °C. The samples are then held at this temperature for 1 hr 45 min in a flow of 1 L/min of argon, followed by a flow of 4 L/min for an additional 30 min. Once the temperature reached 1100 °C, the Ar gas is replaced with a mixture of 50% CO and 50% CO_2 (2 L/min each). The weight change of the sample is continuously monitored to track the reaction between the carbon and CO_2 to produce CO. At 1100 °C, any volatiles and moisture are expected to be removed from the sample. As a result, any weight change observed during the experiment is solely due to the reaction between carbon and CO_2 to CO (Kaffash, Surup and Tangstad, 2021). The test is stopped when a weight loss corresponding to 20% of fixed carbon has reacted. The reaction of carbon results in a percentage mass loss curve that is linear with respect to time, and the slope of the curve corresponds to the CO_2 reactivity or the amount of fixed carbon (% fixed C) that reacts per unit time.

The strength of the materials depends on the extent of their reaction. It is therefore essential to examine the hot strength after the same degree of reaction, ensuring that the materials being compared are reduced by the same amount.

Thermal Abrasion Strength (warm strength)

The reaction of a carbon material with CO/CO_2 gas, along with gradual temperature changes when they descend in the furnace, can lead to a change in its strength. The ability of material to withstand abrasion after reaction is known as its **warm strength**. Loss of strength in carbon material due to their or binder reaction to gas can be measured. Here, the thermal abrasion test is performed on the reaction product obtained from the CO_2 reactivity test to measure the change or loss of strength in carbon material (Monsen et al., 2007). Prior to the test the carbon materials are first screened into specific size fractions.

To determine the thermal abrasion strength, the first step is to calculate the C.I (cohesion Index), which is the fraction of the largest size fraction (>4.75mm) after the CO_2 reactivity test (Monsen et al., 2007). Then, the sample is tumbled in a rotating drum (figure 9) for 10 min at 40 rpm, after which the sample is removed, sieved to 6.3, 4.75, 3.3 and 1.25 mm size fractions and the size distribution measured. The entire sample is placed back in the drum and tumbled for 20 more minutes at 40 rpm before being removed and re-sieved. The fraction of fines formed is reported from this test. In this case, the fraction of materials larger than 3.35 mm after tumbling is used to determine the T.I.3 (Thermal Stability Index), which represents the resistance to degradation and abrasion under furnace conditions.

SINTEF SiO reactivity test

The experimental set up for SINTEF SiO-reactivity tests consist of three separate alumina chambers heated by a graphite tube furnace (Tuset, J. K and Raaness, O., 1976; Lindstad et al., 2007b). The main reactions and distribution of gas flows through the SiO(g) generation chamber, reaction chamber and condensation chamber are illustrated in figure 11. The standard particle size range used for the test is 4–6.3 mm

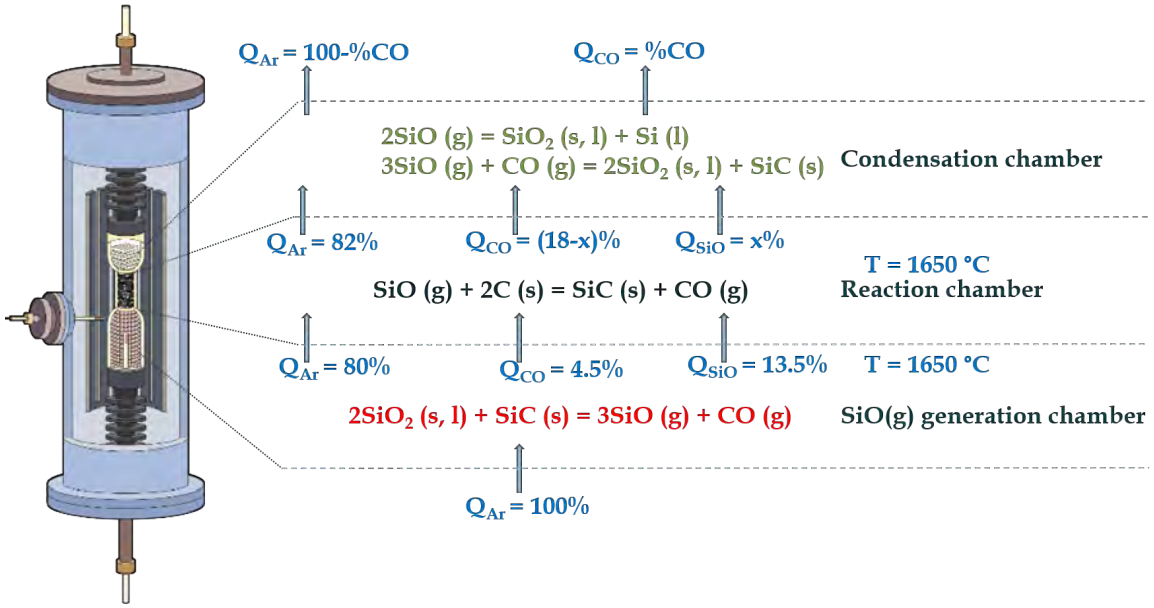

Figure 11. Schematic illustration of the experimental set up for SINTEF SiO reactivity test.

In the generation chamber, SiO(g) is generated at 1650 °C according to reaction 1 from pellets made of SiO_2 and SiC.

$2SiO_2 + SiC = 3SiO + CO$ (1)

The carbon materials, calcined before the test, are placed in the reaction chamber (the sample-bed with height 60 mm and radius 10 mm) which has a volume of 20 mL. During the test, SiO(g) passing though the carbon bed in the reaction chamber reacts to form SiC and CO (reaction 2). The SiO(g) left unreacted is captured and condensed in the condensation chamber. CO in the off gas is continuously measured.

$SiO + 2C = SiC + CO$ (2)

The gas from the generation chamber leaves saturated in SiO and CO. From equilibrium calculation at 1650 °C, this corresponds to a mixture of 13.5% SiO, 4.5% CO and 82% Ar (Lindstad et al., 2007b). When SiO(g) reacts with carbon materials, CO is generated: full conversion of SiO to SiC results in an outlet gas containing 18% CO. When CO drops down to 6%, it indicates that nearly all SiO(g) passes unreacted through the carbon material in the reaction chamber and condenses at the condensation chamber according to reaction 3 and 4.

$2SiO = SiO_2 + Si$ (3)

$3SiO + CO = 2SiO_2 + SiC$ (4)

The time taken for the concentration of CO to decrease from 18% to 6% depends on the properties of the carbon materials. Thus, the reactivity is defined as the volume of SiO(g), in mL, which passes through the carbon layer in the time in which CO decreases from 18% to 10% (R10) or to 6% (R6) as calculated from the equations below (Lindstad et al., 2007b).

$$R10 = \sum_{18\rightarrow 10\%} \frac{Q_{Ar}(18 - \%CO)}{82 - 0.82 * \%CO} * \Delta t$$

$$R6 = \sum_{18\rightarrow 6\%} \frac{Q_{Ar}(18 - \%CO)}{82 - 0.82 * \%CO} * \Delta t$$

3. RESULTS AND DISCUSSION

The results and discussion are mainly divided into two parts: mechanical strength and reactivity. The mechanical strength of the agglomerated materials was evaluated using several methods described in section 2. In addition, the reactivity of the materials was investigated, focusing on CO_2 and SiO reactivity.

3.1 Cold strength

Figure 1, presents the cold strength results for agglomerated pellets and briquettes produced with different binder compositions, along with charcoal (CC-17) and coke (CK-009).

Seven different briquettes (BRQT) and eleven different charcoal pellets (PLT) produced using different binder compositions were selected for the cold strength measurements. Interestingly, pellets made using starch as a binder generate a low amount of fines (<10%) after 30 min of tumbling, comparable to the fines produced by coke (<10%). In contrast, the highest fines generation is observed for pellets produced with SPL as a binder (50 – 80%). As indicated by the CT images, pellets made with SPL exhibit a cracked structure, which weakens the material and leads to increased fines formation. In the case of briquettes, fines generation remains relatively high and shows little variation across different compositions. Among the tested samples, starch-based agglomerates consistently produce the lowest amount of fines.

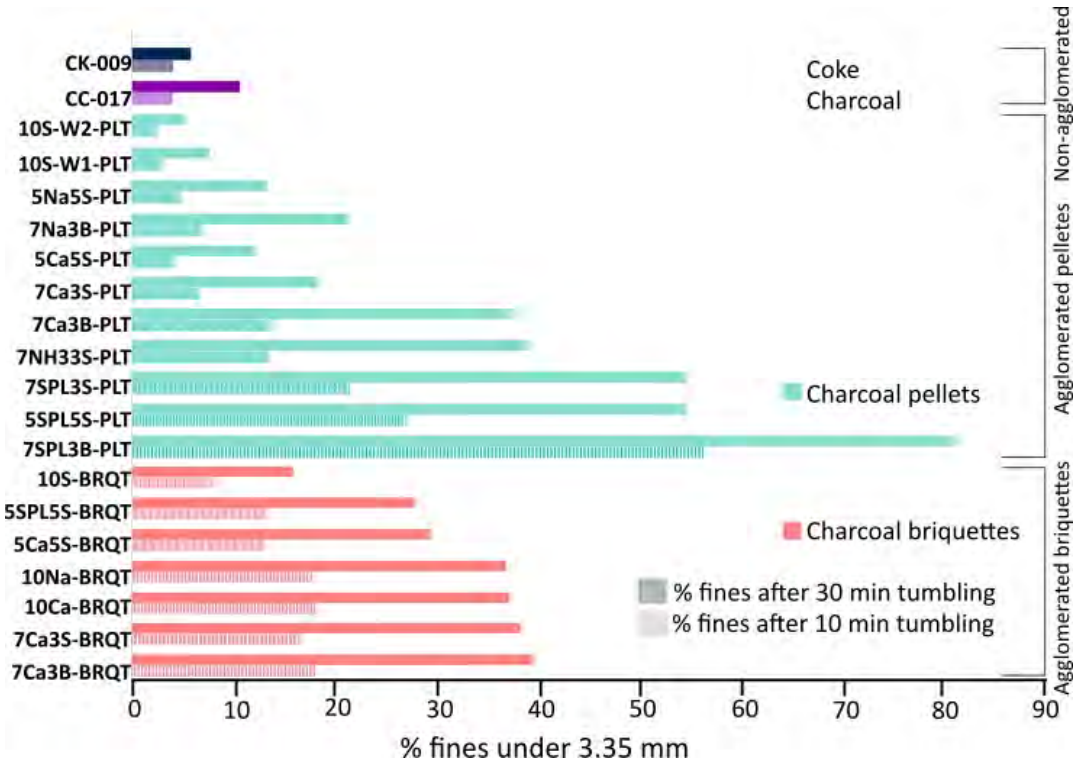

Figure 11. The cold strength results for agglomerated pellets and briquettes produced with different binder compositions, along with charcoal (CC-17) and coke (CK-009). W1 and W2 denote pellets prepared with same binder, differing only in the amount of water used during pelletization.

3.2 Compression strength

To evaluate the effect of furnace conditions on pellet strength, compression tests were performed on pellets both before and after exposure to CO/CO_2 atmosphere at 1100 °C. All pellets had approximately the same dimensions, with a diameter of 15 mm and a length of 15 mm. The results are summarized in Figure 12 and 13, which presents the average peak load for all samples, along with the corresponding minimum and maximum values measured for each type of extruded pellet. In both conditions, pellets produced using starch as a binder exhibit the highest strength, with maximum forces in the range of 1200–1800 N. In contrast, pellets made with SPL show the lowest initial strength (figure 12). However, an increase in strength (figure 13) is observed for SPL-based pellets after exposure to elevated temperature and reactive gas, indicating structural changes during heat treatment. The increase in strength of SPL-based pellets after heat treatment can be attributed to thermal densification and sintering, which enhance inter-particle bonding and reduce pore volume, as reported in previous studies (Chhiti et al., 2012; Branca and Di Blasi, 2025; Pahnila et al., 2026). Previous studies indicate that lignin exhibits thermoplastic behaviour at moderate temperatures, enhancing particle bonding. However, at higher temperatures it undergoes thermal decomposition and carbonization, forming a more rigid carbon structure that can contribute to increased strength after heat treatment (Chhiti et al., 2012). Overall, starch-based pellets exhibited the highest mechanical strength both before and after exposure to furnace conditions.

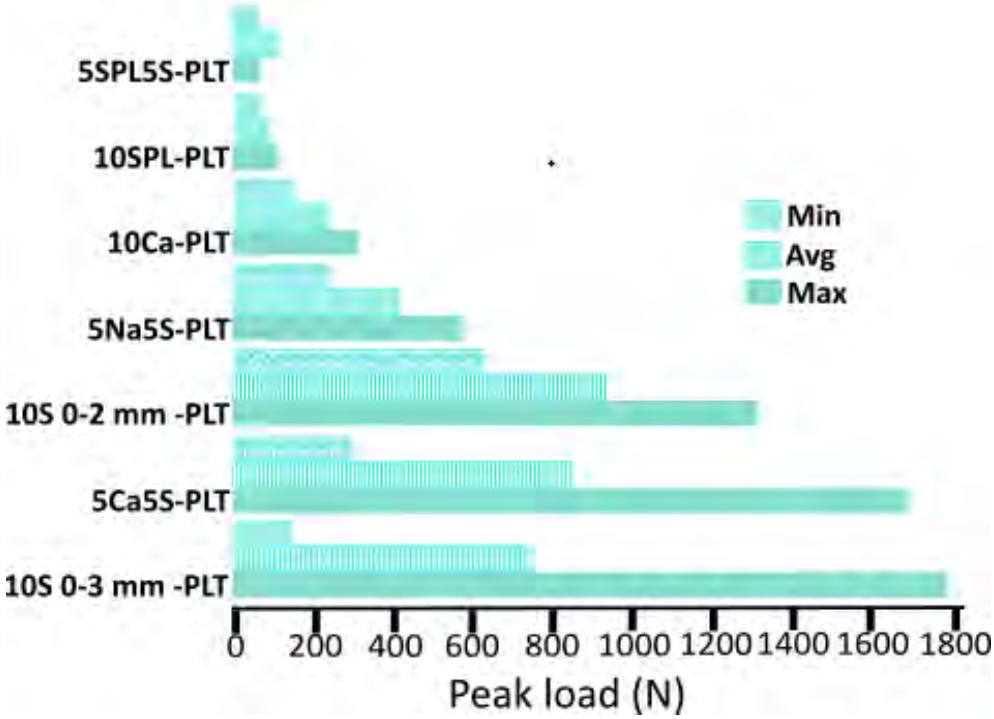

Figure 12. Force at failure in compression test for untreated pellets.

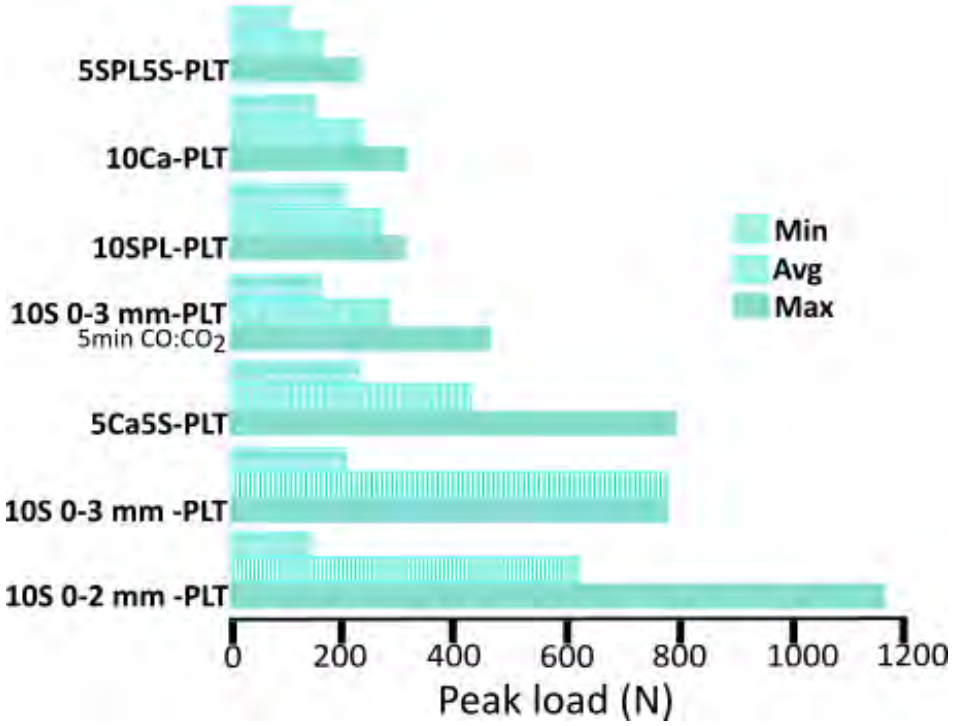

Figure 13. Force at failure in compression test for pellets exposed to CO/CO_2.

3.3 Curing

Figure 14 illustrates the behaviour of various pellets after curing and water exposure for 30 min, 1 h or 24 h. Pellets heat-treated at 200 °C showed poor resistance to water, with disintegration initiating immediately as charcoal fines began to separate, leading to complete dissolution within 1 h. In contrast, pellets cured at 250 °C remained intact in water without noticeable decomposition even after 24 h. A similar behaviour was observed for pellets treated at 300 °C. These results indicate that curing in the temperature range of 250-300 °C is necessary to strengthen the binder network and improve water resistance.

Previous studies have shown that elevated temperatures activate lignosulphonate, enhancing its binding strength (Borregard, n.d.). For example, refractory materials bonded with lignosulphonate are typically cured at 180-220 °C, where the lignin-based binder undergoes activation and improves mechanical integrity. Furthermore, thermal treatment at higher temperatures can lead to carbonization under inert or reducing conditions, contributing to stronger inter-particle bonding. Even under oxidizing conditions, lignin oxidizes relatively slowly, allowing partial char formation if the treatment duration is carefully controlled.

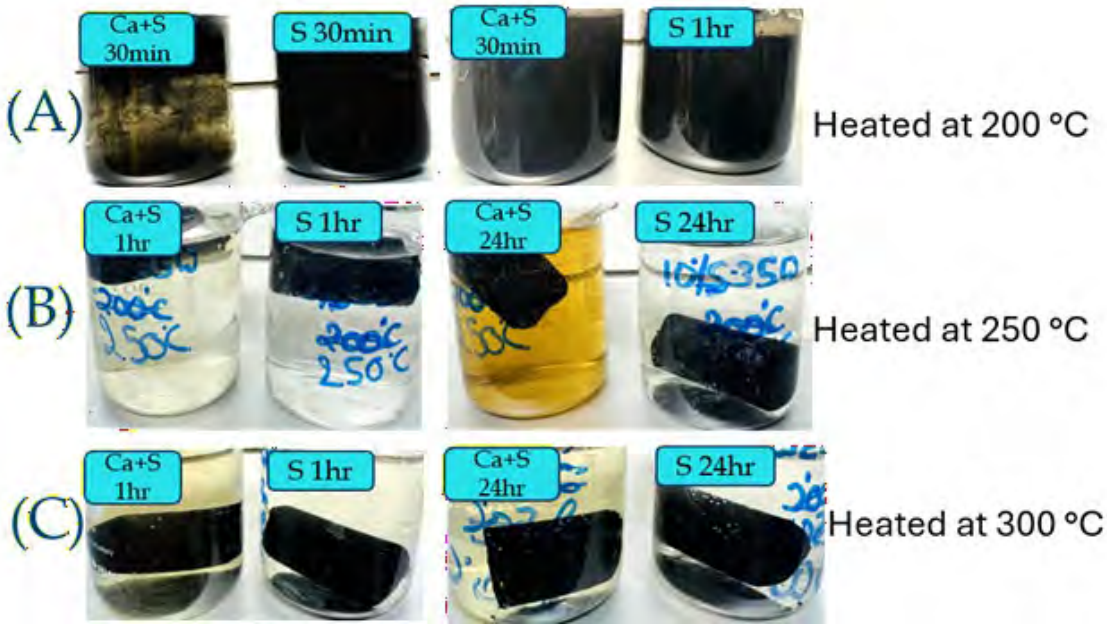

Figure 14. The behaviour of various pellets after curing and water exposure for 30 min, 1 h or 24 h.

The same pellets cured at the three different temperatures were also subjected to a tumbling test. Interestingly, after 30 min of tumbling, pellets cured at 300 °C generated a larger amount of fines, followed by those cured at 250 °C and 200 °C, as shown in figure 15. This suggests that although higher curing temperatures improve water resistance, excessive thermal treatment may lead to increased brittleness, resulting in higher fines generation under mechanical stress. The higher fines generation observed for pellets cured at 300 °C can be directly related to changes in binder chemistry and resulting brittleness. At moderate temperatures (200-250 °C), binders such as starch and lignosulphonate undergo thermal activation and partial cross-linking, which improves inter-particle bonding while still retaining some flexibility in the structure. However, at 300 °C, further heating leads to advanced decomposition and carbonization of the binder, resulting in a more rigid and brittle network. This over-carbonization reduces the ability of the binder to absorb mechanical stress, making the pellets more prone to fracture during tumbling. In other words, while curing at higher temperature improves water resistance and compressive strength, it simultaneously reduces toughness, leading to increased fines generation under dynamic conditions. This could be the reason why pellets cured at 300 °C produced more fines compared to those cured at 250 °C and 200 °C.

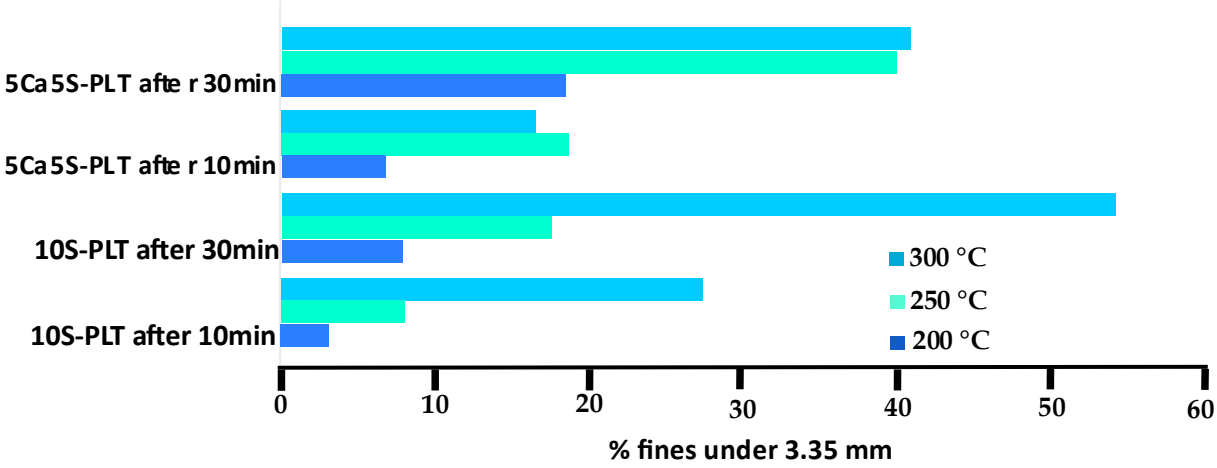

Figure 15. Fines generation during tumbling for samples cured at 200, 250 and 300 °C.

3.4 Thermal Shock Heating

Shock heating tests were performed on laboratory-produced extruded pellets to evaluate fines generation during rapid heating, simulating conditions encountered when materials enter the furnace at approximately 1000 °C. Figure 16 illustrates the cumulative size distribution (percentage passing each sieve) of the pellets after shock heating and 10 min holding at the temperature. The fraction of fines, defined as particles smaller than 3.35 mm, was used as an indicator of mechanical strength. Figure 16 highlights the cumulative percentage below 3.35 mm.

A total of 19 pellets recipes, prepared with different binders and combination of binders, were selected for the test. After sieving, all samples generated less than 5% fines, indicating good resistance to thermal shock-induced disintegration. Similarly, Figure 17 presents the size distribution for four selected briquette samples after shock heating. These briquettes produced even lower fines fractions, below 1% for particles under 3.35 mm. The results demonstrate that both pellets and briquettes exhibit high structural stability under rapid exposure to elevated temperatures (1000 °C), suggesting that they would not undergo significant fragmentation upon entering the furnace. The appearance of the agglomerates after test is shown in Figure 18. While evaluating thermal shock at 1000 °C is relevant to Si production, the furnace top in Mn alloy processes do not reach similar temperatures. Figure 18 shows pellets after shock heating at 500 °C: negligible degradation is observed. This supports customization of these tests for each process.

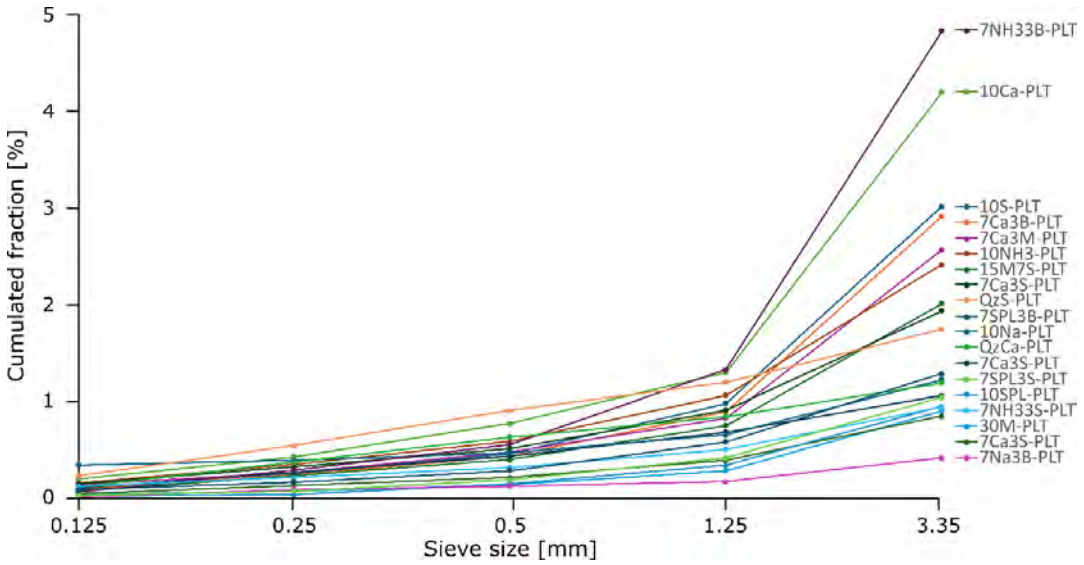

Figure 16. Distribution of fines after shock heating of pellets at 1000 °C.

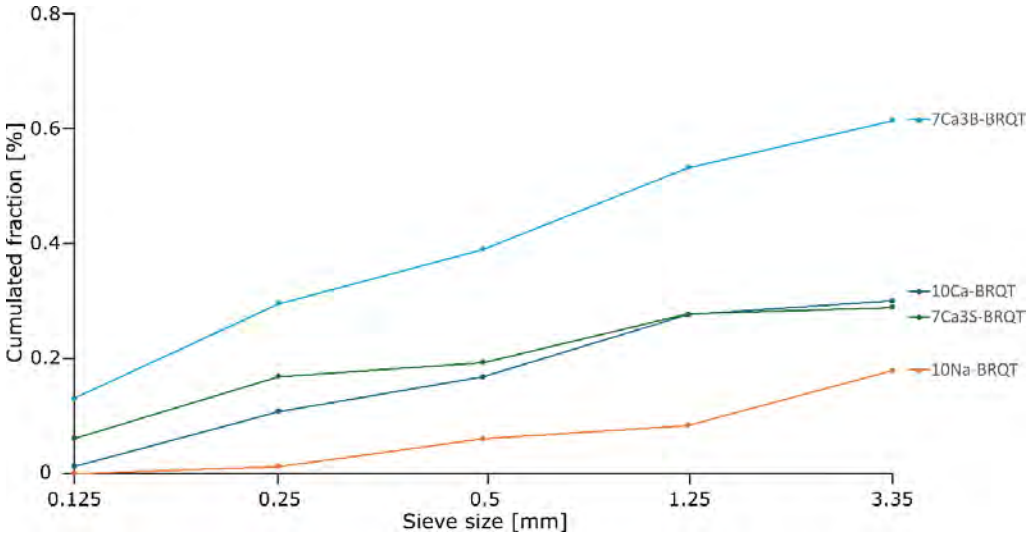

Figure 17. Distribution of fines after shock heating of briquettes at 1000 °C.

Figure 18. Visual aspect of pellets and briquettes after shock heating at 1000 °C.

Figure 19. Visual aspect of pellets after shock heating at 500 °C.

3.5 CO_2 reactivity

CO_2 reactivity tests were conducted on various agglomerated charcoal pellets and briquettes, charcoal, coal, and coke to evaluate their behaviour in a CO/CO_2 atmosphere. In addition, carbon black pellet samples (CB-1, CB-2, CB-3, and CB-4) were also tested. The primary difference among the carbon black samples lies in their composition: CB-1, CB-3, and CB-4 were produced from the same carbon black type with different binder compositions, whereas CB-2 was produced using a different carbon black type. Further details are not disclosed due to confidentiality (see Section 2.1). The results of the tested samples are summarized in figure 20, which presents the CO_2 reactivity of each material expressed as the percentage of fixed carbon (Fix-C) reacted per minute. The calculation of reactivity requires knowledge of the initial fixed carbon content of each sample (Table II). The results show that the biocarbon based

agglomerated pellets and briquettes exhibit CO_2 reactivity values within the same range as coal (CL-017). In contrast, the carbon black pellets demonstrate even lower reactivity than the biocarbon agglomerates. A notable variation is also observed within the carbon black samples, where CB-2 shows significantly lower reactivity compared to the other CB samples produced from the same carbon black type. For comparison, conventional carbon materials were also tested. As expected, charcoal exhibits the highest reactivity, followed by coal and then coke, which is consistent with differences in carbon structure and porosity. In general, the results indicate that while raw charcoal exhibits high CO_2 reactivity, agglomeration of biocarbon can effectively reduce its reactivity to levels comparable to fossil-based carbon such as coal. This highlights the potential of agglomeration processes to tailor the reactivity of biocarbon materials for industrial applications (Monsen et al., 2007; Jayakumari et al., 2023)

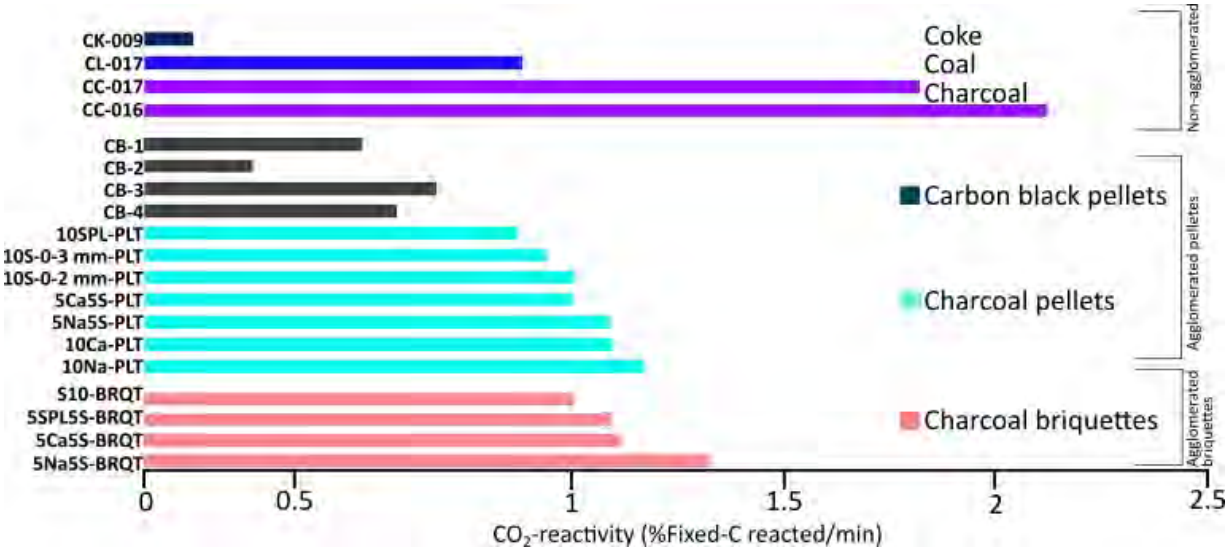

Figure 20. The CO_2 reactivity of each material expressed as the percentage of fixed carbon (Fix-C) reacted per minute.

A visual assessment of the samples was carried out before and after the CO_2 reactivity test, as shown in figure 21. After testing, most samples exhibited degradation primarily at the surface, where the outer layer appeared to be covered with carbon fines, while the internal structure remained relatively intact and hard. This suggests that the reaction was largely limited to the external regions of the pellets.

To verify this observation, one experiment was interrupted after heating the sample in an Ar atmosphere, just before introducing the CO/CO_2 gas mixture (figure 21). Interestingly, no visible changes were observed in the pellet before and after heating under inert conditions. This confirms that the gas-solid reaction predominantly occurs at the surface of the pellets rather than within the bulk.

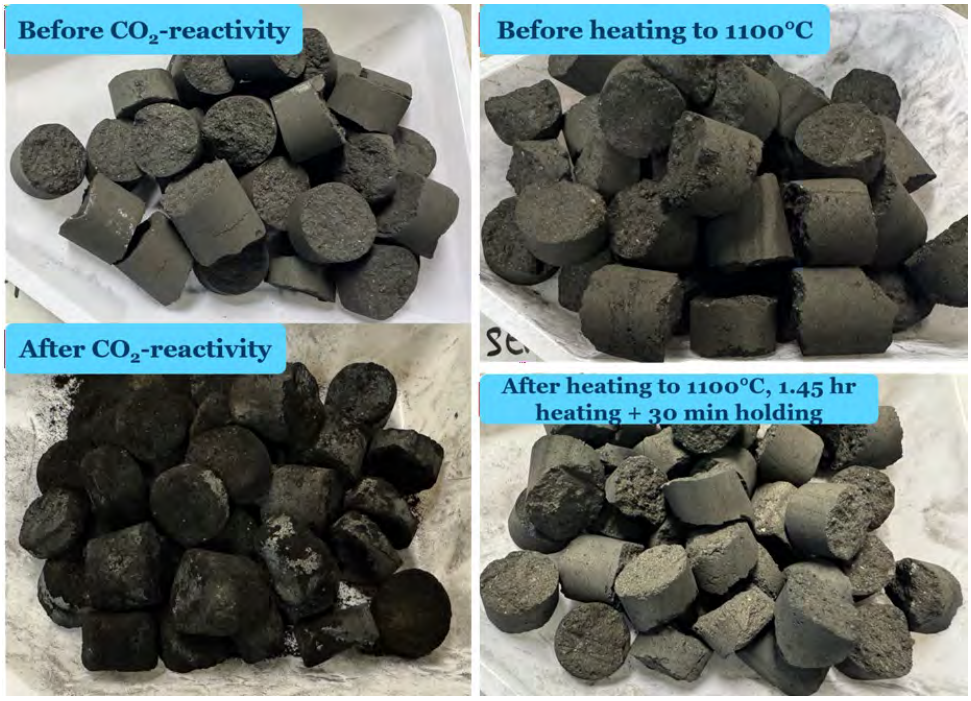

Figure 21. The appearance of sample before and after the CO_2 reactivity test and before and after heating 2 h 15 min at 1100 °C.

3.6 Warm strength after CO_2 reactivity

The warm strength discussed in this study refers to the mechanical integrity of carbon materials after exposure to CO_2 reactivity conditions and represents their abrasion resistance following reactions in a CO/CO_2 gas atmosphere, illustrating what happens in the pre-reduction zone of Mn furnaces. The strength of the samples is evaluated using the cohesion index (C.I.) and the thermal stability index (T.I.3). The C.I. is defined as the fraction of material larger than 4.75 mm after the CO_2 reactivity test, prior to any further handling, and provides an indication of the material's resistance to fines generation under furnace conditions.

Figure 22 presents the investigated samples along with their corresponding C.I. values. Most of the samples exhibit high C.I. values in the range of 80 - 98%, indicating strong resistance to degradation after exposure to reactive gas environments. Such high values are desirable, as they suggest that the materials can maintain their structural integrity during furnace operation.

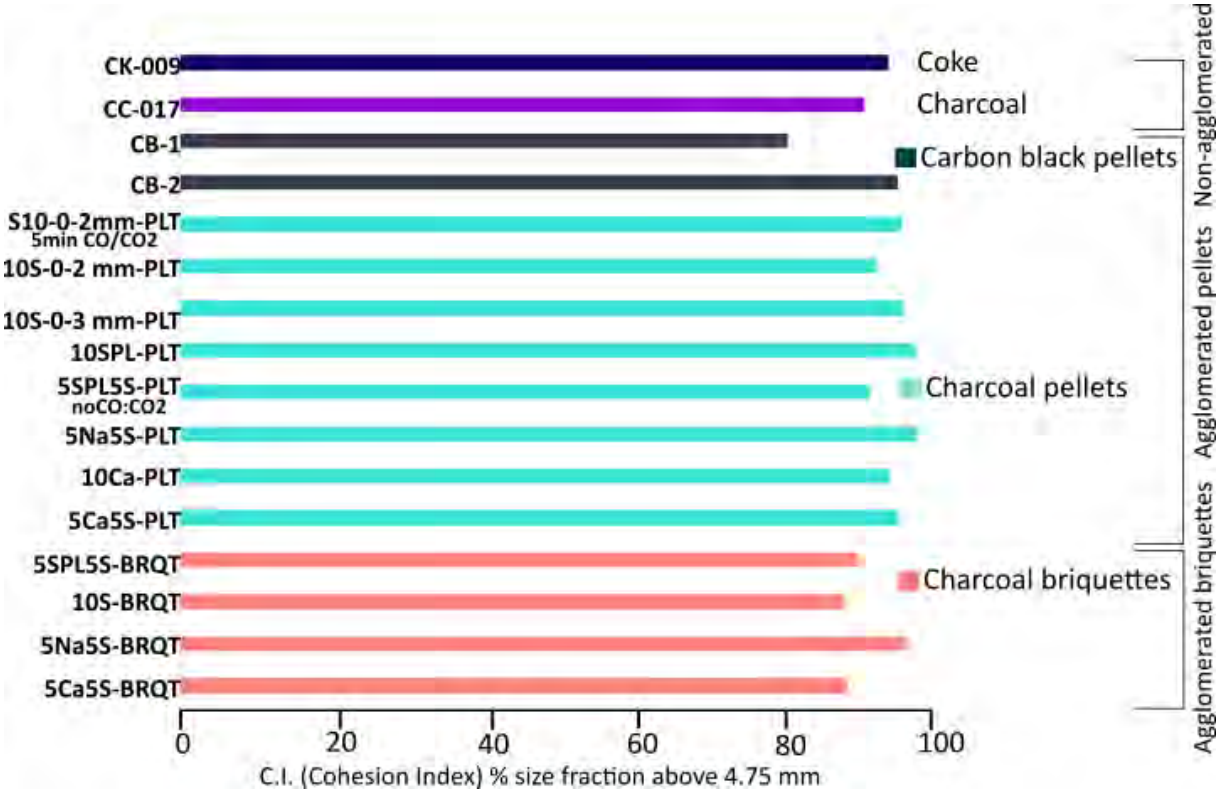

Figure 22. C.I (cohesion index) measured after CO_2 reactivity tests.

The thermal stability index (T.I.3) is defined as the fraction of material larger than 3.35 mm after the CO_2 reactivity test followed by tumbling in a rotating drum. It reflects how the Boudouard reaction influences the abrasion resistance of the materials, where a higher T.I.3 value is preferred. Figure 23 summarizes the T.I.3 values for all samples after 10 and 30 minutes of tumbling. A decrease in T.I.3 is observed for all samples with increasing tumbling time, indicating progressive degradation under mechanical stress. The reduction is more pronounced for the briquettes, where a significant drop in T.I.3 occurs between 10 and 30 minutes.

Among the tested materials, CB-1 pellets exhibit relatively high T.I.3 values, indicating good resistance to degradation, whereas CB-2 pellets were completely disintegrated into fines even after 10 minutes of tumbling. The substantial generation of fines after tumbling suggests that these samples experienced a considerable loss of structural integrity following the CO_2 reaction. In contrast, the conventional carbon materials charcoal, coal, and coke largely retained their mechanical strength after tumbling.

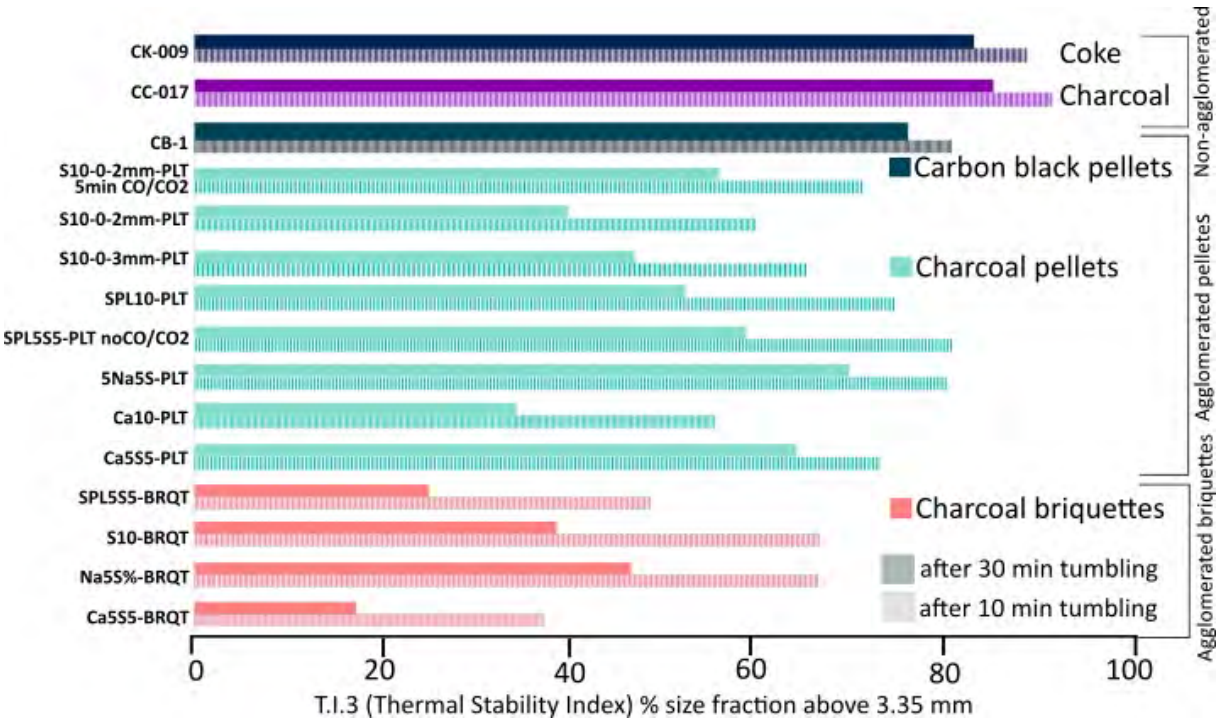

Figure 23. T.I.3 (thermal stability index) measured after CO_2 reactivity test.

3.7 SiO reactivity

The SiO reactivity test measures the ability of a carbon sample to react with SiO gas to form SiC and is expressed as R10. The R10 value is reported in terms of the volume of SiO, where a higher R10 indicates lower reactivity (slower reaction with SiO gas) (Lindstad et al., 2007b). Selected biocarbon agglomerates, carbon black pellets, and conventional carbon materials were subjected to this test, R10 values are shown in Figure 24.

Compared to raw charcoal, the charcoal-based pellets generally exhibit slightly lower reactivity, reflected by higher R10 values. Among the charcoal pellets, those produced with 100% starch and with a 50:50 combination of starch and lignosulphonate binders show higher R10 values compared to pellets made with SPL, Ca-, and NH_4-lignosulphonates, except for Na-lignosulphonate. Consistent with observations from other tests, differences are also seen among the carbon black samples: CB-1 shows slightly lower R10 values (higher reactivity) compared to CB-2, indicating that the type of carbon black significantly influences reactivity.

For reference, conventional carbon materials including charcoal sources (CC-017 and CC-016), coal (CL-017), and coke (CK-009) were also tested. As expected, charcoal exhibits the highest reactivity, followed by coal and then coke. Reproducibility was verified through parallel tests on CL-017 and selected carbon black samples, and average R10 values were used for evaluation. An additional test on CB-2 with a narrower size fraction (4-4.75 mm) showed no significant variation in reactivity. In general, all agglomerated pellets except CB-2 exhibit reactivity values within the range of charcoal to coal, as illustrated in the reactivity scale (Figure 25).

Overall, the results suggest that both SiO and CO_2 reactivity are closely linked to the pore structure of the materials, where higher porosity promotes greater gas accessibility and thus higher reactivity, while agglomeration reduces porosity and moderates reactivity toward levels comparable to conventional carbon materials (Jayakumari and Ringdalen, 2022).

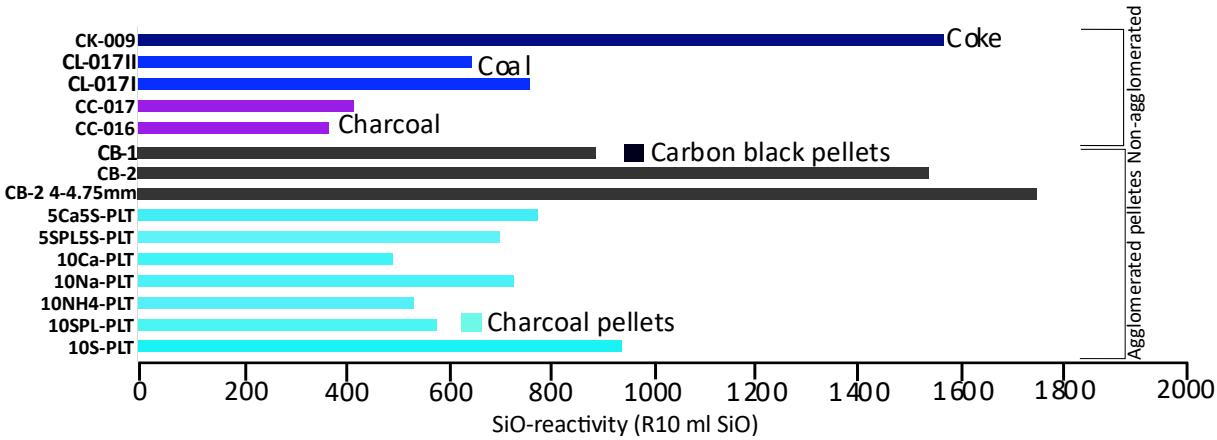

Figure 24. R10 reactivity measured in ml SiO for all the tested carbon samples.

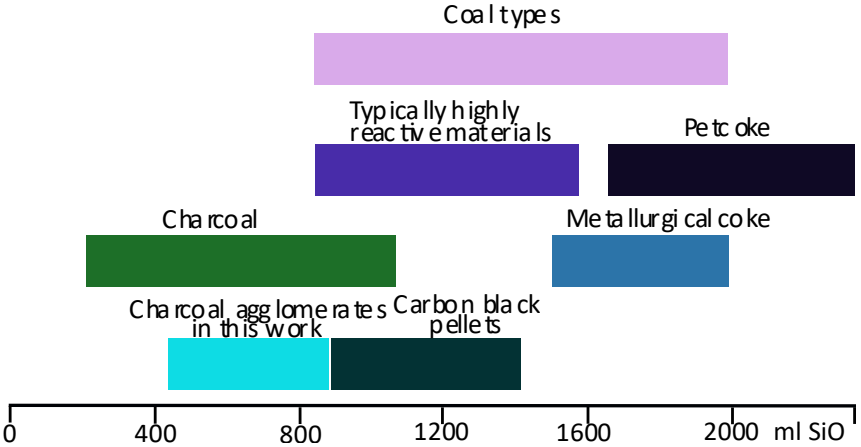

Figure 25. SiO-reactivity of different carbon reductants measured with SINTEF SiO-reactivity test and reactivity values of the agglomerated carbon materials from the current study is also included (Jayakumari and Ringdalen, 2022).

Figure 26 presents CT images of calcined pellets in the size range of 4–6.3 mm (A), partially converted SiC particles (B), and fully converted SiC particles (C), illustrating the transformation behaviour when carbon pellets react with SiO gas. These observations provide insight into the diffusion-controlled mechanisms governing the reaction of SiO gas within agglomerated particles.

In Figure 26 (A), the calcined pellets prior to the SiO test appear relatively dense, with a heterogeneous distribution of coarse and fine particles. In Figure 26 (B), the partially converted samples show grey regions corresponding to SiC formation, while darker regions represent unreacted carbon. The conversion pattern seems to follow the shrinking core model (SCM), where the reaction initiates at the surface of the particle, forming an outer SiC layer that gradually thickens as the reaction proceeds. As described by Schei et al. (Schei, Tuset and Tveit, 1998), the reaction rate decreases with increasing SiC layer thickness, due to the need for SiO(g) to diffuse through this layer to reach the unreacted carbon core.

The present observations confirm that the SCM adequately describes the transformation of charcoal-based agglomerates from carbon to SiC, consistent with previous findings for charcoal (Jayakumari, 2020). However, coal and pet-coke samples exhibit different behaviour and do not strictly follow the SCM mechanism, indicating differences in pore structure and reaction pathways. Previous studies on the kinetics of SiO–carbon reactions also support such material-dependent behaviour (Myrhaug, n.d.,2003).

In Figure 26 (C), the particles are fully converted to SiC, with no remaining unreacted carbon, indicating that SiO gas diffusion is not significantly hindered within the agglomerated structure. This can be attributed to the inherently high porosity of charcoal, characterized by

thin cell walls, which facilitates gas diffusion and promotes complete conversion. Since the agglomerates in this study are produced from charcoal fines, the results demonstrate that agglomeration does not significantly impede SiO diffusion or SiC formation.

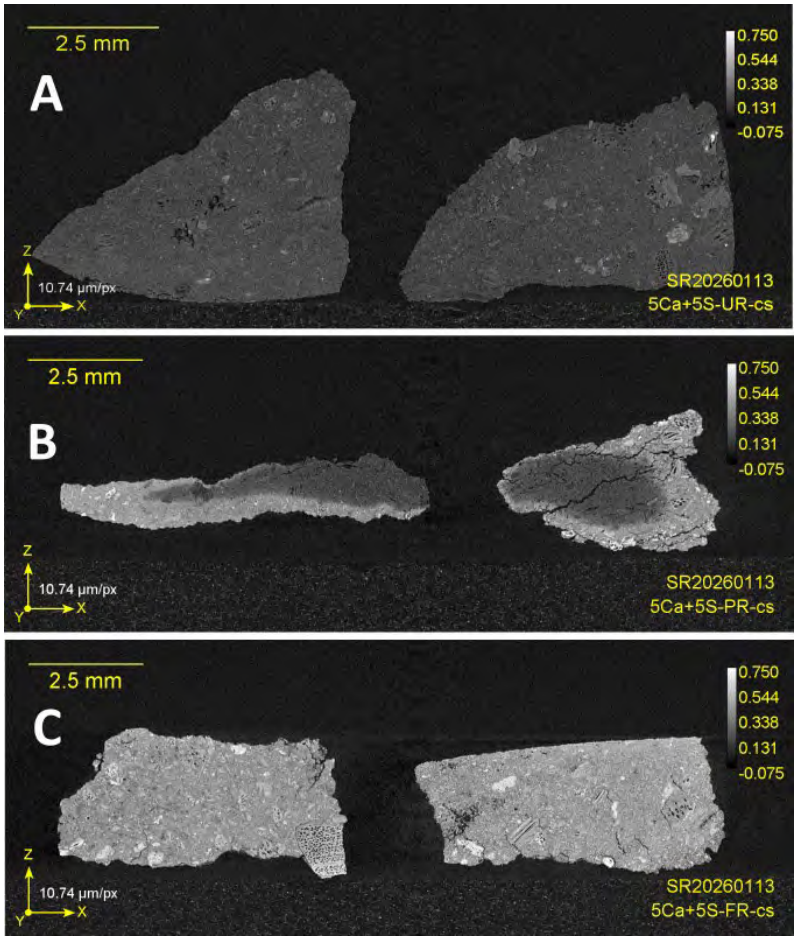

Figure 26. CT of pellets A. unreacted, B. partially reacted and C. Fully reacted to SiC.

Carbon weight gain

At 100% conversion, one mole of SiC is formed from two moles of carbon according to the reaction;

$$SiO(g) + 2C\ (s) = SiC\ (s) + CO\ g)$$

This reaction takes place in the reaction chamber where the carbon particles are located. Based on stoichiometry, 2 moles of carbon (2 x 12.01 g = 24.02 g) form 1 mole of SiC (28.09 + 12.01 = 40.01 g). The theoretical mass increase factor is therefore:

$$\frac{M_{SiC}}{2M_C} = \frac{40,1}{2 \cdot 12,01} = 1,6694 \approx 1,67$$

If a carbon material does not contain ash at all, the theoretical weight gain at full conversion will be 66.9 ≈ 67%. Consequently, the degree of conversion can be estimated directly from the mass increase relative to the theoretical maximum of 67%. The percentage of SiC conversion calculated from the mass gain after the SiO reactivity test for various agglomerated pellets and conventional carbon materials are summarized in Figure 27. The results show that all tested materials, including both agglomerated and conventional carbon samples, achieved SiC conversion levels above 80%, except for coke (CK-009). This indicates that the agglomerated pellets retain a high capacity for SiC formation despite the agglomeration process.

Furthermore, the high conversion levels suggest that SiO gas can effectively diffuse into the agglomerated particles and react with the carbon, resulting in extensive SiC formation.

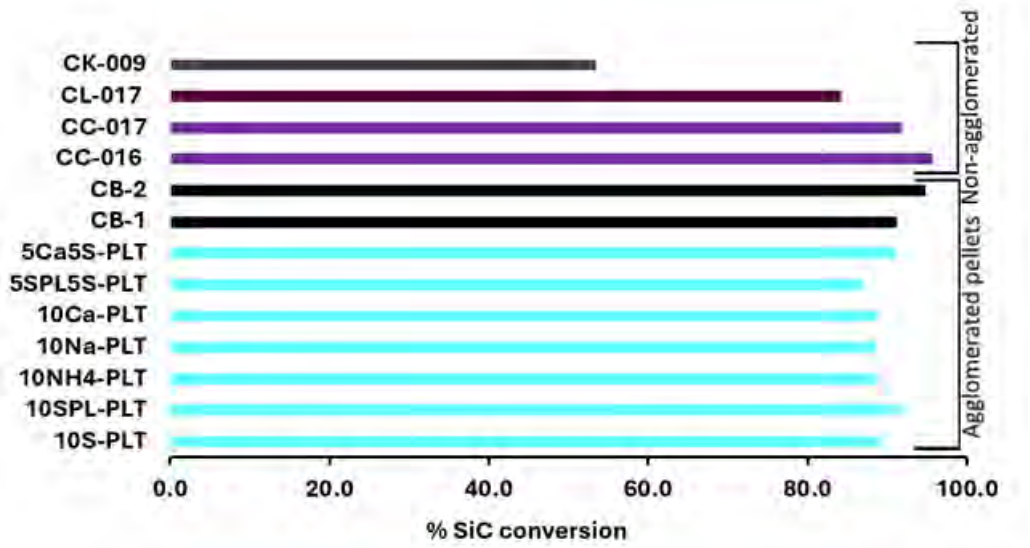

Figure 27. The percentage of SiC conversion calculated from the mass gain after the SiO reactivity test for various agglomerated pellets and conventional carbon materials.

4. CONCLUSIONS

In this study, biocarbon agglomerates in the form of extruded pellets and briquettes produced with different binder compositions were investigated with respect to their physical properties, mechanical strength, thermal stability, and reactivity. The results showed that agglomeration produced materials with a more homogeneous structure, higher bulk density, and lower porosity than raw charcoal. Among the investigated binders, starch-based agglomerates exhibited the highest cold and warm strength, while SPL-based pellets showed improved strength after heat treatment. Both pellets and briquettes demonstrated good resistance to thermal shock, generating only limited amounts of fines after exposure to elevated temperatures.

Furthermore, agglomeration reduced the CO_2 and SiO reactivity of the biocarbon materials to levels comparable to coal, while maintaining high SiC conversion (>80%) in most samples. Overall, the results demonstrate that charcoal fines can be successfully agglomerated into mechanically robust and thermally stable materials with properties suitable for ferroalloy production processes.

5. ACKNOWLEDGEMENTS

This work was carried out through a collaboration between the SINTEF-funded *Forskerinitierte strategiske egnefinansierte prosjekter* (SEP) 2025 initiative and the MECALO project, funded by the EU Horizon Europe programme (Grant Agreement No. 101177480). The Views and opinions expressed herein are those of the author(s) only and do not necessarily reflect those of the European Union or HADEA. Neither the European Union nor the granting authority can be held responsible for them. The support and contributions of both projects are gratefully acknowledged.

We would also like to express our sincere gratitude to Hugo Letartre for his immense contribution to the agglomeration work and various laboratory activities during his internship period with our team. His dedication and valuable support are highly appreciated. All contributions and funding sources are gratefully acknowledged.

6. REFERENCES

Aasly Kurt and, D.V., June 13 - 16, 20016. *Assessment of production performance of quartz in the Si-furnace*.

Borregard, n.d. *TRANSFORMING WASTE INTO VALUE WITH SUSTAINABLE BINDERS*.

Branca, C. and Di Blasi, C., 2025. Packed-Bed Pyrolysis of Alkali Lignin for Value-Added Products. *Recycling*, 10(2), p.66. https://doi.org/10.3390/recycling10020066.

Butler, J.W., Skrivan, W. and Lotfi, S., 2023. Identification of Optimal Binders for Torrefied Biomass Pellets. *Energies*, 16(8), p.3390. https://doi.org/10.3390/en16083390.

Chhiti, Y., Salvador, S., Commandré, J.-M. and Broust, F., 2012. Thermal decomposition of bio-oil: Focus on the products yields under different pyrolysis conditions. *Fuel*, 102, pp.274–281. https://doi.org/10.1016/j.fuel.2012.06.098.

Han, Y. and Tangstad, M., 2024. Metallurgical Properties of Biocarbon in Ferroalloy Production─A Review. *ACS Omega*, 9(23), pp.24142–24162. https://doi.org/10.1021/acsomega.4c00866.

Hoover, H., Bell, R. and Rippy, K., 2024. Emerging Technologies for Decarbonizing Silicon Production. *Journal of Sustainable Metallurgy*, 10(4), pp.1921–1932. https://doi.org/10.1007/s40831-024-00913-3.

Jahrsengene, G., Jayakumari, S., Kero, I.T. and Ringdalen, E., 2023. Sustainable Metal Production: Use of Biocarbon and the Concern of Dusting. In: Metallurgy and Materials Society of the Canadian Institute of Mining Metallurgy and Petroleum (CIM), ed. *Proceedings of the 62nd Conference of Metallurgists, COM 2023*. [online] Cham: Springer Nature Switzerland. pp.1001–1007. https://doi.org/10.1007/978-3-031-38141-6_126.

Jayakumari, S., 2020. *Formation and characterization of β-and α-Silicon Carbide produced during Silicon/Ferrosilicon process*. [online] NTNU. Available at: <https://ntnuopen.ntnu.no/ntnu-xmlui/handle/11250/2678922> [Accessed 21 November 2021].

Jayakumari, S., Jahrsengene, G., Ksiazek, M. and Ringdalen, E., 2023. Investigations on CO2 Reactivity and Thermal Strength of Carbon Sources for Ferroalloy and Silicon Production. In: *Proceedings of the 62nd Conference of Metallurgists, COM 2023*. [online] Conference of Metallurgists. Springer, Cham. pp.1009–1018. https://doi.org/10.1007/978-3-031-38141-6_127.

Jayakumari, S. and Ksiazek, M., 2024. *Fines Generation and Strength of Various Carbon Materials Used in the Ferroalloy Industries*. https://doi.org/10.2139/ssrn.4942468.

Jayakumari, S. and Ringdalen, E., 2022. Effect of Varying SiO Contents on Si and FeSi Production. *SSRN Electronic Journal*. [online] https://doi.org/10.2139/ssrn.4118642.

Jusnes, K.F., 2020. *Phase transformations and thermal degradation in industrial quartz*. [online] NTNU. Available at: <https://ntnuopen.ntnu.no/ntnu-xmlui/handle/11250/2675473> [Accessed 30 September 2022].

Kaffash, H., Surup, G.R. and Tangstad, M., 2021. Densification of Biocarbon and Its Effect on CO2 Reactivity. https://doi.org/https://doi.org/10.3390/pr9020193.

Karunanithy, C., Wang, Y., Muthukumarappan, K. and Pugalendhi, S., 2012. Physiochemical Characterization of Briquettes Made from Different Feedstocks. *Biotechnology Research International*, 2012, p.165202. https://doi.org/10.1155/2012/165202.

Lindstad, T., Gaal, S., Hansen, S. and Prytz, S., 2007a. IMPROVED SINTEF SIO-REACTIVITY TEST. INFACON XI. INFACON XI, India. p.10.

Lindstad, T., Gaal, S., Hansen, S. and Prytz, S., 2007b. IMPROVED SINTEF SIO-REACTIVITY TEST. INFACON XI. INFACON XI, India. p.10.

Makgobelele, N.W., Mbaya, R.K.K., Bunt, J.R., Leokaoke, N.T. and Neomagus, H.W.J.P., 2021. Evaluation of the mechanical properties of wood-derived charcoal briquettes for use as a reductant. *Journal of the Southern African Institute of Mining and Metallurgy*, 121(5), pp.187–192. https://doi.org/10.17159/2411-9717/903/2021.

Monsen, B., Tangstad, M., Solheim, I., Syvertsen, M., Ishak, R. and Midtgaard, H., 2007. Charcoal for Manganese Alloy Production. INFACON XI. India. p.14.

Myrhaug, E.H., n.d. Non-fossil reduction materials in the silicon process - properties and behaviour. p.242.

Narron, R., Wolken, G. and Gargulak, J., 2020. Accelerated Polymerization of Ammonium Lignosulfonate from Loblolly Pine. *Forest Products Journal*, 70(1), pp.134–142. https://doi.org/10.13073/FPJ-D-19-00044.

Obi, O.F., Pecenka, R. and Clifford, M.J., 2022. A Review of Biomass Briquette Binders and Quality Parameters. *Energies*, 15(7), p.2426. https://doi.org/10.3390/en15072426.

Olofsson, J., 2025. Multiple Goals for Biomass Residues in Circular Bioeconomies? Assessing Circularities and Carbon Footprints of Residue-Based Products. *Circular Economy and Sustainability*, 5(1), pp.101–123. https://doi.org/10.1007/s43615-024-00428-9.

Olsen, S.E., Tangstad, M. and Lindstad, T., 2026. *Production of Manganese Ferroalloys by Sverre E. Olsen, Merete Tangstad, Tor Lindstad (9788245046144) | Akademika Bokhandel*. [online] Available at: <https://www.akademika.no/realfag/kjemi/production-manganese-ferroalloys/9788245046144> [Accessed 3 July 2026].

Olugbade, T., Ojo, O. and Mohammed, T., 2019. Influence of Binders on Combustion Properties of Biomass Briquettes: A Recent Review. *BioEnergy Research*, 12(2), pp.241–259. https://doi.org/10.1007/s12155-019-09973-w.

Pahnila, M., Koskela, A., Uusitalo, J., Vitikka, O., Sulasalmi, P. and Fabritius, T., 2026. The Effect of Biomass Species and Pyrolysis Method on Biocarbon Briquette Suitability for Submerged Arc Furnace. *Journal of Sustainable Metallurgy*, 12(1), pp.523–536. https://doi.org/10.1007/s40831-025-01343-5.

Prosess21 ekspertgrupperapport, 2021. *Ny prosessteknologi med redusert karbonavtrykk inkl. CCU*. Available at: <https://www.prosess21.no/informasjon-om-prosess21/Download>.

Ringdalen, E., 2014. Quartz properties in the silicon production. *Silicon for the Chemical and Solar Industry XII*.

Schei, A., Tuset, J.K. and Tveit, H., 1998. *Production of high silicon alloys*. [online] Trondheim: Tapir. Available at: <https://urn.nb.no/URN:NBN:no-nb_digibok_2010021004001> [Accessed 12 April 2022].

Smith-Hanssen, N., Jahrsengene, G. and Ringdalen, E., 2023b. Biocarbon Materials in Metallurgical Processes—Investigation of Critical Properties. In: C. Fleuriault, J.D. Steenkamp, D. Gregurek, J.F. White, Q.G. Reynolds, P.J. Mackey and S.A.C. Hockaday, eds. *Advances in Pyrometallurgy*, The Minerals, Metals & Materials Series. Cham: Springer Nature Switzerland. pp.165–177. https://doi.org/10.1007/978-3-031-22634-2_16.

Sommerfeld, M. and Friedrich, B., 2021. Replacing Fossil Carbon in the Production of Ferroalloys with a Focus on Bio-Based Carbon: A Review. *Minerals*, 11(11), p.1286. https://doi.org/10.3390/min11111286.

Tangstad, M. and Ringdalen, E., 2025. Decarbonization Ferroalloy Production Using Biocarbon. *Minerals*, 15(3), p.228. https://doi.org/10.3390/min15030228.

Tuset, J. K and Raaness, O., 1976. *Reactivity of Reduction Materials for the Production of Silicon, Silicon-rich Ferroalloys and Silicon Carbide*.

Zhang, C., Shao, Y., Zhang, L., Zhang, S., Westerhof, R.J.M., Liu, Q., Jia, P., Li, Q., Wang, Y. and Hu, X., 2020. Impacts of temperature on evolution of char structure during pyrolysis of lignin. *Science of The Total Environment*, 699, p.134381. https://doi.org/10.1016/j.scitotenv.2019.134381.

Sethulakshmy Jayakumari
Research Scientist, SINTEF, Trondheim, Norway

I have completed my master's degree in condensed matter physics (2013) and PhD in process metallurgy (2020) from NTNU, Norway. My PhD project focused on silicon carbide formation

during silicon production. I am currently working as research scientist in process metallurgy and raw materials department in SINTEF. I am involved in several research projects related to silicon and manganese production processes. My work focuses on high-temperature furnace experiments, process optimization, raw material characterization, and the development of sustainable metallurgical technologies.

Eide, G., A. Olivo, K. D. Log, J. O. Odden, O. A. Bariås, H. Rong, and K. Friestad. 2026. Industrial Recycling of Silicon-Containing Materials: From kg scale tests to large scale operation. In *Silicon for the chemical and solar industry XVIII*, edited by M. Tangstad, H. Rong, A. Valderhaug, B. Andresen, H. Dalaker, and I. G. Page. Kristiansand, Norway, September 7–10, 2026.
https://doi.org/10.55669/oa900826

Industrial Recycling of Silicon-Containing Materials: From kg scale tests to large scale operation

G. Eide[1], A. Olivo[1], K.D. Log[1], J.O. Odden[1], O.A. Bariås[2], H. Rong[1] and K. Friestad[1]
[1]Elkem Silicon Products, Norway, gro.eide@elkem.com
[2]Elkem ASA, Norway

Keywords: kerf, silicon, purification, pelletisation, large scale, low-CO_2, sustainability

Abstract - The transition towards lower carbon footprint silicon value chains requires increased utilisation of secondary raw materials across multiple process steps. This work addresses this challenge by developing and demonstrating industrial pathways for recycling silicon-containing materials at Elkem Kristiansand. Two complementary activities are presented.
First, ferrosilicon- and silicon-rich skulls and slags from metallurgical ferrosilicon and silicon production are evaluated as supplementary cementitious materials, partially replacing clinker in cement applications. Material characterisation, processing routes, and performance testing demonstrate the potential for CO_2 reduction.
The activity covers remelting of silicon-rich skulls and slags to recover two distinct product streams: FeSi and a refined slag fraction. Process control focused on stable melting conditions, phase separation, and compositional consistency. Material quality was monitored through chemical analysis and particle-size control, enabling evaluation of both FeSi and slag for downstream cement applications.

Second, recycled silicon from wafer-sawing kerf is upgraded through purification, pellet production, melting, and casting into Si99 grades. Pilot- and industrial-scale trials confirm that recycled silicon can be transformed into consistent, high-quality products suitable for demanding downstream applications. Together, these results demonstrate how integrated recycling solutions can strengthen circularity and sustainability in the silicon industry.
An integrated purification–pelletisation approach was developed to stabilise kerf properties, control organic and oxide behaviour, and produce mechanically robust pellets with predictable performance during subsequent melting. Si99 is produced by remelting kerf-based pellets under controlled furnace conditions. Pellet quality, charge composition, and ramp-up strategy are key process parameters. Stable melting, controlled slag formation, and ladle refining enable consistent chemistry prior to casting. Systematic sampling and online analysis are applied to verify yield, impurity levels, and product stability.

Elkem will in this work present operational data and results from large-scale campaigns at the Fiskaa site in Kristiansand, demonstrating process stability, material quality, and practical feasibility under industrial conditions.

1. INTRODUCTION

The metallurgical silicon industry is increasingly focused on improving resource efficiency and reducing the overall CO_2 footprint of its operations. One potential pathway to achieve this is the recycling of silicon-containing materials, including process residues, off-spec products, and side streams from downstream processing.
Recycling of silicon materials has been successfully demonstrated at laboratory scale (Syvertsen et al., 2018); however, the transition from controlled kg-scale tests to stable industrial operation introduces significant challenges. In particular, recycled materials such as kerf exhibit substantial variability in composition, including organic content, oxide phases, and metallic contaminants. This variability directly affects process stability, product quality, and overall system efficiency.

It is important to distinguish between carbothermic silicon production and remelting-based recycling. Carbothermic silicon production in a reduction furnace is based on the chemical reduction of SiO_2 using carbon, resulting in direct CO_2 emissions (Scope 1). In contrast,

This work is licensed under the Creative Commons Attribution 4.0 International License. To view a copy of this license, visit https://creativecommons.org/licenses/by/4.0/

recycling or remelting in an induction furnace is a purely electric process without direct CO_2 generation, where energy is supplied via electricity. Consequently, the CO_2 footprint of induction furnace operation is dominated by indirect emissions (Scope 2 and 3)
.
This paper will look closer at some aspects related to the transition from kg-scale recycling tests to industrial-scale operation. The impact of recycled material quality and variation on process and product will be evaluated, in addition to the CO_2 implications.

The present article is structured around the challenges related to scaling up to an industrial scale for two cases. The first route addresses recycling of kerf. Kerf supplied in a form of silicon filter cake is a side stream from cutting blocks and wafers in the solar industry (Emil-Kaya et al., 2025). Kerf is converted into pellets and further processed into metallurgical grade silicon (MG-Si). The second route, Slag2Value, focuses on remelting of FeSi slags and skulls to recover FeSi and produce a slag suitable to be used as a replacement for cement. This is one alternative for reducing cement content in order to reach a more sustainable concrete (Jhatial et al., 2023).

Elkem has developed these recycle cases in several R&D projects as indicated in figure 1. In 2025 the development went into a new phase, transferring the processes from lab to industrial scale in an Innovation Norway supported project.

Figure 1: Time line for the development of industrial routes demonstrated at Fiskaa

The emphasis is not only on technical feasibility, but also on the challenges when a concept moves from lab or pilot scale into extended industrial campaigns. Elkem shares some of the gained experience within the area of raw-material stability and safety related to the development.

2. EXPERIMENTAL – TEST INFRASTRUCTURE

2.1 Industrial infrastructure at Fiskaa

The Elkem facilities at Fiskaa Kristiansand provide an unusual combination of equipment relevant for industrial recycling of silicon-containing materials. For the work reported here, the most relevant assets are the pellets plant, the multipurpose melting plant, the crushing/sieving/packing plant, the slag furnace and the analytical laboratory.

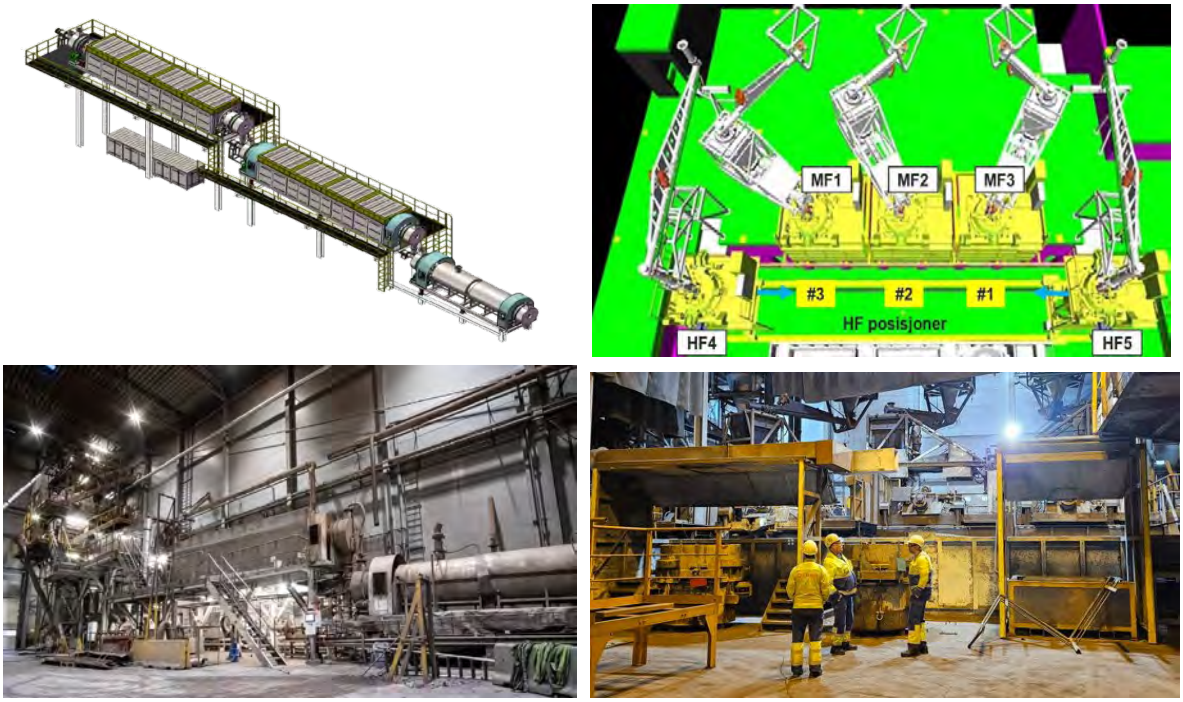

Figure 2: Layout and picture of the pellet and melting plant and at Elkem facilities at Fiskaa, Kristiansand.

Table I: A brief overview of **t**est infrastructure in Kristiansand used in the campaigns

Unit / asset	**Key role in this study**
Pellets plant	Agglomeration, drying, calcination and cooling of kerf
Multipurpose melting plant	Batch melting, slag removal, transfer to holding furnace and ladle refining
Crushing and sieving plant (CSP)	Final sizing and packing of Si products
Analytical laboratory	Routine process and product control

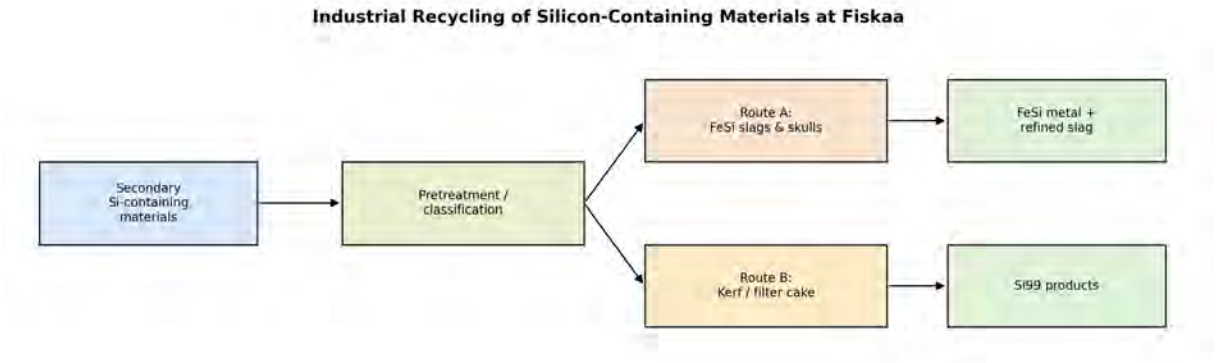

Figure 3: Schematic representation of the two industrial recycling routes demonstrated at Fiskaa

2.2 Route A – kerf upgrading to MG-Si

The kerf route starts with wet filter cake from wafer cutting and uses pelletisation as a controlled pre-treatment step before melting. The pellets line includes mixing/granulation in

an Eirich mixer, drying, calcination under controlled atmosphere, off-gas treatment in an afterburner, and cooling. The pellets are then melted in induction furnaces, cast and crushed to customer size specifications.

Figure 4: Suggested route figure for kerf upgrading to Si99 via pellets, melting, crushing, sizing and packing (CSP)

2.3 Route B – recycling of FeSi slags and sculls

In the remelting route, FeSi slags and sculls are blended with Si-rich adjustment material and CaO in order to reach a process window that supports separation into a FeSi fraction and a lower-Si slag fraction. Earlier pilot and concept work identified basicity (CaO/SiO2), settling time and slag thickness as controlling variables. For rapid cooling of the slag product, thin casting and/or quenching are used before milling.

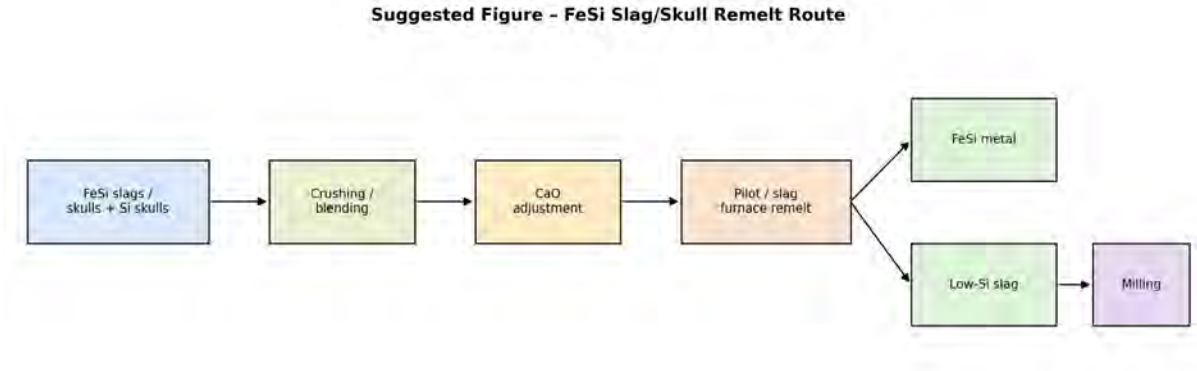

Figure 5: Suggested route figure for FeSi slag/skull remelting and downstream slag milling

2.4 QA and analytical framework

For the pellets and melt line, traceability and online process monitoring were performed through an operational process control system (Predictor). The monitored variables included ID, raw-material properties, process parameters and product quality. Product control was carried out with several different measuring techniques (eg. LECO, XRF, XRD, SEM, etc).

Figure 6: Example of analytical tools used during large scale campaign - Autolab

3. RESULTS & DISCUSSION

3.1 Kerf quality and its impact on pelletisation

Elkem has observed that there is variation in the raw material as indicated in table 2.

Table II: Examples of variation in raw material based on kerf

Parameter	Typical range	Comment
Organic content	1–4 wt%	Originating from cutting fluids / binders
Oxygen content	2–7 wt%	Surface of primary Si particle and organic compounds
Metallic contaminants	0.1–1 wt%	Foreign fragments (wire, bolts, nuts, etc)
Magnetic fraction	Variable	Recoverable
Non-magnetic fraction	Present	Remains in process
Base material	Poly-Si based	Low Fe (sub-ppmw level)

The recycled kerf material shows significant variability in composition, particularly in organic content (~1–4 wt%), oxygen level (~2-7 wt%) and the presence of metallic contaminants originating from mechanical equipment (e.g. wires, bolts, liners, and structural components). While part of the metallic fraction can be removed through magnetic separation and sieving, a non-negligible fraction remains and enters the melting process.

Non-metallic and metallic contaminants that are not removed prior to processing are dissolved into the melt during melting, directly contributing to elevated impurity levels in the final silicon product. Findings from the test campaign with more than 100 MT demonstrate a large range of contaminants, and Figure 7 shows some of the fragments that were identified and removed.

Figure 7: Pictures showing samples of fragments found in the kerf raw material. Scale approximately 1–5 cm.

3.2 Scale-up: industrial campaign on recycling Si

Elkem has selected some key elements in order to follow the material quality through the process steps. For the recycling of Si the focus has been on phosphorus (P) and iron (Fe) as important elements both for process control and as final quality indicator. In addition, carbon, oxygen and humidity are critical elements for the raw materials both for pellets and melting process.

Table III gives an overview of the different steps and observed minimum and maximum values for C, O, humidity, Fe and P. The data are from the large-scale testing carried out at Fiskaa, Kristiansand.

Table III: Overview of key quality indicators for the individual process steps, showing the content and variation of central elements compared with typical values for metallurgical-grade silicon (MG-Si).

Parameter		Raw material	Pellets	Product	Typical MG-Si
C (w%)	Min	0.8	0.1	<0.01	0.01
	Max	4.1	0.7	0.02	0.04
O (w%)	Min	2.4	3.0	-	<0.1
	Max	6.8	6.7	<0.1	
Fe (ppmw)	Min	2	9	151	2000
	Max	512	463	581 (1700)*	4000
P (ppmw)	Min	0.4	0.6	3.1	20
	Max	42	31	7.9	60

* Batches with Fe containing fragments

The P content is lower and more stable with respect to traditional MG-Si due to the general lower content in the main raw material – the KERF. Potential root cause for a slight increase between the different process steps is probably linked to mixing of different raw materials.
Other dopants, like B is not measured on sub-ppmw level in the campaign due to lack of instrumentation for this. However, a current detection limit of 1 ppmw is good enough for the intended use of the final product for MG-Si.

Fe increases with a factor of one order of magnitude from raw material to final product. Fe max increases due to melting of foreign fragments (Fig. 4), following the material stream, but not necessarily being reflected in the chemical analysis in the first part of the raw material handling. Elkem observe that these types of fragments come in waves, indicating that other waste streams occasionally are finding its way into the kerf material stream. Back-calculation from large scale testing at Elkem indicates that the recycled kerf can contain foreign fragments corresponding up to approximately 0.1–0.4 wt% Fe on a dry basis (per kg Si in the kerf as raw material). In addition to Fe, Ni was identified as an additional important metallic impurity in the kerf feedstock. Depending on wafering technology used, concentrations are found in the range from approximately 100 to 600 ppmw in the kerf. The variation in Ni seems to remain during the processing in pellet and melting plant.

3.3 Raw materials and their impact on the remelting process of slag

For the second recycling case, remelting of slags and sculls, control of the chemical composition of raw materials is critical for a successful process design. As the slags and sculls are considered a by-product of the silicon and ferrosilicon production processes, they are usually not analysed extensively. The silicon content in the slags and sculls is usually the only parameter that is analysed, but for remelting purposes a full chemical analysis is necessary.

Slags and sculls are in general inhomogeneous materials. They consist of areas with a lot of silicon and other areas with almost no silicon. In the areas with low silicon content, the slag chemistry may vary a lot in terms of which oxides and silicates are more prominent. Prior to a remelting process, crushing and mixing of the raw materials are thus important. Table IV gives an overview of the typical variations in slags and sculls after such processes for the most important chemical compounds in the large-scale testing carried out at Elkem Kristiansand.

Table IV: Typical variations for some chemical compounds in slags and sculls.

Material	Free silicon (wt. %)	SiO_2 (wt. %)	CaO (wt. %)
Slags	20-40	20-60	5-15
Sculls	25-50	20-70	2-10

3.4 Scale up: industrial campaign of remelting slag and skulls

The most important parameter used to measure product quality was free silicon content in the slag product for a cement or binder application. Elkem had set a target of less than 5 wt. % silicon left in the slag product for this purpose, where levels between 5–10 wt. % were considered acceptable. This parameter was thus monitored for the duration of the campaign, and the results are presented in Figure 7. As can be seen from the figure, the campaign showed a steady decline in free silicon content in the slag product, but achieving the target concentration below 5 wt. % was challenging. Several measures were implemented to optimise the separation of slag and molten FeSi, as reflected by the sudden dips in the figure, but the chemical equilibrium appeared to move towards higher silicon content in the slag product over time. The final measures, from batch 76 onwards, gave the best results. Changes to the practical furnace setup were the main contributor to this improvement. In addition, the operators had gained more experience in sorting slag products with high and low silicon content.

Figure 8: Free silicon content (wt. %) in slag product as a function of batch number.

An important basis for achieving a good separation of slag and silicon is the slag chemistry. A certain difference in density between the slag and silicon is necessary, and the slag must have a certain fluidity. Both properties are adjusted using CaO. Increasing the amount of CaO to the slag melt will increase the density and decrease the viscosity. A decrease in viscosity is positive for the fluidity of the slag melt, but an increase in density is negative in terms of density difference between slag and FeSi. This means the slag chemistry, or the CaO concentration, needed to be monitored closely during the campaign. For this, the term basicity was used, which is in operation mode defined as the ratio between CaO and SiO_2. Basicity measurements were obtained by performing chemical analyses on slag samples taken from the melt. However, this is a slow process which cannot sufficiently be used as a way of controlling the process during operation. Elkem has in the large-scale campaign investigated a new inline method for controlling the basicity of the slag.

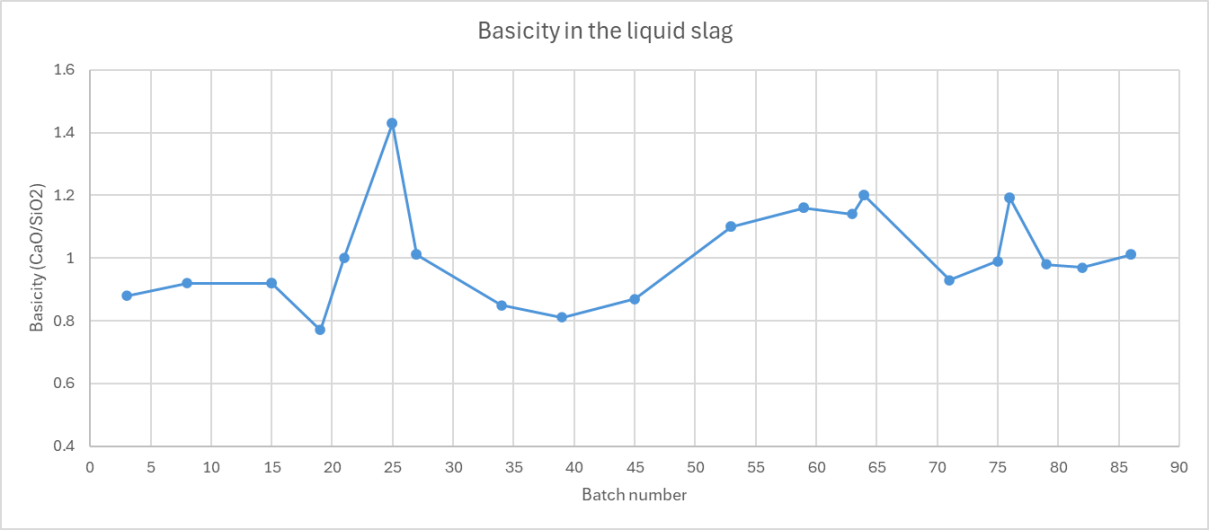

Figure 9: Basicity (CaO/SiO_2) of the liquid slag as a function of batch number.

The new measurement method, under development, generally give higher basicity for the slag than those obtained using chemical analyses. The method will be described on a later stage,

when full validation is completed. In addition, it is observed that the inhomogeneity of the slag results in relatively large variation in basicity. Overall, the average chemistry of the slag was within acceptable areas in terms of density and viscosity. The results compared to small scale test might indicate that scale up and the setup of induction furnaces used for the large scale is the main reason for the challenges related to separation and product quality of slag. In smaller scale, separation of slag and FeSi have been performed successfully with slag products consisting of less than 5 wt. % free silicon (also commonly referred to as metallic silicon content). The root cause for the differences is currently not fully understood, but both design and setup of the systems are under investigation.

3.5 Pellet plant -Experiences and safety issues from the campaign

The pellet step was tested in two separate campaigns conducted in autumn 2025 and spring 2026. The campaigns verified the pellet plant as an industrial pilot and demonstration unit at Technology Readiness Level 7 (TRL7), and the produced material was internally qualified as within specification. At the same time, the campaigns demonstrated that variation in the raw materials is reflected in kerf reactivity during drying and calcination. This directly affects plant capacity, process stability and operational safety. These findings confirm that raw-material control is essential for reliable industrial recycling of silicon from kerf and indicate that tighter raw material specifications are required in future operation.

The campaigns further showed that the pellet line has a demanding process-safety profile, driven by combustible dust, reactive kerf behaviour, plugging in hot process zones, off-gas instability, and a control architecture that still reflects pilot-scale operation. The most critical scenarios are associated with dust fire or explosion, temperature escalation in the dryer and calciner, concealed overheating at blocked transfer points, and operator exposure during manual intervention and upset handling. The overall risk level is strongly influenced by dust containment, the robustness of automation and interlocks, uncertainty in off-gas oxygen measurement, burner-related hazards, and the need for a fully verified philosophy for atmosphere control, ventilation and emergency shutdown.

For further scale-up towards a TRL9 industrial design, the pellet plant should be assessed and developed as an integrated process-safety system. This requires updated HAZID (HAZard Identification) and HAZOP (HAZard and Operability) studies, combustible-dust assessment, hazardous-area classification, and a clearer basis for explosion prevention, atmosphere control strategy and shutdown logic. In parallel, operational robustness should be improved through tighter control of raw material with respect to reactivity, moisture and contamination. In addition, it is necessary to strengthen operating and corrective-action procedures, reduced need for manual intervention, improved housekeeping and maintenance, and systematic operator training. Collectively, these measures are required to close the gap between pilot-scale operation and a robust industrial operating window for kerf-based silicon recycling.

3.6 CO_2 Footprint Impact

Conventional submerged arc furnace (SAF) silicon production is dominated by Scope 1 emissions, with ~4.7–5.0 t CO_2 eq/t Si from carbothermic reduction using carbon reductants. Additional Scope 2 emissions arise from electricity consumption (~11–13 kWh/kg Si), while Scope 3 includes upstream mining of quartz and reductants, and transport of raw materials. For kerf-based recycling, the key shift is the potential of elimination of most Scope 1 emissions,

as no primary reduction is required. The footprint is instead dominated by Scope 2 (electricity, low in Norway) and limited Scope 3 contributions (e.g. additives, logistics). Life-cycle studies indicate up to ~ 77% total emission reduction (Blömeke et al., 2023), implying that the main decarbonisation lever is elimination of most of Scope 1 emissions and that the product will remain with more manageable Scope 2 emissions, which can be reduced further via low-carbon electricity. This redistribution changes the relative contribution of raw material supply, process emissions and electricity consumption, and should therefore be considered when interpreting and comparing carbon footprint results.

In conventional cement production, Scope 1 emissions dominate, primarily from calcination of $CaCO_3$, contributing ~0.5–0.8 t CO_2 eq/t clinker. Scope 2 relates to kiln electricity, while Scope 3 includes raw material supply and downstream use. When slag is used as substitute for cement, most of the avoided emissions are Scope 1, as clinker production is displaced. The residual footprint of slag is largely Scope 2–3, linked to processing (e.g. grinding) and transport. Typical substitution yields ~0.7–0.8 t CO_2 eq savings per tonne of cement replaced. In practice, this shifts emissions away from hard-to-abate Scope 1 towards lower-intensity Scope 2–3 and enabling substantial net reduction in total embodied CO_2 eq in construction materials (He et al., 2022).

3.7 Further work

Future work will focus on expanding the experimental dataset and validating the process under more representative operating conditions. Particular emphasis will be placed on product consistency, silicon recovery, process stability, and environmental performance at increased scale. For silicon products targeting Si99 applications, such as the aluminium and chemical markets, future publications will include a broader characterization of the final product, including key impurity elements (e.g., Al, Ti, and Ca) and life-cycle assessment (LCA) results from regular operation. In addition, further process control needs to be implemented in order to handle the variation in element like Fe and Ni.

Further optimization studies are planned to improve process robustness and resource efficiency. However, several aspects of the technology remain under active development and contain some commercially sensitive know-how. Consequently, detailed information related to intermediate products, operating conditions, and proprietary process parameters is not disclosed at this stage. Such results may be reported in a more aggregated form as the technology matures and progresses towards industrial implementation.

4. CONCLUSION - SUMMARY

This paper presents two large-scale recycling cases at Elkem: recycling of silicon from kerf, and remelting of slags and sculls to produce a cement-replacement material with a lower CO_2 footprint.

Industrial scale testing on kerf recycling shows that silicon from wafer-sawing side streams can be upgraded to Si99 quality. A main finding is that variation in the incoming kerf, particularly in carbon, oxygen, moisture and foreign material, has a direct impact on process stability, safety and intermediate product quality. Among the monitored indicators, Fe has proven to be a practical and important KPI to follow up during processing, as elevated Fe levels reflect contamination from foreign metallic fragments that may enter and follow the process stream. At the same time, the results show that kerf-based recycling has a clear

decarbonisation potential, since production can avoid most of the direct scope 1 CO_2 eq emissions associated with conventional carbothermic silicon production.

Production of slag suitable for replacement of cement by remelting of slag and skulls also demonstrates the importance of controlling the raw materials. The test campaigns show that the raw materials are inherently heterogeneous, with substantial variation in silicon content, SiO_2 and CaO, and that this variation must be managed through crushing, blending and close control of slag chemistry. The large-scale campaign confirmed the technical potential to recover FeSi and produce a slag for use as replacement for cement, but it also demonstrated that there are several challenges related to scale-up that remains to be solved, particularly with respect to stable operation of the process. Nevertheless, this case has a potentially significant CO_2 benefit because the slag product can replace part of the clinker in cement applications and thereby reduce the direct process emissions associated with conventional clinker production

While the results confirm the technical feasibility of the proposed recycling routes, further work is ongoing to establish more detailed product qualification data and environmental performance metrics required for commercial implementation in some selected Si99 markets.

5. ACKNOWLEDGEMENTS

This paper is published by permission of Elkem ASA. The contribution of all our colleagues taking part in the large-scale campaigns are gratefully acknowledged. This work has been funded by Innovation Norway.

6. REFERENCES

M. Syvertsen, T. Halvorsen, K. Mørk, A. Nordmark, T. Kaden and A. Ulyashin, "Remelting and purification of Si-kerf for PV-wafers," in *Proceedings of the Silicon for the Chemical and Solar Industry Conference*, 2018.

E. Emil-Kaya, M. Tellobond, M. Papakci and G. Tranell, "Recycling silicon from secondary sources: waste solar wafers and diamond wire saw kerf slurry in photovoltaic industry," in *Metallurgical & Materials Engineering Congress of South-East Europe*, 6(1), 2025.

S. Blömeke, R. Arafat, J. Yang, J.-P. Mai, F. Cerdas and C. Herrmann, "Environmental assessment of silicon kerf recycling and its benefits for applications in solar cells and Li-ion batteries," *Procedia CIRP*, 116 (2023), pp. 179–184.

A.A. Jhatial, I. Nováková and E. Gjerløw, "A review on emerging cementitious materials, reactivity evaluation and treatment methods," *Buildings*, 13(2) (2023), 526.

S. He, A. Yorulmaz, K. Minalga, M. Fan and J.M. Cullen, "Cement substitution with secondary materials can reduce annual global CO_2 emissions," *Nature Communications*, 13 (2022), 5758.

Gro Eide
Vice President Innovation, ELKEM

Gro Eide holds an PhD in Materials Science from UiO and a MSc in Physics from NTH and has over 30 years of experience in Material product development. She joined Elkem in 1997 and has held several senior leadership roles, including R&D, Laboratory management and product development.

Wellman, S. A., A. Olivo, I. T. Gloppen, and H. Teisrud. 2026. Improved slag estimation in metallurgical grade silicon via temperature-resolved analysis. In *Silicon for the Chemical and Solar Industry XVIII*, edited by M. Tangstad, H. Rong, A. Valderhaug, B. Andresen, H. Dalaker, and I. G. Page. Kristiansand, Norway, September 7–10. https://doi.org/10.55669/oa900827

Improved slag estimation in metallurgical grade silicon *via* temperature-resolved analysis

S.A. Wellman[1,2], A. Olivo[2], I.T. Gloppen[2], and H. Teisrud[2]
[1]Norwegian University of Science and Technology (NTNU), Dept. of Physics, Trondheim, Norway (sophiaaw@stud.ntnu.no)
[2]Elkem ASA, Kristiansand, Norway (alberto.olivo@elkem.com, ida-therese.gloppen@elkem.com, hege.teisrud@elkem.com)

Keywords: slag estimation, silicon production, quality control, oxygen measurements, inert gas fusion

Abstract – Accurate quantification of slag in silicon is essential for quality control in industrial silicon production. Conventional combustion methods provide only total oxygen content and cannot distinguish between slag-derived oxygen and that originating from surface oxides, leading to variability influenced by particle size and sample preparation. This study presents a modified analytical approach based on controlled temperature ramping to selectively differentiate oxygen contributions from surface silicon oxides (SiO_x) and slag phases. The method exploits thermodynamic differences between oxygen containing species, enabling their separation through temperature resolved evolution profiles. Systematic method development was carried out on silicon materials with varying purity, including metallurgical grade (MG-Si) and electronic grade silicon (EG-Si). The results demonstrate that slag-related oxygen is released at higher temperatures than surface oxides, allowing clear signal separation. The proposed method shows strong potential for improving slag estimation accuracy and providing more robust oxygen speciation in silicon quality assessment.

1. INTRODUCTION

Elkem produces a wide range of silicon-based materials, including ferrosilicon (FeSi), magnesium ferrosilicon (FSM), and silicon powders of varying purities, for all of which slag content represents a critical quality parameter (Elkem ASA, n.d.). Quantification of slag is performed using oxygen content as a proxy (Johnston and Barati, 2010). Therefore, the validity of the slag content estimation relies on the reliability of the oxygen measurements. Quantification of slag in silicon materials must be accurate and reproducible to ensure reliable quality control in industrial silicon production (Næss *et al.*, 2014).

In general, the oxygen measurements from which slag content is inferred are obtained by inert gas fusion (IGF) analysis. The standard IGF procedure provides only a total oxygen value and does not distinguish between oxygen originating from slag and oxygen associated with SiO_x (Maslennikova *et al.*, 2025).

To obtain representative results and thus reduce variability, sample homogeneity is crucial: to this purpose, silicon is crushed to micron-range powder prior to analysis. Crushing is a necessary step in samples preparation for IGF and it allows for better mixing of the slag in the silicon (Gruner and John, 1992), even though the material is likely to separate into a heterogeneous mixture where finer particles reside closer to the surface. Crushing and milling increase the surface-to-volume ratio of the sample, thereby enhancing the contribution from surface oxides and introducing errors in the estimated slag content (Petrakis and Komnitsas,

This work is licensed under the Creative Commons Attribution 4.0 International License. To view a copy of this license, visit https://creativecommons.org/licenses/by/4.0/

2022). Generally, crushing is operator-dependent since it is affected by several parameters, such as different equipment type, feed rate, and milling time (Nilssen and Kleiv, 2019). Consequently, particle size distributions vary between specimens and sites so that samples that were crushed for longer or milled finer will suffer to a larger extent from increased oxygen contribution from the surface silicon oxide (Kim *et al.*, 2011). Therefore, measurement errors are both systematic and random in nature: systematic due to the direct correlation of increased surface oxygen with decreasing particle size, and random due to variability in operational conditions (Shen *et al.*, 1997). This challenge is widely recognised within the silicon industry, but available open literature on analytical methods remains limited (Forwald *et al.*, 1994). To the author's knowledge, there is only a patent by Miller, but its applicability is limited to Si powders whose size is suitable for further processing in organohalosilane industry (< 150 µm; Kuivila and Miller, 1999). Furthermore, the patent does not report the extent to which the proposed method improves measurement precision, limiting the assessment of its analytical performance.

Currently, the contribution of SiO_x is not deducted from the total oxygen content when estimating slag content, resulting in the incorrect classification of MG-Si production batches as *off-specification* and subsequently in unnecessary rework. Consequently, there is a need for an analytical approach that can discriminate between oxygen contributions from surface SiO_x and slag phases.
This study investigates a modified analytical method designed to this purpose through a controlled temperature-ramping programme. The approach exploits thermodynamic differences in decomposition reactions among oxygen-containing phases, causing their reactions to occur at distinct temperature intervals (Ostrovski *et al.*, 2010). To the authors' knowledge, no previous studies have reported the use of temperature-resolved inert gas fusion analysis to quantitatively differentiate oxygen associated with surface SiO_x from oxygen originating from slag phases in metallurgical-grade silicon (MG-Si).

A sequence of method iterations was evaluated on silicon samples of varying purity, including metallurgical-grade silicon (MG-Si) and electronic-grade silicon (EG-Si) to confirm that slag-related oxygen evolves at higher temperatures than surface oxides, thereby enabling separation of the two signals. Moreover, an additive was tested to accelerate SiO_x decomposition without affecting slag, thus improving signal resolution.
The method is finally verified through a controlled milling experiment using MG-Si (99 wt. % Si), where increasing milling time, and thus surface area, is expected to increase the oxygen signal associated with SiO_x,while leaving slag-related signal statistically unchanged. The results serve as proof-of-concept for a selective temperature-programmed method capable of separating surface oxide and slag contributions to the total oxygen content.

The approach has the potential to reduce misclassification of silicon batches caused by surface-oxide artefacts, improve analytical robustness across production sites, and strengthen quality-control procedures in silicon manufacturing.

2. EXPERIMENTAL

2.1 Materials

A MG-Si reference sample was used as a model material for initial proof-of-concept testing. It contains more than 99 wt. % elemental Si and the main metal impurities are Fe (0.35 wt. %), Al (0.12 wt. %), C (0.011 wt. %), Ca (350 ppm), and Ti (250 ppm) (Elkem ASA, 2024). Before IGF testing, MG-Si was pulverised in a laboratory planetary mill until D_{50} was lower than 20 µm.

During IGF analysis, oxygen originating both from slag phases and from surface oxides is detected. To verify the assignment of oxygen signals to specific oxygen-containing species in Si-99, the signal profiles of Silgrain® e-Si as a reference EG-Si (purity > 99.9 wt. %, D_{50}=1.50 μm) and wollastonite ($Ca_3(Si_3O_9)$), as a representative pure slag material, were studied. The former has minimal amounts of slag due to its high purity such that the oxygen detected for this material is expected to be mainly from SiO_x. This powder will therefore allow the identification of SiO_x signal assignment in MG-Si. On the contrary, wollastonite was chosen due to its simple chemical composition, absence of free elemental Si, and relevance to silicon metallurgy (Jiang *et al.*, 2014). The tests with wollastonite will then ascribe the signal placement to slag unambiguously.

2.2 Inert gas fusion analysis

For this study, IGF was carried out using a dedicated commercial instrument, LECO ON 836, (LECO, n.d.). Since the instrument operates in inert conditions, leak check and blank correction test are run before each measurements session. For improved homogenisation, the bulk of the sample is first manually mixed prior to the sampling. Before each measurement, approximately a 0.2 g specimen is weighed using tin foil as a container. The foil is subsequently folded and then introduced into a graphite crucible containing graphite powder for IGF in the furnace under helium flow.

Some experiments make use of nickel as a flux medium. The additive was used, as recommended by the instrument supplier, to enhance the reaction kinetics of oxide phases during IGF analysis. For these tests, the sample was placed in a nickel basket before the assembly was introduced to the graphite crucible.

In the analysis, inorganic oxides undergo carbothermic reaction, which is followed by the Boudouard reaction (Eq. [1] and [2]). Added graphite will then act as a reductant for M_xO_y species.

$$M_xO_y + yC \rightarrow yCO + xM \quad [1]$$

$$2CO \rightarrow CO_2 + C \quad [2]$$

where M_xO_y is a general formula for oxide and M its elemental form. Therefore, oxygen signal is calculated *via* the quantification of CO and CO_2, which are detected using a non-dispersive infrared (NDIR) cell. The oxygen concentration is derived using the principle that analyte gas molecules absorb infrared (IR) energy at unique wavelengths and there is a correlation between concentration and IR absorbance (LECO, n.d.). The oxygen signal was recorded as a function of time and furnace temperature and subsequently normalised to sample mass for comparison between measurements. As the aim was to compare relative oxygen-release profiles rather than determine absolute oxygen concentrations, no calibration was applied; the raw detector signal was instead used directly and normalised to sample mass (Skoog *et al.*, 2017). The number of replicates was selected based on the need to ensure sufficient precision and to capture method variability, in line with established principles of analytical chemistry (Skoog *et al.*, 2017). In this study, two to three replicates were applied during exploratory experiments to obtain an initial indication of repeatability. For experiments requiring a more robust statistical evaluation, the number of replicates was increased to five or more, particularly to account for variability associated with sample inhomogeneity.

2.3 Temperature-ramping programme

The oxygen-containing species present in MG-Si include adsorbed water, carbonates, surface silicon oxides, and slag phases. Adsorbed water and carbonates are expected to decompose at

relatively low temperatures (up to approximately 900 °C). Silicon oxides are anticipated to be reduced at intermediate temperatures between 1600 °C and 1700 °C (Lee *et al.*, 2010), whereas slag-related oxygen species are reduced at higher temperatures (above 2200 °C). Accordingly, the temperature ramping programme was designed as a sequence of discrete temperature intervals. Each interval was selected to be sufficiently high to promote decomposition of a specific oxygen-containing species, while minimising overlap with subsequent reactions. The expected sequence of decomposition is illustrated in Figure 1.

The temperature programme was iteratively refined during the experimental campaign to maximise the separation between SiO_x decomposition and the onset of slag reduction. Adjustments included extending the dwell time at the SiO_x decomposition plateau and introducing nickel as a flux to facilitate the reduction of silicon oxides. Efforts were additionally made to improve the signal resolution between the SiO_x and slag-related oxygen signals. To facilitate the interpretation of the oxygen-evolution profiles, the corresponding temperature programme is shown on the secondary y-axis in all plots presented in Chapter 3.

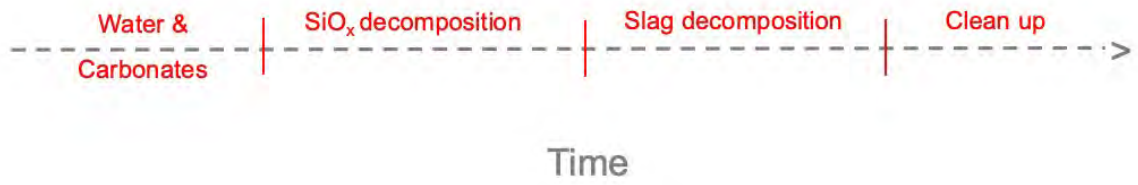

Figure 1: Schematic representation of oxygen-containing species decomposition during temperature ramping

2.4 Proof of concept experiment

To verify the method, a proof-of-concept experiment was conducted using Si-99 samples subjected to varying milling durations, thereby producing different particle size distributions. Increased milling time results in reduced particle size and, consequently, a higher surface-area to-volume ratio, leading to increased surface oxide content. It is therefore expected that the signal corresponding to the SiO_x decomposition interval increases with milling duration, while the signal associated with slag decomposition remains largely unaffected.

For this experiment, as-received MG-Si was milled in a *PULVERISETTE 7 premium line* planetary mill from Fritsch. at 1100 rpm spinning rate for 10 s, 30 s, and 60 s. Specific surface area (SSA) was determined by nitrogen physisorption using a Micromeritics TriStar analyser. Prior to measurement, the samples were degassed to remove adsorbed moisture and volatile species, and the surface area was calculated from the adsorption isotherm in the p/p_0 =0.05-0.30 range using the BET method (Brunauer *et al.*, 1938).
An unmilled sample was also analysed, resulting in four MG-Si samples with distinct particle size distributions and surface oxide contents. Sample preparation otherwise followed the procedure described in Section 2.1 where five replicates were prepared from each sample batch. When needed, pairwise two-sample t-tests were used to assess whether differences in integrated peak areas were statistically significant; $p < 0.01$ was taken as the significance threshold.

3. RESULTS AND DISCUSSION

The carbothermic reduction is generally defined as the chemical reactions that occur between metal oxides and elemental carbon to form carbon monoxide and (semi)metals in their elemental form (see Eq. [1]). These are the same type of reactions that occur in a silicon furnace, therefore similar considerations can be used to describe MG-Si production and oxygen quantification *via* IGF.

The minimum temperature required for carbothermic reduction is defined thermodynamically as the temperature at which the Gibbs free energy of the overall reduction reaction becomes zero ($\Delta G = 0$), corresponding to equilibrium between oxide, carbon, and gaseous species (L'vov, 2000). In this condition, the oxygen affinity to carbon equals that to the oxide, and reduction becomes feasible at higher temperatures (Chahtou *et al.*, 2020). In practical systems, this temperature is not fixed but depends on gas composition, pressure, and reactant activities, which determines the onset of carbothermic reduction in the IGF furnace.
The reaction mechanism is applicable to many elements, such as aluminium, silicon, titanium, iron, etc. (Ostrovski *et al.*, 2010). During the analysis, when a high enough temperature is reached, metal oxides in the sample (i.e. SiO_x and wollastonite) react *via* carbothermic reduction mechanisms with the graphite powder in the crucible.

In the case of SiO_2, this reaction occurs at temperatures higher than 1600 °C (Maeng *et al.*, 2020). The oxidation product, i.e. CO, is then disproportionated to CO_2 and elemental C in the Boudouard reaction (see Eq. [2]). SiO_x reduction proceeds *via* the formation of gaseous SiO, which then can be further reduced to SiC (see Equations [3] and [4]). This reaction pathway introduces a potential source of analytical uncertainty, since SiO is not directly detected by the NDIR system.

$$SiO_x + (x-1)C \rightarrow SiO + (x-1)CO \quad [3]$$
$$SiO + 2C \rightarrow SiC + CO \quad [4]$$

Thermodynamically, low CO partial pressure favours the further conversion of SiO towards either Si or SiC formation (Schei *et al.*, 1998). Under the present analytical conditions, the continuous helium flow may contribute to maintaining a low local pCO, while the addition of fine graphite increases the available carbon surface area and promotes SiO–carbon contact. These conditions are therefore expected to favour SiO conversion and reduce potential losses, improving the reliability of the oxygen measurement.

Whereas, wollastonite carbothermic reduction occurs at temperatures higher than 2000 °C (Swamy and Dubrovinsky, 1997). Therefore, from a thermodynamic point of view, it is possible to separate signals from SiO_x and wollastonite in a IGF spectrum. However, the fast temperature ramp rate requires the optimisation of analysis parameters to improve robustness of results.

To verify the assignment of signal from SiO_x, the temperature-ramping programme was first applied to EG-Si. Its oxygen profile is shown in Figure 2. Two distinct regions of oxygen evolution are present: an early peak at 150-350 s within the designated SiO_x interval (a) and a second peak appearing during the subsequent temperature increase toward the slag plateau (c) at 450-600 s. For EG-Si, the main signal was expected to stay within the designated SiO_x interval. Thus, the resulting splitting of oxygen signal was unexpected. However, upon closer inspection, the onset temperature of the second peak at (c), coincides with that of the SiO_x region (i.e. 1650 °C). Additionally, a sharp decrease in signal is observed upon initiation of the

cooling stage (b) at 350 s, indicating incomplete oxide decomposition in the initial plateau (a). These observations suggest that the second peak represents continued decomposition of residual silicon oxides, temporarily interrupted by the cooling step. This may be attributed to slower reduction kinetics for certain oxide species in SiO_x, requiring higher temperatures to overcome activation barriers for carbothermic reduction, or perhaps the SiO_x quantity is too high to be reduced in that short amount of time.

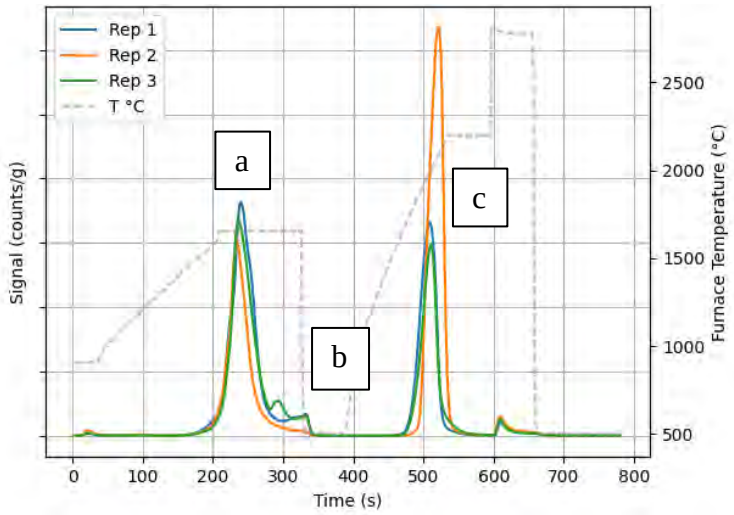

Figure 2: Oxygen signal profiles for temperature-ramped combustion of EG-Si without nickel

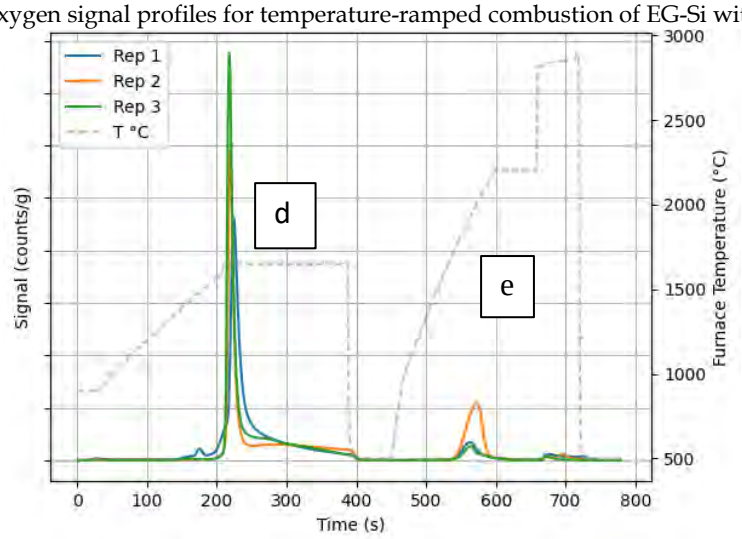

Figure 3: Oxygen signal profiles for temperature-ramped combustion of EG-Si with nickel

To improve the kinetics of SiO_x reduction and thus improve the resolution of oxygen measurements with IGF, one can employ nickel, a commonly used flux medium (Beck and Müller, 1997). There are three main reasons for nickel being a commonly chosen flux. Firstly, elemental nickel's melting point is 1455 °C, meaning it is liquid at the SiO_2 reduction temperature. In its liquid form, nickel has a higher conductivity than the carrier gas helium (54.6 vs. 0.468 $W \cdot m^{-1} \cdot K^{-1}$ at 1750 °C) and thus enhances heat transfer from furnace heating elements to the specimen (Assael *et al.*, 2017). Secondly, it has been recently proved that Ni has a catalytic effect on SiO_2 reduction to Si by weakening bonds in adsorbed CO and SiO and favouring oxygen transfer (Chen *et al.*, 2025). Finally, Ni catalytic effect on CO disproportionation is well-established. The conversion of CO causes a shift in the equilibrium of reaction in Eq. [1], thus boosting metal oxides conversion to their elemental state (Balakos and Chuang, 1993).

As shown in Figure 3, the addition of Ni results in a clear redistribution of the oxygen signal, with a larger fraction occurring within the designated SiO_x interval (d) at 150-300 s. This is evident both qualitatively from peak intensities and quantitatively from peak area analysis (Table I). The fraction of oxygen released at within the designated slag plateau (e) at 450-600 s decreased from 43 % to 9 % upon addition of Ni. These results, summarised in Table I, demonstrate that nickel significantly promotes oxide decomposition at lower temperatures, thereby reducing overlap with the slag-related signal.

Table I: Relative oxygen signal contributions in the SiO_x and slag regions, respectively

Sample	150-350 s	450-600 s
EG-Si without Ni	54.18 %	42.94 %
EG-Si with Ni	88.07 %	9.25 %

Identification of the slag-related signal was performed using wollastonite as a model slag material. Experiments were conducted both with and without nickel to assess its influence on slag decomposition kinetics (Figures 4 and 5). The results confirm that slag reduction occurs exclusively in the high-temperature region, well above the SiO_x decomposition interval. Moreover, under selected analytical conditions, the addition of nickel has no observable effect on slag behaviour, suggesting that Ni acts as a selective flux for silicon oxides without influencing slag reduction.

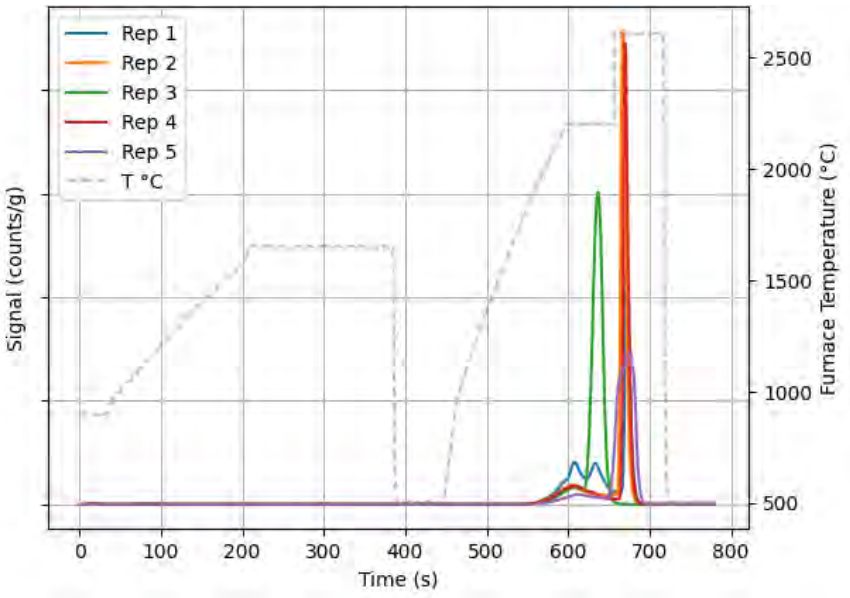

Figure 4: Oxygen signal profiles for wollastonite without Ni

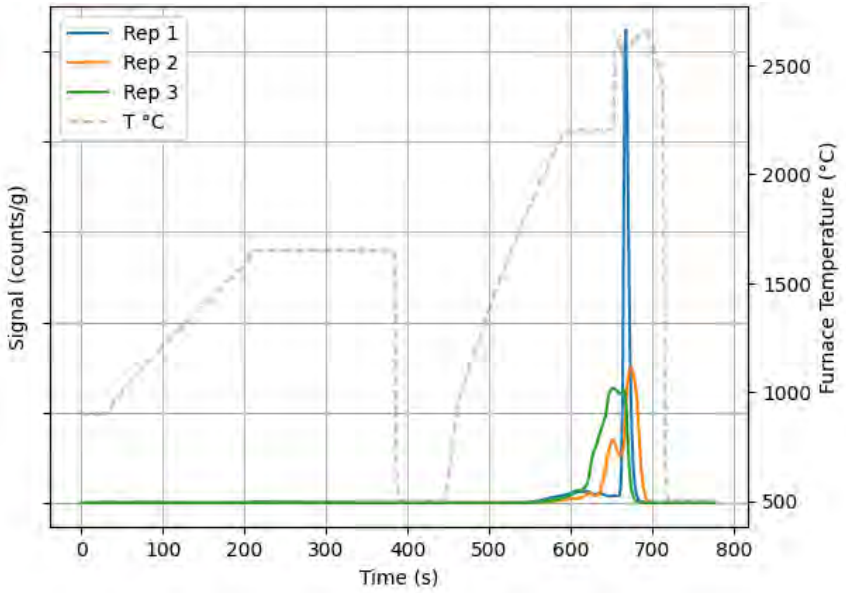

Figure 5: Oxygen signal profiles for wollastonite with Ni

Having established signal assignment and confirmed that SiO_x and slag signals could be almost completely separated, the method was evaluated using Si-99 samples subjected to controlled milling for 10, 30, and 60 s. By increasing the milling time, the mean particle size is reduced. This further size reduction caused an increase in SSA from 0.20 $m^2 \cdot g^{-1}$ to 0.51, 1.96, and 3.17 $m^2 \cdot g^{-1}$, respectively. As previously mentioned, a decreased particle size increases the specific surface area, meaning an increased amount of surface silicon oxide is present. The resulting oxygen signal profiles are shown in Figure 6.

A clear increase in signal intensity within the SiO_x region is observed with increasing milling time, consistent with increased surface area and oxide content. The slightly lower onset temperature observed for the coarser particles may be related to differences in oxide accessibility rather than to a true thermodynamic shift in SiO_x reduction. In fact, as milling increases the specific surface area, it may also increase powder bed porosity and create a more tortuous packed structure (Olivo *et al.*, 2024; Watanabe, 2025). This can introduce additional resistance to mass transport towards the Si/SiO_x–C reaction interface, delaying the effective release of CO/CO_2 from the finer samples. Therefore, the early onset in the coarse sample should be interpreted as a kinetic/sample-heterogeneity effect. In contrast, the signal in the high temperature region remains comparatively stable, both in onset temperature and magnitude.

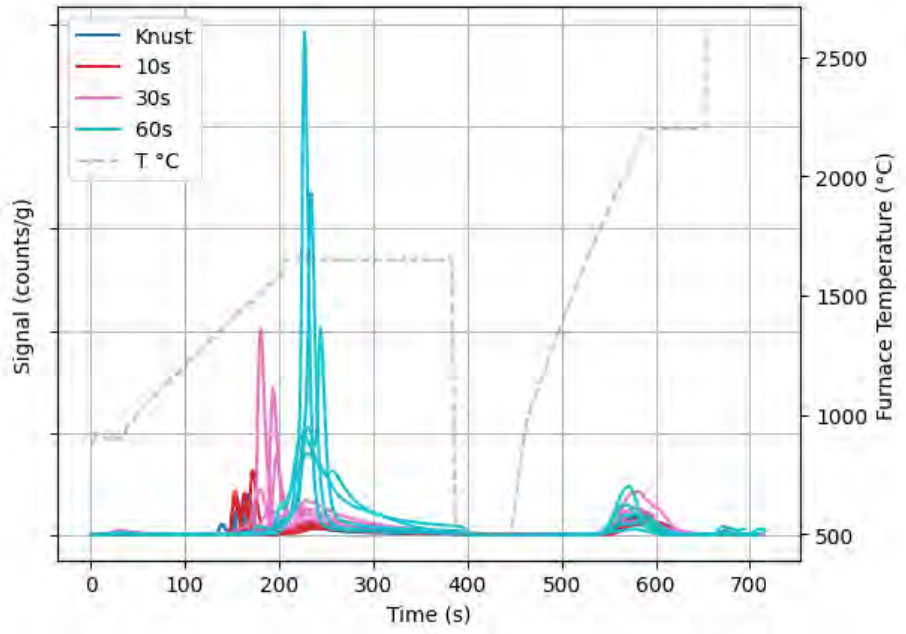

Figure 6: Oxygen signal profiles for MG-Si samples with varying milling durations

Quantitative analysis of peak areas supports these observations. In the SiO_x integration region, the mean oxygen signal increases systematically with milling time, from 4601 counts · s · g^{-1} for the as-received sample to 28419 count · s · g^{-1} after 60 s of milling (Table II). The relative standard deviation (RSD) remains within acceptable limits (7.4 – 15.0 %), considering the inherent inhomogeneity of the material. Statistical analysis (t-tests) confirms that all pairwise differences are significant ($p < 0.001$).

Table II: Statistical measures of peak areas in the SiO_x integration region

	As received	10 s	30 s	60 s
SSA [$m^2 \cdot g^{-1}$]	0.20	0.51	1.96	3.17
Avg. Area [counts • s • g^{-1}]	4601	6282	15447	28419
STD [counts • s • g^{-1}]	513	467	2309	2853
RSD [%]	11.2	7.4	15.0	10.0

In contrast, the slag integration region shows no consistent trend with milling time (Table III). Although RSD values are higher (19.2 – 48.1 %), this is primarily due to lower signal magnitudes rather than increased variability, as indicated by comparable standard deviations. Statistical testing yields $p > 0.01$ for all comparisons, confirming that differences are not significant at the 99 % confidence level.

Table III: Statistical measures of peak areas in the slag integration region

	As received	10 s	30 s	60 s
SSA [$m^2 \cdot g^{-1}$]	0.20	0.51	1.96	3.17
Avg. Area [counts$\cdot s \cdot g^{-1}$]	3654	3156	5515	4777
STD [counts$\cdot s \cdot g^{-1}$]	870	607	2462	2299
RSD [%]	23.8	19.2	44.6	48.1

These results indicate that the low-temperature signal is sensitive to surface oxide content, whereas the high-temperature signal is independent of particle size and can be attributed to slag.

Overall, the findings demonstrate that the temperature-ramped LECO method enables effective separation of oxygen contributions from surface oxides and slag. The systematic increase in the SiO_x signal with milling, combined with the stability of the high-temperature signal, confirms the method's capability to distinguish between these two sources of oxygen.

4. CONCLUSIONS

For industrial silicon production, a reliable slag measurement system based on robust oxygen quantification is critical to ensure consistent quality control and minimise variability arising from sample preparation and measurement uncertainty. This work demonstrates that a temperature-ramped IGF method can significantly improve accuracy in the estimation of slag-bound oxygen in silicon materials. The incorporation of nickel as a selective flux enhances the decomposition of surface silicon oxides, reducing their contribution to the slag-related signal. The effectiveness of the method was confirmed through the milling experiment, which showed that variations in particle size — and thus surface area — affect only the SiO_x signal, while the slag-related signal remains unchanged under selected analytical conditions. This indicates that the combined temperature ramping and nickel-assisted approach reduces the effect of samples particle size on slag-bound oxygen significantly.

Overall, the results establish a proof-of-concept for a temperature-programmed IGF analysis capable of selectively separating and quantifying oxygen contributions from surface oxides and slag. Therefore, the presented method provides a more representative assessment of slag content and has clear potential to improve analytical robustness and quality control in silicon production.

Future work will focus on the full industrial validation of a quantitative method for slag estimation, by verifying accuracy, precision, and reproducibility. The final step will be the transfer of the validated method to quality control laboratories at production sites.

Moreover, the validation of similar methods could be extended also to a broader range of industrial materials, particularly FeSi and FSM, as well as further optimisation of the temperature programme to reduce analysis time while maintaining signal separation.

5. ACKNOWLEDGEMENTS

This paper is published by permission of Elkem ASA. The contribution of our colleague Pål Baggethun is gratefully acknowledged. This work has been funded by Research Council of Norway (RCN) through SFI PhysMet – Centre for Sustainable and Competitive Metallurgical and Manufacturing Industry (Project number: 309584).

6. REFERENCES

Assael M.J., Chatzimichailidis A., Antoniadis K.D., Wakeham W.A., Huber M.L. and Fukuyama H. 2017. Reference correlations for the thermal conductivity of liquid copper, gallium, indium, iron, lead, nickel and tin. *High Temperature High Pressure*, Vol.46(6), pp.391-416. https://doi.org/10.3233/HTHP-170303.

Balakos M.W. and Chuang, S.S.C. 1993. CO disproportionation on Ni-based catalysts. *Reaction Kinetics and Catalysis Letters,* Vol.49, pp.7–12. https://doi.org/10.1007/BF02084022.

Beck H. and Müller H. 1997. Determination of the oxygen content of ceramic materials by Carrier-Gas-Heat-Extraction (CGHE) – feasibility and restrictions of the method. *Fresenius Journal of Analytical Chemistry.* Vol.357, pp.652–655. https://doi.org/10.1007/s002160050229.

Brunauer, S., Emmett, P. H. and Teller, E. 1938. Adsorption of gases in multimolecular layers. *Journal of the American Chemical Society*, 60(2), pp.309–319. https://doi.org/10.1021/ja01269a023.

Cao R., Li Y., Xia J., Chen Z. and Yang J. 2019. $NiSO_4$ as Additive Effect on the Carbothermal Reduction Process of Phosphate Rock and SiO_2. *Silicon,* Vol.11, ..2829–2836. https://doi.org/10.1007/s12633-019-0071-x

Chahtou A., Boucetta A., Benioub R., Boualem A., Hamzaoui S. and Itaka, K. 2020. Study of Carbothermal Reduction of Silica, Alumina and Titania Under Argon Gas. *Proceedings of the 1st International Conference on Renewable Energy and Energy Conversion 2019*. Oran, Algeria, 11-13 November 2019, pp.295-301. https://doi.org/10.1007/978-981-15-5444-5_37.

Chen C., Li W., Zhen Q., Li R., Zhang S., Li X. and Wang J. 2025. Controlled synthesis of silicon carbide whiskers via nickel-based alloy catalyst-assisted carbothermal reduction unraveling vapor-liquid-solid growth and Ni_3Si_2 droplet dynamics. *Ceramics International*, Vol. 51, Issue 19, pp.29770-29780. https://doi.org/10.1016/j.ceramint.2025.04.180.

Elkem ASA (2024). *Product Data Sheet: Metallurgical Silicon (MG-Si), Revision No. 01, 14 March 2024*. Elkem ASA, Oslo, Norway. Available at: Elkem Product Data Sheet MG-Si (Accessed: 23 July 2026).

Elkem ASA (n.d.) Elkem. Available at: https://www.elkem.com/ (Accessed: 13 May 2026).

Gruner W. and John A. Determination of oxygen in solids using a modified carrier gas-hot extraction method. 1992. *Fresenius Journal of Analytical Chemistry,* Vol.342, pp.51–53. https://doi.org/10.1007/BF00321689.

Forwald A.G., Rong H.M. and Vogelaar G.C. 1994. Oxygen in Silicon; occurrence and influence on the direct process to methylchlorosilane. *Proceedings of the Silicon for the Chemical and Solar Industry II*. Loen, Norway, 8-10 June 1994, pp.107-119.

Jiang Y., Lin X., Ideta K., Takebe H., Miyawaki J., Yoon S.H. and Mochida I. 2014. Microstructural transformations of two representative slags at high temperatures and effects on the viscosity. *Journal of Industrial and Engineering Chemistry*, Vol.20, Issue 4, pp.1338–1345. https://doi.org/10.1016/j.jiec.2013.07.015.

Johnston M.D. and Barati M. 2010. Distribution of impurity elements in slag–silicon equilibria for oxidative refining of metallurgical silicon for solar cell applications. *Solar Energy Materials and Solar Cells*, Vol.94, Issue 12, pp.2085-0290. https://doi.org/10.1016/j.solmat.2010.06.025.

Kim B.-C., Uono H., Fuse T., Ishihara T., Senna M. Fabrication of nano-sized Si powders with a narrow size distribution by two-step milling. 2011. *Journal of Materials Research*. Vol.18, Issue 6, pp.1368-1373. https://doi.org/10.1557/JMR.2003.0188.

Kuivila, C.S. and Miller, D.C. 1999. *Method for selecting chemical grade silicon metalloid having improved performance in a direct process for making diorganodihalosilanes*. United States Patent US 5,973,177, issued 26 October 1999.LECO Corporation (n.d.) 836 Series elemental analysis for oxygen, nitrogen and hydrogen detection. Available at: https://www.leco.com/products/836-series/ (Accessed: 13 May 2026).

Lee H.-C., Dhage S., Akhtar M. S., Kwak D.H., Lee W.J., Kim C.-Y., and Yang O-B. 2010. A simulation study on the direct carbothermal reduction of SiO2 for Si metal. *Current Applied Physics*, Vol.10, Issue 2, Supplement, pp.S218-S221. https://doi.org/10.1016/j.cap.2009.11.053.

L'vov, B.V. 2000. Mechanism of carbothermic reduction of iron, cobalt, nickel and copper oxides. *Thermochimica Acta*, 360, pp.109–120. https://doi.org/10.1016/S0040-6031(00)00540-2.

Maeng S.H., Lee H., Park M.S., Park S., Jeong J. and Kim S. 2020. Ultrafast carbothermal reduction of silica to silicon using a CO_2 laser beam. *Scientific Reports,* Vol.10, pp.21730. https://doi.org/10.1038/s41598-020-78562-1.

Maslennikova A.A., Tkacheva O.Y. and Zaikov Y.P. 2025. Carbothermic Reduction for the Quantitative Determination of the Oxygen Content in Various Materials (Review). *Russian Metallurgy*, Vol.2025, pp.1924–1931. https://doi.org/10.1134/S0036029525702957.

Nilssen B.E. and Kleiv R.A. 2020. Silicon powder properties produced in a planetary ball mill as a function of grinding time, grinding bead size and rotational speed. *Silicon*, Vol.12, pp.1–12. https://doi.org/10.1007/s12633-019-00340-0.

Næss M.K., Kero I., Tranell G., Tang K., and Tveit H. 2014. Element Distribution in Silicon Refining: Thermodynamic Model and Industrial Measurements. *JOM*, Vol.66, pp.2343-2354. https://doi.org/10.1007/s11837-013-0797-7.

Olivo A., Michels, L., Høyen M.M., Friestad K. and Di Sabatino, Marisa. 2024 Ageing of micro and nano silicon surface (May 15, 2024). *Proceedings of the Silicon for the Chemical and Solar Industry XVII*. Trondheim, Norway, 7-10 September 2024, pp.295-301. https://doi.org/10.1007/978-981-15-5444-5_37.
http://dx.doi.org/10.2139/ssrn.4941273

Ostrovski O., Zhang G., Kononov R. and Dewan M.A.R. 2010. Carbothermal solid state reduction of stable metal oxides. *Steel Research International*, Vol.81(10), pp. 841–846. https://doi.org/10.1002/srin.201000177.

Petrakis E. and Komnitsas K. 2022. Effect of grinding media size on ferronickel slag ball milling efficiency and energy requirements using kinetics and attainable region approaches. *Minerals*, Vol.12(2), pp.184. https://doi.org/10.3390/min12020184.

Schei A., Tuset J.K. and Tveit H. 1998. *Production of High Silicon Alloys*. 1st ed. Trondheim: Tapir Forlag. ISBN 8251913179

Shen T.D., Shmagin I., Koch C.C., Kolbas R.M., Fahmy Y., Bergman L., Nemanich R.J., McClure M.T., Sitar Z. and Quan M.X. 1997. Photoluminescence from mechanically milled Si and SiO_2 powders. *Physical Review B*, Vol.55(12), pp.7615–7623. https://doi.org/10.1103/PhysRevB.55.7615.

Skoog D.A., Holler F.J. and Crouch S.R. 2017. *Principles of Instrumental Analysis*. 7th ed. Boston: Cengage Learning. ISBN 9781305577213

Swamy V. and Dubrovinsky L.S. 1997. Thermodynamic data for the phases in the $CaSiO_3$ system. *Geochimica et Cosmochimica Acta*, Vol.61, Issue 6, pp.1181-1191. https://doi.org/10.1016/S0016-7037(96)00403-6.

Watanabe T. 2025. Kinetics of thermal oxidation of silicon. *Applied Physics Express*, Vol.18, 120101. https://doi.org/10.35848/1882-0786/ae1f5b.

Sophia Anastasia Wellman
Technical Trainee, Elkem

Sophia holds a Master of Science degree in Applied Physics and Mathematics from the Norwegian University of Science and Technology. During the summer of 2025, she worked as a summer student at Elkem Silicon Products Development in Kristiansand, where she carried out the work presented in this paper.

During the 2025/2026 academic year, she completed both her project work and master's thesis in collaboration with Elkem, focusing on the chemical characterization of oxide layers on silicon powders. In August 2026, she joined Elkem ASA as a Technical Trainee, continuing the research project initiated during her summer internship.

Hoel, J. O., M. O. Victorin, A. Crawford, and H. M. Rong. 2026. Corrosion of Superalloys typically used as reactor material for the reaction between Si, SiCl4 and H2. In *Silicon for the Chemical and Solar Industry XVIII,* edited by M. Tangstad, H. Rong, A. Valderhaug, B. Andresen, H. Dalaker, and I. G. Page. Kristiansand, Norway, September 7–10. https://doi.org/10.55669/oa900828

Corrosion of Superalloys typically used as reactor material for the reaction between Si, $SiCl_4$ and H_2.

J.O. Hoel[1], **M.O. Victorin**[1], **A. Crawford**[2] **and H.M. Rong**[1]
[1]Elkem Silicon Products, Norway, jan-otto.hoel@elkem.com
[2]Alan Crawford Consulting LLC, USA

Keywords: Silicon, Hydrochlorination, Reactor, Corrosion, Alloy, Silicide

Abstract – Superalloys, like for instance Incoloy®800H (UNS N08810), are the preferred construction material in hydrochlorination reactors due to their excellent thermal and chemical stability. These alloys typically contain a high amount of nickel and chromium.
Some of the alloy components will react with the silicon compounds in the hydrochlorination process (for instance $HSiCl_3$) to form silicides on the reactor wall. The silicides will easily oxidize if oxygen and water gets into the reactor, for instance during maintenance or turnaround of the reactor. Some of the oxygen will remain on the reactor wall after restart, and give a permanent reduction in the $HSiCl_3$ selectivity. Silicide formation, and subsequent loss when the reactor is opened for planned and unplanned maintenance, is the main source of internal surface corrosion that ultimately determines the operational life of the very expensive reactor vessel.
The formation of silicide on the superalloy reactor wall is demonstrated with small scale reactors followed by characterization with scanning electron microscope.

1. INTRODUCTION

Elkem is a producer of metallurgical silicon for several applications. To understand and optimize the performance of our silicon, we often develop laboratory test equipment to simulate the performance in the customer processes. Back in 2004 we started to evaluate the performance of silicon in the reaction between silicon, silicon tetrachloride (STC), and hydrogen for the production of trichlorosilane (TCS). See equation 1. This process is often called the HC process, but is also referred to as the hydrogenation process or the dirty recycle process.

$$Si\ (s) + 3SiCl_4\ (g) + 2H_2\ (g) \leftrightarrow 4HSiCl_3\ (g) \qquad (1)$$

Trichlorosilane is the precursor for production of semiconductor and photovoltaic grade of silicon. The advantage with the HC process is that all STC produced in the chemical vapor decomposition step (CVD) can be recycled back to TCS. It is also common to return the HCl produced in the CVD process to the HC process and in more recent years to also use anhydrous HCl as the source of makeup chlorine for the plant instead of purchased STC. None of the original HC industrialization by Union Carbide, including extensive corrosion studies, considered co-feed of any amount of anhydrous HCl – only the system Si, H_2 and STC. The TCS selectivity in the HC process is typically about 25 mole % and therefore the STC must be passed about 4 times though the HC process to be completely consumed. In practical terms, unreacted STC will be recovered from the product gas, mixed with STC from the CVD process and returned (with or without HCl) to the HC process.

This work is licensed under the Creative Commons Attribution 4.0 International License. To view a copy of this license, visit https://creativecommons.org/licenses/by/4.0/

The HC process is typically operated at a pressure of 10 – 35 bars and a temperature of 500 – 600°C. Due to the high temperature combined with excess hydrogen and chloride chemistry, all known industrial HC reactor vessels, including internals and interconnecting piping are fabricated from Alloy 800H (Universal numbering system, UNS, N08810) or special modified Alloy 800H (also N08810) chemistry, also branded as Incoloy® 800H. The main composition of the Alloy 800H material is 30-35% Ni, 19-23% Cr and remaining Fe. The composition of minor elements Al, C and Ti differentiate Alloy 800H from Alloy 800 (N08800) and Alloy 800HT (N08811). Some industrial HC reactors are reported to be fabricated from Alloy 800HT (N08811), HR-120 (N08120) and 347 Stainless (S34700). However this is not confirmed.

One of the earliest HC fluidized bed reactor (FBR) vessel disclosures was by Union Carbide (Union Carbide 1979) of "Incoloy 800". There was not a definitive disclosure of the specific alloy but numerous personal communications through the years indicates the only Incoloy alloy considered and used by Union Carbide was Incoloy® 800H (N08810). As part of the continuing Union Carbide project, Mui and Seyferth (Mui and Seyferth, 1981), discussed specifically Incoloy 800H (N08810) as a preferred material of construction. This is further confirmed in an extended work by Mui (Mui, 1983), where more materials are studied and compared. A former custom industrial equipment fabricator located in the Netherlands, Verolme Special Equipment B.V. (ceased commercial operations in the early 2020's) (Verolme 2011) specified the use of modified Alloy 800H (still N08810) with tighter limits for minor impurities Al, C and Ti along with a special grain size.

The main purpose of building the laboratory test equipment was to study the effect of the silicon quality. Since the Incoloy material was known to be used in industrial reactors, we assumed that the best choice of reactor material would be Incoloy® 800HT (N08811) super alloy. At the time Elkem decided to build the HC lab (2004), more specific information about industrial HC reactor materials of construction was not commonly known. The differences between Alloy 800H (material used in known industrial reactors) and Alloy 800HT should not alter in any way the lab results. Experiments in small laboratory reactors are known to have more interaction with the reactor wall material than an industrial reactor due to the larger reactor wall surface to silicon weight ratio.

Surprisingly, we observed that the performance in the laboratory reactor was heavily influenced by the reactor material and the condition of the reactor wall. In this paper we will discuss the result of more than 20 years of struggle by running the laboratory reactor in Incoloy® 800HT and perhaps the companies running the HC process industrial scale could learn something from our experience.

2. RESULTS AND DISCUSSION

2.1 Reactor design

The main purpose of the apparatus is to measure the production of trichlorosilane (TCS). This is expressed as the so-called "TCS selectivity", which is the molar concentration of TCS in the product gas, excluding hydrogen. Other gas product species, as dichlorosilane, disilanes (Si-Si) and other high boilers (Si-O-Si) are also measured.

The reactant gasses are fed into the bottom of the reactor to react with the fluidized silicon powder. The product gasses and unreacted reactant gasses leave the reactor at the top and are

led through a filter system to a sampling system, to be quantitatively analysed by a gas chromatograph (GC). An automated needle valve downstream of the sampling system controls the pressure in the reactor system. As the silicon in the reactor is consumed, more silicon is automatically added to the reactor from the top to maintain a constant amount of 10g in the reactor. See figure 1 for more details.

All parameters and actions are fully automated, so the reactor can run without any need for attention between normal working hours. Normal runs last over 2-3 days, consuming 3-6 reactor volumes of silicon. Consuming one reactor volume means that 10g of silicon has been consumed and replaced by the addition system.

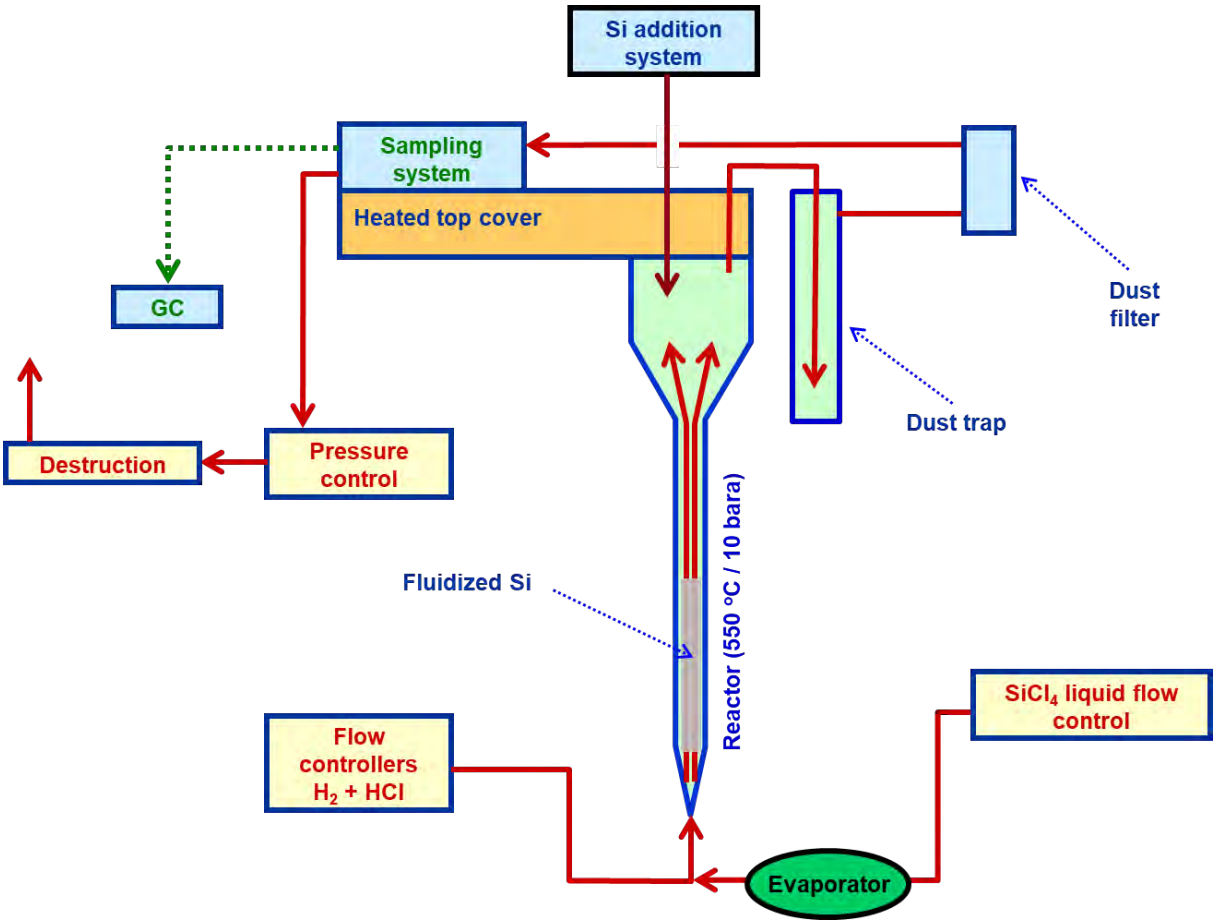

Figure 1: Flow scheme of the apparatus. Liquid silicon tetrachloride (STC) is evaporated and mixed with hydrogen and HCl gas before entering the reactor from the bottom. The silicon powder is fluidized by the upward flow of reactant gasses and product gasses. Overblown Si fines are removed from the product gas by a dust trap and a filter before the product gas enters the sampling system. The sampling system takes out a small volume of the product stream each 16-17 minutes, and send it to a gas chromatograph (GC) for quantitative analysis. The pressure in the reactor system is controlled by an automated needle valve downstream of the sampling system. Silicon powder is added to the reactor from the top to maintain 10 g of silicon in the reactor as silicon is consumed by the reaction.

2.2 Reactor performance deteriorating over time

To check the condition and reproducibility of the reactor, we make standard runs quite frequently. In a standard run, a specific standard Si material is tested with specific standard experimental conditions. These runs should all give equal results over time. However, we observed that the measured TCS selectivities of the standard runs started to become lower. An unfortunate consequence of this is that we cannot compare results between experiments spread over a longer period.

After a lot of investigation, we found that the reactor itself was the cause of the lower TCS selectivity. The selectivity went back up to a normal level after replacing it with a new reactor. See figure 2. All experiments were run with the same silicon sample and the same experimental conditions. The green runs were done when reactor A still was OK. The red runs were done in the same reactor after suspecting issues with the reproducibility. The blue runs were done in reactor B. This reactor was also one that had failed earlier, but it was re-machined internally to get fresh surfaces. As seen, the selectivity went almost up to the original selectivity, and with a good reproducibility

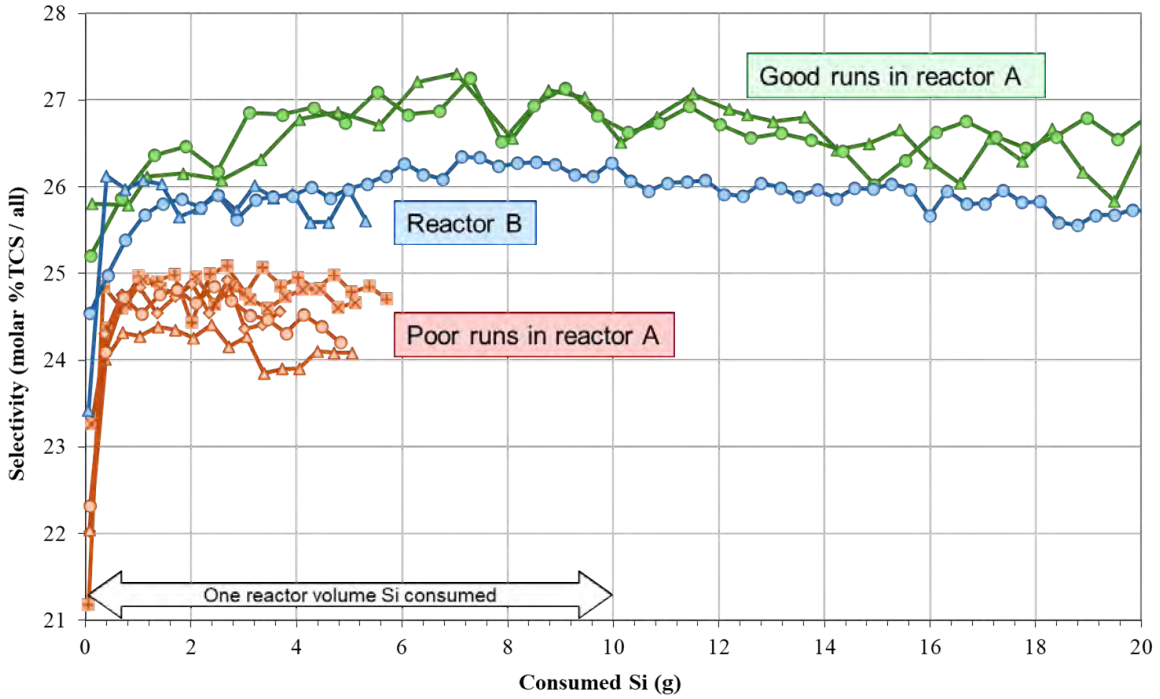

Figure 2: Comparison of TCS selectivities in different reactors and states of the reactors. The x-axis shows the progress as consumed silicon. The y-axis shows the TCS selectivity as the molar concentration of trichlorosilane (TCS).

2.3 The mechanism of reactor deterioration

Hoel and Rong found that oxygen, that was introduced to the reactor as oxide at the surfaces of newly added silicon particles, was able to migrate to older silicon particles and passivate their already active sites. This will in turn reduce the TCS production rate. However, these sites will eventually be reactivated. Selectivity will then also be given by how fast they can regenerate (Hoel and Rong, 2020).

Then it will be reasonable to suspect that oxides on the reactor walls can be sources for oxygen in the reactor as well. Larry Coleman explained that a silicide layer is formed on the reactor wall during the run. This silicide layer is protecting the reactor wall against further corrosion. However, when the reactor is stopped for maintenance and the reactor wall is exposed to humidity and air, this silicide layer will oxidize, and an oxide layer with a thickness of appx. 250 micron will peel off the inner reactor wall (Coleman, 2026). This is in good agreement with the conclusions of Mui and Seyferth (Mui and Seyferth, 1981) and an extended work by Mui (Mui, 1983). Based on that, we propose the following mechanism:

1. <u>During run (hot and with very limited access to oxygen):</u> Gas species with Si, e.g. TCS, will react with the reactor walls. This will allow Si atoms to migrate into the alloy and create a

silicide layer on the reactor surface. Kraus has studied how different alloy qualities corrodes in the HC process (Kraus 2002).

2. During maintenance (cold and with rich access to oxygen): This silicide layer will react with oxygen, creating a flaky layer of silicide oxides that peels of the surface. However, some oxygen will still remain on the inner reactor wall.
3. During next run: The silicide oxide layer will be a source for oxygen to passivate active sites, thus reducing the TCS selectivity. Industrial runs often last for a year. The remaining oxygen on the inner reactor wall will then have time to be consumed, and a protective layer of silicide will reappear on the remaining reactor alloy. This will make the reactor regaining its TCS selectivity. There are, however, not enough time for that in a typical lab run that last only a few days, so the TCS selectivity will not be regained.
4. Further runs and maintenances: In an industrial reactor, the silicide layer created in the previous run will peel off as oxide during each maintenance, and the wall will thus be thinner for each run. In a lab reactor, the silicide oxide layer will grow deeper and contain more oxygen. The TCS selectivity will be permanently reduced.

This mechanism is illustrated in fig 3.

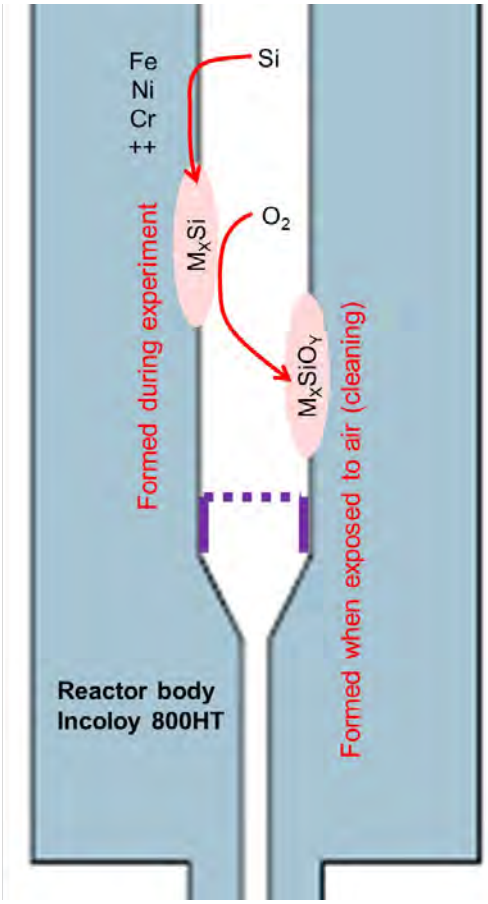

Figure 3: The assumed mechanism for creation of oxides. The left side shows the creation of silicides during experiments, while the right side shows creation of oxides during maintenance between the experiments.

2.4 Examination of the bad reactor

Reactor A was split along its vertical axis, to study the inner walls. One of those parts was cut into pieces small enough to fit into a scanning electron microscope (SEM) chamber. Se figure 4.

The SEM investigation revealed that there were mainly two types of surfaces, see overview in figure 5:

- Flaky material: See figure 6. The flakes contained significant amounts of Fe, Cr, Ni, Si and O. This surface has taken up high amounts of silicon and is partly oxidized.
- Material not covered by flakes: See figure 7. This area has probably been covered by flakes that eventually fell off. This material contained significant amounts of Fe, Cr, Ni and O, but much smaller amounts of Si. The different areas show different states of oxidation. The site "Spectrum 99" shows a surface with no oxidation yet. However, Si has started to infiltrate this site. At the other sites, oxidation has started. Those are probably future flakes.

Figure 8 shows a cross section cut of the inner reactor wall. Si is present not only in the grain boundaries, but also in the bulk reactor material. This shows that Si atoms migrate into the alloy, creating silicides with the metals in the alloy. We also can see that Si, O, and Cl has penetrated the reactor through channels or cracks.
This indicates that the flakes are a result of oxidation, and that the silicide oxidizes easier than the original alloy.

Figure 4: The pieces of the reactor that was examined by SEM. Pieces from left to right is from top to bottom

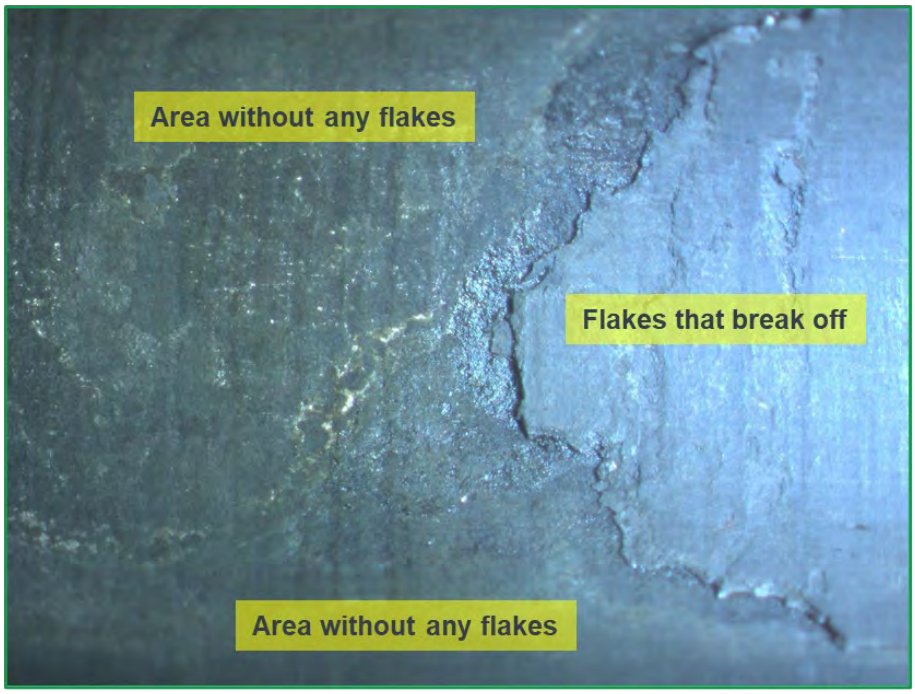

Figure 5: Light microscope picture of the inner reactor surface. Illumination is from the right. On the right side, there is a flake still attached to the reactor inner surface. The shadow line shows the left facing edge of the flake

To check the proposed mechanism for reactor deterioration further, an old reactor was washed thoroughly and then bored with the same diameter as the original bore (10mm) to remove deposits that could not be washed away with a brush. Surprisingly, a lot of torque was needed to re-bore through the reactor that was supposed to have an inner diameter equal to the bore used.

The drilling chips were examined by SEM and found to contain significant amounts of Fe, Cr, Ni, Si and O. An oxide layer should be easy to bore away, but a silicide layer probably not. As silicon atoms migrate into the alloy, they will occupy space, and the volume of the alloy will increase. This will in turn reduce the inner diameter of the reactor alloy, explaining the need for a high torque.

Figures 9 and 10 show SEM pictures of large pieces of the drilling chips, which are assumed to be pieces of the expanded reactor alloy that were cut off during the drilling. They have large amounts of Si in addition to the alloy components. The composition is quite inhomogeneous. Only one of the spectra detects oxygen. This spectrum is close to the surface of the drilling chip. This confirms that silicon species have reacted with the reactor walls to create a layer of silicides, which in turn has reacted with oxygen to create oxides at the reactor walls.

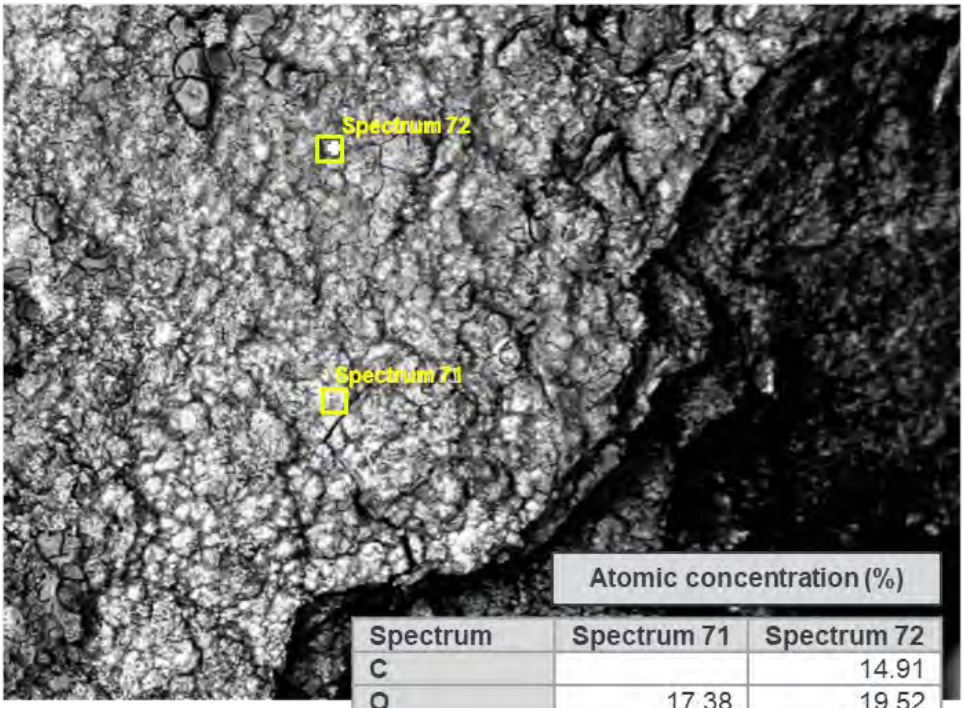

Atomic concentration (%)		
Spectrum	Spectrum 71	Spectrum 72
C		14.91
O	17.38	19.52
Si	24.19	18.76
Cl	2.77	6.26
Ti		3.61
V	0.41	
Cr	10.27	10.38
Mn		0.89
Fe	41.17	14.77
Ni	3.82	10.03
Mo		0.87

Figure 6: Flaky surface with high contents of Si and O in addition to the original reactor material

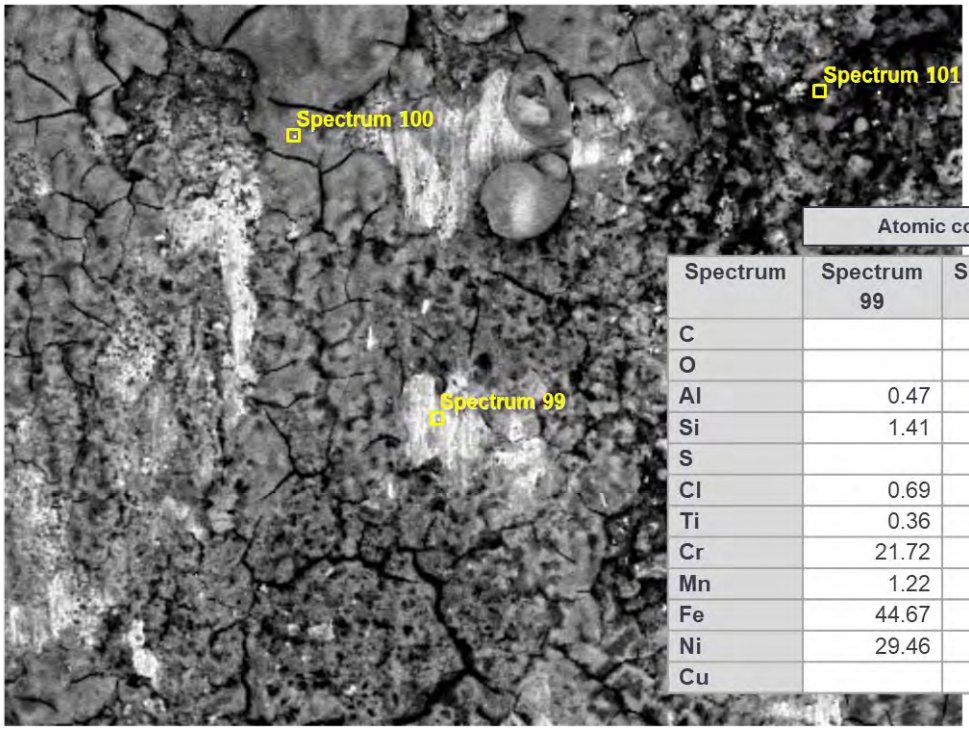

Atomic concentration (%)			
Spectrum	Spectrum 99	Spectrum 100	Spectrum 101
C			52.56
O		49.48	21.78
Al	0.47	0.07	0.18
Si	1.41	0.31	3.04
S			0.39
Cl	0.69	25.50	6.57
Ti	0.36		
Cr	21.72	2.11	6.06
Mn	1.22	0.27	0.20
Fe	44.67	6.35	4.57
Ni	29.46	15.91	4.34
Cu			0.32

Figure 7: Area not covered by flakes. The white areas are uncovered reactor alloy. In the point "Spectrum 99" very little corrosion has occurred yet. The dark areas are thin layers of oxidized reactor material with multiple cracks. In the points 100 and 101, the corrosion has started. Those sites are probably future flakes.

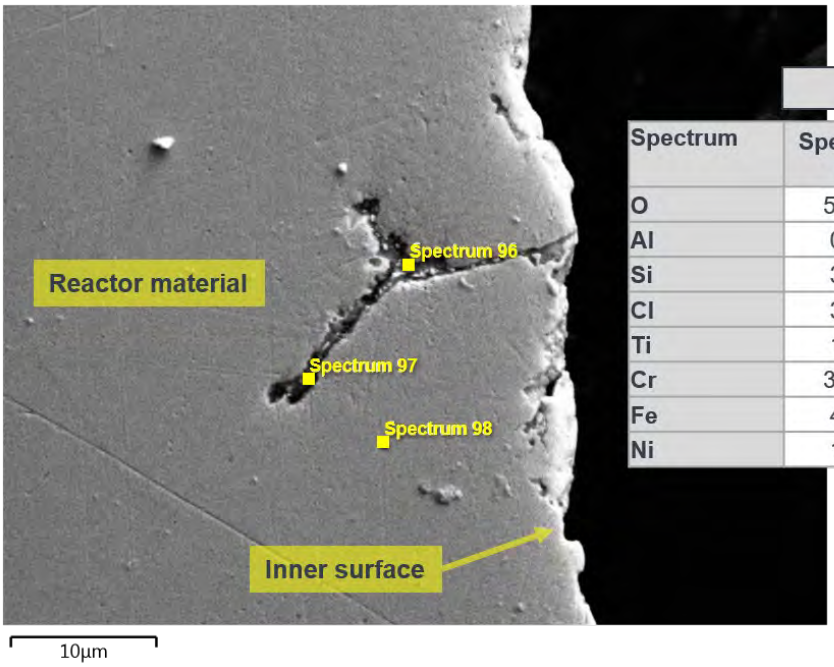

Atomic concentration (%)			
Spectrum	Spectrum 96	Spectrum 97	Spectrum 98
O	55,22	31,47	
Al	0,45		0,83
Si	3,06	2,64	2,43
Cl	3,54	1,69	
Ti	1,11	0,85	
Cr	31,20	27,12	26,19
Fe	4,28	25,10	45,51
Ni	1,15	11,13	25,03

Figure 8: Cross section of the inner reactor surface. Spectrum 98 shows that Si has migrated more than 10 microns into the reactor bulk material. The two other spectra shows that Si, O, and Cl has penetrated the reactor through channels or cracks.

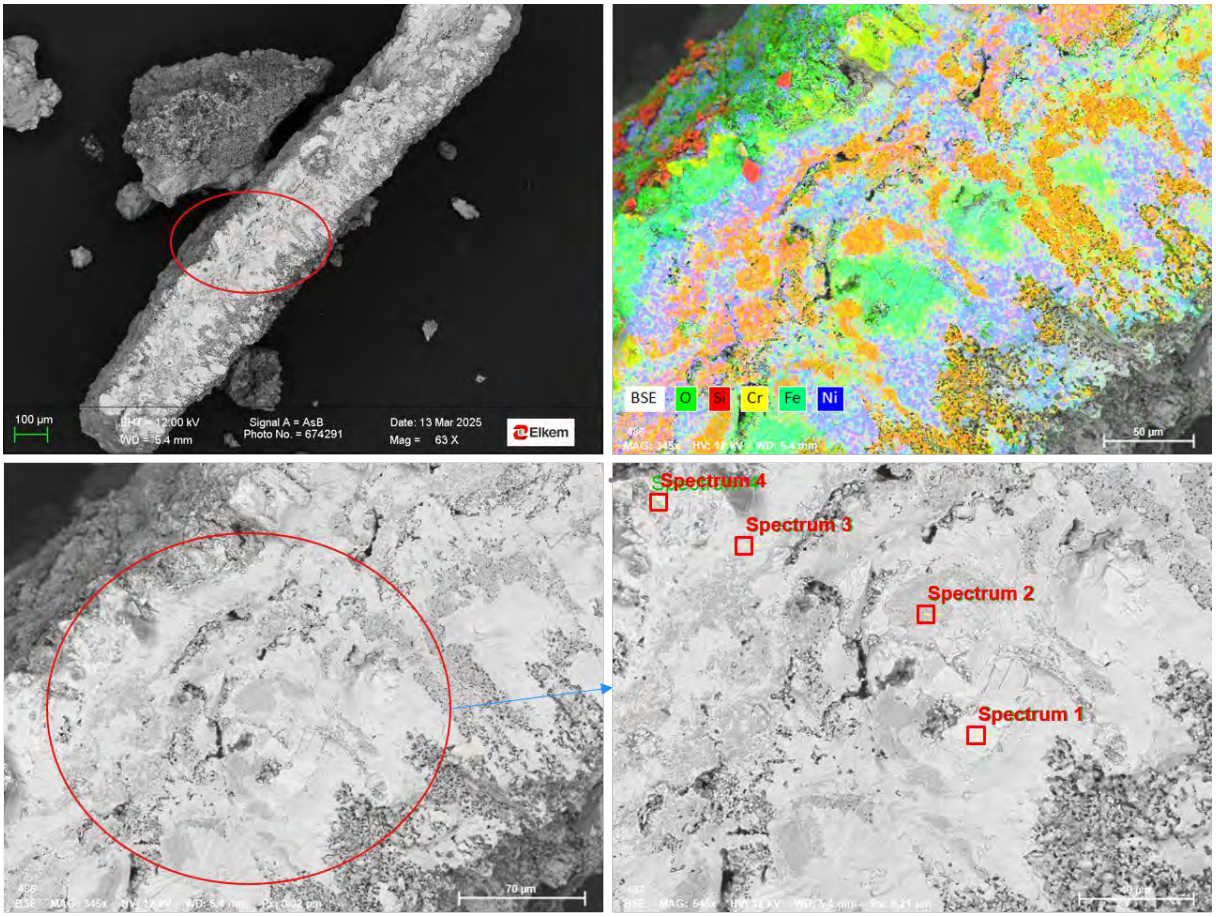

Atomic concentration /%

Spectrum	Si	Cl	Cr	Fe	Ni
Spectrum 1	26.3		2.3	70.0	1.3
Spectrum 2	57.3		27.2	9.2	6.4
Spectrum 3	52.6		2.6	18.7	26.1
Spectrum 4	25.3	0.5	7.2	62.0	5.0

Figure 9: SEM picture of one of the large drilling chip pieces from boring through the reactor. This piece is a mix of silicides with Fe, Ni and Cr. There is no oxygen. This indicates that this is a part of the alloy itself, that expanded due to the infiltration of Si atoms. This corresponds with the high torque needed to bore it out

Figure 11 shows SEM pictures of the smaller drilling chips. These particles contain significant amounts of oxygen as well as Fe, Ni, Cr and Si. This indicates that these are silicide oxides that were easy to crush and machine away from the reactor wall. These small pieces are probably remainders of flakes that still were too rigid to wash away with a brush.

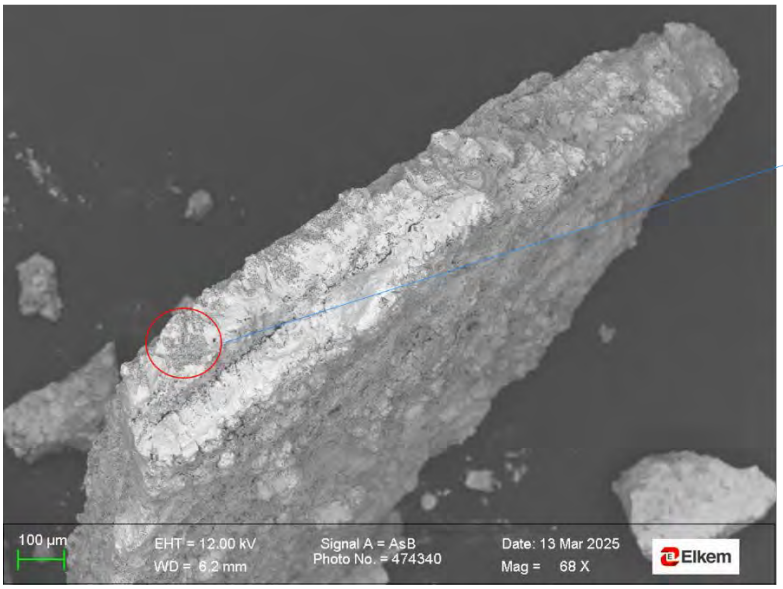

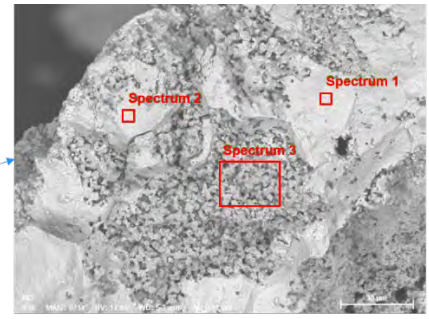

Atomic concentration /%

Spectrum	O	Si	Cl	Cr	Fe	Ni
Spectrum 1		48.2		1.2	24.3	26.3
Spectrum 2		48.3		2.0	39.7	10.0
Spectrum 3	5.6	60.1	0.8	28.3	2.6	2.5

Figure 10: SEM picture of another large drilling chip piece from boring through the reactor. This piece is also a mix of silicides with Fe, Ni and Cr. There is some oxygen on the area spectrum that is close to the surface.

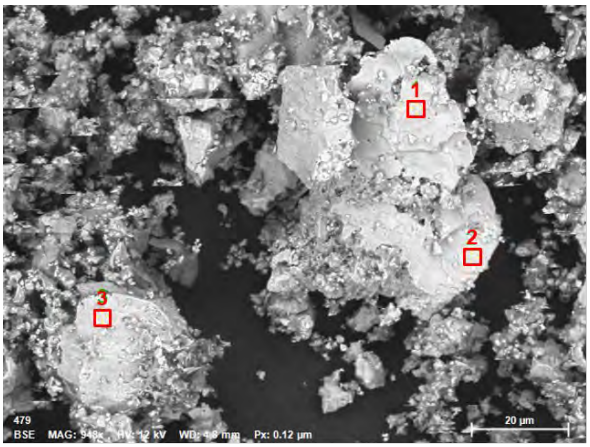

Atomic concentration /%

Spectrum	O	Si	Cr	Fe	Ni
1	6.3	50.8	1.7	18.6	22.5
2		49.2	2.3	25.4	23.0
3	5.9	47.1	1.1	40.4	5.5

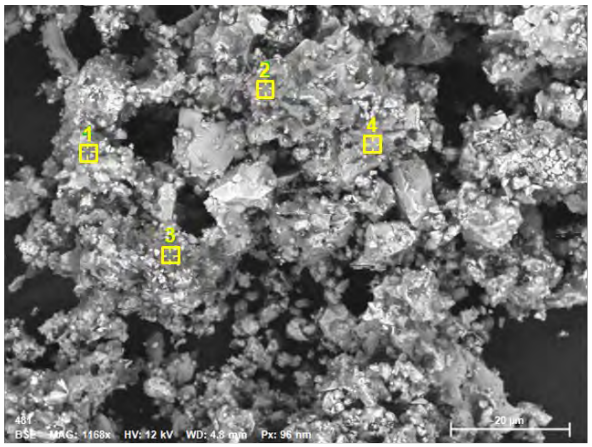

Atomic concentration /%

Spectrum	O	Al	Si	Cl	Ca	Cr	Mn	Fe	Ni
1	4.1		42.8	1.7		8.9		24.8	17.6
2	37.4		38.6	1.8		3.4	0.6	11.0	7.2
3	30.7	3.9	54.6	2.1	2.0	0.8	0.5	4.5	0.9
4	36.3		28.7	7.1		8.5		11.6	7.8

Figure 11: SEM pictures of the smaller particles in the drilling chips from boring through the reactor. These particles contain significant amounts of oxygen as well as Fe, Ni, Cr and Si. This indicates that these are silicide oxides

2.5 Differences between laboratory and industrial operation of the HC process

The industrial HC process is a continuous process where the process can be operated about one year before the reactor system is stopped for maintenance. Contrary to this, a lab scale reactor normally is operated for only a few days between each maintenance. The main reason for this, is to make a full reset of the system between each experiment. This ensures that an experiment is not influenced by the previous experiment.

One consequence of the frequent maintenances is that the inner reactor walls will be exposed to air much more frequently than in an industrial reactor, making this oxidation issue much greater in a lab than at an industrial plant.

2.6 Addressing the laboratory reactor issues

To reduce the oxidation to a minimum, the reactor is immediately connected to an argon supply after emptying it, and flushed continuously while the other parts of the reactor are prepared for the next run. When all these other parts are readied and mounted, the reactor is washed quickly as possible with isopropanol, mounted, evacuated and put on argon flush. In addition, the apparatus is always on continuous Ar flush when "not in duty". We observed a positive effect of minimizing exposure to oxygen during maintenance. However, we cannot do the cleaning without any exposure to air.

Therefore, we have to live with the fact that reactors will deteriorate, also in the future. To reduce the practical and economic consequences of this, a new reactor design with replaceable inner reactor liner has been developed. This makes it easier and cheaper to replace the inner walls of the reactor when needed. This replacement will probably follow "hard time" maintenance principles, by being replaced after a specific number of runs regardless of condition. This will ensure a stable performance of the reactor. We have not concluded yet how many runs each reactor liner can be used before replacement.

This new design also allows easy and cheap changes of reactor material, if desired for the sake of research.

3. CONCLUSIONS

It has been found that the performance of the hydrochlorination process (HC) deteriorates over time, due to corrosions of the reactor inner walls. This has been studied in an Incoloy® 800HT (N08811) reactor at a reactor temperature of 550 ^{o}C and an absolute pressure of 10 bar. We believe that our conclusions also apply to a reactor constructed of Incoloy® 800H (Alloy 800H; N08810), which matches the known material used in many industrial reactors.

Under these conditions, silicon containing gas species will react with the reactor wall, to create silicides of Fe, Ni and Cr. The Si atoms migrate several micrometres into the reactor bulk material.

The formation of silicides on the reactor internal wall destroys the protective properties against corrosion, even of super alloys like Alloy 800HT (N08811). The outer layer of silicides at the reactor walls oxidizes when in contact with air, and will eventually flake off as silicide oxides. This process will continue at the new surfaces behind the flaking.

The peeling of the silicide layer (250 micron thickness) will make the reactor wall thinner after each run. Therefore, an industrial reactor can be exposed to air only a limited number of times before it must be replaced as the design corrosion allowance will have been exceeded. In addition, we observe channels of silicides and chlorides. They can go further into the reactor wall, increasing the potential risk for more dangerous, and difficult to predict, leakages.

Oxygen from the oxidized silicides will in turn contribute to passivate active sites at the silicon powder surfaces in the reactor. The HC process is a reaction from STC to an equilibrium mixture of STC and TCS, see equation 1. The over-all reaction rate in the reactor will become

lower when the surface area of active sites is reduced. This will in turn reduce the amount of TCS produced during the available residence time in the reactor.

Finally, we should note that this work is limited to the HC process chemistry that does not include any external co-feed of anhydrous HCl; only the "classic" HC system of Si, H_2 and STC has been investigated. However, we have recently implemented the option to feed anhydrous HCl into the reactor.

4. ACKNOWLEDGEMENTS

This paper is published by permission of Elkem.

5. REFERENCES

Coleman L, Consultant by demand, 2026. Oral discussions and email correspondences

Hoel J.O. and Rong H.R. 2020. *Activation of silicon in the hydrochlorination process*. Silicon for the Chemical and Solar Industry XV, Trondheim, Norway, June 15 – 18, 2020

Kraus C. 2002. *Korrosionsverhalten metallischer und keramischer Werkstoffe in Prozeßgasen zur Herstellung von Solarsilizium*. PhD. Thesis, Fakultät für Maschinenwesen der Rheinisch-Westfälischen Technischen Hochschule Aachen

Mui, J.Y.P., Seyferth, D.,1981, *Final Report: Investigation of the Hydrochlorination of STC*, see pages 43-51, JPL Contract 955382, http://ntrs.nasa.gov/archive/nasa/casi.ntrs.nasa.gov/19810019076.pdf

Mui, J.Y.P, 1983, *Final Report: Investigation of the Hydrochlorination of STC*, see pages 33-44, JPL Contract 956061

Union Carbide Corporation, 1979, *Final Report Low Cost Solar Array Project Feasibility of the Silane Process for Producing Semiconductor grade Polysilicon,* see Page 45, JPL Contract 954334-10, https://digital.library.unt.edu/ark:/67531/metadc1088825/m2/1/high_res_d/5535914.pdf

Verolme Special Equipment B.V., 2011, web site information accessed 11-October-2011

Jan-Otto Smith-Meyer Hoel

Senior research scientist, Elkem

Jan-Otto Hoel holds a Master's degree in chemistry from NTH (now NTNU) and has worked within the silicon field since 1996, joining Elkem in 2003. His work has largely focused on customer processes within the polysilicon and silicones segments, using lab-scale studies to build understanding and support product development. He is also responsible for the development, construction, and maintenance of laboratory equipment and specialized test setups.

Jacob, L., and M. Tangstad. 2026. Temperature dependence of SiO formation in hydrogen atmosphere. In *Silicon for the Chemical and Solar Industry XVIII,* edited by M. Tangstad, H. Rong, A. Valderhaug, B. Andresen, H. Dalaker, and I. G. Page. Kristiansand, Norway, September 7–10. https://doi.org/10.55669/oa900829

Temperature dependence of SiO formation in hydrogen atmosphere

Liya Jacob[1*] and Merete Tangstad[1]

[1*] Department of Materials Science and Engineering, Norwegian University of Science and Technology, 7491, Trondheim, Norway

*Corresponding author: Liya Jacob, Email: liyamol.jacob@ntnu.no

Keywords: SiO formation, SiO reduction, Hydrogen based reduction, Kinetics

Abstract – The $Si + SiO_2 \rightarrow 2SiO$ reaction was investigated under carbon free conditions in hydrogen and argon atmospheres at 1600–1700 °C to quantify the activation energy and understand how gas environment influences SiO formation. Isothermal mass loss data were evaluated using a diffusion model, which showed linearity across all temperatures (R^2 = 0.92–0.99), suggesting diffusion through a growing SiO_x interfacial layer as the rate controlling step. Arrhenius analysis yielded activation energies (Ea) of 740 kJ·mol^{-1} in Ar and 582 kJ·mol^{-1} in H_2, and the values are consistent with transport limited Si–SiO_2 systems. The high Ea for both argon and hydrogen system also reveals that the reaction on the reactant surface also play an important role in the kinetics along with diffusion. The higher Ea in argon arises from the strongly suppressed SiO formation at 1600 °C, which steepens the temperature dependency. EPMA revealed coarse, sparse Si precipitates in Ar at 1600 °C, whereas hydrogen produced fine, uniformly dispersed Si domains, indicating earlier onset of defect formation and SiO transport. Condensation behaviour followed the amount of SiO formed.

1. INTRODUCTION

Hydrogen is increasingly viewed as a key enabler for carbon-neutral metallurgy because it can replace carbon-based reductants and support process routes that avoid fossil CO_2 emissions. The SiH2 (Ringdalen et al., 2024) concept highlights that future silicon production may rely on hydrogen-based routes. Realizing such a process requires conditions where SiO gas is generated, transported and reduced without rapid back-reaction to Si and SiO_2. The SiH2 investigations show that SiO behaviour is governed by slow and temperature-dependent kinetics, and that suppression of SiO condensation is a central challenge. These findings create a need for fundamental kinetic data for the $Si + SiO_2 \rightarrow 2SiO$ reaction in carbon-free atmospheres, including how hydrogen and argon influence defect formation, interfacial transport and SiO stability.

Although $Si + SiO_2 \rightarrow 2SiO$ reaction has been widely examined in carbon-containing systems, where SiO subsequently reacts with carbonaceous species, its intrinsic kinetics under carbon-free conditions remain poorly understood(Bao et al., 2013). Reported activation energies for SiO-forming reactions span a broad range—from ~380 kJ·mol^{-1} in thin-film geometries to 438–528 kJ mol^{-1} in powders and briquettes, and up to ~557 kJ·mol^{-1} in compacted beds(Sindland and Tangstad, 2021, Andersen, 2010, Leroy et al., 2020). The rate is dependent on microstructure, porosity, and mass-transport. These variations underscore that the apparent activation energy (Ea) is shaped not only by the chemical step but also by diffusion through the evolving SiO_x ($1<x<2$) interfacial layer and by gas-phase transport of SiO away from the reaction front (Li et al., 2016).

This work is licensed under the Creative Commons Attribution 4.0 International License. To view a copy of this license, visit https://creativecommons.org/licenses/by/4.0/

Recent studies have shown that hydrogen further modifies these processes by enhancing oxygen-vacancy formation, increasing defect mobility in SiO_2, and accelerating gas-phase transport (Cartier et al., 1993). Hydrogen has been observed to increase the rate of SiO formation, alter the morphology of condensed Si/SiO_2 products, and thin the gas-boundary layer relative to inert atmospheres. However, despite these mechanistic insights, no systematic determination of the activation energy of the $Si + SiO_2 \rightarrow 2SiO$ reaction has been performed under hydrogen and argon in a carbon-free environment.

In this work, we quantify the activation energy of the $Si + SiO_2 \rightarrow 2SiO$ reaction in hydrogen and argon atmospheres using isothermal kinetic data collected between 1600 and 1690 °C under carbon-free conditions. This will be done by extracting temperature-dependent rate constants from kinetic formulations and construct Arrhenius relationships for each atmosphere. This study will provide direct comparison of the activation energy in H_2 and Ar for SiO formation, offering new insight into how gas atmosphere and temperature affect Si–O kinetics.

2. MATERIALS AND METHODS

Experiments were carried out in an ENTECH 1800 resistance furnace equipped with tungsten carbide (WC) heating elements and capable of reaching 1700 °C. To ensure a fully carbon-free environment and prevent the thermodynamically favorable reaction between SiO and carbon (Bootsma et al., 1971), the hot zone was constructed entirely from alumina components, alumina tubes and Alsint 99.7 crucibles. Temperature control was achieved using a Eurotherm 2408 regulator connected to a custom LabVIEW interface, which continuously logged wall and crucible temperatures as well as furnace power through a National Instruments thermocouple acquisition system. Temperatures were monitored both at the crucible center and along the inner wall. Representative figure of the furnace is given in Figure 1.

16

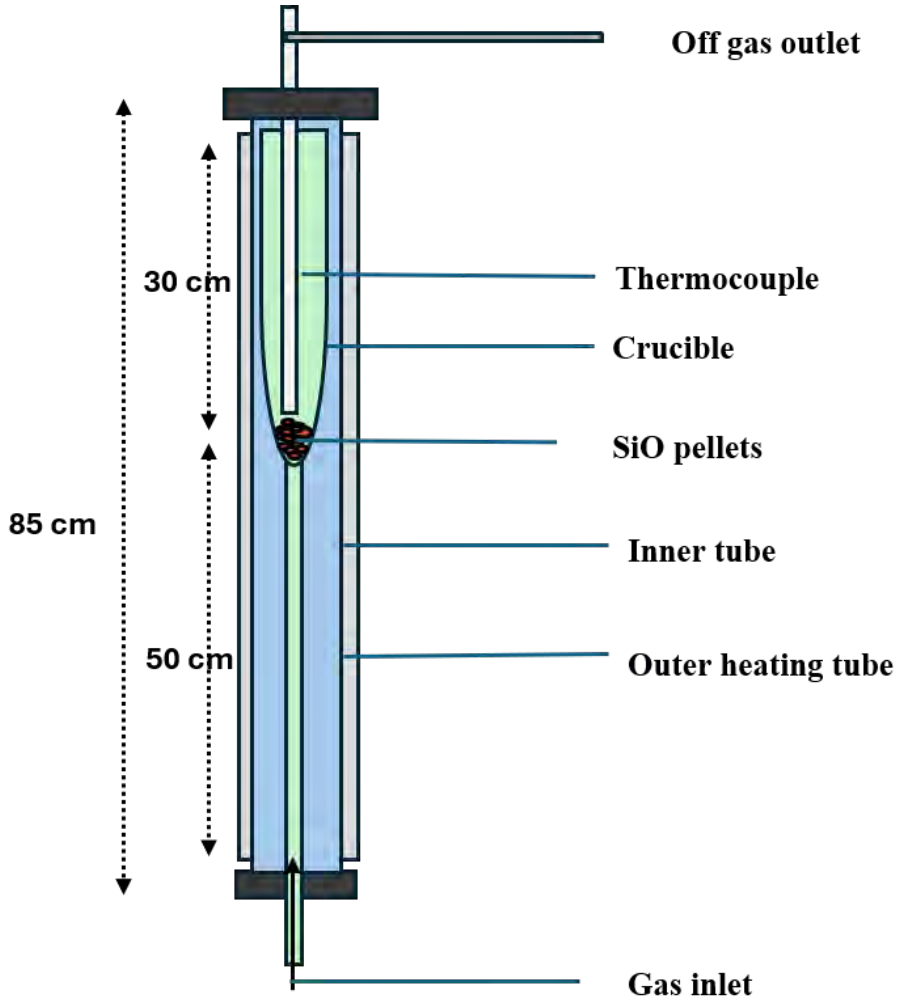

Figure 1. ENTECH 1800 alumina tube furnace used for the SiO formation experiments.

An alumina crucible was positioned at the furnace centre such that its base coincided with the hottest zone. This is where SiO generation takes place. Process gases (Ar or H_2) entered the crucible from below. The crucible remained open to allow off-gas release and to accommodate thermocouple insertion. A small alumina sieve was placed at the bottom of the crucible, and for each experiment, 10 g of SiO granules were distributed in a single layer on the sieve to maintain open gas flow through the bed. The furnace was heated at 10 °C min^{-1} to 1700 ,1650, 1600 °C and held such that the lower crucible region remained at the set temperature for a period of 5, 30, 60 and 90 mins. Argon was supplied at 0.25 L·min^{-1} during heating, while hydrogen was introduced once the temperature reached the set temperature. After cooling down to below 50 °C, the crucible was removed and the products were collected. The crucible was weighed before and after each experiment, and all recovered material, both from the sieve and from the crucible walls, was classified into unreacted pellets and various condensates of different morphologies ("flowers," "plates," and "dust").

Silicon monoxide was supplied as Patinal "SiO" granules (Merck; CAS 10097-28-6) with an Si/O ratio of 1. The granules, 3–5 mm in size (Figure 2), were confirmed by SEM and EPMA to be dense, homogeneous, and free of visible porosity or distinct Si/SiO_2 phase boundaries. High-purity argon (99.9%, Instrument Ar 5) and hydrogen (99.9%, Instrument H_2 4.5) were provided by Linde. The figure of the crucible, and the samples can be seen in our previous publications(Liya Jacob, 2026b, Liya Jacob, 2026a).

2.1. Activation-Energy Determination

The activation energy was obtained from isothermal mass-loss data using a one-dimensional diffusion model D1 (Bieniasz, 2015). Even though, we used a diffusion model, it was the best mechanistic fit rather than a reaction controlled by diffusion alone. Conversion was calculated as,

$$\alpha(t) = \frac{m_0 - m(t)}{m_0},$$

and the rate is given by,

$$\frac{d\alpha}{dt} = \frac{k}{2\alpha}$$

was evaluated for each time point. For each isothermal experiment at 1700, 1650 and 1600 °C, $g(\alpha) = \alpha^2$ was plotted against time and the apparent rate constant $k(T)$ was taken as the slope of a linear least-squares fit to the early-to-mid conversion region, where diffusion control is dominant. The activation energy was found based on the Arrhenius equation:

$$k = k^0 \exp\left(\frac{-E_a}{RT}\right)$$

where k is the experimentally derived rate constant, k^0 is the pre-exponential factor, E_a is the activation energy, R is the gas constant ($R = 8.314\ J \cdot mol^{-1} \cdot K^{-1}$), and T is the absolute temperature in Kelvin. Uncertainty in E_a was estimated from the standard error of the regression slope.

3. RESULTS AND DISCUSSION

The D1 model was chosen because the conversion data showed the typical concave-down behaviour and steady rate decrease. Even though, this method is generally used in diffusion controlled systems, our choice was rather because of good mechanical fit rather than the rate being purely governed by diffusion. When the D1 integral form $g(\alpha) = \alpha^2$ was fitted to the isothermal data, the linear regressions produced R^2 values of 0.92–0.99 both in Ar and H_2 at all three temperatures. Morphological evidence from our earlier publication supports this choice (Liya Jacob, 2026b, Liya Jacob, 2026a). The kinetic profiles at 1700, 1650, and 1600 °C show a consistent enhancement of the $Si + SiO_2 \rightarrow 2SiO$ reaction in hydrogen compared with argon.

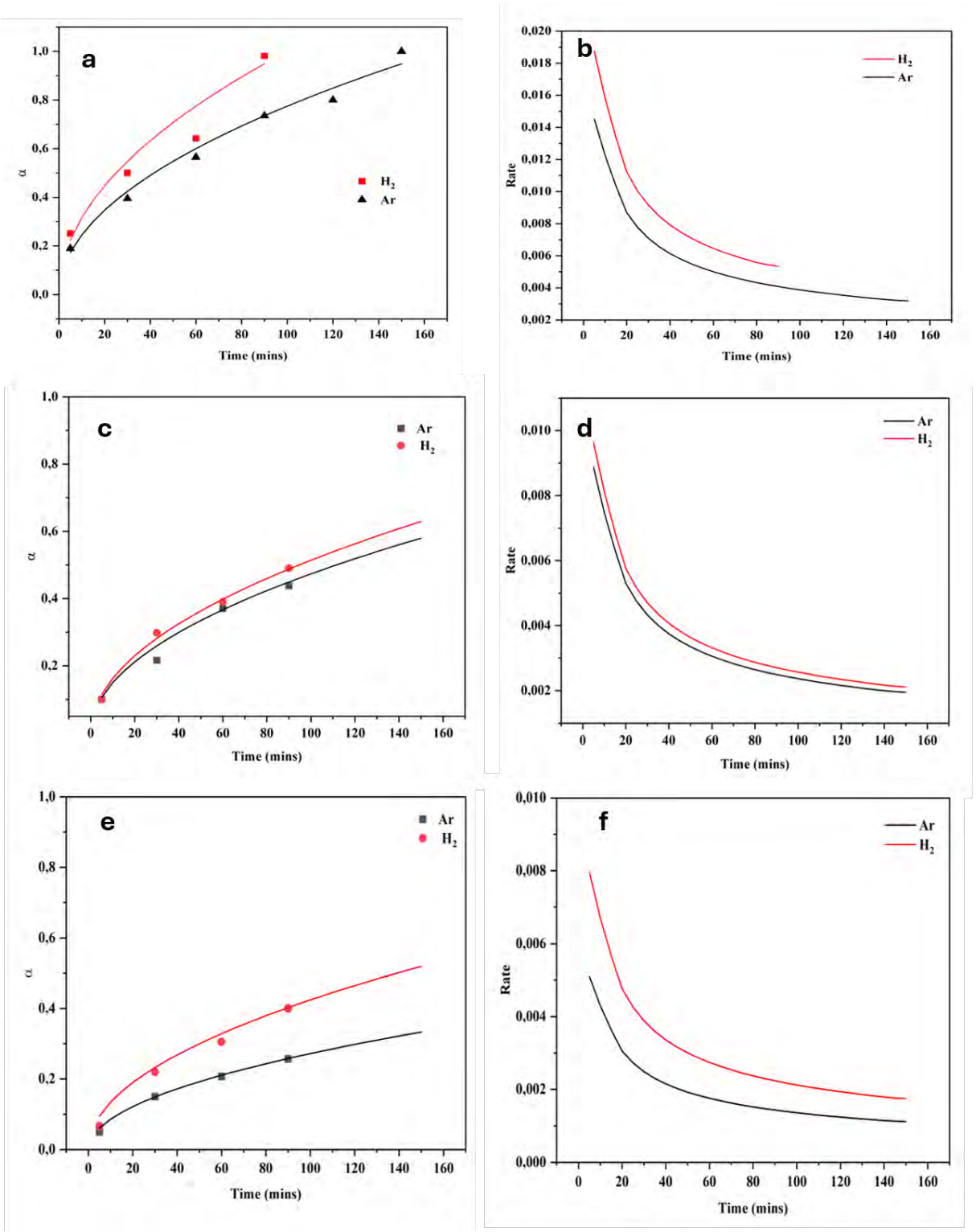

Figure 2. Rate and conversion profile of SiO formation in argon and hydrogen at 1700 °C (a-b), 1650 °C (c-d), 1600 °C (e-f).

In all α–time curves, hydrogen reaches higher conversion at each temperature, and the separation between the two atmospheres becomes more pronounced as temperature decreases. The rate–time plots show the expected decline in reaction rate as the interfacial SiO_x layer thickens, and the rate–α relationships confirm that hydrogen maintains a higher instantaneous rate at equivalent conversion. The Arrhenius analysis yields activation energies 740 kJ·mol^{-1} in Ar and 582 kJ·mol^{-1} in H_2. The Arrhenius fit for hydrogen looks poor because

the three hydrogen rate constants do not fall on a clean straight line, which means the reaction in hydrogen does not follow a single, simple Arrhenius behavior across the temperatures. In hydrogen, the mechanism might change slightly with temperature. Defect formation, surface roughening and SiO transport all increase, so the effective rate constant is influenced by more than just the activation barrier. As a result, the hydrogen points shift up or down relative to the ideal line, giving a weaker linear trend and a lower R^2. Argon behaves more simply and stays closer to a single mechanism, so its points align better.

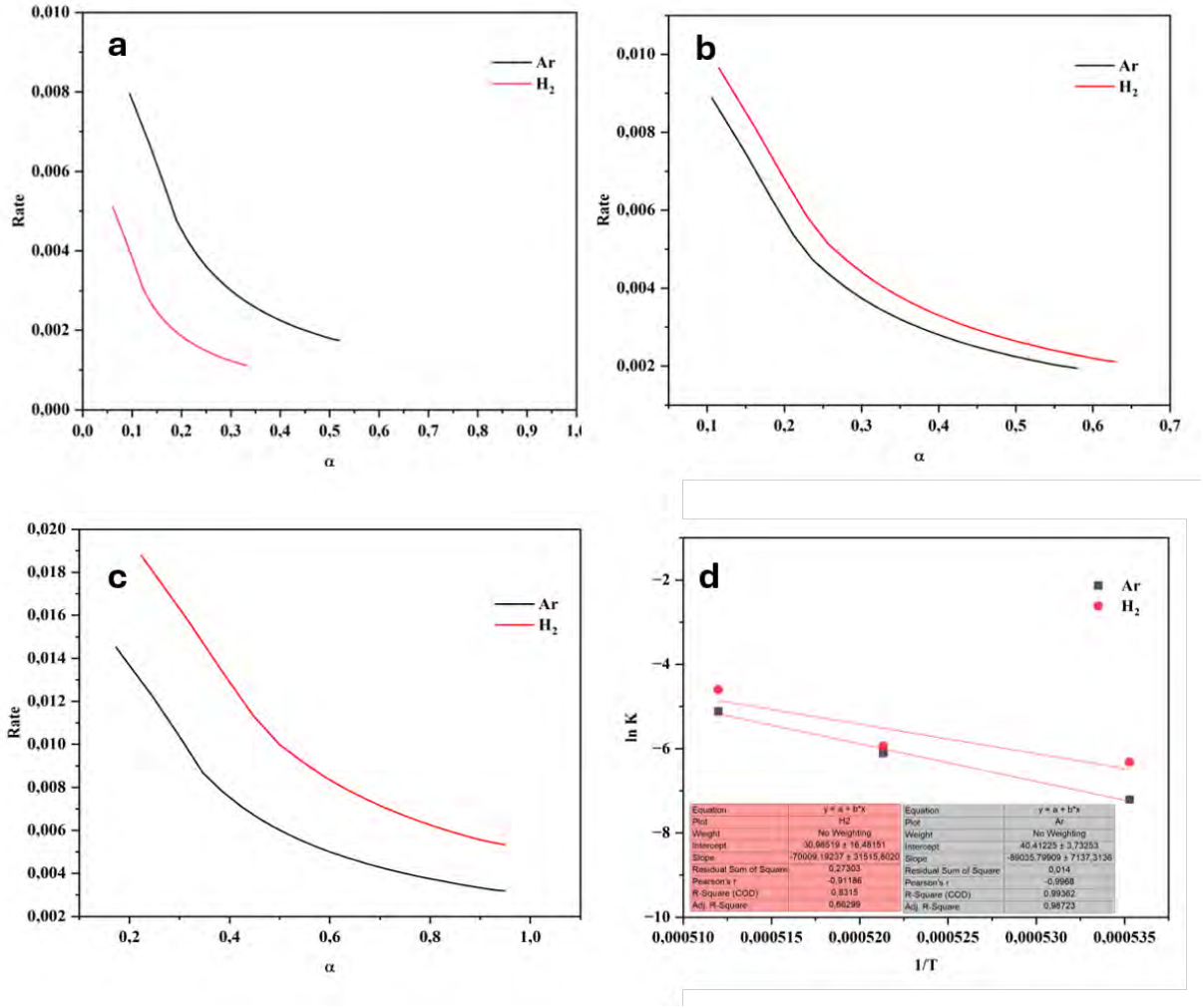

Figure 3. Rate and conversion profiles for a: 1600, b: 1650 and c: 1700 °C. d: Arrehnius plot.

Raider (Raider, 1988) described the formation of sub stoichiometric layers during SiO generation, and Devine et al. (Devine et al., 1996, Devine et al., 1993) demonstrated that oxygen vacancy formation and SiO out diffusion occur readily in SiO_2 at high temperature. Ozturk and Fruehan (Ozturk and Fruehan, 1985) identified gas phase mass transfer as a controlling factor in silica reduction by hydrogen at 1650 °C, and Han and Sohn (Han and Sohn, 2005) reported similar behavior at 1285–1450 °C. The present data follow these trends: at 1700 °C the difference between the two gases is moderate, but at 1650 and 1600 °C hydrogen maintains significantly higher rates and reaches higher conversion within the same reaction time. The overall behavior is consistent with literature showing that apparent activation energies for SiO forming reactions increase with diffusion path length and gas phase resistance (Bongiorno and Pasquarello, 2004, Devine et al., 1996), with powders and briquettes of SiO (Si-SiO_2 interfaces) typically yielding higher values than thin films. The stronger enhancement in hydrogen at

lower temperatures indicates that the effective transport barrier is reduced relative to argon, which agrees with the higher diffusivity and stronger chemical interaction of hydrogen with the SiO_2 network (Watanabe, 2025).

The Arrhenius analysis yields activation energies 740 kJ·mol^{-1} in Ar and 582 kJ·mol^{-1} in H_2, which are high but still consistent with the upper range reported for compact or diffusion limited Si–SiO_2 systems. Powder and briquette studies of Si + SiO_2 → 2SiO typically report apparent activation energies between about 438-528 kJ·mol^{-1} (Andersen, 2010), and ~557 kJ·mol^{-1} (Sindland and Tangstad, 2021) have been obtained for densely packed beds where long solid state and gas phase diffusion paths dominate the overall resistance. In contrast, thin film geometries, where SiO can escape over nanometer scale distances, give significantly lower barriers around 4.0 eV (≈386 kJ·mol^{-1}), and the disproportionation of solid SiO to Si + SiO_2 has been assigned an activation energy of only about 82 kJ·mol^{-1}, reflecting a much shorter transport length and a different rate controlling step (Leroy et al., 2020).

The higher activation energy in Ar compared with H_2 is consistent with the lower gas phase diffusivity of Ar. CO was used as a surrogate for SiO to calculate the diffusivity of H_2 and Ar in SiO, and at 1673 °C, they typically have values of 1.73 × 10^{-3} m^2/s in H_2 and 4.55 × 10^{-4} m^2/s in Ar (Liya Jacob, 2026b). Hydrogen is known to enhance oxygen vacancy formation and defect mobility in SiO_2, to promote Si–H and Si–OH species, and to increase gas phase mass transfer, all of which reduce the effective transport barrier for SiO escape and thus lower the apparent activation energy relative to Ar (Luo et al., 2026, Rashkeev et al., 2001, Bunson et al., 2000, Alkauskas and Pasquarello, 2007). In this context, the value of about 582 kJ·mol^{-1} in H_2 can be viewed as a transport limited activation energy characteristic of a thick, defect rich SiO_x layer under hydrogen.

In addition, as the pellet reacts, its surface becomes rougher, fragmented, and more porous and the pellet becomes smaller. This means the effective reaction area decreases with time**,** so the measured rate constant is not purely intrinsic. It also reflects evolving geometry. In diffusion-controlled systems, the flux of SiO depends on the thickness of the SiO_2 and Si layer, the local porosity and microcracks and the changing surface area**.** When the pellet breaks into smaller pieces or develops pores, or become smaller due to the reaction proceeding, the contact area between Si and SiO_2 increases, which decreases the instantaneous rate even if the intrinsic diffusion coefficient is unchanged. This produces curvature in α–t and rate–t plots and can inflate the apparent activation energy because the Arrhenius fit assumes a constant geometry. Figure 4 shows the proposed mechanism of the reaction. This effect is well-documented in solid–solid reactions where reaction progress changes the interface area, causing deviations from ideal shrinking-core or planar-interface kinetics. Sindland et al. (Sindland and Tangstad, 2021) used the change in contact area for determining the rate of SiO formation.

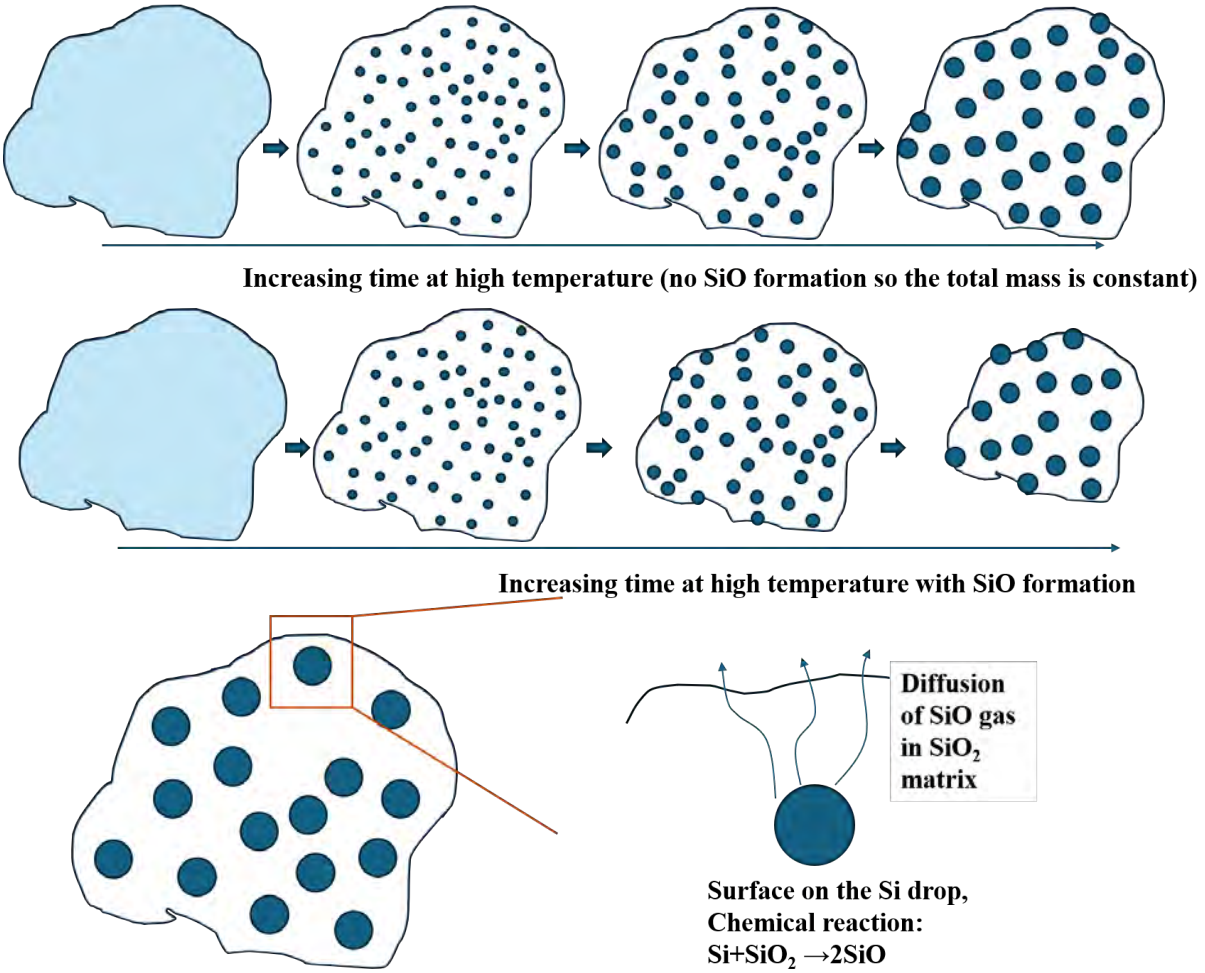

Figure 4. The proposed mechanism of the formation of Si and SiO_2 islands and the diffusion through the interphase.

Bongiorno et al. (Bongiorno and Pasquarello, 2004) studied the transport of O_2 through SiO_2 at Si-SiO_2 interphase using oxidation reactions at different diffusion lengths. They show that the effective diffusion length through a SiO_2 layer is set by the macroscopic diffusivity D of the mobile species and the experimental time scale via the relation $L_D = (4Dt)^{1/2}$. Because D is determined by a broad distribution of local hopping barriers in the disordered oxide, any increase in local barrier heights or reduction in site connectivity produces a strong reduction in D and therefore a rapid shortening of L_D. A thin, higher-density interfacial oxide adjacent to Si acts as a low-permeability layer. It reduces the number of percolating low-energy pathways, lowers the effective D relative to bulk SiO_2 and confines transport when the oxide thickness becomes comparable to or larger than L_D. Because D follows an Arrhenius law, $D \propto \exp(-E_D/RT)$, the diffusion length inherits an exponential temperature sensitivity ($L_D \propto \exp(-E_D/2RT)$), so modest changes in the activation energy for diffusion produce large changes in L_D at the temperatures used here. For our experiments, this provides a consistent explanation of the observed transport limitation and large apparent activation energies. A dense interfacial SiO_x layer and poor percolation in Ar reduce D and L_D, suppressing SiO escape at lower temperatures, whereas hydrogen modifies the local structure and lowers effective barriers, increases D and extends L_D, thereby enhancing SiO flux and lowering the apparent activation energy. Ogawa and Shiono (Ogawa and Shiono, 1995) studied the effect of hydrogen on the interface. They showed that the hydrogen strongly controls reactions at the Si–SiO_2 interface by both creating and removing electrically active defects and by moving through the oxide. From this microscopic understanding of the interface defects, the low-field

instability is closely related to the dissociation chemistry (the reverse of passivation) of hydrogen from hydrogen-passivated dangling Si bonds. The rate at which the reaction causing the generation of interface traps takes place is controlled by the diffusion of hydrogen that has been released from hydrogen-passivated defect sites previously. In plain terms, hydrogen can speed up or slow down interface reactions depending on how easily hydrogen atoms or molecules can move away from the interface. If hydrogen diffuses away quickly the interface becomes more reactive because passivating hydrogen is removed, while slow hydrogen transport lets released hydrogen re-passivate sites and suppress defect growth.

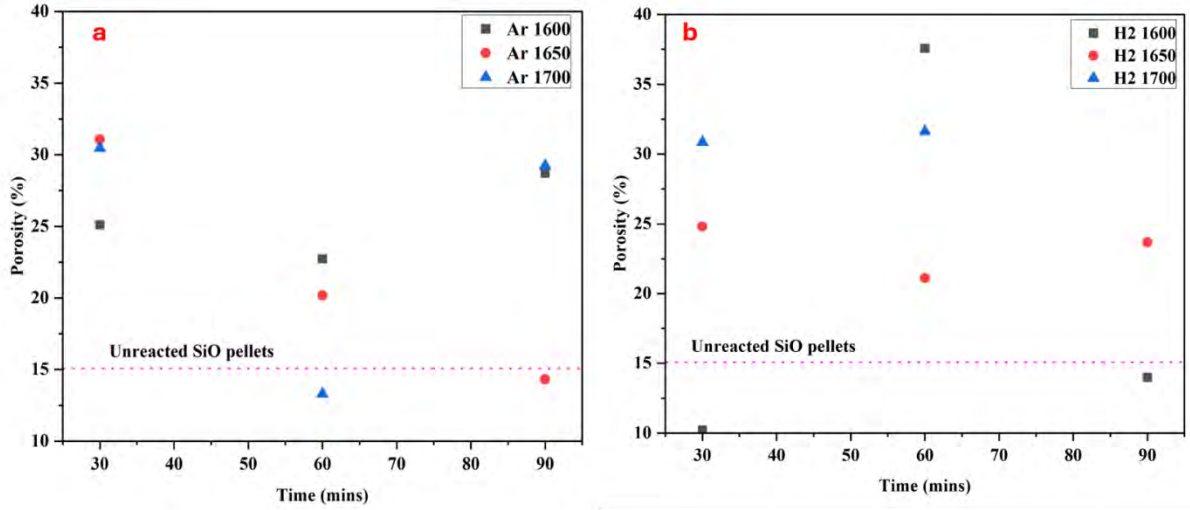

Figure 5. Porosity of the pellets across different temperatures and time.

Porosity measurements as shown in Figure 5 show large scatter because different pellets from the same batch already have different initial porosity and appearance. To reduce this effect, three pellets were selected for each condition and averaged. Even with this variation, the data clearly indicates that porosity can become almost twice that of the unreacted pellets as temperature and reaction time increase, reflecting the progressive opening and fragmentation of the structure. As the reaction approaches completion around 90 minutes, some pores may collapse and merge into thicker, more compact regions, which can reduce the measured porosity and further complicate the trend. Overall, hydrogen tends to give slightly higher porosity values than argon at comparable conditions, but a strict conclusion cannot be drawn because of the pellet-to-pellet variation and the dynamic changes in pore formation and collapse during the reaction.

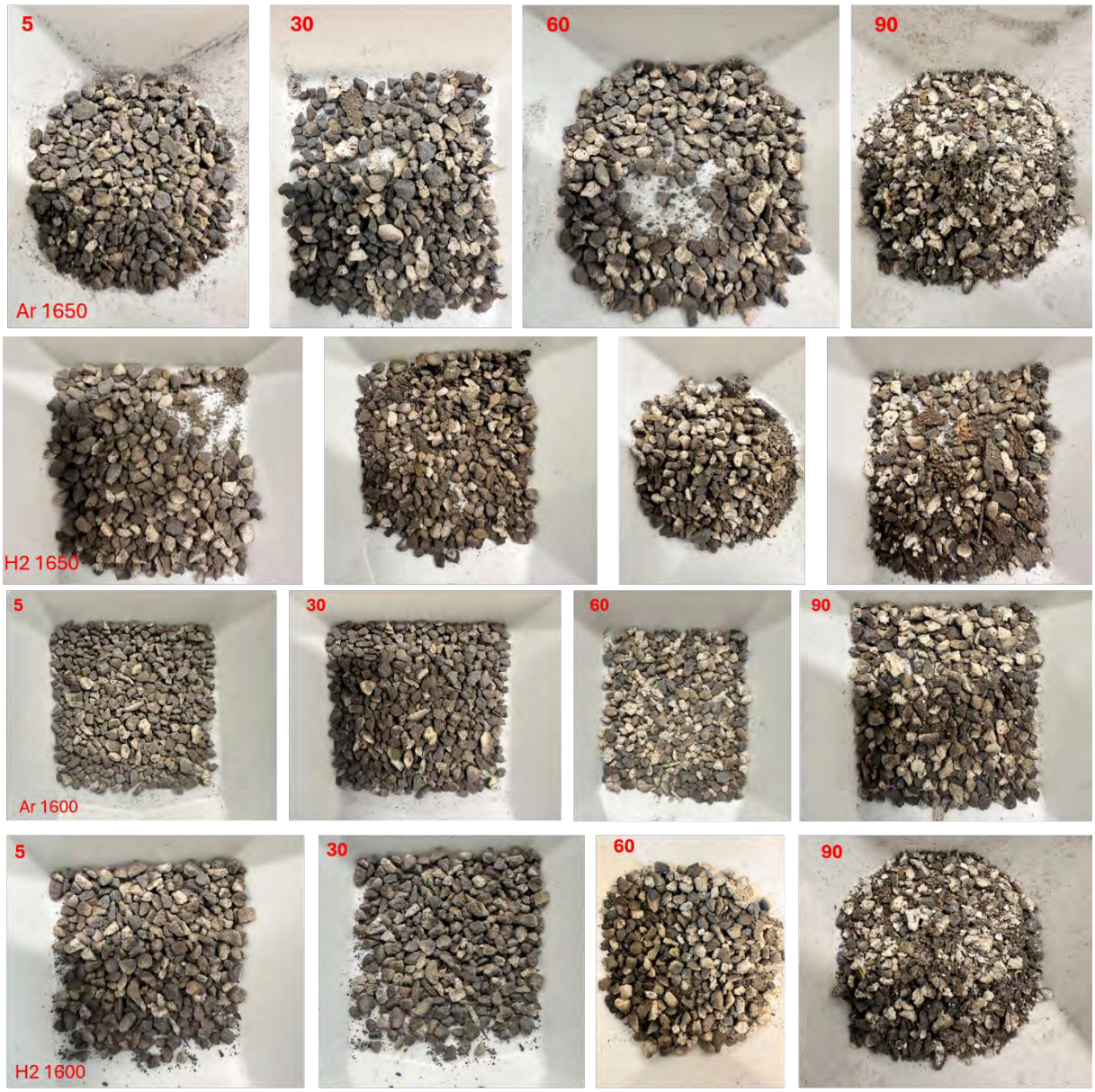

Figure 6. Visual appearance of pellets at different temperatures.

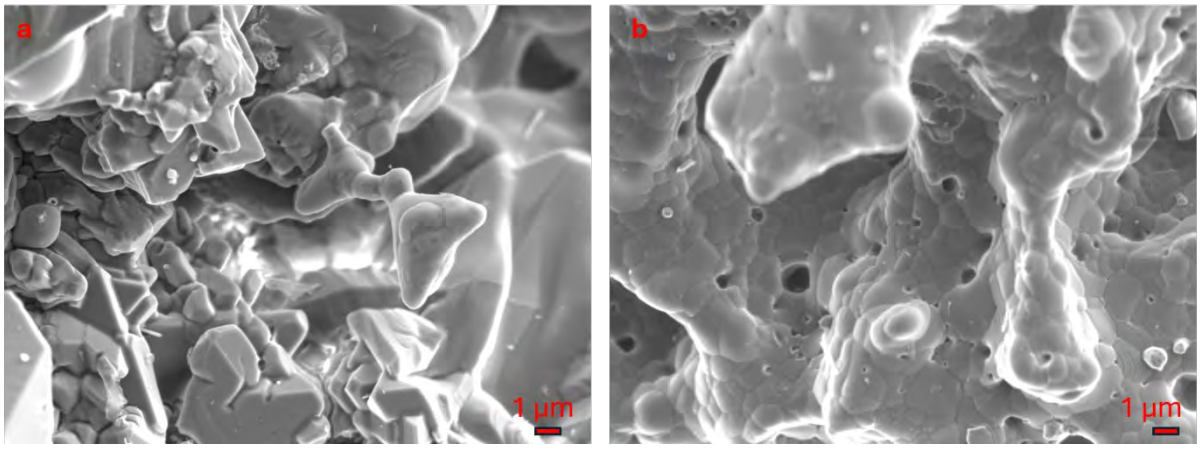

Figure 7. SEM image of the pellets after 30 minutes of experiment in 1700 °C. a: Ar and b: H_2.

Figure 6 and Figure 7 show that the pellets treated in hydrogen develop a noticeably more open and irregular surface, with small voids, pits, and shallow pores scattered across the

grains, while the pellets treated in argon remain much more compact and faceted. This difference does not indicate a fully developed pore network, but it does show that hydrogen slightly roughens and disrupts the SiO_2/Si surface during reaction. Hydrogen promotes local reduction and vacancy formation, so small pockets form where material has been removed or rearranged as SiO leaves the solid. In argon, vacancy formation is weaker and the surface stays dense, so the grains retain their sharp, angular morphology. Overall, hydrogen produces a subtly more porous and irregular microstructure, whereas argon preserves a smoother, more compact surface, even though neither atmosphere creates a continuous pore network.

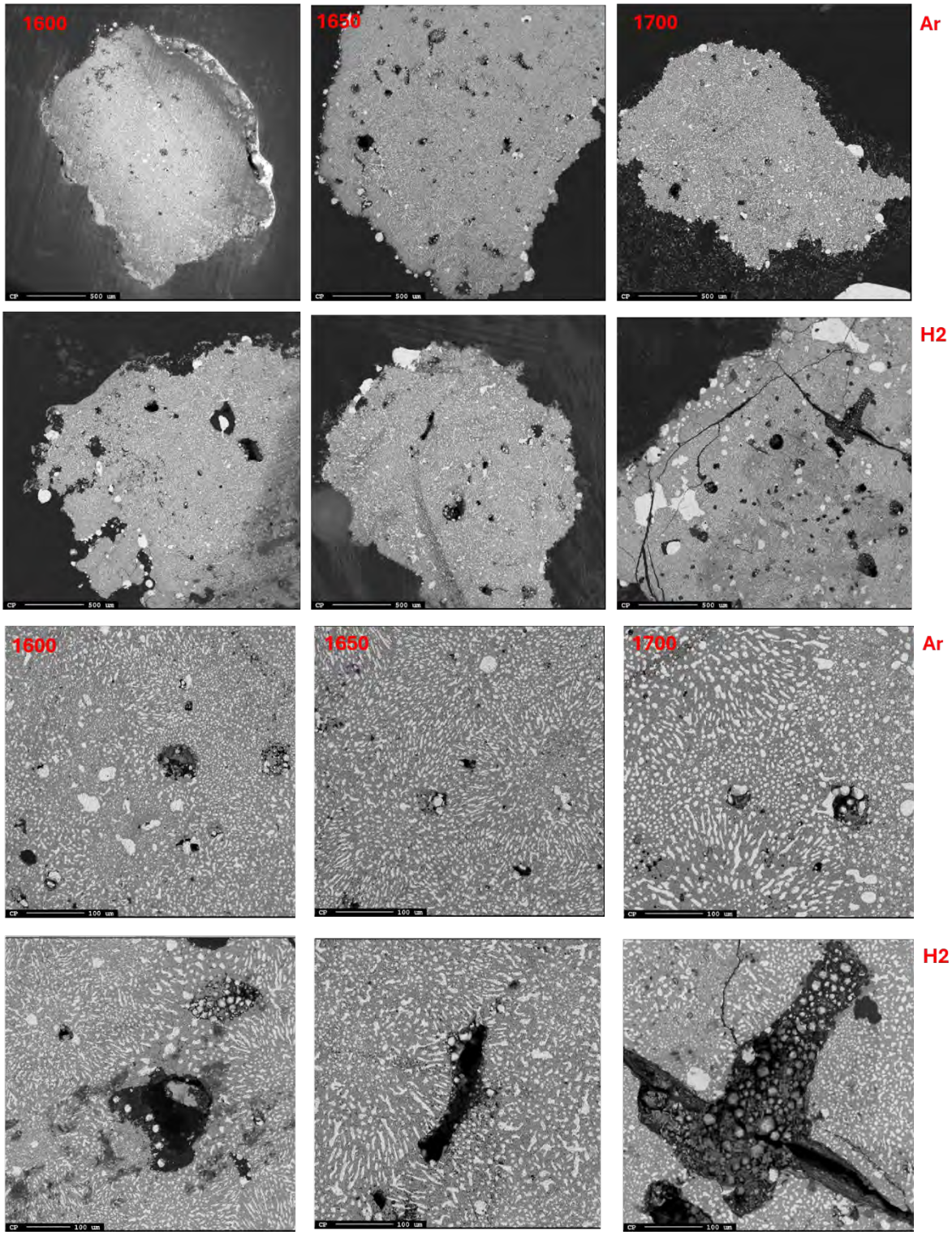

Figure 8. Back-scattered electron-EPMA analysis of the pellets at 500 µmb(200x) and 100 (40x) µm.

Figure 8 shows the back-scattered EPMA cross-sections reveal a clear temperature-dependent transformation of the SiO granules. At 1600 °C, pellets reacted in Ar show coarse, irregular Si precipitates embedded within a largely continuous SiO_2 matrix, indicating limited SiO transport and slow development of the oxygen-depleted interfacial layer. In H_2 at the same temperature, the Si domains are finer and more uniformly dispersed. At 1650 °C, the Ar samples display Si coarsening and the emergence of elongated Si regions, consistent with

slower evacuation of SiO and stronger local disproportionation. The appearance of pores where the formation of Si crystals start also is higher in H_2 pellets.

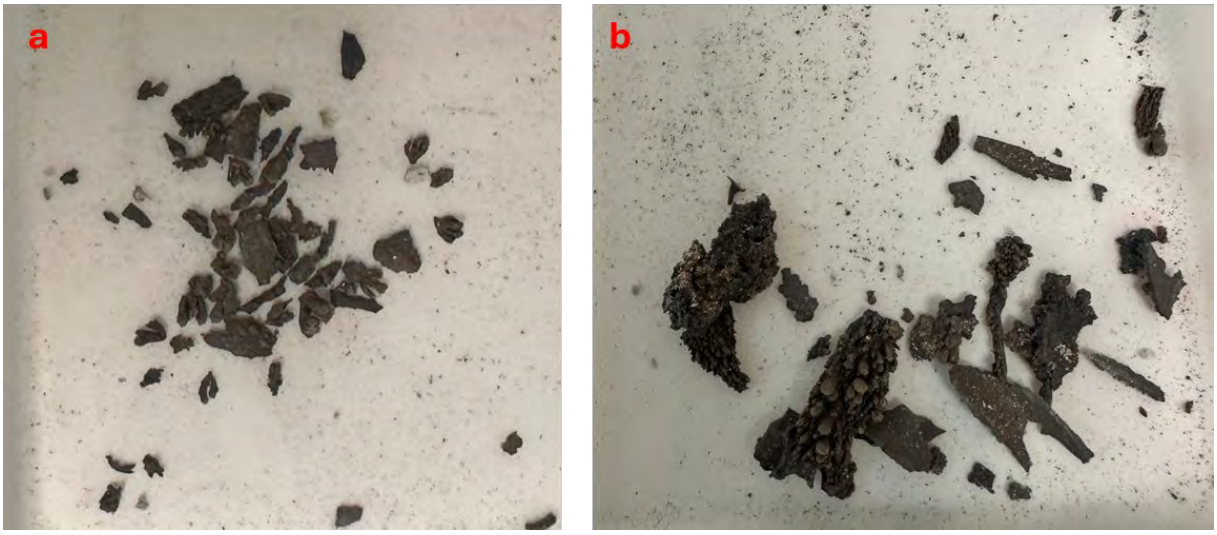

Figure 9. The flower morphology of the condensate in a: Ar and b: H_2

After the SiO is formed, it will be transformed back to $Si+SiO_2$ on the colder crucible walls, and some will fall into the crucible bottom. The flower shaped condensates, found on the crucible, are generally nucleated on the crucible wall, and fall when cooling. The two condensates shown in Figure 9 have a flower-like morphology. This forms in both atmospheres and reflects the way SiO vapor condenses rather than a strong gas-dependent effect. In argon (a), the condensate breaks into many small, brittle fragments with petal-like edges, while in hydrogen (b) the pieces are larger and more clustered, but the overall "flower" appearance is still present. This morphology develops because SiO vapor reaches supersaturation and solidifies in radiating, outward-growing clusters; once cooled and handled, these clusters fracture into petal-shaped pieces. The images therefore show that the fundamental condensation mechanism is the same in both gases, and the flower shape is a natural outcome of SiO vapor condensing and cracking, with only minor differences in size and compactness between argon and hydrogen.

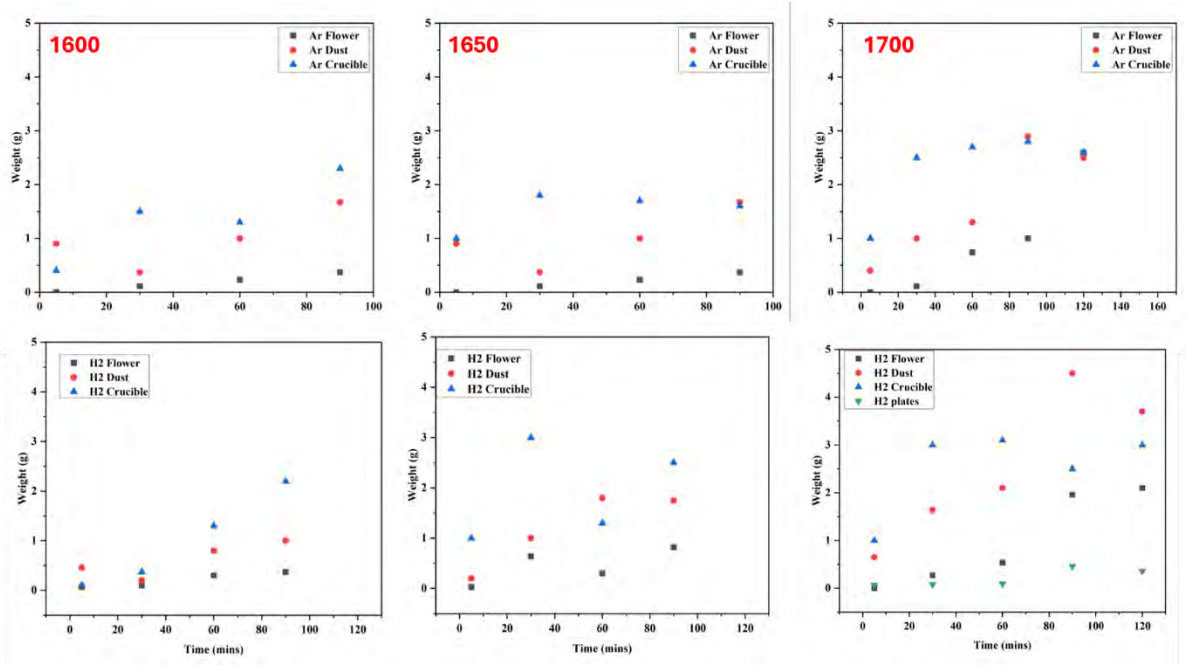

Figure 10. Condensate weight in gram**.**

The condensate collected are shown in Figure 10 broadly similar mass evolution, but the morphology of the recovered material varies with both atmosphere and temperature. In all cases the condensate separates into loose "flower" fragments, fine dust, and a crucible-bound fraction that solidifies directly on the crucible wall and cannot be removed without breaking it, indicating strong adhesion and high local supersaturation. At 1700 °C in hydrogen a distinct plate-like condensate appears, a morphology not observed at lower temperatures or in argon. This suggests that at the highest temperature hydrogen enables a different condensation pathway in which SiO vapor grows as broad, layered structures before fracturing, whereas argon maintains the typical petal-like clusters across all temperatures. The weight trends therefore reflect not only the amount of SiO leaving the pellets but also how the vapor condenses under each atmosphere, with hydrogen at 1700 °C producing a unique structural form while the overall condensate mass remains comparable.

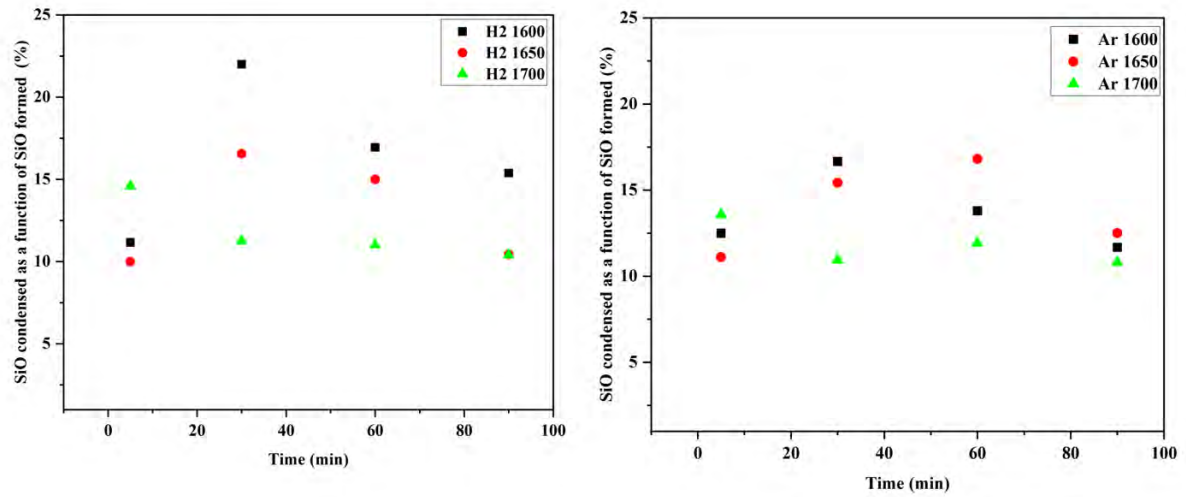

Figure 11. The percentage of SiO condensed at the crucible wall as a function of SiO formed in argon and hydrogen**.**

The percentage of SiO that condenses follows the amount of SiO formed, and the trend is similar in both argon and hydrogen. At all temperatures, the condensed fraction increases steadily as more SiO is produced, confirming that condensation is governed mainly by the SiO supply rate rather than by the gas atmosphere. Hydrogen shows a smoother, more gradual increase in condensed fraction, reflecting faster and more uniform SiO generation and transport. In argon, the condensed fraction shows stronger fluctuations at higher temperatures, which may be due to slower gas-phase transport and more local supersaturation, causing SiO to condense in larger, less uniform aggregates.

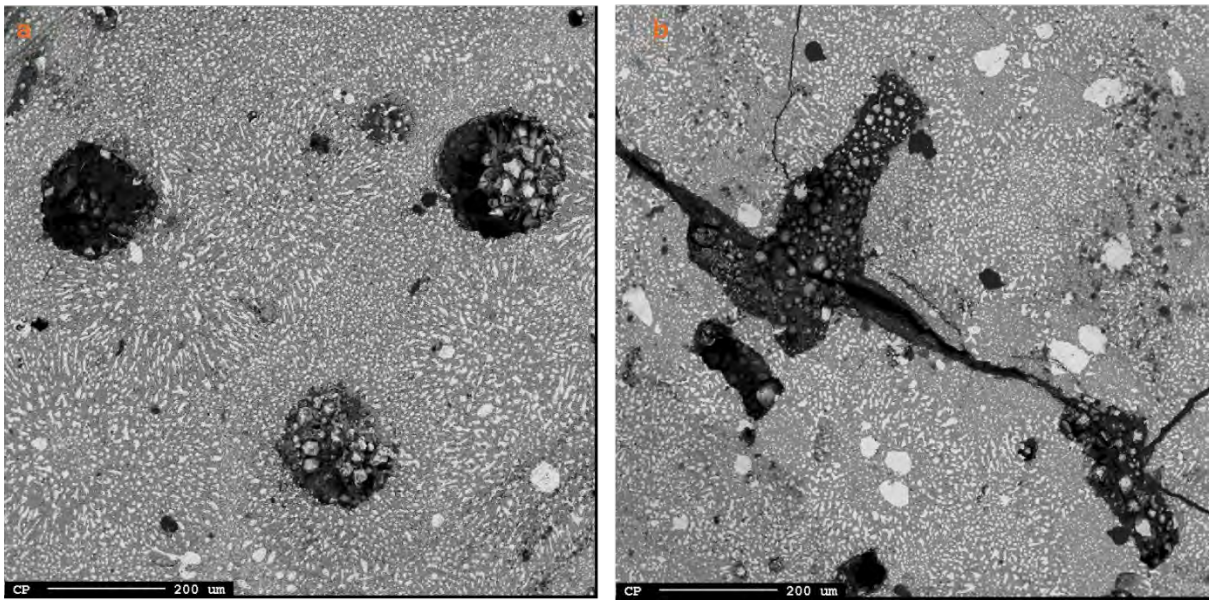

Figure 12. Si formation on the pores of a: argon and b: hydrogen and 1700 °C.

When silicon crystals nucleate and grow on pore surfaces as shown in Figure 12, the process is driven by local supersaturation and heterogeneous nucleation at energetically favorable sites. Pores and internal voids act as microtraps for vapor-phase SiO, increasing local partial pressure and residence time so that supersaturation is reached there before the surrounding flat surfaces. The pore walls and edges lower the critical nucleus size and reduce the surface-energy penalty for nucleation, so condensation begins preferentially inside or at the rim of pores. Once nuclei form, they grow by direct impingement of SiO and by coalescence, producing coarse, clustered grains that fill or rim the pore. This pore-centered growth also reduces the net SiO flux leaving the solid because some vapor is captured and condensed locally, which in turn affects mass-loss measurements and the apparent kinetics. Besides this, most of the condensates starts nucleating around the cooler parts of the crucible (Liya Jacob, 2026a).

4. CONCLUSIONS

This study provides a systematic determination of the activation energy for the $Si + SiO_2 \rightarrow 2SiO$ reaction under hydrogen and argon in a carbon-free environment. Overall, it is shown that SiO formation is faster in H_2 than in Ar at all temperatures. The D1 diffusion model described the kinetics across all temperature's values and EPMA shows progressive development of an oxygen depleted SiO_x interfacial layer. Hydrogen consistently accelerated SiO formation, yielding a lower activation energy (582 $kJ \cdot mol^{-1}$) than argon (740 $kJ \cdot mol^{-1}$). The higher Ea in argon reflects the very slow SiO formation at 1600 °C, where pellets remain largely unmodified and Si precipitation is limited. In contrast, hydrogen promotes early defect formation, finer Si dispersion, and faster SiO removal because of higher diffusion, maintaining measurable reaction rates even at lower temperatures. Condensation behavior is proportional

with SiO formation in both atmospheres. These findings clarify how gas atmosphere governs high-temperature Si–O kinetics and provide a foundation for designing carbon-free silicon processes with improved efficiency and reduced material losses.

5. ACKNOWLEDGEMENTS

This paper is published by the SiH2 project financed by the Research Council of Norway through grant 325464. They are acknowledged. The authors declare no competing interests.

6. REFERENCES

ALKAUSKAS, A. & PASQUARELLO, A. 2007. Alignment of hydrogen-related defect levels at the Si–SiO2 interface. *Physica B: Condensed Matter*, 401**,** 546–549.

ANDERSEN, V. 2010. Reaction mechanism and kinetics of the high temperature reactions in the silicon process. *Norwegian University of Science and Technology, Trondheim***,** 89.

BAO, S., TANGSTAD, M., TANG, K. & RINGDALEN, E. 2013. *Production of SiO Gas in The Silicon Process*.

BIENIASZ, L. K. 2015. Models Involving One-Dimensional Diffusion. *In:* BIENIASZ, L. K. (ed.) *Modelling Electroanalytical Experiments by the Integral Equation Method*. Berlin, Heidelberg: Springer Berlin Heidelberg.

BONGIORNO, A. & PASQUARELLO, A. 2004. Multiscale modeling of oxygen diffusion through the oxide during silicon oxidation. *Physical Review B*, 70**,** 195312.

BOOTSMA, G. A., KNIPPENBERG, W. F. & VERSPUI, G. 1971. Growth of SiC whiskers in the system SiO2-C-H2nucleated by iron. *Journal of Crystal Growth*, 11**,** 297–309.

BUNSON, P., DI VENTRA, M., PANTELIDES, S., FLEETWOOD, D. & SCHRIMPF, R. 2000. Hydrogen-related defects in irradiated SiO/sub 2. *IEEE Transactions on Nuclear Science*, 47**,** 2289–2296.

CARTIER, E., STATHIS, J. H. & BUCHANAN, D. A. 1993. Passivation and depassivation of silicon dangling bonds at the Si/SiO2 interface by atomic hydrogen. *Applied Physics Letters*, 63**,** 1510–1512.

DEVINE, R., MATHIOT, D., WARREN, W. & ASPAR, B. 1996. O interstitial generation and diffusion in high temperature annealed Si/SiO2/Si structures. *Journal of applied physics*, 79**,** 2302–2308.

DEVINE, R. A. B., MATHIOT, D., WARREN, W. L., FLEETWOOD, D. M. & ASPAR, B. 1993. Point defect generation during high temperature annealing of the Si-SiO2 interface. *Applied Physics Letters*, 63**,** 2926–2928.

HAN, G. & SOHN, H. Y. 2005. Kinetics of the Hydrogen Reduction of Silica Incorporating the Effect of Gas-Volume Change upon Reaction. *Journal of the American Ceramic Society*, 88**,** 882–888.

LEROY, F., LANDRU, D., CHEYNIS, F., KONONCHUK, O., MüLLER, P. & CURIOTTO, S. 2020. Kinetics and coupled dynamics of dewetting and chemical reaction in Si/SiO 2/Si system. *Journal of Materials Science*, 55**,** 16074–16082.

LI, X., ZHANG, G., TRONSTAD, R. & OSTROVSKI, O. 2016. Reduction of Quartz to Silicon Monoxide by Methane-Hydrogen Mixtures. *Metallurgical and Materials Transactions B*, 47**,** 2197–2204.

LIYA JACOB, M. K., MERETE TANGSTAD. Silicon Production with Hydrogen as a Reductant: Towards Greener Ferrosilicon. COM 2026, 2026a Canada. Springer.

LIYA JACOB, M. K., MERETE TANGSTAD 2026b. SiO -formation and -condensation with hydrogen in carbon free conditions. *Submitted*.

LUO, H., QI, D., MA, Z., GUO, X., ZHOU, H., LIU, Y. & ZUO, X. 2026. First-principles study of hydrogen-related defects at the a-SiO2/Si(100) interface. *Scientific Reports*, 16**,** 17465.

OGAWA, S. & SHIONO, N. 1995. Generalized diffusion-reaction model for the low-field charge-buildup instability at the Si-SiO 2 interface. *Physical Review B,* 51**,** 4218.
OZTURK, B. & FRUEHAN, R. 1985. The rate of formation of SiO by the reaction of CO or H2 with silica and silicate slags. *Metallurgical Transactions B,* 16**,** 801–806.
RAIDER, S. I. 1988. The Role of SiO in Si Oxidation at a Si-SiO2 Interface. *In:* HELMS, C. R. & DEAL, B. E. (eds.) *The Physics and Chemistry of SiO2 and the Si-SiO2 Interface.* Boston, MA: Springer US.
RASHKEEV, S., FLEETWOOD, D., SCHRIMPF, R. & PANTELIDES, S. 2001. Defect generation by hydrogen at the Si-SiO 2 interface. *Physical review letters,* 87**,** 165506.
RINGDALEN, E., SVENUM, I.-H. & AARNæS, T. 2024. SiH2-A new process for Si-production based on hydrogen. *Available at SSRN 4942625*.
SINDLAND, C. & TANGSTAD, M. 2021. Production rate of SiO gas from industrial quartz and silicon. *Metallurgical and Materials Transactions B,* 52**,** 1755–1771.
WATANABE, T. 2025. Kinetics of thermal oxidation of silicon. *Applied Physics Express*, 18**,** 120101.

Liya Jacob

PhD, NTNU, Norway

Liya Jacob is a PhD researcher in Materials Science and Engineering at NTNU, specializing in hydrogen-based and plasma-assisted reduction pathways for sustainable metallurgical silicon production. Her doctoral work focuses on high-temperature reaction kinetics, sustainable metal production in hydrogen. She maintains strong professional interests in clean-energy process development, advanced furnace technologies, and low-emission materials production.

Yan, G. L., P. L. Biundo, and F. Li. 2026. Mechanism of calcium chloride addition in enhancing the carbothermic reduction of quartz. In *Silicon for the chemical and solar industry XVIII*, edited by M. Tangstad, H. Rong, A. Valderhaug, B. Andresen, H. Dalaker, and I. G. Page. Kristiansand, Norway, September 7–10, 2026.
https://doi.org/10.55669/oa900830

Mechanism of calcium chloride addition in enhancing the carbothermic reduction of quartz

G.L. Yan[1], P.L. Biundo[2], and F. Li[1,3,4*]

[1]Department of Materials Science and Engineering, Lanzhou University of Technology, Lanzhou, P. R. China

[2]Department of Materials Science and Engineering, Norwegian University of Science and Technology, Trondheim, Norway

[3]State Key Laboratory of Advanced Processing and Recycling of Non-ferrous Metals, Lanzhou, P. R. China

[4]Gansu Provincial Engineering Research Center for Industrial Silicon, Lanzhou, P. R. China

*Contact e-mail: li.feicn@hotmail.com

Keywords: Quartz; Calcium chloride; High-temperature melting; Carbothermic reduction; TG–DTG; Thermodynamic analysis

Abstract – The carbothermic reduction of quartz is a key reaction in silicon production and is closely related to quartz softening, mass-loss behaviour of carbon-containing mixtures, and phase evolution. China is a major producer of industrial silicon, and $CaCl_2$ is sometimes added to the furnace burden in Chinese industrial silicon practice to improve furnace operation and productivity. However, its effect on quartz behaviour and carbothermic-reduction-related characteristics remains insufficiently understood. In this study, high-temperature melting experiments, TG–DTG tests, and FactSage equilibrium calculations were used to investigate the effects of $CaCl_2$ addition on high-purity quartz, the SiO_2–C system, and liquid- and gas-phase evolution. The results show that $CaCl_2$ markedly lowers the characteristic temperatures of quartz. As the $CaCl_2$ addition increased from 0 to 1.0 wt.%, the softening temperature (T_S) decreased from 1798 °C to 1745 °C, and the hemispherical temperature (T_H) decreased from 1836 °C to 1776 °C. TG–DTG results showed that the maximum mass-loss rate reached 2.90 % $\cdot min^{-1}$ at 0.8 wt.% $CaCl_2$, compared with 1.48 % $\cdot min^{-1}$ for the additive-free sample. Increasing the addition to 1.0 wt.% further increased the final mass loss, but reduced the maximum mass-loss rate to 2.08 % $\cdot min^{-1}$. FactSage calculations indicated that $CaCl_2$ promotes the formation of liquid salt at approximately 770–1550 °C and shifts the rapid growth of liquid slag from about 1720 °C to 1690 °C. $CaCl_2$ did not markedly change the equilibrium generation window of CO and SiO, whereas chlorine-containing gaseous species increased with addition. These results indicate that, under the present experimental conditions, 0.8 wt.% $CaCl_2$ gave the highest maximum mass-loss rate, while higher additions may contribute additional mass loss through chlorine-containing volatilization.

1. INTRODUCTION

Silicon is an important basic raw material for photovoltaics, silicones, semiconductors, and aluminium–silicon alloys. Its stable supply is therefore important for the development of renewable-energy and electronic-information industries. According to the U.S. Geological Survey, global silicon production in 2024 was about 4.6 million t, of which China accounted for about 3.9 million t, corresponding to approximately 84.8% of the reported global production (U.S. Geological Survey, 2025). In silicon smelting, stabilising the furnace burden, controlling the reaction state in the furnace, and improving the utilization of silicon resources are important operational objectives. According to plant-survey information obtained by the authors, $CaCl_2$ may be added in some Chinese industrial silicon operations at levels up to approximately 10–15 kg per tonne of quartz, depending on furnace condition and raw-material behaviour. The addition range of 0–1.0 wt.% used in this study corresponds to low-level $CaCl_2$ addition and covers additions up to approximately 10 kg per tonne of quartz. This range was selected to examine the effect of low $CaCl_2$ addition under controlled laboratory

This work is licensed under the Creative Commons Attribution 4.0 International License. To view a copy of this license, visit https://creativecommons.org/licenses/by/4.0/

conditions while avoiding excessive salt enrichment and chloride-related volatilization, which would complicate the interpretation of quartz softening, mass-loss behaviour, and gas-phase evolution.

Silicon is mainly produced through the high-temperature carbothermic reduction of quartz by carbonaceous reductants in submerged arc furnaces. This process is not a single reaction, but involves several coupled steps, including intermediate SiC formation, generation and transport of SiO gas, and further reaction between SiO_2 and SiC. It is therefore a typical high-temperature multiphase reaction system (Schei, Tuset, and Tveit, 1998; Ringdalen and Tangstad, 2012; Folstad et al., 2021; Sindland and Tangstad, 2021). Quartz is not only the main silicon source, but also a key raw material affecting the formation of reaction interfaces and mass-transfer conditions. During heating, quartz undergoes polymorphic transformation, volume change, cracking, softening, and melting. The high-temperature morphological evolution of different industrial quartz types can differ substantially and can further influence their behaviour under silicon-production conditions (Li, Tangstad, and Ringdalen, 2018; Metherall et al., 2023). Previous studies have shown that, in SiO_2–SiC systems, increasing temperature and the degree of SiO_2 melting are important for reaction progress, and that the transformation of quartz to cristobalite can promote SiC formation in SiO_2–C systems (Folstad et al., 2021; Tian et al., 2024). Studies on quartz–carbon pellets have also shown that the nature of the carbon source, particle contact state, and gas transport conditions all affect high-temperature reaction behaviour (Li and Tangstad, 2018; Li, Tangstad, and Ringdalen, 2018). Clarifying how $CaCl_2$ affects the high-temperature softening and melting behaviour of quartz and the reaction characteristics of carbon-containing systems is therefore important for understanding its role in industrial silicon production.

Additive control provides a feasible approach for improving the carbothermic reduction behaviour of SiO_2. It has been reported that a small amount of K_2CO_3 can increase the maximum mass-loss rate of silicon-related carbothermic reduction systems, indicating that additives may influence SiO_2 carbothermic reduction by changing the local high-temperature reaction environment (Zhou et al., 2020). However, different additives have different melting behaviours, liquid-phase formation routes, and high-temperature action paths. Therefore, results obtained for carbonate additives cannot be directly used to explain the role of $CaCl_2$. $CaCl_2$ has a relatively low melting point and can form a molten salt phase at an early stage of heating. It may therefore preferentially change the high-temperature interfacial state at the surface of SiO_2 particles and at local contact regions. Phase-equilibrium studies have shown that the introduction of $CaCl_2$ changes the liquid-phase formation conditions in the SiO_2–$CaCl_2$ binary system and the CaO–SiO_2–$CaCl_2$ ternary system (Wang and Morita, 2016). In addition, studies on the dissolution of calcium silicates in molten $CaCl_2$ have shown that silicate species can migrate in the molten-salt medium (Cheng and Yang, 2023). Although these results cannot be directly equated with the reaction mechanism in the SiO_2–C–$CaCl_2$ carbothermic reduction system, they provide useful reference for understanding how $CaCl_2$ molten salt may affect local migration of silicon-containing species and interfacial mass transfer.

Overall, previous studies have clarified the key reaction paths in silicon production, the high-temperature structural and morphological changes of quartz, the effect of additives on carbothermic reactivity, and the regulation of liquid-phase relations in SiO_2-containing systems by $CaCl_2$. However, the specific role of low-level $CaCl_2$ addition in the SiO_2–C carbothermic reduction system is still not well understood. In particular, the relationship between $CaCl_2$ addition, quartz softening and melting, overall mass loss of carbon-containing samples, and liquid-phase evolution remains insufficiently clarified.

In this study, quartz was used as the research object to examine the effect of $CaCl_2$ addition on its high-temperature behaviour and carbothermic reduction process. High-temperature in situ image acquisition was used to record the morphological changes of SiO_2–$CaCl_2$ samples during heating, and the initial deformation temperature (T_D), softening temperature (T_S), and hemispherical temperature (T_H) were determined to analyse the effect of $CaCl_2$ on quartz softening and melting. Thermogravimetric analysis (TG–DTG) was used to compare the mass-loss characteristics of the SiO_2–C system with different $CaCl_2$ additions. FactSage equilibrium thermodynamic calculations were further used to analyse the temperature-dependent evolution of the molten salt phase, liquid slag phase, and main gaseous species. Based on these results, the relationships among $CaCl_2$ addition, high-temperature softening and melting of quartz, mass-loss behaviour of the carbon-containing system, and liquid-phase evolution were discussed to provide experimental evidence and thermodynamic support for understanding the effect of $CaCl_2$ on quartz carbothermic reduction.

2. EXPERIMENTAL MATERIALS AND METHODS

2.1 Experimental materials

The quartz used in the experiments was crushed, ground, and sieved, and the -200 mesh (≤75 μm) powder fraction was used for sample preparation. Its chemical composition was determined by X-ray fluorescence (XRF) and is reported as oxide-equivalent mass fractions in Table I. N911 carbon black was used as the reductant, and analytical-grade anhydrous $CaCl_2$ was used as the additive.

Table I: Chemical composition of the quartz used in this study (wt.%)

Compound	SiO_2	Fe_2O_3	Al_2O_3	CaO	TiO_2	Others
Content	99.760	0.010	0.010	0.001	0.015	0.204

The initial morphology of the quartz powder is shown in Figure 1. After grinding and sieving, the powder particles were irregular in shape and were used for subsequent pellet preparation.

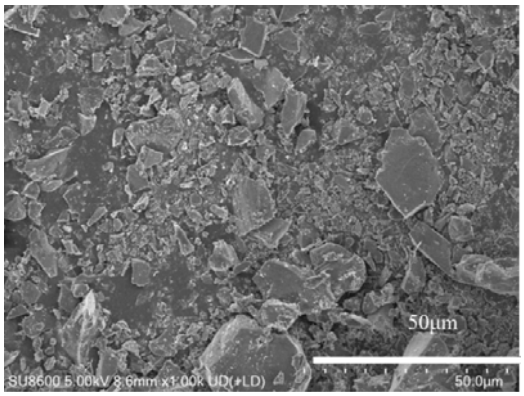

Figure 1: SEM morphology of the quartz powder

2.2 Sample preparation

Samples for the carbon-free high-temperature melting experiments and carbon-containing samples for TG–DTG tests were prepared separately according to the purpose of each test.

The samples for the high-temperature melting experiments were prepared by mixing quartz powder with $CaCl_2$. The $CaCl_2$ additions were 0, 0.1, 0.15, 0.3, 0.6, and 1.0 wt.%, all calculated on the basis of the total mass of the mixed sample. After homogeneous mixing, the powders were pressed into cylindrical specimens with a diameter of 4 mm and a height of 4 mm to

evaluate the effect of $CaCl_2$ on the high-temperature softening–melting behaviour and contour spreading of quartz.

The TG–DTG samples consisted of quartz powder, N911 carbon black, and $CaCl_2$. The quartz powder was passed through a 200-mesh sieve before sample preparation. A deliberately SiO_2-rich charge composition was used for the TG–DTG samples, with a molar ratio of n(C):n(SiO_2) = 1:3. This ratio was not selected as the stoichiometric ratio for SiC formation, but was designed to retain excess SiO_2 after the initial formation of SiC, so that the subsequent reaction between the formed SiC and excess SiO_2 to generate SiO(g) and CO(g) could be considered. The $CaCl_2$ additions were 0, 0.1, 0.5, 0.8, and 1.0 wt.%. Deionized water corresponding to 8 wt.% of the powder mass was added as a temporary binder during pellet preparation. The raw materials for each group were thoroughly mixed and pressed into pellets with a mass of approximately 2.8 g to investigate the effect of $CaCl_2$ addition on the mass-loss behaviour of the carbon-containing system. Different $CaCl_2$ addition levels were used in the high-temperature melting experiments and the TG–DTG tests because the two experiments were designed for different purposes. The high-temperature melting experiments used more closely spaced low-addition levels to resolve gradual changes in quartz softening, hemispherical deformation, and apparent spreading behaviour, whereas the TG–DTG tests used representative addition levels to compare the maximum mass-loss rate and final mass loss of the SiO_2–C system. The 0, 0.1, and 1.0 wt.% additions were included in both experimental series as common reference levels. The sample preparation and TG–DTG testing procedure are shown in Figure 2.

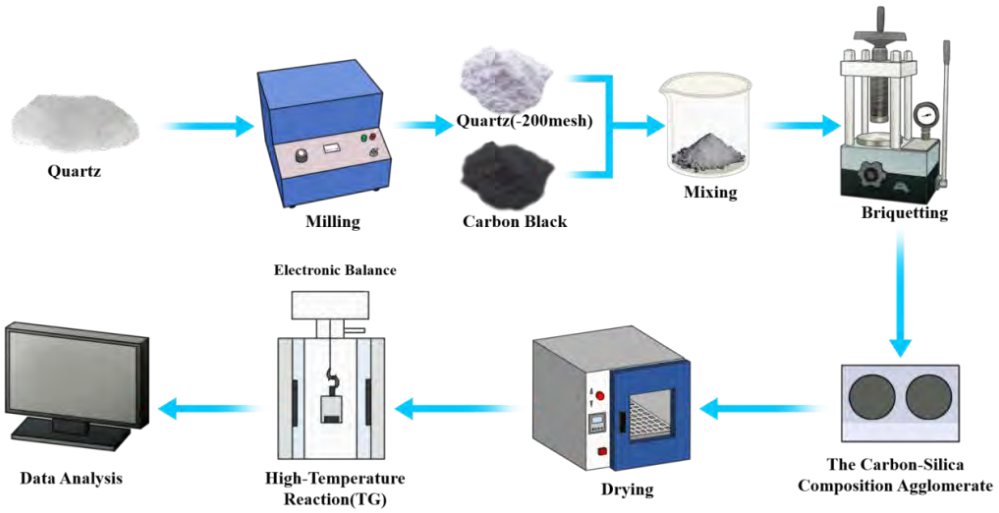

Figure 2: Preparation and TG–DTG testing procedure for carbon-containing samples

Table II: Sample compositions and experimental groups

Experiment	Sample system	n(C):n(SiO_2)	$CaCl_2$ addition / wt.%
High-temperature melting	SiO_2–$CaCl_2$	–	0, 0.1, 0.15, 0.3, 0.6, 1.0
TG–DTG	SiO_2–C–$CaCl_2$	1:3	0, 0.1, 0.5, 0.8, 1.0

2.3 High-temperature melting experiment and characteristic-temperature determination

A high-temperature image-acquisition system was used to observe the morphological evolution of pressed SiO_2–$CaCl_2$ specimens during heating. The specimen was placed on a polished high-purity graphite substrate and heated under high-purity Ar. The heating rate was 20 °C·min^{-1} from room temperature to 1600 °C and 5 °C·min^{-1} above 1600 °C. The contour evolution of the specimen was continuously recorded using a monochrome industrial camera. A schematic of the setup is shown in Figure 3.

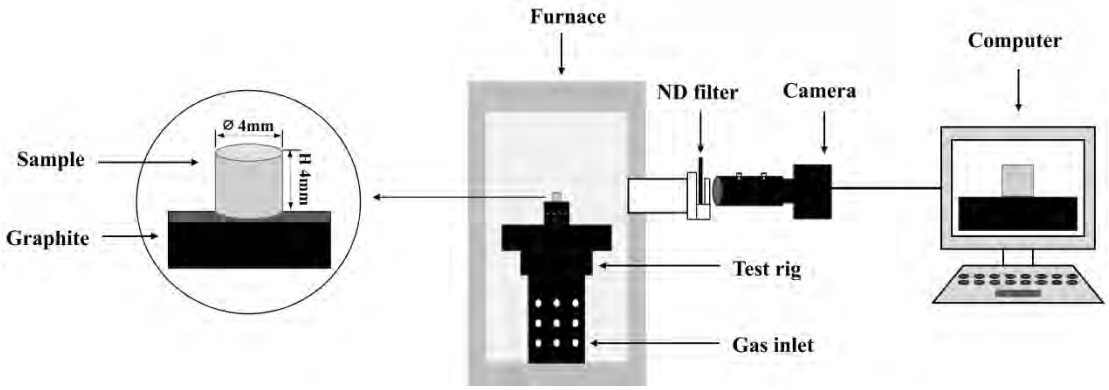

Figure 3: Schematic diagram of the high-temperature in situ morphological observation setup

In silicon-related studies, high-temperature in situ morphological observation has been used to evaluate the softening and melting behaviour of different industrial quartz types, and can reflect differences in the high-temperature morphological stability of quartz in the reaction temperature range (Ringdalen and Tangstad, 2016). Following this approach, the initial deformation temperature (T_D), softening temperature (T_S), and hemispherical temperature (T_H) were used in this study to describe the high-temperature morphological evolution of the specimens during heating. T_D is defined as the temperature at which the specimen first shows identifiable contour deformation relative to the initial cylindrical morphology, and this deformation continues during subsequent heating. T_S is defined as the temperature at which stable edge rounding and a clear increase in sidewall curvature first occur after initial deformation, with the specimen changing from a regular cylindrical contour towards a domed or collapsed morphology. T_H is defined as the temperature at which the specimen contour first forms a hemispherical shape. The apparent contact angle between the deforming SiO_2–$CaCl_2$ specimen and the graphite substrate was determined from the recorded image sequences using a geometric height–base method. The graphite substrate line was used as the horizontal baseline. For each selected image, the specimen height, h, and the apparent base width in contact with the substrate, d, were obtained using image-analysis software. The apparent contact angle was then calculated according to $\theta = 2\arctan(2h/d)$. This calculation is based on a spherical-cap geometric approximation and was used to describe the macroscopic spreading behaviour of the deforming specimen. Because the specimen softened, deformed, and spread during heating, and because possible interfacial reaction with the graphite substrate cannot be excluded, the calculated value is referred to as an apparent contact angle rather than an equilibrium wetting angle. The fitted curves in Figure 6 are empirical fitting curves used only to describe the temperature-dependent trend of the apparent contact angle.

All characteristic temperatures were manually determined from continuous image sequences based on the contour evolution of each specimen, including identifiable contour deformation, edge rounding, sidewall curvature, loss of the initial cylindrical profile, and the formation of a hemispherical shape. For each $CaCl_2$ addition level, one specimen was tested; therefore, the characteristic temperatures are reported as representative values under the present experimental conditions, and no standard deviations are given. The uncertainty in the characteristic-temperature determination was estimated to be approximately ±5 °C because of the image-recording interval and manual identification of the contour transition.

2.4 TG–DTG test

Synchronous thermogravimetric analysis was used to investigate the effect of $CaCl_2$ addition on the mass-loss behaviour of the SiO_2–C system. During the test, each pellet was placed in an isostatically pressed graphite crucible and heated from room temperature to 1800 °C at a

constant heating rate of 20 °C·min^{-1} under flowing Ar. The nominal Ar flow rate was set to 0.5 standard L·min^{-1} using a mass-flow controller. The sample mass was recorded every 5 s. The thermogravimetric (TG) curve and its derivative (DTG) curve were calculated from the mass-change data. One TG–DTG test was performed for each $CaCl_2$ addition level; therefore, the TG–DTG parameters are reported as representative values under the present experimental conditions, and no standard deviations are given.

Previous studies have shown that quartz–carbon pellets undergo several coupled processes in silicon-related high-temperature ranges, including SiC formation, SiO generation, and gas migration. Their mass-loss behaviour is closely related to the carbon source, particle contact state, and gas-transfer conditions (Li, Tangstad, and Ringdalen, 2018; Li and Tangstad, 2018). Therefore, the maximum mass-loss rate and final mass loss were extracted from the TG–DTG curves to compare the effect of $CaCl_2$ addition on the overall mass-loss characteristics of the carbon-containing system. Because $CaCl_2$ addition may also change liquid-phase evolution and introduce high-temperature volatilization of chlorine-containing components, the mass-loss rate in the TG–DTG curves was not directly equated with the rate of a single carbothermic reduction reaction, but was used as an indicator of the overall mass-loss behaviour of the system.

2.5 FactSage equilibrium thermodynamic analysis

Equilibrium thermodynamic analyses for the SiO_2–C–$CaCl_2$ system were carried out using FactSage 8.4. FactSage is a software platform for multicomponent multiphase equilibrium calculations based on thermodynamic databases and Gibbs-free-energy minimization and has been widely used to analyse phase composition and liquid-phase evolution in high-temperature metallurgical systems (Bale et al., 2016).

The FactSage calculations were performed using a fixed input basis of 1000 g SiO_2 and 66.6 g C, corresponding to a molar ratio of n(C):n(SiO_2) = 1:3. The corresponding $CaCl_2$ additions were introduced according to the selected wt.% levels. The pressure was set to 1 atm, and the atmosphere was Ar.

The masses shown in the equilibrium phase-evolution figures are calculated phase masses in grams based on this FactSage input basis, rather than mass fractions or experimentally measured masses.

The focus was on the evolution of liquid-phase composition and major gaseous species with temperature at different $CaCl_2$ additions. The databases used were FactPS, FToxid-SLAGH, and FTsalt-SALTA. FactPS was used to describe pure substances and gas species, SLAGH to describe SiO_2-containing oxide slag liquid, and SALTA to describe $CaCl_2$-containing salt liquid. The calculation temperature range was 600–1800 °C and was used to analyse the equilibrium evolution of liquid and gas phases at different $CaCl_2$ additions. The FactSage results represent equilibrium phase-evolution trends and are not directly equivalent to the reaction rates or mass-transfer processes occurring during actual heating.

3. RESULTS AND DISCUSSION

3.1 Effect of $CaCl_2$ addition on high-temperature morphological evolution and characteristic temperatures

During heating, all specimens evolved from a regular cylindrical contour through initial deformation and obvious softening to a molten morphology. The additive-free specimen still retained a relatively complete cylindrical contour at high temperatures, indicating the high

morphological stability of high-purity quartz. After $CaCl_2$ addition, edge rounding, sidewall bending, and top rounding occurred at lower temperatures. As the $CaCl_2$ addition increased, the development of softening and melting morphologies became more pronounced. Representative morphological changes of the specimens during heating are shown in Figure 4. The apparent specimen height in Figure 4 should be interpreted qualitatively, because the selected images were used mainly to show contour evolution rather than to compare absolute height among different specimens. At T_D, some specimens showed inward contraction of the sidewall and redistribution of the softened body towards the centre, which could make the apparent height remain similar to, or slightly higher than, that at 500 °C. The lower apparent height observed at T_S for some samples may be related to small differences in the initial height of the pressed specimens and to macroscopic softening and collapse of the specimen contour. Therefore, T_D, T_S, and T_H were determined from continuous contour evolution rather than from the absolute height in a single selected image.

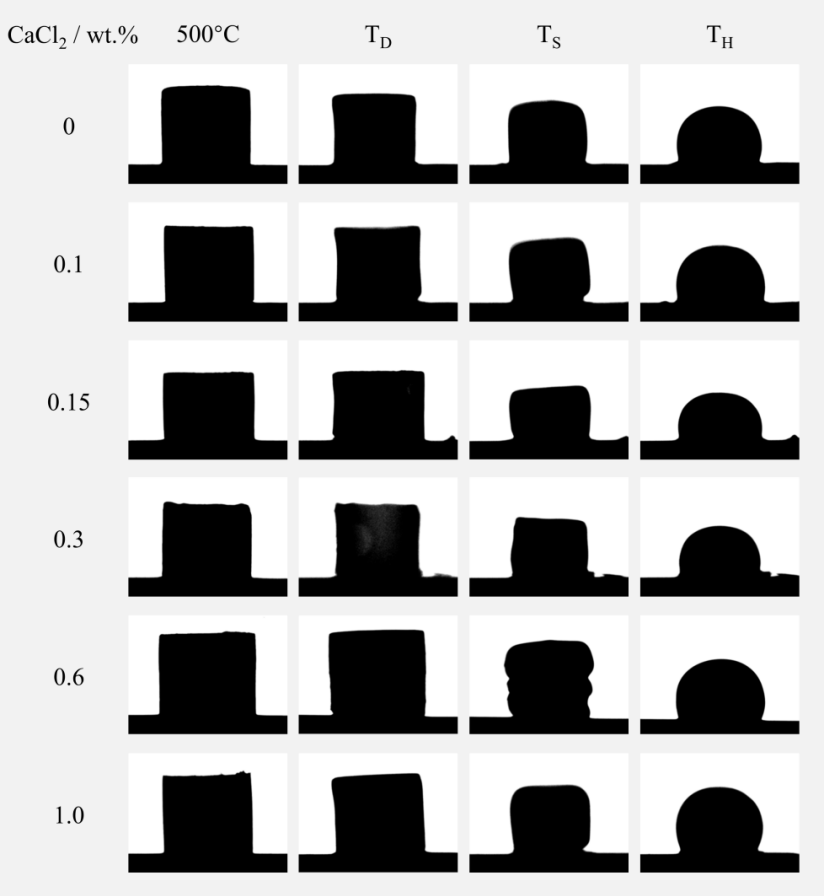

Figure 4: High-temperature morphological evolution of samples modified with $CaCl_2$

To quantitatively compare the effect of $CaCl_2$ on the high-temperature morphological changes of the specimens, the initial deformation temperature (T_D), softening temperature (T_S), and hemispherical temperature (T_H) were determined from continuous image sequences. The results are listed in Table III, and the trends are shown in Figure 5. Because one specimen was tested for each $CaCl_2$ addition level, the following discussion focuses on the overall decreasing trend rather than on small differences between neighbouring addition levels. For the additive-free sample, T_D, T_S, and T_H were 1733, 1798, and 1836 °C, respectively. With increasing $CaCl_2$ addition, all three characteristic temperatures generally decreased. T_D decreased from 1733 °C to about 1715–1716 °C, showing only a small change. In contrast, T_S and T_H decreased more markedly. At 1.0 wt.% $CaCl_2$, T_S decreased from 1798 °C to 1745 °C, a decrease of 53 °C, and T_H decreased from 1836 °C to 1776 °C, a decrease of 60 °C.

Table III: Characteristic temperatures of samples modified with $CaCl_2$

$CaCl_2$ addition / wt.%	T_D / °C	T_S / °C	T_H / °C
0	1733	1798	1836
0.1	1725	1779	1825
0.15	1718	1775	1817
0.3	1717	1766	1810
0.6	1715	1752	1779
1.0	1716	1745	1776

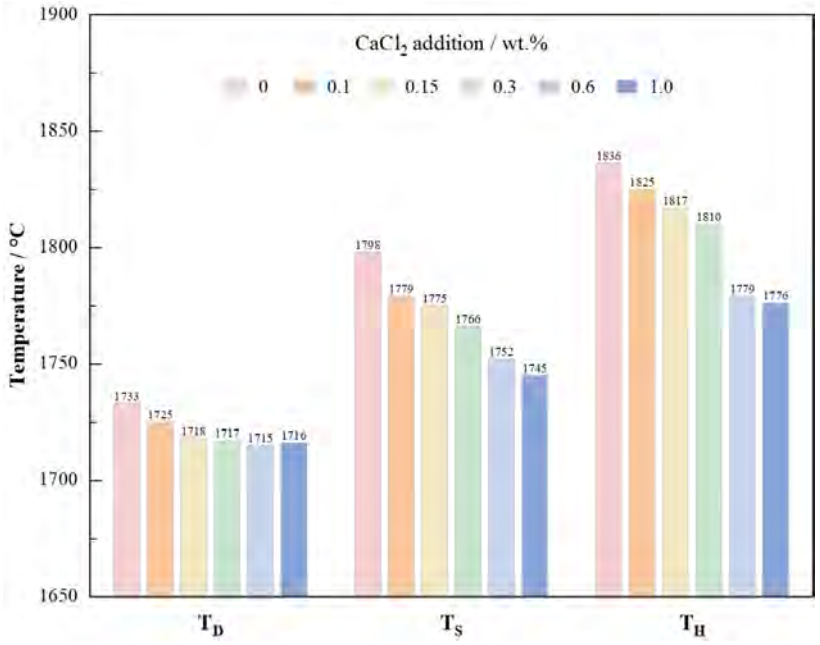

Figure 5: Effect of $CaCl_2$ addition on the characteristic temperatures

In summary, with increasing $CaCl_2$ addition, the initial deformation temperature changed only slightly, whereas the softening and hemispherical temperatures decreased markedly. At 1.0 wt.% $CaCl_2$, T_S and T_H were 53 °C and 60 °C lower than those of the additive-free specimen, respectively. It has been reported that the softening and melting temperature ranges of different industrial quartz types vary significantly, and that the high-temperature morphological state affects their contact and reaction conditions in silicon-related processes (Ringdalen and Tangstad, 2016). For $CaCl_2$-containing SiO_2 systems, phase-equilibrium studies further show that $CaCl_2$ addition can change the liquid-phase formation region (Wang and Morita, 2016). Therefore, the decrease in characteristic temperatures observed in this study may be related to changes in local liquid-phase evolution induced by $CaCl_2$. This relationship is further analysed using FactSage calculations in the following section.

3.2 Effect of $CaCl_2$ addition on apparent contact-angle evolution

The contact angle discussed in this section is the apparent contact angle between the deforming SiO_2–$CaCl_2$ specimen and the graphite substrate during heating. It was calculated from the specimen height and apparent base width using a spherical-cap geometric approximation. Because the specimen softened, deformed, and spread during the test, and because possible interfacial reaction with the graphite substrate cannot be excluded, the calculated angle should not be regarded as an equilibrium wetting angle. Instead, it is used as a macroscopic descriptor of the apparent spreading behaviour of the specimen on the graphite substrate. The apparent contact-angle results are therefore used for qualitative comparison of macroscopic spreading trends rather than for statistical evaluation of equilibrium wetting behaviour. As shown in

Figure 6, after $CaCl_2$ addition, the apparent contact angle decreased more noticeably at lower temperatures.

For the additive-free sample, the apparent contact angle decreased slowly with increasing temperature, from 119.5° at 1733 °C to 109.9° at 1836 °C. After $CaCl_2$ addition, the apparent contact angle decreased more markedly in the lower temperature range. The apparent contact angle of the 0.3 wt.% sample decreased from 116.4° at 1717 °C to 95.1° at 1810 °C, while that of the 0.6 wt.% sample decreased from 123.6° to 109.6° between 1765 and 1779 °C. When the addition increased to 1.0 wt.%, the apparent contact-angle change did not show a further enhancement compared with the 0.6 wt.% sample. In combination with the characteristic-temperature results, this indicates that $CaCl_2$ addition changes the softening, hemispherical deformation, and spreading behaviour of quartz at high temperature, but the effect does not increase monotonically with addition. Because $CaCl_2$ has been reported to modify liquid-phase formation in SiO_2-containing systems (Wang and Morita, 2016), the apparent contact-angle changes observed here may be related to local liquid formation and changes in interfacial spreading conditions induced by the additive. However, because interfacial reaction products and the spatial distribution of the liquid phase were not directly analysed in this study, the apparent contact-angle results are used mainly to characterize macroscopic spreading behaviour and are not taken as direct evidence for a specific reaction mechanism.

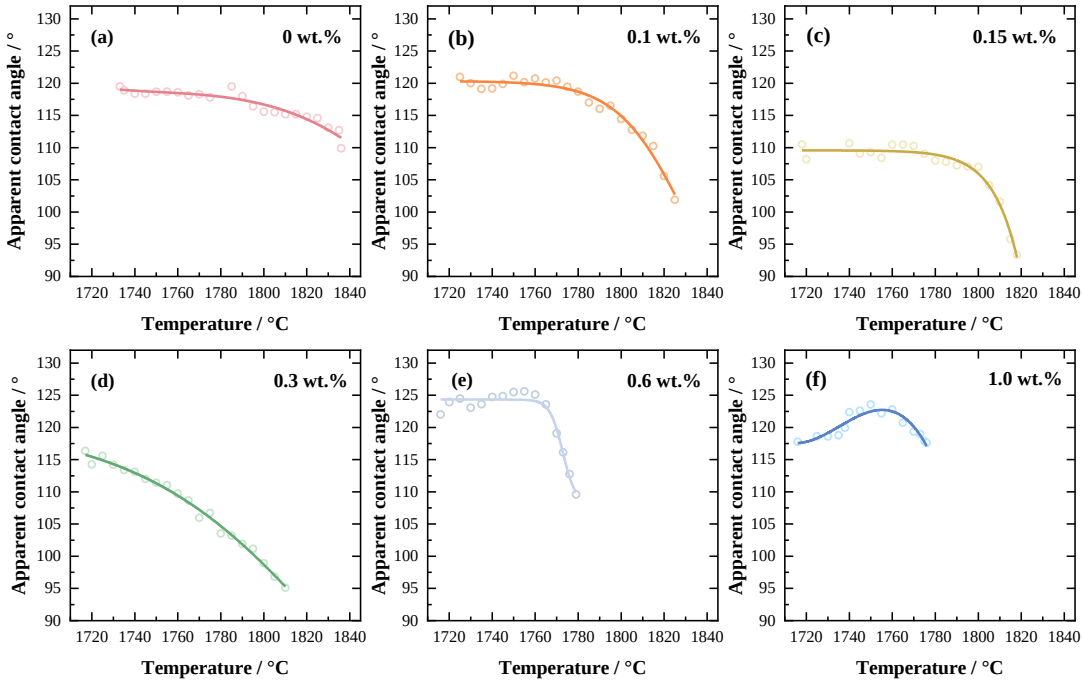

Figure 6: Apparent contact-angle evolution between pressed SiO_2–$CaCl_2$ specimens and the graphite substrate

Symbols represent measured apparent contact angles, and solid lines represent empirical fitting curves.

3.3 Effect of $CaCl_2$ addition on the mass-loss behaviour of the SiO_2–C system

The TG–DTG curves of samples with different $CaCl_2$ additions are shown in Figure 7, and the corresponding characteristic parameters are listed in Table IV. To analyse the stage-wise mass-loss behaviour reflected by the TG–DTG curves, the process was divided into Stage I and Stage II using a common boundary temperature of 1710 °C, which corresponds approximately to the transition region observed in Figure 7(b). Stage I was defined as the cumulative mass loss from the initial sample mass to 1710 °C, and Stage II was defined as the additional mass loss from 1710 °C to the end of the test. This division was used to compare the theoretical mass loss

associated with the main reaction paths with the TG-measured incremental mass loss, and does not imply that only a single reaction occurred in each stage.

Because the TG–DTG samples were prepared with a deliberately SiO_2-rich molar ratio of n(C):n(SiO_2) = 1:3, carbon was the limiting reactant during the initial SiC-forming reaction. Stage I was therefore interpreted as being dominated by mass loss associated with SiC formation, as represented by Equation [1]. Stage II was interpreted as being dominated by the further reaction between the formed SiC and excess SiO_2, accompanied by the release of SiO(g) and CO(g), as represented by Equation [2]. These assignments are used as dominant interpreted reaction paths for theoretical comparison, rather than as proof that the actual TG process occurred through two completely separated reactions.

$$SiO_2(s,l) + 3C(s) \rightarrow SiC(s) + 2CO(g) \quad [1]$$

$$2SiO_2(s,l) + SiC(s) \rightarrow 3SiO(g) + CO(g) \quad [2]$$

The theoretical mass losses in Table V were calculated from the two-stage main reaction paths represented by Equations [1] and [2], together with the corresponding charge basis, and were used for comparison with the TG-measured stage-wise mass losses. The measured Stage I and Stage II values in Table V are incremental mass losses calculated using 1710 °C as the common boundary, and their sum corresponds to the final mass loss listed in Table IV.

For the additive-free sample, the final mass loss was 26.41%, and the maximum mass-loss rate was 1.48 % min^{-1}. After adding 0.1 wt.% $CaCl_2$, the final mass loss increased to 33.49%, but the maximum mass-loss rate was 1.38 % min^{-1}, which was not higher than that of the additive-free sample. When the $CaCl_2$ addition was further increased to 0.5 and 0.8 wt.%, the maximum mass-loss rates increased to 1.96 and 2.90 % min^{-1}, respectively, and the final mass losses reached 33.87% and 39.51%, respectively. The 0.8 wt.% $CaCl_2$ sample showed the highest maximum mass-loss rate, indicating that the mass-loss characteristics of the system were most pronounced at this addition.

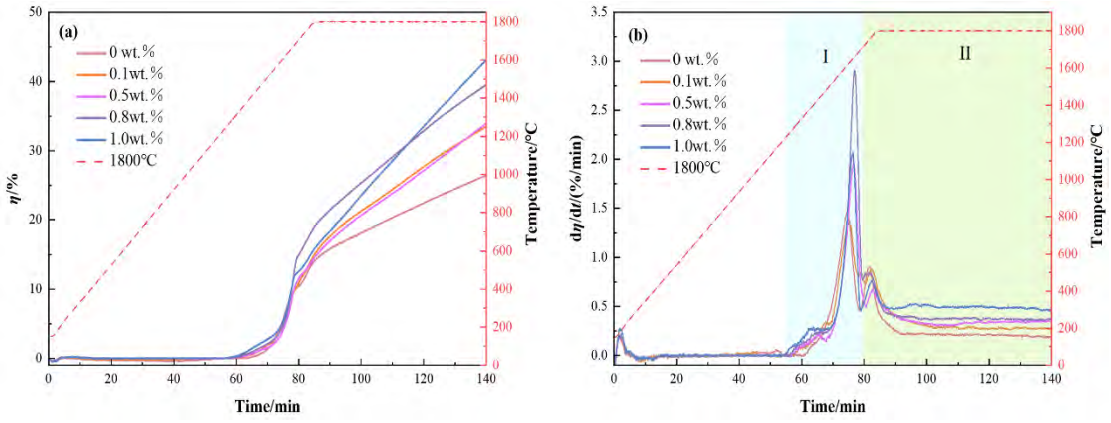

Figure 7: TG–DTG curves of the $CaCl_2$-modified SiO_2–C system

Table IV: TG–DTG characteristic parameters of the $CaCl_2$-modified SiO_2–C system

$CaCl_2$ addition / wt.%	Maximum mass-loss rate / % min^{-1}	Final mass loss / %
0	1.48	26.41
0.1	1.38	33.49
0.5	1.96	33.87
0.8	2.90	39.51
1.0	2.08	42.97

The TG–DTG curves show that, after $CaCl_2$ addition, the mass-loss process during heating shifted overall towards lower temperature, and the corresponding DTG peak also appeared earlier. This indicates that $CaCl_2$ enabled the high-temperature mass-loss behaviour in this stage to occur at lower temperature. When the $CaCl_2$ addition was further increased to 1.0 wt.%, the final mass loss continued to increase to 42.97%, but the maximum mass-loss rate decreased to 2.08 % $\cdot min^{-1}$, lower than that of the 0.8 wt.% sample. Thus, $CaCl_2$ addition increased the overall mass loss of the SiO_2–C system and changed the temperature region in which mass loss occurred during heating, but its promoting effect on the maximum mass-loss rate did not increase monotonically with addition. In the present range, the 0.8 wt.% $CaCl_2$ sample had the highest concentrated mass-loss rate, whereas the 1.0 wt.% $CaCl_2$ sample had the largest cumulative final mass loss.

It should also be noted that the TG curve of the 1.0 wt.% $CaCl_2$ sample showed a different shape from those of the lower-addition samples, with a less distinct initial knee and a higher subsequent mass-loss slope. This difference may be related not only to the nominal $CaCl_2$ addition level, but also to local $CaCl_2$ distribution, mixing homogeneity, pellet structure, gas-escape pathways, and chloride-related volatilization during heating. Therefore, the higher final mass loss of the 1.0 wt.% sample is interpreted cautiously as a larger cumulative mass-loss response, rather than direct evidence of a higher carbothermic reduction degree.

Previous studies have shown that the high-temperature reduction of quartz–carbon pellets involves several coupled processes, including SiC intermediate formation, SiO generation, and gas migration, and that the carbon source and mass-transfer conditions at the particle scale can affect the overall mass-loss behaviour of the system (Li, Tangstad, and Ringdalen, 2018; Li and Tangstad, 2018). It has also been reported that K_2CO_3 can increase the mass-loss rate of silicon carbothermic reduction systems, indicating that additives can affect the high-temperature mass-loss characteristics of silicon-containing carbothermic systems (Zhou et al., 2020). In the $CaCl_2$-containing system investigated here, the mass change during heating may be affected not only by gas generation related to carbothermic reactions, but also by liquid-phase evolution and volatilization of chlorine-containing components. Therefore, the final mass loss and maximum mass-loss rate should be treated as characteristic parameters describing the overall mass-loss behaviour of the system, rather than being directly equated with the degree of carbothermic reduction or the rate of a single reaction.

In addition, the TG–DTG results may be affected by the properties of the pressed composite pellets, including mixing homogeneity, quartz particle-size distribution, local $CaCl_2$ distribution, pellet structure, and gas-escape pathways. Since one TG–DTG test was performed for each $CaCl_2$ addition level, the present results should be interpreted as representative trends under the present experimental conditions rather than as statistically validated differences. Therefore, the comparison among different $CaCl_2$ additions is used mainly to discuss the overall response of the system, and small differences between neighbouring additions should be interpreted with caution.

3.4 Thermodynamic analysis of liquid- and gas-phase evolution

FactSage was used to calculate the equilibrium liquid- and gas-phase evolution of the SiO_2–C–$CaCl_2$ system under Ar in order to analyse the relationship between high-temperature phase changes and the experimental mass-loss behaviour after $CaCl_2$ addition. FactSage equilibrium calculations are based on thermodynamic databases and Gibbs-free-energy minimization, and can be used to predict equilibrium phase-composition changes in high-temperature multiphase systems under specified composition, temperature, and pressure conditions (Bale et al., 2016). The calculation results reflect thermodynamic equilibrium trends rather than the

actual kinetic process during heating, which is jointly controlled by mass transfer, interfacial reactions, and volatilization. The equilibrium liquid-phase evolution at different $CaCl_2$ additions is shown in Figure 8. Enlarged views of 1670–1720 °C are included in Figures 8(b) and 8(c) to highlight the shift of the rapid liquid-phase growth region from approximately 1720 °C in the additive-free system to approximately 1690 °C in the $CaCl_2$-containing systems.

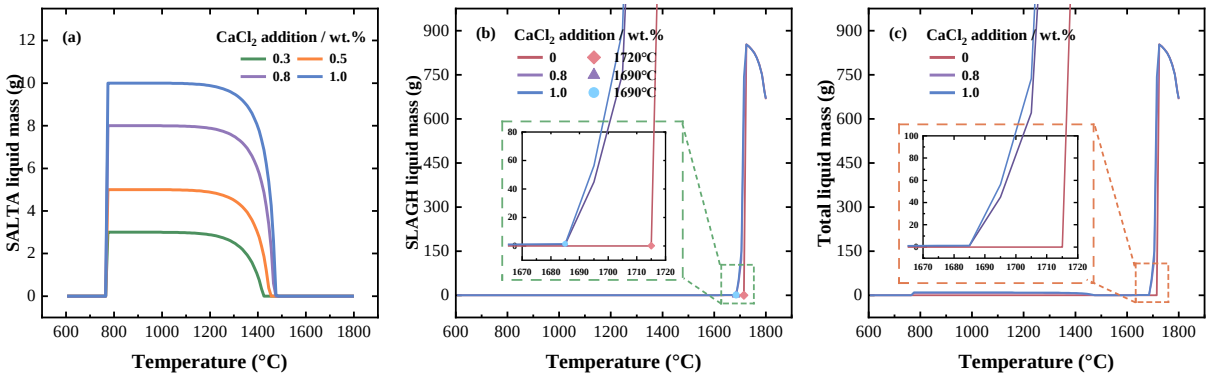

Figure 8: Equilibrium liquid-phase evolution in the SiO_2–C–$CaCl_2$ system: (a) SALTA liquid salt phase; (b) SLAGH liquid slag phase with an enlarged view of 1670–1720 °C; and (c) total liquid phase with an enlarged view of 1670–1720 °C. The y-axis represents the calculated phase mass in grams based on the FactSage input basis.

Figure 8(a) shows that the $CaCl_2$-containing systems began to form a liquid salt at about 770 °C and reached the maximum mass near 775 °C. As the $CaCl_2$ addition increased, the maximum mass of the liquid salt also increased, indicating that $CaCl_2$ first affected the liquid salt composition in the lower-temperature stage. Phase-equilibrium studies of SiO_2–$CaCl_2$ and CaO–SiO_2–$CaCl_2$ systems have shown that $CaCl_2$ addition can change the liquid-phase formation conditions in SiO_2-containing systems (Wang and Morita, 2016). Therefore, the low-temperature liquid salt formation trend calculated in this study is consistent with existing understanding of liquid-phase behaviour in $CaCl_2$-containing silicate systems.

With further increase in temperature, the liquid salt gradually decreased, and the high-temperature liquid-phase evolution became controlled by the liquid slag. As shown in Figure 8(b), especially in the enlarged view, the liquid slag phase in the additive-free system began to increase rapidly near 1720 °C. After $CaCl_2$ addition, the region of pronounced growth shifted to about 1690 °C. The calculation results show that $CaCl_2$ lowered by 30 °C the characteristic temperature at which a large amount of SiO_2 entered the liquid slag. Thus, its effect was not limited to formation of the low-temperature liquid salt, but also included an earlier growth stage of the high-temperature liquid slag.

Figure 8(c) shows that the total liquid phase in the additive-free system mainly increased rapidly after about 1720 °C with the formation of the liquid slag phase. The enlarged view further shows that $CaCl_2$ addition shifted the onset of rapid total-liquid growth to a lower temperature, close to 1690 °C, consistent with the trend observed for the liquid slag phase in Figure 8(b). In contrast, the $CaCl_2$-containing systems exhibited a two-stage evolution feature involving low-temperature liquid salt formation and earlier growth of the high-temperature liquid slag. Because the difference in total liquid mass among the systems was small at high temperature, the role of $CaCl_2$ was mainly reflected in the liquid-formation path and the temperature region of rapid liquid growth, rather than in a marked increase in the final total liquid mass. This trend is consistent with the experimental decrease in T_S and T_H with increasing $CaCl_2$ addition.

The experimental and calculated results are consistent in trend, although the corresponding temperature values are not identical. The high-temperature melting experiments were performed in the carbon-free SiO_2–$CaCl_2$ system, and T_S and T_H describe the macroscopic

response of the specimen when obvious softening and a nearly hemispherical morphology appear. The FactSage calculations were performed for the carbon-containing SiO_2–C–$CaCl_2$ system, and the characteristic temperature range reflects the pronounced growth of the liquid slag under equilibrium conditions. Formation of equilibrium species such as SiC, CO, and SiO in the carbon-containing system changes the consumption path of SiO_2 and the stability range of the liquid phase. In addition, minor impurities in the actual specimen, contact with the graphite substrate, and non-equilibrium spreading and mass-transfer processes may also affect the macroscopic morphological transition temperature. Therefore, the calculation results are used to explain the experimental trend and the direction of liquid-phase evolution, rather than for direct numerical correspondence with T_S or T_H.

It has been reported that molten $CaCl_2$ can participate in the dissolution of calcium silicates and allow silicate species to migrate in the molten-salt medium (Cheng and Yang, 2023). Combined with the present calculations, the formation of low-temperature liquid salt and the forward shift of the liquid slag growth region may change the migration conditions of silicon-containing species at local interfaces. Because intermediate chlorine-containing silicate species or interfacial reaction layers were not directly identified in this study, this analysis should be regarded as a reasonable interpretation of the relationship between liquid-phase evolution and macroscopic high-temperature behaviour, rather than direct proof of specific reaction phases or mass-transfer mechanisms.

On the basis of the liquid-phase evolution analysis, the equilibrium generation of CO and SiO at different $CaCl_2$ additions was compared to further analyse the relationship between mass-loss behaviour during heating in the TG–DTG curves and gas generation related to carbothermic reduction. The results are shown in Figure 9.

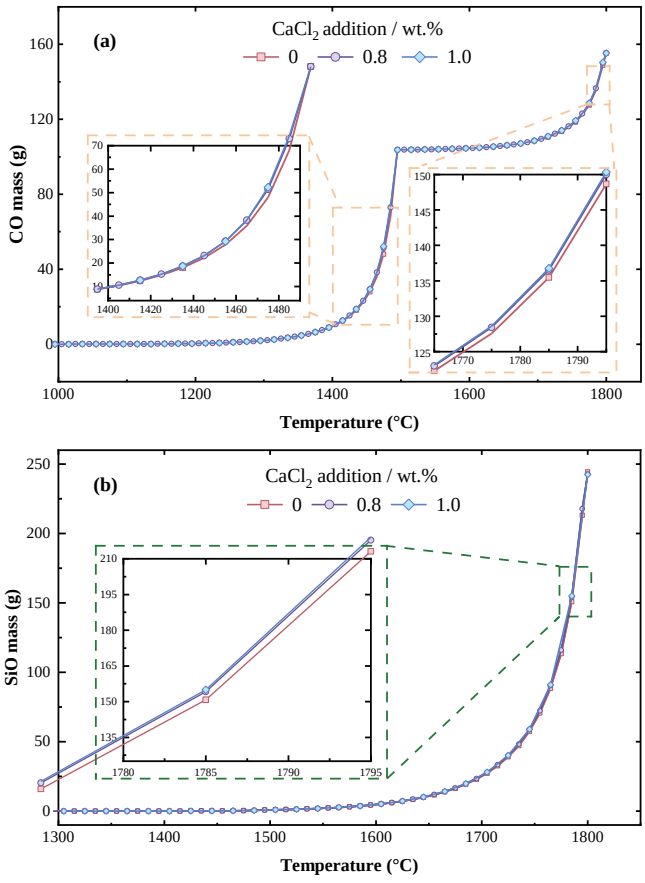

Figure 9: Equilibrium generation behaviour of CO and SiO: (a) CO; and (b) SiO. The insets show enlarged views

Figures 9(a) and 9(b) show that the overall calculated evolution curves of CO and SiO were similar among the different systems, indicating that $CaCl_2$ addition did not markedly change the overall equilibrium generation window of the two major gaseous species. Figure 9(a) shows that the equilibrium CO amount increased in stages with temperature. Enlarged views of the temperature region corresponding to the mass-loss process during heating in the TG–DTG curves show that the equilibrium CO amount in the $CaCl_2$-containing systems was slightly higher than that in the additive-free system. This indicates that $CaCl_2$ may increase the equilibrium tendency for CO-related gas generation in this temperature region. This change is related to the shift of the mass-loss process to lower temperature in the thermogravimetric experiment. However, because the initial equilibrium generation region of CO did not change significantly with $CaCl_2$ addition, the earlier appearance of the mass-loss process in TG–DTG cannot be simply attributed to a decrease in the thermodynamic generation onset of CO. Figure 9(b) shows that SiO increased rapidly mainly in the higher-temperature region. The enlarged view shows that the equilibrium SiO amount in the $CaCl_2$-containing systems was slightly higher than that in the additive-free system during the high-temperature rapid-growth stage, but the differences among the addition levels were small. This result suggests that $CaCl_2$ may have some effect on the SiO generation tendency in the later high-temperature stage, but this effect alone is insufficient to explain all changes in the concentrated mass-loss behaviour observed by TG–DTG.

Combining the TG–DTG experiment with gas-phase equilibrium calculations, the mass-loss process during heating occurred earlier after $CaCl_2$ addition, whereas the initial equilibrium generation regions of CO and SiO did not change markedly. This indicates that the earlier experimental mass loss was not caused by a direct decrease in the thermodynamic generation onset of the relevant gaseous products, but was more likely related to liquid-phase evolution induced by $CaCl_2$. Together with the formation of liquid salt and the shift of the liquid slag growth region shown in Figure 8, $CaCl_2$ may improve interfacial contact and apparent spreading conditions in the actual sample, thereby facilitating local mass transfer and allowing mass loss associated with CO and SiO generation to occur at lower temperature.

Compared with the small differences observed in the CO and SiO curves, the chlorine-containing gaseous species showed a more pronounced response to $CaCl_2$ addition. Their equilibrium evolution is shown in Figure 10.

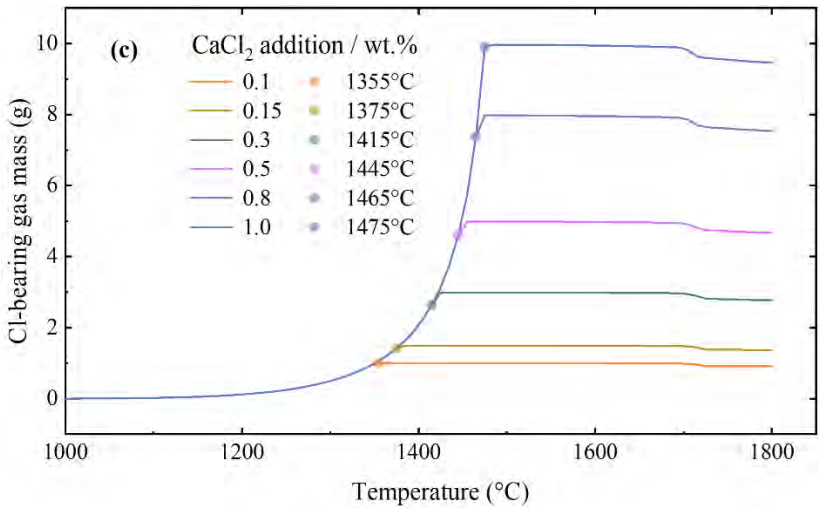

Figure 10: Equilibrium evolution of the total mass of chlorine-containing gaseous species

The chlorine-containing gas mainly formed rapidly in the range of 1355–1475 °C. The 0.8 and 1.0 wt.% $CaCl_2$ systems both reached their maximum values near 1485 °C, with maximum

masses of 7.98 and 9.97 g, corresponding to approximately 0.595% and 0.742% of the total system mass, respectively. This indicates that, with increasing $CaCl_2$ addition, the tendency of chlorine-containing components to volatilize into the gas phase during heating became stronger. To further compare the difference between the theoretical mass loss from the main carbothermic reactions and the experimental stage-wise mass loss, the results are listed in Table V.

Table V: Comparison between stage-wise theoretical mass loss and TG-measured mass loss

$CaCl_2$ addition / wt.%	Stage I theoretical mass loss / %	Stage I measured mass loss / %	Stage II theoretical mass loss / %	Stage II measured mass loss / %
0	9.71	9.95	27.79	16.46
0.1	9.70	11.54	27.76	21.95
0.5	9.66	12.05	27.65	21.82
0.8	9.64	14.76	27.57	24.75
1.0	9.62	12.17	27.51	30.80

Based on the stage-wise mass-loss regions defined in Figure 7 and the main reaction paths represented by Equations [1] and [2], Table V compares the stage-wise theoretical mass losses and TG-measured mass losses at different $CaCl_2$ additions. The theoretical values consider only the mass loss caused by the main SiO_2–C reaction paths and do not include $CaCl_2$ volatilization or the formation of other chlorine-containing gaseous species.

In Stage I, the measured mass loss of the 0.8 wt.% $CaCl_2$ sample was 14.76%, higher than 12.17% for the 1.0 wt.% sample. This agrees with the highest maximum mass-loss rate observed for the 0.8 wt.% sample in the TG–DTG curves, indicating that an appropriate $CaCl_2$ addition is more favourable for the concentrated mass-loss process during heating.

In Stage II, the measured mass loss of the 1.0 wt.% $CaCl_2$ sample reached 30.80%, higher than its theoretical value of 27.51%. In combination with Table IV, the final measured mass losses of the 0.8 and 1.0 wt.% samples were higher than the two-stage total theoretical mass losses by 2.30 and 5.84 percentage points, respectively, with the larger deviation occurring for the 1.0 wt.% sample. This trend is consistent with the increase in chlorine-containing gas mass with $CaCl_2$ addition in Figure 10, indicating that the final mass loss of high-addition samples may include not only gas release related to the SiO_2–C reactions, but also additional mass loss caused by volatilization of chlorine-containing components.

However, the part of the experimental mass loss exceeding the theoretical mass loss cannot be fully attributed to chlorine-containing gas. The FactSage results reflect the gas composition trend under equilibrium conditions, whereas the TG test records cumulative mass loss during actual heating and holding. The experimental mass loss is also affected by liquid formation, interfacial contact, gas escape, and non-equilibrium mass transfer. Therefore, the higher final mass loss of the 1.0 wt.% $CaCl_2$ sample indicates only a larger cumulative mass loss and does not demonstrate a higher degree of carbothermic reduction than that of the 0.8 wt.% sample.

In summary, the effect of $CaCl_2$ on the mass-loss behaviour of the SiO_2–C system is not controlled by a single factor. The formation of low-temperature liquid salt and the forward shift of the high-temperature liquid slag growth region may improve interparticle contact and local mass-transfer conditions, thereby allowing the concentrated mass-loss behaviour during heating to occur earlier and become enhanced. At the same time, the mass of chlorine-containing gas increased with $CaCl_2$ addition, indicating that the increase in cumulative mass loss in high-addition samples may include additive-related volatilization. Thus, 0.8 wt.% $CaCl_2$ was more favourable for increasing the concentrated mass-loss rate, whereas the higher final mass loss of the 1.0 wt.% sample cannot be interpreted directly as a further increase in

carbothermic reduction degree. The detailed mechanism responsible for the weakened rate gain at higher addition still requires further verification based on post-reaction phase analysis, interfacial microstructure, and analysis of evolved or condensed products.

4. CONCLUSIONS

This study investigated the effect of $CaCl_2$ addition on the high-temperature softening and melting behaviour of high-purity quartz, the mass-loss characteristics of the SiO_2–C system, and equilibrium liquid- and gas-phase evolution. The main conclusions are as follows:

(1) $CaCl_2$ effectively lowered the characteristic high-temperature softening and melting temperatures of quartz. As the $CaCl_2$ addition increased from 0 to 1.0 wt.%, the softening temperature T_S decreased from 1798 °C to 1745 °C, and the hemispherical temperature T_H decreased from 1836 °C to 1776 °C, corresponding to decreases of 53 °C and 60 °C, respectively. This indicates that $CaCl_2$ markedly changed the high-temperature morphological evolution of quartz.

(2) $CaCl_2$ addition changed the mass-loss behaviour of the SiO_2–C system. Within the present range, the 0.8 wt.% $CaCl_2$ sample reached a maximum mass-loss rate of 2.90 % $\cdot min^{-1}$, markedly higher than 1.48 % $\cdot min^{-1}$ for the additive-free sample. When the addition increased to 1.0 wt.%, the final mass loss further increased to 42.97%, but the maximum mass-loss rate decreased to 2.08 % $\cdot min^{-1}$. This shows that $CaCl_2$ can increase the cumulative mass loss of the system, but its promoting effect on the mass-loss rate does not continuously increase with addition.

(3) FactSage equilibrium calculations showed that $CaCl_2$ changed the liquid-phase evolution path. In the $CaCl_2$-containing system, the liquid salt mainly existed at approximately 770–1550 °C. At high temperature, $CaCl_2$ lowered the characteristic temperature at which a large amount of SiO_2 entered the liquid slag from 1720 °C in the additive-free system to 1690 °C. This liquid-phase evolution trend corresponds to the decrease in T_S and T_H observed experimentally, indicating that changes in the liquid-formation path may be an important thermodynamic factor for earlier softening and melting of quartz.

(4) Gas-phase equilibrium calculations showed that $CaCl_2$ addition did not markedly change the overall equilibrium generation windows of CO and SiO. However, the equilibrium amounts of CO and SiO in the $CaCl_2$-containing systems were slightly higher in some stage-specific growth regions. In contrast, the total mass of chlorine-containing gaseous species increased markedly with $CaCl_2$ addition. Combined with the comparison between stage-wise theoretical mass loss and TG-measured mass loss, the increase in cumulative mass loss in high-addition samples may include not only gas release related to SiO_2–C reactions, but also additive-related volatilization. Therefore, the higher final mass loss of the 1.0 wt.% $CaCl_2$ sample does not directly indicate a higher degree of carbothermic reduction than that of the 0.8 wt.% sample.

From an industrial perspective, the present results indicate that low-level $CaCl_2$ addition can modify the softening behaviour of quartz and the mass-loss behaviour of SiO_2–C mixtures under silicon-production-related conditions. The non-monotonic response of the maximum mass-loss rate suggests that increasing $CaCl_2$ addition does not necessarily lead to continuous improvement. Excessive addition may increase chloride-related volatilization and should therefore be controlled carefully. Thus, $CaCl_2$ may be considered as a low-level process-adjusting additive, but its application should consider raw-material variability, burden permeability, gas escape, and possible chlorine-containing emissions.

Overall, within the present experimental range, 0.8 wt.% $CaCl_2$ gave the highest maximum mass-loss rate in the SiO_2–C system. The role of $CaCl_2$ is associated with its induction of liquid salt formation, promotion of high-temperature slag-liquid evolution, and influence on high-temperature gas release behaviour. The detailed mechanism behind the weakened rate gain at higher addition still requires further verification through post-reaction phase analysis, interfacial microstructure characterization, and quantitative analysis of volatile components.

5. REFERENCES

Bale C.W., Bélisle E., Chartrand P., Decterov S.A., Eriksson G., Gheribi A.E., Hack K., Jung I.-H., Kang Y.-B., Melançon J., Pelton A.D., Petersen S., Robelin C., Sangster J., Spencer P., and Van Ende M.-A. 2016. FactSage thermochemical software and databases, 2010–2016. *Calphad*, Vol.54, pp.35–53.

Cheng X. and Yang X. 2023. Dissolution of calcium silicates in molten $CaCl_2$. *Metallurgical and Materials Transactions B*, Vol.54, pp.192–202.

Folstad M.B., Ringdalen E., Tveit H., and Tangstad M. 2021. Effect of different SiO_2 polymorphs on the reaction between SiO2 and SiC in Si production. Metallurgical and Materials Transactions B, Vol.52, pp.792–803.

Li F. and Tangstad M. 2018. Kinetic modeling of the reaction rate for quartz and carbon black pellet. Metallurgical and Materials Transactions B, Vol.49, pp.1101–1108.

Li F., Tangstad M., and Ringdalen E. 2018. Carbothermal reduction of quartz and carbon pellets at elevated temperatures. *Metallurgical and Materials Transactions B*, Vol.49, pp.1078–1088.

Metherall B., Breward C.J.W., Please C.P., and Lacey A.A. 2023. Modelling the reduction of quartz in a quartz–carbon pellet. *Journal of Engineering Mathematics*, Vol.141, Article 4.

Ringdalen E. 2015. Changes in quartz during heating and the possible effects on Si production. *JOM*, Vol.67, pp.484–492.

Ringdalen E. and Tangstad M. 2012. Reaction mechanisms in carbothermic production of silicon: Study of selected reactions. In: International Smelting Technology Symposium. Hoboken: John Wiley & Sons, pp.195–204.

Ringdalen E. and Tangstad M. 2016. Softening and melting of SiO2, an important parameter for reactions with quartz in Si production. In: Reddy R.G., Chaubal P., Pistorius P.C., and Pal U., eds. *Advances in Molten Slags, Fluxes, and Salts: Proceedings of the 10th International Conference on Molten Slags, Fluxes and Salts 2016.* Cham: Springer, pp.43–51.
https://doi.org/10.1007/978-3-319-48769-4_4

Schei A., Tuset J.K., and Tveit H. 1998. Production of High Silicon Alloys. Trondheim: Tapir Forlag.

Sindland C. and Tangstad M. 2021. Production rate of SiO gas from industrial quartz and silicon. Metallurgical and Materials Transactions B, Vol.52, pp.1755–1771.

Tian J., Wei K., Deng X., Liu Y., and Ma W. 2024. A study of the effect of quartz-to-cristobalite transformation on SiC generation in metallurgical-grade silicon production. Silicon, Vol.16, pp.3155–3164.

U.S. Geological Survey. 2025. *Mineral Commodity Summaries 2025: Silicon.* Reston, VA: U.S. Geological Survey, pp.160–161.
https://pubs.usgs.gov/periodicals/mcs2025/mcs2025-silicon.pdf

Wang Y. and Morita K. 2016. Measurement of the phase diagram of the SiO_2–$CaCl_2$ system and liquid area study of the SiO_2–CaO–$CaCl_2$ system. *Metallurgical and Materials Transactions B*, Vol.47, pp.1542–1547.

Zhou S., Chen Z., Ma W., Li S., and Zhao Y. 2020. Effect of K_2CO_3 as an additive agent on the carbothermic reduction process of silicon production. *Silicon*, Vol.12, pp.1575–1584.

Fei Li

Associate Professor, Lanzhou University of Technology

Received a Ph.D. degree from the Norwegian University of Science and Technology in 2017. The main research interests include industrial silicon and silicon-based ferroalloy smelting, silicon functional materials, and solid waste recycling. Current work focuses on reaction mechanisms, process optimization, and sustainable utilization of silicon resources and industrial solid wastes.

Lo Biundo, P. L. Z., W., M. Wallin, and M. Tangstad. 2026. Ferrosilicon Alloys for High-Temperature Latent Heat Thermal Energy Storage: Thermophysical Properties and Containment Strategies. In *Silicon for the chemical and solar industry XVIII*, edited by M. Tangstad, H. Rong, A. Valderhaug, B. Andresen, H. Dalaker, and I. G. Page. Kristiansand, Norway, September 7–10, 2026.
https://doi.org/10.55669/oa900831

Ferrosilicon Alloys for High-Temperature Latent Heat Thermal Energy Storage: Thermophysical Properties and Containment Strategies

P.L.Z. Lo Biundo[1*], Wojciech Polkowski[1], Maria Wallin[1], Merete Tangstad[1]
[1]Department of Materials Science and Engineering, Norwegian University of Science and Technology, Norway, paolo.l.z.l.biundo@ntnu.no

Keywords: Ferrosilicon, Silicon Carbide, Wetting, Phase Change Materials (PCM), Latent Heat Energy Storage (LHTES), Refractory Corrosion

Abstract – Latent Heat Thermal Energy Storage (LHTES) based on metallic Phase Change Materials (PCMs) represents a promising solution. Among these materials, ferrosilicon (FeSi) alloys stand out due to their exceptionally high volumetric latent heat, exceeding 1 MWh/m^3, and their ability to operate at temperatures far above those of conventional LHTES systems. Such high temperature operation enables higher theoretical Carnot efficiencies and supports emerging solid state thermophotovoltaic (TPV) concepts, a framework currently being explored within the EU-funded SUNSON project.

This work evaluates the thermophysical properties of available PCMs with a particular focus on the FeSi system and its ternary derivatives zfor high-temperature PCM applications. Attention is given to near-eutectic compositions such as FeSi57 (57 wt% Si), which exhibit a narrow phase transition temperature range of less than 50 °C. Key parameters governing PCM performance, including working temperature, latent heat and density are reported.

A critical challenge in the industrial application of metallic PCMs is the containment of highly reactive liquid phases. Graphite is an attractive and cost-effective refractory option, but its interaction with molten silicon introduces both challenges and potential advantages. This review synthesizes current research on the thermodynamic stability of the resulting silicon carbide (SiC) layer and its potential to act as a self-passivating barrier. The performance of ceramic-coated graphite systems is compared against established non-reactive containment materials used in the silicon industry, such as Si_3N_4 and BN, along with emerging approaches such as microencapsulation.

Overall, Fe–Si-based alloys combined with optimized containment strategies, such as BN-coated graphite represent a promising route toward scalable high temperature thermal energy storage systems.

1. INTRODUCTION

The transition toward renewable energy sources such as solar and wind is essential for reducing greenhouse-gas emissions and achieving a decarbonized energy system. However, the intermittent character of these resources creates a persistent mismatch between energy generation and energy demand. Reliable and scalable energy storage is therefore required if large fractions of renewable electricity are to be integrated into future energy systems (Ramos et al., 2022). Thermal Energy Storage (TES) is one of the main technological pathways to address this challenge because excess electricity or heat can be stored as thermal energy and later returned to the process or converted back into power when required.
Within TES, Latent Heat Thermal Energy Storage (LHTES) has attracted considerable attention because it exploits the enthalpy of phase transformation in a phase change material (PCM) (Fatahi et al., 2022; Imran Khan et al., 2023; Jiao et al., 2023). In comparison with sensible heat

This work is licensed under the Creative Commons Attribution 4.0 International License. To view a copy of this license, visit https://creativecommons.org/licenses/by/4.0/

storage, LHTES offers higher energy density and a comparatively narrow operating temperature interval during charging and discharging.

To maximize energy conversion efficiencies and energy density, recent advancements have focused on high temperature LHTES systems operating well beyond 1000 °C. At these temperatures, the stored heat can be efficiently converted back into electricity on demand using thermophotovoltaic (TPV) energy converters. TPV devices are advanced solid-state converters that produce electricity directly from the radiant heat (photons) emitted by the high-temperature storage system. Because they lack moving parts, are compact, and are perfectly suited for high temperatures, TPV systems represent a highly promising heat-to-power conversion technology for high temperature LHTES applications (Datas et al., 2022).

The selection of a suitable PCM for this temperature range is, however, far from trivial. Organic PCMs, salt hydrates, and many common inorganic storage media are either thermally unstable or chemically unsuitable above approximately 1000 °C. As a consequence, attention has shifted toward refractory salts, oxides, and metallic or metalloid systems (Fernández et al., 2017; Imran Khan et al., 2023; Zhao et al., 2020). Among the latter, silicon-rich alloys stand out because silicon has a very high latent heat of fusion, high thermal conductivity, and a melting point that overlaps well with high temperature storage targets.

In this context, Fe–Si-based alloys have emerged as especially promising candidates. By alloying silicon with iron, the volumetric latent heat can remain high while the density increases and the severe expansion of pure silicon on solidification can be partly mitigated. Near-eutectic Fe–Si compositions also exhibit relatively narrow melting intervals, which is advantageous for LHTES operation. At the same time, the containment problem remains a central bottleneck, because molten Si-rich alloys react with most refractory materials, can infiltrate porous substrates, and may cause rapid vessel degradation (Imran Khan et al., 2023; Jiao et al., 2022; Ma et al., 2014; Zhao et al., 2020).

The present paper therefore reviews two tightly coupled topics: the thermophysical properties of Fe–Si-based high-temperature PCMs and the containment strategies required for their practical implementation. Particular emphasis is placed on FeSi57 and related Fe–Si–B, Fe–Si–Mn, and Fe–Si–Cr alloys, as well as on the role of graphite, SiC, Si_3N_4, and BN as candidate containment materials.

2. Thermophysical Properties of PCMs

2.1 Selection criteria for phase change materials

The criteria traditionally used to assess low-temperature PCMs (Abhat, 1983) remain highly relevant at high temperature, although additional constraints arise from the operating environment (Fernández et al., 2017; Imran Khan et al., 2023; Zhao et al., 2020).

Thermodynamic criteria

- The PCM should have a melting point within the desired operating temperature range. For FeSi-based PCMs intended for use in thermophotovoltaic systems, the ideal temperature range is approximately 1200 °C or higher (Datas et al., 2025).
- High latent heat is required to achieve high energy density. In this work, PCM performance is evaluated on a volumetric basis rather than a gravimetric one (Fernández et al., 2017).

- A high specific heat capacity is also beneficial, as it increases the total amount of energy that can be stored.
- High thermal conductivity is important in order to minimize temperature gradients during charging and discharging.
- Congruent melting is desirable so that the solid and liquid phases have the same composition, thereby avoiding segregation and changes in melting behaviour during cycling.
- Small volume changes during the phase transition are important in order to minimize mechanical stress on the containment vessel. This is a particularly critical property for silicon-rich systems, as silicon can expand by up to 9% upon solidification.

Kinetic criteria

- Supercooling during solidification should be avoided; otherwise, the operating temperature may vary from cycle to cycle.

Chemical criteria

- The material should be chemically stable under the intended operating conditions.
- It should not react with or corrode the containment vessel, as containment remains one of the main challenges for high-temperature metallic PCMs (Imran Khan et al., 2023; Jiao et al., 2022; Ma et al., 2014; Zhao et al., 2020).
- It should possess low volatility at operating temperatures to prevent excessive vapor pressure so the PCM does not evaporate or increase the mechanical stress in a closed system.
- If possible, the material should also be non-toxic, non-flammable, and non-explosive.

Economic criteria are also undoubtedly important, but these will not be further discussed here.

2.2 Candidate high temperature PCMs

In the LHTES literature, temperatures of 600–700 °C are often classified as high temperature (Imran Khan et al., 2023; Jayathunga et al., 2024; Prieto et al., 2022; Yang et al., 2025), since conventional steam turbines for power generation typically have upper operating limit of around 700 °C (Nomoto, 2017; Wright et al., 2004). Temperatures above 1000 °C, however, are generally classified as ultra-high temperature (UHT) and pose substantially greater challenges in terms of materials stability and system design. Under these conditions, many conventional PCMs, such as organic paraffins, fatty acids, and salt hydrates, become thermally unstable. Consequently, candidate materials are largely limited to inorganic salts, oxides, and metallic systems.

Salts and oxides

Table I reports a list of salts and oxides that have melting points above 1000 °C and high latent heat, making them possible candidates as PCM. Fluoride salts are frequently discussed for high-temperature TES because the strong ionic bonding associated with fluorine leads to relatively high melting points and substantial latent heat (Misra, 1988). Nevertheless, toxicity, corrosivity, and materials compatibility remain important drawbacks. Oxides and silicates are often chemically stable and in some cases inexpensive, but many exhibit lower effective thermal conductivity and can form viscous liquids or glassy phases that complicate heat transfer and cycling. Metallic and metalloid PCMs, by contrast, offer rather higher thermal conductivity and can be tuned over a wide temperature range, but they are highly corrosive and present containment challenges in the molten state.

Table I. Inorganic oxides and salts PCM candidates with working temperature above 1000 °C reported in the literature.

PCM Composition	Melting Point	Gravimetric Latent Heat	Solid Density	Volumetric Latent Heat
	°C	J/g	g/cm³	kWh/m³
Magnesium Fluoride (MgF_2) **(Allison, 2013; Cárdenas and León, 2013)**	1263	938-942	3.15	821-824
Calcium Fluoride (CaF_2)**(Allison, 2013; Cárdenas and León, 2013)**	1418	380-391	3.18	336-345
Barium Fluoride (BaF_2)**(Allison, 2013; Cárdenas and León, 2013)**	1320-1368	119-133	4.89	162-181
Strontium Fluoride (SrF_2) **(Allison, 2013; Cárdenas and León, 2013)**	1440-1477	231-236	4.24	272-278
Sodium Metasilicate (Na_2SiO_3)**(Allison, 2013; Cárdenas and León, 2013)**	1088	424	1.749	206
Beryllium Oxide (BeO)**(Allison, 2013; Batutis, 1961)**	2548	3160	3.01	2642

Magnesium fluoride is one of the most promising fluoride candidates as shown in table I because of its combination of high latent heat and melting point. In literature it often appears in several eutectic formulations, reducing the working temperature to below 1000 °C while maintaining substantial storage density (Birchenall and Riechman, 1980; Imran Khan et al., 2023; Kenisarin, 2010; Misra, 1988). However, additional work is still required to validate its long-term cycling stability and containment compatibility under realistic TES conditions.
Among oxides , although some compounds have high melting point, they usually possess low gravimetric latent heat under 200 J/g and densities below 5 g/cm3 (Cárdenas and León, 2013), and may produce highly viscous melts with poor heat-transfer characteristics. Sodium metasilicate has a melting point and latent heat that make it conceptually relevant as a PCM, but translating slags or slag-like systems into practical latent-heat media remains difficult because of low thermal conductivity, glass formation, and complex melting behavior. Beryllium oxide has excellent thermophysical properties (Batutis, 1961) but is included only for completeness because its toxicity makes it unsuitable for practical implementation in addition to its very high melting temperature.

Metallic or metalloid PCM
Metallic PCMs have always been an interesting but extremely challenging system: they can be virtually engineered for any working temperature, they crystallize naturally very easily, they

have high thermal conductivity. On the other hand, molten metals are very reactive, especially with oxygen and the containing vessel.
Table II presents a list of potential PCMs. The containment will be discussed in the next section of this work.

Table II. Representative metallic and metalloid high temperature PCM candidates reported in the literature.

PCM Composition	**Melting Point**	**Gravimetric Latent Heat**	**Solid Density**	**Volumetric Latent Heat**
	°C	**J/g**	**g/cm³**	**KWh/m³**
Silicon (Si)(Homa and Sobczak, 2019; Jiao et al., 2019; Olesinski and Abbaschian, 1984)	1414	~1800	2.330	1150
Boron (B)(Allison, 2013; Olesinski and Abbaschian, 1984)	2077-2092	4644	2.080	2683
Copper (Cu)(Allison, 2013; Sheng et al., 2022)	1063-1085	207 - 210	8.960	514
Si-3.25B (Datas et al., 2020)	1389	1069 - 1853	2.300	693 - 1205
FeSi57 (Lo Biundo et al., 2025a)	1213	930	4.067	1050
Fe-26Si-9B (Polkowski et al., 2025b)	1196 - 1264	834	4.422 (liquid)	1020
Fe-46Si-5B (Polkowski et al., 2025b)	1173 - 1196	960	3.800 (liquid)	1064

Among metallic PCMs, pure silicon is an ideal high temperature storage PCM. At 1414 °C, silicon transforms from a diamond FCC crystal structure to a liquid with metallic character (Eustathopoulos et al., 1999) and exhibits a latent heat of fusion of approximately 1800 J g^{-1}. Despite its moderate density relative to other metals such as iron or copper, its volumetric latent heat remains around 1000–1150 kWh m^{-3}, which is high for a single-component PCM (Datas et al., 2018; Homa and Sobczak, 2019). Silicon is also attractive because both the solid

and liquid phases have comparatively high thermal conductivity, to the extent that molten silicon has even been proposed as a heat-transfer fluid (Amy et al., 2021).
The main drawback of pure silicon is the large volume expansion on solidification of 9%. This expansion can generate severe mechanical stress on the crucible during discharge and may cause cracking or catastrophic failure of the vessel. Alloying offers a way to reduce this problem while preserving much of the latent-heat advantage of silicon.

Boron has an even higher latent heat, reaching above 4600 J/g or 2500 kWh/m³ due to its icosahedral crystalline structure, but its melting point above 2000 °C, high cost, and difficult purification make it unattractive as a standalone.

Several transition metals have been considered as candidate PCMs because of their availability, density, and melting temperature. Among them, copper is often discussed in the literature as a possible phase change material (Datas et al., 2022; Gil et al., 2010; Li et al., 2013; Ma et al., 2014; Sheng et al., 2022). Pure copper melts at slightly above 1085 °C. Its gravimetric latent heat is relatively low, at around 210 J g^{-1}; however, its high density (approximately 8.96 g cm^{-3} in the solid state) results in a volumetric latent heat of about 514 kWh m^{-3}, corresponding to roughly half that of silicon. Copper is particularly attractive because of its excellent thermal conductivity, which supports rapid charging and discharging and enhances heat transfer from the heat source into the bulk PCM. This reduces the risk of localized overheating and helps maintain a more uniform melting front. Additionally, copper is more inert towards the surroundings, compared to many other metallic PCMs.

The Binary Fe-Si System and Near-Eutectic Compositions
When it comes to candidate metallic phase change materials (PCMs), the iron-silicon (Fe–Si) binary system stands out. Silicon provides excellent latent heat, while iron adds density and helps counteract the volume expansion issues common with pure silicon. Near congruent melting compositions are particularly of interest because they keep the phase transition in a narrow temperature range, which is a requirement for efficient latent-heat storage (Fernández et al., 2017; Zhao et al., 2020).

Looking at the Fe–Si phase diagram, most of the phase diagram in figure 1 has solidus between 1200–1400 °C reaching the temperature needed for thermophotovoltaic (TPV). FeSi57, close to the Fe3Si7 phase field, has been reported to provide an energy-storage capacity of approximately 1.05 MWh m^{-3} while operating in the 1150–1250 °C interval, together with a very small volume change on solidification (reported as approximately −0.4%) (Lo Biundo et al., 2025a). This combination of high volumetric latent heat, a narrow phase transition temperature, and almost zero volume change makes FeSi57 one of the most promising Fe–Si proposed options for high temperature LHTES.

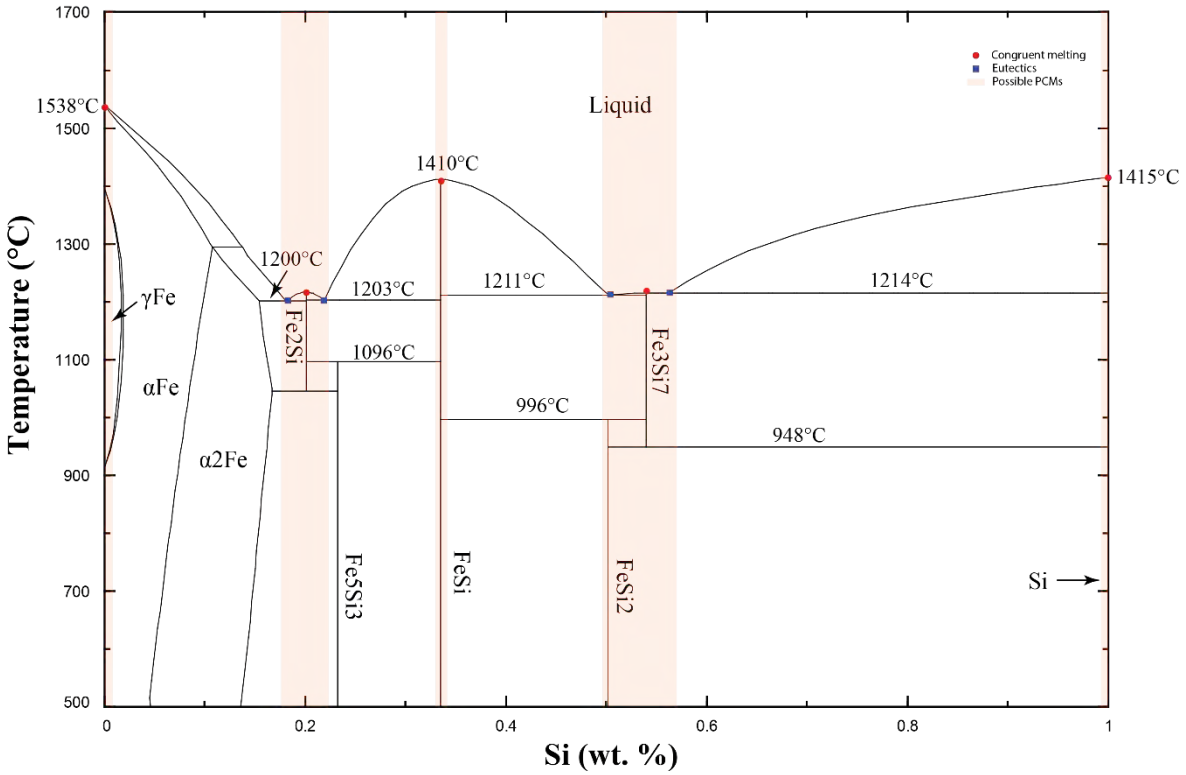

Figure 1. FeSi phase diagram calculated with FactSage. The area near the congruent melting phases and eutectic points are interesting for application as PCM since most of the energy stored is concentrated in a narrow phase transition range. **(Lo Biundo, 2026)**

Further studies have explored the addition of ternary alloying elements to the Fe-Si system to identify new PCM compositions with higher latent heat or tailored operating temperatures. The Fe-Si-B system has gained significant interest, primarily due to the intrinsically high latent heat of boron. In particular, the eutectic composition Fe-26Si-9B (wt.%) has been proposed as a viable PCM (Jiao et al., 2022), showing a latent heat of 1020 kWh/m³ (Polkowski et al., 2025b). Similarly, the Fe-46Si-5B composition has a latent heat of 1064 kWh/m³.

In addition, the Si-B system has been assessed. Its eutectic composition, Si-3.25B, undergoes a 9% volume expansion during solidification (Datas et al., 2020), posing mechanical constraints similar to pure silicon. While this expansion can be suppressed by incorporating 20 wt.% boron, such an addition shifts the liquidus temperature above 1700°C (Jiao et al., 2019).

Beyond boron, the addition of Cr, Ti, and V was calculated utilizing FactSage. These thermodynamic calculations have identified several promising ternary candidates, including Fe-24Si-11B, Fe-34Si-38Cr, Fe-34Si-43Cr, Fe-36Si-14V, Fe-34Si-10V, and Fe-38Si-20Ti. Nevertheless, empirical validation of these theoretical compositions remains to be conducted (Lo Biundo et al., 2025b).

3. Containment Strategies and Refractory Materials

Containment is one of the defining challenges for PCMs above 1000 °C and especially for metallic ones. At these temperatures, silicon rich alloys and halide salts are aggressively corrosive, dissolving, reacting and infiltrating most used materials (Mohan et al., 2019). The long term containment, along thermocycles of melting and freezing, does not depend on the stability of the PCM itself, but on the container-liquid interaction.

The important interfacial phenomena to consider are wetting, chemical reaction (thermodynamic and kinetic), interdiffusion, infiltration in pores or cracks and thermomechanical damage caused by the phase transition (Dezellus and Eustathopoulos,

2010). These effects often affect each other: a reactive melt may lower the contact angle, penetrate a porous body, form a new interfacial phase, and embrittle the container during thermal cycling due to difference in expansion. This paper will focus primarily on metallic silicon-based alloys and recent advancements in their storage technology.

3.1 Refractory metals

Refractory metals used in the aerospace industry such as molybdenum, tungsten, tantalum, and niobium are often considered for high-temperature applications because of their high melting points, mechanical strength, and fabrication potential. In fact, they are used in molten-salt systems below 1000 °C (Kenisarin, 2010). For silicon-rich PCMs and fluorides, however, refractory metals are generally unsuitable because they form silicides and fluorides without developing a passivation layer.

When molten silicon is in contact with a refractory-metal surface, compounds such as $MoSi_2$, WSi_2, or $TaSi_2$ are formed. Tests with silicon in molybdenum crucibles have shown that the metal continuously dissolves into the melt until catastrophic failure. The resulting silicide layer is not truly passivating and cannot prevent further corrosion (Batutis, 1961). For LHTES system that need to withstand thousands of cycles, refractory metals are therefore not considered viable containers for silicon-rich PCMs.

3.2. Oxide ceramics

Oxide ceramics such as silica (SiO_2), alumina (Al_2O_3), and magnesium oxide (MgO) have suitable melting temperature, but they are unfit to store the silicon based alloys. First, oxides will react to make a slag according to the reaction

$$2\underline{MeO}+Si=\underline{SiO2}+2Me$$

where the underscored oxides will form a slag and the metal will dissolve in the PCM.
Second, silicon is known to react with silica according to the equation

$$SiO_2(s) + Si(l) = 2SiO(g)$$

Due to the gas formed, in sessile drop experiments the melt is observed to "oscillate" on the substrate (Drevet and Eustathopoulos, 2012; Jiao, 2020).
The Si/MgO and the Si/Al_2O_3 systems show contact angles of respectively 88° and 86°, and react at the interface, dissolving Mg and Al in the melt and forming silica (Yuan et al., 2004). Thus, oxide ceramics are not suitable for the storage, both for a "pollution" of the melt and the generation of slag and gasses.

3.3. Non-oxide ceramics: SiC, Si_3N_4, BN and graphite

Silicon carbide (SiC)
SiC is inert when in contact with pure silicon, as carbon solubility in silicon is low, at ppm levels. According to sessile-drop studies the contact angle for Si/SiC is in the range of 30–50°, indicating good wetting(Eustathopoulos et al., 1999; Li and Hausner, 1992a). This indicates a good chemical compatibility and favors the infiltration of the melt if the substrate is too porous (Israel et al., 2010). When iron is present, the interfacial behavior depends on alloy composition. Iron-rich melts can react more actively with SiC, dissolving it into silicon and precipitating carbon., while silicon rich ones will form SiC in contact with graphite according to the Si+C=SiC equation. The equilibrium threshold depends on the temperature and SiC stability is achieved for melts above 20 wt% Si at 1200 °C or 30 wt% at 2000 °C as shown in figure 2 [To be published (Lo Biundo et al., 2026)].

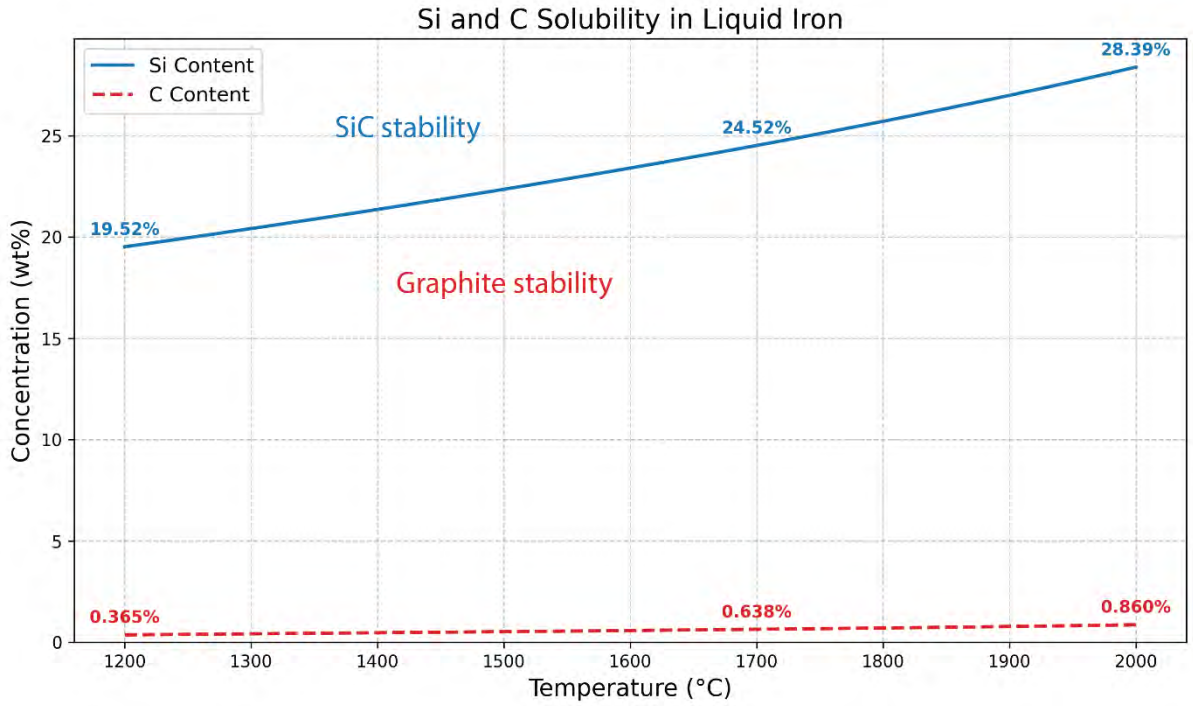

Figure 2. Calculated equilibrium concentrations in (wt%) in liquid iron on SiC substrate using FactSage. (Lo Biundo, 2026)

Silicon nitride (Si_3N_4*)*

Si_3N_4 has been used in the silicon industry because it is non-wetting toward molten silicon. While it is considered non wetting and non reactive, the performance of Si_3N_4 is highly sensitive to oxygen partial pressure and local interfacial chemistry, and complete wetting has been reported under some low-oxygen condition due to the formation of a oxynitride (SiN_xO_y) layer (Li and Hausner, 1992b), exhibiting contact angles from 90° to 40° since the layer eventually evaporates reacting forming SiO (Jiao, 2020).

The addition of boron in the PCM can change its behaviour. For boron containing alloys, higher contact angles of 143° have been reported for FeSiB/Si_3N_4, due to the formation of BN at the interfacial layer (Jiao et al., 2022). The boron nitride formed at the interface is chemically inert and non wettable, improving the barrier properties.

Boron nitride (BN)

Hexagonal BN is another important non-oxide ceramic for silicon-rich systems. For pure silicon, BN generally exhibits non-wetting behaviour, with high contact angles between 90°–145°(Polkowski et al., 2018). However, pure silicon can also dissolve BN during prolonged exposure, forming silicon borides and progressively degrading the barrier (Polkowski et al., 2018). At higher temperature and after repeated cycling, the contact angle decreases.

In boron-rich Fe–Si–B alloys, the thermodynamic driving force for BN dissolution is suppressed because the melt already contains boron (Jiao, 2020). BN is non-wetting over multiple cycles and therefore acting as an efficient barrier. Its main limitation is mechanical rather than chemical: BN is brittle and difficult to use as a standalone structural containment material on a large scale.

Graphite (C)

Graphite is an excellent refractory material, as it withstands easily high temperatures. It reacts with silicon containing melts forming SiC. The Si/SiC system is, in fact, a good description of

the reactive wetting of the Si/C system, where SiC is formed at the interface. According to (Israel et al., 2010), the infiltration of the melt into the porous structure is reaction-limited by the formation of SiC; it follows a linear trend with time and is directly related to the spreading velocity on the surface. These velocities depend heavily on the morphological features of the graphite: the total porosity, the dimension of the pores, and the degree of pore closure, with smaller, closed pores performing significantly better. The high wettability Si/SiC of the system promotes creep along the crucible walls and capillary infiltration into its pores. For this reason, a closed-pore graphite variant like isostatic graphite will perform much better, whereas extruded graphite, which is more porous and features an open-pore structure, is less suitable. Moreover, while graphite can be used because it forms an inert, self-healing SiC layer, the initial interaction involves two distinct mechanisms that alter the PCM composition. First, carbon dissolves directly into the molten PCM. Second, the graphite chemically reacts with the PCM to form the interfacial SiC layer, consuming silicon in the process.

3.4 Container design

A promising candidate as a vessel is graphite crucible coated internally with boron nitride. In this design, a thin BN layer gives the graphite non reactive and non wetting properties towards the Fe–Si melts. If the BN coating is locally damaged or scratched, the exposed graphite will react with the silicon present in the melt to form an inert SiC layer, which acts as a self-healing backup barrier and suppresses further damages. This vessel would benefit on the availability of graphite availability, price and structural strength and use BN as a layer that can last multiple cycles.

For such design to be effective, there are some requirements. First the graphite should not have open porosity, and a denser graphite generally is better at containing the melt and forming a stable SiC layer (Israel et al., 2010). Second the BN layer needs to be adherent to the substrate to postpone the degradation as much as possible during thermocycling. Third, graphite and the other ceramics discussed here are not stable in oxygen atmosphere in the intended temperature range: graphite turns into CO and CO_2 gas and so does the BN, releasing N_2 and forming B_2O_3 which has a “low” melting point of 450 °C. Si_3N_4 and SiC, on the other hand, behave much like BN, where N_2 and CO_2 volatilize, but the resulting SiO_2 oxide can protect the material from further oxidation.

Overall, a BN-coated graphite container appears to be a practical compromise between chemical resistance, mechanical robustness, machinability, and cost. Its success, however, depends on the combined optimization of graphite microstructure, BN coating quality, alloy composition, and operating atmosphere.

3.5. Encapsulation of PCMs

A prominent alternative is the encapsulation of PCM in a shell in order to have a solid material that is easier to handle and has some advantages, like a high surface to volume ratio that improves the charging and discharging and reduces stresses by thermal gradients since the beads are smaller (Imran Khan et al., 2023). An example is the Al-Si PCM growing a self healing Al_2O_3 oxide shell on the PCM droplets, making them inert and easy to use (Nomura et al., 2019) and some studies on the encapsulation of FeSi57 were done, promoting the formation of an SiO_2 layer using microsilica (Polkowski et al., 2025a).

Encapsulating the PCM eliminates direct contact between the liquid melt and containment wall, mitigating crucible corrosion issues. The resulting system behaves like a solid-state material that exhibits a spike in its “effective specific heat capacity” at the phase change temperature.

Despite these benefits, several drawbacks remain. The additional encapsulation step introduces manufacturing complexity and higher costs, while also penalizing the system's

overall latent heat capacity. Operational risks include potential particle leakage and complex manufacturing scalability. Additionally, while individual particle heat transfer can be constrained by the shell, submerging the encapsulated PCMs in a dynamic heat transfer fluid can actually boost the system's effective thermal conductivity rather than decreasing it. This topic, therefore, constitutes a research gap, where a new type of easy to handle and efficient high temperature PCM could be used.

Table III. Studies on microencapsulation of PCMs at high temperature

PCM@capsule	**Melting Point**	**Latent Heat**	**Encapsulation Mechanism**
	°C	**J/g**	
$FeSi57@SiO_2$	1229	890	Ultrasonic atomization to form spherical cores, which are subsequently coated with nano SiO2 and fired to form a layer. (Polkowski et al., 2025a)
$Cu@Al_2O_3$	1063	210	Copper powders are mixed with a CMC gel binder to form a non-densified core. This binder decomposes and leaves behind internal voids. When the copper melts, this porous medium accommodates the liquid's expansion. (Sheng et al., 2022)
Cu@Fe (FeO)	1090	24.6	This core-shell structure naturally forms through the liquid phase separation of undercooled Fe-Cu immiscible alloys during aerodynamic levitation processing. Fe rapidly oxidizes forming a protective FeO (Ma et al., 2014)
NaF@C	988	192 J/g	NaF particles are encapsulated in a resole-type phenolic resin, that then is cured and carbonised to form a carbon shell. (Jiang et al., 2022)
NaCl- Al_2O_3 @SiC@Al_2O_3	800-850	Not specified	Double-layer encapsulation where an intermediate SiC powder layer isolates the highly corrosive molten salt, and the bulk outer Al_2O_3 shell provides strength and oxygen protection (Liao et al., 2024)
Al-Si@Al_2O_3	577	273–301	Two-step fabrication involving a boehmite treatment (boiling) and high-temperature heat oxidation to grow a protective Al_2O_3 shell on the droplets (Nomura et al., 2019)

4. CONCLUSIONS

This work has evaluated the potential of Fe–Si-based alloys as phase change materials for ultra-high-temperature latent heat thermal energy storage, together with the associated challenges of containment and material compatibility.

Among candidate PCMs operating above 1000 °C, metallic systems offer advantages in terms of thermal conductivity and energy density. Silicon-rich materials are particularly attractive due to their exceptionally high latent heat of fusion. However, the large volume expansion of pure silicon during solidification represents a significant limitation for practical implementation.

Alloying with iron provides a solution to mitigate the volume expansion. The Fe–Si system, especially near-eutectic compositions such as Fe–57Si, combines high volumetric latent heat (~1000 kWh m^{-3}), a narrow phase transition interval, and minimal volume change. These characteristics make Fe–Si alloys among the most promising candidates for high temperature LHTES, particularly in combination with thermophotovoltaic conversion technologies.

The containment of molten silicon-rich alloys remains the primary challenge. Refractory metals are unsuitable due to continuous silicide formation, while oxide ceramics suffer from chemical reactivity leading to SiO evolution. Non-oxide ceramics offer improved performance, although each material presents limitations: SiC provides chemical stability but is highly wettable; Si_3N_4 and BN exhibit non-wetting behavior but are sensitive to environment and mechanical constraints. Graphite, while reactive, can form a passivating SiC layer that contributes to system stability.

A graphite vessel coated with boron nitride provides a combination of mechanical robustness, non-wetting behavior, and self-healing capability through SiC formation at coating defects. The biggest drawback of graphite is the need for a non-oxidizing environment.

Encapsulation strategies represent an alternative approach to avoid the melt-container interaction. Although there is active research in this field, there is a lack of technological maturity for temperatures above 1000 °C, particularly for silicon-based alloys.

Future work should focus on the coupled optimization of alloy design, interfacial stability, and container engineering to enable reliable and scalable high temperature thermal energy storage systems.

5. ACKNOWLEDGEMENTS

SUNSON project has received funding from Horizon Europe Research and Innovation Action programme under Grant Agreement No. 101083827, funded by the European Union. Views and opinions expressed are however those of the author(s) only and do not necessarily reflect those of the European Union or CINEA. Neither the European Union nor the granting authority can be held responsible for them.

6. REFERENCES

Abhat, A., 1983. Low temperature latent heat thermal energy storage: Heat storage materials. Solar Energy 30, 313–332. https://doi.org/10.1016/0038-092X(83)90186-X

Allison, T., 2013. NIST-JANAF Thermochemical Tables - SRD 13. https://doi.org/10.18434/T42S31

Amy, C., Pishahang, M., Kelsall, C.C., LaPotin, A., Henry, A., 2021. High-temperature Pumping of Silicon for Thermal Energy Grid Storage. Energy 233, 121105. https://doi.org/10.1016/j.energy.2021.121105

Batutis, E.F., 1961. Thermal Energy Storage Research and Development Program: Final Technical Report (No. 19650001220). National Aeronautics and Space Administration (NASA).
Birchenall, C.E., Riechman, A.F., 1980. Heat storage in eutectic alloys. Metallurgical Transactions A 11, 1415–1420. https://doi.org/10.1007/BF02653497
Cárdenas, B., León, N., 2013. High temperature latent heat thermal energy storage: Phase change materials, design considerations and performance enhancement techniques. Renewable and Sustainable Energy Reviews 27, 724–737. https://doi.org/10.1016/j.rser.2013.07.028
Datas, A., Bondavalli, P., Pantaleo, A.M., 2025. Embracing thermophotovoltaic electricity: Pathways to market adoption. Solar Energy Materials and Solar Cells 283, 113419. https://doi.org/10.1016/j.solmat.2025.113419
Datas, A., Cristobal, A.Belén., del Cañizo, C., Antolín, E., Beaughon, M., Nikolopoulos, N., Nikolopoulos, A., Zeneli, M., Sobczak, N., Polkowski, W., Tangstad, M., Safarian, J., Trucchi, D.M., Bellucci, A., Girolami, M., Marx, R., Bestenlehner, D., Lang, S., Vitulano, A., Sabbatella, G., Martí, A., 2018. AMADEUS: Next generation materials and solid state devices for ultra high temperature energy storage and conversion. AIP Conference Proceedings 2033, 170004. https://doi.org/10.1063/1.5067168
Datas, A., López, E., Ramos, A., Nikolopoulos, N., Nikolopoulos, A., Zeneli, M., Sobczak, N., Polkowski, W., Tangstad, M., Safarian, J., Trucchi, D.M., Bellucci, A., Girolami, M., Bestenlehner, D., Lang, S., Vitulano, A., Sabbatella, G., Cañizo, C. del, Cristobal, A.B., Martí, A., 2020. Ultra-high temperature energy storage and conversion: A review of the AMADEUS project results. AIP Conference Proceedings 2303, 190008. https://doi.org/10.1063/5.0028552
Datas, A., López-Ceballos, A., López, E., Ramos, A., Cañizo, C. del, 2022. Latent heat thermophotovoltaic batteries. Joule 6, 418–443. https://doi.org/10.1016/j.joule.2022.01.010
Dezellus, O., Eustathopoulos, N., 2010. Fundamental issues of reactive wetting by liquid metals. J Mater Sci 45, 4256–4264. https://doi.org/10.1007/s10853-009-4128-x
Drevet, B., Eustathopoulos, N., 2012. Wetting of ceramics by molten silicon and silicon alloys: a review. Journal of Materials Science 47, 8247–8260. https://doi.org/10.1007/s10853-012-6663-0
Eustathopoulos, N., Nicholas, M.G., Drevet, B., 1999. Wettability at High Temperatures. Elsevier.
Fatahi, H., Claverie, J., Poncet, S., 2022. Thermal Characterization of Phase Change Materials by Differential Scanning Calorimetry: A Review. Applied Sciences 12, 12019. https://doi.org/10.3390/app122312019
Fernández, A.I., Barreneche, C., Belusko, M., Segarra, M., Bruno, F., Cabeza, L.F., 2017. Considerations for the use of metal alloys as phase change materials for high temperature applications. Solar Energy Materials and Solar Cells 171, 275–281. https://doi.org/10.1016/j.solmat.2017.06.054
Gil, A., Medrano, M., Martorell, I., Lázaro, A., Dolado, P., Zalba, B., Cabeza, L.F., 2010. State of the art on high temperature thermal energy storage for power generation. Part 1—Concepts, materials and modellization. Renewable and Sustainable Energy Reviews 14, 31–55. https://doi.org/10.1016/j.rser.2009.07.035
Homa, M., Sobczak, N., 2019. Measurements of temperature and heat of phase transformation of pure silicon by using differential scanning calorimetry. J Therm Anal Calorim 138, 4215–4221. https://doi.org/10.1007/s10973-019-08716-5
Imran Khan, M., Asfand, F., Al-Ghamdi, S.G., 2023. Progress in research and development of phase change materials for thermal energy storage in concentrated solar power.

Applied Thermal Engineering 219, 119546. https://doi.org/10.1016/j.applthermaleng.2022.119546
Israel, R., Voytovych, R., Protsenko, P., Drevet, B., Camel, D., Eustathopoulos, N., 2010. Capillary interactions between molten silicon and porous graphite. J Mater Sci 45, 2210–2217. https://doi.org/10.1007/s10853-009-3889-6
Jayathunga, D.S., Karunathilake, H.P., Narayana, M., Witharana, S., 2024. Phase change material (PCM) candidates for latent heat thermal energy storage (LHTES) in concentrated solar power (CSP) based thermal applications - A review. Renewable and Sustainable Energy Reviews 189, 113904. https://doi.org/10.1016/j.rser.2023.113904
Jiang, Y., Wang, Q., Tian, S., Luo, Z., Wang, D., Bai, Y., Lu, W., Zhao, T., 2022. Preparation of NaF Microcapsules for High-Temperature Thermal Storage. ACS Omega 7, 24688–24694. https://doi.org/10.1021/acsomega.2c02539
Jiao, J., Jayakumari, S., Wallin, M., Tangstad, M., 2023. Graphite crucible interaction with Fe–Si–B phase change material in pilot-scale experiments. High Temperature Materials and Processes 42. https://doi.org/10.1515/htmp-2022-0288
Jiao, J., Safarian, J., Grorud, B., Tangstad, M., 2019. High Temperature Interaction of Si-B Alloys with Graphite Crucible in Thermal Energy Storage Systems. 1-20. https://doi.org/10.3390/ma13010029
Jiao, J., Safarian, J., Tangstad, M., 2022. The Use of Fe-26Si-9B Alloy as Phase Change Material in Si3N4 Container. Crystals 12. https://doi.org/10.3390/cryst12030376
Jiao, J.M., 2020. Si-based phase change materials in thermal energy storage systems (Doctoral thesis). NTNU.
Kenisarin, M.M., 2010. High-temperature phase change materials for thermal energy storage. Renewable and Sustainable Energy Reviews 14, 955–970. https://doi.org/10.1016/j.rser.2009.11.011
Li, J.G., Hausner, H., 1992a. Wetting and adhesion in liquid silicon/ceramic systems. Materials Letters 14, 329–332. https://doi.org/10.1016/0167-577X(92)90047-N
Li, J.G., Hausner, H., 1992b. Influence of oxygen partial pressure on the wetting behaviour of silicon nitride by molten silicon. Journal of the European Ceramic Society 9, 101–105. https://doi.org/10.1016/0955-2219(92)90051-E
Li, X., Wang, Hengzhi, Wang, Hui, Kim, S., Esfarjani, K., Ren, Z., Chen, G., 2013. Metallic Composites Phase-Change Materials for High-Temperature Thermal Energy Storage, in: ES2013. ASME 2013 7th International Conference on Energy Sustainability. https://doi.org/10.1115/ES2013-18395
Liao, S., Zhou, X., Chen, X., Li, Z., Yamashita, S., Zhang, C., Kita, H., 2024. Development of Macro-Encapsulated Phase-Change Material Using Composite of NaCl-Al2O3 with Characteristics of Self-Standing. Processes 12, 1123. https://doi.org/10.3390/pr12061123
Lo Biundo, P.L.Z., 2026. FeSi interaction with SiC substrates. https://doi.org/10.18710/H1SPUR
Lo Biundo, P.L.Z., Jiao, J., Wallin, M., Polkowska, A., Nowak, R., Bruzda, G., Kudyba, A., Kateusz, F., Bętkowska, A., Tangstad, M., Polkowski, W., 2025a. Thermophysical properties of eutectic Fe-57Si ultra-high-temperature metallic phase change material. Journal of Thermal Analysis and Calorimetry 150, 9903–9911. https://doi.org/10.1007/s10973-025-14332-3
Lo Biundo, P.L.Z., Polkowski, W., Jiao, J., Wallin, M., Tangstad, M., 2025b. Ferro-alloys as high temperature phase change materials. International Journal of Minerals, Metallurgy and Materials 32, 2177–2188. https://doi.org/10.1007/s12613-025-3187-6

Lo Biundo, P.L.Z., Polkowski, W., Wallin, M., Tangstad, M., 2026. High-Temperature Wetting and Interfacial Stability of FeSi Alloys on SiC: Implications for Smelting and Energy Storage Applications. Presented at the COM - Conference of Metallurgy and Materials, Springer Nature, Calgary, Canada.

Ma, B., Li, J., Xu, Z., Peng, Z., 2014. Fe-shell/Cu-core encapsulated metallic phase change materials prepared by aerodynamic levitation method. Applied Energy 132, 568–574. https://doi.org/10.1016/j.apenergy.2014.07.054

Misra, A.K., 1988. Fluoride Salts as Phase Change Materials for Thermal Energy Storage in the Temperature Range 1000–1400 K: Thermal Analysis and Heat of Fusion Measurements. Journal of The Electrochemical Society 135, 850. https://doi.org/10.1149/1.2095808

Mohan, G., Venkataraman, M.B., Coventry, J., 2019. Sensible energy storage options for concentrating solar power plants operating above 600 °C. Renewable and Sustainable Energy Reviews 107, 319–337. https://doi.org/10.1016/j.rser.2019.01.062

Nomoto, H., 2017. 12 - Development in materials for ultra-supercritical (USC) and advanced ultra-supercritical (A-USC) steam turbines, in: Tanuma, T. (Ed.), Advances in Steam Turbines for Modern Power Plants. Woodhead Publishing, pp. 263–278. https://doi.org/10.1016/B978-0-08-100314-5.00012-9

Nomura, T., Yoolerd, J., Sheng, N., Sakai, H., Hasegawa, Y., Haga, M., Akiyama, T., 2019. Al/Al2O3 core/shell microencapsulated phase change material for high-temperature applications. Solar Energy Materials and Solar Cells 193, 281–286. https://doi.org/10.1016/j.solmat.2018.12.023

Olesinski, R.W., Abbaschian, G.J., 1984. The B−Si (Boron-Silicon) system. Bulletin of Alloy Phase Diagrams 5, 478–484. https://doi.org/10.1007/BF02872900

Polkowski, W., Biundo, P.L.Z.L., Jiao, J., Wallin, M., Kalicki, B., Ciftci, J., Żrodowski, Ł., Polkowska, A., Bętkowska, A., Kateusz, F., Tangstad, M., 2025a. Micro-encapsulation of Si-Fe ultra-high temperature phase change material: Fabrication and basic energy storage properties. Results in Engineering 25, 104191. https://doi.org/10.1016/j.rineng.2025.104191

Polkowski, W., Sobczak, N., Nowak, R., Kudyba, A., Bruzda, G., Polkowska, A., Homa, M., Turalska, P., Tangstad, M., Safarian, J., Moosavi-Khoonsari, E., Datas, A., 2018. Wetting Behavior and Reactivity of Molten Silicon with h-BN Substrate at Ultrahigh Temperatures up to 1750 °C. Journal of Materials Engineering and Performance 27, 5040–5053. https://doi.org/10.1007/s11665-017-3114-8

Polkowski, W., Zhong Lo Biundo, P.L., Jiao, J., Wallin, M., Polkowska, A., Kateusz, F., Tangstad, M., 2025b. Designing new ultra-high temperature phase change materials from the Fe-Si-B system for thermal energy storage density above 1 MWh/m3. Materials & Design 260, 114958. https://doi.org/10.1016/j.matdes.2025.114958

Prieto, C., Vérez, D., Cabeza, L.F., 2022. Active Thermal Energy Storage (TES) With Phase Change Materials (PCM) for High Temperature, in: Cabeza, L.F. (Ed.), Encyclopedia of Energy Storage. Elsevier, Oxford, pp. 470–478. https://doi.org/10.1016/B978-0-12-819723-3.00100-1

Ramos, A., López, E., del Cañizo, C., Datas, A., 2022. Cost-effective ultra-high temperature latent heat thermal energy storage systems. Journal of Energy Storage 49, 104131. https://doi.org/10.1016/j.est.2022.104131

Sheng, N., Ge, Y., Guo, Y., Zhu, C., Rao, Z., 2022. Macro-encapsulated metallic phase change material over 1000 °C for high-temperature thermal storage. Solar Energy Materials and Solar Cells 239, 111655. https://doi.org/10.1016/j.solmat.2022.111655

Wright, I., Maziasz, P., Ellis, F., Gibbons, T., Woodford, D., 2004. Materials issues for turbines for operations in ultra-supercritical steam. Proceedings of the 29th Internal Conf. on Coal Utilization and Fuel Systems.

Yang, Y., Guo, X., Liu, M., Yang, H., Zou, D., 2025. Review on high-temperature macroencapsulated phase change materials: Encapsulation strategy, thermal storage system, and optimization. Journal of Energy Chemistry 104, 324–359. https://doi.org/10.1016/j.jechem.2024.12.052

Yuan, Z., Huang, W.L., Mukai, K., 2004. Wettability and reactivity of molten silicon with various substrates. Applied Physics A 78, 617–622. https://doi.org/10.1007/s00339-002-2001-8

Zhao, Y., Zhao, C.Y., Markides, C.N., Wang, H., Li, W., 2020. Medium- and high-temperature latent and thermochemical heat storage using metals and metallic compounds as heat storage media: A technical review. Applied Energy 280, 115950. https://doi.org/10.1016/j.apenergy.2020.115950

Paolo Lai Zhong Lo Biundo

PhD candidate, NTNU Norges teknisk-naturvitenskapelige universitet

Graduated in Material Science and Engineering from the Norwegian University of Science and Technology (NTNU) and Materials Engineering and Nanotechnology from Politecnico of Milan in 2023. Currently working as a Ph.D. candidate in the REM group at NTNU. The main research interests include FactSage simulations and thermophysical analysis of silicon-based phase change materials and refractory ceramics thermal energy storage.

Straum, I. L., C. Sindland, V. Andersen, and V. Myrvågnes. 2026. High-Temperature Behaviour of Quartz-Charcoal Briquettes in Metallurgical Silicon Production. In *Silicon for the chemical and solar industry XVIII,* edited by M. Tangstad, H. Rong, A. Valderhaug, B. Andresen, H. Dalaker, and I. G. Page. Kristiansand, Norway, September 7–10, 2026. https://doi.org/10.55669/oa900832

High-Temperature Behaviour of Quartz–Charcoal Briquettes in Metallurgical Silicon Production

I.L. Straum[1], C. Sindland[1,2], V. Andersen[2], and V. Myrvågnes[1,2]
[1]Department of Materials Science and Engineering, NTNU, Norway
[2]Elkem ASA, Norway

Keywords: Fines utilization, Agglomerates, Biocarbon, Silicon Production, SiO-reactivity, SiC-formation

Abstract – The high-temperature behaviour of quartz–charcoal briquettes (QCB) and reference charcoal briquettes (CB) was investigated under conditions relevant to metallurgical silicon production. QCB briquettes contained 30 wt.% quartz, 60 wt.% calcined charcoal, and 10 wt.% corn starch binder. Briquettes were heat treated at temperatures between 1400°C and 2000°C, both with and without exposure to externally generated SiO(g), and characterised by thermogravimetric analysis (TGA), X-ray diffraction (XRD), scanning electron microscopy (SEM), image analysis, apparent and envelope density measurements, and off-gas analysis. An initial mass loss of approximately 13 wt.% was observed below 900°C, attributed to binder decomposition, devolatilisation, and moisture removal. SiC formation started at 1400°C, below the thermodynamic equilibrium onset of approximately 1500–1520°C. The main carbothermal reduction stage occurred between 1400°C and 1700°C, during which all crystalline silica phases were consumed and total SiC content reached approximately 22 wt.%, consistent with the theoretical value for complete quartz conversion. The CB briquettes showed no significant phase development in the absence of quartz. Exposure to externally generated SiO(g) resulted in additional SiC formation concentrated at the bottom and sides of both briquette types, and the QCB briquettes retained significant SiO-capture capability after extensive internal reduction. The results demonstrate that composite quartz–charcoal briquettes are reactive under silicon production conditions and show potential for improved utilisation of fine raw material fractions.

1. INTRODUCTION

Silicon is produced industrially through carbothermic reduction of quartz in a submerged arc furnace (SAF), using carbonaceous reductants such as coal, coke, charcoal, and wood chips. The simplified overall reaction is shown in *Equation 1*, although in practice several reactions and phase transformations occur at different temperatures and furnace zones (Schei et al., 1998).

$$SiO_2 + 2C \rightarrow Si + 2CO \quad [1]$$

An important operational challenge is the generation and handling of fine raw material fractions. Fine particles are produced during quartz mining and during the production, transport, and handling of carbonaceous materials. When charged directly to the furnace, fines may reduce charge permeability, disturb upward gas flow, and contribute to unstable furnace operation (Ringdalen et al., 2022; Haugedal, 2025). Fine carbon particles, particularly fractions below 1 mm, may also be carried with the furnace off-gas and subsequently combust in the

This work is licensed under the Creative Commons Attribution 4.0 International License. To view a copy of this license, visit https://creativecommons.org/licenses/by/4.0/

furnace hood or off-gas system, resulting in reductant losses and changes in the carbon balance (Schei et al., 1998).

Agglomeration has been proposed as a route for converting fine quartz and carbon fractions into raw materials with improved properties for furnace use (Schei, 1998; Li, 2017; Kyaw, 2024). By combining quartz and carbon within the same briquette, closer contact between reactants may be achieved while maintaining sufficient permeability in the furnace charge (Li, 2017). Composite agglomerates may also influence local reactions involving SiO(g) and alter the reaction behaviour within the charge.

The close contact between quartz and charcoal particles within the briquette reduces the transport distance for gaseous intermediates and may therefore alter the effective reaction kinetics compared with a conventional loose furnace charge. Wiik (1990) demonstrated experimentally that the reaction between solid silica and solid carbon proceeds primarily via the gas phase rather than as a direct solid–solid reaction, as described in *Equations 2* and *3*. These two reactions combine to give the overall SiC-forming reaction shown in *Equation 4*. This two-step gas-phase mechanism was confirmed by Li (2017), who identified it as the dominant reaction path in the SiC-producing stage of quartz–carbon pellets in both CO and Ar atmospheres.

$$SiO_2 + C = SiO_{(g)} + CO \quad [2]$$

$$SiO_{(g)} + 2C = SiC + CO \quad [3]$$

$$SiO_2 + 3C = SiC + 2CO \quad [4]$$

Although thermodynamic equilibrium calculations predict that the conversion of SiO_2 and C to SiC becomes favourable at approximately 1500–1520°C, Poch and Dietzel observed the onset of SiC formation already at 1350°C in an argon atmosphere (Poch and Dietzel, 1962). This suggests that the close contact of reactants in a composite briquette, combined with the locally reducing gas atmosphere, may further facilitate SiC formation below the thermodynamically predicted onset temperature.

This paper presents results from an experimental investigation of quartz–charcoal briquettes (QCB) heat treated at temperatures between 1400 °C and 2000 °C, both with and without exposure to externally generated SiO(g). The objective was to characterise the reaction behaviour, phase development, and microstructural evolution of composite briquettes relevant to MG-Si and FeSi production.

2. EXPERIMENTAL

2.1 Materials and briquette preparation

Two briquette compositions were investigated. QCB contained 30 wt.% quartz, 60 wt.% calcined charcoal, and 10 wt.% corn starch binder. Reference CB contained 90 wt.% calcined charcoal and 10 wt.% binder. The quartz was dried at 105°C, sieved to 100–250 µm, and characterised by XRF analysis, which showed approximately 99 wt.% SiO_2 with minor impurities.

Two batches of the same charcoal were calcined at 900°C (Batch 2) and 1200°C (Batch 1) to remove PAH-containing volatile matter. After calcination, both batches showed fixed carbon

contents of approximately 94 wt.% (dry basis), ash contents of 4.3–4.9 wt.%, and residual volatile matter of 1.4–1.5 wt.%, as determined by proximate analysis.

Briquettes were prepared by mixing charcoal and quartz with a gelatinised binder paste (corn starch mixed with water), pressed into cylindrical pellets (10 mm diameter, ~12 mm height for CB and ~10 mm for QCB), and dried at 105°C for 24 hours. The binder content of 10 wt.% refers to the dry component mixture; water was added only to facilitate gelatinisation and was largely removed during pressing and drying. A total of 252 briquettes were produced across 21 experimental batches, with batches consisting of 12 briquettes of identical composition and a total dry mass of approximately 10 g.

2.2 High-temperature experiments

Heat treatment was performed in a graphite tube resistance furnace under inert atmosphere (Ar below 2000°C and He at 2000°C to reduce the risk of argon ionisation). Standard experiments used a heating ramp of approximately 40 minutes to the target temperature followed by a 30-minute isothermal hold, except at 1450°C where a 2-hour hold was used to assess time-dependent conversion. Target temperatures were 1400, 1450, 1700, 1900, and 2000°C.

Selected experiments included exposure to externally generated SiO(g). A Si–SiO_2 mixture (0.5–1 mm particle size) placed in a lower crucible within the same furnace assembly served as the SiO source, as shown in *Figure 1*. Off-gas CO and CO_2 concentrations and temperature were monitored continuously throughout all experiments.

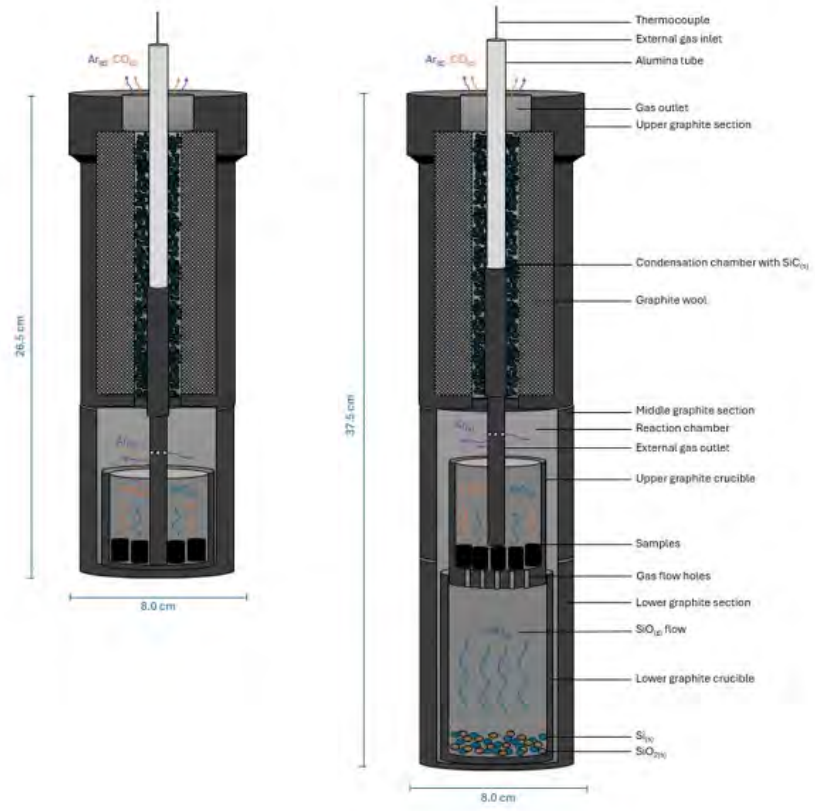

Figure 1: Schematic illustration of the standard furnace setup (left) and the SiO(g) exposure setup (right), showing the graphite crucible assembly, sample placement, and gas flow directions.

2.3 Characterisation

Phase evolution was characterised by XRD. Microstructural development was examined by BSE-SEM, in which contrast distinguishes quartz (bright), SiC (intermediate), and carbon (dark) based on mean atomic number. Each briquette cross-section was reconstructed from approximately 20–40 individual BSE-SEM images. Phase area fractions were quantified from the reconstructed images using a custom Python script applying Otsu-based thresholding. Apparent density and envelope density were determined by Archimedes' method and a GeoPyc analyser, respectively. TGA experiments (50°C/min to 1500°C) were performed to characterise binder decomposition independently of the high-temperature reactions.

3. RESULTS AND DISCUSSION

3.1 Expected reaction sequence

Before presenting the experimental results, it is useful to establish the theoretically expected reaction sequence. *HSC Chemistry* equilibrium calculations for the QCB composition (30 wt.% quartz, 60 wt.% charcoal) predict that SiO_2 remains stable up to approximately 1500–1520°C, above which SiC and CO(g) are formed according to *Equation 4*. Assuming a SiO partial pressure of 1 bar, significant SiO(g) formation from the Si–SiO_2 lower crucible is predicted above approximately 1930–1940°C, consistent with the findings of Sindland (2020), who reported weight losses of 45–50 wt.% from Si–SiO_2 mixtures at 1930–1950°C for a 30-minute hold.

Based on the QCB composition (30 wt.% quartz, 60 wt.% charcoal) and the SiC-producing reaction (*Equation 4*), complete internal carbothermal reduction of the quartz fraction is expected to yield approximately 20 wt.% SiC, with a corresponding CO-related mass loss of approximately 28 wt.%. If 1 g of externally generated SiO(g) additionally reacts with carbon according to *Equation 3*, the expected total SiC content increases to approximately 29 wt.%. These theoretical values provide reference points for interpreting the experimental XRD and mass-loss results.

The expected mass development during heating is illustrated in *Figure 2*. The initial mass loss below approximately 400°C corresponds to decomposition of the binder, residual moisture, and residual volatile matter in the charcoal. The corn starch binder contributes approximately 9.4 wt.% volatile loss when used at 10 wt.% addition (Kyaw, pers. comm., 2026), while the remaining contribution was estimated from the measured moisture and volatile matter contents of the calcined charcoal. This resulted in theoretical low-temperature mass losses of 12.58 wt.% for CB and 11.65 wt.% for QCB. For the QCB briquettes, a further mass loss is expected between approximately 1500°C and 1700°C due to CO(g) evolution accompanying SiC formation. In the SiO-exposure experiments, additional SiC formation from externally supplied SiO(g) above approximately 1930°C may partially offset this mass loss, resulting in an increase in remaining briquette mass relative to the standard experiments. The curves for 25% and 50% SiO utilisation represent scenarios where 25% and 50%, respectively, of the experimentally estimated SiO(g) generated during each experiment (approximately 3.8 g for CB and 5.7 g for QCB) is assumed to react with carbon in the briquette to form SiC.

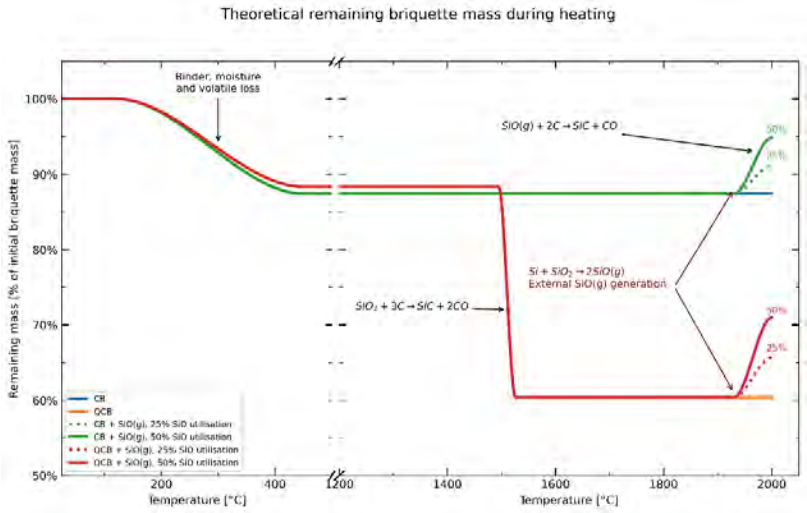

Figure 2: Theoretical remaining briquette mass as a function of temperature for CB and QCB briquettes, with and without exposure to externally generated SiO(g). For the SiO-exposed compositions, theoretical curves assuming 25% and 50% utilisation of the externally generated SiO(g) for SiC formation are shown. The three main stages represent moisture and volatile loss, carbothermal reduction of quartz, and additional SiC formation from externally supplied SiO(g).

3.2 Reaction Sequence from the Long Duration Experiments

Three main reaction stages were identified from the combined off-gas, TGA, and mass-change measurements, and are illustrated in the qualitative CO off-gas profile from a long-duration heating experiment (1400–2000°C) shown in *Figure 3*. The CO measurements are interpreted qualitatively, and the evolution of the CO signal relative to the temperature is used to identify the different reaction stages: (1) binder decomposition and devolatilisation below approximately 900°C, (2) internal carbothermal reduction of quartz between approximately 1400°C and 1700°C, and (3) interaction with externally supplied SiO(g) above approximately 1800°C in the SiO-exposure experiments.

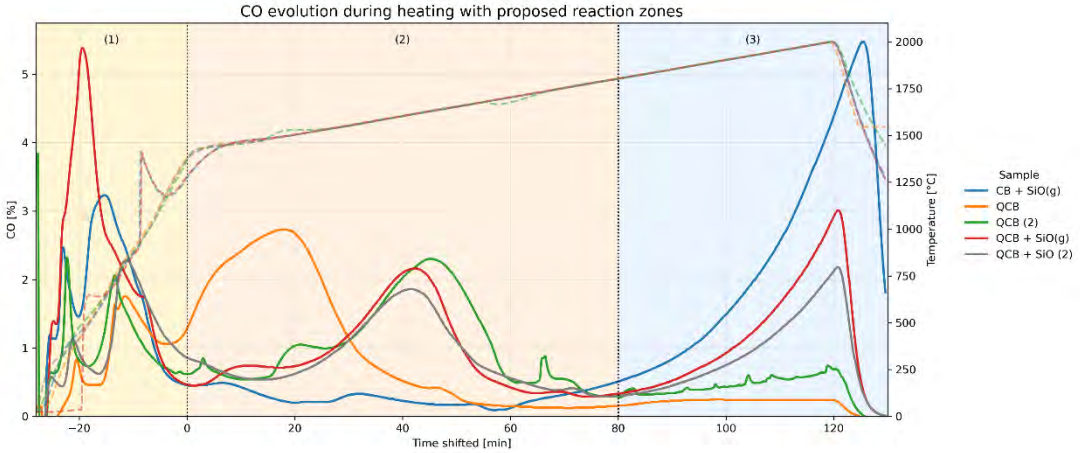

Figure 3: CO off-gas evolution during the long-duration heating experiments, showing the three proposed reaction stages: (1) binder decomposition, (2) carbothermal reduction and SiC formation, and (3) interaction with externally supplied SiO(g). Dashed lines represent the furnace temperature profiles.

3.3 Low-temperature Mass Loss and Binder Decomposition

TGA showed a distinct mass-loss event centred near 300°C for both CB and QCB briquettes, in good agreement with the decomposition range of 280–360°C reported for corn starch (Piglłowska et al., 2020). Total low-temperature mass loss was 13.2 wt.% for CB and 13.1 wt.% for QCB, consistent with the estimates presented in *Section 3.1*. The mass curves stabilised at a clear plateau before the onset of carbothermal reactions, confirming that binder-related processes were complete before the main reduction stage. Net mass losses of CB briquettes after furnace heat treatment were in close agreement with TGA values up to 1900°C (*Table I*), confirming no significant additional reactions in the CB system below this temperature.

Table I: Mass loss of CB briquettes after heat treatment at different temperatures, compared with the TGA baseline. The mass loss remains relatively stable between 1400 and 1900°C.

Condition	Mass loss [wt.%]	Difference from TGA [wt.%]
TGA (CB baseline)	13.2	0.0
CB 1400°C	12.1	−1.1
CB 1700°C	13.3	+0.1
CB 1900°C	13.9	+0.7

3.4 Internal Carbothermal Reduction and SiC Formation

Cross-sectional BSE-SEM images of CB briquettes in the as-prepared state and after heat treatment up to 1900°C are shown in *Figure 4*. The microstructure remained largely unchanged across the investigated temperature range, with no significant phase development or pore formation observed. Note that the dark regions are porosity occurring during sample preparation. This is consistent with the XRD results shown in *Table II*, which confirmed the absence of new silicon-containing phases in the CB briquettes at any temperature. Minor graphitisation of the carbon matrix was observed above 1700°C, but no SiC or other reaction products were detected, confirming that the carbon matrix did not undergo significant chemical reactions in the absence of quartz.

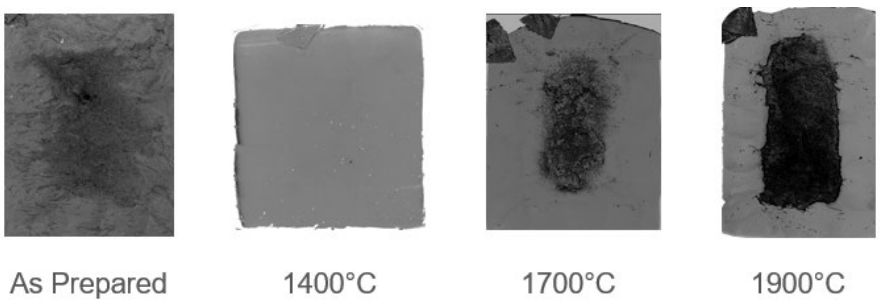

Figure 4: BSE-SEM images of CB briquettes before and after heat treatment, showing limited microstructural change compared with the as-prepared condition. The dark regions correspond to pores, and no significant microstructural changes are observed with increasing temperature

Table II: Phase composition of CB briquettes before and after heat treatment at different temperatures, as determined by XRD. No SiC formation was detected at any temperature.

Temperature [°C]	Phase Composition [wt.%]			
	Amorphous	Graphite 1	Graphite 2	SiC-Cubic
As Prepared	100.00	--	-	-
CB 1400°C	100.00		-	-
CB 1700°C	96.17	1.52	2.31	-
CB 1900°C	97.96	0.07	1.97	-

In contrast, the QCB briquettes underwent significant microstructural changes during heat treatment, as shown in *Figure 5*. At 1400°C, quartz particles are still clearly visible as bright regions distributed throughout the carbon matrix. At 1700°C, these regions have largely disappeared and been replaced by pores and SiC-containing phases. The segmented BSE images illustrate this progression quantitatively, showing the increase in pore fraction and SiC-containing regions with increasing temperature.

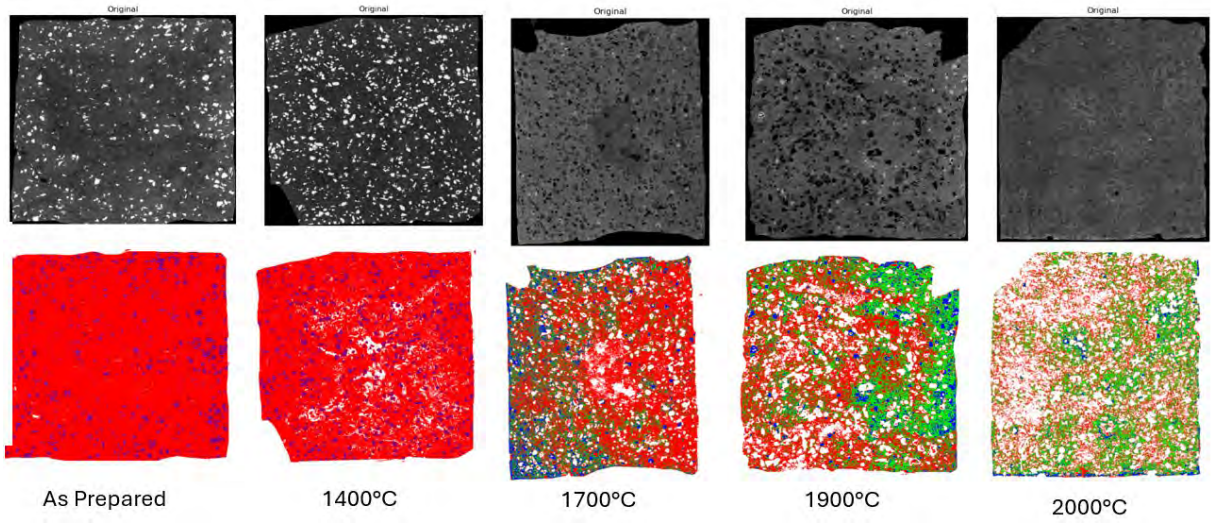

Figure 5: BSE-SEM images and corresponding segmented images from image analysis of QCB briquettes in the as-prepared condition and after heat treatment at 1400°C, 1700°C, 1900°C, and 2000°C. In the segmented images, red represents the carbon phase, purple represents quartz, green represents a mixed SiC–carbon phase, and blue represents SiC clusters.

The XRD results confirm this phase evolution, as shown in Table III. Quartz and cristobalite were detected after heat treatment at 1400°C, whereas no crystalline silica phases were observed at 1700°C and above. The total SiC content at 1700°C reached approximately 22 wt.%, in good agreement with the theoretical value of approximately 20 wt.% expected from complete conversion of the quartz fraction according to *Equation 4*, indicating extensive quartz conversion by 1700°C. The consistently high amorphous fraction across all temperatures is expected to be dominated by unreacted carbon, although a contribution from amorphous silica cannot be excluded based on the XRD results.

Table III: Phase composition of QCB briquettes after heat treatment at different temperatures, as determined by XRD. No crystalline quartz or cristobalite was detected at 1700°C and above, with a corresponding increase in SiC content.

Temperature [°C]	Phase Composition [wt.%]				
	Amorphous	Quartz	Cristobalite	SiC-Cubic	SiC-2H
As Prepared	81.67	18.33	-	-	-
QCB 1400°C	77.98	10.44	9.28	2.30	-
QCB 1450°C[1]	79.69	4.22	6.25	9.04	0.80
QCB 1700°C	77.74	-	-	20.87	1.39
QCB 1900°C	78.96	-	-	17.51	3.53
QCB 2000°C	81.15	-	-	17.67	1.18

[1] *Longer holding time (2 h).*

3.5 Reaction with externally generated SiO(g)

The segmented BSE-SEM images in *Figure 6* illustrate the difference in microstructural response between CB and QCB briquettes exposed to externally generated SiO(g). In both briquette types, SiC formation is concentrated at the bottom and along the sides of the briquette cross-section, as indicated by the blue regions, consistent with SiO(g) entering the briquette from below and reacting with carbon at the exposed surfaces. Both CB and QCB briquettes reacted with externally supplied SiO(g), although the amount of SiO(g) generated differed between experiments, which should be considered when comparing the extent of SiC formation between the two briquette types.

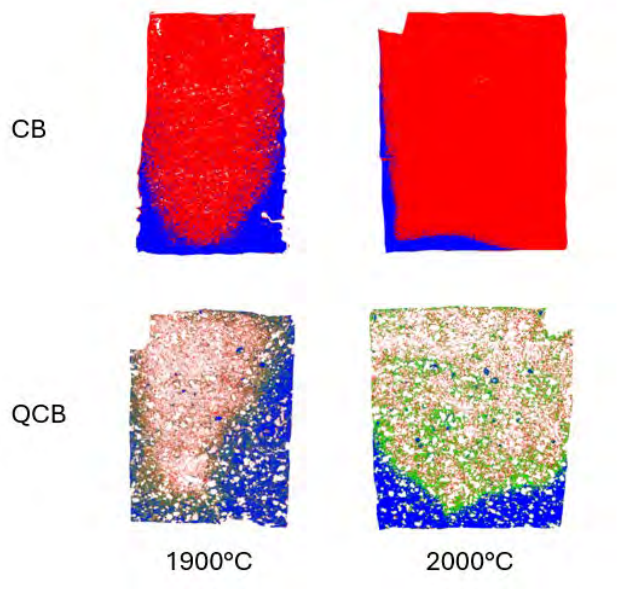

Figure 6: Segmented BSE-SEM images of CB and QCB briquettes after exposure to externally generated SiO(g) at 1900°C and 2000°C. Red represents the carbon phase, green represents a mixed SiC–carbon phase, and blue represents SiC clusters.

The SiO(g) generation and corresponding SiC formation from XRD are summarised in *Table IV*. Exposure to externally generated SiO(g) resulted in additional SiC formation in both briquette types. The additional SiC content (ΔSiC) was calculated relative to the corresponding standard experiments without external SiO(g), and no parallel experiments were conducted, so the values should be interpreted as indicative rather than statistically confirmed. The amount of SiO(g) generated was lower than theoretically expected (Sindland, 2020), suggesting incomplete reaction or SiO losses within the experimental setup.

When normalised to the amount of SiO(g) generated, comparable levels of additional SiC formation were observed for both CB and QCB briquettes, suggesting a comparable ability to react with externally supplied SiO(g). Nevertheless, the QCB briquettes retained a substantial SiO-capture capability despite extensive prior internal reduction, indicating that reactive carbon surfaces remained available for further SiC formation. This is consistent with Li et al. (2018), who reported that good matching between quartz–carbon reactivity and SiO reactivity reduces SiO losses.

Table IV: Estimated SiO(g) generation and corresponding crystalline SiC content in briquettes exposed to external SiO(g). The additional SiC content (ΔSiC) was calculated relative to the corresponding samples treated without external SiO(g).

Condition	SiO generated [g]	SiO generated [%]	SiC without SiO [wt.%]	SiC with SiO [wt%]	ΔSiC [wt.%]
CB 1900°C + SiO(g)	4.05	20.25	0.00	4.39	4.39
CB 2000°C + SiO(g)	3.56	17.8	0.00	8.55	8.55
QCB 1900°C + SiO(g)	5.72	28.6	21.04	29.59	8.55
QCB 2000°C + SiO(g)	5.62	28.1	18.85	28.91	10.06

3.6 Comparison of measured and theoretical mass loss

The measured mass changes are compared with the theoretical mass balance in Figure 7. For both CB and QCB briquettes without external SiO(g), the measured values are in good agreement with the theoretical predictions, indicating that the low-temperature mass loss and carbothermal reduction account for most of the observed weight changes. For the experiments with external SiO(g), the measured mass changes were consistently smaller than the theoretical predictions. Since the theoretical curves assume complete utilisation of the estimated SiO(g) generated, the discrepancy indicates that only a fraction of the generated SiO(g) reacted with the briquettes. This is consistent with transport limitations, incomplete gas–solid contact, and the non-uniform distribution of SiO(g) within the experimental setup, as discussed in *Section 3.5*.

Although the total SiC content was higher in the QCB briquettes than in the CB briquettes, this was primarily a consequence of the internal carbothermal reduction that had already occurred prior to SiO(g) exposure. When normalised to the amount of SiO(g) generated, comparable levels of additional SiC formation were observed for both briquette types, suggesting a similar ability to react with externally supplied SiO(g). Nevertheless, the QCB briquettes retained a substantial SiO-capture capability despite extensive prior internal reduction, indicating that reactive carbon surfaces remained available for further SiC formation.

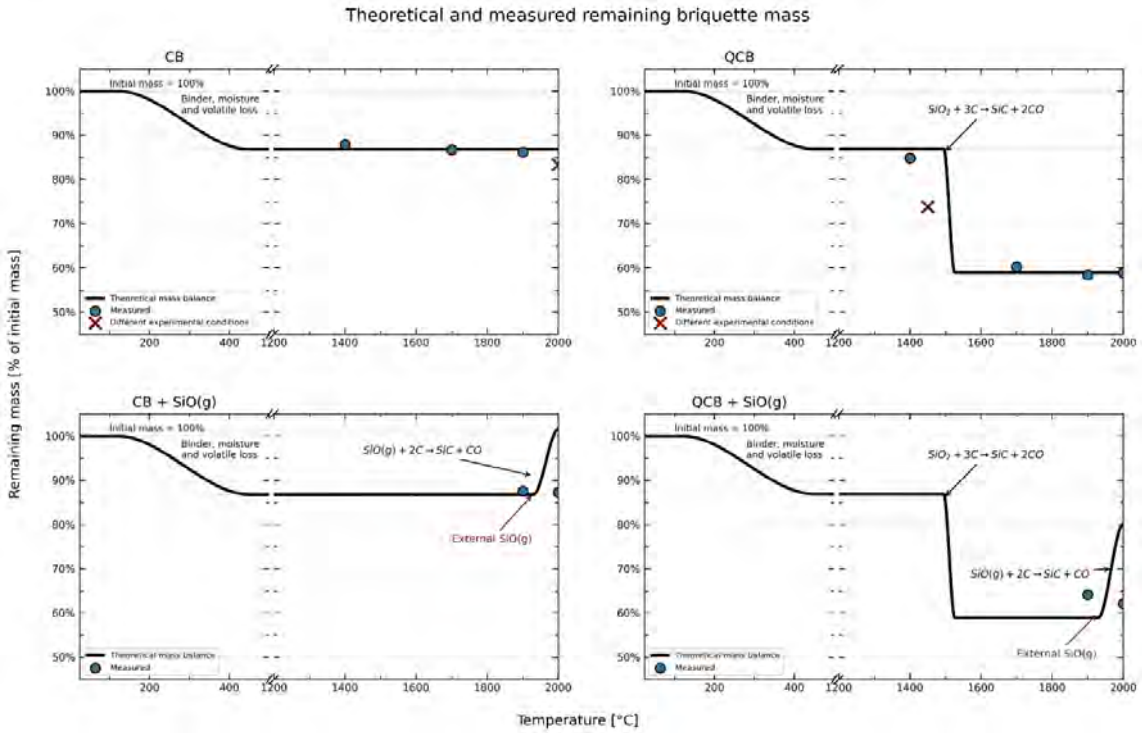

Figure 7: Theoretical and measured remaining briquette mass as a function of temperature for CB and QCB briquettes, with and without exposure to externally generated SiO(g). The theoretical curves assume complete low-temperature volatile loss, full carbothermal reduction of quartz, and complete utilisation of the estimated SiO(g) generated. Measured values are shown as individual data points.

3.7 Future work

The present work investigated a wide range of temperatures and reaction conditions relevant to silicon production. Future studies should focus on obtaining a more detailed understanding of the high-temperature behaviour of these briquettes. During sample handling, the QCB briquettes appeared to exhibit a higher mechanical strength than the CB briquettes once substantial SiC formation had occurred. Although this observation was not quantified, it represents an interesting topic for future investigation through dedicated mechanical strength measurements. Further studies should also investigate whether the increased porosity generated during internal carbothermal reduction contributes to the substantial SiO(g) capture observed in the QCB briquettes by increasing the available reactive surface area.

4. CONCLUSIONS

The high-temperature behaviour of QCB and reference CB briquettes was investigated at temperatures between 1400°C and 2000°C, with and without exposure to externally generated SiO(g). Both briquette types showed an initial mass loss of approximately 13 wt.% below approximately 900°C, attributed to corn starch decomposition, devolatilisation of residual volatile matter, and moisture removal, which were complete before the onset of carbothermal reduction.

The QCB briquettes underwent extensive phase development between 1400°C and 1700°C. SiC formation started at 1400°C, below the thermodynamic equilibrium onset of approximately 1500–1520°C. All crystalline silica phases were consumed by 1700°C, and the total SiC content reached approximately 22 wt.%, in good agreement with the theoretical value of 20 wt.% for complete quartz conversion.

Exposure to externally generated SiO(g) resulted in additional SiC formation concentrated at the bottom and sides of both briquette types, consistent with SiO(g) entering from below. A portion of the generated SiO(g) reacted with both CB and QCB briquettes. Although the QCB briquettes exhibited a greater increase in total SiC content, comparable levels of additional SiC formation were observed for both briquette types when normalised to the amount of SiO(g) generated. The substantial SiO-capture capability observed for the QCB briquettes may be related to the increased porosity developed during internal carbon–quartz reactions at elevated temperatures, which could provide a larger reactive surface area for subsequent reactions with SiO(g).

5. ACKNOWLEDGEMENTS

This work was carried out as part of the QUEEN (Quartz Enrichment Enabling Near-Zero Silicon) project, funded by the European Union's Horizon Europe research and innovation programme.

6. REFERENCES

Haugedal, H. 2025. *The Effects of Biocarbon on Permeability and Wind-Sieving of Charge for Silicon Production*. MSc thesis. Trondheim: NTNU.

Kyaw, T.T. and Tangstad, M. 2024. Use of Agglomerates in Silicon Production. *SSRN Electronic Journal*. doi:10.2139/ssrn.4945352.

Li, F. 2017. *SiC Production Using SiO_2 and C Agglomerates.* PhD thesis. Trondheim: NTNU.

Li, F., Tangstad, M., and Ringdalen, E. 2018. Carbothermal Reduction of Quartz and Carbon Pellets at Elevated Temperatures. *Metallurgical and Materials Transactions B*, 49B, 1078-1088.

Pigłowska, M., et al. 2020. Kinetics and Thermodynamics of Thermal Degradation of Different Starches and Estimation the OH Group and H_2O Content on the Surface by TG/DTG-DTA. *Polymers*, 12(2), 357.

Poch, W. and Dietzel, A. 1962. The Formation of Silicon Carbide from Silicon Dioxide and Carbon. Berichte der Deutschen Keramischen Gesellschaft, 39, 413-426.

Ringdalen, E., Einarsrud, K.E., and Nordhus, A. 2022. Gas Flow and Pressure Drop in Charge Material in Silicon Production. *JOM,* Vol.74, pp.3971-3979.

Schei, A., Tuset, J.K., and Tveit, H. 1998. *Production of High Silicon Alloys*. Trondheim: TAPIR Forlag.

Sindland, C. 2020. *Production Rate of SiO Gas from Industrial Quartz and Silicon*. MSc thesis. Trondheim: NTNU.

Surup, G.R., Trubetskaya, A., and Tangstad, M. 2020. Charcoal as an Alternative Reductant in Ferroalloy Production: A Review. *Processes*, Vol.8, No.11, p.1432.

Wiik, K. 1990. *Kinetics of Reactions Between Silica and Carbon*. Dr.ing. thesis. Trondheim: NTH.

Ingeborg Lillevik Straum

MSc Student, Department of Materials Science and Engineering, NTNU

Ingeborg Lillevik Straum completed her Master's degree in Materials Technology at NTNU in June 2026. Her thesis investigated the high-temperature behaviour of quartz–charcoal briquettes relevant to metallurgical silicon production and was conducted as part of the Horizon Europe QUEEN project. Her research interests include pyrometallurgy, raw material agglomeration, and sustainable production routes for silicon and ferrosilicon.

Øvrelid, S. J. S. 2026. Transition to Carbon Neutral Silicon Production at Wacker Holla. In *Silicon for the chemical and solar industry XVIII*, edited by M. Tangstad, H. Rong, A. Valderhaug, B. Andresen, H. Dalaker, and I. G. Page. Kristiansand, Norway, September 7–10, 2026.
https://doi.org/10.55669/oa900834

Transition to Carbon Neutral Silicon Production at Wacker Holla

Sigurd J.S. Øvrelid
Wacker Chemicals Norway AS, Holla Metall, Sigurd.oevrelid@wacker.com

Keywords: Silicon, biocarbon, industrial testing, carbon neutrality, dust, safety

Abstract – This paper describes ongoing work carried out at Wacker Chemicals Norway AS, Holla Metall, to make the silicon plant carbon neutral by 2030 through large-scale substitution of fossil reductants with biocarbon. The transition requires changes to logistics, especially related to handling and use of low-density and mechanically weak materials that generate fines and dust. Full-scale industrial test campaigns have been conducted with biocarbon shares exceeding 50% of the total carbon demand, demonstrating that stable furnace operation is possible. During testing, temporary fluctuations in silicon yield are observed, mainly associated with ramp-up phases, variability in fines generation, and controlling the effective carbon input. The work highlights differences between charcoal and agglomerated biocarbon materials in terms of reactivity, mechanical stability, and operational behavior, and highlights the need for improved control of material properties and operating strategies. A structured qualification methodology combining laboratory testing and industrial validation has been developed to support implementation. The results show that successful use of biocarbon requires looking at the full process. Major research and development projects are carried out in-house as well as in collaboration with universities, research companies and other industry including both established and new producers of biocarbon materials.

1. Introduction

In recent years, the importance of biocarbon has grown. Driven by carbon neutrality targets and supported by the development of agglomerated products, significantly higher substitution levels have become technically feasible. Industrial experience from Brazil and other parts of South America shows that silicon production with mainly biogenic reductants is possible when the process is designed accordingly (Minasligas, 2026; LIASA, 2026). However, these operations face similar challenges related to variability in charcoal quality, which affects carbon utilization (Isbaex, 2014).

In a previous publication, Wacker Chemicals Norway AS, Holla Metall, hereafter referred to as Wacker Holla, presented its strategy towards carbon neutral silicon production, emphasizing the role of biocarbon substitution and outlining key technical challenges associated with this transition (Halland, 2024). Particular attention was given to the variability in mechanical and thermal strength, fines and dust generation, which highlighted the need for industrial validation to fully understand the implications of this transition. The overall objective of significantly reducing greenhouse gas emissions remains unchanged. Wacker Holla continues to target carbon neutral silicon production by 2030 through large-scale substitution of fossil reductants with sustainable biocarbon materials, combined with adaptation of raw material systems and furnace operation.

This article builds on the consideration already set out and presents operational experience from multiple industrial test campaigns. While the previous study focused on feasibility and strategy, the present work documents the behavior of biocarbon under full-scale furnace

This work is licensed under the Creative Commons Attribution 4.0 International License. To view a copy of this license, visit https://creativecommons.org/licenses/by/4.0/

conditions. The analysis is based on campaigns starting in 2020 and subsequent tests with increasing operational experience. Attention is given to the differences between charcoal and agglomerated biocarbon, and their impact on furnace behavior, process stability, and material handling. The evolution of operating strategy is also described, reflecting the transition from exploratory testing to more controlled implementation.

2. Role of Biocarbon in Silicon Furnace Operation

In the carbothermic silicon process, carbon (C) acts as the reducing agent for silica and participates in reactions involving silicon monoxide (SiO) gas, including the formation of silicon carbide (SiC) and subsequent silicon production. The ability to capture SiO gas directly influences silicon yield and energy efficiency. In addition, carbon affects gas generation, burden permeability, and electrical resistance, making its properties critical for stable furnace operation.

A key reaction is the capture of ascending SiO gas through SiC formation, shown in following reaction:

$$SiO_{(g)} + 2C_{(s)} = SiC_{(s)} + CO_{(g)} \quad [1]$$

The efficiency of this reaction depends on the availability and reactivity of carbon surfaces, as well as the distribution of carbon in the charge. In this respect, biocarbon behaves quite differently from conventional fossil carbon materials. In general, its higher porosity and reactivity can improve the reaction rates, but at the same time it can become less stable, as it tends to break down and form finer fractions. Because of this, biocarbon needs to be considered not only as a chemical reactant, but also as part of the furnace structure, influencing permeability, gas flow, and electrical behavior.

3. Qualification Methodology for Biocarbon Materials

Due to the variability and complex behavior of biocarbon materials, a structured qualification methodology is required prior to industrial use. Experience has shown that neither appropriate material properties nor furnace behavior can be predicted from a single dataset. An iterative approach combining supplier data, laboratory testing, and industrial validation is therefore applied. Evaluation is carried out stepwise, starting with simple and low-cost assessments, and progressing to more detailed testing only for materials that demonstrate acceptable performance. This approach minimizes the use of resources on unsuitable materials.

The process begins with a review of supplier-provided data, including chemical composition, ash chemistry, and basic physical properties. In parallel, supplier capability, scalability, logistics, and compliance with sustainability requirements are evaluated. Materials that pass this stage are tested by an in-house laboratory, using small sample quantities. This includes verification of full chemical analysis, thermal behavior, and resistance to degradation during handling. Mechanical stability is first assessed through a drop test, designed to simulate the maximum drops encountered in the raw material handling system. In addition, a simple but informative crushing test is performed, where the material is deliberately broken using momentum transfer and localized pressure to provide a qualitative, comparative assessment of its mechanical strength and how it breaks up. Moisture behavior is also evaluated, both in terms of uptake and resistance. Thermal resistance is evaluated by heating the material to approximately 1000 °C for 10 minutes in an inert atmosphere, providing an indication of its stability during the early stages of furnace exposure.

Further testing is conducted externally, including SiO reactivity and mechanical strength by tumble testing. Materials that pass these stages are considered for pilot-scale tests. Such tests are intended to expose the material under more representative conditions. However, while these evaluations provide valuable information, they are not sufficient to fully predict industrial behavior. As a result, controlled full-scale trials remain a necessary step in the qualification process, representing the final validation before potential implementation.

Industrial testing is performed by gradually introducing the material into our dedicated test furnace of about 17 MW. For new products we will use enough material for a trial lasting about a month on 30% of the total carbon demand, ramping up from 20% as the starting point.
If we consider the industrial test a success, we will either start testing on higher shares, exceeding 50% of the total carbon demand, or use one of the larger furnaces which has semi-continuous filling through charging tubes instead of the batchwise filling by truck on the smaller test furnace. The larger furnaces also have higher accumulation of drop length throughout the raw material handling system, increasing the risk of fines and dust generation.

Wacker Holla has already run several full industrial scale tests for biocarbon materials. During these campaigns, key performance indicators such as furnace stability, dust formation, silicon yield, and electrical response are closely monitored. Only materials that demonstrate stable and predictable behavior under these conditions are approved for long-term use. This structured process has proven essential for managing the risks associated with introducing new biocarbon materials.

In 2025 Wacker reached a new milestone: a long-term contract with a US-based producer of biogenic carbon and biohydrogen products. The contract came into force following a successful completion of the full qualification process. The biogenic carbon is to be produced in a new manufacturing plant built in the USA. The agreed volumes will cover a substantial portion of Wacker Holla's total carbon demand, marking a major step towards climate neutral silicon production.

4. Industrial test development and learning progression

Historically, the use of small amounts of charcoal and wood chips in the carbon mix has been common industry practice. Charcoal has typically served as a supplementary carbon source, mainly due to its relatively low impurity levels and high porosity. For most producers its use has nevertheless been limited, as large-scale substitution has been restricted by low density, high fines/dust generation, and challenges related to stability, supply and cost. This is also the case for Wacker Holla.

4.1 Operational and HSE challenges

At Wacker Holla, initial industrial campaigns were carried out to test high levels of biocarbon substitution under conditions largely based on conventional operation. Operation could be maintained at moderate substitution levels, confirming that biocarbon can function as a reductant. At the same time, several challenges were identified, including increased gas generation, variability in furnace stability, reduced yield, and changes in by-product composition.

In this work, particle fractions are differentiated based on their impact on handling and furnace operation. *Dust* refers to particles on the micrometer scale, which are prone to becoming airborne during handling and transport, representing the main Health, Safety and Environment (HSE) concern. *Fines* refer to particles that may leave the furnace with the off gas,

depending also on particle density and gas flow conditions, or that may accumulate within the burden and disrupt gas flow and permeability.

Significant HSE challenges were also observed. Dust formation occurred throughout the material handling chain, including unloading, storage, transport, weighing, and charging. This led to accumulation of dust in several areas, increasing the risk of self-heating and ignition, as well as explosion. Dust was also found to accumulate in critical equipment, such as feeding systems, leading to failures and unplanned stoppages. Mitigation measures were implemented to address these issues. Dust suppression systems were introduced, cleaning routines intensified, and monitoring of material temperatures in storage and silos was improved.

One of the most important process-related observations was the extent of variability in raw material behavior. Fluctuations in moisture content and fines distribution were much greater than typically observed for fossil carbon materials. This introduces a significant unknown variation in the carbon loss and complicates process control. The fines that are not blown off with the process gas can end up altering the permeability of the burden and hindering uniform gas flow. Uneven gas distribution reduces the effective SiO-reactivity of the charge, which is unwanted. The extent of these fluctuations is shown in Figures 1 and 2.

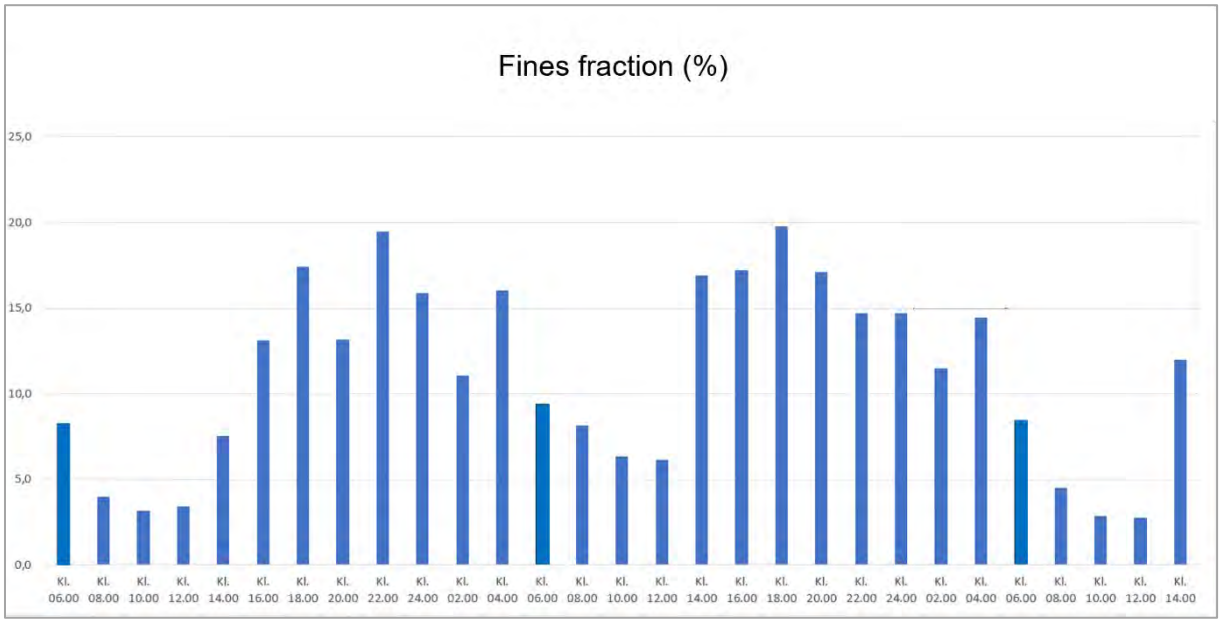

Figure 1: Fines fraction (%) for charcoal in the weighing cell as a function of time.

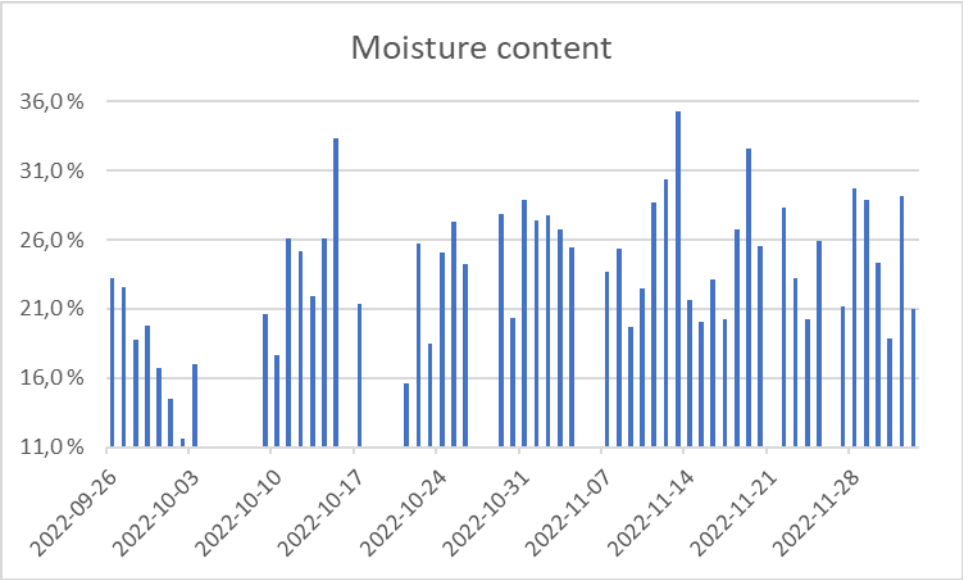

Figure 2: Moisture content (%) of charcoal as a function of time.

A distinct daily variation in fines fraction was observed, linked to filling of the day bins. This indicates that segregation during storage and handling was a major source of variability in the weighed charge mix. Part of the observed instability was also related to operating practice. Furnace parameters were adjusted frequently in response to uncertainty in material behavior. The resistance set point was often changed based on assumed differences in electrical properties, and the carbon balance was repeatedly adjusted to compensate for assumed daily variations in blow-off and burn-off. Frequent changes reduced process stability and made it difficult to identify the underlying causes of instability. Operation became reactive, with adjustments made to short-term fluctuations rather than allowing the furnace to stabilize.

It became clear that stable furnace operation required more consistent input materials. Stable moisture content, controlled particle size distribution with low fines content and predictable carbon input are all necessary to maintain predictable furnace conditions. Later campaigns were conducted with improved control of both materials and operation. Methods reducing segregation significantly were developed and implemented. Adjustments were made more conservatively and typically one at a time, allowing the response of the furnace to be observed before further changes were introduced. This marked a transition from reactive to controlled operation.

Additional improvements were made to charge composition, layering, and material flow through the furnace. Greater control of residence time and charge burden structure contributed to more stable reaction conditions. These changes resulted in a clear improvement in furnace stability, even at substitution levels above 50% of the carbon demand. The results show that many of the challenges observed in early campaigns were not only inherent to biocarbon but also related to operating strategy.

4.2 Impact on silicon yield and carbon balance

The sensitivity of silicon yield to carbon balance makes accurate control particularly important during biocarbon testing. From our experience, for a well-operated silicon furnace, a 1%

reduction in effective carbon balance typically corresponds to approximately a 2% reduction in silicon yield. Variations in fines generation and carbon losses can therefore have a significant impact on furnace performance and complicate interpretation of test results. The development of silicon yield during a full-scale campaign on our designated test furnace, using agglomerated biocarbon, is shown in Figure 3.

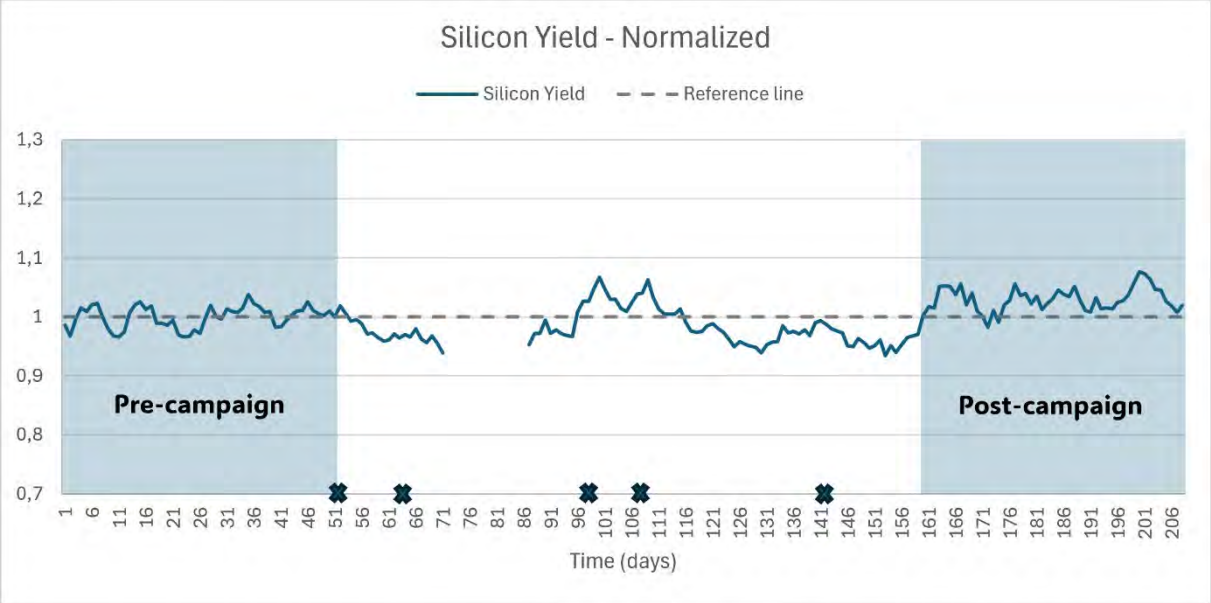

Figure 3: Normalized silicon yield relative to the average value of the 50-day pre-campaign period. Shaded regions indicate pre- and post-campaign operation. Crosses mark the ramp-up steps. The curve is a five-day symmetrical average. Days with furnace load less than 90% are removed from the data set. The break in the curve is a yearly maintenance stop including the following ramp up period. The stepwise increases in biocarbon share are shown with "X".

The results show that, although temporary fluctuations and short-term reductions in silicon yield occur during the campaign period, the average yield remains close to the reference level. The initial drop in silicon yield in the 95-day long biocarbon test indicates the learning curve for adjustments of electrical setpoints and carbon content at the start. The observed decreases in silicon yield coincide, with one exception discussed below, with the stepwise increases in biocarbon substitution. Following each increase, the process is stabilized on an acceptable yield before further ramp-up steps are introduced. This sometimes takes more time than in the original test plan, but the curve shows the empirical learning process done after every biocarbon increase.

The behavior observed in Figure 3 must be interpreted in the context of the time required to evaluate process performance when introducing new biocarbon materials. Several months of stable operation are needed to determine the actual impact on carbon losses and corresponding silicon yield, particularly for materials that generate significant amounts of fines. Variations in fines content influence the effective carbon input and may only become evident over extended periods. Similarly, determination of optimum electrical operating conditions requires time, since changes in raw material properties affect burden resistivity and furnace response. Temporary reductions in silicon yield of approximately 2–3% should therefore be expected during industrial qualification campaigns and are not necessarily an indication of poor material performance. Similar behavior is frequently observed during testing of new fossil carbon materials, where both furnace operation and carbon balance require optimization before representative performance can be established.

The post-campaign period shows a clear increase in normalized silicon yield relative to both the campaign and reference periods, providing additional insight into the overall carbon balance of the process. This behavior is consistent with a temporary excess of carbon during the biocarbon campaign, resulting in accumulation of (SiC) in the furnace. The subsequent increase in yield corresponds to operation at lower fixed carbon input, where this accumulated SiC is gradually consumed, leading to improved silicon recovery. Similar behavior is observed during the campaign period between approximately day 95 and 115, where an increase in silicon yield coincides with reduced fixed carbon input following a period of higher carbon addition. This boosts the silicon yield temporarily and delays the expected decrease in yield from the ramp ups on day 98 and day 107.

A contributing factor to this behavior may be overestimation of carbon losses associated with increased fines generation, resulting in operation with a higher effective carbon input than intended. These effects tend to be particularly pronounced with increasing biocarbon shares, as both fines generation and changes in burden resistance are amplified.

Another factor influencing furnace performance is the volumetric nature of biocarbon materials. Because biocarbon generally contains less fixed carbon per unit volume than fossil reductants, larger material volumes must be charged to maintain the desired carbon balance. This may reduce the residence time of other carbon materials in the furnace. As a consequence, fossil reductants may participate less effectively in SiO capture reactions and subsequent SiC formation, reducing their effective reactivity. The influence of this mechanism is expected to diminish at very high biocarbon substitution levels because the remaining fraction of fossil carbon becomes progressively smaller.

Overall, the results indicate that the process was not fully optimized during the campaign period. Nevertheless, stable operation was maintained at biocarbon substitution levels exceeding 50% of the total carbon demand, while the average silicon yield remained close to the reference level. The remaining yield differences are believed to be largely related to carbon balance control, electrical optimization, and operational adaptation, rather than to fundamental limitations of the biocarbon materials themselves.

4.3 Charcoal versus agglomerated biocarbon

The industrial campaigns highlighted significant differences between charcoal and agglomerated biocarbon products. Although both material types can function as reductants in silicon production, their properties differ considerably. Charcoal represents the simpler form of biocarbon and is characterized by a highly porous structure and high reactivity towards SiO. Industrial experience shows that charcoal-rich charges often promote uniform gas distribution and material flow, both of which increase the silicon yield.

However, the same porous structure that gives charcoal its high reactivity also results in lower mechanical strength. Material degradation during transport, handling, and charging therefore remains a significant challenge. The resulting particle-size variability complicates process control and can make furnace behavior less predictable. Industrial implementation of high charcoal shares therefore requires careful control of raw material quality and handling conditions.

Agglomerated biocarbon products, including briquettes and extruded materials, are produced through densification of finer carbon fractions, typically with the addition of binders. The principal advantage of these materials is improved mechanical robustness. Densification reduces particle degradation, improves particle-size consistency, and enables more

predictable feeding behavior throughout the raw material handling system. From an operational perspective, these properties contribute to greater process stability.

The improved mechanical durability of agglomerated products is reflected both in laboratory testing and industrial operation. Figure 4 compares tumble-test performance and fines generation measured during plant trials. Materials with higher tumble-test retention generally produced less fines during industrial use.

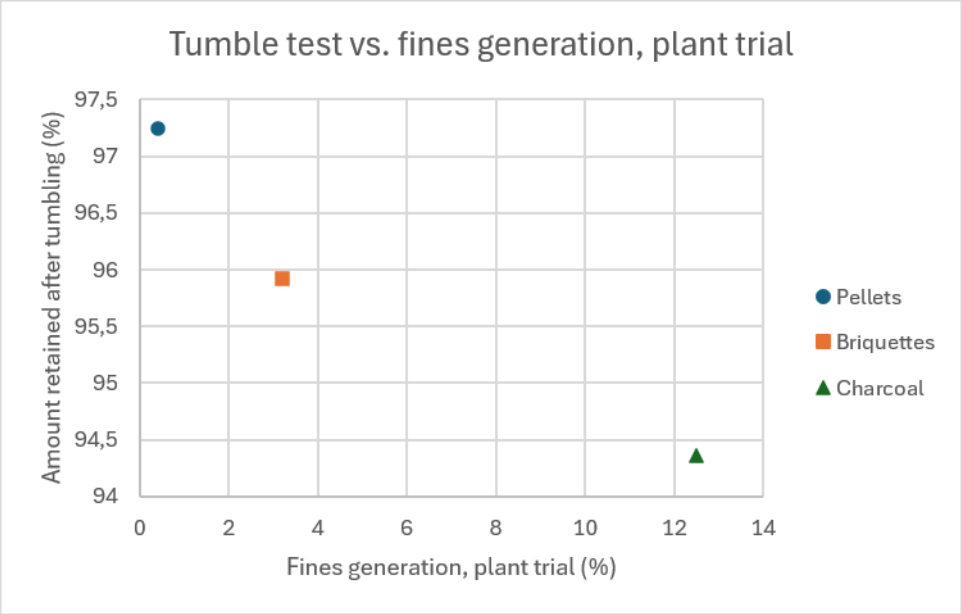

Figure 4: Relationship between tumble-test retention and fines generation during industrial trials. Tumbling results are based on the average of several pellets, briquettes and charcoal types.

The results show clear reduction in fines generation for the agglomerated products compared with charcoal. However, during industrial testing it was observed that dust formation during handling of briquettes was similar to amounts observed during handling of charcoal. While agglomeration can reduce the formation of larger fine fractions and improve process control, the generation of airborne particles may still remain sufficiently high to require dedicated dust mitigation measures.

Thermal stability is another consideration. While agglomerated materials are mechanically robust, partial disintegration during heating has been observed, indicating that their behavior under furnace conditions is strongly dependent on the type and performance of the binder system used. The moisture resistance of agglomerated materials is strongly dependent on both the type of binder system and the agglomeration method; while some combinations provide improved resistance to water uptake, others may promote moisture absorption and lead to deterioration during storage and handling. The selection of binder is therefore critical, as it directly impacts not only the chemical purity of the material, but also its thermal stability and resistance to moisture.

Overall, charcoal offers superior reactivity but suffers from handling and stability issues, whereas agglomerated biocarbon provides operational robustness at the expense of reduced reactivity. One way to compensate for the lower reactivity of agglomerates is to reduce the final particle size, thereby shortening diffusion distances and increasing the available reactive surface area. In practice, agglomerate development requires balancing multiple properties,

including reactivity, mechanical strength, thermal stability, impurity levels, and moisture resistance. The optimal solution represents a compromise between these factors, while remaining cost-effective for industrial use.

5. Conclusion

This work presents industrial experience with the introduction of biocarbon in silicon furnace operation and demonstrates that stable operation is achievable at substitution levels exceeding 50% of the carbon demand. This was validated on a 17 MW furnace without long-term loss of average silicon yield.

The work further demonstrates that successful implementation depends not only on material properties but also on operating practices. The structured qualification methodology and transition from reactive to controlled operation were essential for achieving stable furnace performance.

The comparison between charcoal and agglomerates highlights the trade-off between reactivity and handling strength, emphasizing the need for optimized material selection and properties.

Continued research and development, both in-house and in collaboration with universities, research institutions, and industry partners, strongly supports Wacker Holla in progressing toward its climate goals.

6. References

LIASA (2026). *Produtos: Silício Metálico*
https://liasa.com.br/nosso-negocio/produtos

Minasligas (2026). *Silício Metálico*
https://www.minasligas.com.br/portal/produtos/silicio-metalico/

Isbaex, C. 2014. *Influência da densidade do carvão vegetal na produção de silício metálico*. Master's dissertation. Universidade Federal de Viçosa.
https://locus.ufv.br/items/7a55fe76-17f9-4fcf-8fec-67be8ffd2bc2

Halland, T. and Øvrelid, S. 2024. Roadmap to carbon neutrality, *Proceedings of the Silicon for the Chemical and Solar Industry XVII - ISBN 978-82-692919-3-3*, Trondheim, Norway, 10-13 September 2024, pp. 1-7.
SSRN: https://ssrn.com/abstract=4944161 or DOI: http://dx.doi.org/10.2139/ssrn.4944161

Sigurd Johannes Slåtsve Øvrelid
Metallurgist, Wacker Chemicals Norway AS, Holla Metall

Master in process metallurgy from NTNU, Norway. Worked as a trainee and metallurgist in Eramet Norway, Porsgrunn before joining Wacker in 2023. Currently working with raw materials and process support at the Holla site in Kyrksæterøra.

Ringdalen, E., S. Jayakumari, T. Aarnæs, and A. Anderson. 2026. SiO-generation for H2 reduction with SiH2 process. In *Silicon for the Chemical and Solar Industry XVIII*, edited by M. Tangstad, H. Rong, A. Valderhaug, B. Andresen, H. Dalaker, and I. G. Page. Kristiansand, Norway, September 7–10. https://doi.org/10.55669/oa900836

SiO- generation for H2 reduction with SiH2 process

E. Ringdalen[1], S Jayakumari[1] TAarnæs[1], A. Anderson
[1]SINTEF, Norway, *eli.ringdalen@sintef.no*

Keywords: Silicon, hydrogen, SiO-gas, quartz

Abstract The SiH2 process is a concept for production of silicon by H_2 as reductant. The idea is to produce SiO gas by reaction between SiO_2 and internal recycled Si. Produced SiO is reduced by H_2 to Si and H_2O. The two reactions take place at different temperatures. To realise the proposed concept, knowledge about the kinetics for the involved reactions is needed. Reaction between SiO_2 and Si to produce SiO is discussed here. In the experiments, flow of warm SiO gas from the reaction has been measured continuously by a new method. This method shows that the reaction rate varies with time and have a peak with very high SiO generation that start as the temperature reach around 1750 °C to 1800 °C and then reduces rapidly until a lower rate is reached. Effects on reaction SiO_2 + Si ⇄2SiO of various other parameters such as gas composition, gas flow rates, temperature and properties of SiO_2 and Si source is also discussed.

1. INTRODUCTION

The SiH2 project proposes a novel process concept, SiH2 process shown in Figure 1where hydrogen substitutes carbon as reductant resulting in Si-production with no CO_2 emissions (Ringdalen et al., 2024).

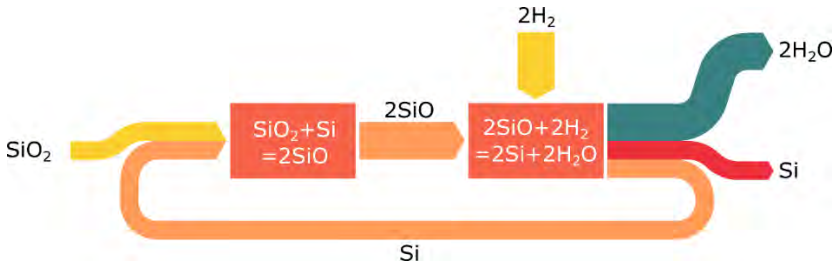

Figure 1 Concept for SiH2 process.

The process is based on two main reactions. First SiO-gas is produced by reaction (1) between liquid Si and solid or liquid SiO_2. Produced SiO is then reduced by hydrogen by reaction (2) to water (H_2O) and Si. Half of the produced Si is recirculated back to be used as reductant for production of SiO from SiO_2 by reaction (1). Remaining produced Si go to the final product. If other Si-sources are used for reaction (1), more of the produced Si will end up in the final product. Final Si production by reaction (2) require that SiO gas is available as reactant. It is thus crucial for the process that SiO produced by reaction (1) do not react back to SiO_2 and Si by the condensation reaction, reaction (3). This is the reverse of reaction (1).

$$SiO_2(s, l) + Si(l) = 2SiO(g) \quad (1)$$

$$SiO\ (g) + H_2(g) = Si\ (l) + H_2O\ (g) \quad (2)$$

$$2SiO\ (g) = Si\ (l) + SiO_2\ (l, s) \quad (3)$$

This work is licensed under the Creative Commons Attribution 4.0 International License. To view a copy of this license, visit https://creativecommons.org/licenses/by/4.0/

Reaction (1) and reaction (2) will at a pressure of 1 atm not be in equilibrium or run to left within the same temperature range. Production of SiO by reaction (1) in reasonable amounts will take place above around 1750 °C, close to the melting point of SiO_2, while reaction (2) between SiO and H_2 will take place below around 800 °C. Production of Si by this process will thus require either to find conditions where SiO can be produced by reaction (1) with lower temperatures, conditions where SiO can be reduced by H_2 by reaction (2) at higher temperatures, or conditions where SiO can be cooled down to a temperature where it can be reduced with H_2 according to reaction (2) before it reacts back to SiO_2 by reaction (3). Based on the known slow kinetics for reaction (3) (Schei et al., 1998),(Broggi A, 2021), cooling of produced SiO gas is regarded as the most probable alternative. Production of Si-H compounds instead of Si is another alternative.

Revealing the potential for the SiH2 process require knowledge of all the involved reactions and how they are affected by different parameters. Reaction (1) is an important part of existing Si-production. It is also important for producing SiO to be used in investigations of reactions involving SiO. Results from different studies not targeted towards, but involving reaction (1) between SiO_2 and Si are here summarised together with studies of reaction (1) done as part of the SiH2 project

2. SiO generation from reaction between SiO_2 and Si, background.

The main reaction studied here is reaction (1), production of SiO gas from SiO_2 and Si. This is an endothermic reaction with $\Delta H_{1800\,°C}$ = 598 kJ/mol. Produced SiO gas is stable only at high temperatures and will react back to SiO_2 + Si during cooling(Broggi A, 2021). The reaction is mostly studied at conditions where the gas phase contain CO-gas in addition to SiO, as is the case in industrial Si-production. Since there are limited data available about SiO-generation from SiO_2 + Si in a carbon free system, data from investigations in a system with carbon and at 1 atm total pressure is included in the discussion. The system will then include both SiO-generating and SiO consuming reactions. The most important are

$$SiO_2(s) + Si(l) = 2SiO(g) \qquad \Delta H_{1800} = 598\ kJ/mol \quad (1)$$

$$2SiO_2(s, l) + SiC(s) = 3SiO(g) + CO(g) \qquad \Delta H_{1800} = 1367\ kJ/mol \quad (4)$$

$$SiO(g) + 2C(s) = SiC(s) + CO(g) \qquad \Delta H_{1500} = -74\ kJ/mol \quad (5)$$

$$SiO(g) + SiC(s) = 2Si(l) + CO(g) \qquad \Delta H_{1800} = 171\ kJ/mol \quad (6)$$

The equilibrium content of SiO in a CO-SiO gas mixture at a total pressure of 1 atm at different temperatures is given by Figure 2

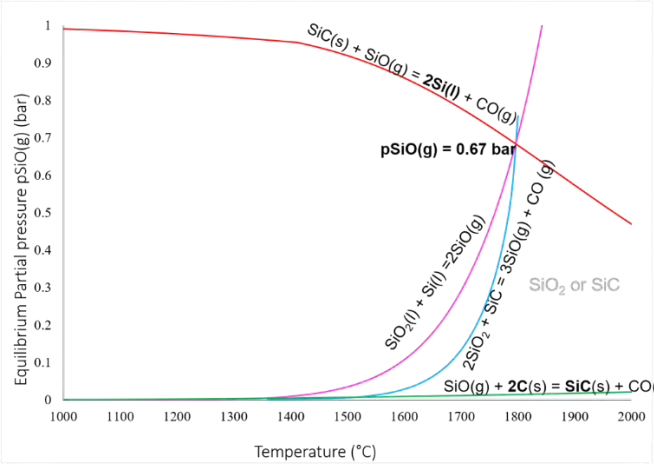

Figure 2 Stability diagram showing equilibrium pSiO for different reactions of importance for the Si process **(Jayakumari and Ringdalen, 2022)** The gas phase is a mixture of SiO+CO with a total pressure of 1 atm. Adapted from (Schei et al., 1998).

This illustrates that the stable partial pressure of SiO above a mixture of SiO_2+ Si i very low at temperatures below around 1650°C but increase fast with increasing temperature. In a system containing carbon, produced SiO can be consumed by reactions with carbon. SiO generated above around 1500 °C, reacts to SiC according to reaction (5) at low partial pressures of SiO. Produced SiC can react further with SiO_2 according to reaction (4) producing SiO. Above a temperature of 1800 °C and a partial pressure of SiO between around 0.5 to 0.67 bar, SiO reacts with SiC to Si according to reaction (6) Si. For the SiH2 process where the aim is a carbon free system, reaction (4) to (6) will not take place. Since most of the investigations of reaction between SiO_2 and Si are done in a carbon containing system, they and especially the consumption of produces SiO will be an important part of the evaluation of the obtained results.

SiO generation from SiO_2 + Si by reaction (1) has been found (Andersen, 2010) (Bao et al., 2013) to have a slow reaction rate at 1550 °C. The rate increased with temperature with a slight decrease around melting point for SiO_2, followed by a fast increase in rate at temperatures above the melting point. Sindland (Sindland and Tangstad, 2021) found that the rate of reaction (1) increased with reaction area and temperature. It was not affected by quartz source. The rate could be expressed by equation (7). Reaction area is corrected for melting of SiO_2 by an agglomeration factor F described by (Sindland and Tangstad, 2021).

$$\frac{d\alpha}{dt} = 6.25x10^8 A exp(-\frac{557x10^3}{RT}) \qquad (7)$$

A similar expression was found (Tangstad et al., 2019) for rate for SiO-generation by reaction (4) between SiO_2 and SiC. Kinetic parameters as activation energies and frequency factors found in different other investigations are summarised in the paper. Comparison of rate for reaction (1) and reaction (4) by Sindland (Sindland and Tangstad, 2021) show that with the same reaction areas, the rate for SiO generation from the two reactions are within the same range, but that SiO generation from SiO_2 + Si is faster than SiO generation from SiO_2 + SiC at all temperatures with largest difference at the highest temperatures. Rate for SiO-generation by reaction (4) SiO_2+ SiC was in the investigations by Tangstad (Tangstad et al., 2019) and by Folstad (Folstad et al., 2021) found not to be affected by ratio between the different SiO_2 polymorphs for the investigated quartz source.

Physical and chemical properties of quartz and their changes during heating vary between commercial available quartz sources (Ringdalen, 2015). This might have an effect on both design and operating conditions for reactors for SiO generation from reaction between SiO_2 and Si and also for investigations of this reaction. Parameters that are found to vary are thermal stability, (Ringdalen, 2014) (Jusnes, 2020), rate for transformations to different SiO_2 polymorphs (Ringdalen and Tangstad, 2016), (Jusnes, 2020),(He et al., 2021), volume changes during heating and melting properties (Ringdalen et al., 2020). Molten silica has a high viscosity which can be lowered by content of minor elements in the quartz source.(Dalaker, 2025). Operating conditions as heating rates, gas flow rates and temperature gradients may affect the observed differences between quartz sources. They may also affect agglomeration and segregation between the reacting phases and the rate for SiO-generation.

2. Investigations of reaction between SiO_2 and Si

SiO has been generated by reaction (1) as a part of other studies where this reaction was not the main focus. Results and observations from such investigations will give useful information about reaction (1) between SiO_2 and Si. Parameters. conditions and results from different investigations are here summarised and compared. The presented results are generated as a "byproduct" from other investigations targeted at other objectives and does not systematically investigate reaction (1). Results from the following studies are included: Production of SiO gas from SiO_2+ Si with different partial pressures of SiO for bio carbon investigations(Ringdalen, E and Jayakumari S, 2025), investigations of properties of remaining SiO_2 after reactions between SiO_2 and Si, and investigations of SiO_2 + Si reaction for the SiH2 process. The presented investigations are done in two different resistance heated graphite tube furnaces for investigations of 10-40 gram samples, with on-line gas measurement. The main difference is that the two-zone furnace has two chambers with individually controlled temperatures and the possibility for on-line measurement of SiO-content in the flow of warm gas between these. Set-up in the furnaces varied between the different investigations and are presented as a part of these.

2.1 Production of SiO gas from SiO_2+ Si with different partial pressures of SiO

Methodology

As a part of an investigation of reactions between SiO and carbon (Ringdalen, E and Jayakumari S, 2025),. SiO-gas was produced in the ReSiNa furnace by reaction between SiO_2 and Si by two different set-ups shown in Figure 3. The main difference between these is the larger size of the crucible and higher amount of SiO_2+ Si in series B compared to series A. There is a temperature gradient in the lower part of the crucible of around 15°C/cm. Reported temperature is measured at the top of the graphite sieve. Temperature in the bottom of the Si + SiO_2 bed is around 75-85 °C higher than this. Gas, either Ar or CO was introduced at the top of the graphite sieve. Gas flow varied between the experiments. The materials were heated by 25 °C/min to 1750 °C and held at this temperature for the designated time of 5 or, 15 but most often 30 min and then cooled down to 25 °C. SiO generation was determined through mass loss of the sample.

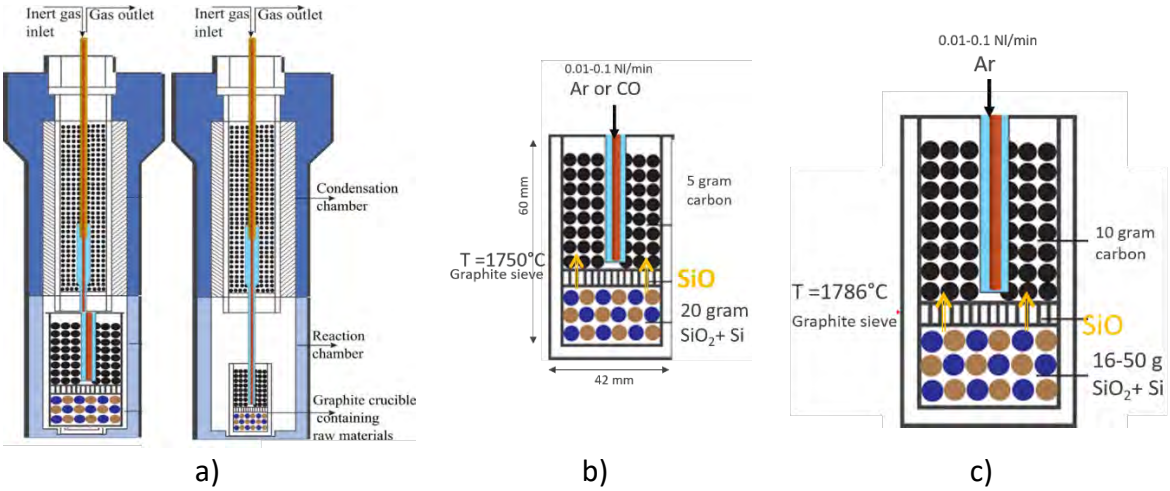

Figure 3 Set-up for investigations of SiO_2 + Si reaction to produce different $p_{SiO.}$ (a) furnace set-up, b) Set-up series A, c) set-up series B.

Two different sources of SiO_2 + Si was used: 1) SiO granules, which is commercially available 2-4 mm granules of an amorphous mixture of SiO_2+ Si. Particle size of the individual grains is to small to be seen in EPMA and thus in µm size or smaller. 2)Pieces of SiO_2 + Si is a stoichiometric mixture of individual 1-4 mm particles of quartz and pure Si.

The aim of this work was to generate a known partial pressure of SiO from the lower chamber in order to investigate how partial pressure of SiO would affect its rection with carbon. In series A the aim was to have the same SiO flow from the lower chamber in all the experiments and to obtain different SiO content in the gas in the various experiments by varying the flow of introduced Ar or CO gas. Both total gas flow and SiO-content in the gas are then varied. In Series B, the aim was to have the same total gas flow in all the experiments and to vary the SiO-content in the gas, by vary both flow of generated SiO-gas and flow of introduced gas. Flow of generated SiO-gas was varied by varying amount of SiO_2 + Si and thus contact areas between SiO_2+ Si. Planned flow of SiO was for both cases calculated by the kinetic equation found by Sindland (Sindland and Tangstad, 2021), equation (7). The experiments behind the work of Sindland is done in the apparatus described in Figure 3 with a set up similar to set-up b) with 20 grams of separate 1-5 mm pieces of SiO_2+ Si. Gas was introduced above the SiO_2 + Si bed in both the experiments by Sindland and those discussed here, but in the experiments by Sindland there were no graphite sieve and no carbon bed in the crucible. In the experiments by Sindland the temperature was measured at the bottom of the crucible in contrast to the current experiment where it was measured at the top of the sieve.

Results

Planned and obtained combinations of gas flow and partial pressure of SiO for the current experiments are compared in Figure 4. For Series A, the obtained combination of gas flow and p_{SiO} are close to the planned trend although it is a lot of scatter. SiO-generation and consequently total gas flows are in general lower when CO gas is used instead of Ar-gas. The slightly higher than planned SiO-generation for experiments with Ar is assumed to be a consequence of the different locations for temperature measurement, just above the SiO_2 + Si bed in series A and at the bottom of the layer in the experiments by Sindland. In series B all experiments had a higher generation of SiO gas than expected and consequently a higher total gas flow than planned. SiO-generation was lower from pieces of SiO_2+ Si than for granules with SiO_2+ Si.

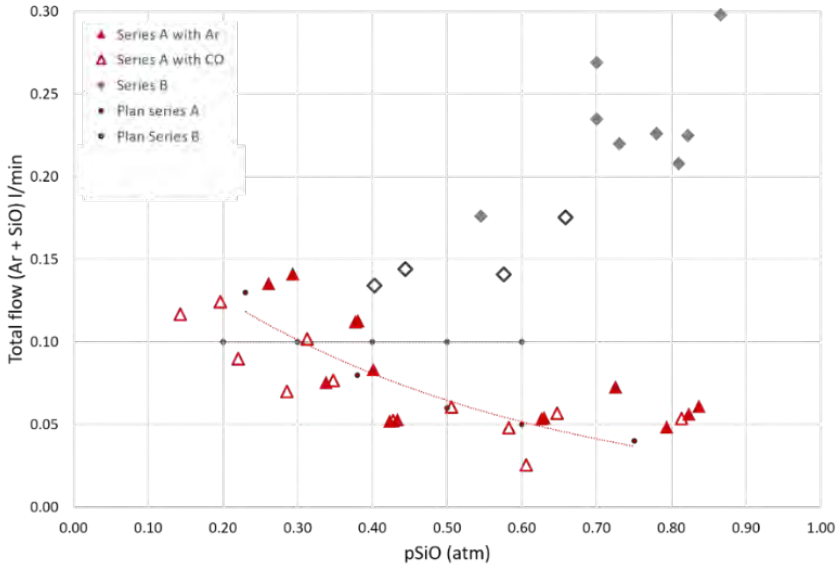

Figure 4 Planned and obtained combinations of gas flows and partial pressure of SiO for the experiments of series A and Series B In series A markers for experiments with CO instead if Ar gas is not filled. I series B, markers for experiment with pieces of SiO_2 + Si instead of granules are not filled. A trendline is included for the planned combinations. One point in series B (pSiO= 0.93, gas flow= 0.53) is regarded as an outlier and not included.

In the kinetic equation (equation 7) for reaction (1), gas flow is not included as a variable. The varying gas flows used in the experiments will thus not affect the calculated combination of total gas flow and partial pressure of SiO. The relatively good correlation between planned and obtained values in series A indicate that this assumption is valid and that the flow of gas introduced above the Si+ SiO_2 bed will not affect the rate for SiO-generation. The lower rate for SiO-generation when CO was used instead of Ar indicate that the gas atmosphere will be of importance for rate of SiO-generation. This should thus be taken into account when the kinetic equation is used in systems with CO-gas, as in industrial furnaces for Si-production. For SiH2 process that is carbon free, the higher rate for SiO-generation in Ar is expected to be an advantage. The higher than calculated SiO-generation in all experiments in series B shows that for other conditions and other raw materials, another kinetic expression with other parameters must be used.

The relative effects of different variables are compared in Figure 5. Average SiO flow during the experiments were expected to increase with increasing amount of material since this gives a higher total contact area between SiO_2 and Si. This seems not to be the case. For granules of SiO_2+Si, average flow of SiO did not increase when the amount of material was doubled. The comparison of two different amounts of pieces of SiO_2 + Si indicates the same also for this source, although the difference might be within the experimental uncertainty. Both Figure 4 and Figure 5 indicate that SiO-generation from SiO_2 + Si granules are much higher than from separate pieces of SiO_2 + Si. This might be attributed to the very low grain size for particles in the granules of SiO_2+Si giving a higher contact area, or to a higher reactivity of the amorphous SiO_2 in the granules compared to SiO_2 in the larger SiO_2 pieces from quartz origin. Amorphous silica in granules of SiO_2+ Si may also have other melting properties than crystalline SiO_2 in the pieces of SiO_2 and Si. Other explanation might also possible. The main parameter that affects average SiO flow seems to be reaction time. Average flow of SiO gas is higher when the holding time is shorter. Average flow rate was nearly 3 times higher with 5 minutes holding time than with 30 minutes holding time. This indicates that after an initial high rate for generation of SiO, the reaction will slow and maybe stop completely.

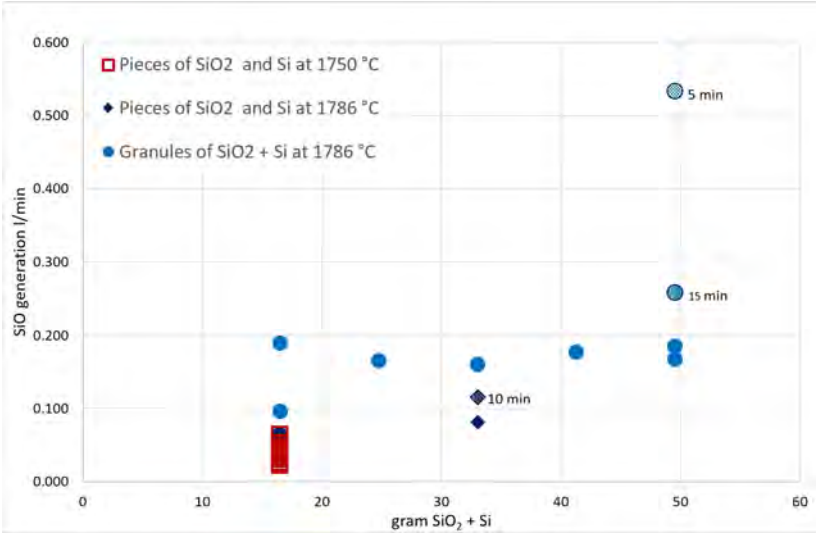

Figure 5 Generation of SiO gas in l/min from different amounts of either pieces of SiO_2 and Si or granules of SiO_2+Si in 1750 or 1786 °C. When nothing else is specified in the figure, the holding time was 30 minutes.

2.2 Investigations of reaction between SiO_2 + Si

Methodology

Reaction between SiO_2 and Si is currently investigated in an on-going work in SiH2 project to study SiO-generation. Results from this will be published separately, but some initial results are presented here. Preliminary investigations of slag formation from quartz, done with the same methodology, generated as a side result information about the reaction between SiO_2 and Si that also will be presented

The experiments were done in the two zone furnace, shown in Figure 6. It has two separately controlled heating zones, both resistances heated. Composition of gas flowing from lower to upper crucible are measured on-line with FTIR (Hestnes Bakke, 2026). In the current work, SiO-content was measured. Composition of cold off gas are measured on-line with µGC. Changes in material during the experiments are found through visual assessments, weight changes and characterisation by EPMA. In both sets of experiments, the raw materials were a mixture of industrial quartz (Qz42) with more than 99 % purity and PV grade Si. In each experiment 75 gram of a 1:1 molar mixture of SiO_2+ Si was used In the slag formation experiments, the raw materials had a size of 1-3 mm and in the SiH2 experiments either 0.5-1 mm or 1-1.5 mm. Ar with a flow of 0.2-0.4 l/min was introduced at the bottom of the crucible and flushed through the SiO_2+Si bed. The materials were heated with 50 °C/min to the designated temperature varying between the experiments from 1650 °C to 2000 °C and held at this temperature for the designated time varying between 5 and 30 minutes in the slag formation experiments and 180 minutes in the SiH2 experiments. Temperature difference between bottom and top of the 80 mm high lower crucible was in the newer experiments found to be around 10 °C. The apparatus was improved both between and within the two series. The exact values of data generated in the different experiments are thus not directly comparable, but general trends can be found.

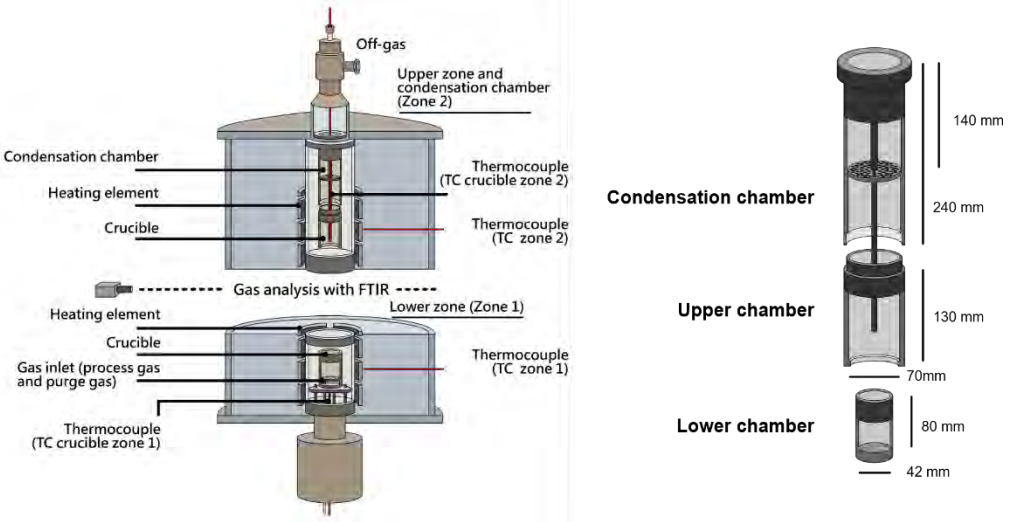

Figure 6 Sketch of two zone furnace. Overview to the left, Crucible sizes to the right.

Results

When the SiO_2 + Si mixture is heated to above approximately1400 °C, Si will melt, and above 1750 °C SiO_2 will melt. Contact area between the two materials will then change as Si flows down. Examination of the crucibles after the experiments revealed that at 1800 °C, Si and SiO_2 was fully separated with a layer of molten SiO_2 above a layer of Si, as seen in Figure 7. This will lower contact area and are thus expected to reduce the reaction rate. Since this is a graphite furnace, carbon is present in the system. A layer of SiC had, as shown in Figure 8, formed around the Si particles in most of the experiments. Such a layer was also seen in the experiments for SiO formations and in the experiments by Sindland. This layer between the SiO_2 and the Si particles is expected to affect the rate of reaction between these.

Figure 7 Crucible after experiment at 1800 ° C showing segregation with Si at bottom with melted SiO_2 above. Diameter of crucible is 42 mm.

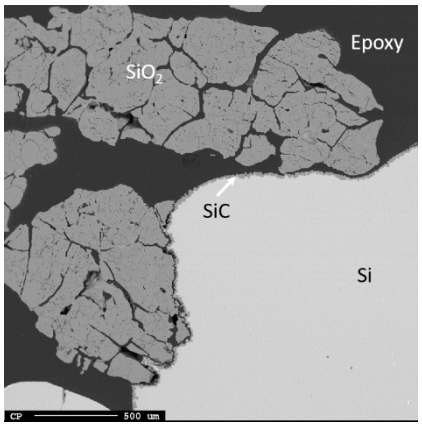

Figure 8 EPMA picture showing SiC formed around the molten Si at the interface between SiO_2 and SiC.

Since the only product from the reaction is a gas, weight loss will, if side reactions are disregarded, show amount of reacted material. As expected, this increased with temperature as shown in Figure 9 for preliminary experiments for slag formation and in Figure 10 for SiH2 experiments. They both show the same trends with very little reaction until the temperature is above 1750 °C and that not all material had reacted when the experiments were finished, even

after 3 hours reaction time. The main difference between the two sets of results is the longer holding time for the SiH2 experiments and the difference in particle size. The different sizes of raw materials used in the SiH2 process experiments did not seem to affect amount of reacted. The small difference in amount of reacted after 5 minutes and 30 minutes seen in Figure 9 indicate that the reaction rate is much faster in the start and then slow down. This might also explain the relatively small difference between amount of reacted after 30 minutes seen in Figure 9 and after 180 minutes seen in Figure 10.

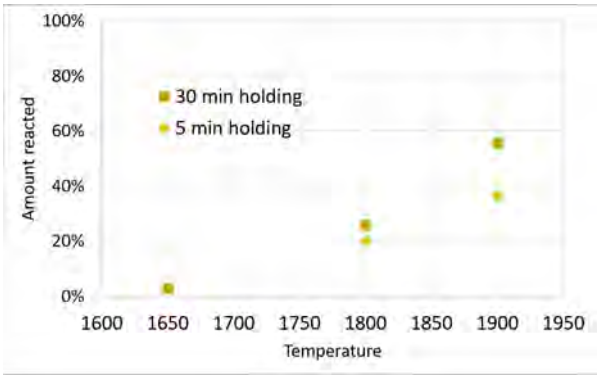

Figure 9 Amount of reacted SiO_2 + Si at different temperatures and holding times in slag formation experiments, 1-3 mm particle size.

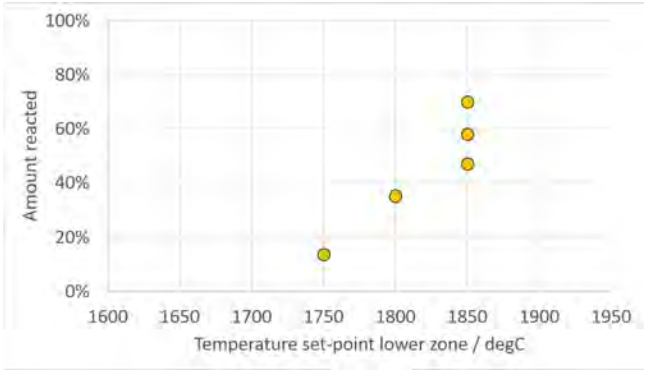

Figure 10 Amount of reacted SiO_2 + Si in SiH2 process experiments with 180 minutes holding time and 0.5-1 and 1-1,5 mm particle size.

Continuous measurement of SiO formation with time in the slag formation experiments presented in Figure 11 shows that generation of SiO is very fast in the beginning with the highest rates and most of the SiO evolution in the first 10 minutes after the rapid reaction starts. After 15- 20 minutes holding time, there is very little SiO generation indicating that the reaction has nearly stopped. The high rate of SiO generation starts around 1750 °C to 1800 °C. Similar behaviour is also indicated from the on-going SiH2 experiments. Also, in these there seems to be a peak in SiO generation when a temperature around 1800 °C is reached with a very high generation of SiO in the first 15-30 minutes of the holding time but declining with time in this period.

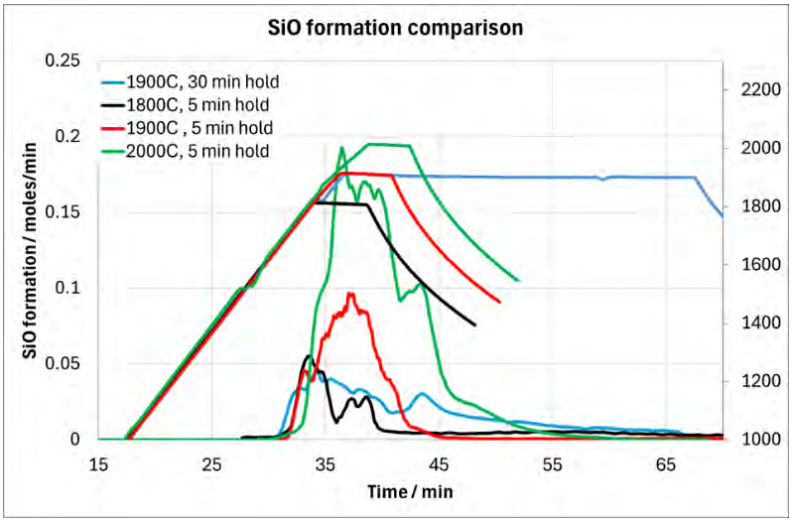

Figure 11 Variation with time in flow of warm SiO gas from reaction between SiO_2+ Si at different temperatures.

3. Discussion

The presented results cover different experimental set-ups, variations in raw material sources and sizes, gas atmospheres and flows as well as reaction temperatures. Based on this, some

general features and effects of parameters on reaction (1) between SiO_2 and Si, can be discussed. There are not enough directly comparable experiments to generate kinetic parameters or to quantify uncertainties in the measurements.

The kinetic equation and parameters for rate for reaction (1) found by Sindland(Sindland and Tangstad, 2021) was found to be valid for reaction between pieces of quartz and Si with a similar set-up to that used by Sindland. It was found also to be valid for different flow rates of gas although this is not a parameter in the equation. This indicates that mass transfer in the gas phase is not rate determining. Substituting Ar-gas with CO gave a lower rate showing that that gas atmosphere can be of importance for the rate of reaction. In further development of the SiH2 process this can be useful in finding a process design that gives the desired partial pressures of SiO. For SiO_2 and Si pieces a set-up with larger crucibles and more materials gave a higher SiO-generation than predicted in the kinetic equation. This might be within the uncertainty of the experiments or a result of other parameters such as segregation or variation in rate with time.

Segregation between SiO_2 and Si with accumulation of Si at the bottom of the crucible below SiO_2 has been observed in several experiments. This will reduce the contact area between SiO_2 and Si and is thus expected to reduce the reactions rate. The mechanism behind the segregation is believed to be that at temperatures above 1400 °C, Si melts and may start to flow downwards out of the quartz particles while quartz is either solid or acting as a solid due to its high viscosity.

When granules of SiO_2 + Si were used as raw material instead of pieces of quartz and Si, the reaction rate was much higher than predicted. The granules are a 1:1 mol mixture of ultrafine particles of Si and amorphous SiO_2. The higher reaction rate can either be a result of the ultrafine particle size or a higher reaction rate for amorphous SiO_2 compared to pieces of quartz. At temperatures where SiO_2 is molten, the raw material source is not expected to have any impact. With the slow melting of quartz (Ringdalen et al., 2020), the quartz is expected to be partly molten at 1750 °C, and a difference in reaction rates for different sources at this temperature can not be excluded. Since Folstad (Folstad et al., 2021) found that this is not the case for reaction (4) between SiO_2 and SiC, and Sindland reported that quartz source will not affect reaction between SiO_2 and Si, the higher rate for reaction with granules is expected to be a result of the ultra-fine grain size. This will both give a higher contact area between the phases and most likely lower the downward flow of Si and thus give less segregation. If the case is that amorphous silica gives a higher reaction rate, this can be an advantage for the SiH2 process. Amorphous SiO_2 as microsilica, could then be a good alternative as SiO_2 source. Higher amount of SiO_2 + Si will give a higher contact area between the two phases and was thus expected to give a higher reaction rate and generation of more SiO. This was as seen in Figure 5 not the case for granules of SiO where SiO generation in l/min was independent of amount of material.

Reaction rate will as shown in the kinetic equation increase exponentially with increased temperature. This was also seen in the experiments shown in Figure 9 and Figure 10. Very little SiO is formed below 1750 °C. Total amount of reacted material depends in addition to the temperature on the holding time. With a constant rate of SiO generation, measured average rate for SiO formation in l/min SiO should at the same temperature be the same independent of holding time. Total amount of reacted will then increase approximately linearly with time. This is not case here. SiO generation in l/min is higher with shorter holding times, and it is as seen in Figure 9 not much difference between amount reacted after 5 minutes and 30 minutes. This indicates a higher reaction rate when the reaction temperature is reached and that this

slows down with time. This is confirmed with on-line measurements of generated SiO as seen in Figure 11. The on-set temperature for the rapid reaction and high generation of SiO is around 1750 °C to 1800 °C. This is assumed to be connected to melting of SiO_2 and its lower viscosity with increased temperature. This has not been investigated and the mechanism behind this change in rate with time is thus not established. The variation in SiO generation with time has an impact on experiments where a known or stable SiO flow is needed for upstream reactions, and for evaluation and modelling of processes where SiO is involved. For design of the SiH2 process where partial pressure of SiO will affect both condensation of SiO and its further reaction with H_2, the variation in SiO generation with time must be included in the evaluation.

4. Conclusions

The kinetic equation and kinetic parameters for reaction (1) between SiO_2 and Si developed by Sindland (Sindland and Tangstad, 2021) was found to be valid for reaction between pieces of SiO_2 and Si in comparable conditions to the experiments they are based on. Flow of Ar gas is not included in the equation, but this was shown not to affect rate of SiO generation. CO-gas will slightly reduce the rate of SiO-generation. Granules with a 1:1 molar mixture of SiO_2+Si will give a higher reaction rate than predicted. This will not increase with increasing amount of granules. Rate for reaction (1) between SiO_2 and Si is not constant with time for a given temperature. At a temperature between 1750 °C and 1800 °C it will become very fast with a high peak and then decline rapidly during the next 15-30 minutes until the reaction nearly stop. As a consequence of this average SiO-flow for a given period vary strongly with length of the period it is averaged over and will be higher for shorter periods averaged around the peak.

For the SiH2 process the aim is to first have a high productivity of SiO, then cool the gas down without condensation and finally reduce it with H_2 to Si with a high yield. The partial pressure of SiO is critical in all these parts of the process. Having the knowledge that partial pressure vary considerably with time is thus important for the further development of the process, and methods to mitigate this should be pursued. If the reaction rate for granules is due to its content of amorphous SiO_2, use of amorphous SiO_2 sources such as microsilica could be beneficial for the SiH2 process.

Acknowledgements

This work has been funded by the Research council of Norway through project 325464 FP SiH2 and by the Research council of Norway and FFF (The Norwegian Ferroalloy producers Research association) through the projects 336175 KSP BioMet and 326581 KSP Recursive. They are all acknowledged.

5. REFERENCES

Andersen, V., 2010. Reaction mechanism and kinetics of the high temperature reactions in the silicon process (MSc thesis). NTNU, Trondheim, Norway.

Bao, S., Tangstad, M., Tang, K., Ringdalen, E., 2013. Production of SiO Gas in the Silicon Process. Presented at the INFACON XIII, Almaty, Kazakhstan, pp. 273–282.

Broggi A, 2021. Condensation of SiO and CO in silicon and ferrosilicon production (PhD Thesis). NTNU.

Dalaker, H., 2025. FactSage Calculations on the viscosities of silica melts (SINTEF Report No. 2025:00140). SINTEF.

Folstad, M.B., Ringdalen, E., Tveit, H., Tangstad, M., 2021. Effect of Different SiO2 Polymorphs on the Reaction Between SiO2 and SiC in Si Production. Metall. Mater. Trans. B. https://doi.org/10.1007/s11663-020-02053-x

He, J., Jusnes, K.F., Tangstad, M., 2021. Phase Transformation in Quartz at Elevated Temperatures. Asp. Min. Miner. Sci. 6, 691–699.

Hestnes Bakke, 2026. Non-Intrusive Monitoring of Silicon Monoxide gas using Infrared Spectroscopy. Appl. Spectrosc. Submitted.
Jayakumari, S., Ringdalen, E., 2022. Effect of Varying SiO Contents on Si and FeSi Production. https://doi.org/10.2139/ssrn.4118642
Jusnes, K.F., 2020. Phase transformations and thermal degradation in industrial quartz. NTNU, Trondheim, Norway.
Ringdalen, E., 2015. Changes in Quartz During Heating and the Possible Effects on Si Production. JOM 67, 484–492. https://doi.org/10.1007/s11837-014-1149-y
Ringdalen, E., 2014. Quartz properties in the silicon production. Presented at the Silicon for the Chemical and Solar Industry XII, Trondheim, Norway.
Ringdalen, E., Bao, S., Tveit, H., 2020. Effect of melting properties of quartz on industrial Si and FeSi production, in: Proceedings of Silicon for the Chemical and Solar Industry XV. Trondheim, Norway, pp. 101–118.
Ringdalen, E, Jayakumari S, 2025. Effect of gas flow and partial pressure on the reaction between SiO(g) and C (SINTEF Report No. 2025:01082).
Ringdalen, E., Svenum, I.-H., Aarnæs, T., 2024. SiH2- A new process for Si-production based on hydrogen. https://doi.org/10.2139/ssrn.4942625
Ringdalen, E., Tangstad, M., 2016. Phase transformations in quartz and its effect on furnace operation. Presented at the Proceedings of Silicon for the Chemical and Solar Industry XIII, Kristiansand, Norway, pp. 269–278.
Schei, A., Tuset, J.K., Tveit, H., 1998. Production of high silicon alloys. Tapir Trondheim.
Sindland, C., Tangstad, M., 2021. Production Rate of SiO Gas from Industrial Quartz and Silicon. Metall. Mater. Trans. B 52, 1755–1771. https://doi.org/10.1007/s11663-021-02143-4
Tangstad, M., Safarian, J., Bao, S., Ringdalen, E., Valderhaug, A., 2019. Reaction Rates of 2SiO2+SiC=3SiO+CO in Pellets at Elevated Temperatures. Asp. Min. Miner. Sci. 3. https://doi.org/10.31031/AMMS.2019.03.000558

Eli Ringdalen
Senior Research Scientist, SINTEF

MSc. in ore geology from NTNU, Norway in1979. PhD in Metallurgy at NTNU, Norway in 1999. Subject of PhD thesis was HCFeCr process. Worked in various mining and metallurgical companies including Mn-alloy and silicon plants until 2006. From then working at SINTEF with projects within FeSi and Si, Mn-alloys, HCFeCr, as well as with environmental challenges, CO_2 emissions and development of new process, especially based on gas- metal reactions. Main research field: pyrometallurgy, ores, quartz, carbon and biocarbon reductants, use of gases, H_2 and CH_4 in metal production.

Ganesan, N. S., B. Ryningen, K. D. Log, Y. Xu, W. Palitzsch, and M. Bellmann. 2026. Assessment of the Availability and Recovery Potential of Silicon from Discarded Solar Panels. In *Silicon for the chemical and solar industry XVIII*, edited by M. Tangstad, H. Rong, A. Valderhaug, B. Andresen, H. Dalaker, and I. G. Page. Kristiansand, Norway, September 7–10, 2026. https://doi.org/10.55669/oa900838

Assessment of the Availability and Recovery Potential of Silicon from Discarded Solar Panels

Nagarajan Somi Ganesan[1], Birgit Ryningen[1], Kristina Dyrli Log[2], Yijiang Xu[1], Wolfram Palitzsch[3], Martin Bellmann[1]

[1]SINTEF Industry, Trondheim, Norway, nagarajan.ganesan@sintef.no

[2]Elkem Silicon Product Development AS, Kristiansand, Norway

[3]LuxChemTech GmbH, Freiberg, Germany

Keywords: Circular Economy, EOL-PV Panels, Recycling , Silicon Recovery, Secondary Raw Materials

Currently, silicon is a base material for more than 95% of photovoltaic (PV) modules. The deployment of PV modules is expected to increase significantly across the European Union (EU), leading to generation of millions of tons of cumulative end-of-life photovoltaic (EOL PV) waste in the coming decades. This huge expansion and waste accumulation emphasize the need for a circular economy approach. QUASAR, an EU-funded project, aims to develop a holistic recycling approach to manage the growing volume of EOL PV panels. With the help of advanced recycling technologies, QUASAR aims to enable efficient recovery of materials such as silicon, silver, polymers, glass, and other metals. As part of QUASAR, this study assesses the expected quantities of EOL PV modules and the silicon embedded within them under chosen scenarios based on historical PV installation data, EU-level installation forecasts, dynamic module mass-to-power ratios, and material composition data. In addition, the characteristics of a recovered silicon sample obtained from a preliminary refining step were evaluated using Inductively Coupled Plasma Mass Spectrometry (ICP-MS) and LECO analysis. Based on the quantity and quality assessments, the potential demand for silicon recovered from EOL PV panels as a secondary raw material in PV and other value chains has been discussed in the context of a circular economy approach.

1. INTRODUCTION

The goal of carbon neutrality drives the photovoltaic (PV) deployment at a faster pace, with terawatt annual installations anticipated globally by the end of this decade (Goldschmidt et al. 2021) (ITRPV 2025). In the European Union (EU), PV installation has reached 406 gigawatts (GW) in 2025 (Jäger-Waldau 2025) and is expected to reach 2.3 terawatt (TW) by 2050, according to long-term projections by the EU Joint Research Centre (JRC) (Chatzipanagi et al. 2025). This rapid expansion is expected to result in a substantial accumulation of end-of-life photovoltaic (EOL PV) modules in the coming decades, demanding effective waste management strategies and the valorisation of the recoverable materials. The profitability threshold for the sustainable recycling sector is reported to be 19000 tonnes/year (Bošnjaković et al. 2023). Therefore, understanding future EoL-PV waste generation is essential for planning effective collection, recycling, and material recovery strategies (Mahmoudi, Huda & Behnia 2021). In addition, assessing the quality of recovered materials is crucial to determine their suitability for reuse. QUASAR[1]is an EU-funded project that aims to develop a holistic approach for EOL PV panels, enabling the efficient recovery of key materials such as silicon, silver, polymers, glass, and other metals using advanced recycling technologies such as the water-jet delamination method and the pyrolysis process . Although QUASAR covers the

[1] https://quasar-project.eu/

This work is licensed under the Creative Commons Attribution 4.0 International License. To view a copy of this license, visit https://creativecommons.org/licenses/by/4.0/

entire PV recycling value chain, this study focuses specifically on PV waste estimation and the characterization of a recovered silicon sample.

Recent studies (Foster et al. 2025; Kastanaki 2025) estimate that PV waste will reach around 6 million tonnes (mt) and 23 mt of PV waste by 2040 and 2050 based on earlier National Energy and Climate Plans (NECPs) targets of 624 GW by 2030 and 1,116 GW by 2040. This study reassesses future crystalline silicon (c-Si) PV waste generation under the Early Loss scenario using the EU JRC net-zero projection of 2.3 TW installed PV capacity by 2050. A silicon sample recovered from EOL PV panels using the waterjet delamination method and preliminary chemical etching processes was assessed through Inductively Coupled Plasma Mass Spectrometer (ICP-MS) and LECO analysis to identify the presence of metallic and non-metallic impurities. Based on the quantity and quality of the recovered silicon, its suitability as a raw material and potential market demand were discussed. Evaluating the quantity of PV waste and the quality of recovered silicon is essential for supporting circular economy approaches through sustainable resource utilization and secondary raw material integration.

2. METHODOLOGY AND MATERIALS

2.1 Data

Historical and projected deployment of crystalline silicon (c-Si) PV was derived from PV installation data and the market share of c-Si technology. The mass of c-Si PV was estimated using a dynamic power-to-mass conversion factor (tonnes per megawatt). Based on the Weibull Early Loss (EL) scenario, the distribution of EOL PV waste and embedded silicon was estimated. The methodology of the waste estimation is shown in Figure 1 and the data sources and other assumptions are given in Table I.

Figure 1: Methodology for calculating EOL-PV waste and embedded silicon

Table I Data sources and assumptions

PV deployment data in the EU – (1996 – 2021)	(Czajkowski et al. 2023)
PV deployment data in the EU – (2021 – 2025)	(Solar Power Europe 2025)
Market share data for c-Si PV	(Philipps et al. 2025)(Foster et al. 2025)
Dynamic power-to-mass ratio	(Ovaitt et al. 2022)
Dynamic Si content in PV modules	(Ovaitt et al. 2022)
Specific polysilicon consumption (2026-2030)	(Taylor et al. 2025)
Specific polysilicon consumption (2030-2050, assumed constant)	1.5 tonnes/MW
Assumptions on PV deployment projections from (2026-2050)	
2026-2030 (750 GW by 2030 - Solar Power Europe 2025)	68.7 GW (annual average installations)
2030-2050 (2.3 TW by 2050 - Chatzipanagi et al. 2025)	77.8 GW (annual average installations)

PV Lifespan - Weibull Early Loss Scenario: The Early Loss Scenario is modelled using a Weibull function (Equation 1)

$$F(t) = 1 - e^{\left(\frac{t}{\beta}\right)^{\alpha}} \quad (1)$$

Where t is the lifetime of the panel in years, α and β are the shape factors. The failure probability curve is governed by the shape factors α (2.4928) and β (30) (Kastanaki & Giannis 2022); (Joseph M Kuitche 2010). The corresponding failure probability curve is shown in Figure 2. The detailed assumptions of the EL Scenario are provided elsewhere (IRENA 2016).

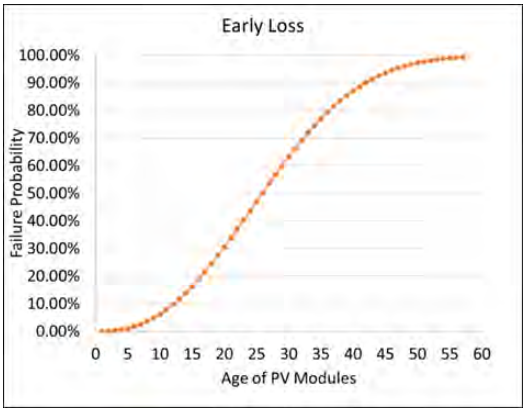

Figure 1: Shape function - Early Loss

Silicon content in PV modules: The dynamic silicon composition in PV modules was obtained from (Ovaitt et al. 2022) as shown in Figure 3, to estimate the potential availability of Si embedded in EOL c-Si PV modules

Average specific polysilicon consumption: In 2025, the average polysilicon consumption was around 2 tonnes per MW. Figure 3 shows the average specific polysilicon consumption estimated from the JRC report *Deep Dive on Critical Raw Materials for Solar Photovoltaics in the EU* for 2026-2030 (Taylor et al. 2025). From 2031 to 2050, it is assumed to remain constant at 1.5 tonnes/MW.

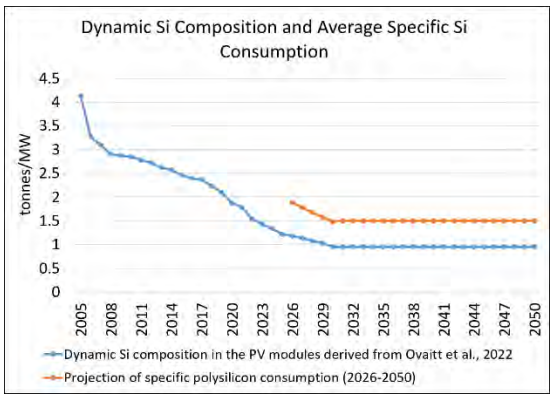

Figure 3: Dynamic Si composition in PV modules and Average Specific polysilicon consumption

2.2 Experimental Methods

Recovered silicon from EOL PV Modules: The recovered silicon sample was obtained from Luxchemtech GmbH, which uses the water-jet delamination process to separate the cell and polymer layers from the glass, enabling intact glass recovery and producing polymer flakes containing silicon cells. The silicon is then recovered from the polymer fraction through chemical processes. The details of the water-jet delamination and chemical processing steps can be found elsewhere (PVPS Task 12 2024) (Dimd et al. 2026).

Characterization techniques: ICP-MS and LECO analyses were carried out on the recovered silicon sample. ICP-MS detects the presence of metal impurities at the ppm level. For ICPMS, the sample was decomposed in 65% HNO_3 and 40% HF in a Milestone microwave and was further diluted with 5% HNO_3 and analyzed on an Agilent 8800 Triple Quadropole ICP-MS (ICP-QQQ) with an SPS 4 Autosampler. Further, They were quantified against standards from Inorganic Ventures, with ^{115}In as the internal standard. LECO analysis uses infrared absorption and thermal conductivity to measure combustion gases within a sample. This process determines the presence and concentration of C, O and N. LECO analysis converts the elements in a sample into their oxidized forms using either the gas fusion method (hydrogen, nitrogen, and oxygen) or the combustion method (carbon).

3. RESULTS AND DISCUSSION

3.1 Quantity Estimation of EOL PV Modules

Based on historical and projected cumulative PV installations by 2050 and the dynamic market share of c-Si PV modules, approximately 2.25 TW of the total 2.3 TW is estimated to comprise c-Si technology. This corresponds to an estimated mass of 121.14 mt. Under the EL scenario, almost all modules installed by 2050 are projected to reach end-of-life by 2100, resulting in approximately 120.54 mt of cumulative EOL PV waste. Accordingly, cumulative EOL PV waste is estimated to reach 2.31 mt, 9.99 mt and 28.30 mt by 2030, 2040, and 2050, respectively. The annual distribution is expected to increase in the coming years, reaching a maximum of 3.15 mt in 2060 as shown in Figure 4. It should be noted that these estimates are based solely on PV installations up to 2050. Consequently, PV capacity added after 2050 would further contribute to both cumulative and annual EOL PV waste generation beyond 2050 and up to 2100.

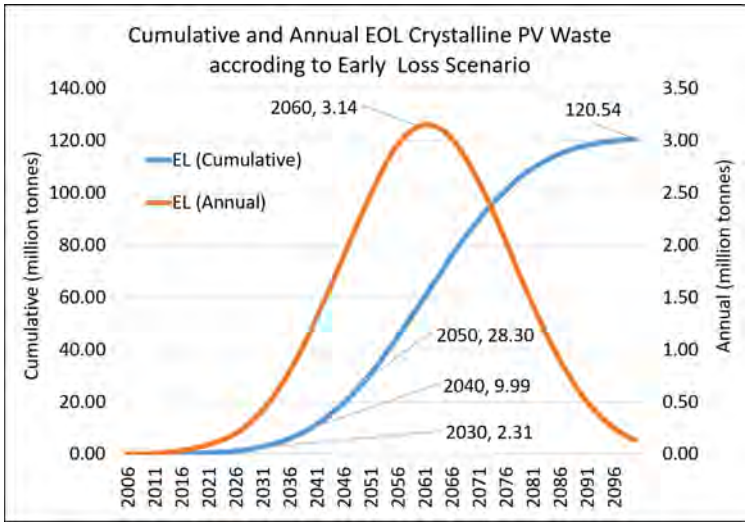

Figure 2 Cumulative and Annual EOL PV waste generation according to EL scenario

3.2 Quantity Estimation of Silicon in EOL PV Modules

Based on the dynamic silicon composition of PV modules, the estimated 121.14 mt of cumulative EOL PV waste contains approximately 2.45 mt of embedded silicon. The embedded silicon in EOL PV modules is estimated to be around 79.4 kt (1000 tonnes (kt)), 289.8 kt, and 706.5 kt by 2030, 2040, and 2050, respectively, as shown in Figure 5.

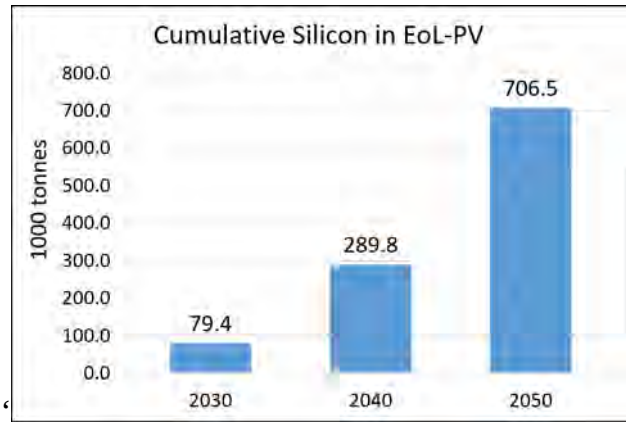

Figure 5: Cumulative embedded silicon in EOL PV according to EL scenario

Based on the projected PV deployment from 2026 to 2050 and the average specific polysilicon consumption, the cumulative polysilicon demand of the EU PV industry during 2026–2050 is estimated to reach 2.83 mt. On the other hand, the valorisation of the silicon in the EOL PV waste mainly depends on the recycling practices such as EOL PV modules collection efficiency, silicon recovery efficiency and refining efficiency. Table II shows the assumed efficiencies for the recycling practices under high, medium and low scenarios.

Table II Assumptions on recycling efficiencies

Scenarios	Collection efficiency	Recovery efficiency	Refining efficiency
High	100%	100%	100%
Medium	85%	85%	85%
Low	70%	70%	70%

Based on these assumptions, the silicon availability from EOL PV waste was estimated. Figure 6 shows the cumulative polysilicon demand in the EU PV industry and the cumulative silicon availability from EOL PV waste under low, medium, and high scenarios. By 2050, the amount of silicon recoverable from EOL PV waste is estimated to reach 706.5 kt, 433.9 kt, and 242.3 kt under the high, medium, and low scenarios, respectively, corresponding to 25.0%, 15.3%, and 8.6% of the cumulative silicon demand of the EU PV industry.

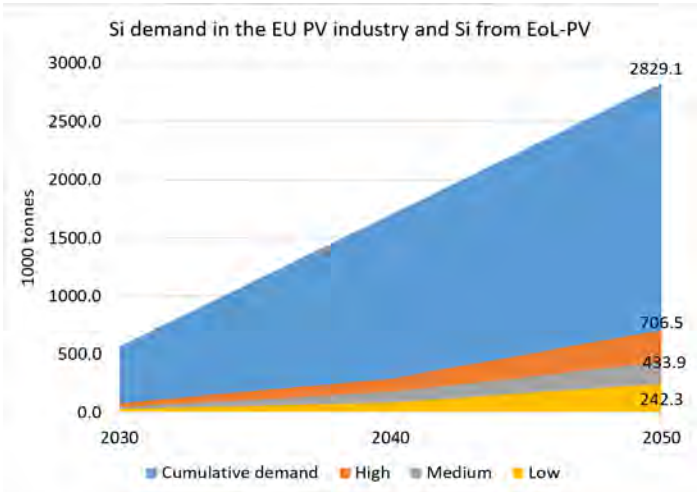

Figure 3 Polysilicon demand in the EU PV industry and silicon from EOL PV modules

3.3 Quality of Recovered Silicon from EOL PV Modules

The results of the ICP-MS analysis, along with the impurity levels in metallurgical-grade silicon (MGS) and compensated solar-grade silicon (SGS) are shown in Table III, where compensated SGS refers to silicon of sufficient quality to manufacture standard solar cells without significant efficiency losses. The compensated SGS values reported by Coletti (2011) are used only as a reference benchmark representing a minimum quality level, as silicon purity requirements have evolved with the development of advanced PV cell technologies. Most impurities in the recovered silicon are significantly lower than those in MGS (Mallah et al. 2025) and approach or fall within compensated SGS-level thresholds (Gianluca Coletti 2011), indicating effective purification during recycling process. Elements such as Fe, Ti and Cu are present at relatively low concentrations, while boron and phosphorus remain below or close to detection limits. However, the recovered silicon exhibits a comparatively high silver concentration (182 ppm) and slightly high aluminium concentration (47 ppm) likely

originating from PV cell metallization, highlighting the need for further refining for high-purity applications.

Table III Metallic impurities in the recovered silicon by ICP-MS

Element	MGS	Compensated SGS	Si from EoL-PV	RSD
		In ppmw		(%)
B	14.51	<0.45	<0.052	-
Al	4689.30	<5	45	4.8
P	8.11	<0.6	<5.2	-
Sb	123.44	<0.05	0.43	0.8
Ti	733.94	<0.05	5.6	5.2
Fe	8230.86	<5	2.9	2.8
Ni	92.10	<1	<0.52	-
Cu	54.65	<1	14	0.9
Na	35.16	<0.008	6.7	6.8
Ag	1	<0.1	182	0.7
Sn	<0.1	<0.1	0.28	3.2
Pb	<0.1	<0.05	<0.52	-

The LECO analysis measures the concentrations of C, N and O and the results are shown in Table IV. The recovered silicon contained 244 ppmw C and 940 ppmw O while nitrogen is below the detection limit, indicating the effective removal of Si_3N_4 anti-reflection layer. The C and O content remains higher than the low trace-level limits (<1 ppmw) required for SGS (Gianluca Coletti 2011), indicating the need for further process optimization or additional refining before direct reuse in the PV value chain.

Table IV Carbon, nitrogen and oxygen in recovered silicon by LECO

	C	N	O
ppmw	244	<20	940
RSD (%)	6.93	-	6.03

3.4 Secondary Raw Material Suitability

To reach the level of solar grade polysilicon (SGS), the purity of the recovered silicon should be in the range of 6N to 9N. However, the purity of the recovered silicon from the preliminary refining processes exhibits a purity of approximately 3N when considering all metallic and non-metallic impurities. Upgrading the preliminary recycling and refining processes to increase the purity of recovered silicon from 3N to 6N may enable its direct use in the PV industry. Several studies report that, despite relatively higher metal concentrations, comparable solar cell performance can still be achieved compared to that obtained by the solar grade feedstock. The typical parameters that differentiate the impact of each element are diffusivity and segregation coefficients. The metal impurities are categorized into three groups: fast diffusing (Cu, Ni, etc.), relatively fast (Fe, Cr, etc.) and slow (Ti, Mo, V, etc.). Al and Ti specifications should not be relaxed because they are not gatterable. The metal impurities with high and relatively high diffusivity in silicon can be better tolerated than slowly diffusing ones, since they can be more easily manipulated during the gettering process in cell manufacturing (Gianluca Coletti 2011). In such cases, the recovered silicon at the current purity level may be considered for blending with pure polysilicon feedstock. However, the impact of different impurities on advanced cell technologies such as tunnel oxide passivated contact (TOPCon) and heterojunction (HJT) cells still requires further investigation.

On the other hand, compared to MGS, EOL PV-derived silicon exhibits much lower metallic impurities. MGS is primarily used in Al-Si alloying, Silicone production and polysilicon

production industries. The current purity level of the recovered silicon enables its direct substitution for MGS in Al–Si alloy production, silicone manufacturing, and polysilicon industries. However, from a circular economy perspective, these applications offer relatively low economic value compared to higher-value reuse pathways.

4. CONCLUSIONS

This study provides a comprehensive assessment of PV waste generation under the chosen scenarios and the quantity of silicon recoverable from EOL PV modules based on low, medium and high recycling efficiency assumptions. Based on the EL scenario, the cumulative EOL PV waste in the EU is projected to reach 2.31 mt, 9.99 mt and 28.30 mt by 2030, 2040, and 2050, respectively. The estimations indicate that silicon recovered from EOL PV waste could make a meaningful contribution to the EU PV industry's silicon demand, supplying up to 25.0% by 2050 under the high scenario, compared with 15.3% and 8.6% under the medium and low scenarios, respectively. Apart from Al, Ag, O, and C, most impurities in the recovered silicon are considerably lower than those in MGS and are close to or within compensated SGS specifications, indicating effective purification during the recycling process. Although the current purity level of recovered silicon is sufficient for substituting MGS in several applications, its use in PV applications may require either blending with high-purity feedstock or further refining. These findings can support the development of circular economy strategies in the PV value chain.

4. ACKNOWLEDGEMENTS

This work is part of the QUASAR project funded by the European Union's Horizon Europe research and innovation programme under grant agreement number 101122298.

5. REFERENCES

Bošnjaković, M., Galović, M., Kuprešak, J. & Bošnjaković, T., 2023, 'The End of Life of PV Systems: Is Europe Ready for It?', *Sustainability*, 15(23), 16466.

Chatzipanagi, A., Jaeger-Waldau A, Letout, S., Mountraki, A. & Gea Bermudez, J., 2025, *Clean Energy Technology Observatory: Photovoltaics in the European Union - 2025 Status Report on Technology Development, Trends, Value Chains and Markets,* Publications Office of the European Union.

Czajkowski, A., Wajda, A., Poranek, N., Bhadoria, S. & Remiorz, L., 2023, 'Prediction of the Market of End-of-Life Photovoltaic Panels in the Context of Common EU Management System', *Energies*, 16(1).

Dimd, B.D., Palitzsch, W., Xu, Y., Ryningen, B., Ganesan, N.S. & Bellmann, M., 2026, 'Material recovery and characterization from end-of-life photovoltaic modules using water-jet delamination', *Solar Energy Materials and Solar Cells*, 306.

Foster, G., Kastanaki, E., Marschinski, F., E., B.J., Neuwahl, F. & Marschinski, R., 2025, *Circular Economy Strategies for the EU's Renewable Electricity Supply*, Publications Office of the European Union.

Gianluca Coletti, 2011, 'Impurities in silicon and their impact on solar cell performance'.

Goldschmidt, J.C., Wagner, L., Pietzcker, R. & Friedrich, L., 2021, 'Technological learning for resource efficient terawatt scale photovoltaics', *Energy and Environmental Science*, 14(10), 5147–5160.

IRENA, 2016, *End-of-Life Management: Solar Photovoltaic Panels*.

ITRPV, 2025, 'International Technology Roadmap for Photovoltaics (ITRPV) 16th Edition'.

Jäger-Waldau, A., 2025, 'Snapshot of photovoltaics - March 2025', *EPJ Photovoltaics*, 16.

Joseph M Kuitche, 2010, 'Statistical Lifetime Prediction for Photovoltaic Modules'.

Kastanaki, E., 2025, 'Dynamic assessment of photovoltaic waste streams in the EU-27 countries under the circular economy principles of "Reduce, Reuse and Recycle"', *Resources, Conservation and Recycling*, 214.

Kastanaki, E. & Giannis, A., 2022, 'Energy decarbonisation in the European Union: Assessment of photovoltaic waste recycling potential', *Renewable Energy*, 192, 1–13.

Mahmoudi, S., Huda, N. & Behnia, M., 2021, 'Multi-levels of photovoltaic waste management: A holistic framework', *Journal of Cleaner Production*, 294.

Mallah, A.R., Saevarsdottir, G., Heuer, M. & Svavarsson, H.G., 2025, 'Advancing Sustainability in Solar-Grade Silicon Production: Enhanced Boron and Phosphorus Removal via Silicon Refining from Al–Si Melt', *JOM*.

Ovaitt, S., Mirletz, H., Seetharaman, S. & Barnes, T., 2022, 'PV in the circular economy, a dynamic framework analyzing technology evolution and reliability impacts', *iScience*, 25(1).

Philipps, S., Ise, F., Warmuth, W. & Projects GmbH, P., 2025, *Photovoltaics Report*.
PVPS Task 12, 2024, *Advances in Photovoltaic Module Recycling Literature Review and Update to Empirical Life Cycle Inventory Data and Patent Review Task 12 PV Sustainability Activities*.
Solar Power Europe, 2025, 'EU Solar Market Outlook 2025-2030'.
Taylor, N., Kuzov, T., Chatzipanagi, A., Carrara, S., Jakimów, M., Materna, F., Espinosa, N., Latunussa, C., Bobba, S., Jaeger-Waldau & Leccisi, A., 2025, *D E E P D I V E SOLAR PHOTOVOLTAICS IN THE EU*, Publications Office of the European Union.

Nagarajan Somi Ganesan *is a Research Scientist at SINTEF Industry, Norway. His research focuses on silicon crystal growth, end-of-life PV recycling, silicon recovery, and circular economy strategies.*

Victorin, M. O., A. Sengoku, H. Kjønli, and H. M. Rong. 2026. Effect of Copper, Zinc and Tin on the reaction between silicon and hydrogen chloride. In *Silicon for the chemical and solar industry XVIII*, edited by M. Tangstad, H. Rong, A. Valderhaug, B. Andresen, H. Dalaker, and I. G. Page. Kristiansand, Norway, September 7–10, 2026. https://doi.org/10.55669/oa900840

Effect of Copper, Zinc and Tin on the reaction between silicon and hydrogen chloride

M.O. Victorin [2], A. Sengoku[1], H. Kjønli[2] and H.M. Rong[2]
[1]Elkem Japan, Japan
[2]Elkem Silicon Products, Norway

Keywords: Trichlorosilanes, direct chlorination, Tin, Zinc, Copper, High boilers

Abstract – Direct chlorination (DC) of metallurgical-grade silicon with anhydrous HCl is an industrial route to trichlorosilane (TCS), typically operated without intentional catalysts. In contrast, the methylchlorosilane direct synthesis (MCS) uses catalyst/promoter elements such as Cu, Zn and Sn, whose individual effects on silicon surface reactivity remain difficult to isolate because of CH_3Cl cracking and coke formation. In this work, DC was used as a simplified model system to evaluate the influence of typical MCS catalyst elements on TCS selectivity, reactivity and high-boiler formation. A synthetic silicon sample containing controlled amount of Fe, Al and Ca was tested with additions of Cu, Zn or Sn in a continuous lab-scale fluidized-bed reactor at 340 °C and 1.15 barg, with continuous silicon feeding to maintain a constant reaction mass. Product gases were analysed by online GC, and reacted residues were characterized by SEM–EDS. Cu increased silicon reactivity, lowering the reaction start temperature from 366 °C to 338 °C, without significantly affecting selectivity. Zn maintained high TCS selectivity but increased HCl loss, suggesting progressive surface deactivation through chloride-rich deposits. Sn had the strongest detrimental effect, decreasing TCS selectivity and preferentially increasing Si–Si bonded high boilers. SEM–EDS showed both Sn-rich particles and dispersed Sn in reacted Si-rich regions, indicating surface modification. These results identify Sn as a critical impurity for TCS production.

1. INTRODUCTION

1.1. Direct Synthesis

The Direct Synthesis (DS), also called the methylchlorosilanes synthesis (MCS), is a key step in silicone production. The direct process, discovered by Rochow-Müller in 1939, uses a copper-based catalyst for the reaction of Metallurgical grade silicon (MG-Si) powder with gaseous methyl chloride. Zinc (Zn), tin (Sn), and aluminum (Al) act as promoters to boost efficiency. Dimethyldichlorosilane ($(CH_3)_2SiCl_2$, M2), is the main product of the reaction but it is produced together with many by-products.

$$Si\ (s) + 2CH_3Cl\ (g) \rightarrow (CH_3)_2SiCl_2\ (g) \qquad (1)$$

Industrially this heterogeneous reaction takes place in a fluidized bed reactor under a pressure between 2.5 and 4 bars and a temperature around 300°C (Kanner & Lewis, 1993). Common objective of the MCS producers is to perform the reaction with a high productivity (50-80% of the methyl chloride consumed in the first pass), a high selectivity in M2 (more than 80% M2) and good silicon utilization (min 95% of the silicon converted to products).

Despite numerous studies and publications, today the mechanism of the direct synthesis of MCS has not been fully established. One challenge is that the direct synthesis suffers from a side-reaction where the CH_3Cl reagent cracks and forms carbonaceous compounds such as

This work is licensed under the Creative Commons Attribution 4.0 International License. To view a copy of this license, visit https://creativecommons.org/licenses/by/4.0/

CH_4 and solid carbon, which degrade the performance (Blaser et al., 2021). Formation of carbon compounds on the surface also makes it very difficult to characterize the reacting powder.

1.2. Direct Chlorination

The process to produce Trichlorosilane (TCS; $HSiCl_3$)) by reaction of Si and anhydrous HCl has been given several names. Direct chlorination (DC) has become a common name and is used in this paper. Alternate names for the reaction are low-pressure chlorination, direct TCS process and, to make things a bit confusing, hydrochlorination. But today, hydrochlorination is commonly used for the process to produce TCS by reaction of silicon, hydrogen and silicon tetrachloride (STC; $SiCl_4$). This process is not discussed in this paper.

TCS is the basis compound for semiconductor silicon (Ashworth, Bunge and Colomb, 2024) as well as silicon for photovoltaic applications and a wide range of materials known as organofunctional silanes.

In the direct chlorination process, hydrogen chloride gas fluidizes a bed of metallurgical grade silicon powder. TCS is produced at a high rate according to equation 2 and STC is formed in a consecutive reaction between TCS and HCl according to equation 3 and also according to equation 4A and 4B (Dropka et al., 2006).

$$Si\ (s) + 3HCl\ (g) \rightarrow HSiCl_3\ (g) + H_2\ (g) \quad (2)$$
$$HSiCl_3\ (g) + HCl\ (g) \rightarrow SiCl_4\ (g) + H_2\ (g) \quad (3)$$
$$Si\ (s) + 4HCl\ (g) \rightarrow SiCl_4\ (g) + 2H_2\ (g) \quad (4A)$$
$$HSiCl_3\ (g) + HCl\ (g) \rightarrow SiCl_4\ (g) + H_2\ (g) \quad (4B)$$

In addition to STC, the other typical by-products are dichlorosilane (DCS), and the so-called "high-boilers", which comprise several silanes compounds with Si-Si and Si-O-Si bonds.

Industrially this reaction takes place in a fluidized bed reactor under a pressure between 2 and 5 bars and a temperature between 300-400°C. The DC reaction is typically conducted in fluid bed reactors that contain a large internal heat exchanger to remove the high heat of reaction generated by the exothermic reaction. The DC process is typically operated without any catalysts since the impurities present in the metallurgical silicon are enough to ensure high HCl conversion.

Higher reaction temperatures favor higher STC yields and lower TCS yields. While not a topic of this paper, the DC reaction can be run in a fixed bed reactor with lumps of metallurgical grade silicon at ~1100°C-1200. (Crawford et al., 2022).

1.3. Industrial operation conditions

Table 1 : Comparison of Direct Chlorination and the Rochow-Müller reaction

	Direct Chlorination	**Direct Synthesis or Rochow-Müller Reaction**
Reactants	MG-Si + anhydrous HCl	MG-Si + methyl chloride CH_3Cl
Temperature[°C]	300-400	265-310
Pressure[bar]	2-5	2-4
Catalyst	No	Cu, Zn, Sn, P Different form
Target products	Trichlorosilane $HSiCl_3$	Dimethyldichlorosilane - $(CH_3)_2SiCl_2$
By-products	Silicon tetrachloride - $SiCl_4$ Dichlorosilane - SiH_2Cl_2 Several High Boilers (HB), primarily chlorinated disilanes, like hexachlorodisilane (Si_2Cl_6)	Methyltrichlorosilane – CH_3SiCl_3 – M1 Methyldichlorosilane - $(CH_3)SiCl_2$ – MH Trimethylchlorosilane – $(CH_3)_3SiCl$ – M3 Tetramethylsilane – $(CH_3)_4Si$ – M4 Several High Boilers (HB) $(CH3)_xSi2Cl_y$, (x+y = 6)

1.4. Why this study

Direct synthesis is more complex than direct chlorination because it involves interactions among catalysts and promoters such as Cu, Zn, Sn, and other elements. In addition, methyl chloride introduces carbon into the system. During direct synthesis, CH_3Cl can crack in a side reaction, forming H_2, HCl, CH_4, and solid and liquid hydrocarbons (Blaser et al., 2021). These hydrocarbons, commonly referred to as coke, may deposit on active sites, lowering the productivity of $(CH_3)_2SiCl_2$, and lead to deactivation. (Blaser et al., 2021). CH_3Cl cracking also results in production of higher levels of lower value compounds such as methyldichlorosilane [MH; CH_3SiCl_2H] and methyltrichlorosilane [M1; CH_3SiCl_3].

In MCS chemistry, Zn and Sn are also known as important promoter elements, which have long been used to influence catalyst performance and product selectivity in the Rochow-Müller reaction. Although their beneficial effects have been widely recognized, their mechanistic roles remain not fully understood. Previous studies suggest that these elements can modify the electronic structure and adsorption behavior at active silicon surface sites, thereby affecting the dissociation of reactant molecules and subsequent surface reactions (Tanaka et al., 2003). In particular, Zn and Sn have been reported to exhibit distinct adsorption characteristics on Si surfaces, implying potentially different impacts on catalytic activity and by-product formation.

In addition, Cu and Zn may be present as trace elements in silicon raw materials. Tveit and Myrhaug (2000) describe that electrodes could contain some copper and biocarbon (charcoal and woodchips) could contain some zinc. Lindstad and Forseth (2024) show that the origin of the raw material for pyrolysis to make biocarbon will influence the trace element content in the silicon, especially the zinc. Switching from fossil carbon (coal, coke) to biocarbon (charcoal, woodchips) is a major lever for silicon producers to decrease their emissions (Ausland and Rong, 2020).

The recycling of crystalline silicon photovoltaic modules inherently reintroduces metallic impurities originally present in the panel structure, including Cu and Sn (Chen *et al*., 2024). These elements are integral to solar panel components and are quantitatively identified within the silicon cell fraction of the module composition (Chen *et al*., 2024). During recycling processes these metals may be recovered together with silicon, thereby creating a pathway for Cu and Sn contamination in recycled silicon feedstock (Chen *et al*., 2024).

This study, therefore, investigates whether typical MCS catalyst elements influence DC performance and how these catalysts deposit on the silicon surface.

2. EXPERIMENTAL SECTION

A series of laboratory experiments was conducted on a laboratory reactor to evaluate the effect of MCS catalysts (Cu, Zn, and Sn) on DC performance, including TCS selectivity, reactivity, and by-product formation. The study also aimed to investigate the distribution of the different catalysts on the silicon surface. This is why SEM-EDS analyses were performed to examine how the catalysts were deposited on the silicon after the reaction.
These experimental results are presented in this section.

2.1. Sample preparation

Five experiments were run in the lab scale DC reactor. The Al, Ca and Fe have been measured while the Cu, Zn and Sn have been calculated.

Table 2 : Composition of Samples with trace metal additions

Experiment	Al (weight %)	Ca (weight %)	Fe (weight %)	Cu (weight ppm)	Zn (weight ppm)	Sn (weight ppm)
Si-Fe-Al-Ca	0,11	0,006	0,27	-	-	
Si-Fe-Al-Ca 1000 ppm Sn	0,11	0,006	0,27	-	-	1 000
Si-Fe-Al-Ca 100 ppm Sn	0,11	0,006	0,27	-	-	100
Si-Fe-Al-Ca 1000 ppm Cu	0,11	0,006	0,27	1 000	-	-
Si-Fe-Al-Ca 1000 ppm Zn	0,11	0,006	0,27	-	1 000	-

The Si-Fe-Al-Ca sample has been made from pure silicon (polysilicon supplied by Wacker Chemie GmbH) melted and alloyed with iron (Fe), aluminum (Al) and calcium (Ca) in Elkem laboratory in Kristiansand (Norway). The level of Fe, Al and Ca has been decided to be close to typical value for MG-Si and pure silicon was used as a starting material to avoid any impact of other trace elements that can be found in MG-Si.
The tin was used as powder metallic form from Alfa Aesar®, with a top size of maximum 150 µm and purity of 99,995 % on metal basis.
The zinc was used as a powder metallic form from Alfa Aesar® with a top size of maximum 150 µm and a purity of 99,9%.
The Cu catalyst is added as a master alloy made from high purity Si and Cu. This master alloy is mixed with the Si sample to get the desired level of Cu, the fraction 125-180 µm used during the experiment had a content of 3,2 % Cu measured by XRF.

2.2. Lab-scale fluidized-bed DC reactor

The five experiments were run under identical reaction conditions described above. Experiments were conducted in a continuous laboratory-scale fluidized-bed DC reactor

operated at 1.15 barg and 340 °C. Silicon samples with very low reactivity will not react at 340 °C and need higher temperature (360 °C) to complete the experiment. The energy produced by reacting the HCl is important in maintaining the reaction rate. If the reaction stops it is typical that the reaction has to be restarted at a higher temperature.
Ground silicon was continuously added to maintain 5 g of reaction mass, using a particle size range of 125–250 µm. A continuous feed of anhydrous HCl with a small amount of argon was supplied to the reactor, with argon serving as an internal standard for the online gas chromatograph (GC). A filter positioned outside the reactor captured entrained fines and removed some impurities during operation. The process gas was then automatically analyzed by the online GC.
TCS selectivity is defined as the molar percentage of TCS in the product stream relative to the total chlorosilanes produced (TCS, STC, DCS, and high boilers). It is reported on a hydrogen-free and HCl-free basis. DCS and high-boiler selectivity are calculated in the same way. High boilers are defined in Table 3.
HCl loss is defined as the fraction of HCl that is not converted in the reactor, determined by measuring the residual HCl concentration in the reactor off-gas (Hesse and Pätzold, 2006). In a highly reactive system, most of the supplied HCl is consumed, and the residual HCl concentration may therefore fall below the gas chromatograph (GC) detection limit. Conversely, in a system with low reactivity, a larger fraction of HCl remains unreacted and can be detected by GC. HCl loss is used as an inverse indicator of silicon reactivity: low HCl loss indicates high reactivity, whereas high HCl loss indicates low reactivity.
The main performance indicators were total silicon consumption (up to 70 g, 12 reactor volumes), TCS selectivity, HCl loss (or reactivity), DCS selectivity, and high-boiler selectivity.

2.3. Gas chromatograph measurements

All selectivity measurements and the other quantified gas analyses are produced by a Varian 3900 gas chromatograph (GC). The GC is equipped with a packed column (30% QF1, 80/100 Chromosorb PAW) and a thermal conductivity detector (TCD). The product gas is sampled about each 19 minutes.

It was previously shown that by selecting appropriate chromatographic columns and optimizing the sample amount, various high-boiling components were successfully detected and quantified (Hoel and Rong, 2020). At present, the five types of high boilers given in Table 3 can be identified. Of the five compounds, three are siloxane species (HB1, HB2 and HB3) containing Si–O–Si linkages, while the remaining two (HB4 and HB5) are high-boiling species with Si–Si bonds:

Table 3 : list of High Boiler observed

HB	Formula	Likely name
HB1	$SiHCl_2$-O-$SiHCl_2$	Tetrachlorodisiloxane
HB2	$SiCl_3$-O-$SiHCl_2$	Pentachlorodisiloxane
HB3	$SiCl_3$-O- $SiCl_3$	Hexachlorodisiloxane
HB4	Cl_3Si-$SiHCl_2$	Pentachlorodisilane
HB5	Cl_3Si-$SiCl_3$	Hexachlorodisilane

2.4. SEM-EDS characterization of reaction residues

The solid residues obtained from the reactor after the reaction were characterized by scanning electron microscopy (SEM) coupled with energy-dispersive X-ray spectroscopy (EDS). The samples were mounted on aluminum stubs without further treatment.

SEM observations were carried out in backscattered electron (BSE) mode at an accelerating voltage (EHT) of 15 kV to examine the morphology and microstructure of the residues.
In addition, elemental distribution was evaluated by EDS mapping to visualize the spatial distribution of Si, Fe, Al, Ca, Cu, Zn and Sn in the samples.
Figure 1 presents representative SEM images of unreacted silicon particles with an initial size of 125–250 µm (a) and reacted particles collected after the experiment (b), showing consumed regions and crater-like reaction sites.

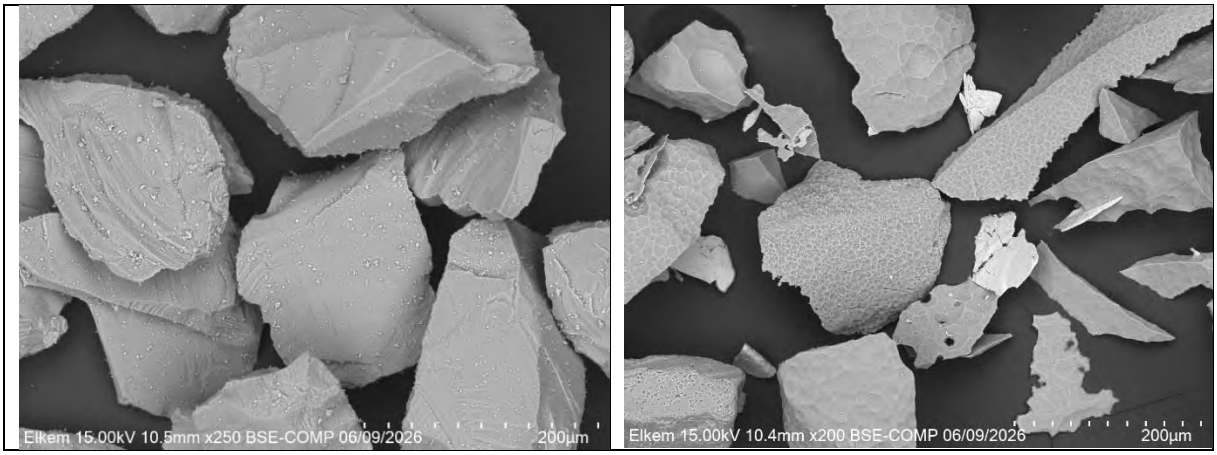

Figure 1: Unreacted silicon at 250x (a) and reacted silicon at 200x (b)

3. RESULT and DISCUSSIONS

3.1. Impact of Copper

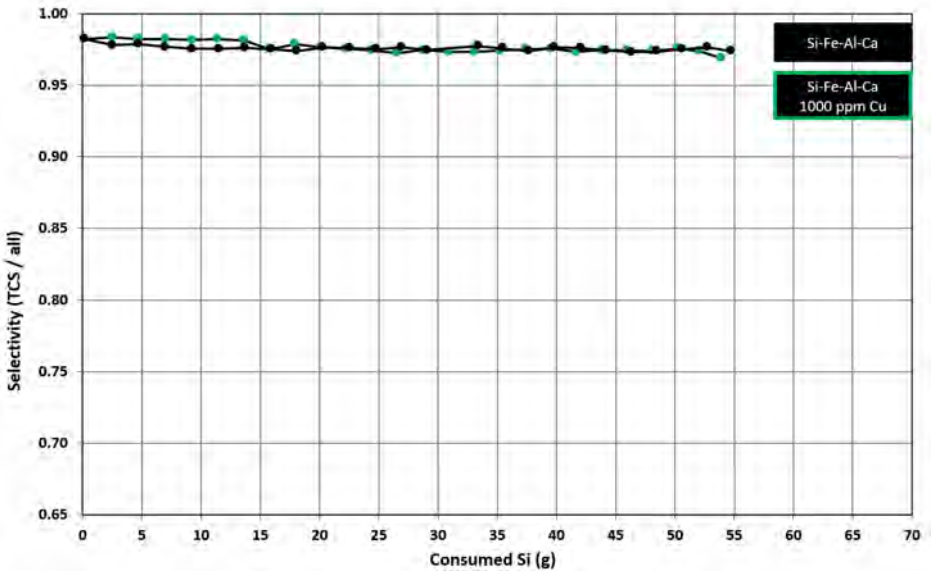

Figure 2 : Evolution of the TCS selectivity for reference sample and sample with 1000 ppm Cu

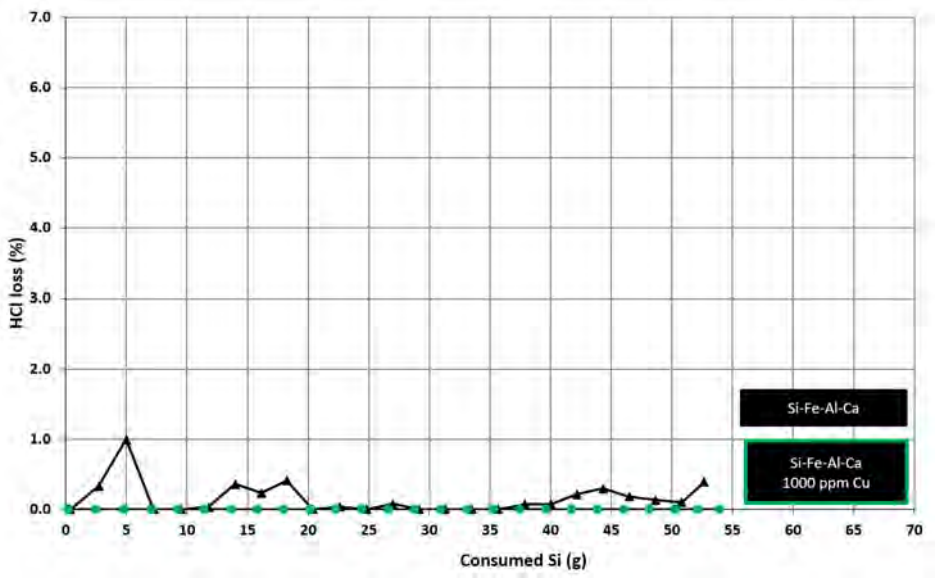

Figure 3 : Evolution of the HCl loss (%) for reference sample and sample with 1000 ppm Cu

The TCS selectivity of the reference material and the experiment with copper is shown in Figure 2. It should be noted that the reference material gives a TCS selectivity of about 97% and compared to typical MG-Si material this is a very high TCS selectivity and therefore it is the trace elements that are not present in the reference material that is impacting the TCS selectivity. There is no significant difference in TCS selectivity for the two experiments. The HCl loss is shown in Figure 3.

The experiment with 1000 ppm Cu shows no HCl loss, indicating high reactivity. This catalytic effect is also reflected in the reaction onset temperature, defined as the reactor-wall temperature required to initiate direct chlorination. In fact, each reaction is initially started by charging 5 grams of silicon to the reactor, starting gas (HCl + argon) feed and gradually increasing the reactor temperature to 380 °C by applying heat to the reactor. When the reaction starts, observed by a decrease in the reactor overhead pressure, the temperature controller is placed in automatic at a setpoint of 340 °C. The reaction onset temperature is the temperature when the pressure decreases.

The reference sample starts reacting at 366 °C, whereas the sample with 1000 ppm Cu starts at 338 °C, corresponding to a 28 °C decrease. In addition, *Figure 4* shows clear differences in reactor residue morphology. The Cu-containing residue (b and d) appears more fragmented, with more fine debris and disrupted particles. This may indicate that freshly added silicon requires time to react in the reference system, whereas in the presence of Cu the reaction proceeds faster and consumes the newly added particles. Ehrich et al. (1998) demonstrate that the silicon reactivity dramatically increases in presence of copper.

No significant differences are observed on TCS selectivity or DCS and High boiler formation. Cu is mainly impacting the reactivity.

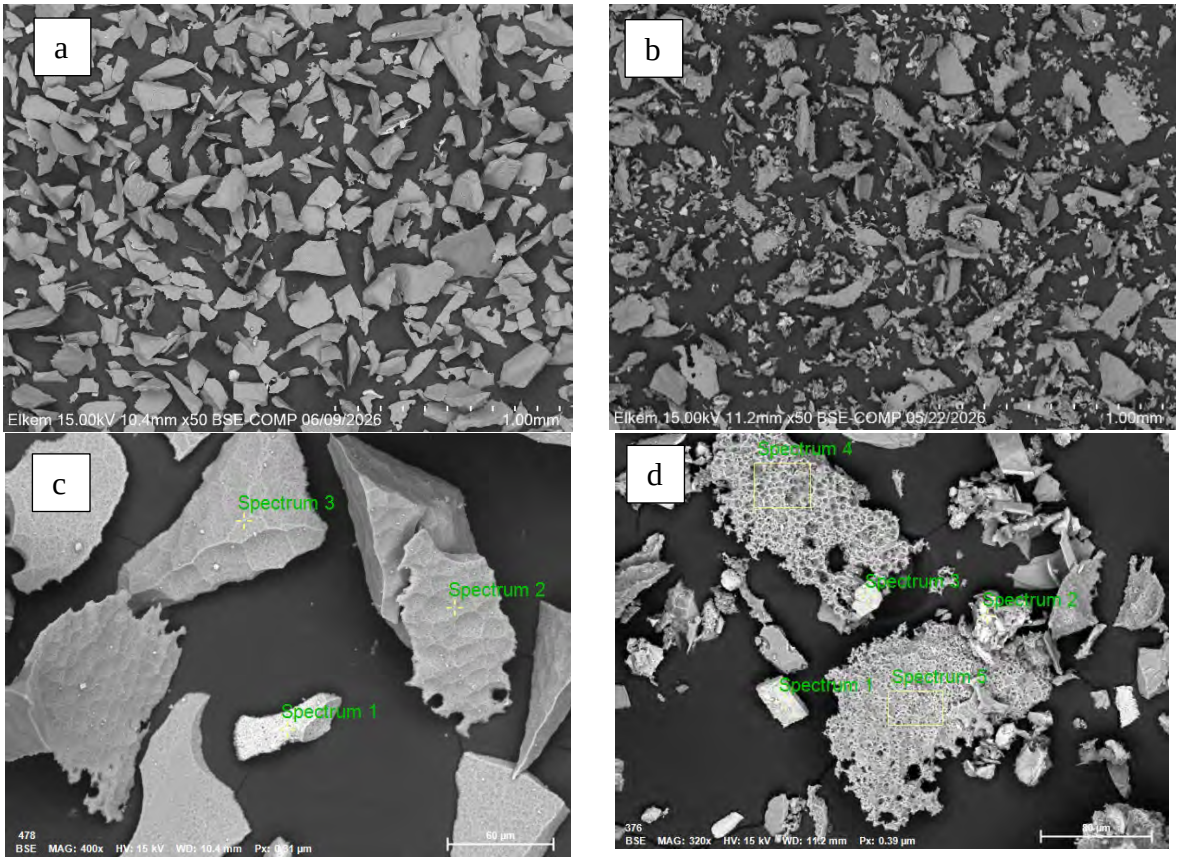

e

Atomic concentration /%

Spectrum	O	Al	Si	Cl	Ca	Fe	Pt
Spectrum 1	16.77	13.55	43.06	1.18	0.47	24.97	0.00
Spectrum 2	13.51	0.46	83.89	0.99		1.14	0.00
Spectrum 3	7.77		91.18	0.35		0.69	0.00

f

Atomic concentration /%

Spectrum	O	Al	Si	Cl	Ca	Fe	Cu	Pt
Spectrum 1	33.50	8.48	32.90	3.32	1.20	20.17	0.43	0.00
Spectrum 2	30.59	1.19	17.39	33.58		4.62	12.62	0.00
Spectrum 3	6.67	33.22	35.10	0.57		24.43		0.00
Spectrum 4	17.47	0.71	79.49	0.95		1.39		0.00
Spectrum 5	10.84	0.50	84.66	1.78		1.29	0.93	0.00

Figure 4 : Reacted silicon particles from reference sample (a at 50x and c at 400x) and from sample with 1000 ppm Cu (b at 50x and dat 320x) and semi quantitative composition of spectrum for reference sample (e) and sample with 1000 ppm Cu (f)

The SEM analysis of the experiment performed with 1000 ppm of Cu shows a homogeneous distribution of Cu across the silicon surface (c and d, *Figure 5*)). The silicon particles appear to be significantly consumed over most of the surface (a, *Figure 5*). Small craters can be observed, corresponding to areas where silicon has been locally consumed (b, *Figure 5*). Inside these craters (c, *Figure 5*), a porous structure with small holes is visible, suggesting localized material consumption.

The semi-quantitative EDS analysis (d, *Figure 5*) indicates that silicon is the dominant element in all analyzed areas (>85 at.%), with minor amounts of O, Fe, Al, Cl, and Cu. Oxygen is found due to oxidation of the surface after removing from the reactor. Copper is detected in all spectra at low concentration and appears to be homogeneously distributed.

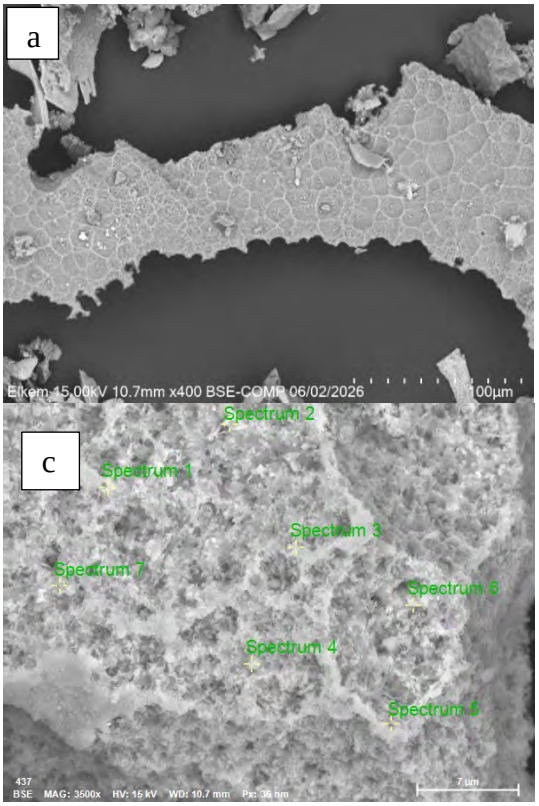

d

Atomic concentration /%

Spectrum	O	Al	Si	Cl	Ca	Fe	Cu	Pt
Spectrum 1	18.57	0.63	77.59	1.16	0.16	1.44	0.45	0.00
Spectrum 2	16.80	0.73	79.18	1.29		1.53	0.47	0.00
Spectrum 3	11.01	0.66	86.34	0.95		0.75	0.29	0.00
Spectrum 4	14.53	0.70	81.71	1.15		1.34	0.58	0.00
Spectrum 5	19.55	1.02	74.97	2.01		1.40	1.04	0.00
Spectrum 6	19.54	0.82	75.90	1.68	0.08	1.47	0.51	0.00
Spectrum 7	8.20	0.58	89.57	0.67		0.55	0.43	0.00

Figure 5 : Reacted silicon particles form sample with 1000 ppm Cu at 400x (a), 2300x µm (b), 3500x (c) and semi quantitative composition of spectrum (d)

3.2. Impact of Zinc

The impact of Zn addition on both TCS selectivity and reactivity was evaluated by comparing a reference sample with a sample containing 1000 ppm Zn.
As shown in *Figure 6*, the experiment with Zn gives slightly higher TCS selectivity than the reference.

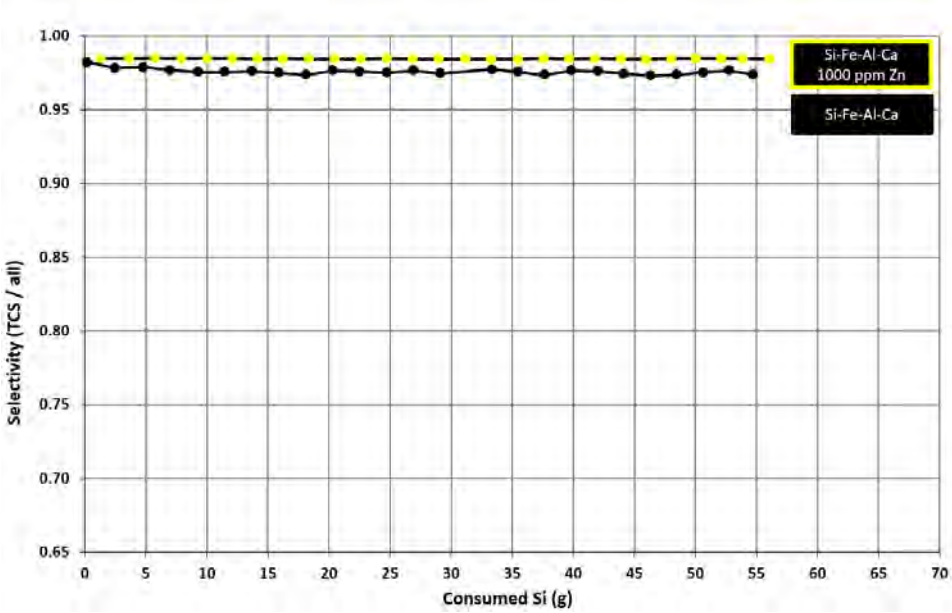

Figure 6 : Evolution of the TCS selectivity for reference sample and sample with 1000 ppm Zn

Figure 7 shows a significant increase in HCl loss in the presence of Zn, particularly at higher silicon conversion levels, where values exceed 5–6%, whereas the reference sample remains close to zero.
These results suggest that Zn does not affect the selectivity toward TCS formation, but a lower reactivity demonstrated by an increasing fraction of unreacted HCl over time compared to the reference system.

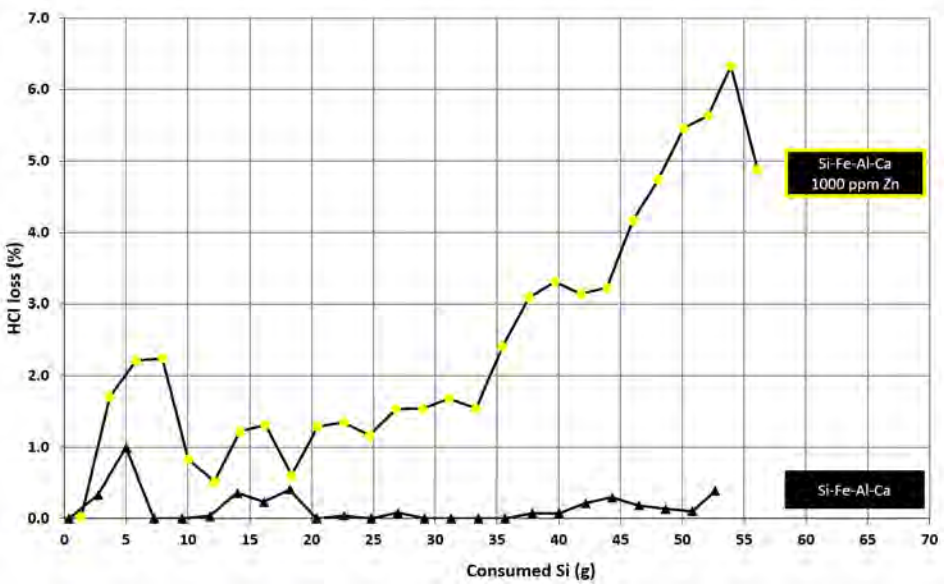

Figure 7 : Evolution of the HCl loss (%) for reference sample and sample with 1000 ppm Zn

Very small white deposits can be observed on the surface, *Figure 8* a, b and c. These deposits correspond to spectra 1 and 2 (*Figure 8* (d)) and contain Zn, Fe and Cl. They likely originate from a Zn–Fe chloride-derived phase. Over time, this phase could accumulate and limit access to Si surface.
Spectra 3, 4 and 5 correspond to the Si-rich matrix (>90 at.% Si), which represents the primary reaction surface. The presence of residual Zn in these regions suggests partial incorporation or surface interaction of Zn species within the active silicon phase.

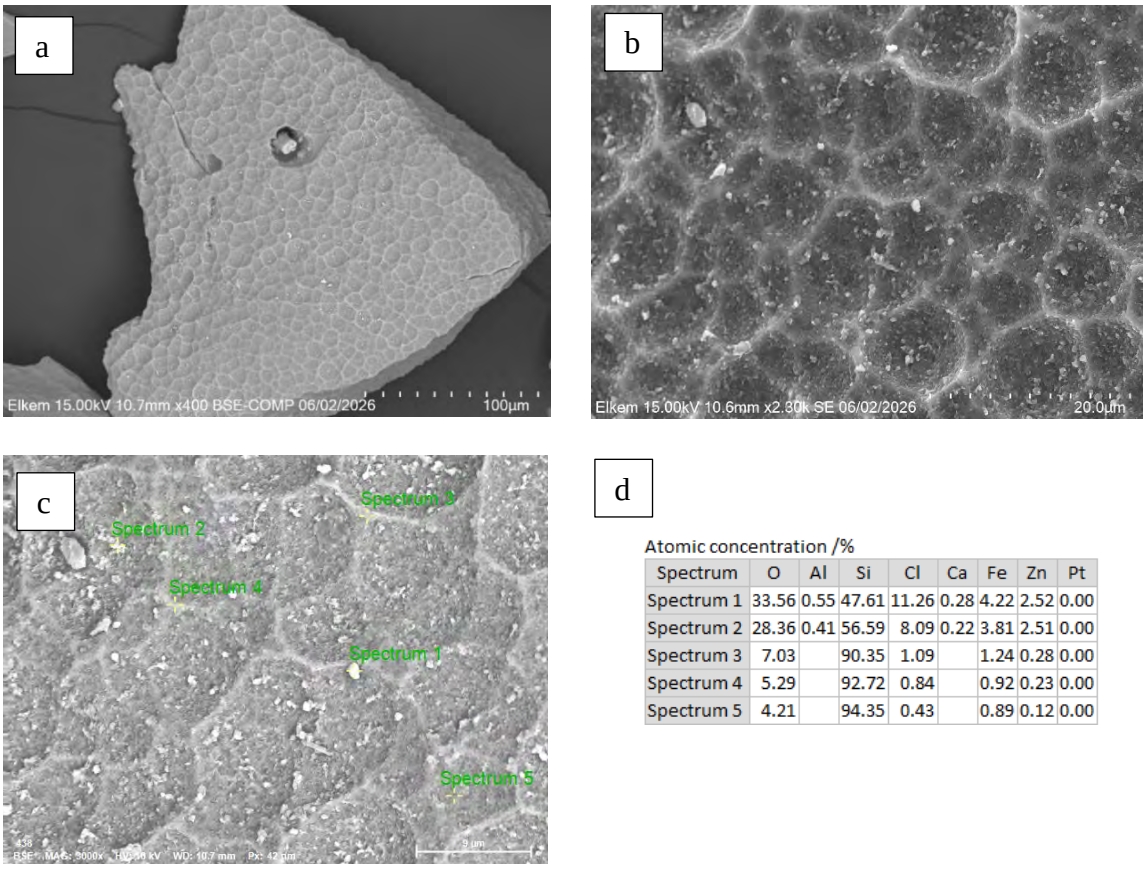

Atomic concentration /%

Spectrum	O	Al	Si	Cl	Ca	Fe	Zn	Pt
Spectrum 1	33.56	0.55	47.61	11.26	0.28	4.22	2.52	0.00
Spectrum 2	28.36	0.41	56.59	8.09	0.22	3.81	2.51	0.00
Spectrum 3	7.03		90.35	1.09		1.24	0.28	0.00
Spectrum 4	5.29		92.72	0.84		0.92	0.23	0.00
Spectrum 5	4.21		94.35	0.43		0.89	0.12	0.00

Figure 8 : Reacted silicon particles from sample with 1000 ppm Zn at 100 µm (a), 20 µm (b), 7 µm (c) and semi quantitative composition of spectrum (d)

3.3. Impact of tin

It was found that tin, tested at two different levels, has a large negative impact on TCS selectivity, (*Figure 9*). The experiment with 1000 ppm Sn in the feed gave a very strong negative effect on TCS selectivity and at the end of the experiment the TCS selectivity was only about 70%. Originally, the plan was to only run experiments with 1000 ppm Cu, Zn or Sn in the feed, but due to the very strong effect of Sn it was decided to run a new experiment with 100 ppm Sn in the feed.

The sample containing 1000 ppm Sn showed approximately 10% lower TCS selectivity than that containing 100 ppm Sn (*Figure 9***)**. This trend suggests that the detrimental effect of Sn addition on selectivity becomes increasingly significant with higher Sn content. While the reference sample maintains a high and stable TCS selectivity at 98%, the addition of 100 ppm Sn leads to a noticeable decline to approximately 85%, and further addition to 1000 ppm results in an even lower selectivity in the range of 70%.

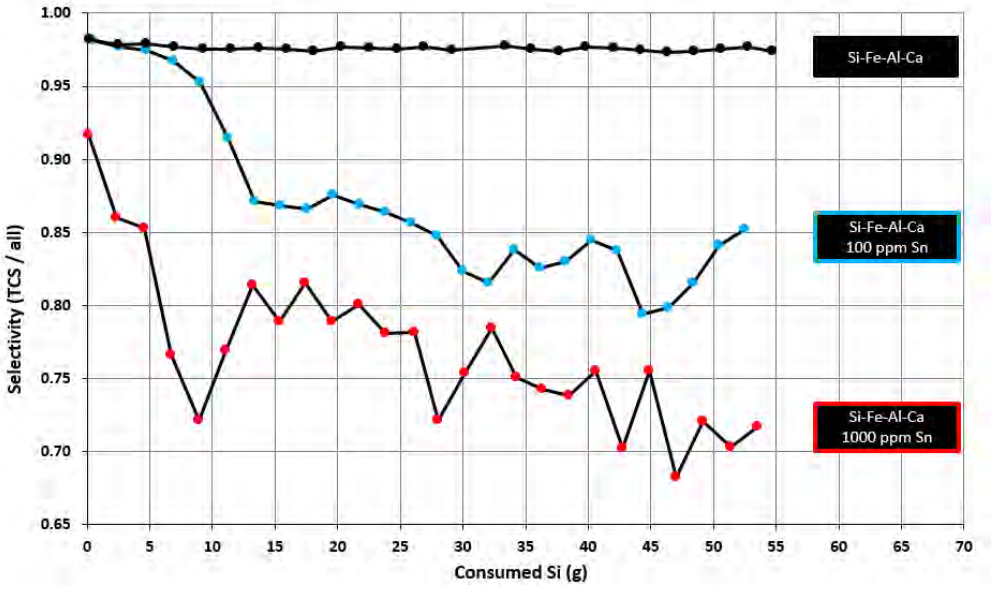

Figure 9 : Evolution of the TCS selectivity for reference sample, sample with 1000 ppm Sn and sample with 100 ppm

In addition, Figure 10 shows that HCl loss is strongly affected by Sn addition. The reference sample exhibits negligible HCl loss, whereas the 100 ppm Sn sample shows a substantial increase, reaching up to ~5%, and the 1000 ppm Sn sample maintains elevated values around ~1–2%.

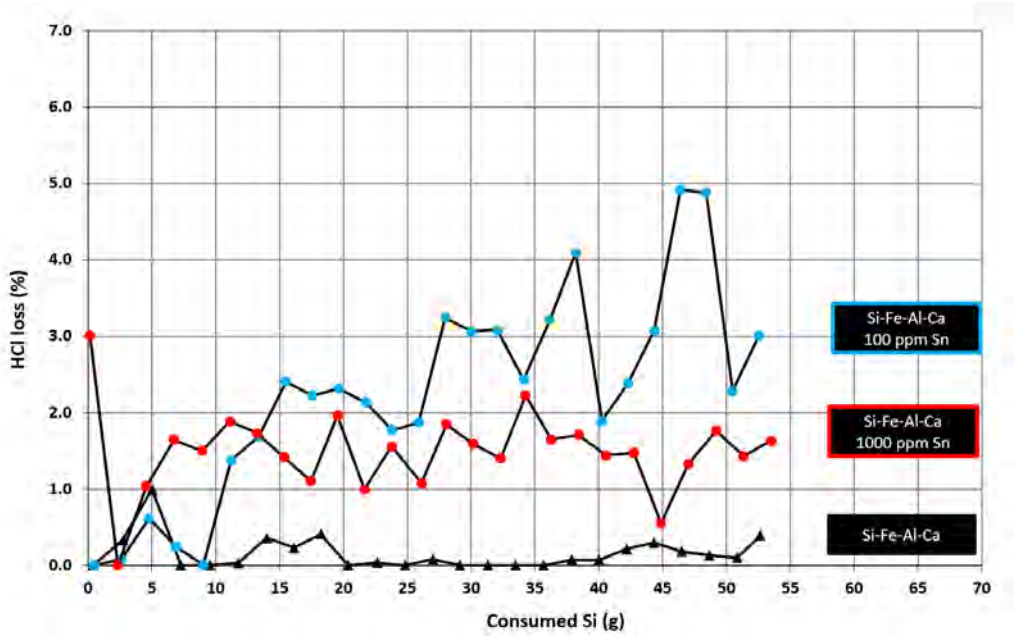

Figure 10 : Evolution of the HCl loss (%) for reference sample, sample with 1000 ppm Sn and sample with 100 ppm

The SEM observations first reveal the presence of numerous white particles distributed on the silicon surface (*Figure 11*), corresponding to Sn-rich regions. EDS analysis (*Figure 11*) confirms that these particles contain a high concentration of Sn, indicating a strong accumulation of Sn in some areas.

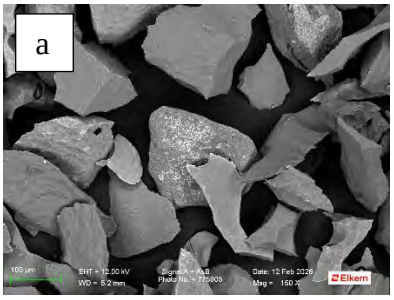

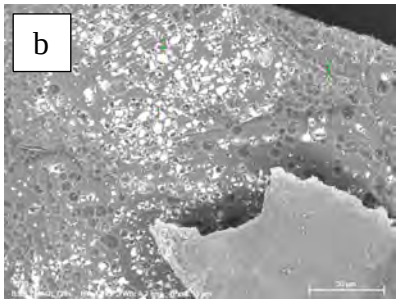

c

Atomic concentration /%

Spectrum	O	Si	Cl	Cr	Fe	Sn	Au
1	27.7	29.6	0.8		1.0	40.8	0.0
2	12.4	26.3		2.0	9.9	49.3	0.0
3	2.7	95.3			2.0		0.0

Figure 11 : Reacted silicon particles form sample with 1000 ppm Sn at 100 µm (a), 30 µm (b), and semi quantitative composition of spectrum (c)

At higher magnification, the silicon surface appears heterogeneous (c *Figure 12*), with the presence of crater-like regions associated with silicon consumption and regions with "white deposit". These crater areas do not necessarily contain visible Sn-rich particles (spectrum 1, 2 and 5 d *Figure 12*). EDS analysis performed in these regions shows that Sn is still systematically present on the silicon surface, with typical concentrations in the range of 1–5 %.
This demonstrates that Sn is not only present as "white deposit" but is also distributed within the reacted silicon regions. Two distinct types of Sn-containing domains can therefore be identified: (i) localized region with high Sn content, and (ii) Si-rich regions containing a lower amount of Sn (d *Figure 12*).

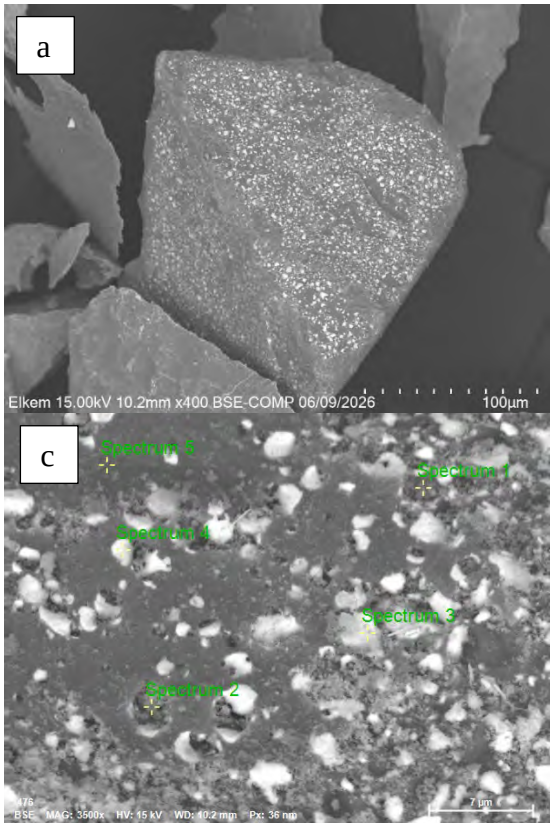

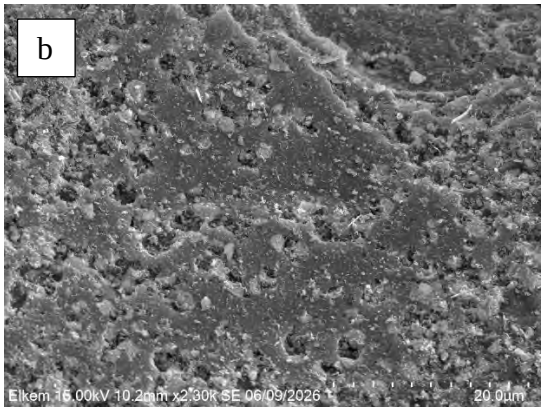

d

Atomic concentration /%

Spectrum	O	Si	Cl	Cr	Fe	Sn	Pt
Spectrum 1	11.36	84.50	0.87		0.38	2.89	0.00
Spectrum 2	20.18	71.97	1.71		2.73	3.41	0.00
Spectrum 3	15.19	40.27	0.88	1.13	11.72	30.81	0.00
Spectrum 4	16.31	43.47	0.88	1.43	9.57	28.35	0.00
Spectrum 5	6.62	90.70	0.30		0.36	2.03	0.00

Figure 12 : Reacted silicon particles form sample with 1000 ppm Sn at 100 µm (a), 20 µm (b), 7 µm (c) and semi quantitative composition of spectrum (d)

The influence of Sn on the formation of high-boiling (HB) components was further analyzed by monitoring the evolution of individual HB species, which were quantified by gas chromatography (GC).
As shown in *Figure 13*, the formation of HB1 and HB3 (siloxane species containing Si–O–Si linkages) remains relatively low and exhibits only a weak dependence on Sn concentration. The amount of oxygen containing high boilers is limited by the availability of oxygen (mainly surface oxygen introduced with the silicon powder). Although a slight increase can be observed for the Sn-containing samples, the overall contribution of these oxygen-bridged species is limited.

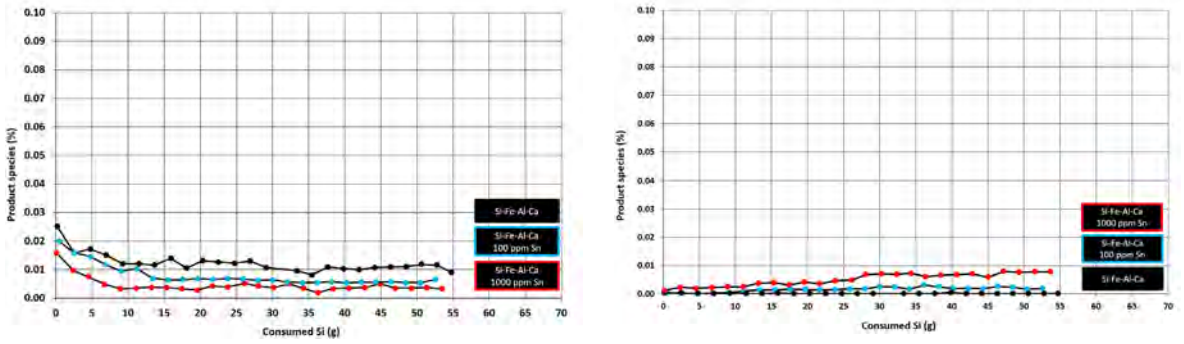

Figure 13 : Evolution of the HB1(left) and HB 3(right) for reference sample, sample with 1000 ppm Sn and sample with 100 ppm

In contrast, *Figure 14* reveals a pronounced increase in HB4 and HB5, which correspond to Si–Si bonded high-boiling species. This increase is particularly significant for the sample containing 1000 ppm Sn, where both HB4 and HB5 rise sharply with increasing silicon consumption and Sn accumulation, reaching substantially higher levels than those observed for the reference and 100 ppm Sn samples. For the sample containing 100 ppm Sn, the impact is mainly on HB5. These results indicate that Sn promotes the formation of Si–Si bonded high-boiling species.

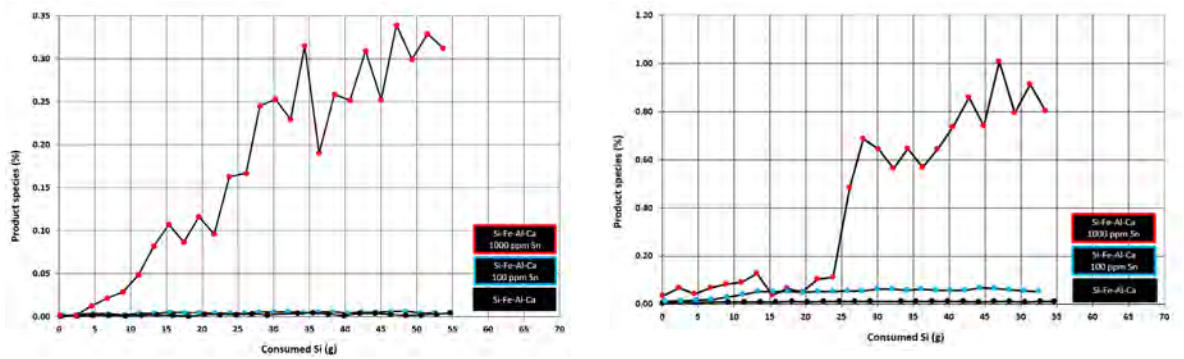

Figure 14 : Evolution of the HB4(left) and HB 5(right) for reference sample, sample with 1000 ppm Sn and sample with 100 ppm

In summary the Sn-containing experiment exhibits a significant increase in the formation of high-boiling species, particularly Si–Si bonded compounds, together with a lower TCS selectivity and incomplete HCl conversion.
This behavior can be correlated with the surface structure revealed by SEM–EDS, which shows that Sn is present in high concentration level and as a dispersed phase on the silicon surface. The industrial relevance of the observed Sn effect is particularly important when considering

high-boiling residue formation in TCS production. High boilers are undesirable because they represent both a loss of valuable chlorosilanes and an additional downstream treatment burden. In industrial direct chlorination, the production of trichlorosilane generates significant volumes of by-products with boiling points above 100 °C (boiling point of Hexachlorodisilane (HB 5) is 144 °C), predominantly disilanes and disiloxanes. These residues have traditionally been removed from the product stream together with silicon fines and aluminum chloride solids and disposed of as slurry, leading to losses of valuable TCS and STC in the waste stream (Kroupa, 2002). In the present study, Sn addition strongly decreased TCS selectivity and preferentially increased the formation of Si–Si bonded high-boiling species, especially HB4 and HB5. This indicates that Sn contamination may not only reduce the yield of the desired TCS product but also increase the load on downstream high-boiler recovery, residue treatment and waste-management systems. From an industrial perspective, Sn should therefore be considered a critical impurity in silicon feedstocks for direct chlorination.

3.4. Proposed role of Sn in promoting Si–Si bond formation during direct chlorination

Sn present on the reacting silicon surface may first modify the local active sites. This can occur by interaction with exposed silicon atoms, by formation of small Sn aggregates, or by possible partial incorporation of Sn into the near-surface region. This interpretation is consistent with surface-science studies of Zn and Sn on clean Si(111)-7×7 (Tanaka et al., 2003). These observations suggest that Sn can locally change the structure of the silicon surface.

The possible role of Sn in forming Si–Si bonded species is also supported by the work of Shimada, Nagashima and Aramata (2006). They studied Sn-containing contact masses for phenylchlorosilane synthesis and observed white precipitates on silicon wafer surfaces when Sn was present. These precipitates were identified as chlorine-rich branched polysilanes. The authors proposed that reactive silylene-like species formed on the silicon surface and contributed to the formation of these precipitates. Their system was based on chlorobenzene and not HCl, but it gives a useful analogy. It suggests that Sn can favor the formation of silylene-like species on silicon surfaces, which may then lead to Si–Si coupling.

The Photo-EMF study of Lorey et al. (2000) gives another indication that Sn may affect silicon reactivity through electronic effects. In this work, the electronic state of the silicon was shown to influence both selectivity and the amount of disilanes in the crude silane mixture. A higher Sn concentration relative to phosphorus was associated with p-type Photo-EMF behavior, while a higher P/Sn ratio shifted the silicon toward stronger n-type behavior. This study was performed for organohalosilane direct synthesis and not for HCl direct chlorination. However, it supports the general idea that Sn can change the electronic character of reactive silicon surfaces and impact disilane formation.

In the present direct chlorination system, Sn-modified areas may therefore favor the formation of silylene-like species during the reaction with HCl. If these intermediates couple together, they can form new Si–Si bonds. This gives a possible explanation for the increased formation of Si–Si-containing high boilers observed in the Sn-containing samples.

Crawford et al (2022) showed that Germanium (Ge) had a strong impact on TCS selectivity. Although Ge and Sn may act through different mechanisms, the reported effect of trace Ge on direct chlorination supports the broader hypothesis that Group 14 impurities can strongly influence silicon surface reactivity and selectivity. Lead (Pb), known as dangerous inhibitor in the direct process, could also be a good candidate for a similar study.

4. CONCLUSION

Beyond the direct effect of Cu, Zn, and Sn on DC performance, this work demonstrates the value of combining controlled laboratory-scale reaction testing with SEM–EDS characterization of reactor residue. Laboratory reactor data provide quantitative information on reactivity, TCS selectivity and high-boiler formation, while SEM–EDS reveals how the added elements are distributed on the reacted silicon particles. This combined methodology makes it possible to make the link between lab results and visual observation at silicon surface level.

Direct chlorination was used as a simplified model system to study MCS catalyst elements without the additional complexity of CH_3Cl cracking and coke formation. This allowed the intrinsic effect of Cu, Zn, and Sn on the silicon surface to be evaluated more directly. One learning for MCS is that high level of Sn could probably increase Si–Si bonded high-boiler formation.

Industrially, the most important finding is that Sn is a critical impurity for direct chlorination. Even at low concentration, it decreases TCS selectivity and promotes Si–Si bonded high boilers, increasing product losses and residue-management challenges. Zn is less harmful to selectivity, but it may reduce reactivity over time through chloride-derived surface deposits.

These findings have significant implications for future silicon feedstocks, notably recycled silicon recovered from end-of-life solar modules, potentially containing residual tin from solder materials, and biocarbon-based silicon, for which Sn and Zn concentrations may vary according to the origin and composition of the biocarbon feedstock.

5. REFERENCES

Ausland, G. and Rong, H.M., 2020. Silicon production with high energy efficiency and low CO_2 footprint. In: Silicon for the Chemical and Solar Industry XV, Trondheim, Norway, 15–18 June 2020.

Ashworth, A., Bunge, M. and Colomb, M.A., 2024. Effect of calcium on the direct chlorination process. In: M. Tangstad, H. Rong, A. Valderhaug, B. Andresen and I.G. Page (eds.), Silicon for the Chemical and Solar Industry XVII, Trondheim, Norway, 10–13 September 2024.

Blaser, E., Rosier, C., Huet, M., Chaurand, P., Geantet, C. and Loridant, S., 2021. Thermal cracking of CH_3Cl leads to auto-catalysis of deposited coke. Catalysis Science & Technology, 11(2), pp.469–473. https://doi.org/10.1039/d0cy01725f

Chen, P.-H., Chen, W.-S., Lee, C.-H. and Wu, J.-Y. (2024) Comprehensive review of crystalline silicon solar panel recycling: From historical context to advanced techniques. Sustainability, 16, 60. https://doi.org/10.3390/su16010060

Crawford, A., Rong, H.M. and Kjønli, H., 2022. *Investigation of the effect of a newly identified trace impurity on the reactivity and selectivity of the direct chlorination trichlorosilane synthesis reaction*. In: M. Tangstad, H. Rong, Aa. Valderhaug, B. Andresen, H. Tveit and I.G. Page (eds.), Silicon for the Chemical and Solar Industry XVI, Trondheim, Norway, 14–16 June 2022

Dropka, N., Hoang, D.L., Kürschner, U., Martin, A., Pätzold, U., Hesse, K. and Lieske, H., 2006. Kinetic studies on trichlorosilane synthesis. In: H.A. Øye, H. Brekken, T. Foosnæs and L. Nygaard (eds.), Silicon for the Chemical Industry VIII, Trondheim, Norway, 12–15 June 2006.

Ehrich, H., Lobreyer, T., Hesse, K. and Lieske, H., 1998. *Action of copper in trichlorosilane synthesis*. In: H.A. Øye, H.M. Rong, L. Nygaard and G. Schüssler (eds.), *Silicon for the Chemical Industry IV*, Geiranger, Norway, 3–5 June 1998.

Hesse, K. and Pätzold, U., 2006. Survey over the TCS process. In: H.A. Øye, H. Brekken, T. Fosnes and L. Nygaard (eds.), Silicon for the Chemical Industry VIII, Trondheim, Norway, 12–15 June 2006

Hoel, J.-O. and Rong, H.M., 2020. Activation of silicon in the hydrochlorination process. In: Silicon for the Chemical and Solar Industry XV, Trondheim, Norway, 15–18 June 2020.

Kroupa, M.G., 2002. High Boiling Residue Recovery Process for the Synthesis of Trichlorosilane, in Øye, H.A., Rong, H.M., Nygaard, L., Schüssler, G. and Tuset, J.Kr. (eds.) Silicon for the Chemical Industry VI. Loen, Norway, 17–21 June 2002

Lindstad, C.N. and Forseth, T., 2024. Feedstock for biochar variation in crucial elements for metal production. In: Silicon for the Chemical and Solar Industry XVII.

Lorey, L., Roewer, G. and Damm, C., 2000. The effect of the electronic state of the educt silicon in the direct synthesis. In: H.A. Øye, H.M. Rong, L. Nygaard, G. Schüssler and J.Kr. Tuset (eds.), Silicon for the Chemical Industry V, Tromsø, Norway, 29 May–2 June 2000

Shimada, S., Nagashima, H. and Aramata, M., 2006. *A study about the mechanism of catalysts and promoters in the Rochow process and the development of a new contact mass without copper for phenylchlorosilanes synthesis*. In: H.A. Øye, H. Brekken, T. Foosnæs and L. Nygaard (eds.), Silicon for the Chemical Industry VIII, Trondheim, Norway, 12–16 June 2006.

Tanaka, K.-I., Xie, Z.-X., Egawa, T. and Aramata, M., 2003. Dynamics of Sn and Zn atoms on a Si(111)-7×7 surface. Journal of Molecular Catalysis A: Chemical, 199, pp.19–26.

Tveit, H. and Myrhaug, E., 2000. Important sub-processes in the silicon process: The behavior of trace elements. In: H.A. Øye, H.M. Rong, L. Nygaard, G. Schüssler and J.Kr. Tuset (eds.), Silicon for the Chemical Industry V, Tromsø, Norway, 29 May–2 June 2000

6. ACKNOWLEDGEMENTS

This paper is published by permission of Elkem.

Marc-Olivier Victorin
Silicon specialist, Elkem

Marc-Olivier Victorin is an Engineer from IMT Mines Albi (France) Graduate School of Engineering, where he graduated in 2007. He has 19 years of industrial experience, including 14 years at Elkem across different divisions and international environments. He is currently a Silicon Specialist at Elkem, based in Trondheim (NO). He is supporting polysilicon customers using Direct Chlorination (DC) and Hydrochlorination (HC) processes, focusing on product development, product qualification, and sustainable silicon solutions.

Korol, N., and V. Yankovych 2026. Extruded Charcoal Briquettes with a Protective Organic. In *Silicon for the chemical and solar industry XVIII*, edited by M. Tangstad, H. Rong, A. Valderhaug, B. Andresen, H. Dalaker, and I. G. Page. Kristiansand, Norway, September 7–10, 2026. https://doi.org/10.55669/oa900841

Extruded Charcoal Briquettes with a Protective Organic Polymer Binder for Barbecue and Metallurgical Applications

Nataliya Korol[1,2] and Viktor Yankovych[1]
[1]R&D Department, Perechin Timber and Chemical Plant, 25 Uzhanska str., 89200 Perechin, Ukraine, korolni@lxk.com.ua
[2]Department of Organic Chemistry, Educational and Research Institute of Chemistry and Ecology, Uzhhorod National University, Fedyntsa str. 53/1, 88000 Uzhhorod, Ukraine

Keywords: extruded charcoal briquettes, organic polymer binder, mechanical strength, water resistance, thermal shock, metallurgical reductant

Abstract – Charcoal continues to be a strategically important carbonaceous reductant for the metallurgical industry, including the production of metallurgical-grade silicon and ferrosilicon, due to its low ash and sulphur content and its renewable origin. However, the mechanical, thermal and water-resistance properties of conventional roller-pressed charcoal briquettes are often insufficient for the demanding handling and high-temperature conditions of submerged-arc furnaces. In the present work, cylindrical extruded charcoal briquettes (20 mm in diameter, 30–150 mm in length) were manufactured on a laboratory extruder from milled hardwood charcoal fines and a self-developed protective organic polymer binder — a water-soluble, carboxyl-functional polymer — used at a low loading, and were characterised against the requirements of EN 1860-2 and DIN 51729-10. Proximate analysis gave a fixed-carbon content of 74.0 % and an ash content of 4.5 %, with a typical alkaline-earth-rich ash composition (36.76 wt-% CaO, 16.10 wt-% SiO_2, 8.59 wt-% K_2O). The briquettes withstood axial compression loads of 0.5–0.9 MPa, lost only 14.4 ± 0.56 % of mass after 30 min of drum abrasion, absorbed 36.1 % water after five days of immersion without disintegration, and retained their cylindrical shape after rapid heating to 900 °C, losing 24 % of mass. The proximate and abrasion data are means ± standard deviation of three independently produced batches (n = 3); the ash analysis is a single accredited determination, the compression result is the observed range, and the water-uptake and thermal-shock values are single determinations. The combined results indicate that the obtained briquettes meet the basic mechanical, hydrothermal and thermal-shock criteria required for both barbecue applications and for use as a carbonaceous reductant in metallurgical processes.

1. INTRODUCTION

Charcoal is one of the few carbonaceous materials that combines a renewable origin with very low ash and sulphur content, and for this reason it has been widely investigated as a partial or complete substitute for fossil reductants in the production of silicon, ferrosilicon and manganese ferroalloys (Monsen *et al.*, 2007; Surup, Trubetskaya, and Tangstad, 2020; Ringdalen, 2025). The replacement of fossil coke by charcoal in submerged-arc furnaces is

This work is licensed under the Creative Commons Attribution 4.0 International License. To view a copy of this license, visit https://creativecommons.org/licenses/by/4.0/

regarded as one of the most accessible short-term measures for reducing the CO_2 footprint of the silicon and ferroalloy industries (Surup, Trubetskaya, and Tangstad, 2020).

At the same time, a significant fraction of industrial charcoal is generated as fines (typically below 6 mm) during carbonisation, screening, transport and storage. According to data reported for the silicon industry, more than 10 % of the charcoal feed can be lost as fines during processing, which is normally too small to be charged directly into the furnace and is therefore discarded or used as a low-value by-product (Makgobelele *et al.*, 2021). Conversion of these fines into mechanically and hydrothermally stable briquettes is therefore both an economic and an environmental objective.

A wide range of organic and inorganic binders has been proposed for charcoal briquetting, including starches, molasses, lignosulphonates, polyvinyl alcohol (PVA), bentonite and combinations thereof (Korol and Yankovych, 2025a; Yankovych and Korol, 2025). Recent work by the authors has shown that the binder molecular structure and the densification pressure jointly govern the mechanical integrity of charcoal briquettes, with modified polysaccharides offering the best compromise between cold mechanical strength, ash contribution and cost (Yankovych and Korol, 2025). Polyvinyl-alcohol-based binder systems, in particular, have been shown to give a useful combination of dry strength and water resistance when combined with molasses and a small amount of surfactant (Korol and Yankovych, 2025a). At the same time, the surface chemistry of the charcoal fines and the influence of mild chemical pre-treatments on their adhesive interaction with binders have also been studied (Korol and Yankovych, 2025b).

Most of the published work, however, has focused on roller-pressed or piston-pressed briquettes. Extrusion, by contrast, allows higher and more uniform compaction pressures and longer residence times in the die, which in principle reduces the amount of binder required and yields more compact briquettes. The shape obtained, a cylinder of well-defined diameter, is also better suited to bulk handling and to the gas-permeability requirements of metallurgical furnaces.

The objective of the present work is to characterise a new type of extruded charcoal briquette manufactured at the Perechin Timber and Chemical Plant (Ukraine) using an alternative technology based on a protective organic polymer binder. The proximate composition, elemental composition of the ash, compression strength, abrasion resistance, water resistance and thermal-shock behaviour of the briquettes are evaluated against the requirements of EN 1860-2 (CEN, 2005) and the elemental-analysis standard DIN 51729-10 (DIN, 2011), and the results are discussed in the context of barbecue and metallurgical applications.

2. MATERIALS AND METHODS

2.1 Sample preparation

The briquettes were manufactured from hardwood charcoal produced by Perechin Timber and Chemical Plant from 100 % hardwood feedstock of legal origin. The raw material for briquetting was the charcoal fines fraction (0–6 mm) generated during carbonisation, screening, handling and storage. Before briquetting the fines were milled and homogenised, and the particle-size distribution of the milled feed was determined by dry sieving in triplicate; it is given in Table I. The distribution is markedly bimodal: 35 wt-% of the material lies in the coarse 2.00–6.00 mm fraction, while 50 wt-% is finer than 0.50 mm, with a pronounced minimum of only 3 wt-% in the 0.50–1.00 mm interval. The mass-median size d_{50} is accordingly 0.50 mm and the d_{90} is approximately 4.4 mm. A bimodal feed of this kind is favourable for

extrusion: the fine mode fills the interstices between the coarse particles and so raises the packing density of the extrudate, while the coarse particles carry the load and limit shrinkage during drying. Together with the continuity of the binder film, this packing behaviour governs the compactness, the cold mechanical strength and the abrasion behaviour of the finished briquette.

Table I: Particle-size distribution of the milled hardwood charcoal fines used as the feed for extrusion, determined by dry sieving (n = 3). The mass-median size d_{50} falls on a sieve aperture and requires no interpolation; d_{90} was obtained from the cumulative undersize curve by linear interpolation on a logarithmic size scale, the coarsest fraction being taken as 2.00–6.00 mm.

Size fraction	Mass fraction (wt-%)
2.00 – 6.00 mm	35
1.00 – 2.00 mm	12
0.50 – 1.00 mm	3
0.25 – 0.50 mm	22
0.125 – 0.25 mm	7
< 0.125 mm	21
Mass-median size, d_{50} (mm)	**0.50**
d_{90} (mm)	**4.4**

The protective organic polymer binder used in this work is a self-developed, water-soluble organic polymer that carries a high density of carboxyl groups along its chain, used as the sole binding component: no co-binder, plasticiser or surfactant is added. It is dissolved in the process water at room temperature and introduced at a loading well below the 15–25 wt-% that the pressed formulations of our earlier work require (Yankovych and Korol, 2025). The binder and process parameters are collected in Table II. Two features of this chemistry bear directly on the results reported below. First, polymers of this class are efficient film formers: on drying they leave a continuous, cohesive film that bridges the charcoal particles, which is what allows a mechanically coherent extrudate to be obtained at so low a binder loading. Second, the carboxylate groups of the polymer can form ionic crosslinks with the alkaline-earth and alkali cations that are abundant in hardwood charcoal ash — the ash of the present material contains 36.76 wt-% CaO and 8.59 wt-% K_2O (Table IV). The calcium salts of polycarboxylates are sparingly soluble in water, so the crosslinked film is not removed by immersion. We propose this in-situ ionic crosslinking as the mechanism underlying the water resistance reported in Section 3.4, where the briquettes retained their shape after five days of full immersion. The proposal is consistent with the behaviour observed, but a direct spectroscopic confirmation was outside the scope of the present study and is planned as part of the continuing programme. This binder therefore works by a different mechanism from the hydrogen-bond-dominated polysaccharide and polyvinyl-alcohol systems examined in our earlier work (Korol and Yankovych, 2025a; Yankovych and Korol, 2025): ionic crosslinking rather than hydrogen bonding. Those studies established that polysaccharides give the highest cold strength, but none of the five binders screened there delivered water resistance at a low loading, which is what motivated the change of binder chemistry reported here.

Table II: Composition of the protective organic polymer binder system and the extrusion and drying parameters used for the briquettes characterised in this work.

Parameter	Value
Binder type	self-developed, water-soluble organic polymer bearing carboxyl groups
Co-binder, plasticiser or surfactant additions	none – single-component binder system
Preparation of the binder	dissolved in the process water at room temperature
Binder loading and exact composition	commercially protected – see text
Separate mixing stage	none – mixing takes place inside the extruder
Extruder	laboratory single-screw extruder, model PBE-133
Drive	5.5 kW; motor 1500 rpm through a two-stage gear reducer (Ts2U-160)
Die diameter (mm)	20
Barrel and die heating	none – the mass is warmed by shear during repeated passes
Nameplate throughput (kg h^{-1})	300
Throughput achieved on charcoal fines (kg h^{-1})	≤ 5
Machine dimensions (mm) and mass (kg)	1600 × 1050 × 850; ≤ 300
Drying regime	ambient air, to constant mass
Moisture content of the dried briquettes (wt-%)	4.3

The exact composition of the binder system, and its loading on dry charcoal, are commercially protected by Perechin Timber and Chemical Plant and are not disclosed here. Table II therefore reports the functional chemistry of the polymer, the preparation route and the complete set of machine and process parameters, but not the formulation itself. We recognise that this places a limit on strict reproducibility, and we state it openly rather than leaving it implicit: the results below can be reproduced qualitatively with a commercial water-soluble polycarboxylate of comparable charge density on the equipment described, but the exact values will depend on the grade and loading chosen.

No separate mixing stage was available: the milled charcoal fines, the dissolved binder and the process water were fed directly to a laboratory single-screw extruder (model PBE-133, 5.5 kW, motor speed 1500 rpm through a two-stage gear reducer), in which mixing, densification and shaping all take place. The barrel is not externally heated; the mass is warmed by shear, and homogenisation is achieved by passing the charge through the extruder several times before the final pass through the 20 mm die. This is the main process limitation of the present work and it is quantified in Table II: against a nameplate throughput of 300 kg h^{-1}, no more than 5 kg h^{-1} could be achieved on charcoal fines, because the mixture has to be prepared and warmed inside the extruder itself. Continuous operation would require a heated, agitated mixing vessel upstream so that a ready, warm mass is delivered to the die in a single pass. The extrudates were cut to the required length and dried under ambient conditions until the final moisture content was stabilised at 4.3 wt-%. The resulting briquettes are cylindrical agglomerates with a diameter of 20 mm and a length of 30–150 mm, the length being adjustable according to customer requirements. The general appearance of the briquettes, together with a calliper verification of the nominal diameter, is shown in Figure 1.

Figure 1: General appearance of the extruded charcoal briquettes and calliper verification of the nominal 20 mm diameter.

2.2 Proximate and ash analysis

The proximate composition (moisture, ash, volatile matter, fixed carbon) of the briquettes was determined in accordance with EN 1860-2 (CEN, 2005). The elemental composition of the ash was determined by Ruhr Lab GmbH (Germany) following DIN 51729-10 (DIN, 2011) and is reported as oxide percentages.

2.3 Compression (strength) test

Cylindrical briquettes were placed in a hydraulic press and loaded both along (axial) and across (radial) the cylinder axis (Figure 2). The pressure at which a briquette failed was recorded with a calibrated pressure gauge and converted into a nominal compressive stress.

Figure 2: Compression test on the extruded charcoal briquettes: hydraulic press with pressure gauge (left), briquette under axial load (centre) and broken sample after failure (right).

2.4 Abrasion (tumble/drum) test

Mechanical durability under handling was assessed by a tumble test. A weighed sample of briquettes was placed in a rotating drum of 30 cm internal diameter and rotated at 40 rpm for 30 min. After the test the sample was removed and sieved through 3.35 mm and 0.5 mm sieves, and the mass fraction of each size class was calculated relative to the initial mass (Figure 3).

Figure 3: Abrasion (tumble) test: briquettes before testing (left) and after 30 min in the rotating drum at 40 rpm together with the fines and broken fragments generated (right).

2.5 Water-resistance test

To assess the protective effect of the organic polymer binder, weighed briquettes were fully immersed in a container of distilled water at room temperature for five days (Figure 4). At the end of the immersion the briquettes were removed, the surface water was wiped off, and the samples were weighed and visually inspected for cracking and disintegration. Water uptake was calculated as the relative mass gain with respect to the initial dry mass.

Figure 4: Water-resistance test: extruded charcoal briquettes after five days of full immersion in distilled water, with no visible disintegration of the cylindrical agglomerates.

2.6 Thermal-shock test

Thermal-shock behaviour was evaluated by rapid heating in an oxygen-free sealed container at 900 °C for 10 min, followed by cooling under oxygen-free conditions to room temperature (Figure 5). The samples were inspected for shape retention, and the relative mass loss was determined gravimetrically.

Figure 5: Thermal-shock test sequence: muffle furnace at 900 °C (left), briquettes in the sealed oxygen-free container during heating (centre-left), the container during cooling (centre-right) and the briquettes after cooling with shape retention (right).

2.7 Statistical analysis and repeatability

The replication of the individual tests differs, and is stated here explicitly rather than left to be inferred. The proximate analysis and the abrasion test were each carried out on three independently produced batches of briquettes, manufactured from the same charcoal lot and the same binder formulation under nominally identical conditions ($n = 3$); for these indices the results are given as the arithmetic mean ± one sample standard deviation, the SD being calculated with the $n - 1$ denominator, and the values appear in Tables III and V. The ash analysis of Table IV is a single determination carried out under accreditation by an external laboratory (Ruhr Lab GmbH) on the batch characterised here; rather than replicate it, we quote in Section 3.1 the range observed over eight production batches analysed in the same campaign, which is the more informative measure of the variability that a furnace operator would actually encounter. The compression test was carried out on several individual briquettes, and the result is reported as the observed range of failure stresses rather than as a mean with a standard deviation: the failure of a brittle cylindrical agglomerate is governed by

the largest defect present in the particular specimen, so the distribution is markedly non-Gaussian and a standard deviation would convey a misleading impression of precision. The water-resistance and thermal-shock results are single determinations on one charge of briquettes each, and are therefore quoted without a dispersion estimate; mass changes were determined gravimetrically to ± 0.01 g. Extending the water-resistance and thermal-shock measurements to full triplicate determination, and establishing the specimen statistics of the compression test, are part of the continuing work.

3. RESULTS AND DISCUSSION

3.1 Proximate composition and ash chemistry

The proximate analysis of the extruded charcoal briquettes is summarised in Table III; all values are means of three independently produced batches, with the corresponding standard deviations. The fixed-carbon content (74.0 %) exceeds the 60 % minimum required by EN 1860-2 for charcoal briquettes, and the ash content (4.5 %) is well below the maximum value of 18 % allowed by the same standard (CEN, 2005). The total moisture content (4.3 %) is consistent with values reported for industrially dried charcoal briquettes. The volatile-matter fraction of 21.5 % is somewhat higher than that of pure metallurgical-grade lump charcoal, which can be attributed to the residual organic polymer binder; this is acceptable for barbecue applications and is not detrimental for metallurgical use, since the volatiles are released in the upper part of the furnace shaft before the briquettes reach the reaction zone. It is instructive to set these figures beside those of the conventional roller-pressed briquette manufactured at the same plant from the same hardwood charcoal, which has a moisture content of 5.5 %, an ash content of 4.5 %, a volatile-matter content of 24.5 % and a fixed-carbon content of 71.5 % at an apparent density of 0.34 g cm^{-3}. The ash contents of the two products are identical, as they must be when the charcoal and its source are the same, but the extruded briquette is drier, contains three percentage points less volatile matter and correspondingly more fixed carbon. Both differences follow from the process rather than from the feedstock: the low binder loading contributes less volatile organic matter than the 15–25 wt-% of polysaccharide required by the pressed product, and the shear-heated extrudate leaves the die warm and dries to a lower residual moisture. For a metallurgical reductant, both differences are in the useful direction.

Table III: Proximate composition of the extruded charcoal briquettes, determined in accordance with EN 1860-2. Values are means of three independent batches (n = 3); SD = sample standard deviation. Ash, volatile matter and fixed carbon are given on a dry basis.

Parameter	Value (wt-%)	SD (±, wt-%)
Moisture content	4.3	0.72
Ash content	4.5	0.33
Volatile matter	21.5	0.56
Fixed carbon (C-fix)	74.0	1.96

The elemental composition of the ash is given in Table IV. The ash is dominated by CaO (36.76 wt-%), SiO_2 (16.10 wt-%) and K_2O (8.59 wt-%), with smaller amounts of MgO, P_2O_5, SO_3, Na_2O and Fe_2O_3. This alkaline-earth-rich, low-iron ash chemistry is typical of hardwood charcoal and is advantageous for silicon metallurgy: the low Fe_2O_3 content (0.97 wt-%) limits iron contamination of the silicon product, while the high CaO/K_2O ratio is favourable for slag basicity control. Two qualifications belong with these figures. Table IV is a single accredited determination on the batch of briquettes characterised here, and the ash chemistry of hardwood charcoal varies appreciably from batch to batch: in the same laboratory campaign, eight production batches of charcoal briquettes from this plant, of which the present sample is one, gave 23.0–46.1 wt-% CaO, 8.6–27.5 wt-% K_2O and 2.5–16.1 wt-% SiO_2. The silica content

of the present batch is therefore the highest of that set, and the 16.10 wt-% in Table IV should not be read as typical of the product; the batch mean over the eight was 6.0 wt-%. The Fe_2O_3 content, by contrast, was consistently low across all eight batches (0.62–1.58 wt-%, mean 1.01 wt-%), so the argument on iron contamination does not rest on a single favourable analysis. The CaO and K_2O contents were above 23 and 8.5 wt-% respectively in every batch, which matters for the crosslinking mechanism proposed in Section 2.1: the cations required for it are present in abundance whatever the batch.

Table IV: Elemental composition of the ash of the extruded charcoal briquettes, determined according to DIN 51729-10. Single accredited determination on the batch characterised here; the batch-to-batch range over eight production batches is given in the text.

Oxide	Value (wt-%)
CaO	36.76
SiO_2	16.10
K_2O	8.59
MgO	2.32
SO_3	2.30
P_2O_5	1.80
Fe_2O_3	0.97
Na_2O	0.72

3.2 Compressive strength

The extruded briquettes withstood axial and radial loads in the range 0.5–0.9 MPa before failure — the observed range over the individual specimens tested, reported as a range rather than as a mean with a standard deviation for the reason given in Section 2.7, with the typical failure mode shown in Figure 2 (right). For hydraulically pressed charcoal briquettes intended for use as a carbonaceous reductant in silicon production, Makgobelele *et al.* (2021) reported cold compressive strengths of 2 kg cm^{-2} (0.20 MPa) without binder, 40 kg cm^{-2} (3.9 MPa) at 3 wt-% PVA and 115 kg cm^{-2} (11.3 MPa) at 5 wt-% PVA after seven days of curing, against 31 kg cm^{-2} (3.0 MPa) for the parent lump charcoal, and quoted 3.8 kg cm^{-2} (0.37 MPa) as the compressive strength accepted industrially for coal briquettes. The values obtained in the present work therefore exceed that industrial acceptance threshold by a factor of 1.4 to 2.4 and are an order of magnitude above a binderless agglomerate, while remaining below the heavily PVA-loaded pressed briquettes and below the parent lump charcoal; a fuller comparison is given in Section 3.6. The comparison is nevertheless an imperfect one, since the binder chemistry differs and the binder loading of the present briquettes is not disclosed. It should also be noted that the failure load of a 20 mm cylindrical extrudate is not strictly comparable with values measured on short pressed pellets of a different geometry. The level of strength obtained is sufficient to allow the briquettes to be handled, bagged, transported and charged into a furnace without significant breakage, and is consistent with the general observation that hydraulically pressing or extruding the charge produces briquettes two to four times stronger than the equivalent roller-pressed product (Yankovych and Korol, 2025).

3.3 Abrasion resistance

After 30 min in the rotating drum, the briquettes broke approximately in the middle but the resulting pieces retained their cylindrical shape, as visible in Figure 3 (right). The mass fractions obtained after sieving are summarised in Table V. The total mass of material lost as fines below 3.35 mm is 14.4 ± 0.56 % (mean ± SD, n = 3) (11.3 % below 0.5 mm and 3.14 % in the 0.5–3.35 mm range), with a further 0.3 % in the >3.35 mm fines fraction. This corresponds to a mechanical durability of 85.6 ± 0.83 %, which is acceptable for industrial handling and, as

shown in Section 3.6, is of the same order as the abrasion resistance index of 85 % reported for hydraulically pressed charcoal briquettes bound with 3 wt-% PVA, although still below the 96 % of the parent lump charcoal (Makgobelele *et al.*, 2021). The relatively high amount of very fine material (<0.5 mm) is associated with surface attrition of the cylindrical extrudates rather than with bulk fracture, and could be further reduced by optimising the binder/charcoal ratio and the curing time, as discussed by Korol and Yankovych (2025a).

Table V: Particle-size distribution of the briquette fines generated by the abrasion (drum) test. Values are means of three independent tests (n = 3); SD = sample standard deviation.

Fraction	Mass loss (wt-%)	SD (±, wt-%)
0.0 – 0.5 mm	11.30	0.74
0.5 – 3.35 mm	3.14	0.13
> 3.35 mm	0.30	0.06
Total below 3.35 mm	**14.44**	**0.83**

3.4 Water resistance

After five days of full immersion (Figure 4), the briquettes retained their original cylindrical shape and did not disintegrate. The water uptake corresponded to 36.1 % of the initial dry mass; as stated in Section 2.7, this is a single determination and is therefore quoted without a dispersion estimate. This behaviour is in good agreement with the protective effect expected from the organic polymer binder. As set out in Section 2.1, the polymer film is expected to be ionically crosslinked in situ by the calcium and potassium released from the charcoal ash, and the calcium carboxylate so formed is only sparingly soluble; the film therefore survives the immersion and continues to hold the agglomerate together, while water is still taken up through the open pore network of the charcoal itself. The uptake measured here is thus a measure of pore filling rather than of binder dissolution, which is consistent with the complete absence of disintegration. Comparable five-day water uptake values of the order of 30–40 % have been reported for PVA- and PVA/molasses-bound briquettes (Korol and Yankovych, 2025a). It is also instructive to compare these figures with the values obtained on the same type of test by Makgobelele *et al.* (2021), who measured a five-day water absorption of 42 % for lump charcoal and of 25–27 % for hydraulically pressed briquettes containing 3–5 wt-% PVA, while their binderless briquettes disintegrated completely (water-resistance index 0 %). The present briquettes therefore take up less water than the parent lump charcoal and, unlike a binderless agglomerate, survive the immersion intact. The combination of full shape retention and moderate water absorption is sufficient for outdoor storage in temperate climates, although a protective packaging is still recommended for prolonged exposure to rain.

3.5 Thermal-shock behaviour

After rapid heating to 900 °C in an oxygen-free environment and subsequent cooling (Figure 5), the briquettes retained their cylindrical shape and showed no through-thickness cracking. The associated mass loss was 24.0 % of the initial mass; this is a single determination on one charge of briquettes, and its extension to triplicate measurement is part of the continuing work (Section 2.7). This value is consistent with the release of residual moisture, volatile matter and pyrolysis products of the organic polymer binder, and is in the range expected for carbonaceous materials of the present composition. For comparison, Ringdalen (2025) reported that charcoal heated to 800 °C generated only about 2 % of fines below 3.35 mm and that biocarbon agglomerates remained largely undecrepitated, which is consistent with the complete shape retention observed here. The shape retention is the property of practical interest for metallurgical use, since it indicates that the briquettes will not collapse to fines in

the upper, low-temperature zone of a silicon or ferrosilicon submerged-arc furnace, where rapid temperature gradients of the same order of magnitude are encountered. The result therefore supports the suitability of the present extruded briquettes as a carbonaceous reductant in metallurgical processes, in line with the broader trend of substituting fossil reductants by biocarbon-based materials (Surup, Trubetskaya, and Tangstad, 2020; Ringdalen, 2025).

3.6 Comparison with lump charcoal and other carbonaceous materials

Since the briquettes are intended to substitute both lump barbecue charcoal and part of the fossil carbon charged to a submerged-arc furnace, it is useful to place the values measured here in the context of the corresponding data for lump charcoal, for conventionally pressed charcoal briquettes, for binderless agglomerates and for fossil reductants. Such a comparison is collected in Table VI.

Table VI: Comparison of the extruded charcoal briquettes of the present work with lump charcoal, conventionally pressed charcoal briquettes, binderless agglomerates and fossil reductants. Compressive strengths taken from the literature have been converted from kg cm^{-2} (1 kg cm^{-2} = 0.0981 MPa). For rows 2–5 the abrasion figure is the abrasion resistance index (mass % retained) defined in the cited study; for the present work it is the mass % retained above 3.35 mm after 30 min at 40 rpm. The two procedures differ in detail, so the comparison is indicative rather than strictly quantitative.

Material	Fixed C (wt-%)	Ash (wt-%)	VM (wt-%)	Compressive strength (MPa)	Abrasion / durability (%)	Water uptake, 5 d (%)	Source
Extruded charcoal briquettes, 20 mm	74.0	4.5	21.5	0.5 – 0.9	85.6	36.1	This work
Lump (coarse) hardwood charcoal	66.1	2.5	19.2	3.0	96	42	Makgobelele *et al.* (2021)
Pressed charcoal briquettes, 3 wt-% PVA	63.3	7.7	22.0	3.9	85	25	Makgobelele *et al.* (2021)
Pressed charcoal briquettes, 5 wt-% PVA	62.6	6.6	20.6	11.3	82	27	Makgobelele *et al.* (2021)
Binderless charcoal briquettes	58.3	8.0	22.8	0.20	3	disintegrated	Makgobelele *et al.* (2021)
Fossil reductant (coal / coke), typical requirement	> 85	< 12	–	–	–	–	Surup *et al.* (2020)
EN 1860-2, barbecue charcoal briquettes	≥ 60	≤ 18	–	–	–	–	CEN (2005)
EN 1860-2, lump barbecue charcoal	≥ 75	≤ 8	–	–	–	–	CEN (2005)

Chemically, the extruded briquettes are closer to lump charcoal than to a conventional briquetted product. Their ash content of 4.5 wt-% is only about twice that of the parent coarse charcoal (2.5 wt-%) reported by Makgobelele *et al.* (2021), less than half the 6.6–8.0 wt-% measured for the PVA-pressed and binderless briquettes of the same study, and far below the 18 wt-% permitted for briquettes by EN 1860-2 (CEN, 2005). The fixed-carbon content of 74.0 wt-% is higher than that of any of the briquettes in the cited work (58.3–63.3 wt-%) and even higher than that of the parent coarse charcoal itself (66.1 wt-%); it falls only marginally short of the 75 wt-% minimum that EN 1860-2 sets for lump barbecue charcoal, a class in which the present product is not required to qualify. Relative to fossil reductants, for which a fixed carbon above 85 wt-% and an ash content of up to 12 wt-% are typical (Surup, Trubetskaya, and Tangstad, 2020), the briquettes offer a lower carbon density but a markedly cleaner, alkaline-earth-rich and low-iron ash, and a sulphur content roughly two orders of magnitude below that of metallurgical coke (Ringdalen, 2025).

Mechanically, the ranking is the one expected for an agglomerate. Lump charcoal remains the strongest and most abrasion-resistant material of the set (3.0 MPa, abrasion resistance index 96 %), but it cannot be produced from fines, cannot be given a defined shape and absorbs more water (42 %) than the present briquettes. Binderless agglomerates sit at the opposite extreme, at 0.20 MPa, an abrasion resistance index of only 3 % and complete disintegration in water. The extruded briquettes of the present work occupy an intermediate position, with a durability of 85.6 ± 0.83 % that matches the 85 % reported for hydraulically pressed briquettes containing 3 wt-% PVA, and a water uptake of 36.1 % with full shape retention. Their unconfined compressive strength of 0.5–0.9 MPa is lower than that of lump charcoal and of the heavily bound pressed briquettes, but it is 1.4 to 2.4 times the value of 3.8 kg cm^{-2} (0.37 MPa) quoted as the industrially acceptable compressive strength for coal briquettes (Makgobelele *et al.*, 2021). It should also be borne in mind that the failure load of a 20 mm cylindrical extrudate is not strictly comparable with values measured on short pressed pellets of a different geometry. Overall, Table VI shows that the present technology recovers the chemical quality of lump charcoal from a material that would otherwise be discarded, at a handling durability equivalent to a well-bound pressed briquette and with far better water resistance than a binderless product, at the cost of a lower single-particle compressive strength.

3.7 Implications for industrial use

Taken together, the results presented in sections 3.1–3.6 show that the extruded charcoal briquettes meet the EN 1860-2 requirements for barbecue charcoal briquettes (CEN, 2005) with a fixed-carbon content well above 60 % and an ash content well below 18 %, and that their mechanical, hydrothermal and thermal-shock properties are adequate for routine industrial handling. The low ash and very low Fe_2O_3 content, together with the shape retention at 900 °C, also make these briquettes a credible candidate as a partial substitute for fossil coke in silicon and ferrosilicon production. Additional pilot-scale testing in a submerged-arc furnace will be required to confirm the reactivity (Boudouard) and electrical-resistivity behaviour of the briquettes, in line with the experimental approach recently described for biocarbon by Ringdalen (2025). Finally, given the importance of carbonaceous materials in the wider field of separations and adsorption, it can be noted that the same hardwood charcoal feedstock has been shown to be an effective precursor of activated carbon for the removal of organic micropollutants from aqueous and ethanol solutions (Korol *et al.*, 2026).

4. CONCLUSIONS

A new type of cylindrical extruded charcoal briquette (diameter 20 mm, length 30–150 mm) has been manufactured on a laboratory extruder from hardwood charcoal fines and a protective organic polymer binder, and has been characterised against the requirements of EN 1860-2 and DIN 51729-10. The replication of the individual tests differs and is stated in Section 2.7: the proximate and abrasion indices are means ± standard deviation of three independently produced batches (n = 3), the ash analysis is a single accredited determination reported together with the batch-to-batch range, the compressive strength is reported as the observed range of failure stresses, and the water-resistance and thermal-shock results are single determinations. The main conclusions of the work can be summarised as follows.

The proximate analysis gave a fixed-carbon content of 74.0 % and an ash content of 4.5 %, both well within the EN 1860-2 limits for charcoal briquettes. The ash is dominated by CaO (36.76 wt-%), SiO_2 (16.10 wt-%) and K_2O (8.59 wt-%), with a very low Fe_2O_3 content (0.97 wt-%) that is favourable for silicon metallurgy.

Mechanically, the briquettes withstand compression loads of 0.5–0.9 MPa, and lose only 14.4 ± 0.56 % of mass as fines below 3.35 mm after 30 min of drum abrasion at 40 rpm, which corresponds to a mechanical durability of 85.6 ± 0.83 %.

The protective organic polymer binder gives a clear water-resistance benefit: after five days of full immersion the briquettes retained their cylindrical shape and showed no disintegration, with a moderate water uptake of 36.1 % of the initial dry mass (single determination).

Under rapid heating to 900 °C in an oxygen-free environment the briquettes retained their shape with a mass loss of 24.0 % (single determination), demonstrating acceptable thermal-shock resistance and supporting their suitability as a carbonaceous reductant in metallurgical applications, including silicon and ferrosilicon production.

The results reported above are, however, subject to a number of limitations that should be borne in mind when interpreting them and that define the boundaries of the present study. First, the briquettes were produced in discrete batches on a laboratory single-screw extruder; a continuous industrial extrusion line differs in shear and thermal history, throughput, die wear and drying regime, so the strength, durability and water-resistance values reported here must be confirmed on industrially produced material before they can be transferred to plant scale. The throughput actually achieved is itself a limitation of the present configuration: against a nameplate capacity of 300 kg h^{-1}, no more than 5 kg h^{-1} could be produced from charcoal fines, because the charge has to be warmed and homogenised by repeated passes through the extruder itself. Closing that gap requires a heated, agitated mixing vessel upstream of the die rather than a change to the binder or to the formulation, and this is the first step of the planned scale-up. Second, the thermal-shock test was carried out at 900 °C, which reproduces the rapid heating experienced by the charge in the upper, low-temperature zone of a submerged-arc furnace but is well below the temperatures prevailing in the coke bed and in the reaction zone of silicon and ferrosilicon production; the behaviour of the briquettes at those temperatures, together with their Boudouard (CO_2) reactivity and their electrical resistivity, has not been assessed here and is the subject of ongoing work. Third, the abrasion test generated 11.3 wt-% of material below 0.5 mm, which is higher than desirable for a furnace feed and would represent a real material loss in industrial handling; reducing this very fine fraction — most probably by increasing the binder dosage, extending the curing time or introducing a short thermal-curing step — remains the single most important target for further optimisation. Finally, all data reported here refer to one binder formulation and one hardwood charcoal source, so the sensitivity of the results to feedstock variability and to binder composition still has to be established. A further limitation concerns the reporting itself: the water-resistance and thermal-shock results rest on single determinations and the compressive strength is given as an observed range, so only the proximate and abrasion indices carry a measured dispersion; and the exact binder composition and loading are commercially protected, which restricts strict reproduction of the formulation by other laboratories.

Further work will focus on pilot-scale testing of the briquettes in a submerged-arc furnace and on the optimisation of the binder formulation in order to reduce the proportion of very fine material generated during abrasion, while preserving the favourable water-resistance and thermal-shock characteristics demonstrated in the present study.

5. ACKNOWLEDGEMENTS

This paper is published by permission of Perechin Timber and Chemical Plant. The authors gratefully acknowledge the support of the R&D Department of Perechin Timber and Chemical

Plant and of Uzhhorod National University in carrying out the experimental work. The elemental analysis of the ash was kindly performed by Ruhr Lab GmbH (Germany). The present study was carried out within the framework of the joint research programme of Perechin Timber and Chemical Plant and Uzhhorod National University on the valorisation of hardwood charcoal fines, which also supported the previous publications of the authors cited in this work (Korol and Yankovych, 2025a, 2025b; Yankovych and Korol, 2025; Korol *et al.*, 2026).

6. REFERENCES

CEN. 2005. *EN 1860-2: Appliances, solid fuels and firelighters for barbecuing – Part 2: Barbecue charcoal and barbecue charcoal briquettes – Requirements and test methods*. European Committee for Standardization, Brussels.

DIN. 2011. *DIN 51729-10: Testing of solid fuels – Determination of chemical composition of fuel ash – Part 10: X-ray fluorescence analysis (XRF)*. Deutsches Institut für Normung, Berlin.

Korol, N.I., Zhukova, Yu., Kulia, D., Haleha, O.V., and Yankovych, V. 2026. Adsorption of salicylic acid from ethanol solutions onto activated carbon: kinetics and equilibrium studies. *Results in Materials*, Vol.29, 100866.

Korol, N. and Yankovych, V. 2025a. Polyvinyl alcohol-based binder systems for biomass and charcoal briquettes. *Fuels*, Vol.6, No.4, 81. https://doi.org/10.3390/fuels6040081

Korol, N. and Yankovych, V. 2025b. Optimizing coal fine properties for industrial applications through chemical treatments. *Proceedings of the 5th International Scientific Conference "Chemical Technology and Engineering – 2025"*, Lviv, Ukraine, 23–26 June 2025, pp.99–104.

Makgobelele, N.W., Mbaya, R.K.K., Bunt, J.R., Leokaoke, N.T., and Neomagus, H.W.J.P. 2021. Evaluation of the mechanical properties of wood-derived charcoal briquettes for use as a reductant. *Journal of the Southern African Institute of Mining and Metallurgy*, Vol.121, No.5, pp.187–194.

Monsen, B., Tangstad, M., Solheim, I., Syvertsen, M., Ishak, R., and Midtgaard, H. 2007. Charcoal for manganese alloy production. *Proceedings of INFACON XI – Innovations in the Ferro-Alloy Industry*, New Delhi, India, 18–21 February 2007, Vol.1, pp.297–310.

Ringdalen, E. 2025. Decarbonization of ferroalloy production using biocarbon. *Minerals*, Vol.15, No.3, 228. https://doi.org/10.3390/min15030228

Surup, G.R., Trubetskaya, A., and Tangstad, M. 2020. Charcoal as an alternative reductant in ferroalloy production: a review. *Processes*, Vol.8, No.11, 1432. https://doi.org/10.3390/pr8111432

Yankovych, V. and Korol, N. 2025. Mechanochemical and molecular analysis of organic binders in charcoal briquetting for enhanced cold mechanical strength. *Cleaner Engineering and Technology*, Vol.29, 101113.

Nataliya Korol

Researcher, R&D Department, Perechin Timber and Chemical Plant; Associate Professor, Department of Organic Chemistry, Uzhhorod National University

Nataliya Korol holds a PhD in chemistry from Uzhhorod National University, where she is an Associate Professor in the Department of Organic Chemistry, and is also part of the R&D team of Perechin Timber and Chemical Plant. Her research is focused on the valorisation of hardwood-derived carbonaceous materials, including the development of organic binder systems for charcoal briquettes, the chemistry of coal and charcoal fines, and the use of activated carbons as adsorbents for organic micropollutants. She has co-authored several recent publications on charcoal briquetting and adsorption, and is the presenting author of the present contribution.

Danzi, E., and S. H. Spitzer. 2026. Safety Aspects of Silicon as a Clean Energy Transition Element. In *Silicon for the chemical and solar industry XVIII*, edited by M. Tangstad, H. Rong, A. Valderhaug, B. Andresen, H. Dalaker, and I. G. Page. Kristiansand, Norway, September 7–10, 2026. https://doi.org/10.55669/oa900842

Safety Aspects of Silicon as a Clean Energy Transition Element

Enrico Danzi[1], and Stefan H. Spitzer[1,2]

[1]VSB-Technical University of Ostrava, Czechia, enrico.danzi@vsb.cz

[2]European Institute for Innovation - Technology, Germany, s.spitzer@eifi-tech.eu

Keywords: MeCRE, SSE-Chart, Safety Characteristics, Metal Explosions

Abstract – The shift to clean energy from fossil fuels will depend heavily on metals. Silicon is one of the top elements, playing a key role in the transition to green energy due to its abundance and importance in developing essential technologies. The main energy sectors are the PV industry and the new application of Si-anode elements in EV production. These industries will increase silicon output and promote new recycling methods. Economic and security concerns are present, as China holds a monopoly on production, and Europe must address the challenge of energy costs associated with smelting and refining silicon. Because of its high energy density and specific energy, silicon is also an excellent candidate as a metal fuel. Its widespread availability in silica form, commonly used in glass manufacturing, is environmentally friendly and non-toxic, requiring no specialized waste processing. Furthermore, a clean, energy-efficient method for producing hydrogen from silica has been demonstrated. Still, little is known about the combustion behaviour and explosibility parameters of pure silicon dusts or Si-H2 mixtures. This work will provide data on explosibility characterization and establish a reliable, reproducible dataset for use in risk assessment of silicon metal powder-based energy processes. The silicon powder sample tested exhibited relatively high values for overpressure and rate of pressure rise, respectively, 8.1 bar and 440 bar/sec.

1. INTRODUCTION

Metals will play a central role in the energy transition by supporting the EU in building its clean energy value chain and driving it towards achieving the goals of the Sustainable Development Scenario 2050. In this scenario, elements could be sorted by their relevance and application: renewable technologies such as electric vehicles, photovoltaic modules, wind turbines, and hydrogen energy applications require a high load of specific materials relative to their conventional counterparts. Silicon is listed in the first tier for its relevance in the KU Leuven (2022) report on critical materials for the energy transition, and an increase of about 60 per cent in its production is forecast if the SDS scenario is to be reached within the 2050 deadline.

Silicon will likely drive the energy transition due to its potential enhanced utilisation in two sectors: the photovoltaic modules industry (JRC, 2024), and silicon adoption in replacing carbon-based anodes (graphite) in electric vehicle batteries (Feyzi, 2024). In these perspectives, the EU silicon market has a potential growth of 600-700 ktonn/y in 2030 to 900 ktonn/y in 2050 (KU Leuven, 2022). Actually, this further rise in PV production is connected to the

This work is licensed under the Creative Commons Attribution 4.0 International License. To view a copy of this license, visit https://creativecommons.org/licenses/by/4.0/

perspectives of decarbonising the EU according to the Paris Treaty, thus requiring about 60% more silicon than is now required.

The current silicon market consists mostly of chemical and metallurgical applications. Silicon is widely used as a fluidising agent in the aluminium melting process and is included in the production of Al--Si alloys. A significant share of silicon extraction is used in silicones and silane production, while electronic applications account for a small contribution.
Both metallurgical-grade and solar-grade polysilicon (>99.9999%) are produced from silica mineral ore extraction followed by carbothermal reduction, a process generating 4.3 ton CO2 per ton of Si produced (Hoover, 2024), making decarbonisation of Si production one of the most pressing open challenges. Metallurgical grade silicon is converted to a volatile compound that is condensed and refined by fractional distillation. Ultra-pure silicon is then extracted from this refined product (CRM Alliance, 2026).

Alternative reduction pathways have been proposed, such as bio-carbon coupled with CCU/CCS (Hoover, 2024), solid-state electrolysis with molten salts (Maldonado2020), and high-temperature solar furnaces (Loutzenhiser, 2010), though these remain at lab or pilot scale. Silicon, together with Aluminium, iron, and magnesium, is among the best potential candidates as an energy carrier, due to its high energy density, high abundance, non-toxic oxidised form, and high transportability (see also Wronksy & Sciacovelli, 2024).

A promising pathway for silicon's high energy content is its direct combustion in air or by steam to generate heat and power outputs. This process is among the most effective metal-enabled energy cycles (MeCRE, see Figure 1), although renewable sources are demanded to close the silica-to-silicon metal loop effectively.

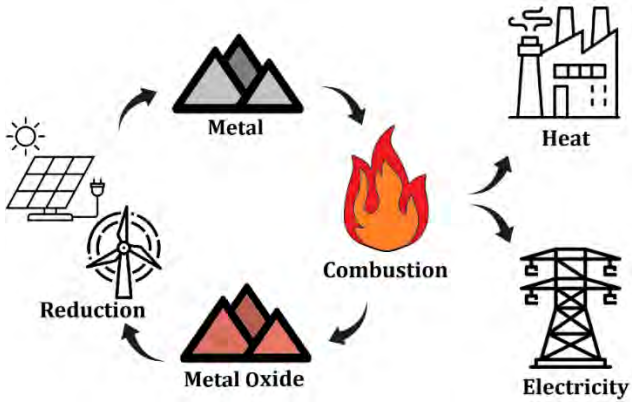

Figure 1: Schematic of the cycle using metals as an energy carrier: If renewable energy is available in surplus, the metal oxide gets reduced. If energy or heat is needed, the metal is burned, from Semenova, (2026)

The technical feasibility of a silicon powder burner has recently been demonstrated (Heng, 2025a, Heng, 2025b), laying the foundation for silicon as a direct energy carrier, a concept first proposed by (Bardsley, 2008).

In selecting silicon as an energy carrier, several criteria must be assessed: availability, cost, energy storage density, safety in handling, potential for closing the material cycle, reactivity during activation, and simple, loss-free storage (Bergthorson, 2018).

While technical constraints have been addressed, and intrinsic properties give this metal relevant advantages among others, availability and accessibility are still problematic. According to the European Commission report (JRC, 2024) and Ramírez-Márquez, C. (2025), China produces over 65% of the world's metallurgical-grade silicon (silicon metal) and

accounts for over 80% to 90% of global solar-grade polysilicon output. China is associated with significant overcapacity, raising concerns about supply security and sustainable pricing rather than material abundance. European Union demand currently relies on imports from Norway (EU Commission, 2023), with Scandinavian supply offering sustainability advantages through green energy availability (Akyıldız, 2024). Silicon end-of-life recycling rates remain near zero today (KU Leuven, 2022), though this will become increasingly important as the first large volumes of PV module waste arise around 2040.

1.1 The safety perspective

Given these supply-chain and market constraints, the safe handling and processing of silicon and its compounds are critical and often underappreciated dimensions of any large-scale silicon energy economy. It is clear from the literature (Kletz & Amyotte, 2010) that increasing the adoption scale of a hazardous material (or a hazardous process) without any adequate risk assessment will produce a coherent increase in related accidents, as maximising the inventory of a hazardous material would increase the cumulative exposure of targets (workers, installations, and surrounding communities).

The risk level is heightened by several factors, such as underestimating actual risks, assuming that "green processes" are intrinsically safer (Casson Moreno, 2019), and uncritically relying on proven materials or processes while disregarding site-specific variables and variability in conditions. In the Silicon industrial chain, certain hazards could exacerbate the risk of explosions and fires, as demonstrated by recent accidents discussed below.

Silicon and its key process intermediates, including silane (flashpoint 27 °C, pyrophoric) and trichlorosilane, are highly flammable, and fine silicon powder forms explosive dust clouds with ignition energies in the range of 5--100 mJ and minimum explosive concentrations of approximately 100-200 g·m-3.

Actually, the specific process layout for polysilicon manufacturing requires chemical engineering know-how and strict process management due to the use of flammable, toxic, and hazardous materials. Three significant industrial accidents illustrate these hazards across more than five decades of Silicon processing.

In 1972, a catastrophic silicon dust explosion at Elkem's Bremanger plant in Norway killed five workers and severely injured four more, destroying the entire grinding facility; the cause was a hot-work operation on a powder-conveying pipe that had not been cleaned, which dispersed and ignited a fine dust layer and propagated a secondary explosion throughout the building (Eckhoff, 2003). This case reflected some key common failures while dealing with combustible dust: i) poor housekeeping, letting dust pile up; ii) inadequate hot-work procedure, providing an efficient ignition source; iii) unawareness or failure to recognise material-specific hazards.
In January 2014, a fire and explosion occurred at the Mitsubishi Materials polysilicon plant in Yokkaichi, Japan, during maintenance cleaning of a heat exchanger in the hydrogen recycling section; chlorosilane polymer residues had accumulated inside the exchanger, and their hydrolysis under dry, low-temperature conditions produced highly ignition-sensitive compounds whose decomposition — identified as involving $Si_8H_{10}O_{14}$ — triggered the explosion when the cover was opened (Kudo et al., 2016).

A recent series of major accidents across the polysilicon supply chain — the 2024 explosion at OCI's plant in Malaysia and the 2020–2021 fires and explosions at Xinjiang facilities (Bernreuter, 2020, 2024; Crawford, 2025a, 2025b; Wood-Black et al., 2021) — shows that solar-

grade silicon production still handles highly hazardous materials with little cross-industry safety information sharing. Although these events concerned chlorosilane, hydrogen, and siloxane process hazards rather than silicon metal powder, their concentration in Xinjiang, which holds most of the world's polysilicon capacity, means even localised incidents can disrupt global PV feedstock supply. This context motivates a fuller characterisation of the fire and explosion behaviour along the silicon value chain, including the silicon-particle hazards addressed here. Taken together, these cases demonstrate that the hazards of silicon chemistry — whether in powder grinding, reactive gas processing, or maintenance operations — demand the most rigorous process safety discipline, and that this dimension must be integral to any strategy for scaling Silicon in the renewable energy transition.

1.2 Metal dust explosions

Metal dust explosions present particular hazards compared to organic dust: the high heat of combustion per mole of oxygen, exceeding that of carbon by a factor of two to three, drives adiabatic flame temperatures above 3000 K, generating intense thermal radiation and severe burn injuries (Reding, 2018).

Yet safety literature on silicon combustion behavior and its metal-to-energy cycle remains scarce, and the assumption that silicon powder is harder to ignite than aluminum or magnesium should not be equated with low explosion sensitivity under all conditions.

This latter statement came with the actual difficulty of maintaining stable silicon particle flames in burner applications (Weiser et al., 2026, Heng et al., 2025b). Even Eckhoff's pioneering work (Eckhoff, 1986) underlined the lower ignition sensitivity of Si compared with Al powders, but this should be regarded as a relative assumption, consistent with the specific testing in terms of materials and equipment.

Among other metal dusts, silicon was less tested, and scarce data could be found in the literature. The science community has recently focused on silicon-to-energy applications, investigating combustion behavior, while the safety parameters have been less in the spotlight, according to the authors' literature analysis. This could have reflected on ultimate safety assumptions, or underestimation of the actual explosibility characterization of a combustible powder, which resulted in a misunderstanding of the ignition sensitivity ranking of silicon metal particles.

Jacobson and coworkers (Jacobson, 1964) tested several elemental metal powders. A silicon sample, defined as collected from a bag filter before grinding, exhibited Pmax = 5.6 bar and $(dp/dt)_{max}$ = 827.4 bar·sec^{-1}, corresponding to a K_{St} value of about 225 bar·sec^{-1}·m^{-1}. The sample was sized 100% under 74 μm.

In the aftermath of the reported accident, Eckhoff (1986) conducted an experimental campaign in which very fine silicon samples were analysed. In this, the explosion testing was conducted in the modified Hartmann tube, with an electric spark as the ignition source, as was common at the time. He concludes that fine silicon powders could present a significant explosion hazard, although not as severe as that of equally fine aluminium powders. This is reflected in both the rate of pressure rise and the MIE values. By decreasing the particle size, Silicon ignited more easily and generated higher rates of pressure rise, although these were lower than those of Al at any given particle diameter. In terms of $(dp/dt)_{max}$, this gap is almost equal to four times.

The explosion behaviour of silicon powders in vented tubes is investigated later (Eckhoff, 1988) to identify the actual response of bag-filter equipment to internal overpressure and the reliability of the VDI 3673 standard for explosion-venting design. The silicon sample reported a d50 of about 50 μm and was also tested for its explosibility parameters. When the silicon dust cloud was ignited by a silicon dust flame, the measured reduced overpressure (p_{red}) was correctly predicted by the standard, whereas with a nitrocellulose flame, the p_{red} was very low and inconsistent with the standard.

Skjold (2013) also studied the silicon flame propagation behaviour using a 20 L spherical device by measuring the impact of the ignition delay time (and hence the turbulence level in the vessel) on overpressure and pressure rise over time. A relevant finding was the rapid decrease in dust concentration with increasing ignition delay time, which could be regarded as a critical constraint on the applicability of results from constant-volume explosion vessels at the laboratory scale. Both particle size and shape would have impacted the dust settling in the vessel.

Hybrid mixtures of silicon dust and hydrogen were also investigated. They demonstrated how typical parameters used in the design of explosion protection systems, such as p_{max} and $(dp/dt)_{max}$, are affected by mixture composition and can vary significantly when hydrogen is introduced.

2. MATERIALS AND METHODS

Dust explosion safety characteristics are conventionally grouped into three groups according to their physical meaning and practical role in hazard assessment (Eckhoff, 2003, Bartknecht, 1993). Primary characteristics define the fundamental boundaries of the explosive regime: the lower explosion limit (LEL, also called the minimum explosible concentration, MEC) and the limiting oxygen concentration (LOC) (EN14034-3, EN14034-4). Together they describe the compositional space — in terms of fuel concentration and oxygen availability — within which a self-sustaining deflagration can exist, and they are therefore the quantities most directly relevant to the design of inerting, dilution, and ventilation strategies aimed at preventing an explosive atmosphere from forming in the first place. Secondary characteristics describe the sensitivity of the dust cloud to ignition once an explosive atmosphere is present: the minimum ignition energy (MIE) and the minimum ignition temperature (MIT) of the dust cloud (EN13821, ISO 80079). These determine the type and strength of ignition source capable of initiating an explosion, and so govern the selection of electrical equipment categories, the permissibility of hot-work operations, and the adequacy of electrostatic bonding and earthing measures. Tertiary characteristics quantify the destructive severity of the explosion event itself and are the parameters on which passive and active explosion protection systems such as venting, suppression, and containment are dimensioned. The two principal tertiary parameters are the maximum explosion pressure pmax and the maximum rate of pressure rise (dp/dt)max, from which the scale-normalized deflagration index $KSt = (dp/dt)_{max} \times V^{1/3}$ is derived (EN14034-1, EN14034-2). These were determined experimentally using the standardized 20-liter sphere (see Fig. 2).

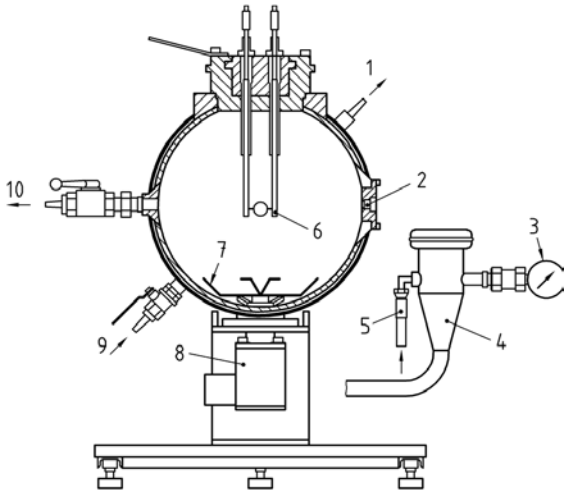

Figure 2: Schematic of the standard 20-L sphere apparatus for the determination of safety characteristics of dusts (EN14034-1), 1) Cooling water outlet 2) Pressure transducers 3) Manometer 4) Dust container 600 ml 5) Air inlet 6) Ignition source 7) Nozzle 8) Fast-acting valve 9) Cooling water inlet 10) Vent (Air, reaction products)

In this vessel, a weighed quantity of dust is loaded into an external 0.6-liter pressurized reservoir (4) at approximately 20 bar, while the sphere is simultaneously pre-evacuated to around 0.4 bar absolute, ensuring that the combined initial condition at the moment of dispersal is atmospheric. Upon actuation of the solenoid valve (8), dust is ejected through a rebound nozzle within the sphere, generating a turbulent suspended cloud representative of worst-case process plant conditions. After a standardized ignition delay time of 60 ms, two opposing pyrotechnic chemical ignitors mounted at the geometric center of the sphere (6) fire simultaneously, supplying a combined ignition energy of 10 kJ. Two piezoelectric pressure transducers flush-mounted in the vessel wall (2) record the complete pressure–time trace of the event, from which p_{max} is extracted as the highest pressure attained and $(dp/dt)_{max}$ is determined as the maximum slope of the rising portion of that trace. The procedure is repeated three times across a systematic range of dust concentrations spanning from low concentrations up to fuel-rich compositions, since neither p_{max} nor $(dp/dt)_{max}$ necessarily occurs at the same concentration for all materials, and both the stoichiometric and the moderately fuel-rich regimes must be covered to ensure the true peak values are captured. The average of the three highest values recorded across the entire concentration series is reported as the characteristic severity parameters of the material. The cubic-root normalization embedded in K_{St} is what enables results measured in the 20 L laboratory vessel to be applied to the sizing of explosion protection systems on vessels of arbitrary industrial scale.

The $(dp/dt)_{max}$ is converted to the K_{St} form through the cubic-root normalisation equation, as this latter value is independent of testing vessel size and could be used as a design parameter for protection systems on vessels of arbitrary industrial scale. In this work, the safety characteristics of a silicon dust sample were tested using a 20 L sphere, in air and mixed with hydrogen, to assess the enhanced synergistic effect of the hybrid mixture (see tests specifications in Table 1). The sample was a 99% pure commercial silicon powder, with a mean diameter of about 20.2 um.

For the silicon-hydrogen tests, the 20L sphere was evacuated to a pressure below the initial 0.4 bar and then filled with hydrogen so that the desired concentration is reached after the dust-air mixture is injected (DIN/TS 31018-1).

Table I: Tests performed and standards of reference

Parameter	Standard
Maximum explosion pressure p_{max}	EN 14034-1:2011
Maximum rate of pressure rise $(dp/dt)_{max}$	EN 14034-2:2011
Maximum explosion pressure p_{max} (hybrid mixture)	DIN/TS 31018-1:2024-05
Maximum rate of pressure rise $(dp/dt)_{max}$, (hybrid mixture)	DIN/TS 31018-1:2024-05

3. RESULTS AND DISCUSSION

This work's results are presented in Figures 3 and 4, respectively, for the maximum pressure and the maximum pressure rise at any tested dust concentration.

.

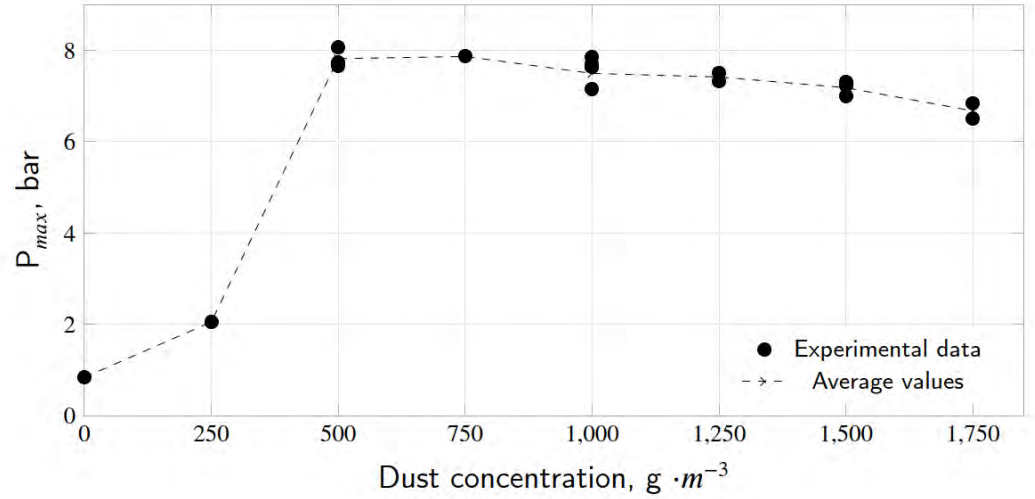

Figure 3: Rate of pressure rise test for this work's silicon sample

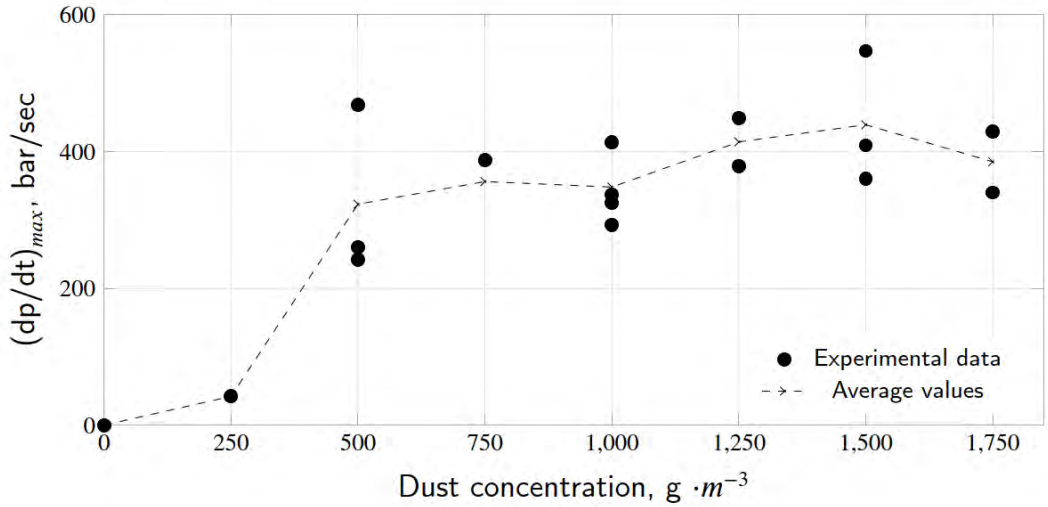

Figure 4: Rate of pressure rise test for this work's silicon sample

The maximum overpressure found was 8.1 bar at 500 g/m3, and the maximum rate of pressure rise was about 440 bar/sec at 1500 g/m3 (these are averages of the maximum values obtained across the different test series). The explosion curve obtained is typical for a metal powder, as

it peaks, then settles or slightly decreases in a plateau-like shape. Higher concentrations will likely result in a decrease in both parameters, as they enter a rich fuel mixture and the mass exceeds the dispersion device's effectiveness.

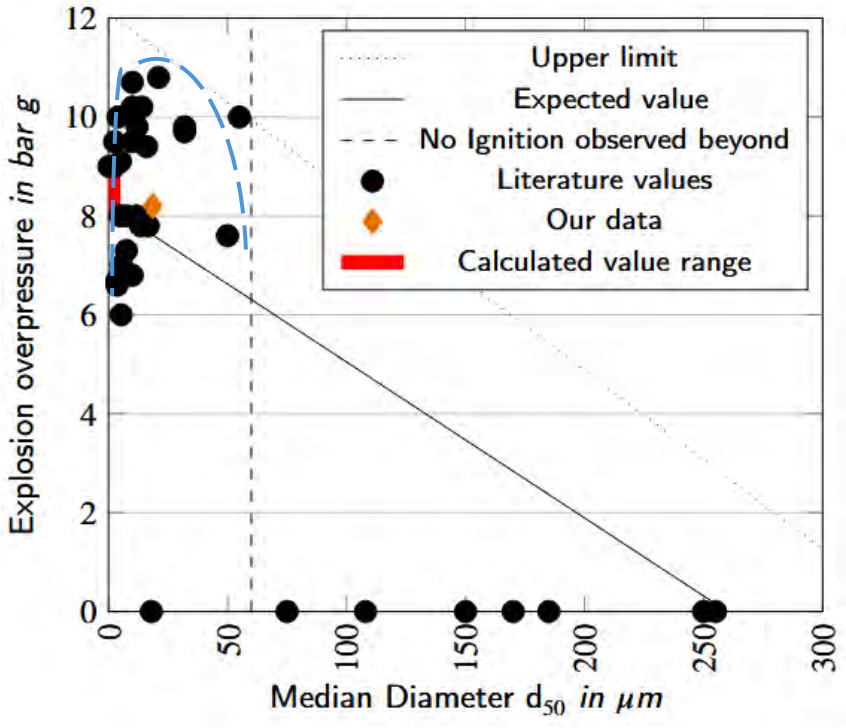

Figure 5: SSE-Chart: Explosion pressures for several silicon dusts against the stated $d_{50,}$ data collected from Lucas (1994), Eckhoff, (1988 & 1992), Cashdollar, (2007), Matsuda, (2001), Taveau, (2018), Hertzberg, (1992), and GESTIS (2026).

Data from explosion testing are collected and organised in the plot in Figure 5, which reports the maximum overpressure against the 50th percentile of the dust particle size distribution. This is a coherent and reliable representation of combustible dust safety parameters, since PSD strongly affects both pmax and $(dp/dt)_{max}$.

From a closer look at the curve in the vicinity of the lower size area, the curve seems to assume a bell-shaped form, with a peak at about 20 microns (around 10 bars, the blue dashed line in Figure 5). Smaller sizes reported lower overpressures. The reasons could be associated with: higher agglomeration (as inter-particle forces grow with reducing diameters), so that agglomerates accounted for the explosion dynamics and then lower overpressures than expected were found; or with passivation enhancement at smaller size, this has been reported by Mittal (2014), for magnesium, but could likely be concerning silicon (although Mittal's data dealt with micro- and nanometric dust samples too). Another alternative explanation could be as a result of data scattering, since some referenced values (such as those from GESTIS database) only reported a median value, but any other information was not disclosed. Particle size distribution parameters could refer to the 50th percentile or average diameter based on volume or weight distribution or even refer to Sauter diameter (the diameter of a sphere that has the same ratio of volume to surface area as the whole group of particles).

For relatively larger diameters, the agglomeration seemed negligible, and higher overpressures are reported, in the range 15-20 µm, while larger diameters tend to give lower overpressures, coherently with the literature, up to a likely threshold where no explosion is reported anymore. This threshold could be identified from the dataset around 70 um. Only

one point stood as an outlier at 18 um, with no ignition; this corresponded to a test of Eckhoff (1986) using a different ignition source and device, as reported above. Silicon has clearly lower sensitivity to ignition, as stated before, even though the ignition type is crucial.

The calculated range values are derived from different methods, from analytical to adiabatic equilibrium models, such as CANTERA (Goodwin et al., 2025) and the CEA-NASA codes (Gordon et al., 1994). The predicted pressure range of approximately 7.9–10.5 bar g is particularly uncertain, as the experimental data show large scatter values exceeding the calculated upper bound. This may be due to additional high-temperature reaction pathways, such as silicon nitride formation and the further oxidation of SiO to SiO2, as well as pressure-piling effects in the confined vessel. Therefore, the upper limit should be regarded as preliminary, and further tests considering particle size, morphology and oxidation state are needed before using these values for explosion protection design (see also Morra, D. et al., 2026).

.

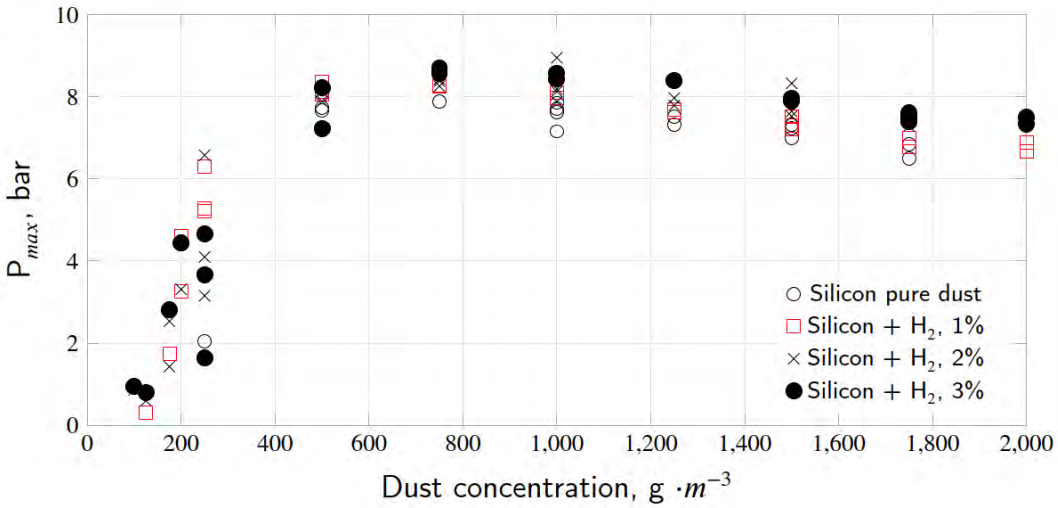

Figure 6: Preliminary results of hybrid silicon-Hydrogen mixtures, overpressure against dust concentration.

Figure 6 presents the preliminary test results for hybrid mixtures (Si-H2). Here, only 3 hydrogen concentrations were tested, all below its LEL (4%). Although further validation and testing are needed, some considerations are warranted. At lower dust concentrations (around the silicon dust LEL), hydrogen addition has a higher effect on the overpressure. As dust mass increases, the differences between pure dust explosions and hybrid mixtures become less relevant, although it seems that the higher the hydrogen share, the higher the overpressure at any given concentration. These assumptions pointed to the existence of a "synergistic" zone, where, despite neither component's LEL being reached, the explosion parameters exceed those of the individual components.

4. CONCLUSIONS

Silicon dust has been investigated for its explosion pressure and maximum rate of pressure rise. This sample exhibited 8.1 bars and 440 bar/sec, respectively, for p_{max} and $(dp/dt)_{max}$. It has also been compared with literature data, and the first upper-bound estimates of its safety characteristics were presented. Further tests are needed to verify the presented approach, but eventually, this will lead to predictable safety characteristics that are easy to implement and remain reliable and independent of the testing facility.

The future perspective is to further examine silicon powders with coarser diameters (in the 70-100 um range), to replicate the different sizes across the silicon processing industry and verify the diameter vs overpressure correlation. Even though no ignition has been observed thus far above median particle sizes above ~70 μm, it is too early to regard silicon powders exceeding that diameter as safe. Other metals such as aluminium and iron show rather flat behaviour, similar to the dotted and straight lines of Fig. 5; hence, further investigation is needed to clarify which assumption is most correct. An experimental campaign is planned in the next research step with coarser samples.

Future work will also focus more on hybrid mixtures of silicon dust and hydrogen. These materials are encountered in the same process facilities along the silicon metal industrial chain, and a synergistic effect on the overpressure of the pure single components is possible (Spitzer, 2026). Preliminary results have already demonstrated that, even with hydrogen content below its LEL (4%), the overpressure of the silicon-H2 mixture increases, confirming the synergistic effect between the two materials.

5. ACKNOWLEDGEMENTS

This work was supported by the European Union under the Horizon Europe project CESAR (Centre of Excellence for Safety Research, GA No 101186946).

6. REFERENCES

Akyıldız, O. (2024) 'The importance of silicon metal on the green transition and the role of Northern Countries in the silicon metal market', European Geosciences Union General Assembly 2024 (EGU24), EGU General Assembly Conference Abstracts, p. 4042. doi: 10.5194/egusphere-egu24-4042.

Bardsley, W.E. (2008) 'The sustainable global energy economy: Hydrogen or silicon?', Natural Resources Research, 17(4), pp. 197–204. doi: 10.1007/s11053-008-9077-6.

Bartknecht, W. (1993) Explosionsschutz: Grundlagen und Anwendung, Springer

Bartknecht, W. and Zwahlen, G. (1993) Explosionsschutz: Grundlagen und Anwendung. Berlin: Springer. ISBN: 978-3-540-55464-6.

Bergthorson, J.M. (2018) 'Recyclable metal fuels for clean and compact zero-carbon power', Progress in Energy and Combustion Science, 68, pp. 169–196. doi: 10.1016/j.pecs.2018.05.001.

Bernreuter Research (2020) Lessons from the polysilicon plant accidents at Daqo and GCL. Available at: https://www.bernreuter.com/newsroom/polysilicon-news/article/lessons-from-the-polysilicon-plant-accidents-at-daqo-and-gcl/ (Accessed: 30 June 2026).

Bernreuter Research (2024) Accident at OCI Malaysia's polysilicon plant injures ten workers. Available at: https://www.bernreuter.com/newsroom/polysilicon-news/article/accident-at-oci-malaysia-s-polysilicon-plant-injures-ten-workers/ (Accessed: 30 June 2026).

Crawford, A. (2025a) The accident at OCIM's polysilicon plant shouts for more safety. Available at: https://www.bernreuter.com/newsroom/polysilicon-news/article/the-accident-at-ocim-s-polysilicon-plant-shouts-for-more-safety/ (Accessed: 30 June 2026).

Crawford, A. (2025b) OCIM 14-August-2024 fatal hydrochlorination accident analysis. Available at: https://www.bernreuter.com/files/data/newsroom/polysilicon-news/2025/2025-01-06-Alan-Crawford-OCIM-August-2024-Fatal-Accident-Analysis.pdf (Accessed: 30 June 2026).

Critical Raw Materials Alliance (CRM Alliance). https://www.crmalliance.eu/silicon-metal. Last accessed 27 July 2026.

DIN (2024) DIN/TS 31018-1:2024-05 — Determination methods for safety-related parameters of explosion protection for hybrid mixtures of substances — Part 1: Gases. Berlin: DIN Deutsches Institut für Normung.

DIN. DIN/TS 31018-1 Bestimmungsverfahren für sicherheitstechnische Kenngrößen des explosionsschutzes für hybride stoffgemische - Teil 1: gase. German pre-standard, Deutsches Institut für Normung; 2024, http://dx.doi.org/10.31030/3530706

Eckhoff, R.K. (2003) Dust Explosions in the Process Industries. Amsterdam: Elsevier Science. doi: 10.1016/B978-0-7506-7602-1.X5000-8.

Eckhoff, Rolf (2003) Dust Explosions in the Process Industries, 3rd ed., Gulf Professional Publishing

EN 14034-3:2006+A1:2011 — MEC/LEL

EN 14034-4:2004+A1:2011 — LOC

European Commission, Joint Research Centre (2024) Clean Energy Technology Observatory: Photovoltaics in the European Union – 2024 status report on technology development, trends, value chains and markets. Luxembourg: Publications Office of the European Union. JRC139297. doi: 10.2760/1812909.
European Commission, Joint Research Centre, Chatzipanagi, A., Jaeger-Waldau, A., Letout, S., Mountraki, A., Gea Bermudez, J., Georgakaki, A., Ince, E. and Schmitz, A., Clean Energy Technology Observatory: Photovoltaics in the European Union - 2024 Status Report on Technology Development, Trends, Value Chains and Markets, Publications Office of the European Union, Luxembourg, 2024, https://data.europa.eu/doi/10.2760/1812909, JRC139297.
European Commission. Study on the Critical Raw Material for the UE 2023 – Final report
European Committee for Standardization (2002) EN 13821:2002. Potentially explosive atmospheres — Explosion prevention and protection — Determination of minimum ignition energy of dust/air mixtures. Brussels: CEN.
European Committee for Standardization (2011) EN 14034-1:2004+A1:2011. Determination of explosion characteristics of dust clouds – Part 1: Determination of the maximum explosion pressure pmax of dust clouds. Brussels: CEN.
European Committee for Standardization (2011) EN 14034-2:2006+A1:2011. Determination of explosion characteristics of dust clouds – Part 2: Determination of the maximum rate of explosion pressure rise (dp/dt)max of dust clouds. Brussels: CEN.
European Committee for Standardization (2011) EN 14034-3:2006+A1:2011. Determination of explosion characteristics of dust clouds – Part 3: Determination of the lower explosion limit LEL of dust clouds. Brussels: CEN.
European Committee for Standardization (2011) EN 14034-4:2004+A1:2011. Determination of explosion characteristics of dust clouds – Part 4: Determination of the limiting oxygen concentration LOC of dust clouds. Brussels: CEN.
European Committee for Standardization. (2011). *Determination of explosion characteristics of dust clouds — Part 1: Determination of the maximum explosion pressure (pmax) of dust clouds* (EN 14034-1:2004+A1:2011), and *Part 2: Determination of the maximum rate of explosion pressure (dp/dt)max (*EN 14034-2:2004+A1:2011). Brussels: CEN.
Feyzi, E., Kumar M R, A., Li, X., Deng, S., Nanda, J. and Zaghib, K. (2024) 'A comprehensive review of silicon anodes for high-energy lithium-ion batteries: Challenges, latest developments, and perspectives', Next Energy, 5, p. 100176. doi: 10.1016/j.nxener.2024.100176.
Goodwin, D.G., Moffat, H.K., Schoegl, I., Speth, R.L. and Weber, B.W. (2025) Cantera: An object-oriented software toolkit for chemical kinetics, thermodynamics, and transport processes. Version 3.2.0. Available at: https://www.cantera.org. doi: 10.5281/zenodo.17620923.
Gordon, S. and McBride, B.J. (1994) Computer Program for Calculation of Complex Chemical Equilibrium Compositions and Applications. Part I: Analysis. NASA Reference Publication 1311. Cleveland, OH: NASA Lewis Research Center.
Heng, H., Keck, H., Chauveau, C., Goroshin, S., Bergthorson, J. and Halter, F. (2025) 'Combustion behaviour of single silicon particles in different oxidizing environments', Combustion and Flame, 283, p. 114625. doi: 10.1016/j.combustflame.2025.114625.
Heng, H., Mani, C., Chepel, N., Mangalvedhe, K., Antar, E., Goroshin, S. and Bergthorson, J. (2025) 'Silicon dust flames: A pathway to using silicon as a carbon-free energy carrier', Proceedings of the Combustion Institute, 41, p. 105940. doi: 10.1016/j.proci.2025.105940.
Hoover, H., Bell, R. and Rippy, K. (2024) 'Emerging technologies for decarbonizing silicon production', Journal of Sustainable Metallurgy, 10, pp. 1921–1932. doi: 10.1007/s40831-024-00913-3.
Institute for Occupational Safety and Health of the German Social Accident Insurance. Gestis staubex - database for dusts, 2026
International Organization for Standardization (ISO) (2006) ISO 80079-20-2:2006: Explosive atmospheres — Part 20-2: Material characteristics — Combustible dusts test methods. Geneva: ISO.
Jerome Taveau, Saul Lemkowitz, Simone Hochgreb, and Dirk Roekaerts. Scaling up the severity of metal dusts deflagrations. In Twelfth International Symposium on Hazards, Prevention, and Mitigation of Industrial Explosions (ISHPMIE XII), Kansas City, USA, 2018
Joachim Lucas. Explosionsfähige staub/luft-gemische - bewertung von explosionskenngrößen, die in verschiedenen apparaturen ermittelt wurden. Technische Überwachung, pages 61–68, 19
Kenneth L. Cashdollar and Isaac A. Zlochower. Explosion temperatures and pressures of metals and other elemental dust clouds. Journal of Loss Prevention in the Process Industries, 20(4–6):337–348, 2007.
Kletz, T.A. and Amyotte, P.R. (2010) Process Plants: A Handbook for Inherently Safer Design. 2nd edn. Boca Raton, FL: CRC Press.
KU Leuven (2022) Metals for clean energy: Pathways to solving Europe's raw materials challenge. Leuven, Belgium: KU Leuven. Commissioned by Eurometaux
Loutzenhiser, P.G., Tuerk, O. and Steinfeld, A. (2010) 'Production of Si by vacuum carbothermal reduction of SiO_2 using concentrated solar energy', JOM, 62, pp. 49–54. doi: 10.1007/s11837-010-0137-0.

Martin Hertzberg, Isaac A. Zlochower, and Kenneth L. Cashdollar. Metal dust combustion: Explosion limits, pressures and temperatures. Twenty-Fourth Symposium (International) on Combustion, pages 1827–1835, 1992
Moreno, V. C.; Danzi, E.; Marmo, L.; Salzano, E.; Cozzani, V. Major Accident Hazard in Biodiesel Production Processes. *Saf Sci* **2019**, *113* (December 2018), 490–503. https://doi.org/10.1016/j.ssci.2018.12.014.
Morra, D., Duenas Santana, J. A., Danzi, E., Taveau, J., Salzano, E., Semenova, A., Eckart, S., Spitzer, S. H. (2026). Explosion Pressures of Metals - Theoretical Values and Experimental Results, submitted to Advanced Powder Technology, Special Issue: Metal Powder: From Preparation to Combustion Processes.
R. K. Eckhoff, F. Alfert, and K. Fuhre. Venting of dust explosions in a 5.8m³ bag filter under realistic conditions of dust cloud generation. VDI-Berichte, 701:695–722, 1988
Ramírez-Márquez, C. (2025). Solar-Grade Silicon in the Energy Transition: A Strategic Commodity for the Global Photovoltaic Market. Commodities, 4(3), 18. https://doi.org/10.3390/commodities4030018
Reding, N.S. and Shiflett, M.B. (2018) 'Metal dust explosion hazards: a technical review', Industrial & Engineering Chemistry Research, 57(34), pp. 11473–11482. doi: 10.1021/acs.iecr.8b02465.
Semenova, A. *et al.* (2026) 'Towards standardized safety protocols for iron-based energy carriers: International alignment through round robin testing on safety characteristics', *Open Research Europe*, 6, 54. doi: 10.12688/openreseurope.22839.1.
Spitzer S.H., Sr., Amyotte P., Salzano E. (2026). Explosion behavior of hybrid mixtures. Progress in Energy and Combustion Science, 113, DOI: 10.1016/j.pecs.2025.101276
T. Matsuda, M. Yashima, M. Nifuku, and H. Enomoto. Some aspects in testing and assessment of metal dust explosions. Journal of Loss Prevention in the Process Industries, 14, 2001
Tomasz Wronski, Adriano Sciacovelli, Analysis of the potential of four reactive metals as zero-carbon energy carriers for energy storage and conversion, Journal of Energy Storage, Volume 100, Part A, 2024, 113514, ISSN 2352-152X, https://doi.org/10.1016/j.est.2024.113514.
U.S. Chemical Safety and Hazard Investigation Board (CSB) (2006) Combustible Dust Hazard Study. Investigation Report No. 2006-H-1. Washington, DC: U.S. Chemical Safety and Hazard Investigation Board. Available at: https://www.csb.gov/assets/1/20/dust_final_report_website_11-17-06.pdf
U.S. Chemical Safety and Hazard Investigation Board (CSB) (2018) Dust Incidents 2006–2017. Washington, DC: U.S. Chemical Safety and Hazard Investigation Board. Available at: https://www.csb.gov/assets/1/6/csb_dust_incidents.pdf
Verein Deutscher Ingenieure (VDI) (2002) Pressure venting of dust explosions. VDI-Richtlinie 3673 Blatt 1. Berlin: Beuth Verlag.IEEE Style
Weiser, V., Kelzenberg, S., Knapp, S. and Koleczko, A. (2026). Investigation on the Combustion of Silicon as a Carbon-free Energy Carrier. In Energetic Materials and Techniques (eds L.T. DeLuca and R.M. Doherty). https://doi.org/10.1002/9783527853267.ch05
Wood-Black, F., Blayney, M. B., Reid, M., Hicks, K. E. and Wiliams, O. F. ACS Chemical Health & Safety 2021 28 (4), 229-231. DOI: 10.1021/acs.chas.1c00057
Yan, X. Q.; Yu, J. L. Dust Explosion Incidents in China. Process Safety Progress 2012, 31 (2), 187–189. https://doi.org/10.1002/prs.11482.
Yuan, Z.; Khakzad, N.; Khan, F.; Amyotte, P. Dust Explosions: A Threat to the Process Industries. Process Safety and Environmental Protection 2015, 98, 57–71. https://doi.org/10.1016/j.psep.2015.06.008.

Enrico Danzi

Scientist, VSB – Technical University of Ostrava

Enrico Danzi is a Chemical Engineer with a PhD in Metrology. His research addresses industrial safety and fire risk assessment. Since September 2025, he has been a researcher in the CESAR project (Centre of Excellence for Safety Research) at VSB–Technical University of Ostrava, Czech Republic, focusing on the safety aspects of clean energy processes. His work explores the explosibility of metal powders–H2 mixtures and H2 jet-fire testing. He is involved in COST actions NERO (extreme wildfires) and REInvent (biomass valorisation) and received the 2026 RISENERGY Transnational Access grant for research on biomass–plastic pyrolysis and explosibility. He has authored more than 30 scientific papers and presented at international safety science conferences since 2014.

Buseth, T., B. R. Henriksen, M. G. Dolmen, T. Skjold, A. M. Mork, and G. H. Pedersen. 2026. The Effect of Particle Size Distribution on the Explosibility of Silicon Dust Clouds. In *Silicon for the chemical and solar industry XVIII*, edited by M. Tangstad, H. Rong, A. Valderhaug, B. Andresen, H. Dalaker, and I. G. Page. Kristiansand, Norway, September 7–10, 2026. https://doi.org/10.55669/oa900843

The Effect of Particle Size Distribution on the Explosibility of Silicon Dust Clouds

T. Buseth[1], B.R. Henriksen[1], M.G. Dolmen[1], T. Skjold[2], A.M. Mork[2] and G.H. Pedersen[3]
[1]Elkem ASA Technology / Process Development, Norway, bjorn-rune.henriksen@elkem.com
[2]University of Bergen, Norway, [3]Gexcon AS, Bergen, Norway

Keywords: Silicon, dust explosions, explosive properties, particle size distribution

Silicon dust—metallurgical and higher-purity grades—exhibits ignitability and explosibility characteristics that underpin industrial applications as energetic material. Silicon has also been proposed as a possible "green fuel" for energy production through controlled combustion. However, the same energetic properties that enable these applications can, under unfavourable conditions, create hazardous situations and trigger industrial accidents. This is well recognised across the industry. Elkem has firsthand experience, including the devastating dust explosion in Bremanger in 1972. Since then, Elkem has maintained a long-standing focus on dust explosions hazards and the mechanisms that influence the explosion risk. Relevant test data for silicon dust that could be identified within the company have now been consolidated for a comprehensive review. This effort has led to an updated understanding of the behaviour and properties of silicon dust, particularly regarding the influence of dynamic variables. Among these, particle size distribution (PSD) is the most critical parameter affecting dust explosibility. Notably, PSD is not a fixed property; it is dynamic and evolves with time, mechanical forces, and degree of turbulence. Standardized dust-testing methods capture only a controlled subset of these variables, enabling comparisons across samples while simplifying the complexity of real-world conditions.

1. INTRODUCTION

This paper discusses the explosibility of silicon dust, as expressed through the maximum explosion overpressure P_{max} (bar) and the maximum rate of pressure rise $(dP/dt)_{max}$ (bar/s), also expressed as the K_{St} value (bar m/s). Other explosion-related properties of silicon dust, such as minimum ignition energy (MIE) and limiting oxygen concentration (LOC), are outside the scope of the present work. The main objective is to illustrate the effects of particle size distribution on the explosive properties of silicon dust.

Silicon is widely used as an energetic material. This includes applications such as igniters and delay charges, pyro mixtures, and general explosives (Koch & Clément, 2007). Silicon and other metals (e.g. iron) are also considered as potential green and recyclable energy carriers in controlled combustion processes (Bergthorson, 2015; Weiser et al., 2023; Heng, 2025; Baum et al., 2026). However, the same energetic properties that enable these applications can, under unfavourable conditions, create hazardous situations and trigger accidents with disastrous consequences. Dust explosions are recognized as a serious hazard in the industry and have been a recurring topic in this conference series (e.g. Tveit & Breidenthal, 2018).

A silicon dust explosion occurred at Elkem Bremanger in October 1972 (Eckhoff, 1994, 2003). This disastrous accident resulted in five casualties and four life-altering injuries. The plant area involved was destroyed and later redesigned as a wet process. The likely ignition source was hot work, with (accidental) penetration of a ventilation duct resulting in dispersion and ignition of accumulated dust, and flame propagation inside the ventilation system. The thermal effects of the secondary fireball, with flame temperatures possibly exceeding 2 000 °C, gave permanent burn injuries on unprotected skin over large distances.

This work is licensed under the Creative Commons Attribution 4.0 International License. To view a copy of this license, visit https://creativecommons.org/licenses/by/4.0/

Both General Electric and Dow have shared information about explosions in silicon milling installations. This includes the G.E. Waterford explosions up to 1967, and the Dow Corning mill explosion in December 1987. Back in 1969, Elkem had discussions about silicon milling explosions with Midland Silicones in UK. In August 1995, the Elkem Metals Alloy plant had an explosion in a ball mill, with a secondary filter explosion. Other resources have information about later silicon-related incidents in the industry.

Our current focus is on the coarser dusts that result from handling bulk material, and to a lesser extent the very fine particles intentionally manufactured by milling processes. Elkem also has products in the fine sized material ranges and need to handle safety aspects for these processes. Another approach is to increase the understanding on how coarse the silicon particles must be to become un-ignitable and hence safe to handle (i.e. inherently safer design).

The properties measured in standardised tests of explosion properties provide information on the amount and rate of energy release in the rapid combustion we in ordinary terms call a dust explosion. This information is important for the design of consequence-reducing measures, such as venting devices, suppression systems, and isolation systems (e.g. fast-acting valves). The parameters determined in a constant volume explosion vessel with volume V include the maximum overpressure, P_{max}, the maximum pressure rise rate, $(dP/dt)_{max}$, and the size-corrected maximum pressure rise rate, $K_{St} = V^{1/3} (dP/dt)_{max}$ (St = 'Staub', German). The testing is covered through ISO/IEC, ASTM and EN standards, some detail will be discussed later.

Other explosion related properties include the minimum ignition energy (MIE), the lower explosion/flammability limit (LEL/LFL) or minimum explosive concentration (MEC), and the limiting oxygen content (LOC). MIE and LEL/LFL/MEC or LOC are necessary data for understanding ignition properties and implementing ignition controls.

Particle size is acknowledged as the major parameter influencing ignitability and explosivity in different samples of the same material. Moisture is an important parameter with organic materials, but less important for metal dusts. Various researchers have addressed the influence of the particle size distribution (PSD) on the explosion properties of metal dust (e.g. Castellanos et al., 2014). The properties of the PSD of a given material are typically expressed by percentile diameters such as D_{10}, D_{50} (median), and D_{90}, the surface mean diameter $D_{3,2}$ (Sauter mean), the volume mean diameter $D_{4,3}$, the specific surface area (SSA), and various measures that reflect the width and degree of symmetry of the distribution (e.g. span, polydispersity, skewness, kurtosis, rank, etc.).

2. A COLLECTION OF HISTORIC SILICON DUST TESTING DATA

Over half a century, Elkem has accumulated more than 100 reports from dust explosion testing of silicon, ferro-silicon, and magnesium-ferro-silicon (FSM) samples. Most of the testing was conducted by the dust explosion laboratory at Chr. Michelsen Institute (CMI), which later became part of Gexcon AS. In addition, some 40 reports from different risk assessments or hazardous area classifications conducted on behalf of Elkem, and various literature sources, also contain relevant data on ignition and explosion properties for silicon. Overall, the reports illustrate a development in dust testing over time.

We assume there is a large volume of similarly unpublished or internal test reports within the individual companies in the silicon industry, and we welcome any additional reports for inclusion into our compilation!

From the literature: The US Bureau of Mines report from 1964 on ignitability of metal dusts, includes 11 different silicon samples (Jacobson et al., 1964): It is the oldest silicon and dust explosion related publication we have currently found. Noteworthy is also the Dow Corning

letter in a local Carrollton paper (C+E News) on observed low ignition energies for milled silicon (Halm, 1979), and Elkem Metals' (Allenbach, 1984) warning on materials finer than 44 µm (325 US Mesh). Later came a report on silicon testing from Japan National Institute of Occupational Safety & Health, NIOSH (Matsuda, 1984), and an article on fine sized silicon properties from Eckhoff, 1986. Some additional published data from this silicon conference series are Crawford, 2000; Wineland, 2002 and van Noort, 2002. Other important data sets are from research by Skjold, 2003, 2013 and 2026, and recent Master projects by students at the University of Bergen (Østgård, 2021; Faye & Bjørnsen, 2023; Mork, 2026). Our latest external testing data addition is on explosion testing of silicon made for Li-ion batteries (Lee, 2025).

Data from the online Gestis Dust-Ex database of combustion and explosion characteristics of dusts (Dustex, 2026) has also been included into our data collection with 22 different samples. This appears to be all the current entries identified as silicon. These will be discussed later.

The Elkem data collection today comprises silicon, ferro-silicon and magnesium-ferro-silicon data, with some additional silicon-related alloys and materials. One or several different properties have been tested and reported for each sample. The reported properties for one sample may be the result of an underlying larger test series, i.e., at different dust concentrations. An important addition is that reports of zero (i.e., not ignitable samples) are included as necessary data points.

Table I: Count of different silicon only data collected from existing test reports or from literature.

	Explosibility			Ignitability			Particle size data (µm)		
Property	K_{St}	P_{max}	$(dP/dt)_{max}$	MIE	LEL	LOC	D_{50}	D_{10} and D_{90}	$D_{3,2}$ and $D_{4,3}$
Silicon count	132	151	97	82	40	28	137	70	50
Elkem reports	78	79	44	58	19	19	65	36	18
Literature	54	72	53	24	21	9	72	34	32

For silicon we cover a total of 530 data points on explosibility and ignitability combined. It is obvious that the explosive properties have been tested the most (380 data), and that the ignition properties are probably not sufficiently investigated with 150 data points.

3. SUMMARIZING EXPLOSIVE EFFECT AGAINST PARTICLE DIMENSIONS

3.1 Samples particle size information

Information about particle sizes is rudimentary or missing for a lot of both internal and public samples. Size information from the Gestis Dust-Ex database is also limited. We were able to identify mean diameter, or D_{50}, for several samples, as indicated in Table 1. These values may be from sieving (mass), optical methods (typically volume) and other methods.

Van Wingerden, 2019 discussed the use of public test data information for a general understanding of explosive effects from different dusts, including silicon. This was based on the publicly available Gestis Dust-Ex data with D_{50} information. Those data were only 11 values for P_{max} and K_{St}, from six ignitable and five not ignitable samples. All of these were already included in the 1997 printed edition of the database. We have reproduced this in Figure 1:

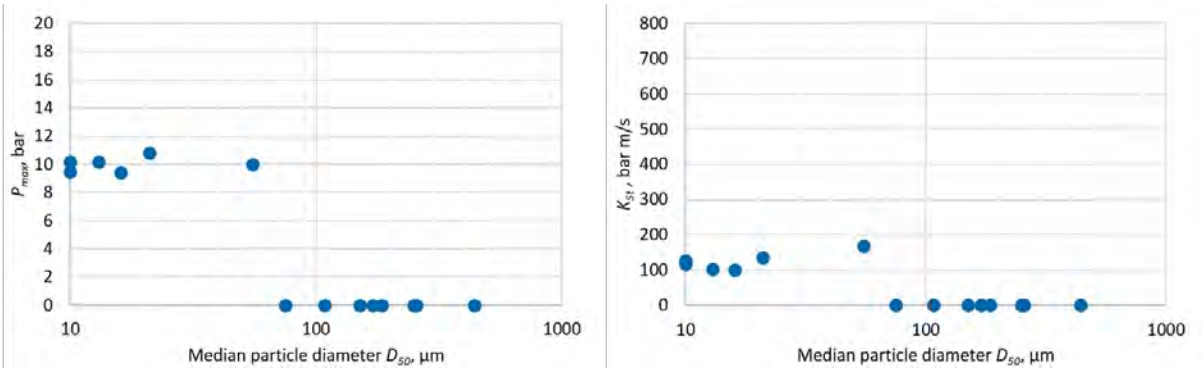

Figure 1: Maximum explosion pressure (left) and K_{St}-value (right) as function of median particle diameter D_{50}. Silicon data from the Gestis Dust-Ex database only, reproducing van Wingerden, 2019.

In the graphs there are now 6 samples with ignition, 7 with no ignition. Two newer samples have been added in the Gestis Dust-Ex data base since the original publication, both not ignitable. Max ignited D_{50} is 55 µm, lowest no ignition D_{50} is at 75 µm. These charts could possibly open for a misunderstanding that silicon samples with D_{50} higher than 55 µm would not be ignitable. This can also demonstrate a clear warning on estimating properties from literature data only, without testing of a sample from the actual process in question.

Updates to the testing standard (like ISO/IEC 80079-20-2:2016) have also introduced an additional 'hard to ignite' test requirement with significantly increased ignition energy (2 x 1 kJ), after earlier dust testing reported samples as not ignitable at 1-10 Joule and industrial incidents demonstrated otherwise. Older test reports may have stated such samples as not ignitable. Coarser metal dusts can come into this category. For 'high density material such as metals' it is in addition permitted in the standards also to test at higher dust concentrations (up to 2 500 g/m^3, versus normally up to 1 500 g/m^3).

The following two graphs from our historic data was used to build an internal general engineering guideline for materials with a D_{50} coarser than 10 µm. The data points earlier shown in reproducing the van Wingerden paper are also included here. For P_{max} we have 83 data points and 20 values of no ignition (zero). For K_{St} we have 72 data point and 20 no ignition values. The uncertainties around the use of D_{50} as parameter will be discussed further.

For P_{max} at D_{50} larger than 20 µm there are a four individual points with pressures above 9.0 bar out of 32. For K_{St} there are no data above 190 bar m/s until D_{50} is finer than 10 µm. Our interpretation was that a K_{St} should not be expected to exceed 190 bar m/s for D_{50} higher than 10 µm, but there is some residual risk that pressures may exceed 9.0 bar for materials with D_{50} above 20 µm.

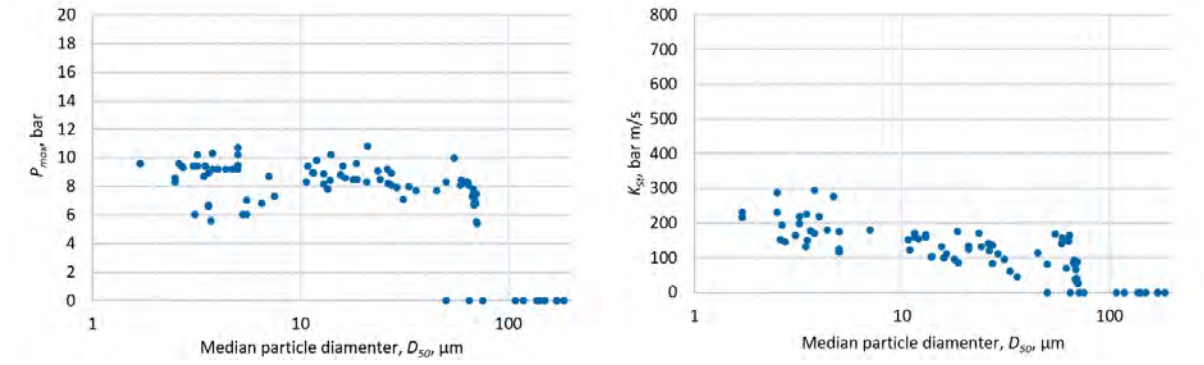

Figure 2: Currently collected silicon explosivity data with D_{50} information.

The highest D_{50} with reported P_{max} and K_{St} in the data set is 70,5 µm. We have however registered ignition for a sample with a D_{50} at 113 µm, so *the information here is also insufficient to establish a D_{50} limit for explosibility*. Literature cites avoiding particles finer than 70 to 80 µm to safeguard that no ignition may occur. In the fine end of the particle size range, data for silicon particle distributions with D_{50} finer than 10 to 20 µm must be assessed on a case-by-case basis. Here the explosive properties rapidly escalate, as can be seen by some very high K_{St} values.

For completeness, the following graphs show all the registered K_{St} and P_{max} collected, in a sequence from increasing D_{50}, and then from decreasing K_{St} without D_{50} information. A total of 152 P_{max} (119 ignition, 33 no ign.) and 132 K_{St} points (102 ignition, 30 no ign.) are included.

Overall, there are 39 out of 152 P_{max} values at > 9.0 bar. There are 13 K_{St} values > 190 bar m/s for D_{50} finer than 10 µm, and 5 high K_{St} values with no D_{50} information attached.

Table II: K_{St} and P_{max} data, with and without D_{50} information

Count of:	P_{max} data	K_{St} data
Ignition data, with D_{50}	83	72
No ignition data, with D_{50}	20	20
Ignition data, no D_{50}	36	30
No ignition data, no D_{50}	13	10

This information can now be used for preliminary discussions and to add content for analysis of new test results. The conservative approach is to set a baseline along the upper values, i.e., a K_{St} of 190 bar m/s for material coarser than a 10 µm D_{50}. But there is also possibility for a risk-based approach through a better understanding of test results that report lower values.

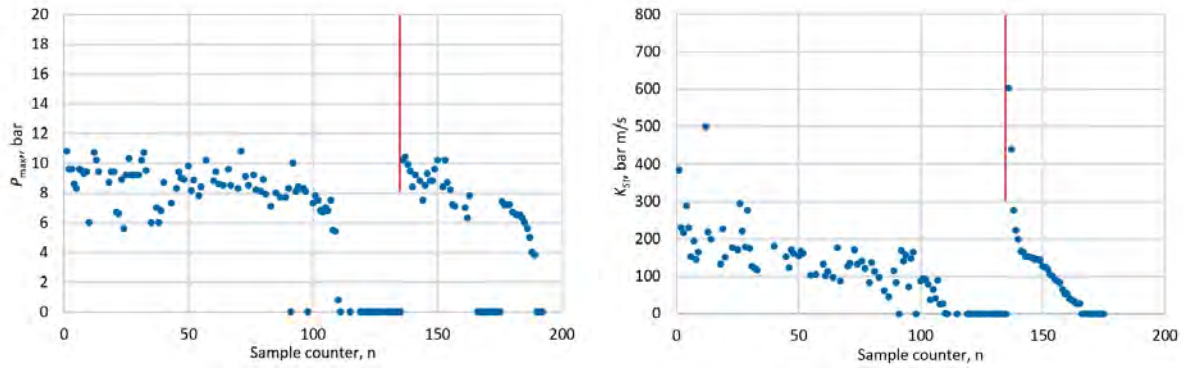

Figure 3: All our collected P_{max} and K_{St} values, the red lines separating data with and w/o D_{50} information.

At the same time, the bandwidth spread in data illustrates the risks and uncertainties in sampling, testing and then estimating ignition and explosion properties from any dust sample.

3.2 Median particle size as an indicator of explosion hazard

A major limitation of using a single D_{50} value is that different samples with similar D_{50} values may represent widely different size distributions, as the D_{50} does not reflect the distribution in the fine or coarse particles content. In the current understanding of metal dust ignition and explosions, it is the finer sized particles that carry the hazards of ignition and combustion.

Polydispersity or span, kurtosis and other values can be used as indicators of such variations. Castellanos et al., 2014 tested different distributions in aluminium dusts, including constructed

distributions with approximately the same median particle diameter. The size distributions tested are shown in figure 5. Test results ranged from P_{max} 9.0 to 10.0 bar and K_{St} from 231 to 403 bar m/s for aluminium with increasing content of fine particles in the wider distributions.

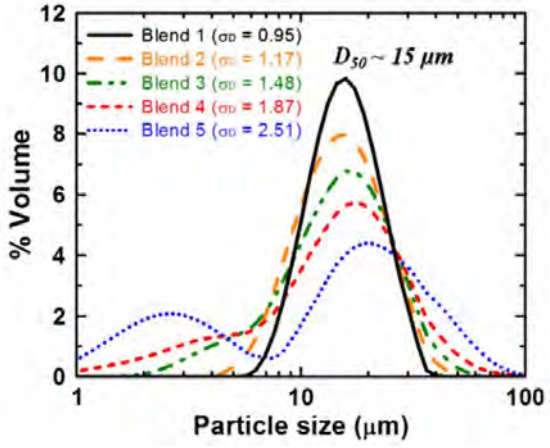

Figure 5: Different particle distributions with the same median particle size (Copy from Castellanos et al., 2014)

4. NEWER TEST DATA WITH CONTINUOUS PARTICLE SIZE DISTRIBUTIONS

Elkem has started using a Malvern Mastersizer to obtain continuous size distribution data on the dust testing samples. The laser diffraction method is not expected to report a totally 'true' distribution but is seen as a consistent indicator of the particle sizes. Additional parameters can be derived, like D_{10}, D_{90}, $D_{3,2}$ and $D_{4,3}$. We can also report a calculated specific surface area, but from the same underlying measurement data.

In combustion analysis, ignition and combustion are seen as surface-oriented processes, but the ending total combustion (burnout) is more related to the volume of droplets or particles. In dust combustion (flash fires or dust explosions) normally only a fraction of the total available dust is consumed, i.e. 25 %. A surface area-weighted or Sauter mean diameter $D_{3,2}$ and a De Brouckere or volume-weighted mean diameter $D_{4,3}$ should provide information relevant to these situations.

Master students from University of Bergen have performed dust testing for a more detailed understanding of particle distribution effects in cooperation with Elkem. Their testing is reduced from a standard program, as we try to work within a limited field of parameters. Specific reductions are restricting max dust loads to avoid operational problems, and not running complete series and repetitions with the different dust loads as required in standards.

Our focus has been to identify particle size limits for explosive behaviour – what are the hazardous size ranges that must be removed for a safe product and a safe process, and how much coarse or fine particles involved will influence the explosive properties.

Larger particles included in a dust sample may act as heat sinks in the system. This is especially valid for metal dusts with high melting points, where there are no sensible vapour pressures for a gas-phase combustion onset at lower temperatures. High dust concentrations may counter these effects, with the presence of a very large number of small particles that are easily heated to ignition by a (sufficiently strong) flame front.

Especially Mork, 2026 have compiled series of material mixes going from a coarse silicon with an increasing addition of fine sized particles, and also from fine sized silicon with a gradual addition of coarser particles. This was all based on jet milled pure silicon materials from the Elkem Silgrain® production line at Elkem Bremanger. Variability reduction was addressed

through Theory of Sampling -aligned use of a rotary divider and manual bed blending methods (more about this later).

The coarse starting material is close to non-ignitable and only yields a very limited effect at a very high dust concentration, 3 000 g/m³. Explosivity and particle size information is given in Table III. Two very fine materials were used to control the content of fine particles.

Table III: Materials used for testing changes in particle size distribution.

	Explosive data		Size range	Particle size data (µm)				
Material	P_{max}	K_{St}	(µm)	D_{10}	D_{50}	D_{90}	$D_{3,2}$	$D_{4,3}$
Fine 'A'	9.5	152	< 8	0.6	2.6	5.0	1.3	2.8
Fine 'B'	9.4	226	2-7	1.9	3.5	6.0	3.1	3.8
Coarse 'E'	0.8	1	> 40	43.2	71.4	117	66.4	76.4

It is assumed that the higher K_{St} value for the slightly coarser material B is linked to agglomeration effects in material A.

Adding a very fine material, starting at 2 wt%, immediately gives a clear explosive effect with the coarse material. The effect is increasing with higher fines content. Adding 2 % of A or B changes the surface mean diameter $D_{3,2}$ from 66.4 to 53.8 (A) or 51.6 µm (B), whereas the average diameter D_{50} changes from 71.4 to 70.5 and 70.1 µm. The explosion pressure increases significantly (Figure 6), whereas pressure rise rate shows a more gradual increase (Figure 7).

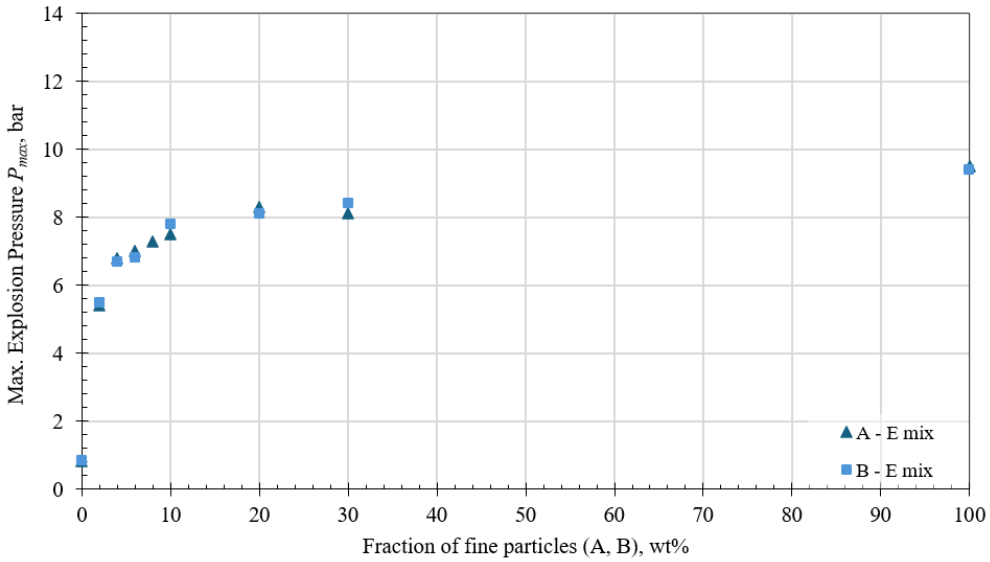

Figure 6: Changes in P_{max} from increasing fine particles content in coarse material (based on Mork, 2026)

The other observation is from the very fine end; adding increasing amounts of coarse particles up to 80 wt% do not shift P_{max} or K_{St} values of the fine materials significantly.

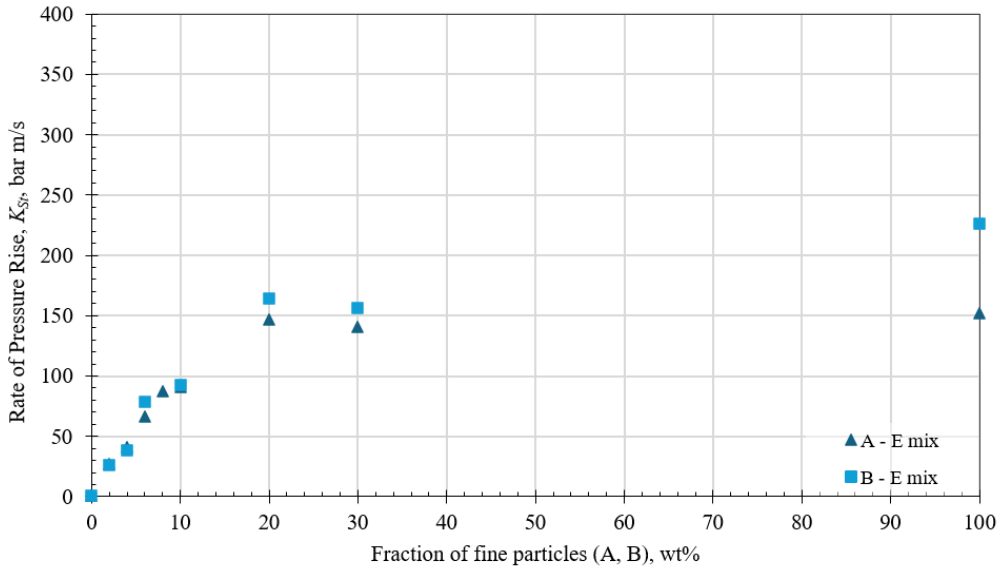

Figure 7: Changes in pressure rise rate K_{St} from increasing fine particles (based on Mork, 2026)

The change in explosive effect by particle size can be further illustrated by looking at individual results from the varying dust loads. In figures 8 and 9 the detailed results from one of the test series are shown. From the equipment limitations we chose not to test at the initially very high ignitable concentration, but the graphs indicate that maximum effect is not determined at lower concentrations until a 30 – 70 % mix ratio of fine to coarse material.

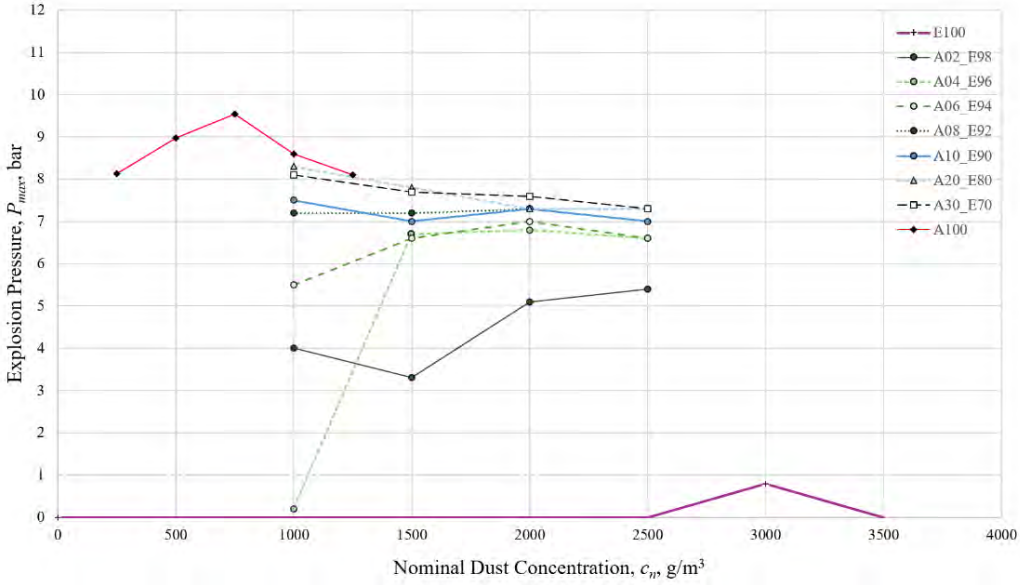

Figure 8: Changes in pressure P_{max} at different dust loads (from Mork, 2026)

The pressure measurements are a clear indication on how little fine particles are needed to render a coarser distribution highly ignitable, across a wide range of dust concentrations. The pressure rise rate demonstrates a more gradual effect.

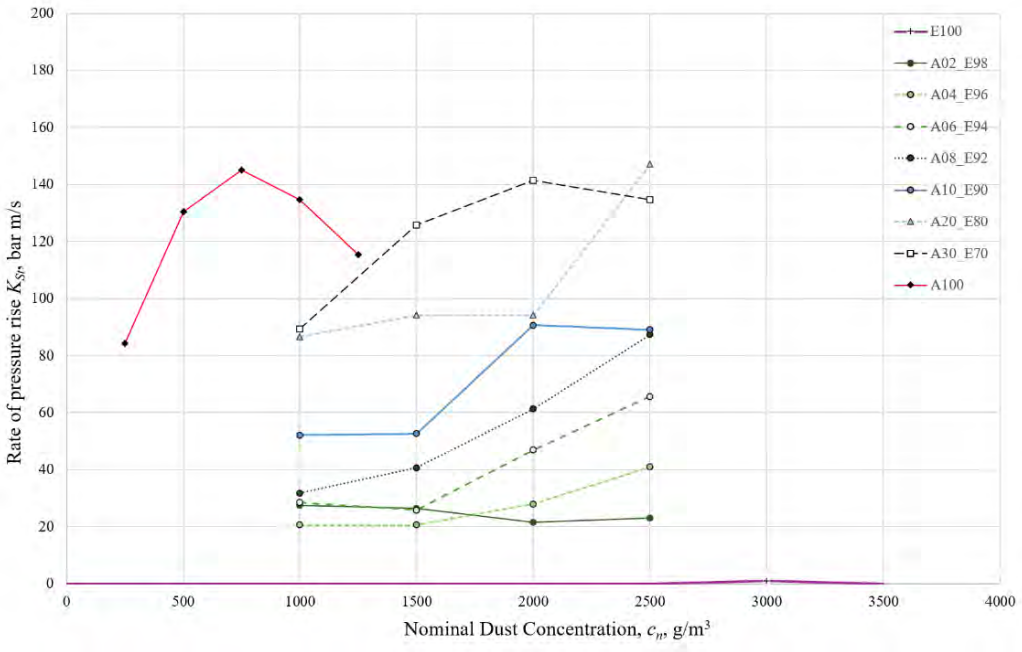

Figure 9: Changes in pressure rise rate K_{St} from increasing content of fine particles at various dust loads.

Adding an increasing mass of coarse particles to fine sized shifts the maximum points to higher dust concentrations, from 500 g/m³ for the finest material and into the only 3 000 g/m³ concentration for the coarse material without any fines addition.

In figures 10 and 11 below, P_{max} and K_{St} values are summarized as a function of the measured surface mean diameter $D_{3,2}$, from Mork, 2026. The surface mean diameter offers a better correlation than any of the other tested size variables like D_{10} or $D_{4,3}$.

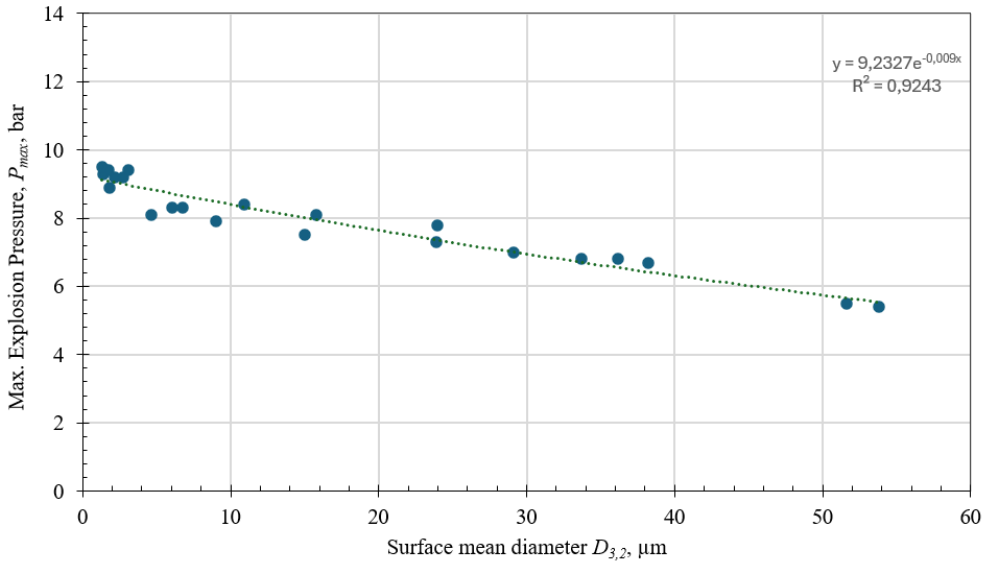

Figure 10: Overall P_{max} versus surface mean diameter $D_{3,2}$ from current testing.

The trendlines are indicative, but please observe that any safety or engineering related information must be based on the max values. This is indicated in the following graph for K_{St} values.

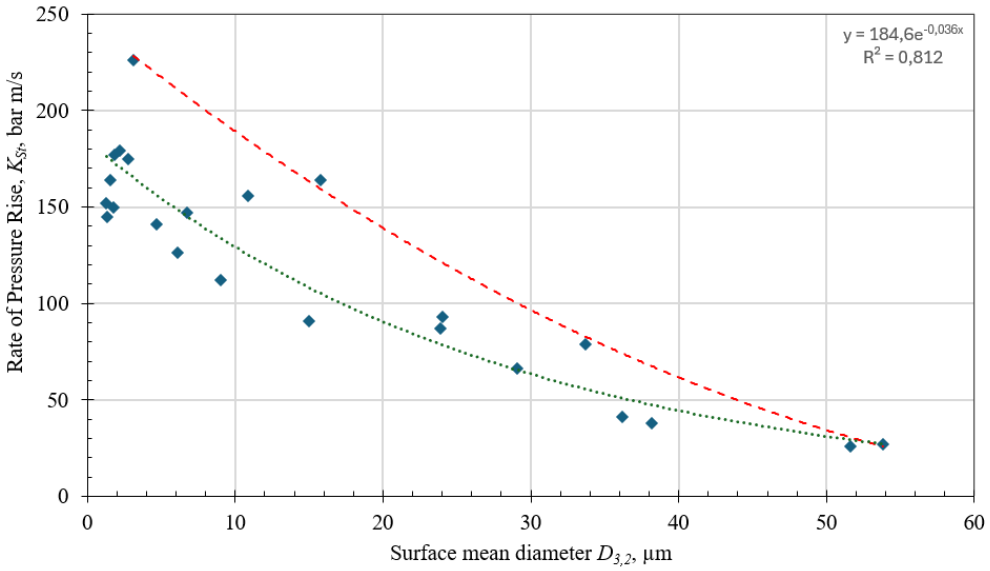

Figure 11: Max pressure rise rate K_{St} versus surface mean diameter. Added red indicator for a safety-related line.

Remark the spread with a few high data points. These might be discussed as possible outliers, but they also indicate that the correlation is still not strong enough to be used as a predictive indicator of explosivity. More work is needed to increase the fundamental consistency in dust testing.

5. OTHER INFLUENCING FACTORS IN SILICON DUST TESTING

5.1 The combustion mechanism of silicon

The silicon combustion mechanism has been discussed as a homogenous (gas phase) versus a heterogeneous (gas-solid or gas-liquid) combustion. Light elements like Al and Mg combust in the gas phase (homogenous reaction) and Fe combust from the solid/liquid state in a heterogenous reaction. Gas phase reactions can see free mixing, whereas phase interface reactions can be controlled by diffusion phenomena. For some metals, a start from heterogenous combustion with an outside (solid or liquid) oxide layer can then transfer into an exploded particle and a homogenous combustion (Lu et al, 2026). Melting and boiling temperatures of the elements and their oxides can indicate this.

Van der Wel, 1993 discussed that hybrid and heterogenous combustion mechanisms would lead to max explosive effects at dust loads high above stochiometric composition, which is typically seen for most metal dusts. The melting and boiling temperatures of silicon and the silicon oxides indicate the potential for a hybrid combustion mechanism for silicon. The silicon and the oxide SiO_2 are in a liquid state at observed and adiabatic flame temperatures, and there should be a limited vapour pressure of silicon. The additional complicating element is the monoxide SiO in a gaseous state at these temperatures, and the SiO then has a condensation reaction balance forming Si + SiO_2 at lower temperatures. The complete silicon combustion mechanism is complex, both chemically andthermodynamically. Several earlier authors model or discuss silicon combustion only from the overall reaction and omit or do not realise the importance of the suboxide $SiO_{(g)}$.

Arntzen, 2025 and MSc students at University of Bergen are developing the thermodynamic modelling of the metal dust combustion processes for implementation in the Gexcon FLACS code. Østgård 2022, Liland 2025, and now Andersen 2026 have been working in this direction. Heng et al, 2025 and 2026 documents the silicon combustion process, especially from observations of combustion of single silicon particles in their 2026 paper. Here they confirm a

shrinking core model with a d^2 rate of reaction with a SiO gaseous layer outside of the combustion liquid silicon droplet.

5.2 Elements in dust testing equipment and methods

The dust testing situation and equipment is by itself a highly variable process, mostly governed by controlling a range of variables though the relevant standards. These variations may also be seen as consequences of the dust testing situation being a combination of physical and dynamic properties: Material properties versus time dependent variables like dust concentration, particle size distribution and dispersion turbulence level. A dispersed dust cloud is a short-lived phenomenon. The settling process may also create pockets within a dust cloud with narrow fine sized domains, with high sensitivity for ignition (a low MIE situation). The standards allow for a deviation in results at up to 10 % (EN 14034-1).

A general factor in the setup and testing of borderline explosion limits is the use of pyrotechnic igniters. The pyro igniters yield an inherent pressure effect in the test equipment, and any direct measurements must be corrected for those effects. This complicates the interpretation between an ignitable and a non-ignitable material.

Turbulence and wall effects in the 20 litre sphere are controlled through timing of the ignition from initial start of dispersion. A study on modified ignition timing highlighted the effects of turbulence; igniting a fine sized silicon sample at 30 ms versus the standardised 60 ms after dust dispersion increased the pressure rise rate from 219 to 500 bar m/s (Cruz, 2019). This indicates that a real life event under circumstances that deviate insignificantly from the standardised testing situation may yield very different effects. There can be a (theoretical) possibility of releasing energies in excess from what testing results indicate.

For the 20 litre spheres, the testing standards also require additional recalculation of values to align data with the 1 m^3 test data. The reported P_{ex} is not identical to the measured P_{meas}.

There is also a discussion for reactive metals that the smaller 20 l sphere may underreport explosive effects. Tests by Elkem together with Fike indicate that silicon is not in the highest reactivity class.

5.3 Particle samples and representativity

Sampling and splitting approaches and particle representativity considerations is an element to introduce here. Grab samples seem to have been the routine within dust testing, and this is far from modern understanding, as established through Theory of sampling (TOS) like from Esbensen, 2017 and the horizontal sampling standard DS 3077, 2024. Particle representativity is a necessity for testing of fine sized materials properties, as would be well known to operators of the Rochow-Müller synthesis.

To continue working with the detailed results at different dust concentrations we will need a more stable test and measurement system. We have so far not seen any publication of data on repeatability and reproducibility (i.e., Gauge R&R or MSA) in dust testing with metal dusts. Semenova et al., 2026 reports on a round robin of four hard to ignite iron powders. Dust lab round robin tests (Cesana AG) show 10 % variation in results on an organic dust (niacin), and do not use metal dust.

6. CONCLUSIONS AND FUTURE WORK

This work offers an update in the understanding of the ignition and explosion properties of silicon, with some additional special cases. For an installation in operation the data gives an indication about what particles must be securely removed to avoid explosion hazards in fine sized products. The results also demonstrate the influence of varying fine particle content and

highlight how even a small fraction of fines can significantly increase the potential for dust explosion under favourable conditions.

A D_{50} value as a particle size indicator is poorly connected to K_{St}, or $(dP/dt)_{max}$ and P_{max} values, as seen in the first part of our data. Instead of using a D_{50} for particle size information we indicate that surface mean diameter, $D_{3,2}$ is a better indicator of explosive effects (Østgård, 2022; Mork, 2026).

Coarser materials with low fines content can be ignitable at higher dust concentrations. High dust loads are for example found in fugitive dust situations and inside dust-gas separators (filter housing, etc.), and normally not present inside well-ventilated processing equipment.

Assuming a P_{max} of 9 bar may be acceptable for pressure tolerance in an inerted installation, but oxygen concentrations above LOC may increase pressure effects up to or possibly beyond this value. A K_{St} of 190 bar m/s may appear safe as an engineering value for size ranges over 10 µm from the presently available data. However, reassessment of new data based on alternative values such as $D_{3,2}$ may be a better option and should provide better values. And – any engineering assessment must be validated by appropriate verification activities in as-built and operative situations.

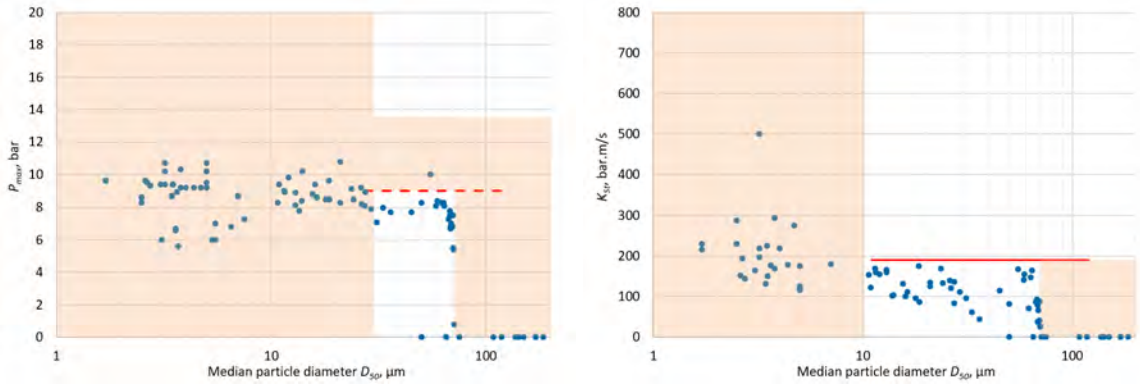

Figure 12: Indication of regimes of high uncertainty in explosive effects from median particle diameter D_{50}.

6.1 Possible future work

Currently, there is not sufficient information on ignitability properties like minimum explosive concentration MEC / lower explosive limit LEL, or the minimum ignition energy MIE. The available data are limited, and further work is required. We have reviewed the available LOC data, but do not yet have a full review with particle size effects included. Liquid silicon is a valid dust ignition source, and any ignited metal / silicon dust will represent a very strong ignition source due to the very high flame temperature.

There are indications in literature that a thermodynamic modelling related back to particle size distribution may be possible. We have so far not seen this established and validated for any materials.

The recent tests have used pure Silgrain®, avoiding any effects of impurity elements and intermetallic phases. There is a threshold where silicon composition effects influence the ignitability and explosivity through effects of intermetallic phase compositions. Silicides formation will affect the composition of individual dust particles. Some intermetallic phases are more brittle and naturally enrich into fines. Crawford, 2000 reported some data on minimum ignition energies for specific intermetallic phases.

A final general remark: Any additional historical or new test data to expand the current compilation are welcome!

8. ACKNOWLEDGEMENTS

This paper is published by permission of Elkem ASA. The contributions of our colleagues are gratefully acknowledged; Especially Christa Nimbona and Pål Baggethun at Elkem, several earlier MSc students at University of Bergen, and several resources at Gexcon.

9. REFERENCES

Allenbach C.R. 1984, Combustibility Characteristics of fine sized ferroalloys and metals, *42nd Electric Furnace Conference*, Toronto, 1984.

Andersen E. 2026, *Development of Combustion Model for Silicon Dust Explosions in FLACS-DustEx*, MSc Thesis, University of Bergen, June 2026.

Arntzen B.J., Lucas M. & Ghaffari M, 2025, An Arrhenius reaction rate based burning model for simulation of dust explosions, *J Loss Prev in the Proc Ind*, 97 (2025), 105638

Bjørnsen A. 2023, *Experimental Investigation of Silicon Dust Explosions in Pipes*, MSc thesis, University of Bergen, 2023.

Bergthorson J.M., Goroshin S., Soo M.J., Julien P., Palecka J., Frost D.L. & Jarvis D.J. 2015, Direct combustion of recyclable metal fuels for zero-carbon heat and power, *Applied Energy* 160 (2015) 368-382

Castellanos D., et al. 2014, *The effect of particle size polydispersity on the explosibility characteristics of aluminium dust,* Powder Technology 254, 2014, 331-337

Cesana AG, CH – Internet page with annual round robin results https://www.cesana-ag.ch/Calibration.shtml

Crawford A.C. 2000, Silicon grinding safety: The effect of calcium disilicide on the explosion potential of silicon powder, in *Silicon for the Chemical Industry V*, Tromsø, Norway, May 29 – June 2, 2000

Cruz O.C.C. 2019, *Study of the effect of dust dispersion and turbulence on explosion properties of atmospheres of fine ferro-silicon powders*, BSc thesis, Instituto Tecnológico De Altamira (Mexico) (With Gexcon, Norway)

Esbensen K. & Wagner C. 2017 *Get your sampling right*, Spectroscopy Europe, (eBook from the Sampling Column) Sampling Columns | Spectroscopy Europe/World, alternatively through (Introduction to Theory and Practice of Sampling available as eBook | Spectroscopy Europe/World)

Eckhoff R.K., Parker S.J., Gruvin B., Hatcher M. and Johansson T. 1986, *Ignitability and Explosibility of Silicon Dust Clouds. Influence of Dust Fineness*. Journal of the Electrochemical Society, 133, 12, 1986

Eckhoff R.K. 1991, *Dust Explosions in the Process Industries*, Butterworth Heinemann, Oxford, 1st ed. 1991 (later editions available). ISBN 0 7506 1109 X

Eckhoff R.K. 1994, Dust explosion hazards in the ferro-alloys industry, *Proceedings 52nd Electric Furnace Conference,* Nov 13-16, 1994, Nashville, TN, USA, pp 283-302

Gestis Dust-Ex online data base IFA - Databases on hazardous substances: GESTIS-DUST-EX, accessed June 2026.

Halm R, 1979, Letter to the local newspaper *C+E News*, 13.8.1979 (personal copy)

Heng H., Mani C., Chepel N., Mangalvedhe K., Antar E., Goroshin S. & Bergthorson J. 2025, Silicon dust flames: A pathway to using silicon as a carbon-free energy carrier, *Proceedings of the Combustion Institute*, 412 (2025) 105940

Heng H., Keck H., Chauveau C., Goroshin S., Bergthorson J. & Halter F. 2026, Combustion behaviour of single silicon particles in different oxidizing environments, *Combustion and Flame* 283 (2026) 11 4625

Jacobson M., Cooper A.R. & Nagy J. 1964. *Explosibility of metal powders*, Report of investigations 6516, US Dept of Interior; Bureau of mines (The USBM reports on explosibility of metal powders date back at least to 1943).

Koch E.-C. & Clément D. 2007. Special Materials in Pyrotechnics: VI. Silicon – An Old Fuel with New Perspectives. *Propellants, Explosives, Pyrotechnics* **32**, No.3 (2007)

Lee H.H. 2025, *A Study on the Ignition Energy and Explosion Limits of Sust Generate in the Anode Material Manufacturing Process for Lithium-ion Batteries*, PhD Dissertation, Chungbuk National University, Cheongju, Korea, August 2025

Lu Y., Xingyan C., Wang Z., Xu S. & Sun S 2026, A review of metal dust explosion characteristics and protection technologies, *Journal of Safety and Sustainability*, (in press) doi: 10.1016/j.jsaus.2026.01.001

Liland E.B. 2025, *Developing Aluminium Dust Explosion Modelling Capabilities for FLACS-Dust-Ex*, MSc thesis., University of Bergen, 2025.

Matsuda T. 1993, *8. Dust Explosion Hazards of Metallic Silicon*, in Specific Research Report of the Research Institute of Industrial Safety, RIIS-SRR-No.12 (1993) (Chapter 8)

Mork A.M. 2026, *The Effect of Particle Size Distribution on Explosion Indices for Silicon dust*, MSc thesis, University of Bergen, 2026

Semenova A *et al*. 2026, Towards standardized safety protocols for iron-based energy carriers: International alignment through round robin testing on safety characteristics, *Open Research Europe* (in peer review), Towards standardized safety protocols for ... | Open Research Europe

Skjold, T. 2003, *Selected aspects of turbulence and combustion in 20-litre explosion vessels,* Cand. Scient thesis, University of Bergen 2003.

Skjold T. 2013, An experimental investigation of flame propagation in clouds of silicon dust dispersed in air, hydrogen-air mixtures, and hybrid Si-H2-air mixtures, *24th ICDERS*, Taipei, July 28 – Aug 2, 2013. (Including references to earlier MSc and PhD publications with results on Silicon)

Skjold T., Faye A., Bjørnsen A., van Wingerden M., Buseth T. 2026, Silicon dust explosion in ducts and pipes, *Journal of Loss Prevention in the Process Industries* **103**, Doi: 10.1016/j.jlp.2026.106111

Tveit H. & Breidenthal M. 2018, The EHS Achilles Heel of the Silicon Furnace – the Potential for Energy out of Control, *Silicon for the Chemical and Solar Industry XIV*, Svolvær, Norway June 11-14, 2018

van der Wel P.G.J. 1993 *Ignition and propagation of dust explosions*, PhD dissertation, Delft University Press, 1993 (Including articles 1991, 1992)

van Noort W.C.J., van der Stap P. & van der Waal J. 2014, Silicon milling & Explosion Prevention, in *Silicon for the Chemical and Solar Industry XII*, Trondheim, Norway, June 24-27, 2014

van Wingerden K. 2019, Application of Laboratory-scale Determined K_{St}-values of Metal Dust to Industrial Scale Processes, *Chemical Engineering Transactions*, 77, 2019, pp 679-684. Doi: 10.3303/CET1977114

Wineland J. 2002, Silicon crusher explosion hazards, in *Silicon for the Chemical Industry VI*, Loen, Norway, June 17-21, 2002

Weber V., Kelzenberg S., Koleczko A., Knapp S., Raap A., Roth E. Schäfer T. 2023, *Silicon – an established pyrotechnic fuel as zero-carbon, high-density energy carrier*, 46th International Pyrotechnics Seminar 2023, Sept 11-14, San Malo

Østgård T. 2022, *En eksperimentell studie av partikkelstørrelsesfordelingens innvirkning på utvalgte eksplosjonsparametre for silisiumstøv*, MSc thesis, University of Bergen, 2022.

Relevant standards:

DS 3077:2024 *Representative Sampling – Horizontal Standard* (Danish Standard).

ISO/IEC 80079-20-2:2016 Explosive atmospheres Part 20-2: *Material characteristics Combustible dusts test methods.*

EN 14034-1:2024+A1:2011 *Determination of explosion characteristics of dust clouds Part 1: Determination of the maximum explosion pressure P_{max} of dust clouds.*

EN 14034-2:2006+A1:2011 *Determination of explosion characteristics of dust clouds Part 2: Determination of the maximum rate of explosion pressure rise $(dp/dt)_{max}$ of dust clouds.*

ASTM E1226-19(2025) *Standard Test Method for Explosibility of Dust Clouds.*